

Interaction Between Forming and the Crash Response of Aluminium Alloy S-Rails

by

Dino Alberto Oliveira

A thesis
presented to the University of Waterloo
in fulfillment of the
thesis requirement for the degree of
Doctor of Philosophy
in
Mechanical Engineering

Waterloo, Ontario, Canada, 2007

© Dino Alberto Oliveira 2007

Author's Declaration

I hereby declare that I am the sole author of this thesis. This is a true copy of the thesis, including any required final revisions, as accepted by examiners.

I understand that my thesis may be made electronically available to the public.

Abstract

One of the principal energy absorbing structural components that influences the crashworthiness of a vehicle is the side-rail, which is also commonly referred to as an s-rail due to its shape that is reminiscent of an “s”. To improve the crashworthiness of a vehicle, in the wake of significant environmental pressures requiring vehicle light-weighting, the parameters that govern the crash response of the s-rail and the implications of light-weight material substitution need to be better understood.

In this work, the main parameters that govern the crash response of an s-rail and the variables that influence them were identified and assessed through a combined experimental and numerical modelling programme. In particular, the as-formed properties of aluminium alloy s-rails, due to the tube bending and hydroforming fabrication route were examined.

Tube bending, hydroforming and crash experiments were conducted to examine and assess the effects of initial tube thickness, strength, geometry, bend severity, work hardening, thickness changes and residual stresses on the crash response of the s-rail. The forming process variables, springback, thickness, strains, and force and energy response measured in the experiments were used to validate the finite element models developed herein. The validated numerical models of tube bending, hydroforming and crash provided additional insight and also allowed further investigation of the parameters governing the crash response of s-rails.

The relevant parameters governing the crash response of s-rails were isolated and the basis for a set of design guidelines, in terms of maximizing energy absorption or minimizing mass, was established. The overall size is the most influential design parameter affecting the energy absorption capability of the s-rail, followed by the initial thickness, material strength, cross-sectional geometry, bend severity and hydroforming process employed, and finally

boost in bending. The most significant conclusion made based on this research is that the effects of forming history must be considered to accurately predict the crash response of the s-rail. There are additional conclusions with respect to the tube bending and hydroforming processes, as well as s-rail crash response, that will contribute to improving the design of s-rails for better crashworthiness of vehicles.

Acknowledgements

There have been a number of people that have been instrumental in allowing this research to be conducted and this thesis to be written in fulfillment of the requirement for the degree of Doctor of Philosophy. I am indebted to my supervising Professor, research partners, colleagues, friends and family for their continual motivation and support.

I would like to express gratitude towards Professor Michael Worswick for his supervision and guidance. I am grateful for his generosity and the positive impact he has had in the development of my career. This research was made possible through funding from General Motors of Canada, the NRC Aluminum Technology Centre (ATC), and by the Natural Science and Engineering Research Council (NSERC). The collaborations with Robert Mayer, Scott Lawson, Ruth Gusko and Nancy Johnson, from General Motors, as well as Ahmed Rahem, Guillaume D'Amours, Hamid Shakeri and Jean-Pierre Martin, from the ATC, have been important in performing this research. In particular, I would like to thank Robert Mayer for his guidance and supervision of the crash experiments that were conducted at the GM Technical Centre in Warren, Michigan. I would like to acknowledge Bill Barber and his support team at Tycos Tool and Die for manufacturing of the s-rail die.

I am indebted to my colleagues Bruce Williams, Christopher Salisbury, Blake Hodgins, Hari Simha, Rassin Grantab and Javad Gholipour, for their insightful input and discussion. I must also express thanks to the various support staff at the University including Howard Barker, Richard Gordon, Eckhard Budziarek, Jim Baleshta, Tom Gawel, Laurie Young, Marlene Dolson and Jian Zou. Having been surrounded at the University by such good people as Jose Imbert, Rafal Smerd, Zengtao-Chen, Alan Thompson, Alex Bardelcik, Oleg Orlov, Mikhail Sorine, Sooky Winkler and Nader Abedrabbo has made my experience a great one.

During my time at the University, I have formed a number of strong friendships with several people that have made my day-to-day activities very enjoyable. I would particularly like to express my appreciation to Blake Hodgins, Christopher Salisbury, Jose Imbert and Rafal Smerd for their help, support and great friendship throughout all these years.

My sincerest thanks to all those that
have made the experience of
conducting this research
memorable.

*This thesis is dedicated to
all of those who have had faith in me,
my family,
and most of all my wife Tara.*

Table of Contents

<i>Author's Declaration</i>	<i>ii</i>
<i>Abstract</i>	<i>iii</i>
<i>Acknowledgements</i>	<i>v</i>
<i>Dedications</i>	<i>vii</i>
<i>Table of Contents</i>	<i>viii</i>
<i>List of Tables</i>	<i>xiii</i>
<i>List of Figures</i>	<i>xv</i>

CHAPTER 1 INTRODUCTION	1
1.1 Bending	4
1.2 Mandrel-Rotary Draw Tube Bending	5
1.3 Significant Contributions to Rotary Draw Tube Bending.....	7
1.3.1 Tube Characteristics and Limitations.....	7
1.3.2 Effect of a Mandrel on Ovalization, Thinning and Wrinkling.....	8
1.3.3 Strains and Work Hardening due to Bending	9
1.3.4 Springback	10
1.3.5 Lubrication and Friction.....	10
1.3.6 Process Variables in Bending.....	11
1.3.7 Boost	12
1.3.8 Significant Contributions to the Analytical and Numerical Modelling of Tube Bending	13
1.4 Hydroforming.....	14
1.4.1 Significant Contributions to the Hydroforming Process.....	15
1.4.1.1 Tooling and Workpiece Properties.....	15
1.4.1.2 Pressurization and End-Feed	17
1.4.1.3 Lubrication and Friction	18
1.4.2 The Low-Pressure Process.....	19

1.4.3 Interaction Between Tube Bending and Hydroforming	21
1.5 Crash Response	22
1.5.1 Significant Contributions to Understanding the Bending Mode of Collapse in S-Rails	23
1.5.1.1 Bending Collapse in a Section.....	23
1.5.1.2 S-Rail Collapse	25
1.5.1.3 Stiffening of S-Rails	27
1.5.2 Interaction Between Forming History and Crash Response of S-Rails	27
1.6 Summary	28
CHAPTER 2 EXPERIMENTS	31
2.1 S-rail Geometry and Test Matrix	35
2.2 Material Characterization.....	37
2.3 Tube Bending Experiments.....	41
2.3.1 Mandrel-Rotary Draw Tube Bender and Tooling.....	43
2.3.2 Process Parameters, Methods and Measurements	44
2.4 Hydroforming Experiments	47
2.4.1 S-Rail Die and Press.....	48
2.4.2 Process Parameters, Methods and Measurements	51
2.5 Impact Experiments	52
2.5.1 Deceleration Sled.....	53
2.5.2 Impact Parameters and Measurements.....	54
2.6 Annealing of S-Rails	55
CHAPTER 3 NUMERICAL MODELLING.....	59
3.1 Modelling Program and Implementation	59
3.1.1 Strategy	59
3.1.2 Numerical Investigations Based on Experiments.....	62
3.1.3 Numerical Investigations Further Examining and Isolating Physical Variables Governing the Crash Response of S-Rails.....	63
3.1.4 Modelling Approach and Implementation	64
3.2 Tube Bending Simulation	65
3.2.1 Bending with Additional Boost.....	71
3.3 Hydroforming Models.....	71
3.3.1 Low-Pressure Process.....	73

3.3.2 <i>High-Pressure Process</i>	75
3.4 <i>Crash Simulation</i>	78
3.5 <i>Material Models</i>	79
3.5.1 <i>Johnson-Cook Model</i>	81
3.5.2 <i>Zerilli-Armstrong Model</i>	83
CHAPTER 4 EXPERIMENTAL RESULTS	85
4.1 <i>Tube Bending Results</i>	85
4.1.1 <i>Process Variables and Ovality</i>	86
4.1.2 <i>Thickness</i>	88
4.1.3 <i>Strains</i>	90
4.2 <i>Hydroforming Results</i>	93
4.2.1 <i>Thickness</i>	93
4.2.2 <i>Strains</i>	94
4.3 <i>Interaction of the Tube Bending and Hydroforming Processes</i>	96
4.4 <i>Crash Results</i>	98
4.4.1 <i>Examination of Testing Repeatability</i>	100
4.4.2 <i>Effect of Initial Tube Thickness on Crash Response</i>	103
4.4.3 <i>Effect of Bend Severity on Crash Response</i>	104
4.4.3.1 <i>Non-Hydroformed S-Rails</i>	104
4.4.3.2 <i>Hydroformed S-Rails</i>	106
4.4.4 <i>Effect of Hydroforming on Crash Response</i>	107
4.4.5 <i>Effect of Annealing on Crash Response</i>	109
4.5 <i>Summary</i>	112
4.5.1 <i>Tube Bending and Hydroforming of S-Rails</i>	112
4.5.2 <i>Crash Response of S-Rails</i>	115
CHAPTER 5 NUMERICAL RESULTS	117
5.1 <i>Tube Bending Predictions</i>	118
5.1.1 <i>Predictions of Bending Process Variables</i>	120
5.1.2 <i>Predicted Thickness after Bending</i>	124
5.1.3 <i>Strains</i>	132
5.2 <i>Hydroforming Predictions</i>	138
5.2.1 <i>Predicted Thickness after Hydroforming</i>	141

5.2.2 Predicted Strains after Hydroforming	143
5.3 Crash Results.....	146
5.3.1 Geometry Predictions	146
5.3.1.1 Development of Plastic Hinges during Deformation of the S-Rails	148
5.3.2 Understanding the Force-Time Response in S-Rail Crash	152
5.3.2.1 Oscillatory Nature of Early Force-Time Response	153
5.3.2.2 Wave Propagation in S-Rail Crash	154
5.3.3 Predicted Force and Energy Response	158
5.3.3.1 Non-Hydroformed S-Rails.....	158
5.3.3.2 Hydroformed S-Rails.....	159
5.3.4 Predicted Force and Energy Response of Annealed S-Rails	160
5.3.5 Effect of Strain Rate Sensitivity and Thermal Softening on Crash Response	162
5.3.5.1 Johnson-Cook Predictions.....	167
5.3.5.2 Zerilli-Armstrong Predictions.....	168
5.4 Sensitivity of Models to Element Formulation and Size	170
5.4.1 Computational Cost of Mesh Size	174
5.5 Summary	175
5.5.1 Tube Bending and Hydroforming Models.....	175
5.5.2 Crash Models.....	178

CHAPTER 6 NUMERICAL INVESTIGATIONS INTO THE VARIABLES GOVERNING THE PHYSICAL CHARACTERISTICS AND CRASH RESPONSE OF S- RAILS

6.1 Effect of S-Rail Geometry on Crash Response	182
6.1.1 R/D Ratio and Section Lengths	182
6.1.2 S-Rail Cross-Section	186
6.2 Effect of Forming Parameters on Crash Response	191
6.2.1 Material Strength	191
6.2.2 Bending Boost	193
6.2.2.1 Effect of Boost on Thickness and Strain.....	194
6.2.2.2 Effect of Boost on Crash Response.....	197
6.2.3 Forming History.....	198
6.3 Effect of Hydroforming Process Type	201
6.3.1 Overview	201
6.3.2 Results	201

6.3.2.1 High-Pressure Hydroforming Predictions	201
6.3.2.2 Crash Response of High-Pressure Hydroformed S-Rails	205
6.3.3 Summary.....	206
CHAPTER 7 DISCUSSION	208
7.1 Influence of Tube Bending and Hydroforming on the Characteristics of S-Rails	208
7.2 Variables Governing the Crash Response of S-Rails.....	214
7.3 Demonstration of S-Rail Crash Response Improvement through Better Design and Forming Techniques	222
7.3.1 Crash Results and Summary	223
CHAPTER 8 CONCLUSIONS AND RECOMMENDATIONS	226
8.1 Conclusions	226
8.1.1 S-Rail Crash Response.....	226
8.1.2 Tube Bending	227
8.1.3 Hydroforming.....	227
8.1.4 Numerical Modelling	228
8.2 Recommendations	229
REFERENCES	230
<i>APPENDIX A: TWIST COMPRESSION TESTS FOR TUBE BENDING AND HYDROFORMING OF AA5754 TUBE.....</i>	<i>240</i>
<i>APPENDIX B: RESULTS FOR THE 2 AND 3.5 MM EN-AW5018 S- RAILS.....</i>	<i>251</i>
<i>APPENDIX C: PREDICTED TUBE BENDING, HYDROFORMING AND CRASH RESULTS</i>	<i>258</i>
<i>APPENDIX D: UNDERSTANDING THE FORCE RESPONSE IN S-RAIL CRASH.....</i>	<i>275</i>
<i>APPENDIX E: NUMERICAL INVESTIGATIONS INTO THE VARIABLES GOVERNING THE CHARACTERISTICS AND CRASH RESPONSE OF S-RAILS.....</i>	<i>288</i>

List of Tables

Table 1.1: Classification of bending operations [3].....	5
Table 2.1: S-rail dimensions for each R/D ratio. Units are in millimeters.	36
Table 2.2: Test matrix for s-rail crash tests.	37
Table 2.3: Nominal composition of AA5754 and EN-AW5018 tubes [105].	38
Table 2.4: Material specifications on bending and hydroforming tooling used in experiments.....	44
Table 2.5: Process parameters for the 3 mm AA5754 tube bending experiments.....	45
Table 2.6: Process parameters for the 2 and 3.5 mm EN-AW5018 tube bending experiments.	47
Table 2.7: Crash test parameters for 3 mm AA5754, and 2 and 3.5 mm EN-AW5018 s-rails.	55
Table 2.8: Average hardness measurements on 3 mm AA5754 non-annealed and annealed hydroformed s-rails. Hardness is reported using a Rockwell-Superficial 15N (15 kg diamond) scale.	57
Table 2.9: Average hardness measurements on 3 mm AA5754 non-annealed and annealed non-hydroformed s-rails. Hardness is reported using a Rockwell-Superficial 15N (15 kg diamond) scale.	57
Table 3.1: Summary of the variables governing the crash response of s-rails that are investigated through simulation of the forming and crash experiments.....	62
Table 3.2: Summary of the additional variables that govern the crash response of s-rails that were not investigated through simulation of the forming and crash experiments.	63
Table 3.3: Coefficients of friction used in tube bending and hydroforming models.	71
Table 3.4: Summary of the second moment of area about the neutral axis of bending for the various cross-sections examined in the s-rail.	75
Table 3.5: Test matrix examining the effect of the hydroforming process on the crash response of AA5754 s-rails. *Strain localization occurred; **Strain localization could not be avoided with end-feed.	77
Table 3.6: Barlat (1989) model parameters. Lankford parameters provided by tube supplier [109]. 80	
Table 3.7: Johnson-Cook model parameters employed based on Hopkinson bar experiments by Salisbury et al. [106,107] using a power law work hardening term, and parameters determined in this work using a Voce law work hardening term.	82
Table 3.8: Zerilli-Armstrong model parameters employed based on Hopkinson bar experiments by Salisbury et al. [106,107].	84
Table 4.1: Ovality ratios in various sections of the 3 mm AA5754 s-rails.....	88
Table 4.2: Peak force, crush displacement, energy absorbed at 250 mm crush displacement and the percent change in these quantities with respect to the R/D=1.5 condition for 3 mm AA5754 hydroformed and non-hydroformed s-rails at each bend severity.....	109
Table 4.3: Peak force, crush displacement, energy absorbed at 250 mm crush displacement and the percent change in these quantities with respect to the R/D=1.5 condition for 3 mm	

AA5754 hydroformed and non-hydroformed s-rails at each bend severity that have been fully annealed.....	112
Table 4.4: Summary of the effect of changes in bend severity on forming process variables and strains within hydroformed s-rails.	113
Table 5.1: Predicted second moment of area for the round (non-hydroformed) and square (hydroformed) cross-section of the hinge location corresponding to section D of the 3 mm AA5754 s-rails bent at R/D=2.5.	152
Table 5.2: Duration of the various models computation used to simulate the forming and crash response of a 3 mm AA5754s-rail bent at R/D=2.0. The durations of the models computation are for 2.5, 5 and 7.5 mm element size discretizations. A single Pentium-4 3.06 GHz processor was used for each simulation.	175
Table 5.3: Summary of the measured process variables, thickness and strain in a 3 mm hydroformed s-rail versus the predictions using the isotropic von Mises, anisotropic Barlat and Zerilli-Armstrong material models.....	176
Table 5.4: Summary of the measured peak load and energy absorption for 3 mm AA5754 hydroformed s-rails that have been annealed and not-annealed prior to the crash experiments versus the predictions utilizing the various material models.....	178
Table 6.1: Peak load and energy absorbed for the s-rails with varying cross-sections examined considering and not considering forming history.	190
Table 6.2: Summary of peak load and energy absorption at 250 mm of crush distance for the various forming history conditions considered in the s-rail crash simulation.	199
Table 6.3: Summary of s-rail crash results for each hydroforming process.	206
Table 7.1: Axial and circumferential strain measured at the center of the inside and outside of the bend for various tubes bent under a 100% boost condition. Theoretical estimate of axial strain at outside of bend is based on beam bending theory [112]. The strain data sources for the various materials are: (i) Δ - Oliveira et al. [6] and Gholipour et al. [137]; (ii) ϕ - Grantab [138]; (iii) ξ - Dymant [18]; (iv) β - Bardelcik [139]; and (v) α - Sorine [140]. .	210
Table A.1: Tube bending and hydroforming tooling specification.	242
Table A.2: Estimates of interface pressures.	243
Table A.3: Test plan for twist compression tests.....	244
Table A.4: Summary of the friction coefficients for bending of AA5754 tube.....	250
Table A.5: Summary of the friction coefficients for hydroforming of AA5754 tube.	250
Table D.1: Wave property relations at free and rigid boundaries. Note that the incident, reflected and transmitted wave properties are denoted by sub- and super-script symbols I, R and T, respectively [127]. U_p refers to the particle velocity.....	278
Table D.2: Material properties and parameters utilized within the Ogden linear viscoelastic formulation within LS-DYNA [30,31] that was used to represent the rubber pad within the simulation prediction. Parameters provided by Cronin [145].	284

List of Figures

Figure 1.1: 2006 Corvette frame showing the location of a one piece aluminium hydroformed s-rail that incorporates a frontal axial crush zone [1].	2
Figure 1.2: Axial crush members after impact [].	2
Figure 1.3: Schematic of s-rail collapse.	3
Figure 1.4: Mandrel-rotary draw tube bending schematic.	6
Figure 1.5: Schematic depicting bending terminology used to describe bent tubes.	7
Figure 1.6: Three methods of providing boost during bending: (a) frictional boost; (b) boost block; and, (c) independent collet boost.	12
Figure 1.7: (a) Typical hydroforming process sequence; and, (b) variation of internal pressure, axial feeding and stroke during hydroforming [36].	14
Figure 1.8: The limits and working range in tube hydroforming [56].	18
Figure 1.9: (a) Section formation during low, high and multi-pressure hydroforming, with (right) and without (left) water pressure; and, (b) comparative pressure sequences for low, high and multi-pressure hydroforming [64].	20
Figure 1.10: Evolution in shape of a square thin-walled column under torsional load [78].	24
Figure 1.11: Static collapse modes of mild steel square columns with the L/C ratio increasing from left to right. (L is the length of the column and C is the width of a side face of the square column) [80].	25
Figure 2.1: Photos of hydroformed s-rail crash structure set-up: (a) before impact; (b) after impact; and, (c) close-up of s-rail after impact.	33
Figure 2.2: Flow chart of experimental program. Note that the high-pressure process was not considered in the experiments (model-only).	34
Figure 2.3: (a) Hydroformed (top) and non-hydroformed s-rail (bottom); and, (b) various sections comprising the s-rail.	35
Figure 2.4: Cross-section of hydroformed and non-hydroformed s-rails.	36
Figure 2.5: Significant locations around the section of a tube.	38
Figure 2.6: True stress versus true plastic strain curve for 3 mm AA5754, and 2 and 3.5 mm EN-AW5018 tubes. The measured constitutive data was curve fit using the classical Voce equation to tensile data up to the point of necking and the rest of the curve was extrapolated.	39

Figure 2.7: Engineering stress versus engineering strain for 3 mm AA5754 tube tensile samples cut at the 3, 6 and 9 o'clock positions and from flat sheet (rolling direction).	40
Figure 2.8: Engineering stress versus engineering strain response of 3 mm AA5754 flat sheet samples cut from the 0, 45 and 90 degree locations.	41
Figure 2.9: Photograph of rotary draw tube bending apparatus showing bend tooling (bend die is at 90°). Tube is not shown.	42
Figure 2.10: Locations of thickness and strain measurements along the (a) inside and outside of the bend; and (b) around the circumference of the bend at the 22.5° location of the bend. Note that the schematic is shown for a hydroformed tube. The same conventions were used for both hydroformed and non-hydroformed s-rails.	46
Figure 2.11: S-rail die photos: (a) isometric view of upper and lower dies; (b) front view of lower die; (c) isometric view of lower die; (d) close-up view of die insert within lower die; and (e) various die inserts.	48
Figure 2.12: Schematic of s-rail lower die: (a) isometric view of lower die; (b) front view with die inserts; (c) front view without die inserts; (d) close-up of transition region; and (e) die insert.	49
Figure 2.13: Schematic of a hydroformed s-rail before end-trimming: (a) full view, and (b) close-up of trimmed section.	50
Figure 2.14: End-plugs used in hydroforming of s-rails.	51
Figure 2.15: S-rail crash structure and load cell arrangement schematic. View looking down on assembly from above.	53
Figure 3.1: Flow chart outlining the parameters governing s-rail crash response.	60
Figure 3.2: Variables governing the crash response of s-rails: (a) initial thickness; (b) cross-section geometry; and (c) material properties. Note that the variables examined in the experiments are shaded.	60
Figure 3.3: Variables that influence the as-formed properties of the s-rail. Note that the variables examined in the experiments are shaded.	61
Figure 3.4: Prescribed displacement and loads of the moving tools within the tube bending simulation.	67
Figure 3.5: Finite element discretization used to model the tube bending operation.	68
Figure 3.6: Non-hydroformed and hydroformed s-rails with element size discretizations of (a) 2.5; (b) 5; and, (c) 7.5 mm.	68
Figure 3.7: Predicted deformation of tube during second bend for models utilizing and not utilizing a prescribed motion boundary condition on nodes near the clamp die end of the tube. Predicted deformation is shown at (a) 0 ms; (b) 10 ms; (c) 18 ms; and (d) 20 ms.	70
Figure 3.8: (a) Die surfaces and tube for simulating the hydroforming s-rails of square, and rectangular cross-sections with aspect ratios of 1:2 and 2:1. Close-up view of the transition region of the finite element discretization of the: (b) square; (c) rectangular with aspect ratio of 2:1; and (d) rectangular with aspect ratio 1:2 die cross-sections.	72
Figure 3.9: Prescribed sequence of die closure and internal pressure within the low-pressure hydroforming simulation.	73

Figure 3.10: (a) Round; (b) square; (c) rectangular with an aspect ratio 2:1; and, (d) rectangular with an aspect ratio of 1:2 cross-section s-rails. Units are in millimeters.....	74
Figure 3.11: Typical internal pressure and end-feed schedule used in the high-pressure hydroforming simulations.	76
Figure 3.12: Typical buckling experienced due to excessive end-feed without sufficient internal pressure.	76
Figure 3.13: Schematic of undeformed tubes outer diameter and final hydroformed perimeter (width and corner radius). Units are in millimeters.....	78
Figure 3.14: Crash model schematic and boundary conditions.....	79
Figure 3.15: Voce curve fit based on ASTM data and predicted effective stress versus the effective plastic strain using a Johnson-Cook model with a Voce hardening term and a power-law hardening (standard) model. Stress-strain responses are at quasi-static strain rates.....	83
Figure 3.16: Effective stress versus effective plastic strain for a Voce fit based on ASTM data at quasi-static strain rates and predicted using the Zerilli-Armstrong model with parameters determined by Salisbury et al. [106,107] over a range of strain rates of 0.0033-500 s ⁻¹ . 84	84
Figure 4.1: Bend die torque for 3 mm AA575 s-rails.....	86
Figure 4.2: Pressure die boost load for 3 mm AA5754 s-rails.	87
Figure 4.3: Mandrel load for 3 mm AA5754 s-rails.....	87
Figure 4.4: Thickness along the inside of the first bend for 3 mm AA5754 s-rails.	89
Figure 4.5: Thickness along the outside of the first bend for 3 mm AA5754 s-rails.	89
Figure 4.6: Thickness around the circumference of the first bend, at the center of the bend angle, for 3 mm AA5754 s-rails.....	90
Figure 4.7: Major and minor engineering strain along the inside of the bend for 3 mm AA5754 tubes bent at R/D ratios of 2.5, 2.0 and 1.5.	91
Figure 4.8: Major and minor engineering strain along the outside of the bend for 3 mm AA5754 tubes bent at R/D ratios of 2.5, 2.0 and 1.5.....	92
Figure 4.9: Major and minor engineering strain around the circumference of the bend for 3 mm AA5754 tubes bent at R/D ratios of 2.5, 2.0 and 1.5.....	92
Figure 4.10: Typical thickness distribution measured around the circumference of a straight section of a 3 mm AA5754 hydroformed s-rail. Weld seam is located at the 0-degree location. 93	93
Figure 4.11: Thickness distribution around the circumference of the bend, at the center of the bend angle, for 3 mm AA5754 s-rails bent at R/D ratios of 2.5, 2.0 and 1.5.	94
Figure 4.12: Major and minor engineering strain around the circumference of the center of a straight section in a 3 mm AA5754 hydroformed s-rail.	95
Figure 4.13: Major and minor engineering strain around the circumference of a bend region, at the center of the bend angle, in 3 mm AA5754 hydroformed s-rails bent at an R/D ratio of 2.5, 2.0 and 1.5.....	96
Figure 4.14: Measured thickness around the circumference of a bend, at the center of the bend angle, in a 3 mm AA5754 s-rail bent at R/D=2.0 before and after hydroforming.	97

Figure 4.15: Measured major and minor engineering strain around the circumference of a bend, at the center of the bend angle, in a 3 mm AA5754 s-rail bent at R/D=2.0 before and after hydroforming.	98
Figure 4.16: (a) Crushed; and (b) non-crushed non-hydroformed s-rails; and, (c) crushed; and (d) non-crushed hydroformed s-rails. The 3 mm AA5754 s-rails shown were bent at R/D=2.5.....	99
Figure 4.17: (a) Inboard; and, (b) outboard deformation modes at the fixed end of the 3 mm AA5754 s-rail.	100
Figure 4.18: (a) Force; and (b) energy versus crush distance for three impact tests on 3 mm AA5754 hydroformed s-rails bent at R/D=2.5.	101
Figure 4.19: (a) Force; and (b) energy versus crush distance of 3 mm AA5754 hydroformed s-rails bent at R/D=2.0 and impacted at 3.00 and 3.33 m/s.	102
Figure 4.20: (a) Force; and (b) energy versus crush displacement response of 2 and 3.5 mm EN-AW5018 non-hydroformed s-rail structures bent at an R/D=2.0 [5].	104
Figure 4.21: (a) Force; and (b) energy versus crush displacement of 3 mm AA5754 non-hydroformed s-rails bent at an R/D ratio of 2.5, 2.0 and 1.5.	105
Figure 4.22: (a) Force; and (b) energy versus crush distance for 3 mm AA5754 hydroformed s-rails bent at R/D ratios of 2.5, 2.0 and 1.5.	106
Figure 4.23: (a) Force; and (b) energy versus crush displacement for 3 mm AA5754 non-hydroformed and hydroformed s-rails bent at R/D=2.0.....	107
Figure 4.24: (a) Peak force; and (b) energy absorbed at 250 mm of crush distance for 3 mm AA5754 non-hydroformed and hydroformed s-rails at each bend severity.	108
Figure 4.25: (a) Force; and (b) energy versus crush displacement for hydroformed and annealed 3 mm AA5754 s-rails bent at the three bend severities. Also shown is the force response of a non-annealed s-rail bent at R/D=2.0.	110
Figure 4.26: (a) Peak force; and (b) energy absorbed at 250 mm of crush distance for 3 mm AA5754 hydroformed and non-hydroformed s-rails at each bend severity that were annealed prior to the crash experiments. The corresponding data for the non-annealed s-rails from Figure 4.24 is also shown.....	111
Figure 4.27: (a) Percent thickness reduction; and (b) axial; and (c) circumferential engineering strains measured at the center of the bend. (d) Circumferential engineering strain measured at corners of the bend.....	113
Figure 4.28: Summary of the effects of the s-rail cross-section, bend severity, low-pressure hydroforming process employed, and annealing prior to the crash experiments on the crash response of s-rails.	116
Figure 5.1: Predicted deformation at various stages of simulating the bending of a 3 mm AA5754 s-rail at R/D=2.5: (a) first bend; (b) tube reposition and re-orientation between bends; and (c) second bend. Note that the springback stage after each bend is not shown. The initial and final simulation times for each stage are denoted by t_0 and t_f , respectively.	119
Figure 5.2: (a) Actual 3 mm AA5754 s-rail after bending at R/D=2.5 and trimming. Predicted s-rail geometry after bending and trimming operations with contours of (b) thickness (mm); (c) major strain; and (d) minor strain.	120

Figure 5.3: Measured bend torque for the first bend of the s-rail bent at the R/D ratios of 2.5, 2.0 and 1.5, and predictions using the piecewise linear material model with a von Mises yield criterion.....	121
Figure 5.4: Measured pressure die boost load for the first bend of the s-rail bent at the R/D ratios of 2.5, 2.0 and 1.5, and predictions using the piecewise linear material model with a von Mises yield criterion.	121
Figure 5.5: Measured mandrel load for the first bend of the s-rail bent at the R/D ratios of 2.5, 2.0 and 1.5, and predictions using the piecewise linear material model with a von Mises yield criterion.....	122
Figure 5.6: Predicted bend torque for the first and second bend of the s-rail at the R/D ratios of 2.5, 2.0 and 1.5.....	123
Figure 5.7: Predicted pressure die boost load for the first and second bend of the s-rail at the R/D ratios of 2.5, 2.0 and 1.5.....	123
Figure 5.8: Predicted mandrel load for the first and second bend of the s-rail at the R/D ratios of 2.5, 2.0 and 1.5.....	124
Figure 5.9: Measured thickness along the inside of the bend for R/D=2.5 and the predictions using the isotropic von Mises (ISO) and anisotropic Barlat (1989) material model.	125
Figure 5.10: Measured thickness along the inside of the bend for R/D=2.0 and the predictions using the isotropic von Mises (ISO) and anisotropic Barlat (1989) material models.....	125
Figure 5.11: Measured thickness along the inside of the bend for R/D=1.5 and the predictions using the isotropic von Mises (ISO) and anisotropic Barlat (1989) material models.....	126
Figure 5.12: Measured thickness along the outside of the bend for R/D=2.5 and predictions using the isotropic von Mises (ISO) and anisotropic Barlat (1989) material models.....	127
Figure 5.13: Measured thickness along the outside of the bend for R/D=2.0 and predictions using the isotropic von Mises (ISO) and anisotropic Barlat (1989) material models.....	127
Figure 5.14: Measured thickness along the outside of the bend for R/D=1.5 and predictions using the isotropic von Mises (ISO) and anisotropic Barlat (1989) material models.....	128
Figure 5.15: Measured thickness around the circumference of the bend for R/D=2.5 and predictions using the isotropic von Mises (ISO) and anisotropic Barlat (1989) material models. ...	129
Figure 5.16: Measured thickness around the circumference of the bend for R/D=2.0 and predictions using the isotropic von Mises (ISO) and anisotropic Barlat (1989) material models. ...	129
Figure 5.17: Measured thickness around the circumference of the bend for R/D=1.5 and predictions using the isotropic von Mises (ISO) and anisotropic Barlat (1989) material models. ...	130
Figure 5.18: Predictions of thickness along the inside of the bend using the anisotropic Barlat (1989) material model for R/D ratios of 2.5, 2.0 and 1.5.	131
Figure 5.19: Predictions of thickness along the outside of the bend using the anisotropic Barlat (1989) material model for R/D ratios of 2.5, 2.0 and 1.5.....	131
Figure 5.20: Predictions of thickness around the circumference of the bend using the anisotropic Barlat (1989) material model for R/D ratios of 2.5, 2.0 and 1.5.....	132
Figure 5.21: Measured major and minor engineering strains and predictions using the isotropic von Mises (ISO) and anisotropic Barlat (1989) material models along the inside of the bend for R/D=2.5.....	133

Figure 5.22: Measured major and minor engineering strains and predictions using the isotropic von Mises (ISO) and anisotropic Barlat (1989) material models along the inside of the bend for R/D=2.0.....	133
Figure 5.23: Measured major and minor engineering strains and predictions using the isotropic von Mises (ISO) and anisotropic Barlat (1989) material models along the inside of the bend for R/D=1.5.....	134
Figure 5.24: Measured major and minor engineering strains and predictions using the isotropic von Mises (ISO) and anisotropic Barlat (1989) material models along the outside of the bend for R/D=2.5.....	134
Figure 5.25: Measured major and minor engineering strains and predictions using the isotropic von Mises (ISO) and anisotropic Barlat (1989) material models along the outside of the bend for R/D=2.0.....	135
Figure 5.26: Measured major and minor engineering strains and predictions using the isotropic von Mises (ISO) and anisotropic Barlat (1989) material models along the outside of the bend for R/D=1.5.....	135
Figure 5.27: Measured major and minor engineering strains and predictions using the isotropic von Mises (ISO) and anisotropic Barlat (1989) material models around the circumference of the bend for R/D=2.5.....	136
Figure 5.28: Measured major and minor engineering strains and predictions using the isotropic von Mises (ISO) and anisotropic Barlat (1989) material models around the circumference of the bend for R/D=2.0.....	136
Figure 5.29: Measured major and minor engineering strains and predictions using the isotropic von Mises (ISO) and anisotropic Barlat (1989) material models around the circumference of the bend for R/D=1.5.....	137
Figure 5.30: Major and minor engineering strain predictions around the circumference of the bend at R/D ratios of 2.5, 2.0 and 1.5 using the anisotropic Barlat (1989) material model.....	138
Figure 5.31: Predicted deformation of a 3 mm AA5754 s-rail bent at R/D=2.5 at several instants in time during the low-pressure hydroforming operation. (a) Die surfaces and s-rail; (b) s-rail; (c) cross-section view of straight section A of the s-rail; and (d) cross-section view of bent section D of s-rail.....	139
Figure 5.32: (a) Actual 3 mm AA575 s-rail bent at R/D=2.5 after hydroforming and trimming. Predicted s-rail geometry after low-pressure hydroforming and trimming operations and contours of (b) thickness (mm); (c) major strain; and (d) minor strain.....	140
Figure 5.33: Predicted thickness distribution around the straight section C of s-rails bent and hydroformed at R/D ratios of 2.5, 2.0 and 1.5 using the isotropic material model.....	141
Figure 5.34: Measured thickness around the circumference of the bend and predictions using the isotropic von Mises and anisotropic Barlat (1989) material models for hydroformed s-rails bent at R/D=2.5.....	142
Figure 5.35: Measured thickness around the circumference of the bend and predictions using the isotropic von Mises and anisotropic Barlat (1989) material models for hydroformed s-rails bent at R/D=2.0.....	142
Figure 5.36: Measured thickness around the circumference of the bend and predictions using the isotropic von Mises and anisotropic Barlat (1989) material models for hydroformed s-rails bent at R/D=1.5.....	143

Figure 5.37: Measured versus predicted major and minor engineering strains using the isotropic von Mises material model around the circumference of straight section C of the hydroformed s-rail.	144
Figure 5.38: Measured major and minor engineering strains and predictions using the isotropic von Mises and anisotropic material models around the circumference of a bend in a hydroformed s-rail bent at R/D=2.5.	145
Figure 5.39: Measured major and minor engineering strains and predictions using the isotropic von Mises and anisotropic material models around the circumference of a bend in a hydroformed s-rail bent at R/D=2.0.	145
Figure 5.40: Measured major and minor engineering strains and predictions using the isotropic von Mises and anisotropic material models around the circumference of a bend in a hydroformed s-rail bent at R/D=1.5.	146
Figure 5.41: (a) Actual and (b) predicted 3 mm AA5754 crushed non-hydroformed s-rail geometry with contours of effective plastic strain. S-rail was bent at R/D=2.5.	147
Figure 5.42: Top view of (a) actual and (b) predicted 3 mm AA5754 crushed hydroformed s-rail geometry with contours of effective plastic strain. S-rail was bent at R/D=2.5.	147
Figure 5.43: Isometric view of (a) actual and (b) predicted 3 mm AA5754 crushed hydroformed s-rail geometry with contours of effective plastic strain. S-rail was bent at R/D=2.5.	148
Figure 5.44: (a) Isometric; (b) front; and (c) front sectioned views of deformation in the 3 mm AA5754(bent at R/D=2.5) non-hydroformed s-rail at various increments in time.	149
Figure 5.45: (a) Isometric; (b) front; and (c) front sectioned views of deformation in the 3 mm AA5754(bent at R/D=2.5) hydroformed s-rail at various increments in time.	150
Figure 5.46: Predicted deformation of a cross-section of the hinge in section D of 3 mm AA5754 non-hydroformed and hydroformed s-rails bent at R/D=2.5.	151
Figure 5.47: Predicted second moment of area for the round (non-hydroformed) and square (hydroformed) cross-section of the hinge location corresponding to section D of the 3 mm AA5754 s-rails bent at R/D=2.5.	152
Figure 5.48: Predicted, filtered and non-filtered crush force versus time for a 3 mm AA5754 hydroformed s-rail bent at an R/D=2.0. Level of deformation, instant of first contact, peak load and time duration that wave propagation effects are significant are shown. .	154
Figure 5.49: (a) Traverse distances; and (b) time intervals for a stress wave to propagate between the geometric and rigid boundaries of the s-rail.	155
Figure 5.50: Contours of stress in the z-direction at various instants in time due to impact showing the progression of first loading wave. The units of stress are MPa.	156
Figure 5.51: Predicted force versus time signature of s-rail. Points in time that the stress waves reflected from the first and second bends, and the fixed end of the s-rail reach the impact plate.	158
Figure 5.52: Measured and predicted (a) force; and (b) energy versus crush distance for a 3 mm AA5754 non-hydroformed s-rail bent at R/D=2.0 using the isotropic von Mises and anisotropic Barlat (1989) material models.	159
Figure 5.53: Measured and predicted (a) force; and (b) energy versus crush distance for a 3 mm AA5754 hydroformed s-rail bent at R/D=2.0 using the isotropic von Mises and anisotropic Barlat (1989) models.	160

Figure 5.54: Measured and predicted (a) force; and (b) energy versus crush distance for 3 mm AA5754 annealed and non-annealed non-hydroformed s-rails bent at an R/D ratio of 2.0 using the isotropic von Mises material model.	161
Figure 5.55: Measured and predicted (a) force; and (b) energy versus crush distance for 3 mm AA5754 annealed and non-annealed hydroformed s-rails bent at an R/D ratio of 2.0 using the isotropic von Mises material model.	162
Figure 5.56: Location of maximum strain rate.	163
Figure 5.57: Predicted (a) maximum strain rate; (b) crush distance; and, (c) effective plastic strain versus time experienced in an element at the hinge location of the s-rail.	164
Figure 5.58: Contour plot of temperature in the s-rail. Units are in degrees Celsius.	165
Figure 5.59: Predicted temperature versus (a) crush distance, and (b) time in the element experiencing the largest adiabatic temperature rise and strain rate.	166
Figure 5.60: Predictions of (a) force; and (b) energy versus crush distance using the Johnson-Cook UMAT with a Voce hardening law for 3 mm AA5754 hydroformed s-rails bent at R/D=2.0.	168
Figure 5.61: Measured (a) force; and (b) energy response and predictions using the Zerilli-Armstrong material model for 3 mm AA5754 hydroformed s-rails bent at R/D=2.0.	170
Figure 5.62: Predicted: (a) force; and, (b) energy response of 3.5 mm EN-AW5018 s-rails bent at an R/D=2.0, simulated using fully-integrated (FI) and Belytschko-Lin-Tsay (BT) elements and 2.5, 5 and 7.5 mm element sizes.	172
Figure 5.63: Predicted (a) force; and (b) energy versus crush distance using 2.5, 5 and 7.5 mm element size discretizations for 3 mm AA5754 hydroformed s-rails bent at an R/D=2.0 and the isotropic von Mises material model.	174
Figure 5.64: Summary of measured and predicted (a) thickness reduction; (b) axial strain; (c) circumferential strain; and (d) circumferential strain at the corners in a 3 mm hydroformed s-rail bent at various bend severities.	177
Figure 5.65: Summary of the measured peak load and energy absorption for 3 mm AA5754 hydroformed s-rails that have been annealed and not-annealed prior to the crash experiments versus the predictions utilizing the various material models.	179
Figure 6.1: Predicted (a) force; and (b) energy versus crush distance for 3 mm AA5754 hydroformed s-rails with uniform thickness and virgin material properties bent at R/D ratios of 2.5, 2.0 and 1.5.	183
Figure 6.2: Schematic of centre line geometry of s-rails bent at R/D ratios of 2.5 (green), 2.0 (blue), and 1.5 (red): (a) links 1, 2 and 3; (b) close-up of the distance between the fixed end of the s-rail and the location of hinge in the linkage corresponding to section E; (c) length of the bar linkage (section C) between hinges in bend regions; (d) distance between the fixed end of the s-rail and the location of hinge in linkage corresponding to section A; and (e) close-up view of the hinge location occurring at the bends of the s-rail. Units are in millimeters.	185
Figure 6.3: (a) Section view of hydroformed s-rail (time=0 ms); (b) contours of effective plastic strain in the corresponding cross-section (time=12 ms); and, (c) contours of effective plastic strain in of the hinge in region 1 of three s-rails with different bend severities superimposed on one another (time=12 ms).	186

Figure 6.4: Predicted (a) thickness; and (b) major and minor strain around the circumference of the center section of the bend for the various s-rail cross-section geometries.	188
Figure 6.5: Predicted contours of effective plastic strain in the rectangular cross-section s-rails with aspect ratios of 2:1 and 1:2 at a time of 0 ms and 35 ms.	189
Figure 6.6: Predicted (a) peak load; and (b) energy absorbed for the s-rails with varying cross-sections examined considering and not considering forming history.	191
Figure 6.7: Predicted (a) force; and (b) energy versus crush distance for 3 mm AA5754 and 3 mm EN-AW5018 hydroformed s-rails bent at R/D=2.0, and fabricated under the same prescribed conditions.	193
Figure 6.8: Predicted thickness along the inside of the bend for (i) 100% frictional boost; (ii) 104% frictional boost; and (iii) 104% independent collet boost bending conditions.	194
Figure 6.9: Predicted thickness along the outside of the bend for (i) 100% frictional boost; (ii) 104% frictional boost; and (iii) 104% independent collet boost bending conditions.	195
Figure 6.10: Predicted effective plastic strain along the inside of the bend for (i) 100% frictional boost; (ii) 104% frictional boost; and (iii) 104% independent collet boost bending conditions.	196
Figure 6.11: Predicted effective plastic strain along the outside of the bend for (i) 100% frictional boost; (ii) 104% frictional boost; and (iii) 104% independent collet boost bending conditions.	196
Figure 6.12: Predicted (a) force; and (b) energy absorption for hydroformed s-rail bent under the three boost conditions.	197
Figure 6.13: Summary of predicted (a) peak load and (b) energy absorption of non-hydroformed and hydroformed s-rails bent at R/D=2.0 for the various forming history considerations. ...	200
Figure 6.14: Contours of (a) thickness; and (b) effective plastic strain: (i) zero-percent expansion and zero end-feed; (ii) four-percent expansion and zero end-feed; (iii) four-percent expansion with a frictionless condition and 80 mm of end-feed; (iv) four-percent expansion with 30 mm of end-feed; (v) nine-percent expansion with zero end-feed; and (vi) nine-percent expansion with a frictionless condition and 100 mm of end-feed.	203
Figure 6.15: Strain localization observed in high-pressure hydroforming simulations using: (a) four-percent expansion with zero end-feed; and, (b) nine-percent expansion with zero end-feed.	204
Figure 6.16: Predicted (a) force; and (b) energy per unit mass versus crush distance for hydroformed s-rails: (i) zero-percent expansion and zero end-feed; (ii) four-percent expansion and zero end-feed; (iii) four-percent expansion with 30 mm of end-feed; (iv) four-percent expansion with a frictionless condition and 80 mm of end-feed; (v) nine-percent expansion with zero end-feed; and (vi) nine-percent expansion with a frictionless condition and 100 mm of end-feed.	206
Figure 7.1: Axial and circumferential strain measured at the center of the inside and outside of the bend for various tubes bent under a 100% boost condition at: (a) R/D=2.5; (b) R/D=2.0; and (c) R/D=1.5. Theoretical estimate of axial strain at outside of bend is based on beam bending theory [112]. The strain data sources for the various materials are: (i) Δ -Oliveira et al. [6] and Gholipour et al. [137]; (ii) ϕ - Grantab [138]; (iii) ξ - Dymant [18]; (iv) β - Bardelcik [139]; and (v) α - Sorine [140].	211

Figure 7.2: Ranking chart indicating variables and the degree to which they affect the crash response of aluminium alloy hydroformed s-rails.	214
Figure 7.3: Predicted (a) force and (b) energy absorption of the various parameters affecting s-rail crash response.	215
Figure 7.4: Increase in energy absorption versus increase in material strength data for various material substitutions. The data for the HSLA350 and DP600 substitutions for DDQ steel are taken from Grantab [138].....	217
Figure 7.5: Predicted (a) peak load and (b) energy absorption for hydroformed AA5754 s-rails that were bent at R/D=2.0: (i) utilizing the various material models examined, and (ii) with various forming history effects isolated.....	220
Figure 7.6: Influence of element formulation and mesh size on the predicted energy absorption of hydroformed s-rails. B.L.T.- Belytschko-Lin-Tsay [121]; F.I.-fully integrated [31]. ..	222
Figure 7.7: (a) Baseline s-rail; and, (b) improved s-rail before and after impact.	224
Figure 7.8: (a) Force; and, (b) energy absorption comparison between the baseline and improved s-rails.....	225
Figure A.1: (a) Twist compression test rig; (b) close-up of test rig; and, (c) anvil and workpiece...	241
Figure A.2: Schematic of the tool/workpiece interaction.....	241
Figure A.3: Coefficient of friction for hardened 4130 steel interacting with a lubricated and dry workpiece.....	245
Figure A.4: Coefficient of friction for hardened 4130 steel interacting with a dry workpiece at 2 and 19 rpm.	245
Figure A.5: Coefficient of friction for non-hardened 4130 steel and the Drawsol AL20 lubricant at 6.9 and 13.8 MPa.	246
Figure A.6: Coefficient of friction for non-hardened 4130 steel at 2 and 19 rpm.....	246
Figure A.7: Coefficient of friction for 8620 chromed steel interacting with lubricated and dry workpiece.....	247
Figure A.8: Coefficient of friction for 8620 chromed steel at 6.9 and 13.8 MPa.....	247
Figure A.9: Coefficient of friction for 4140 steel and Hydrodraw625 lubricant at various levels of interface pressure.	248
Figure A.10: Coefficient of friction for 4140 steel at 0.4 and 4 rpm.....	248
Figure A.11: Coefficient of friction for 4140 steel with various lubricant film thicknesses using a rotational speed of 0.8 rpm.	249
Figure B.1: Measured and predicted thickness results along the circumference of the 3.5 mm s-rail bent at an R/D=2.0.	251
Figure B.2: Measured and predicted thickness results along the: (a) lower path; and, (b) upper path of the 3.5 mm s-rail bent at an R/D=2.0.....	252
Figure B.3: Measured and predicted: (a) major; and, (b) minor strain along the circumference of the first bend of a 3.5 mm s-rail bent at an R/D=2.0.	253

Figure B.4: Measured and predicted strains for a 3.5 mm s-rail, bent at an R/D=2.0, along the lower path: (a) major strains; and, (b) minor strains.	254
Figure B.5: Measured and numerically predicted: (a) force; and, (b) energy versus displacement response of 3.5 mm s-rail structures bent at an R/D=2.0 for various mesh sizes. Analytical prediction is included for comparison purposes.	255
Figure B.6: Measured and predicted: (a) force; and, (b) energy versus displacement response of 2 mm s-rail structures bent at an R/D=2.0 for various mesh sizes. Analytical prediction is included for comparison purposes.	256
Figure B.7: The effect of considering forming history on the: (a) force; and, (b) energy versus displacement response of a 2 and 3.5 mm s-rail crash structure bent at an R/D of 2.0. Crush response was calculated using the 2.5 mm sized elements.	257
Figure C.1: Predicted bend torque using the isotropic von Mises versus anisotropic Barlat (1989) material models.	258
Figure C.2: Predicted pressure die boost load using the isotropic von Mises versus anisotropic Barlat (1989) material models.	259
Figure C.3: Predicted mandrel load using the isotropic von Mises versus anisotropic Barlat (1989) material models.	259
Figure C.4: Measured and predicted bend torque using 2.5, 5 and 7.5 mm element sized mesh discretizations for s-rails bent at R/D=2.0 using the anisotropic Barlat (1989) material model.	260
Figure C.5: Measured and predicted pressure die boost load using 2.5, 5 and 7.5 mm element sized mesh discretizations for s-rails bent at R/D=2.0 using the anisotropic Barlat (1989) material model.	260
Figure C.6: Measured and predicted mandrel load using 2.5, 5 and 7.5 mm element sized mesh discretizations for s-rails bent at R/D=2.0 using the anisotropic Barlat (1989) material model.	261
Figure C.7: Predictions of thickness along the inside of an R/D=2.0 bend using 2.5, 5 and 7.5 mm element size discretizations and an isotropic von Mises material model.	262
Figure C.8: Predictions of thickness along the outside of an R/D=2.0 bend using 2.5, 5 and 7.5 mm element size discretizations and an isotropic von Mises material model.	262
Figure C.9: Predictions of major and minor engineering strains along the inside of an R/D=2.0 bend using 2.5, 5 and 7.5 mm element size discretizations and an isotropic von Mises material model.	263
Figure C.10: Predictions of major and minor engineering strains along the outside of an R/D=2.0 bend using 2.5, 5 and 7.5 mm element size discretizations and an isotropic von Mises material model.	263
Figure C.11: Predicted bend torque using the rate-insensitive material model and rate-sensitive Zerilli-Armstrong material model.	264
Figure C.12: Predicted boost load using the rate-insensitive material model and rate-sensitive Zerilli-Armstrong material model.	264
Figure C.13: Predicted mandrel load using the rate-insensitive material model and rate-sensitive Zerilli-Armstrong material model.	265

Figure C.14: Predicted thickness along the inside of the bend using the rate-insensitive material model and rate-sensitive Zerilli-Armstrong material model.....	265
Figure C.15: Predicted thickness along the outside of the bend using the rate-insensitive material model and rate-sensitive Zerilli-Armstrong material model.....	266
Figure C.16: Predicted thickness around the circumference of the bend using the rate-insensitive and rate-sensitive Zerilli-Armstrong material models.....	266
Figure C.17: Predicted major and minor engineering strains along the inside of the bend using the rate-insensitive material model and rate-sensitive Zerilli-Armstrong material model. .	267
Figure C.18: Predicted major and minor engineering strains along the outside of the bend using the rate-insensitive material model and rate-sensitive Zerilli-Armstrong material model. .	267
Figure C.19: Predicted major and minor engineering strains around the circumference of the bend using the rate-insensitive and rate-sensitive Zerilli-Armstrong material models.	268
Figure C.20: Measured thickness and predictions using 2.5, 5 and 7.5 mm element size discretizations and the rate-insensitive isotropic von Mises material model around the circumference of the hydroformed bend section R/D=2.0.....	269
Figure C.21: Measured major and minor engineering strains and predictions using the rate-insensitive isotropic von Mises material model with element size discretizations of 2.5, 5 and 7.5 mm around the circumference of the hydroformed bend section R/D=2.0.....	269
Figure C.22: Predicted thickness around the circumference of the bend region after hydroforming using the rate-insensitive and rate-sensitive Zerilli-Armstrong material models.	270
Figure C.23: Predicted major and minor engineering strains around the circumference of the bend region after hydroforming using the rate-insensitive and rate-sensitive Zerilli-Armstrong material models.....	270
Figure C.24: Measured and predicted (a) force; and (b) energy versus crush distance for a 3 mm AA5754 non-hydroformed s-rail bent at R/D=2.5 using the isotropic and anisotropic models.....	271
Figure C.25: Measured and predicted (a) force; and (b) energy versus crush distance for a 3 mm AA5754 non-hydroformed s-rail bent at R/D=1.5 using the isotropic and anisotropic models.....	272
Figure C.26: Measured and predicted (a) force; and (b) energy versus crush distance for a 3 mm AA5754 hydroformed s-rail bent at R/D=2.5 using the isotropic and anisotropic models.	273
Figure C.27: Measured and predicted (a) force; and (b) energy versus crush distance for a 3 mm AA5754 hydroformed s-rail bent at R/D=1.5 using the isotropic and anisotropic models.	274
Figure D.1: Predicted, filtered and non-filtered crush force versus time for a 3 mm AA5754 hydroformed s-rail bent at an R/D=2.0. Level of deformation, instant of first contact, peak load and time duration that wave propagation effects are significant are shown. .	276
Figure D.2: Impact of two cylindrical bars: (a) before impact; (b) at the moment of impact; (c) shortly after impact; and, (d) after the stress wave from the striker bar has been transferred to the incident bar.	277
Figure D.3: (a) Geometric; and, (b) material impedance changes.....	278

Figure D.4: (a) Traverse distances; and (b) time intervals for a stress wave to propagate between the geometric and rigid boundaries of the s-rail.	279
Figure D.5: Contours of stress in the z-direction at various instants in time due to impact showing the progression of first loading wave.	280
Figure D.6: Predicted force versus time signature of s-rail. Points in time that the stress waves reflected from the first and second bends, and the fixed end of the s-rail reach the impact plate.	282
Figure D.7: Experimental and predicted (filtered and non-filtered) force versus time data.	283
Figure D.8: Schematic of s-rail impact interface for the model considering a rubber damper.	284
Figure D.9: Predicted force versus time response with and without a rubber pad at impact interface. The output interval of the data is shown within brackets within the legend.	285
Figure D.10: Predicted force-time response of s-rail considering various forming history effects.	286
Figure E.1: (a) Peak load; and (b) energy absorbed for the s-rails with varying cross-sections examined considering forming history.	288
Figure E.2: (a) Peak load; and (b) energy absorbed for the s-rails with varying cross-sections examined not considering forming history.	289
Figure E.3: Predicted (a) force; and (b) energy versus crush distance for non-hydroformed s-rails with (i) entire forming history considered; (ii) residual stresses removed; (iii) residual stresses and work hardening removed; and, (iv) residual stresses, work hardening and thickness changes removed.	290
Figure E.4: Predicted (a) force; and (b) energy versus crush distance for hydroformed s-rails with (i) entire forming history considered; (ii) residual stresses removed; (iii) residual stresses and work hardening removed; and, (iv) residual stresses, work hardening and thickness changes removed.	291
Figure E.5: Predicted (a) force; and (b) energy per unit mass versus crush distance for hydroformed s-rails: (i) zero-percent expansion and zero end-feed; (ii) four-percent expansion and zero end-feed; (iii) four-percent expansion with 30 mm of end-feed; (iv) four-percent expansion with a frictionless condition and 80 mm of end-feed; (v) nine-percent expansion with zero end-feed; and (vi) nine-percent expansion with a frictionless condition and 100 mm of end-feed.	292

Chapter 1

Introduction

The movement towards light-weight vehicles represents a significant engineering challenge for design and manufacturing within the automotive industry, which must now consider aluminium alloys and advanced high strength steels as potential light-weight replacements for mild steel automotive structural components. Such a substitution must not jeopardize the structural integrity of the components nor sacrifice the energy absorption characteristics of the vehicle in a crash event. To this end, the effects of the manufacturing process on the crash performance of light-weight automotive structural components must be better understood, ultimately, to ensure sufficient protection to the occupants.

Within a vehicle, there are generally two main types of energy absorbing members that undergo axial and/or bending modes of collapse during a collision. Such members are often referred to as either axial or side-rail (s-rail) crush structures, and are shown in Figure 1.1 [1]. An axial crush member is designed to undergo a progressive folding type of collapse (Figure 1.2) that absorbs most of the impact energy due to a collision while isolating deformation to local regions of the front or rear of the vehicle (front and/or rear) outside of the occupant zone. The so-called s-rail provides structural strength throughout the vehicle and must also exhibit excellent energy absorption characteristics during a crash event. S-rail deformation generally occurs through bending collapse after the energy absorbing capability of the axial members has been exhausted. To better understand the global response of a vehicle during crash, it is important to first isolate and investigate the two main energy absorbing structural components. The research comprising this thesis focuses on the interaction between the fabrication and crash response of s-rail structural components.



Figure 1.1: 2006 Corvette frame showing the location of a one piece aluminium hydroformed s-rail that incorporates a frontal axial crush zone [1].



Figure 1.2: Axial crush members after impact [2].

During an impact event, an s-rail structure undergoes a three-hinge bending mode of collapse, as illustrated in Figure 1.3. The hinge locations on the s-rail occur at locations of greatest local bending moment, which are the two bend regions and near the base of the longest outer straight section. Typically in a vehicle, there are many subcomponents and parts attached to the s-rail that will affect the energy absorption during a crash event. In the current research, the crash response of the s-rail itself, measured in terms of force and energy absorption, is the primary focus and lateral supports are neglected. One manufacturing route used to fabricate s-rail components involves tube bending followed by hydroforming. The objective of this research is to understand the parameters that govern the crash response of s-

rails fabricated from aluminium alloy, seam welded tubes. The emphasis here is on the effects of the tube bending and hydroforming processes on the as-formed properties of the s-rail and the subsequent crash response.

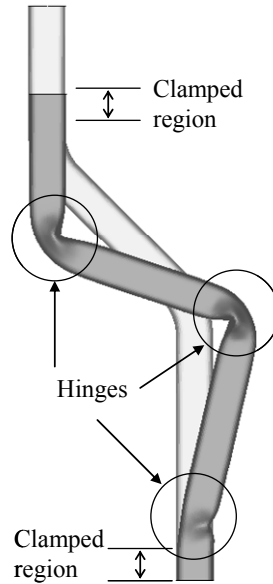


Figure 1.3: Schematic of s-rail collapse.

The automotive manufacturing sector is now beginning to shift its fabrication techniques for structural parts towards the tube bending and hydroforming processes due to several structural performance and economic advantages they offer (Section 1.4). In the past, s-rails have been manufactured using stamped sheet metal components that are subsequently welded together. With the emergence of hydroforming techniques that allow the forming of closed-section complex parts, the use of welded sheet metal structural components represents an inferior means of fabricating structural components. The current and future demands for hydroformed components of increasingly complex shape and tight dimensional tolerances, sets additional requirements on pre-hydroforming shaping processes, such as tube bending. Mandrel-rotary draw tube bending is the most common bending process that ensures that pre-formed parts have the dimensional accuracy requirements of the hydroforming process. A typical s-rail made from tube stock requires two or more bends using a mandrel-rotary draw tube bender, after which the pre-formed part is then placed in a hydroforming die to impart the final desired cross-sectional shape after pressurization.

There has been little research into the effect of rotary draw bending and hydroforming on the crash performance of s-rail structures. This knowledge is necessary in design, particularly in support of the adoption of advanced light-weight materials, such as aluminium alloys, that are subjected to crash conditions. The research conducted as part of this doctoral thesis has served to isolate and identify the relevant manufacturing parameters in the tube bending and hydroforming processes that exert a significant influence on the crash response of s-rail structures. In addition, advanced numerical simulation techniques were developed and used to complement the experimental investigation and further understand the crash response of automotive structural components. Through this work, the foundation has been put in place to bridge the gap of knowledge concerning the interaction between manufacturing and crash response, hence ensuring better design for vehicle crashworthiness.

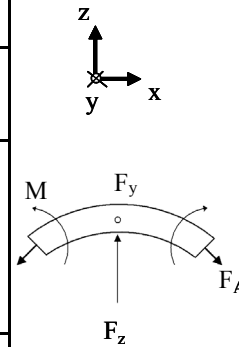
The balance of this chapter provides a review and assessment of the state-of-the-art in tube bending, hydroforming and structural crash research, followed by an introduction to the current research presented in this thesis.

1.1 Bending

Bending processes can be categorized as (i) kinematic shaping; or, (ii) forming with shape defining tools, as described by Vollersten *et al.* [3]. Kinematic shaping is based on forming by defined relative motion between the workpiece and tool and allows a wide variety of bending profiles. Forming with shape defining tools utilizes tools with the desired final part geometry, after accounting for springback during unloading, and yields a highly reproducible product and short processing time. Table 1.1 [3] provides a summary of these bending processes that are further categorized in terms of the nature of the externally applied bending moment and force. The most common processes for bending pipe and tube are ram, roll, heat-induction, sand packing and hot-slab forming, and rotary draw bending. These tube and pipe bending processes require increased precision for automotive applications and generally require forming with shaping tools that induce a locally variable moment. Ultimately, the selection of tube bending process depends on the desired center-line radius, wall thickness, quality of the bend, production rate required, outer diameter and cost. The most commonly employed bending method used in automotive structural applications, and a focus of the current research, is the rotary draw bending process.

Table 1.1: Classification of bending operations [3].

	Without moment		Locally constant moment	Locally variable moment		
	No external forces	F_y	M	$M(F_z), F_z$	$M(F_z), F_z, F_y$	$M(F_z), F_z, F_A$
Kinematic bending	thermally induced bending	thermally induced bending under compressive force	bending with a pure moment	air bending		
Forming with shaping tools				Press bending, rotary draw bending	Sand-packing and hot slab forming	Roll bending, heat induction bending



1.2 Mandrel-Rotary Draw Tube Bending

Mandrel-rotary draw tube bending utilizes five major tools (Figure 1.4) that all interact with one another via the tube during bending. The tools required are: (i) bend die; (ii) clamp die; (iii) pressure die; (iv) wiper die; and, (v) mandrel. At the start of the bend process the bend die, clamp die, pressure die and tube are all oriented parallel to one another, as shown in Figure 1.4. The wiper die is positioned at a small angle to the tube axis, which is usually referred to as the “rake angle”. This angle minimizes frictional drag from the wiper during bending, while assisting in preventing wrinkling on the inside of the bend [4]. The location of tangency is determined by the line perpendicular to the tube axis that intersects the center of the bend die rotation [5,6]. The mandrel prevents collapse of the tube and limits tube ovalization. In addition, the mandrel transfers the clamping load from the pressure die to the inside of the tube and ultimately to the bend and wiper dies to prevent wrinkling. The wiper die may be lubricated while the bend die, clamp die and pressure die are kept dry to minimize slip during bending. Once the tube is positioned over the mandrel, the clamp and pressure dies are closed under displacement- or load-control, applying clamping forces on the tube. The bend die and wiper die serve to react these clamping loads while the mandrel prevents the tube from collapsing. The bend and clamp dies then rotate synchronously, pulling the tube around the bend die, while the pressure die advances parallel to the mandrel axis, hence pushing material into the bend region.

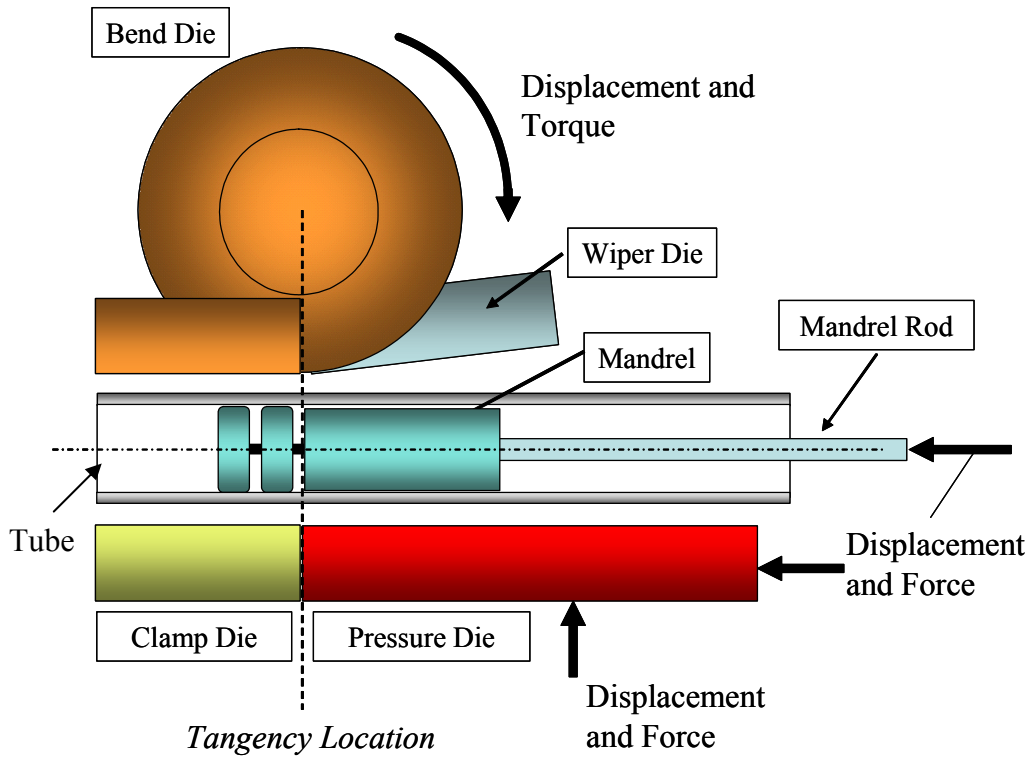


Figure 1.4: Mandrel-rotary draw tube bending schematic.

When discussing the rotary draw tube bending process, it is important to be familiar with terminology common used within the industry, as presented in Figure 1.5. The center-line (CL) of the tube and neutral axis (NA) refer to continuous lines that connect every center and neutral point of the cross-section of the tube, respectively. The center-line radius (CLR) of the bend or “bend radius” refers to the distance between the center of rotation and the center-line of the tube. Bend severity is typically described in terms of the ratio of center-line bend radius to tube outer diameter or CLR/OD, where OD is the outer diameter of the tube. The short form notation that is used throughout this work is the R/D ratio. The tangent line refers to the line along which the bend starts or ends. During bending, the tube wall at the outside and inside of the bend will tend to thin and thicken, respectively. In addition, the walls collapse and move toward the neutral axis, which results in ovalization of the cross-section and a shift in the neutral axis toward the inside of the bend. Due to this shift, the length of the center-line is longer than the neutral axis, along which the tube retains its original length; therefore, there is an elongation of the tube [7]. Mandrel-rotary draw tube bending provides a controllable and accurate method of bending tube into complex shapes and is therefore a common choice for numerically controlled bending of high volume, high accuracy parts.

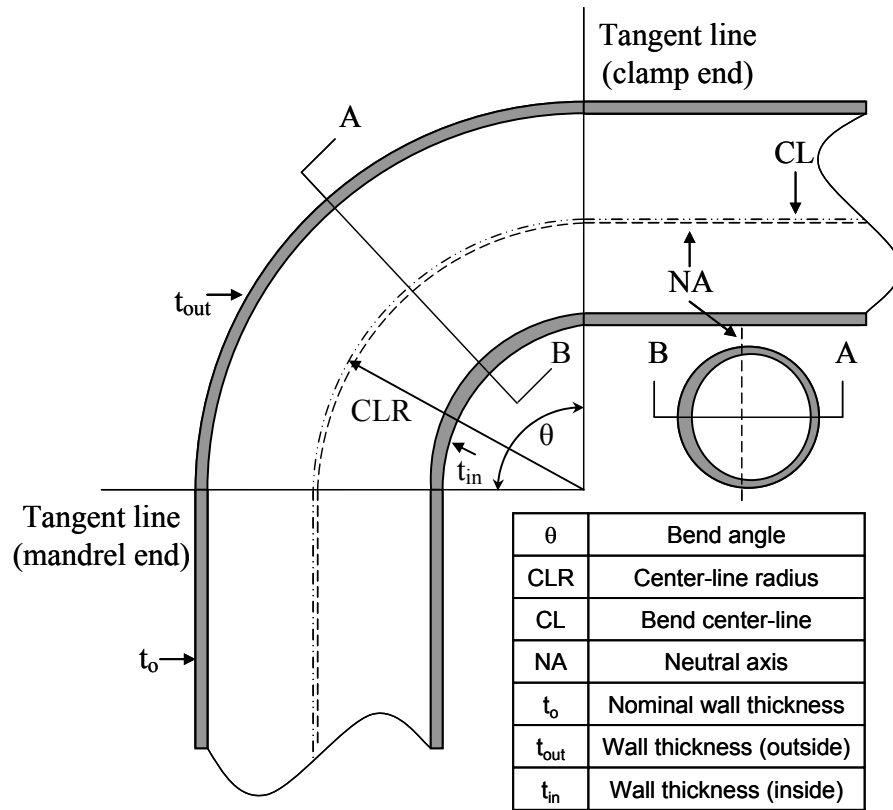


Figure 1.5: Schematic depicting bending terminology used to describe bent tubes.

1.3 Significant Contributions to Rotary Draw Tube Bending

1.3.1 Tube Characteristics and Limitations

The main parameters defining a tube bending operation are: (i) the tube material characteristics; (ii) the tube outside diameter; (iii) the wall thickness; (iv) the center-line radius of bend; and (v) the bend angle. Two key factors are commonly used to determine the feasibility of the bending process and tooling selection: (i) the wall factor; and, (ii) the bend factor [7,8]. The wall factor refers to the ratio of tube outer diameter to the tube thickness (OD/t), while the bend factor is the R/D ratio. The limiting bend radius (LBR) is often used to determine the bendability for a specific value of the wall factor, the details of which are given by Gillanders [9]. The limiting bend radius ultimately depends on the total elongation of the tube material and the tooling design. A typical “safe” design guideline for the bending radius is that it be greater than two times the outer diameter of the tube [7]; however, extreme values of 0.7 times the tube outer diameter have been reported [10]. Guidelines for proper selection of bend tooling material and geometry are provided by [7,8].

1.3.2 Effect of a Mandrel on Ovalization, Thinning and Wrinkling

Bending with a mandrel reduces ovalization of the tube cross-section and assists in the prevention of buckles or wrinkles on the inside of the bend [4,5,11,12,13]. There are a wide variety of mandrels that may be used in bending, depending on the R/D ratio and wall factor (outer diameter of tube/wall thickness), which are further discussed in [8]. Guidelines for the selection and use of mandrel types are given by Luk'yanov *et al.* [14] and tube bend tooling suppliers [8].

Wrinkling in tube bending is a phenomenon resulting from the compressive stresses at the inside of the bend reaching the buckling point and thus collapsing the tube wall. Wrinkling becomes a larger concern for thin walled tubes and tight bend radii. Bending without a mandrel can result in buckling or wrinkling of the tube, especially if a wiper die is not used. Traditionally, the wiper die suppresses buckling and wrinkling on the compressive side (inside of the bend) of the tube during bending by preventing the compressed tube wall from buckling and/or wrinkling. Friction between the wiper die and the tube also retards material flow into the bend region, which reduces the compressive strains on the inside of the bend. The effectiveness of the wiper die is largely dependant on the amount of clamping force and the axial displacement of the pressure die. High boost increases the compressive strains and the likelihood of wrinkling because more material is pushed into the bend. In contrast, high pressure die clamping load increases friction at the wiper die interface, thus further retarding material flow and suppressing wrinkling.

Yang *et al.* [4] investigated bending of 48 mm outer diameter thin-wall low-carbon steel tubes at R/D ratios of 1.15, 1.35 and 1.58 using a rotary draw bender. In this work, they report that although the use of a mandrel limited ovalization and collapse of the tube, the thickness reduction in the tube wall was greater when using a mandrel. In work by Trana [13], it was found that changing from a solid cylindrical mandrel to a mandrel with balls connected by links, improved formability to allow hydroforming without bursting. Paulsen *et al.* [12] have shown that the anisotropy of a material is a significant factor influencing the cross-sectional distortion when bending with a mandrel.

Another phenomenon associated with the mandrel, known as humping can occur on the outside of the bend. Typically this occurs when the tube is compressed against the balls of a

mandrel. To reduce the appearance of this wrinkling or humping on the outside of the bend, Inoue and Mellor [11] suggest that the mandrel position should be adjusted such that the leading edge of the base of the mandrel is moved ahead of the bend tangency point by an increasing amount for increasing bend radii. Work by Oliveira *et al.* [5] found that retraction of the mandrel near the end of the bending process “ironed” out wrinkles and removed bumps on the outside of the tube, and that thicker tubes may be bent with a larger mandrel clearance since they are less likely to ovalize and wrinkle along the inside of the bend.

1.3.3 Strains and Work Hardening due to Bending

Pre-strain through cold-working of a material has been shown by several researchers to result in an increase in the local material strength or flow stress [15,16]. Consequently, a material that has undergone pre-straining will have a higher yield stress upon subsequent deformation than in its undeformed state. Therefore, it is important to consider and quantify the level of pre-strain in a material due to the bending operation since it will affect the local strength properties of the bend region in subsequent processing, such as hydroforming or crash.

Local strains in bent tubes have been shown by Oliveira *et al.* [5,6], Dwyer *et al.* [17], Dymant *et al.* [18] and Barldelcik *et al.* [19,20] to be mainly governed by the bend severity and level of boost in bending. They found that the local strains in bent tubes are reduced through increased levels of boost and bending at larger R/D ratios. More specifically, the level of axial strain along the outside of a pre-bent tube increases by approximately 4-5% strain when bending at an R/D ratio of 2.0 as opposed to 2.5 in EN-AW5018 aluminium alloy [5,6], DQAK [18] and DP600 steel tubes [19,20]. Minimal changes in hoop strain were measured and greater thinning was observed on the outside of the bends for the smaller R/D ratio. Similarly, Inoue and Mellor [11], and Gholipour *et al.* [21,22] examined bending of stainless steel tube at R/D ratios in the range 4.0 to 1.5, and EN-AW5018 aluminium alloy tubes bent at R/D=2.5 and 2.0, respectively. Inoue and Mellor [11] found that a decrease in the R/D ratio resulted in an increase in axial strain by as much as 8% strain, and that thickness strain increased by up to 4% strain. Gholipour *et al.* [21,22] found that a decrease in the R/D ratio resulted in a 3% increase in the magnitude of thickness and axial strains at the location of greatest tensile strain, but report that the circumferential strain (hoop strain)

did not appreciably change around the outside of the bend. Similar changes in strain with R/D ratio were found along the inside of the bend.

1.3.4 Springback

Springback in tube bending is caused by the extremely complex stress state resulting from the bending process and must be accounted for to obtain correct final part shapes. The inside and outside of the bend experience compressive and tensile stresses, respectively. When the tube is removed from the bend tooling, the elastic components of the stress cause the bend angle to decrease and the bend radius to increase. Consequently, the tube has to be bent to a greater bend angle and smaller radius to compensate for springback. In general, the springback and radial growth of the tube increase with the R/D ratio and wall thickness [7]. A more advanced method of compensating for springback was developed by Wang *et al.* [23], where the final prescribed bend angle is precisely offset using a compensation system that measures the bending moment and bending angle on-line.

Work by Oliveira *et al.* [5,6] on bending of 2 and 3.5 mm EN-AW5018 aluminium alloy tubes found that the amount of springback increased at lower levels of boost and did not change significantly when bending at an R/D ratio of 2.5 and 2.0. Inoue and Mellor [11] noted a different effect from Oliveira *et al.* [5,6] when they performed similar experiments on stainless steel tubes over a wider range of R/D ratios: 1.5-4.0. They noted that as the bend radius (or R/D ratio) decreased, angular springback decreased as well.

1.3.5 Lubrication and Friction

Lubricant is normally pumped through the mandrel, which contains channels that feed lubricant to the inside surface of the tube [8]. The application of lubricant to the wiper die in an automated fashion is a more challenging task due to confinement issues; however, wiper dies have been recently developed with built in nozzles to distribute lubricant to the tooling surface [8]. There are numerous available lubricants and coatings for bend tooling, all of which claim to provide excellent frictional environments for bending; however, there is little in terms of actual published information on lubricants and coatings directed specifically towards tube bending applications. In addition, there is very little specific information

readily available on lubricant properties, such as pressure-viscosity and temperature-viscosity parameters.

Inoue and Mellor [11] performed a parametric study on the strains and mandrel loads during bending of stainless steel tubes using three lubricants. They reported up to a 20% decrease in thickness due to lubricant substitution and a 40% reduction in mandrel tension.

Oliveira *et al.* [24] performed a parametric study on various lubricants for bending AKDQ galvanized steel and EN-AW5018 aluminium tubes. The mandrel load and the bend head torque were recorded as a function of lubricant and displayed similar trends to the results of Inoue and Mellor [11]. Interestingly, Oliveira *et al.* [24] reported that the optimum lubricant for steel performed poorly on the aluminium samples, and *vice versa*. They also noted that material pick-up on the mandrel is common when bending aluminium tubes, and that this pick-up likely changes the clearance between the mandrel and the tube, reducing the quality of the bend. Certain lubricants are able to protect against this build-up better than others [24].

1.3.6 Process Variables in Bending

There have been few attempts to measure process variables during the rotary draw bending process; the earliest attempt was by Inoue and Mellor [11], who recorded the bend head torque and the tension in the mandrel rod (Figure 1.4) during bending. They found that the mandrel load increased by about 100% for a change in R/D ratio from 4.0 to 1.5.

Oliveira *et al.* [5,6,24], Dwyer *et al.* [17], and Dymant *et al.* [18,25] have all monitored the process variables during the tube bending process using an Eagle EPT-75 fully instrumented mandrel-rotary draw tube bender at the University of Waterloo. In particular, load and displacement data on the bend die, pressure die, clamp die and mandrel were recorded. The process variables have been found to be very sensitive to tooling set-up, lubrication conditions, bend radius, tube thickness, boost force and material type [11,24]. Applying higher upsetting axial forces (commonly known as boost [6,19,20,25]) on the tube will reduce the amount of bend die torque and thinning during bending [6,11,25].

1.3.7 Boost

An effective way to control the thickness and strain levels in the tube during the bending process is to apply either a tensile or compressive axial force to the portion of the tube being bent. This technique is generally known as “boost” and takes advantage of the superposition of compressive axial stresses on the bending stresses in the longitudinal direction.

To apply an axial boost force on the tube during bending, there are three types of boost conditions that may be enforced within either a displacement- or load-controlled scheme: (i) frictional boost; (ii) boost-block loading; and, (iii) independent collet boost application, as depicted in Figure 1.6. Frictional boost refers to the condition under which the frictional forces from the pressure die movement in the axial direction push the tube into the bend. The second condition utilizes an additional boost-block fixture attached to the pressure die that pushes directly on the end of the tube. Lastly, the independent collet boost condition utilizes an additional actuator that pushes directly on the back of the tube independently from the axial pressure die displacement. For the first two conditions, boost is defined as the ratio of the axial pressure die displacement (δ_{pd}) to the tangential displacement of a point on the center-line radius (CLR) of the bend die [6,18,26]. The bend die rotates by an angle θ , thus the boost ratio is given by

$$Boost = \frac{\delta_{pd}}{\theta * CLR} \quad (1.1)$$

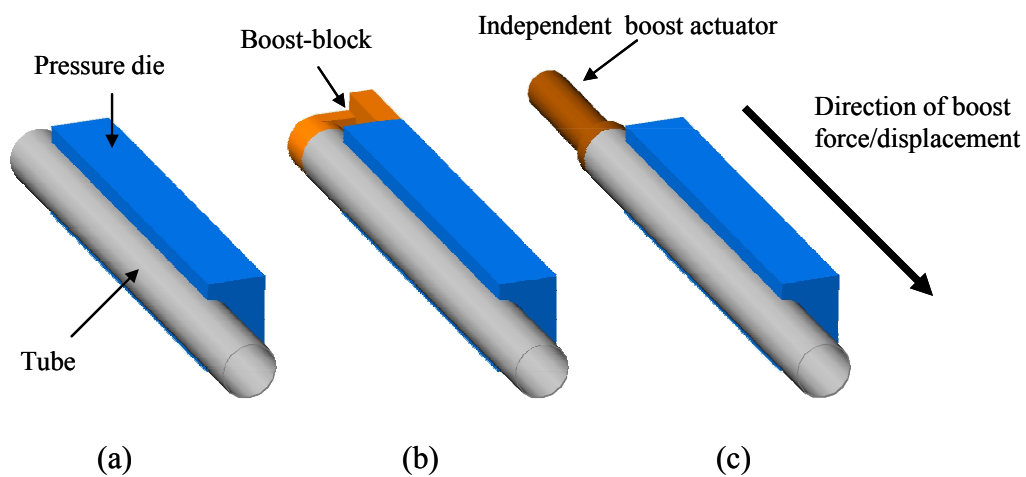


Figure 1.6: Three methods of providing boost during bending: (a) frictional boost; (b) boost block; and, (c) independent collet boost.

Boost is often expressed as a percentage; hence 100% boost refers to the condition when the pressure die velocity is equal to the tangential velocity of the bend die. The independent collet boost, can be independent of the other tools and would therefore be expressed in terms of load or displacement.

Inoue and Mellor [11] were among the earliest researchers to investigate the effect of boost during rotary draw bending by using a frictional boost condition. Since then, Oliveira *et al.* [6], Dymant [25], Stachowicz [27] and Bardelcik [19,20] have shown that increased levels of boost reduces wall thinning and strain on the outside of the bend, which could potentially increase the residual ductility available for subsequent forming operations.

1.3.8 Significant Contributions to the Analytical and Numerical Modelling of Tube Bending

Normani [26] found that analytical studies predicting the strains and stresses during tube bending are rather limited. There is little work that considers the membrane strain due to axial boost force in processes such as rotary draw bending. Despite these limitations, the mathematical developments in the literature do prove useful for giving a good physical understanding of the tube-bending problem, and how one can approach its solution from a mathematical point of view [26].

In practice, the simulation of the bending process is often accomplished using so-called one-step solvers to obtain estimates of thickness change and strain within the tube prior to a hydroforming operation. However, several investigations into the predictive ability of these one-step solvers have shown significant inaccuracies concerning the wall thickness and strains [26]. With improvements in contact algorithms and computer processing technology, explicit and implicit finite element techniques have been used quite successfully for the simulation of various bending processes [6,7,17,18,21,25,26,28,29].

Models of mandrel-rotary draw tube bending using LS-DYNA [30,31], an explicit dynamic finite element code, have been developed by a number of researchers and have provided predictions of the final shape, thickness and strains in tubes that are in good agreement with experimental results [5,6,17,18,21,26,32,33,34]. Different measures of validation have been adopted to compare these models to corresponding experimental tests.

1.4 Hydroforming

A typical tubular hydroforming process sequence is shown in Figure 1.7a. The tube, which is often pre-bent, is first placed within the die and, upon die closure, the end-seals are pressed into the ends of the tube to begin the pressurization sequence. Internal fluid pressure is increased to force material into the deformation zones within the die. During this process, axial feeding and internal pressure are controlled simultaneously, as shown in Figure 1.7b, which increases the material shaping capability of the process tremendously [35]. The axial forces play a significant role in this process by placing the tube under compressive axial stresses to increase ductility. Very large pressures (approximately 200 MPa) are typically required to form small corner radii at the end of the process due to increased work hardening of the material and high corner radius to wall thickness ratio (r/t) in those local regions. Due to the large pressures at this later stage, it is not possible to axially feed additional material into the deformation zone due to large frictional forces [36]. Thus, the die closure process is often used as a pre-forming process to pre-shape the tube in preparation for hydroforming.

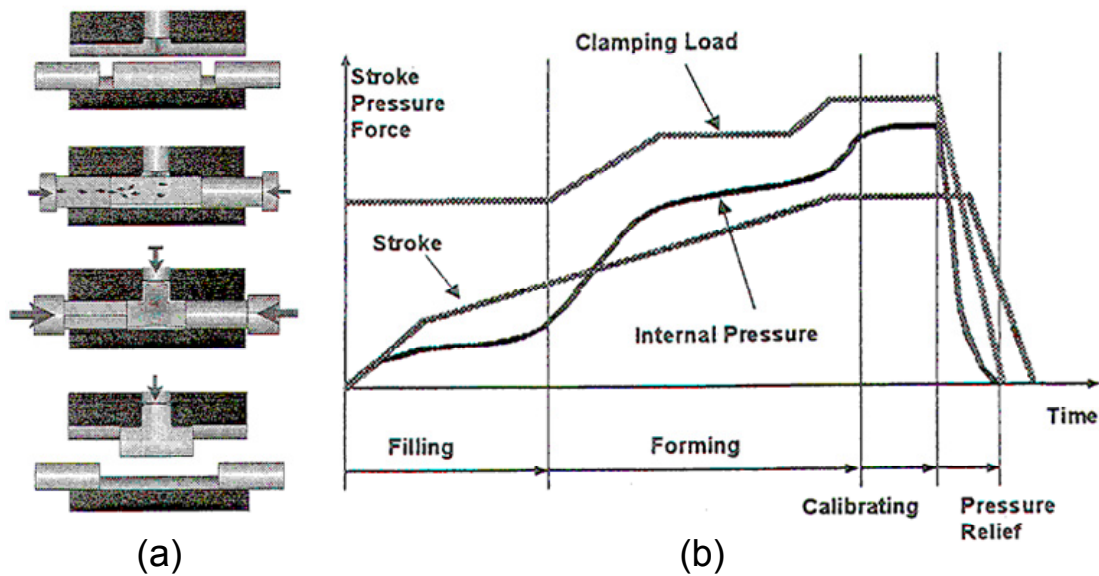


Figure 1.7: (a) Typical hydroforming process sequence; and, (b) variation of internal pressure, axial feeding and stroke during hydroforming [36].

The hydroforming process offers several advantages over conventional metal stamping processes. The main advantages include: part consolidation, weight reduction, improved structural strength and stiffness, lower tooling costs due to fewer numbers of parts to be

produced, tight dimensional tolerances, low springback and reduced scrap [7,36,37]. The disadvantages to the hydroforming process include slow cycle time, high equipment cost and a lack of extensive knowledge base for process and tool design [36]. Consequently, computer simulation techniques provide an important means to provide insight into control strategies for axial feed and internal pressure sequencing to improve the overall effectiveness of the process.

A review of the significant contributions to the hydroforming process is presented. In particular, contributions with respect to hydroforming tooling, pressurization and end-feed, and lubricant and friction are discussed. The “so-called” low-pressure hydroforming process is then presented followed by a review of research contributions examining the interaction between tube bending and hydroforming.

1.4.1 Significant Contributions to the Hydroforming Process

A technological review of the hydroforming process, from its early years to recent dates is given by Koc and Altan [38], on various topics such as material, tribology, equipment, and tooling, some of which is also considered herein. Dohmann and Hartl [39] provide an overview of the fundamental principles of hydroforming processes and their variants. The most significant conclusion they make is that hydroforming has moved into many different applications over the past decades [39]. The technology available to produce more complex shaped parts, with favourable strength, has grown. The key contributions to hydroforming technology can be categorized into three main areas: (i) tooling; (ii) pressurization and end-feed scheduling; and, (iii) lubricant and friction.

1.4.1.1 Tooling and Workpiece Properties

Tooling and fixtures used in the hydroforming process include: the upper and lower dies, the die holder, end-plugs for sealing, actuators for end-feed, the clamping cylinder for opening and closing the die, and cylinder holders to align and react the axial forces during end-feed. In hydroforming, as in many other forming processes, the dies are at the heart of the manufacturing process. A review of challenges and design guidelines are presented by Leitloff and Pohler [40], and Birkert *et al.* [41].

Asnafi *et al.* [37] examined the tube bending, pre-forming and hydroforming of aluminium side members for Volvo and found that proper alignment of the press table, adaptors and die plays a significant role in the hydroforming process. They identify that buckling in the hydroforming process is attributed to: (i) air between the tool and part during hydroforming; (ii) flexing of the tool, adaptors and press table; (iii) tool matching in another press than actually used; (iv) tool separation; and (v) a combination of factors mentioned above. A number of authors have demonstrated that finite element simulation of the hydroforming process can be an invaluable tool in design of tooling and optimizing process parameters [42,43,44,45,46,47].

A sealing system for hydroforming can be classified under two broad categories: expansion and expansion-upsetting type sealing [48]. In the case of tube expansion only, the sealing is required to withstand the forces to seal the tube. When end-feeding is desired, the sealing has to withstand the sealing force as well as the friction force. Krei [48] presents a number of sealing concepts and classifies them based on their material type: metallic or elastomer seals.

Kridli *et al.* [49] used plane strain finite element analysis to study the effects of the strain-hardening exponent, initial tube wall thickness, and die corner radii on corner-filling and thickness distribution within a straight hydroformed tube, inside a square die cavity. It was concluded that the thickness distribution is a function of the die corner radius and strain-hardening behaviour of the material. A greater amount of variation was observed for lower strain hardening (lower n-value) materials. A tube material with a high strain-hardening exponent can be formed without failure to a smaller die corner radius than a material with a low strain-hardening exponent.

Chow and Yang [50] found formability (the relative ease with which metal can be shaped through plastic deformation) during free expansion to be proportional to the strain hardening n-value and Lankford anisotropy parameter, or r-value, under axial plane stress loading. If the ends of the tubes were fixed, however, the formability was observed to be independent of the r-value. Also, burst pressure increased with increasing anisotropy (r-value), for both free and fixed ends, but decreased with decreasing n-value. Furthermore, they concluded that the formability of the tube was strongly dependent on the load path, demonstrating that the end

feeding condition has a significant effect on the onset of bursting. Work by Xia [51] also supported the claims by Chow and Yang, that material anisotropy plays an important role in the failure development within tubes during hydroforming. Interestingly, Mellor [52] examined the tensile instability of thin-walled tubes and suggests that a given material has the greatest ductility when the ratio of the hoop stress to axial stress is equal to one-half.

1.4.1.2 Pressurization and End-Feed

The internal pressurization of the tube provides the forces responsible for expansion and reshaping of the tube. The hydroforming fluid used by most industrial hydroforming systems is an emulsion of water and oil, which also aids in preventing corrosion [7]. Asnafi *et al.* [37] found that buckles can be prevented during hydroforming by prescribing a small internal pressure during die closure. This small pressure also serves to pre-shape the tube before the high-pressure process begins. Tirosh *et al.* [53] demonstrated that thicker tubes are less likely to buckle prematurely than thinner tubes. Wrinkling of a tube, which is another issue encountered in the hydroforming process, can be caused by excessive axial force and can usually be eliminated by increasing the internal pressure during the expansion process [54]. Bursting or fracture occurs as a result of excessive wall thinning, which can be caused by frictional lock-up of the material as it flows over the die or when the ultimate tensile strength of the material is exceeded during expansion due to excessively high internal pressure [54]. In simulating the hydroforming process using finite element techniques, Ahmegotlu [36] demonstrated that both explicit and implicit techniques could model the process; however, it is important that the load on the elements remain normal [55] to mimic the fluid pressure. Internal pressure is usually prescribed as a pressure versus time function, which can sometimes cause stability problems; however, these may be eliminated by using a rate of change of volume versus time function [36].

A major concern in hydroforming is the investigation of loading paths for axial end-feed as a function of pressurization, over time. There is an operating “window”, as shown in Figure 1.8 [56], in which one can form an ideal part, avoiding: (i) wrinkling due to excessive end-feed; and (ii) excessive thinning (leading to bursting) due to too little end-feed. Such failure predictions and optimal operating “windows” are useful to engineers and designers,

even if based on simple models, since they allow early process optimization. The risk of wrinkling or axial collapse is greatest at the beginning of the hydroforming process.

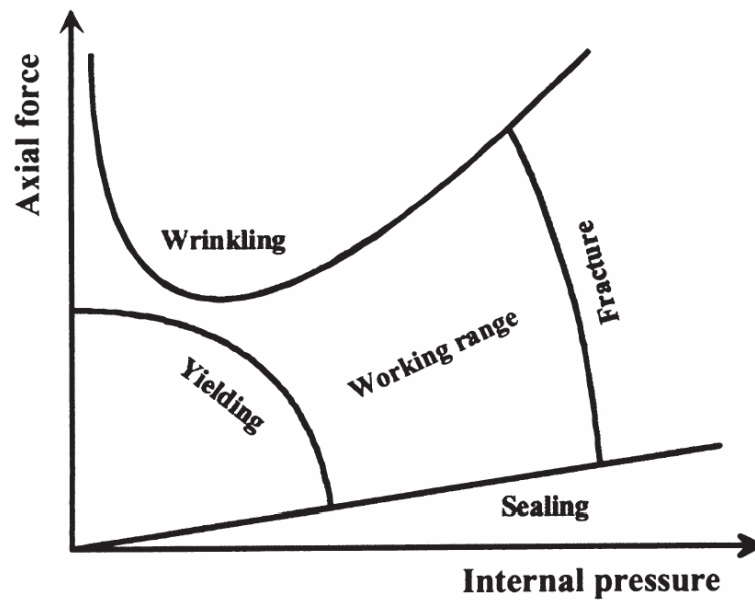


Figure 1.8: The limits and working range in tube hydroforming [56].

End-feed in hydroforming is either force- or stroke-controlled; the choice of either depends on the desired loading path relationship required to optimize formability. MacDonald *et al.* [46,47] investigated the bulge forming of cross-joint components using the finite element method and found that hydroforming with end-feed reduced the thinning and increased the material formability significantly. Asnafi *et al.* [57] found that wall thinning in free-forming can be minimized when the loading path lies between uniaxial tension and pure shear. Determination of the loading path is usually done experimentally; however, the use of simulation tools for optimization has seen some promising development. Abedrabbo *et al.* [58] used an optimization software, HEEDS, in conjunction with LS-DYNA to maximize the formability of a tube by identifying an internal pressure and end-feed rate that satisfies the forming limit diagram.

1.4.1.3 Lubrication and Friction

Lubrication is an important consideration in hydroforming and also one of the least understood from a modeling point of view. Good lubrication conditions allow a tube to reach its final desired expansion and shape in the die, whereas poor lubrication often results in premature failure due to excessive local thinning [37,59,60,61]. The main parameters

affecting the frictional forces in tube hydroforming are the lubricant itself, the tube material (surface roughness and yield strength), the internal pressure and the die surface (surface finish, hardening, coatings).

One technique for measurement of friction that is suitable for hydroforming and tube bending applications is the so-called twist compression test (TCT) [62]. This test considers large interface pressures and sliding distances. Vollertsen and Plancak [63] discuss an alternative approach for determining the coefficient of friction (COF) between die and workpiece. This method is based on the upsetting of a tube and measuring the sliding friction.

1.4.2 The Low-Pressure Process

The so-called “low-pressure” hydroforming process consists of two stages: (i) low pressure die closure; and, (ii) higher-pressure corner expansion. The unique aspect of this process is that the perimeter of the die cavity cross-section is sized to be close to the perimeter of the tube at the beginning of the process; hence, the tube does not fit into the die. During the low-pressure die close, the tube is pressurized to a low pressure such that the fluid-filled tube is supported on the inside to prevent collapse, as shown in Figure 1.9 [64]. The tube undergoes deformation as it is forced to flow into the corner regions of the die without stretching or expansion of the perimeter to fill the die cavity. The corner-radii are formed by deforming the tube wall in a bending mode, whereas in conventional or “high-pressure” hydroforming the deformation mode is tensile and requires an increase in the tube circumference to fill the die cavity. After the low pressure die close, a second higher pressure stage follows in which the pressure within the tube is increased to ensure that the tube completely fills the corners of the die cavity. As a consequence of the lower circumferential strains and reduced work hardening of the material in this process, the pressures associated with this stage are typically much lower than in the high-pressure process, generally less than 83MPa [64]. The low-pressure process typically does not require end-feeding to achieve the final desired shape since there is little or no expansion of the tube. A further advantage of this process is that the lower pressures generate lower frictional conditions which allow the tube to slide more easily along the die surface and into the corner regions; hence reducing thinning and resulting in a more uniform wall thickness. The resulting tube wall thickness varies by only 3-5% with

low-pressure hydroforming, compared to 15-20% thickness reductions using high-pressure hydroforming [65].

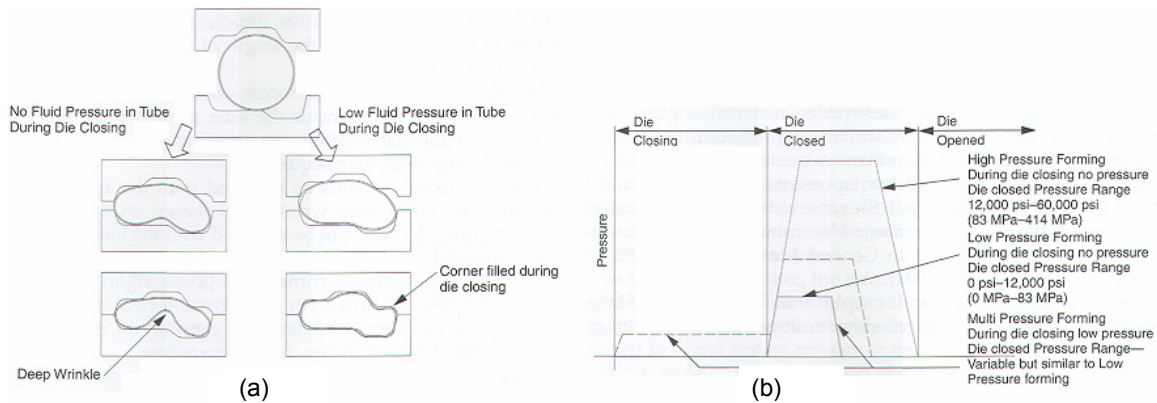


Figure 1.9: (a) Section formation during low, high and multi-pressure hydroforming, with (right) and without (left) water pressure; and, (b) comparative pressure sequences for low, high and multi-pressure hydroforming [64].

The low-pressure hydroforming process is also known as “pressure-sequenced” hydroforming and was developed in the 1980-1990s [66]. There is very little in the literature on the low-pressure process as it is a relatively new technology that had seen little in terms of published research.

Work by Hwang *et al.* [67] represents one of the few studies in low-pressure hydroforming. They used the FEA method to explore the plastic flow pattern of a circular tube that is hydraulically expanded (i.e. high-pressure process), compared to that in tubes crushed into a rectangular cross-section and then expanded using a low-pressure process. Simulation results for thickness distributions, clamping forces, and forming pressures are compared between high and low-pressure processes [67]. They found:

- The maximum forming pressure needed by the low-pressure process is only 5% of the pressure required by high-pressure processes
- The maximum crush force needed in the low-pressure process is about 7% of the clamping force (force required to keep the two die halves together) in the high-pressure process.
- The thickness distribution of the formed product obtained by the low-pressure process is much more uniform than that via the high-pressure expansion process.

1.4.3 Interaction Between Tube Bending and Hydroforming

In hydroforming of complex-shaped parts, a workpiece must often be pre-formed to fit into a shaped die. One such pre-forming operation is the bending of tube using rotary bending, a focus of the proposed research. Clearly, the effect of the pre-forming operation on ductility can be significant in determining the formability of the final hydroformed part. Therefore it can be quite important to adjust forming parameters in such pre-form operations to reduce any negative impact on hydroforming. Of the various tube bending methods, Asnafi *et al* [37] showed that rotary draw bending yielded the best subsequent hydroformability within AA6063-T4 aluminium alloy extruded tube for an underbody side-member.

Pre-bending operations affect the thickness, stress and strain distributions within a tube, which in turn leads to changes in the material hydroformability, as shown by several researchers [4,6,13,17,18,25,59,60,68]. All of these studies serve to demonstrate the need to consider pre-bending effects on the subsequent hydroformability, when developing numerical models of the hydroforming process. For brevity, only some of the more interesting findings are presented here. Yang *et al.* [4] showed that the use of a mandrel in rotary-draw tube bending provides the most favourable properties in bent tubes for the hydroforming process. Trana [13] later found that tube bending with a mandrel with balls resulted in an increase in expansion to burst during hydroforming. He also noted that material data from tensile specimens cut from tube samples instead of sheet properties should be used in simulations of tube bending and hydroforming. A number of researchers [6,11,17,19,20,25,26] have found that rotary bending with boost can reduce work hardening and thinning in the bend region of the part, which is favourable for subsequent hydroforming. It has also been shown that the strain path experienced in bending is significantly different from that during hydroforming, and this change in strain path affects the onset of failure during hydroforming [17,21]. Consequently, the use of a strain-based forming limit diagram may not be appropriate due to large changes in strain path between processes. A stress-based forming limit criterion might be a better approach than the conventional forming limit curve, as proposed by Stoughton [69] and Simha [70,71].

The literature also establishes that finite element simulations of the hydroforming process that consider forming history can provide good predictions of final geometry, thinning and

strains [4,13,17,18,25,37]. Furthermore, numerical models developed by Gholipour *et al.* [21], Lei *et al.* [59] and Kim *et al.* [60] that consider a ductile fracture criterion, were able to accurately predict the failure location during hydroforming, which was shown to be dependant on the inclusion of strains, stresses, thickness changes and damage due to pre-bending.

1.5 Crash Response

In the automotive industry, the understanding of and ability to reliably predict crash response is of vital importance in designing vehicles for the safety of passengers. In the past, analytical methods and experimentation were relied upon heavily to assist design engineers in predicting the crash performance of structures. With increasing computer capacity, numerical methods such as the finite element method have emerged as powerful design tools in optimizing crash response and minimizing design costs, especially with the current push towards automobile weight reduction.

Energy absorbers, such as bumpers and crash boxes are incorporated at the front and rear of the vehicle structure and are used to protect passengers and the structure during impact. These energy absorbers control the dissipation of the automobile kinetic energy during impact, while the force levels are kept sufficiently low to avoid permanent deformation within the rest of the frame. Although these energy absorbers can absorb all the kinetic energy of the vehicle during a low-speed crash, a high-speed crash will activate the crushing of a larger part of the structure in order to absorb all of the energy. With the energy absorbers exhausted, the energy from an impact is converted to work through deformation of the front and side rails of the vehicle in a short period of time, resulting in a dynamic impact [72]. Although most of the studies into the crash performance of structural components have been conducted using quasi-static tests, it is important to also consider the dynamic high-speed crash response of these structures.

During a crash event, structural components will seldom be subjected to either a pure axial or bending collapse, but rather a combination of the two modes. Here, the bending collapse of thin walled extruded tube is reviewed, with an emphasis placed on the s-rail structure. The s-rail usually has an s-shape to avoid interference with other automotive

components, such as the engine, fuel-tank, and wheels, and is shown in Figure 1.1 and Figure 1.3. These members play a critical role in absorbing crash energy during frontal or rear collisions [73].

1.5.1 Significant Contributions to Understanding the Bending Mode of Collapse in S-Rails

1.5.1.1 Bending Collapse in a Section

The uniaxial bending collapse of thin walled rectangular and square section tubes was investigated theoretically and experimentally by Kecman [74]. A limit analysis technique was employed and a set of formulae relating the hinge moment and the associated angle of rotation was derived to predict the hinge moment-rotation curves and energy absorbed during uniaxial bending collapse. A similar technique was developed independently by Abramowicz [75]. The limiting moment that a thin-walled tube can support is brought about by local buckling of the compression wall of the section. This buckling may or may not be accompanied by plastic deformation, depending on the thickness-to-side ratio of the section walls and material properties [76]. The post-buckling behaviour of thin walled tubes involves local folding and rolling of the wall material in a hinge mechanism of “yield” lines at the collapsed hinge. It is characterized by a considerable reduction of resisting moment as hinge rotation is increased [76]. Brown and Tidbury [77] extended this work and examined the collapse of thin-walled square and rectangular cross-section beams in biaxial bending. Due to the limited scope of their research, only narrow conclusions were made: (i) the failure loci for both sections lay near or partially within the fully plastic region and are similar to each other; and, (ii) the sections appeared to obey the normality condition at failure.

Chen and Wierzbicki [78] examined the torsional collapse of square and rectangular cross-section columns both analytically and numerically. The evolution of the cross-sectional shape is shown in Figure 1.10 [78]. Three successive deformation phases were identified based on the physical understanding of the collapse behaviour: (i) pre-buckling; (ii) post-buckling; and, (iii) collapse spreading. They identified that in real applications, torsion seldom acts alone since it is usually combined with compression and/or bending.

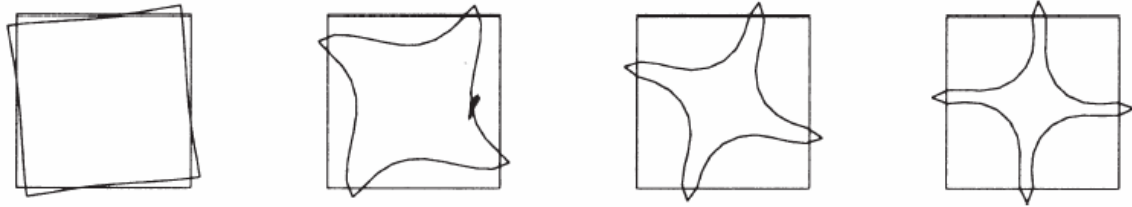


Figure 1.10: Evolution in shape of a square thin-walled column under torsional load [78].

Reyes *et al.* [72] examined the crash response of AA6060-T4 aluminium alloy square cross-section extrusions subjected to oblique loading, through quasi-static experiments and simulation. The extrusions under oblique loads reached the initial peak load when the first lobe formed. Thereafter, the collapse mode switched to global bending and no additional lobes were created, with the exception of the loading case where the oblique loading angle was less than 5-degrees, which was closest to the axial loading condition. Both one and two lobes were observed to form under this condition; thus, the deformation mode depends on load angle and thickness. The prediction of force versus displacement using explicit dynamic modelling techniques underestimated the softening region of the force versus displacement response, resulting in a conservative prediction of the mean loads. The energy absorption drops drastically for load angles greater than 5-degrees and for further increasing load angles (greater than 15-degrees), the absorbed energy does not change significantly. The most dominant parameter in energy absorption was the thickness, which became more pronounced with increasing load angle. The influence of length and temper are also quite important, but are independent of the load angle. The velocity of the impact had no effect on the mean load when the column was dominated by bending.

It is necessary to predict the actual collapse mode that is activated in a structural member in order to design for good crashworthiness. Tubular members are often designed to collapse progressively throughout the entire crushing process. It is important to estimate the factor of safety against a global collapse mode that would otherwise lead to large deformations with potentially catastrophic consequences. Abramowicz *et al.* [79] and Jones [80] addressed this concern by examining the transition from initial global bending to progressive buckling of tubes loaded statically and dynamically in the axial direction, as shown in Figure 1.11 [80]. For a given cross-section, as the length of the column increases, the deformation mode changes from progressive local folding to global buckling.

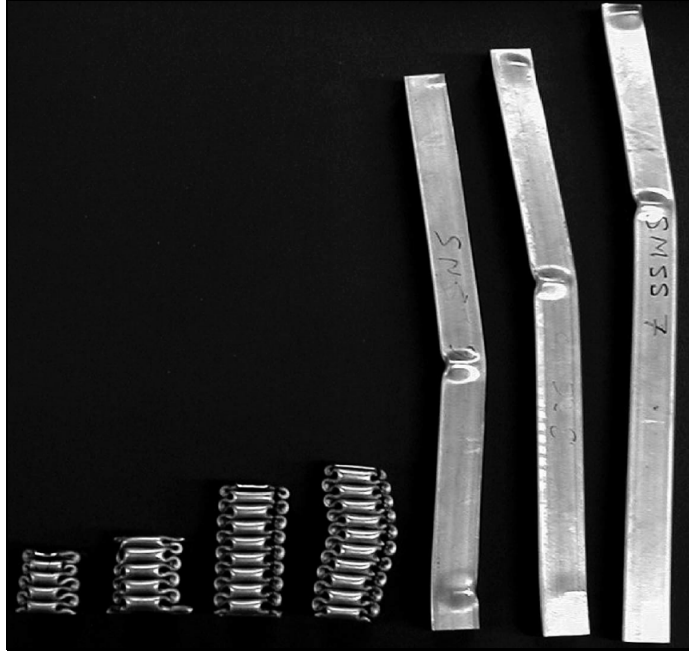


Figure 1.11: Static collapse modes of mild steel square columns with the L/C ratio increasing from left to right. (L is the length of the column and C is the width of a side face of the square column) [80].

1.5.1.2 S-Rail Collapse

Most of the studies on s-rails have been performed on columns made from extrusions or welded sheet metal components. Steel s-rails have been investigated more so than aluminium and there has been no study found in the literature into the crash response of seam welded and hydroformed aluminium alloy tube, which is the focus of the research presented herein.

Chung *et al.* [81] investigated the crash performance of an aluminium automotive space-frame in a frontal impact barrier test through simulation and experiment. The energy absorption of the s-rail component of the frame represented 25% of the total energy absorbed; whereas the bumper absorbed about 15%, from which they concluded that the s-rail component plays a significant role in the crashworthiness of the vehicle structure.

Ni [82] used a numerical approach based on a lumped mass model to investigate the impact response of steel and AA6061-T6 square cross-section s-rails under high-speed impact. Both the analytical and experimental results for the force versus displacement response indicate that the resistance to collapse dropped significantly after the initial fold of

the rail. The reason for this drop may be considered to be due to: (i) the change of curvature of the s-rail after collapse, which causes the previously compressed fibers of the cross-section to be in tension, hence increasing the bending moments but decreasing the axial forces; and, (ii) the local cross-sectional collapse in the bend region which reduces the stiffness of the structure considerably. Ni [82] neglected the effects of section changes in analytical analyses for the purpose of engineering approximation. This was done because there was an inherent difficulty in relating parameters of the local sectional collapse to the global deformation of the frame. Ni [82] found that by not considering the effect of sectional changes, a significant over-prediction of the crush force could result. With the advancement of computational efficiency, the effect of changes in cross-sectional shape on the crush response of s-rails is easily considered using finite element techniques [5,73,83,84].

Reid [85] examined the sensitivity of steel s-rails to thickness and material in crash conditions. A general design guideline for crash response was suggested as follows: for every 10% change in thickness there is approximately a 14% change in energy absorption capability for a crushing s-rail, while for every 10% change in material strength there is approximately a 7% change in energy absorption.

Nishimura *et al.* [86] examined two- and three-dimensional spot-welded s-rails, and demonstrated the accuracy of numerical simulations in predicting the dynamic impact response. The resulting force-deflection response consisted of an initial peak load followed by a gradual reduction in force. It was also shown that an added mass along the rail can change the deformation pattern and that increasing the thickness can increase the peak load.

Kim and Wierzbicki [83] examined the crushing behaviour of thin-walled rectangular cross-section three-dimensional s-rails subjected to complex loading cases by applying techniques developed in previous work [73]. Up to this point, the major difficulties in developing an analytical solution to this problem were the presence of vertical and horizontal eccentricities associated with the three-dimensional s-rail, which results in axial forces, bending and torsion on the s-rail. Consequently, most of the published work on this subject was either experimental or numerical [87,88,89]. The analytical solution of the crushing resistance was derived and the two types of deformation modes, global bending and progressive buckling, were identified using the analysis of the fully plastic bending moment

with a different orientation angle of the bending axis. It was shown that the critical aspect ratio of the rectangular cross-section separating the two deformation modes is 1.36. The analytical predictions were verified through finite element simulation.

1.5.1.3 Stiffening of S-Rails

In order to achieve greater weight efficiency in energy absorption for crash members in vehicle structures such as an s-rail, the concept of introducing light-weight metal filler into the structure enhances the energy absorption capacity considerably [90,91,92,93,94,95,96]. Low density aluminium honeycomb or foam is generally 5-20% lighter than solid aluminium [97]. However, it is the current high cost of this filler material that limits its use in the automotive industry; nonetheless, there remained a significant amount of work in this area. Santosa *et al.* [98] studied the effect of foam filling on the bending crush resistance of a thin walled beam through quasi-static three point bending simulations and experiments. It was found that the foam filler retards the inward sectional collapse at the compressive flange and changes the crushing mode from a single stationary fold to a multiple propagating fold and therefore prevents the drop in the load carrying capacity due to local sectional collapse. Kim and Wierzbicki [73] investigated the effect of cross-sectional shape of hat-type cross-sections on the crush resistance of a steel s-rail. The concept of foam-filling with 3 MPa aluminium foam was applied to the s-rail and the specific energy absorption increased by a factor of 2.84. Through simulation they also found that an s-rail could absorb up to 200% more energy than a typical double-cell profile member when an internal stiffener is diagonally positioned.

1.5.2 Interaction Between Forming History and Crash Response of S-Rails

A review of the interaction between forming and crash response of s-rails manufactured by tube bending and hydroforming is focused upon herein. Within the literature there exists only limited experimental and numerical investigations that consider the effects of forming on the subsequent crash response of structural components. Dutton *et al.* [99,100] have investigated the effects of forming history, such as thinning, strains and stresses, on the crushing behaviour of a steel side-rail through simulation. The effects of thinning and residual stresses due to forming were isolated to determine the effects on crush response. Consideration of thickness changes and residual stresses from the forming operation did not

significantly affect the crush distance of the s-rail; however, consideration of thickness changes within the crush simulation did result in a slightly stiffer crushing response due to thickening of the tube on the inside of the bends. The plastic strains from the bending and pre-forming operations had a significant effect on the crushing response, since the crush distance was reduced by 45% over the base-line case. Oliveira *et al.* [5] found that accounting for the work hardening and thickness changes in the material due to the bending process in models of the crash event increased the peak force by 25-30% and the energy at the point of tearing by 18%. In addition, Ryou *et al.* [101] found that including the forming history of a stamped aluminium alloy s-shaped component in a crush simulation led to a peak acceleration prediction that was 20% higher than a model that did not account for forming history effects.

Using finite element techniques, Kaufman *et al.* [102] also found consideration of the s-rail forming effects resulted in a considerably different force versus deflection response during crash. In addition, the strain rate sensitivity of aluminium alloy tube has been often neglected in simulation, as there is evidence that this material is strain rate insensitive at elevated strain rates [82,103,104].

1.6 Summary

The foregoing review of the literature pertinent to tube bending and hydroforming, as well as structural crash response, has revealed a number of areas requiring further work. Most of the studies examining forming and crash response of tube have been conducted on extruded tubes. Further investigation of seam welded aluminium alloy tube in bending, hydroforming and crash is necessary as this product gains greater acceptance within the automotive industry. There have been a number of studies examining the effect of rotary draw tube bending on the hydroformability of steel tubes; however only a few studies have been conducted on aluminium alloys. Most of these studies have examined the high-pressure hydroforming process and the effect of bending parameters on the low-pressure process has seen little research. The effect of the tube bending process on the formability of tubes during high-pressure hydroforming has been shown to be significant. In particular, the thinning, work hardening and severe changes in strain path all play a significant role in the

hydroformability of a given alloy. There is a lack of research that has focused on the low-pressure hydroforming process itself, which is one aim of the work comprising this thesis.

There have not been any experimental investigations into the effects of rotary draw bending and hydroforming on the crash response of s-rails, which is needed to provide pertinent information for better crashworthiness design. Numerical simulation techniques have been used to investigate some aspects of forming effects on the crash response of stamped structures; while these studies have provided some insight, they are limited, since the models have never been validated experimentally. There have been no publications that have isolated the effect of hydroforming on the crash response of s-rail structures. Hence, examination of the hydroforming processes that can be applied to an s-rail would represent a unique contribution to the area of crash response. Thus, the primary objective of the research presented herein is to determine the interaction between tube bending and hydroforming on the crash response of wrought seam-welded 5XXX-series aluminium alloy tubes, and to identify the parameters that govern the crash response of s-rail structures.

In order to meet the objectives of this research, a large parametric study has been conducted that considers the role of a number of parameters that potentially govern the crash response of s-rails. The material and tube stock parameters examined include:

- the tube thickness; and,
- the tube strength (alloy);

while the forming process parameters include:

- the bend severity and boost;
- the hydroforming process (low-pressure versus high-pressure); and,
- the as-hydroformed s-rail cross-section.

These tube and material parameters, as well as the forming process parameters, are examined using both experimental and numerical modelling programmes. Not all of the parameters could be addressed directly within the experiments due to either limitations of the tube bender and the clamping capacity of the hydroforming press, as well as the availability (and cost) of tooling to examine many different s-rail geometries. A detailed description of the

experimental programme undertaken as part of this parametric study is outlined in Chapter 2. The numerical modelling programme, outlined in Chapter 3, is used to further examine the parameters investigated experimentally, which allows validation of the model and provides further insight into the variables influencing the crash response. In addition, the numerical models are used to investigate the effects of boost and the nature of the hydroforming process (ie. low- versus high-pressure), as well as additional variables that affect the crash response of s-rails such as cross-section and geometry. The results from the experiments are presented in Chapter 4, followed by the results from the supporting numerical simulations in Chapter 5. The results from simulations of s-rail crash scenarios that go beyond the scope of the experiments are presented in Chapter 6. A thorough discussion of the parameters governing the crash response of s-rails and preliminary design guidelines for optimizing crash response are given in Chapter 7. Finally, the conclusions and recommendations stemming from this work are presented in Chapter 8.

Chapter 2

Experiments

The overall aim of the experimental program undertaken as part of this research is to evaluate and understand the pertinent material, process and design variables that govern the crash response of s-rail structures. Crash experiments were conducted simultaneously on two opposing s-rails, shown in Figure 2.1, using a deceleration sled test. The crash response is quantified based on the force and absorbed energy versus time, measured using an arrangement of load cells and a high speed data acquisition system.

A chart outlining the research strategy, including the flow of the as-received tube stock through the s-rail fabrication and crash testing steps, is shown in Figure 2.2. The experimental plan was developed to consider the entire s-rail fabrication route, beginning with tube bending and hydroforming experiments, and followed by crash tests. The materials considered in this research include 3 mm AA5754 and 2 and 3.5 mm EN-AW5018. Material characterization tests were also conducted on the as-received aluminium alloy tubes and the sheet stock from which the tubes were fabricated. The material characterization data was used to determine the constitutive response of the tubes and then used as an input for the numerical models that are presented in Chapter 3.

Three bend severities were examined in the tube bending experiments since the bend regions of the s-rail are important locations in which two of the three hinges form (Figure 1.3). Varying the severity of the bends in the s-rail causes local changes in geometry, thickness, work hardening and residual stress, which potentially influence the behaviour of the hinge during impact. The hydroforming experiments utilized a low-pressure process that changed the s-rail cross-section from round to square. Note that high-pressure hydroforming

experiments were not performed since the cost of the additional acquisition of tooling and tube stock to allow hydroforming of s-rails with circumferential expansion was well beyond the budget available; however the high-pressure hydroforming process was investigated through numerical simulation, as presented in Section 6.3. Finally, crash experiments were conducted on two types of s-rails: (i) non-hydroformed and (ii) hydroformed, which allowed the effect of the hydroforming operation on the crash response to be isolated and assessed.

In addition to investigating the effects of forming variables on the crash response of s-rails, the effects of material strength and initial thickness of the as-received tube were investigated through the three different tube stock materials. To further examine the effects of material strength on the crash response, one-half of the formed s-rails were fully annealed to the O-temper to recover the as-received material properties. The anneal also allows the effects of residual stress and work hardening to be isolated from the effect of thickness change due to the bending and hydroforming.

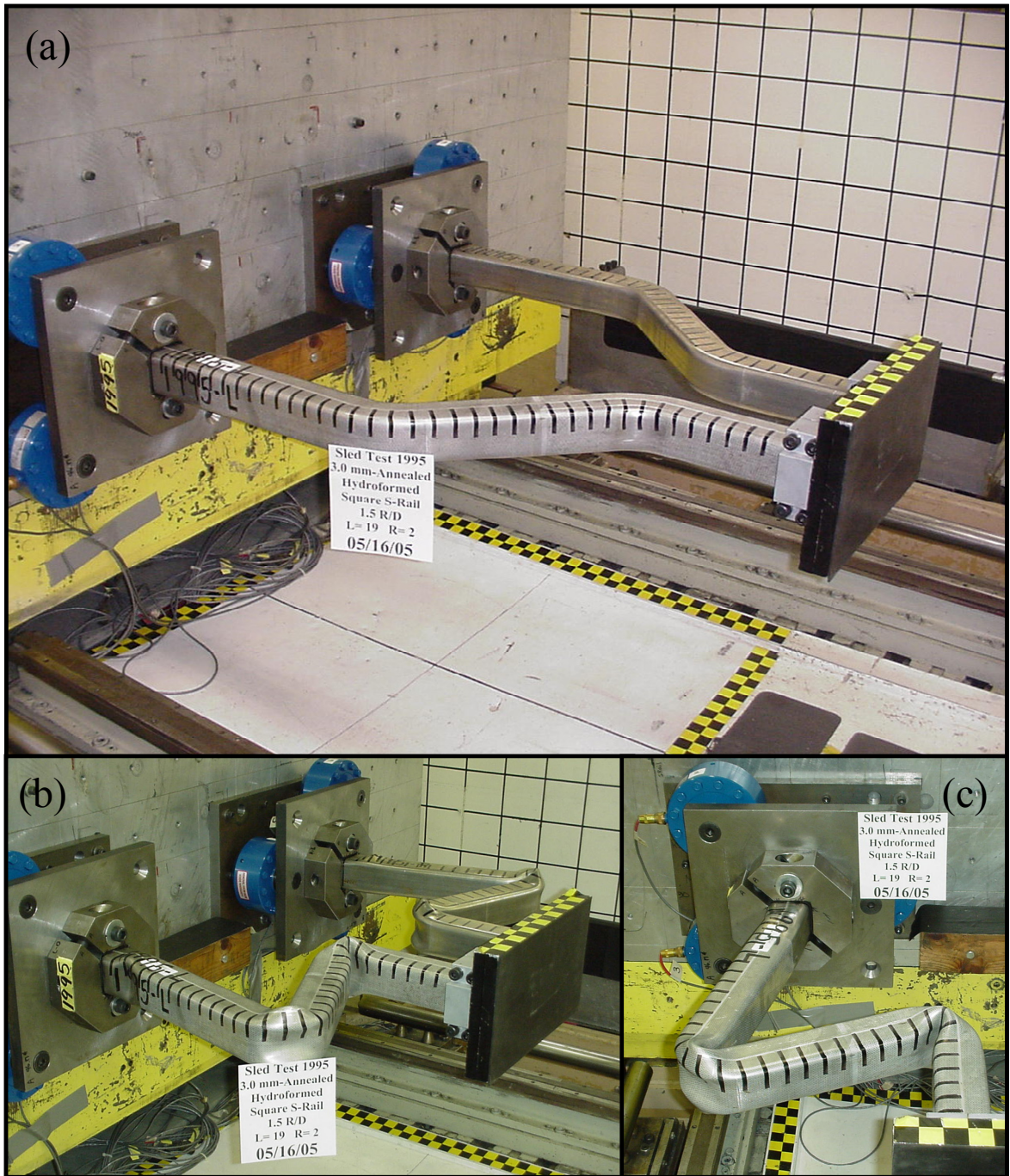


Figure 2.1: Photos of hydroformed s-rail crash structure set-up: (a) before impact; (b) after impact; and, (c) close-up of s-rail after impact.

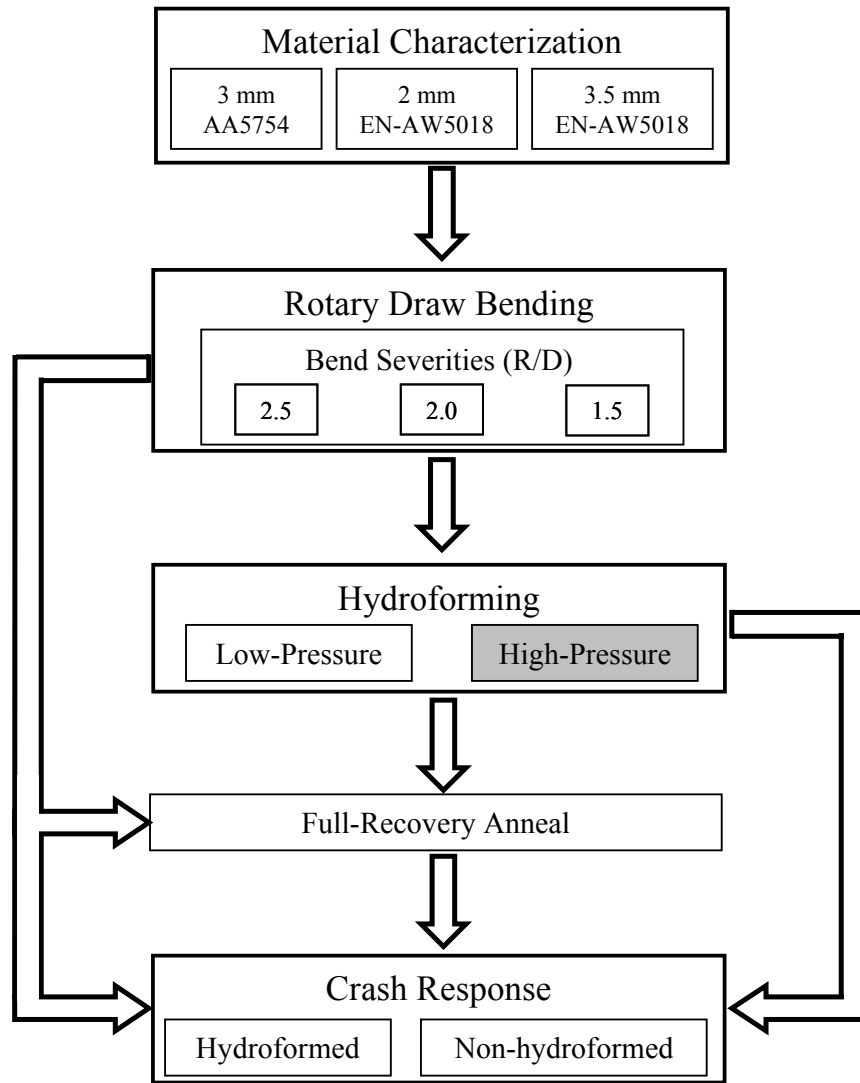


Figure 2.2: Flow chart of experimental program. Note that the high-pressure process was not considered in the experiments (model-only).

The data generated from the experiments allows assessment of the predictive ability of the numerical models developed in this research. The validated models are then used to provide additional insight into the s-rail response by considering crash scenarios outside of the test matrix.

The remainder of this chapter includes a detailed description of the adopted test matrix, followed by the material characterization results. The tube bending, hydroforming and crash experiments are presented thereafter. This chapter concludes with an assessment of the effects of the annealing process on the properties of the non-hydroformed and hydroformed s-rails.

2.1 S-rail Geometry and Test Matrix

The hydroformed and non-hydroformed s-rails examined in this work incorporate two 45-degree bends and are shown in Figure 2.3a. The s-rail is divided into five distinct sections, labeled A-E, and the geometrical properties corresponding to each bend severity or R/D ratio (ratio of centre-line bend radius to tube outer diameter) are shown in Figure 2.3b and listed in Table 2.1. The cross-sections of the non-hydroformed and hydroformed s-rails are shown in Figure 2.4. The hydroformed s-rail has a 65.5 mm square cross-section with a section corner-radius of approximately 12 mm, while the non-hydroformed s-rail has a circular cross-section with a 76.2 mm outer diameter. The size of the s-rail was chosen to be representative of a structural component in a small sized vehicle.

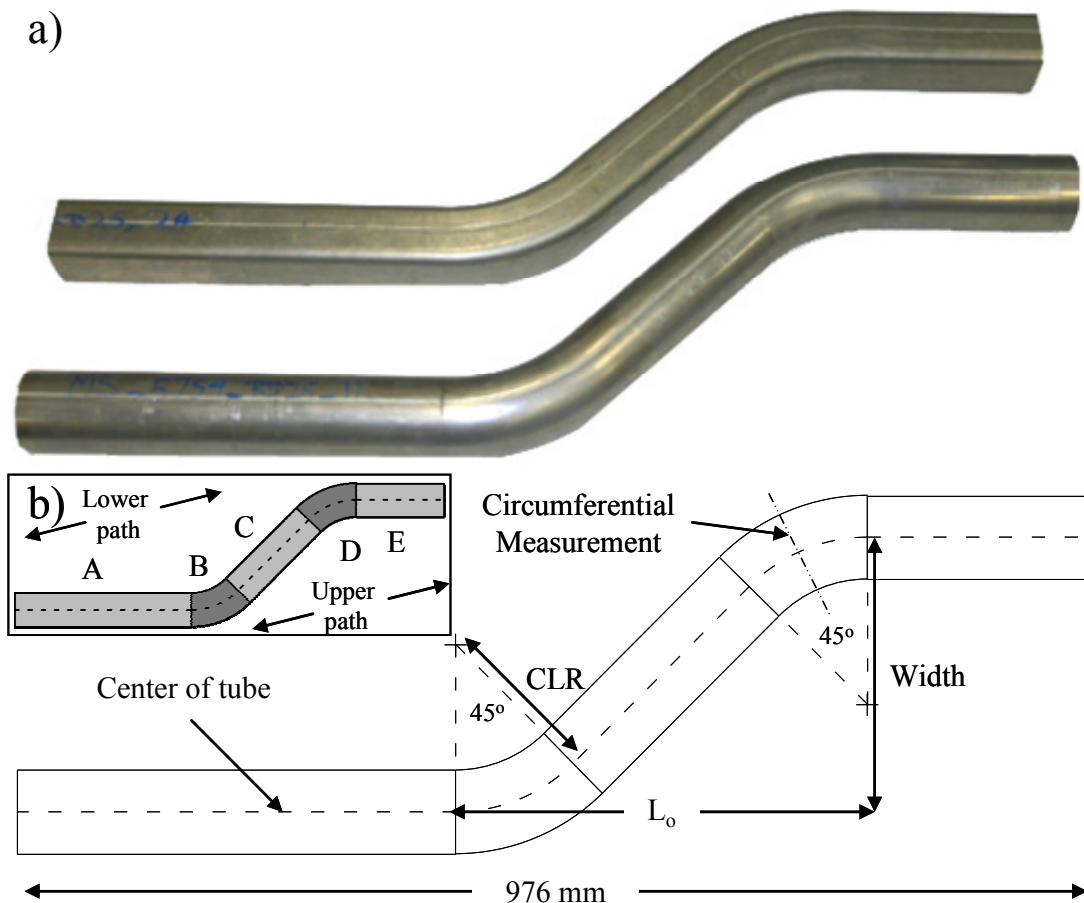


Figure 2.3: (a) Hydroformed (top) and non-hydroformed s-rail (bottom); and, (b) various sections comprising the s-rail.

Table 2.1: S-rail dimensions for each R/D ratio. Units are in millimeters.

R/D Ratio	Width	L _o	Section length		
			A	C	E
2.5 (CLR=190.5)	250	408	384	195.7	184
2.0 (CLR=152.4)	250	376	400	227.0	200
1.5 (CLR=114.3)	250	344	416	260.7	216

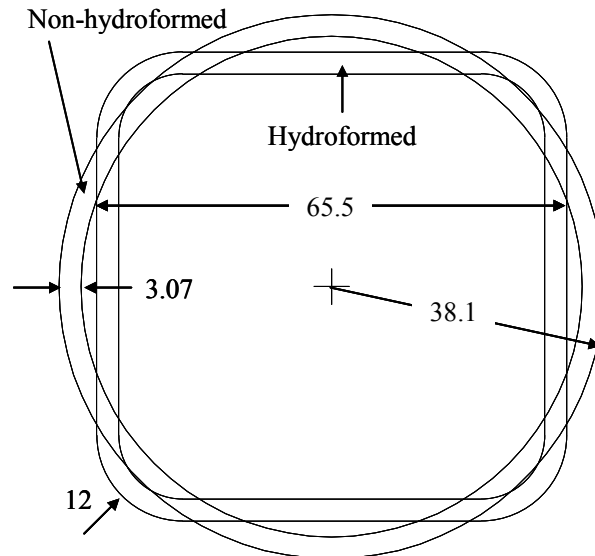


Figure 2.4: Cross-section of hydroformed and non-hydroformed s-rails.

A summary of the crash tests performed for each material, thickness, s-rail type, heat treatment condition and bend severity is given in Table 2.2. Note that each crash test considers one crush structure, which is comprised of two opposing s-rails (Figure 2.1). Three tests were performed for each condition listed in Table 2.2. The experiments considered either hydroformed or non-hydroformed s-rails with a range of bend severity (R/D ratio). Some s-rails were annealed to the O-temper before impact testing, the anneal serving to remove most of the work hardening and residual stresses resulting from the forming operations. The crash tests on annealed specimens allowed the effects of residual stresses and work hardening to be decoupled from the effects of thickness and geometry changes on the crash response. Through simulation, the effect of these variables on crash response is further isolated in Chapter 5 and Chapter 6.

Table 2.2: Test matrix for s-rail crash tests.

Material	Nominal Thickness (mm)	Hydroformed (H) or Non-Hydroformed (NH)	Annealed (A) or Non-Annealed (NA)	Bend Severity (R/D)	Number of crash tests
AA5754	3.0	H	NA	2.5	3
				2.0	3
				1.5	3
			A	2.5	3
				2.0	3
				1.5	3
		NH	NA	2.5	3
				2.0	3
				1.5	3
			A	2.5	3
				2.0	3
				1.5	3
EN-AW5018	2.0	NH	NA	2.5	3
				2.0	3
		H	NA	2.5	3
				2.5	3
	3.5	NH	NA	2.5	3
				2.0	3

2.2 Material Characterization

The materials examined in this work, AA5754 and EN-AW5018, are so-called 5000-series alloys that were tubed using a roll-forming and induction seam welding process and then post-tube annealed. The nominal chemical compositions of the tubes are given in Table 2.3 [105]. Initial thickness measurements [106] were taken around the circumference at the 3, 6 and 9 o'clock positions of the as-received 3 mm AA5754 tubes (Figure 2.5) and revealed a mild variation in thickness. The 3 and 9 o'clock positions have similar thickness ranges of 3.10-3.16 mm, while the 6 o'clock position ranged from 2.99-3.01 mm. The thickness in the 2 and 3.5 mm nominal thickness EN-AW5018 tubes was 2.04 ± 0.02 mm and 3.56 ± 0.02 mm, respectively [5]. The EN-AW5018 tubes were first tubed oversized and then drawn down to the 76.2 mm outer diameter before annealing, which may be the reason for the reduced thickness variation relative to the AA5754 tubes. It should be noted that the majority of the forming and crash experiments were performed on the AA5754 tubes. The EN-AW5018 tubes offered the opportunity to consider a somewhat higher strength material and two different thicknesses.

Table 2.3: Nominal composition of AA5754 and EN-AW5018 tubes [105].

Material	Composition (weight percent)							
	Mg	Mn	Fe	Si	Zn	Cu	Cr	Ti
AA5754	2.8	0.3	0.3	0.2	0.01	0.02	0.02	0.01
EN-AW5018	3.4	0.5	0.3	0.1	0.01	0.02	0.16	0.04

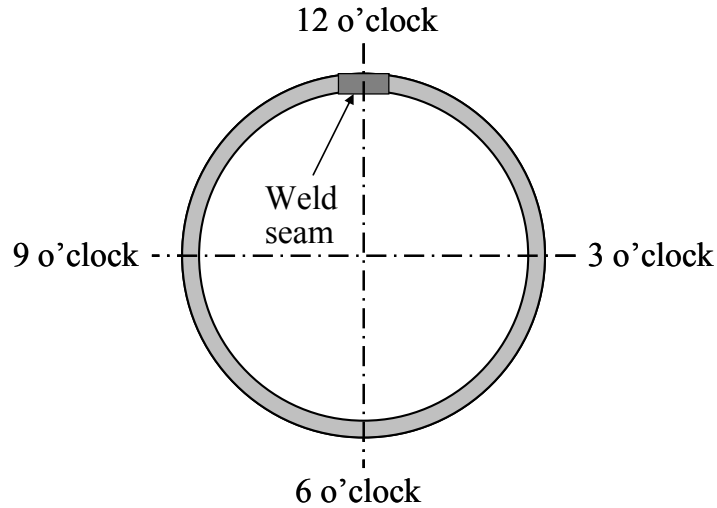


Figure 2.5: Significant locations around the section of a tube.

Tensile tests were performed on the 3 mm AA5754 tube and sheet, and 2 and 3.5 mm EN-AW5018 tube (only) to determine the respective stress versus strain response. Tensile samples were machined from the tubes at the 3, 6 and 9 o'clock positions to determine any variation in stress-strain response around the circumference. For brevity, only the results from these tests are discussed here; the methodology and specific details of the tensile testing have already been documented elsewhere [5,6,24,106,107].

The true stress versus true plastic strain curves for the 3 mm AA5754, and 2 and 3.5 mm EN-AW5018 as-received tubes are shown in Figure 2.6. In general, EN-AW5018, with its higher Mg and Mn content, exhibits a higher strength than AA5754. The measured constitutive data was curve fit using the classical Voce equation [108] to tensile data up to the point of necking and the rest of the curve was extrapolated, as also shown in Figure 2.6. The point of necking occurred at true strains of 0.18 ± 0.01 , 0.18 ± 0.01 and 0.17 ± 0.01 for the 3 mm AA5754, and 2 and 3.5 mm EN-AW5018 tubes, respectively.

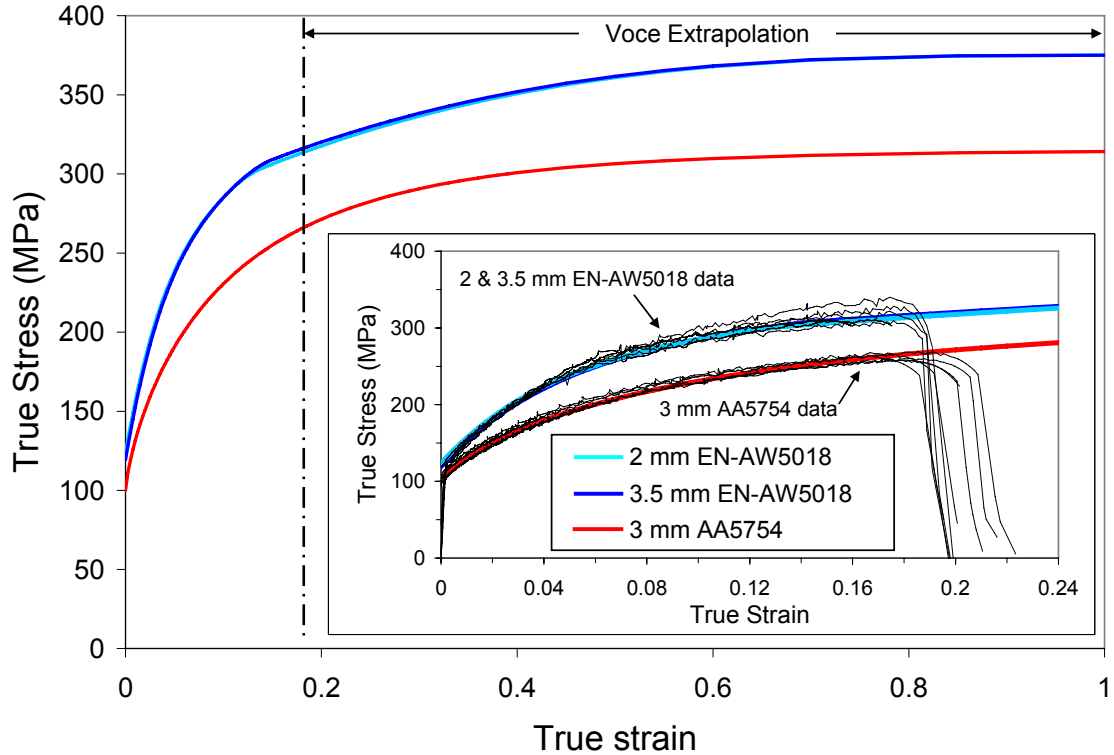


Figure 2.6: True stress versus true plastic strain curve for 3 mm AA5754, and 2 and 3.5 mm EN-AW5018 tubes. The measured constitutive data was curve fit using the classical Voce equation to tensile data up to the point of necking and the rest of the curve was extrapolated.

Tensile test results from samples machined at the 3, 6 and 9 o'clock positions in the 3 mm AA5754 tube, and sheet stock from which the tubes were fabricated, tested along the rolling direction, are shown in Figure 2.7. The stress versus strain response for the 3 and 9 o'clock locations of the tube are indistinguishable, while the 6 o'clock position exhibits a 3-5% higher strength, which is likely due to greater work hardening occurring in that location of the tube during tube fabrication. Although the tubes have been post-tube annealed, the activation energy necessary to begin the recrystallization stage of the annealing process has probably not been reached due to the minimal deformation induced during tube fabrication. The main difference between the sheet and tube samples appears to be in the yield point, which is 90 versus 100 MPa, respectively. Beyond a strain of approximately 0.05, the material response of the sheet samples is almost identical to that of the tube samples in the 3 and 9 o'clock positions. The stress versus strain response from samples around the circumference of the EN-AW5018 tubes (not shown) exhibited no dependency on sample location [106], which may be due to the drawing and subsequent annealing operations that

were used in reducing the outer diameter to 76.2 mm. Sheet stock was not available for this alloy.

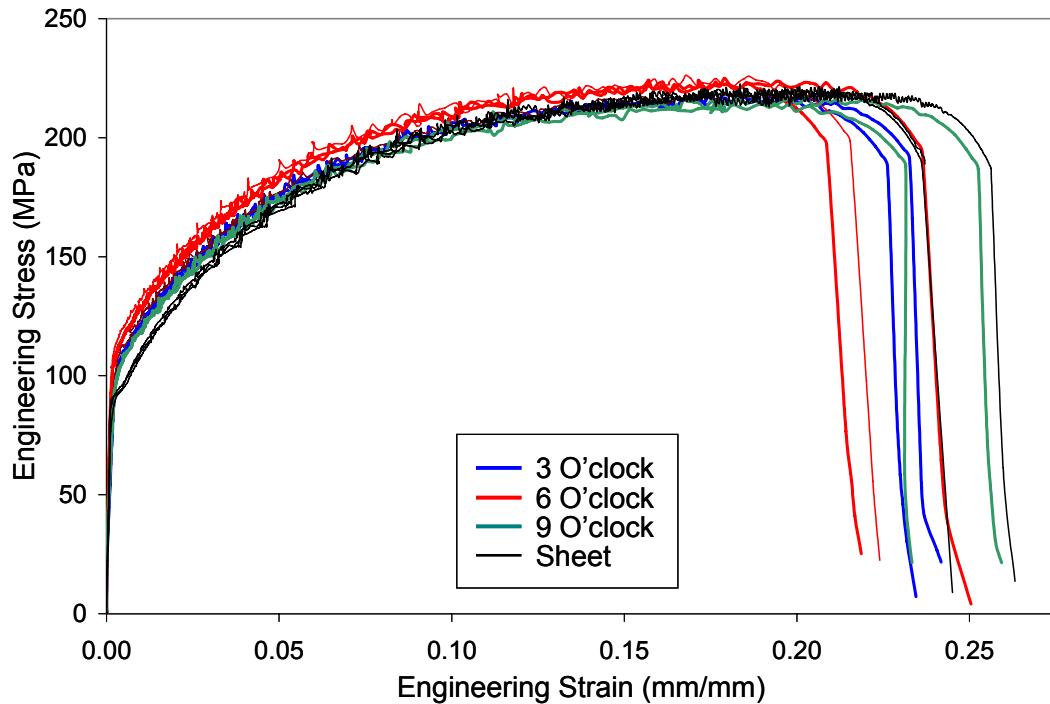


Figure 2.7: Engineering stress versus engineering strain for 3 mm AA5754 tube tensile samples cut at the 3, 6 and 9 o'clock positions and from flat sheet (rolling direction).

To determine the degree of in-plane anisotropy in the 3 mm AA5754 sheet, tensile tests were conducted using samples cut from the 0, 45 and 90 degree locations with respect to the rolling direction (0 degrees) of the sheet. The engineering stress versus strain response for the sheet samples pulled to failure is shown in Figure 2.8. The material strength in the 45 and 90 degree directions is approximately 7% and 8% lower than in the rolling direction, respectively. In addition to specimens that were pulled to failure, tensile tests were interrupted at strains of 10% and 20% for each sheet orientation. The width and thickness were measured at five locations in the gauge section of each sample both before and after they were pulled to an axial strain of 10% and 20%. The r-values or Lankford parameters (ratio of width to thickness strain) were calculated based on the principle of volume conservation and are 0.67, 0.76 and 0.60 for the 0, 45 and 90 degree orientations, respectively. These are similar to the values provided by the tube supplier of 0.64, 0.76 and 0.64 in the 0, 45 and 90 degree directions, respectively [109]. The Lankford parameters for

the 2 and 3.5 mm EN-AW5018 tube were not measured as part of the current research, but were listed by the tube supplier as being equal to 0.75 in the three primary sheet directions [109].

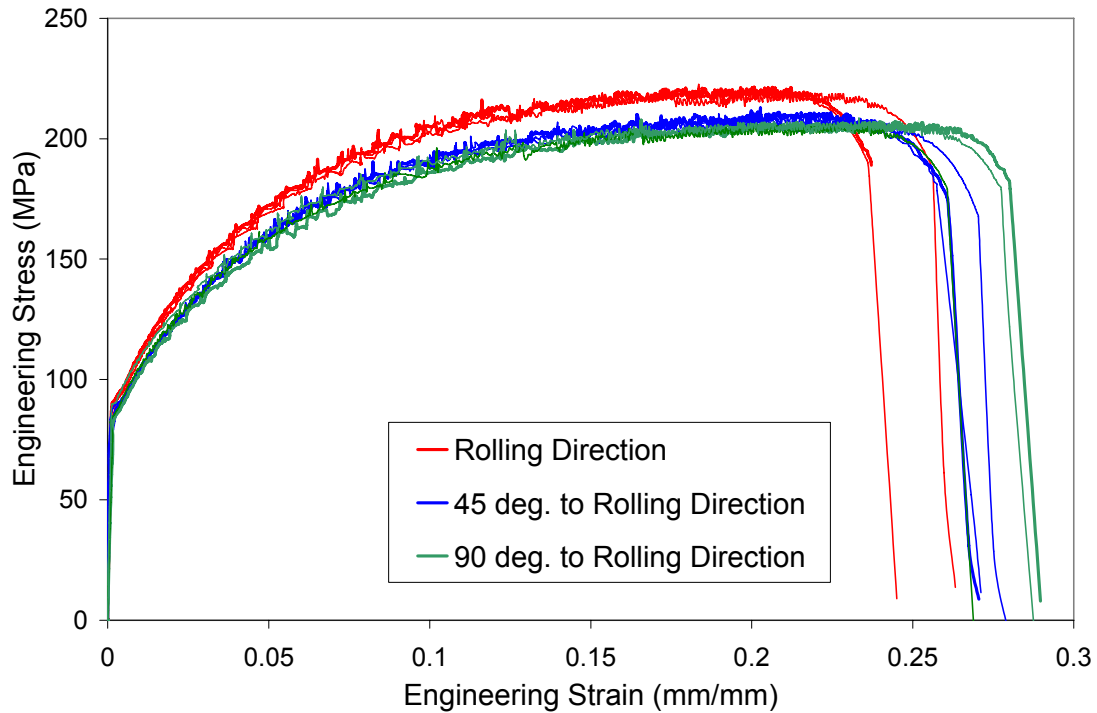


Figure 2.8: Engineering stress versus engineering strain response of 3 mm AA5754 flat sheet samples cut from the 0, 45 and 90 degree locations.

2.3 Tube Bending Experiments

The mandrel-rotary draw tube bending in this work utilized five major tools that interact with one another via the tube during bending (Figure 1.4 and Figure 2.9). The tools required are: (i) bend die; (ii) clamp die; (iii) pressure die; (iv) wiper die; and (v) mandrel. Initially, the bend, clamp and pressure dies are all oriented parallel to the tube axis, as shown in Figure 1.4. The wiper die is positioned at a small angle from the tube, which is usually referred to as the “rake angle”. This angle is set to minimize frictional drag from the wiper during bending and prevent wrinkling on the inside of the bend. The mandrels used in this work consist of a cylindrical mandrel body with two or three mandrel balls utilizing swivel connectors. The mandrel position is specified as the position of the end of the mandrel body relative to the bending tangency point. The location of tangency is determined by taking the

line perpendicular to the tube when clamped and that passes through the center of the bend die rotation axis. The mandrel body is hollow and incorporates lubricant channels that allow lubricant to be pumped to the inside surface of the tube. The wiper was lubricated manually prior to bending, while the bend, clamp and pressure dies were kept dry to minimize slip.

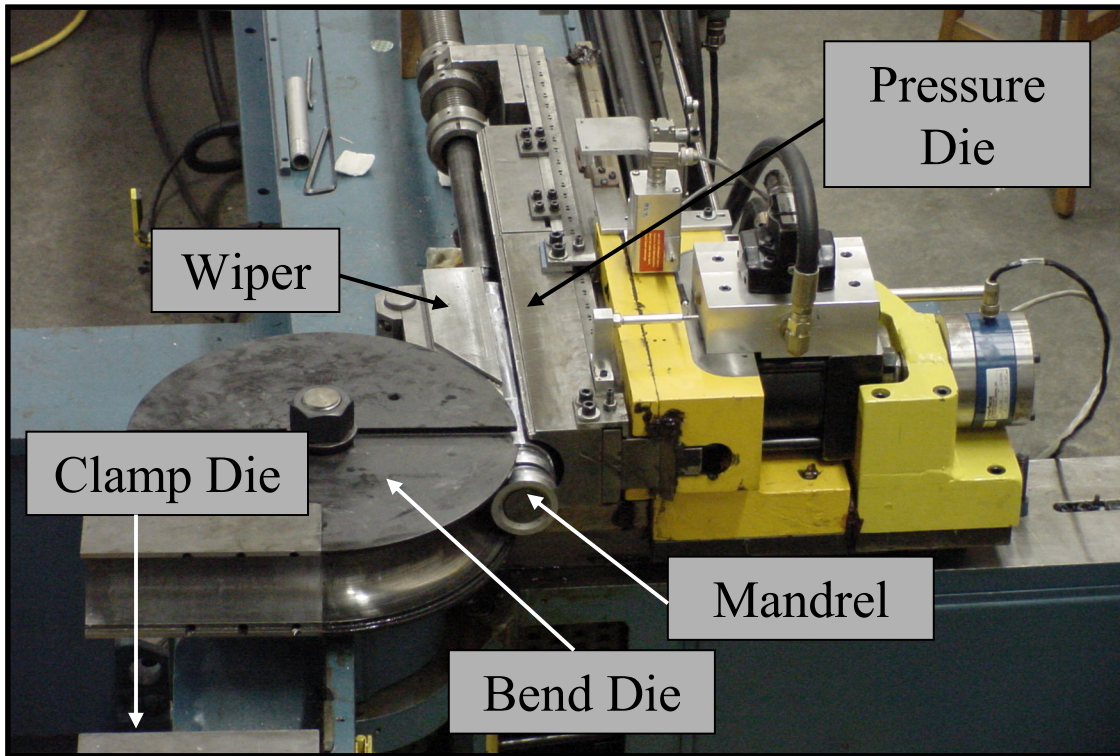


Figure 2.9: Photograph of rotary draw tube bending apparatus showing bend tooling (bend die is at 90°). Tube is not shown.

The tubes were lubricated using Drawsol Al 20 lubricant [110] that was applied using the method described by Oliveira *et al.* [5,6,24]. Once the tube was slid into position over the mandrel, the clamp die was closed, applying a force on the tube by means of a locking toggle mechanism. The pressure die clamping action is actuated under displacement or load control; the latter was used in this work to impose a constant clamping force on the tube. The bend and wiper dies serve to react these clamping loads while the mandrel prevents the tube from collapsing. After clamping, the bend die and clamp die then begin to rotate synchronously, drawing the tube and the bend die, while the pressure die advances parallel to the tube axis, thereby pushing material into the bend region.

Using the instrumented rotary draw tube bender, the aluminium alloy tubes were first bent to 45-degrees after springback over a 3 second period. The tube was then advanced the appropriate distance corresponding to the length of section C of the s-rail (Table 2.1), and rotated about the mandrel by 180-degrees, after which the second 45-degree bend was conducted. A 100% frictional boost condition was employed in bending, which is representative of current industrial practice in rotary draw tube bending. The tube was oriented such that the weld seam was located at the neutral axis in bending, hence minimizing the influence of the weld properties on the deformation of the tube during forming and crash.

A typical “safe” bend radius for the tube size and materials examined, is two times the outer diameter of the tube [111], in this case 152.4 mm, which corresponds to $R/D=2.0$. This value was considered as well as larger, less severe, and smaller, more challenging, bend radii corresponding to R/D ratios of 2.5 and 1.5, respectively. The three levels of bend severity were chosen to induce varying degrees of strain and thickness change in the tube. As a first estimate of bend severity, the bending strain levels were determined using simple bending theory [112] and are 20%, 25% and 33% for R/D ratios of 2.5, 2.0 and 1.5, respectively.

2.3.1 Mandrel-Rotary Draw Tube Bender and Tooling

The tube bender used in this work is an instrumented version of an Eagle EPT-75 bender [5,6,24] and is operated using a closed-loop servo-hydraulic control system. Through the use of actuators, load cells and displacement transducers, the tooling can be independently controlled. A custom PC-based Labview software interface is used to generate program signals to the servo-controllers and to record load and displacement data for the bend die, pressure die (clamping and boost directions) and mandrel throughout the bend. The tooling and control data recorded during bending for the various tools are shown schematically in Figure 1.4. The material specifications for the bend and hydroforming tooling used in the experiments are presented in Table 2.4.

Table 2.4: Material specifications on bending and hydroforming tooling used in experiments.

Tool	Material	Heat or Surface Treatment	Hardness
Bend die	4130 steel	Nitrided	60-62 Rc
Clamp die	4130 steel	Nitrided	60-62 Rc
Pressure die	4130 steel	Nitrided	60-62 Rc
Wiper die	4130 steel	None	N/A
Mandrel	8620 steel	Chromed	58-62 Rc
Hydroforming die body	P20 steel	None	290-330 HB
Hydroforming die inserts	P20 steel	Nitrided	55 Rc
Hydroforming end-plungers	P20 Steel	None	290-330 HB

2.3.2 Process Parameters, Methods and Measurements

The bending parameters for the 3 mm AA5754 tubes are presented in Table 2.5. A fixture was created using the tube geometry dimensions in Table 2.1 with a 2 mm diametral clearance that was used to ensure the s-rails maintained consistent geometrical properties after bending. The ovality ratio (ratio of major to minor axis diameters) was determined from measurements taken from sections A-E in three of the s-rails for each R/D ratio.

Thickness and strain measurements were taken around the circumference and along the inside and outside of the bend in section D (Figure 2.10), which corresponds to the first of the two bends that comprise the s-rail. There were minimal differences in the measured process variables, and thickness and strain distributions between the two bends comprising the s-rail. Approximately one-half of the tubes were circle-gridded prior to bending using electrochemical etching techniques and strain measurements were conducted to a precision of 3% strain on two s-rails per condition [113]. Thickness measurements were taken from the s-rails using a non-destructive ultrasonic probe. Thickness and strains were measured at approximately 5 mm increments for two s-rails at each R/D ratio along the circumference, and along the outside of the bend, as well as into the neighbouring straight sections C and E.

Table 2.5: Process parameters for the 3 mm AA5754 tube bending experiments.

BEND PARAMETER	R/D		
	2.5	2.0	1.5
Bend die radius (mm)	188.6	150.4	113.7
Prescribed bend angle (degrees)	45.5	45.5	46.5
Percentage boost	100		
Pressure die clamp load (kN)	35		
Time (s)	3		
Lubricant	Drawsol Al 20		
Wiper angle (degrees)	0-0.5		
Mandrel balls	2	2	3
Radial mandrel clearance (mm)	0.32		
Mandrel location w.r.t tangency (mm)	0±2		

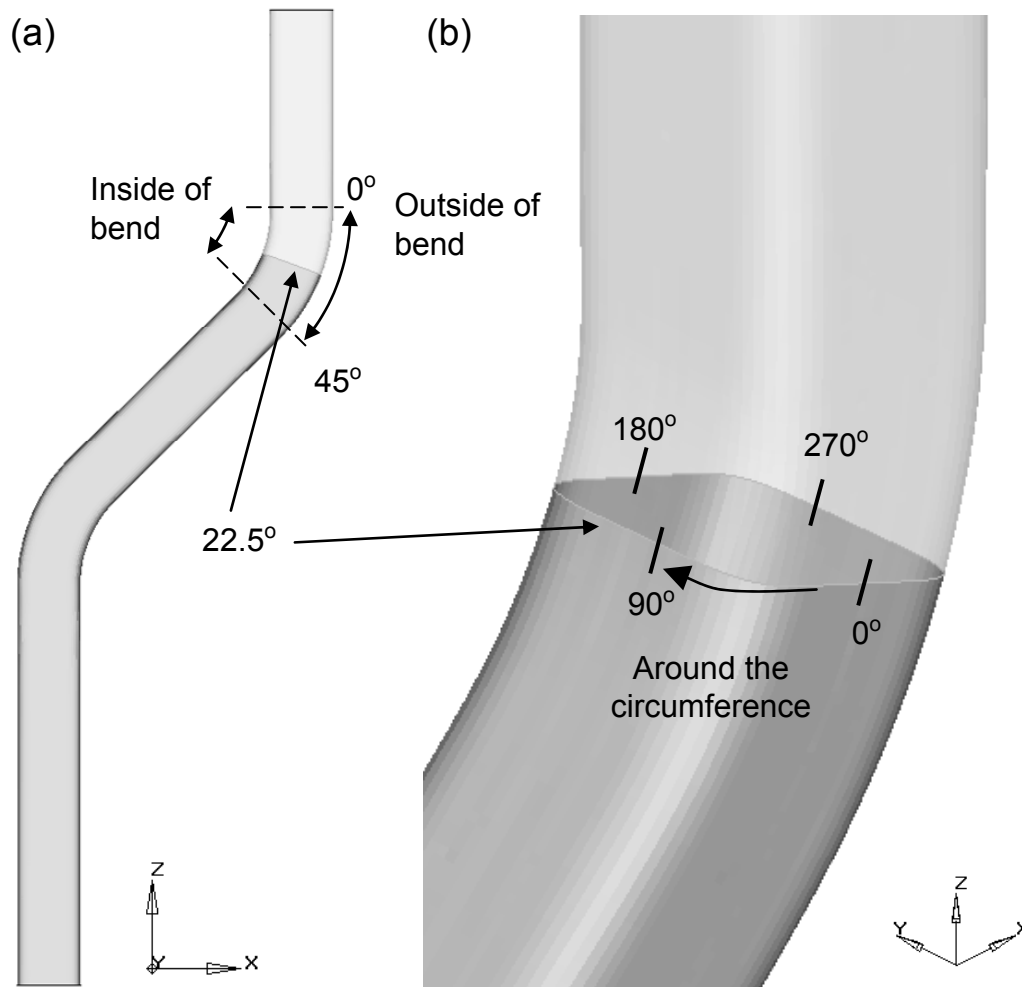


Figure 2.10: Locations of thickness and strain measurements along the (a) inside and outside of the bend; and (b) around the circumference of the bend at the 22.5° location of the bend. Note that the schematic is shown for a hydroformed tube. The same conventions were used for both hydroformed and non-hydroformed s-rails.

The process parameters for the 2 and 3.5 mm EN-AW5018 tubes are shown in Table 2.6. For these tubes, the thickness and strain measurements were taken around the circumference, at the center of the first bend, and along the lower and upper paths shown in Figure 2.3b and Figure 2.10. Measurements were taken at 10-degree increments around the circumference of the tube and approximately 10 mm increments along the lower and upper paths. Measurements were not taken on the 2 mm s-rails bent at $R/D=1.5$ since this bending condition was more thoroughly examined using the 3 mm AA5754 tubes.

Table 2.6: Process parameters for the 2 and 3.5 mm EN-AW5018 tube bending experiments.

Bending Parameter	2 mm, R/D=2.5	2 mm R/D=2.0	2 mm R/D=1.5	3.5 mm R/D=2.5	3.5 mm R/D=2.0
Bend time (s)	3				
Prescribed bend angle (degrees)	47	46.5	46.5	47	46.5
Angle after springback (degrees) ($\pm 1^\circ$)	45				
Percentage boost	100				
Constant pressure die clamp load (kN)	40,000	40,000	40,000	35,000	35,000
Wiper die rake angle (degrees)	0.18-0.30				
Mandrel location w.r.t. tangency (mm) (± 2 mm)	0				
Radial mandrel clearance (mm)	0.33	0.33	0.33	0.57	0.57
Bend die radius (mm) (cut for springback)	188.6	150.4	113.7	188.6	150.2

2.4 Hydroforming Experiments

The published literature often distinguishes between the “low” and “high” pressure hydroforming processes in terms of the pressure attained. This can be misleading since both of these processes can form tubes using the same maximum pressure. In the current thesis, the distinction between the two processes is made in terms of the percent circumferential expansion and use of end-feed. In the current experiments, the s-rails were hydroformed into square cross-sections using near zero-percent expansion without end-feed, which corresponds to a so-called “low-pressure” process in which the circumference of the tube is nearly equal to the perimeter of the die. The tube experiences a mild expansion since the die incorporates a 0.508 mm diametral clearance. The main advantage of this process is that the tubes undergo less than 1% circumferential expansion and do not require end-feed to fill the cavity of the die. In addition, the hydroformed section has a more uniform thickness distribution than if the tube underwent greater circumferential expansion, as in the so-called “high-pressure” process. High-pressure hydroforming experiments were not performed; however, simulations of this process are presented in subsequent chapters.

One consequence of the low-pressure process adopted in the current research is that the tube does not initially fit into the die and must be preformed into the die section during die closure. A low internal pressure of 2.8-6.9 MPa (400-1,000 psi) is applied during die closure, as depicted in Figure 1.9, to prevent buckling.

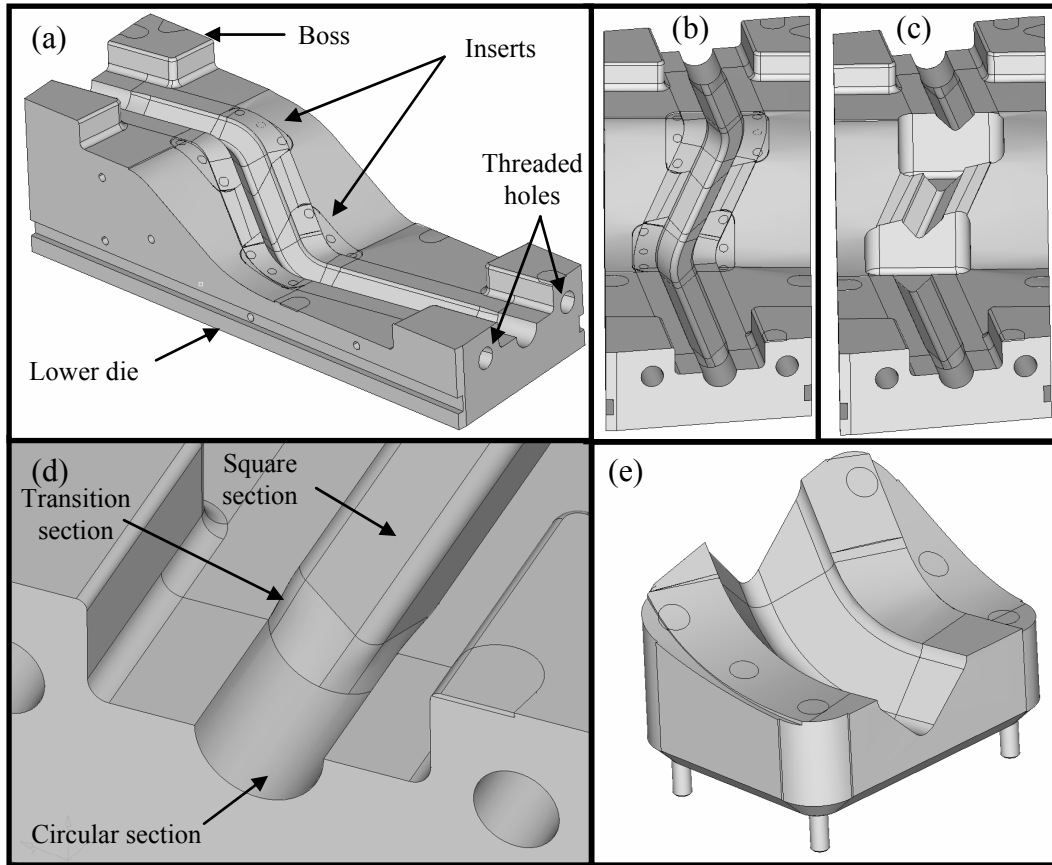


Figure 2.12: Schematic of s-rail lower die: (a) isometric view of lower die; (b) front view with die inserts; (c) front view without die inserts; (d) close-up of transition region; and (e) die insert.

The die cavity extends past the s-rail part geometry in order to accommodate the transition from a square to round cross-section (Figure 2.12d) needed to allow insertion of the cylindrical end-plugs. A schematic of an as-hydroformed s-rail, with a close-up of the transition and circular sealing regions at the ends, is shown in Figure 2.13. The transition regions (Figure 2.13b) are 50 mm long. The straight circular sections at the ends of the die are 100 mm long with a diameter of 76.2 mm, plus a 0.254 mm (0.01 inch) clearance. The square cross-section region has a 0.508 mm (0.02 inch) total clearance. As a consequence of these addenda at the ends of the as-hydroformed s-rail, the tubes were pre-bent with an additional length of 150 mm at each end (sections A and E). After hydroforming, the s-rails were placed into a fixture to trim the end regions of the s-rail and to ensure geometric accuracy for the crash tests.

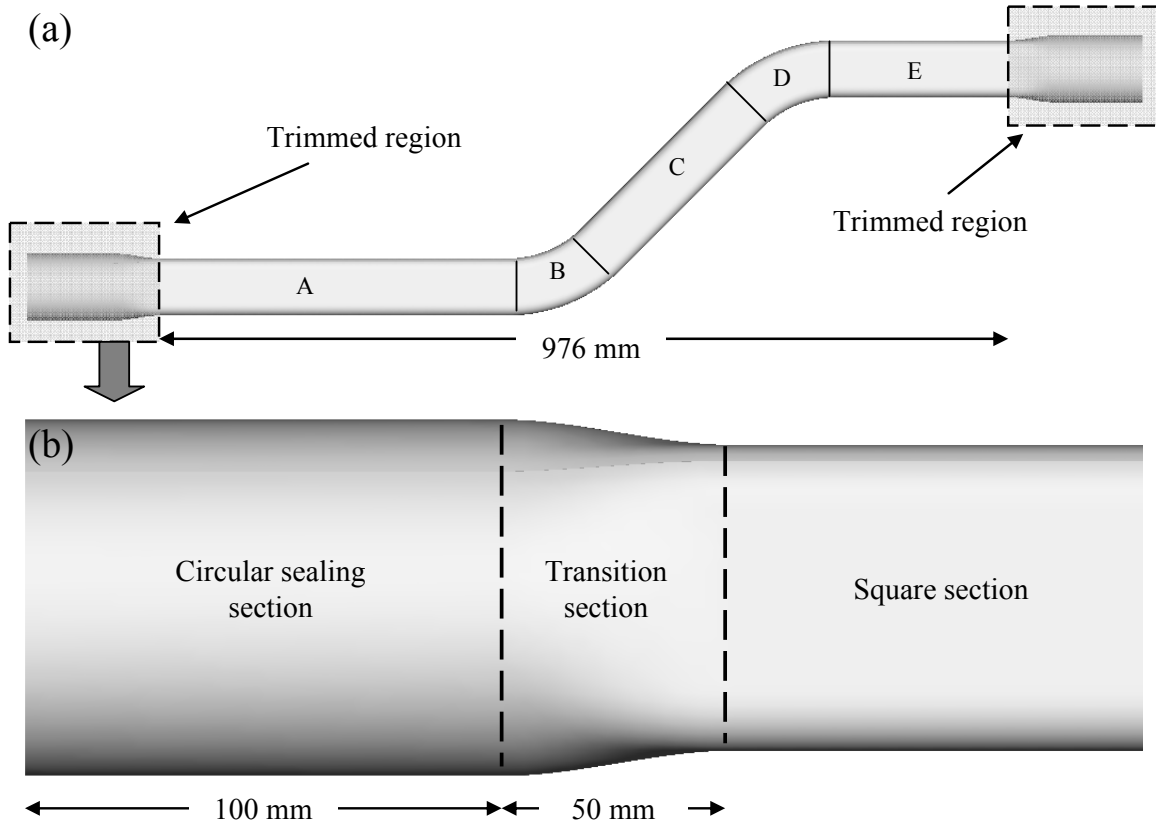


Figure 2.13: Schematic of a hydroformed s-rail before end-trimming: (a) full view, and (b) close-up of trimmed section.

End-plugs to seal the tube ends were designed and manufactured utilizing Parker Polypak high-pressure elastomer seals and are shown in Figure 2.14. These “floating” end-plugs are inserted into the tube ends using an in-house hydro/mechanical fixture. During hydroforming, the axial force resulting from the internal pressure acting on the end-plugs is reacted by 50 mm thick support plates bolted to the ends of the hydroforming die.

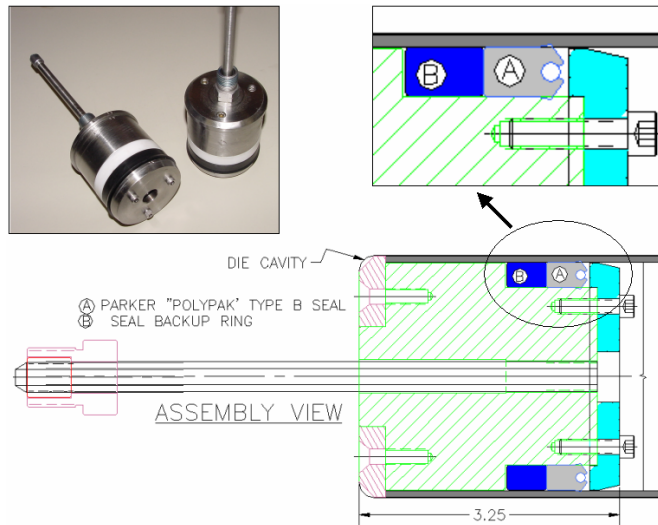


Figure 2.14: End-plugs used in hydroforming of s-rails.

The corner inserts were ion-nitrided to a hardness of approximately 55 Rc. The die bodies were not hardened since this would have represented a large cost and was not necessary when forming soft aluminium tubes. There are four large bosses (Figure 2.12a) on the four corners of the parting surface, which ensure proper mating and alignment of the two die halves and provide resistance to lateral loads during hydroforming. The top die incorporates replaceable wear plates that can be seen in Figure 2.11a. The bottom die has two 50.8 mm diameter threaded holes on each end for attachment of end-feed actuators or in the case of the current research, reaction plates.

A Macrodyne 1,000-tonne hydroforming press at the University of Waterloo was used to conduct the experiments. Closed loop servo-control provided the die closure and pressurization processes. An in-house Labview program generates program signals for the servo-hydraulic controllers and provides data acquisition.

2.4.2 Process Parameters, Methods and Measurements

Prior to hydroforming, the tubes were lubricated with a D.A. Stuart Hydrodraw 625 solid film lubricant [114], which prevented pick-up on the die surfaces and was shown to provide a low coefficient of friction for hydroforming. Twist compression tests were performed to determine the coefficient of friction between the tube and various tooling surfaces. The details of the twist-compression tests and the measured friction coefficient data are given in Appendix A.

The first step in the hydroforming process was to displace the upper die towards the lower die in several incremental steps until it was fully closed; this allowed increases in the tube internal pressure to be relieved due to the reduction in volume of the tube as it was crushed in the die, hence minimizing internal pressure fluctuations. The internal pressure was prescribed to be 4.5 ± 2.5 MPa during the die closure stage of the process. Upon die closure, the pressurization stage was conducted by prescribing an internal pressure that linearly increased with time up to 65 MPa over a period of 70 seconds.

The nominal bending (circumferential) strain at the outside of the corners of the straight sections comprising the hydroformed s-rail can be estimated using an analytical approach that expresses the engineering strain in terms of the r/t (radius of bend/wall thickness) ratio [115]. The bending strain, which is expressed in terms of the engineering strain as

$$e = \frac{1}{(2r/t) + 1} \quad (2.1)$$

is compared to the measured and predicted results in Chapter 4 and Chapter 5. Thickness and strain were measured for the 3 mm AA5754 tubes around the circumference of the center of the first bend region and at the center of the straight section between the bends, which correspond to sections D and C of the s-rail, respectively. Measurements were conducted using the techniques described in Section 2.3.2, for the pre-bent tubes.

2.5 Impact Experiments

Crash experiments were performed using a deceleration sled facility [5,116] at the GM Technical Centre in Warren, Michigan. The testing arrangement requires two s-rails to be tested simultaneously, as shown in Figure 2.15 and Figure 2.1. The s-rails were mounted on 19 mm thick steel plates with rigid bosses that allow clamps to be tightened onto the tube without collapse. The two ends of the s-rail are fixed to provide a boundary condition that can be readily modeled in simulations. The bosses are 50.8 mm in height and are located at the ends of the s-rail, on the inside of the tube. The base plates of the structure are fastened to the vertical impact wall (Figure 2.1) such that the s-rails lie in a horizontal plane to limit friction and lateral side loads on the sled. The clamps are bolted to the top cover plate and load cell cover plate. The clamps at the base of each s-rail are 50.8 mm in height, while two

25.4 mm height clamps are used at the top cover plate for each s-rail. The s-rails were found to be less prone to slip within the clamps at the shorter end. In addition, the clamping surface of the base clamps was grooved to prevent slippage of the tube during the crash event. A sheet of plywood and a rubber cover were placed on the top cover plate to reduce ringing in the system, which could damage the load cells. To some extent, the plywood and rubber mimic a vehicle test condition where bumper foam attenuates the loading [5,116].

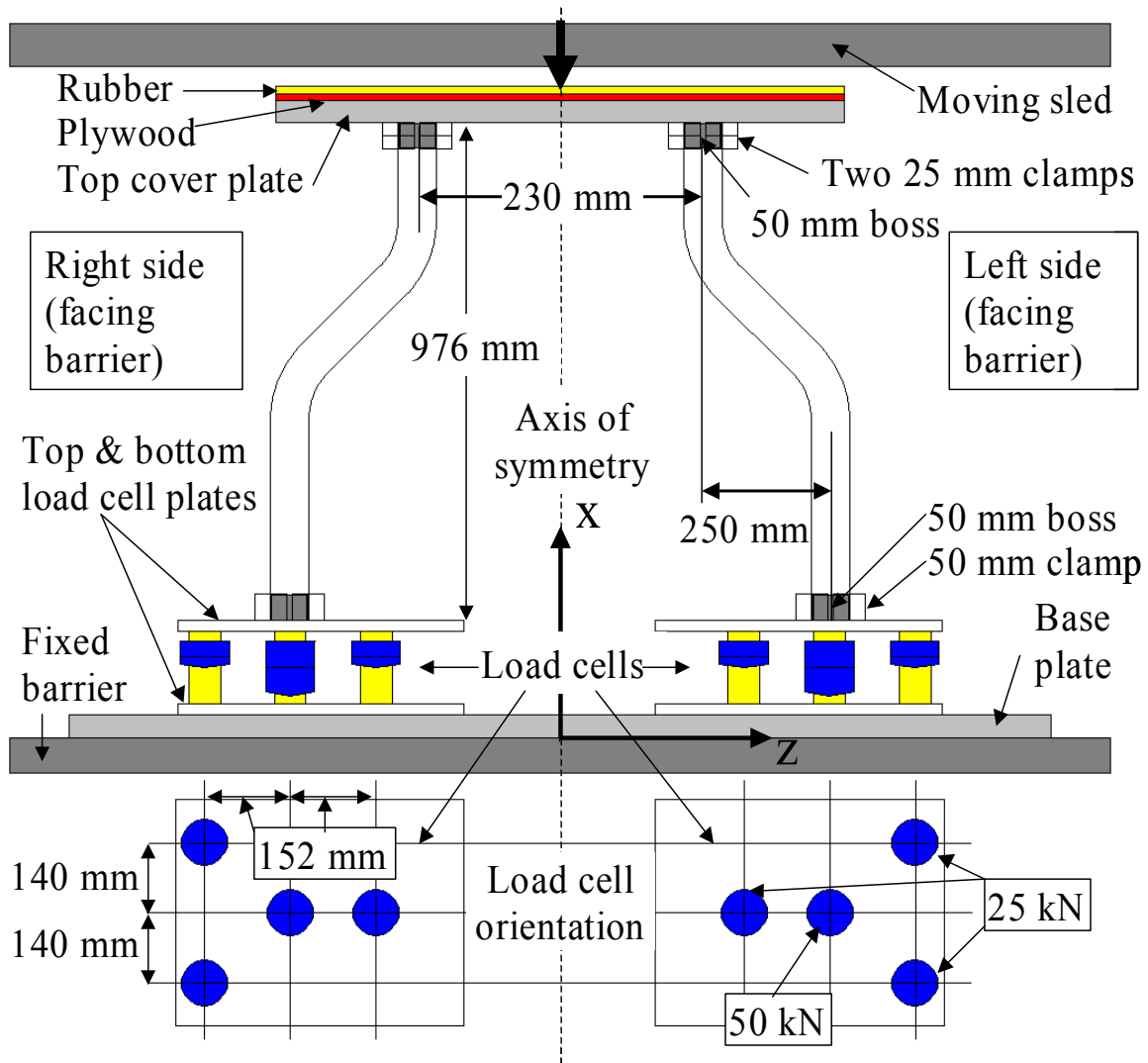


Figure 2.15: S-rail crash structure and load cell arrangement schematic. View looking down on assembly from above.

2.5.1 Deceleration Sled

The deceleration test sled allows variation of the sled mass and impact velocity to control the impact energy. The detailed methods and procedures for testing are described by Mayer *et*

al. [116]. The sled is accelerated using compressed gas towards a rigid vertical wall via a rail system that prevents lateral displacements, and process data is collected at 10,000 samples per second, such that a sample rate of 0.1 ms is used. A low-pass Butterworth 1 kHz electronic filter [117] was applied to the data to pass low frequencies and attenuate frequencies higher than 1 kHz, hence smoothing the data.

Load cells were mounted between the load cell plates, which were 19 mm thick. One 50 kN load-cell was mounted directly beneath the base of the s-rail, with three 25 kN load cells surrounding it, as shown in Figure 2.15. The load cell arrangement was designed using a theoretical analysis performed by Mayer *et al.* [116] and allowed force and moment data to be obtained for each s-rail comprising the impact structure.

2.5.2 Impact Parameters and Measurements

The crash test conditions and final measured crush distances are summarized in Table 2.7 for each s-rail configuration. Numerical simulations were used to estimate the velocity and energy necessary to deform the s-rail structure to the desired maximum distance, which was roughly 275-300 mm. Further deformation would result in reversed loading that would put the s-rail center section in tension and could possibly overload the load-cells. The sled mass was held constant at 1,120 kg for all tests, with the impact plate mass being 15.1, 15.7 and 15.41 kg for the 3 mm AA5754, and 2 and 3.5 mm EN-AW5018 non-hydroformed s-rails, respectively. The mass of the impact plate for the 3 mm AA5754 and 2 mm EN-AW5018 hydroformed s-rails was 14.7 and 14.4 kg, respectively. The small difference in the impacted plate mass is due to the different boss geometry for each thickness and cross-section. The impact velocities for the three R/D ratios within each forming condition are within 2%, indicating excellent repeatability within the experiments. The masses of the 3 mm AA5754, and 2 and 3.5 mm EN-AW5018 hydroformed and non-hydroformed s-rails were measured for each crash test and were 1.99 ± 0.01 , 1.36 ± 0.007 and 2.30 ± 0.02 kg, respectively. Tearing occurred in the EN-AW5018 non-hydroformed s-rails at the point of contact of the clamp and boss interface late in the test. This damage was not judged significant since it occurred beyond the point at which the crush distance is no longer representative of a typical automotive crash event. Tearing of the s-rails was eliminated in the AA5754 tests by introducing a 6.35 mm radius on the edge of the boss.

Table 2.7: Crash test parameters for 3 mm AA5754, and 2 and 3.5 mm EN-AW5018 s-rails.

Material	Nominal Thick. (mm)	Hydro-(H) or Non-Hydroformed (NH)	Annealed (A) or Non-Annealed (NA)	Bend Severity (R/D)	Average Impact Velocity (m/s)	Variation in Impact Velocity (m/s)		Average Kinetic Energy (kJ)	Average Total Crush Distance (mm)	Variation in Crush Distance (m)		Average Crush Distance at Tearing Initiation (mm)
						(+)	(-)			(+)	(-)	
AA5754	3.0	H	NA	2.5	3.35	0.01	0.00	6.3	262	2	2	Not Applicable
				2.0	3.33	0.00	0.00	6.2	292	5	5	
				1.5	3.36	0.02	0.02	6.3	357	4	4	
			A	2.5	3.00	0.00	0.00	5.0	302	8	8	
				2.0	3.00	0.01	0.01	5.0	351	3	3	
				1.5	3.00	0.01	0.00	5.0	387	3	5	
		NH	NA	2.5	2.99	0.01	0.01	5.0	241	1	1	
				2.0	3.02	0.01	0.00	5.1	300	13	12	
				1.5	3.02	0.01	0.01	5.1	419	35	31	
			A	2.5	2.78	0.00	0.01	4.3	222	3	3	
				2.0	2.76	0.03	0.06	4.3	305	39	84	
				1.5	2.77	0.03	0.03	4.3	402	18	13	
EN-AW5018	2.0	NH	NA	2.5	2.28	0.00	0.00	2.9	290	50	30	160
				2.0	2.32	0.01	0.01	3.0	343	97	53	183
	3.5	NH	NA	2.5	4.01	0.02	0.02	9.0	430	10	20	170
				2.0	4.03	0.00	0.00	9.1	470	10	20	200

Two 1,000 fps high-speed cameras recorded the overhead and side-view of the crush structure during each experiment. In addition, a third high-speed camera provided a close-up view of the clamps at the base of the s-rail to observe whether slippage occurred. All of the recorded data was used to assess the crash response of the structures and validate the numerical models of the event.

2.6 Annealing of S-Rails

Both hydroformed and non-hydroformed 3 mm AA5754 s-rails were fully annealed to an O-temper, prior to crash testing, to remove work hardening and residual stresses after forming. An annealing schedule prescribed by the tube manufacturer, Hydro Aluminium [118] was adopted. The s-rails were first cleaned to remove any residual bending or hydroforming lubricant prior to annealing. The tubes were heated in a temperature- and time-controlled furnace to 340-degrees Celsius for two hours, then subsequently cooled to 250-degrees Celsius within three hours, and removed from the furnace where they were cooled to room

temperature. To assess whether the annealing process was successful in removing work hardening effects, Rockwell-Superficial 15N (15 kg diamond) hardness tests were conducted on flat-sheet stock, undeformed tube and on the various sections A-E (Figure 2.3b) in the hydroformed and non-hydroformed s-rails. The hardness tests allowed a relatively easy method to assess changes in material strength without having to conduct sophisticated and time-consuming metallographic investigation or local tensile testing.

Hardness measurements were conducted at ten different locations on each side of three different sheets of AA5754, which were cut from the coil slits from which the tubes were fabricated. Note that the sheet-stock was annealed by the manufacturer using the method employed herein prior to tube fabrication. The hardness was similar for both sides of the sheet and an average hardness of 27 ± 3 (15N) was determined.

Ten hardness measurements were performed at the 3, 6 and 9 o'clock positions (Figure 2.5) for three different as-received tubes. The average hardness in the as-received tubes at the 3, 6 and 9 o'clock positions are 29, 27 and 28 (15N), respectively. The average hardness of an undeformed tube is 28 ± 4 , which is within 1 hardness unit of the flat sheet.

A summary of the average hardness measurements performed on hydroformed and non-hydroformed s-rails in the non-annealed and fully-annealed condition is given in Table 2.8 and Table 2.9. Ten hardness measurements were conducted at various locations on two tubes per condition and a scatter of plus or minus 4 relative to each other was observed. For the non-annealed tubes, the hardness of the as-hydroformed corner regions was greater than the flat regions in all sections A-E of the hydroformed s-rail, while little difference in the hardness was observed between the inside and outside of the bend sections, B and D. Within the non-hydroformed (non-annealed) s-rails, little difference in hardness was observed in the 3, 6 and 9 o'clock positions of sections A and E, and between the inside and outside of the bend in sections B and D.

The fully annealed hydroformed s-rails exhibited a much lower hardness in the flat and corner regions. The hardness of the flat sections in regions A, C and E did not change due to annealing and remained low. The hardness of the annealed hydroformed and non-hydroformed s-rails at the outside of the bend was slightly lower than at the inside of the bend, which is attributed to the greater strain levels on the outside of the bend region, as will

be shown in Chapter 4. The greater strain levels at the outside versus the inside of the bend within the s-rails results in a greater potential level of activation energy available for recrystallization to occur, which will soften the material. The final hardness in the bend regions of the annealed hydroformed and non-hydroformed s-rail were roughly 7 (15N) hardness points below that of the as-received tube or sheet.

Table 2.8: Average hardness measurements on 3 mm AA5754 non-annealed and annealed hydroformed s-rails. Hardness is reported using a Rockwell-Superficial 15N (15 kg diamond) scale.

	Sections of S-Rail					
	A, C & E		B & D			
	Location on Tube		Inside of Bend		Outside of Bend	
S-Rail Type	Flat	Corner	Flat	Corner	Flat	Corner
Hydroformed (non-annealed)	30	36	37	39	37	40
Hydroformed (annealed)	31	21	23	21	22	17

Table 2.9: Average hardness measurements on 3 mm AA5754 non-annealed and annealed non-hydroformed s-rails. Hardness is reported using a Rockwell-Superficial 15N (15 kg diamond) scale.

	Sections of S-Rail								
	A & E			B & D		C			
	Location on Tube			Location on Tube		Location on Tube			
S-Rail Type	3	6	9	Inside	Outside	3	6	9	
Non-hydroformed (non-annealed)	29	30	28	37	36	27	28	29	
Non-hydroformed (annealed)	28	27	28	23	18	26	25	26	

It is evident from Table 2.9 that the annealed s-rails do not have a uniform strength distribution as indicated by the variation in hardness in the sections of the s-rail. The degree of material softening during annealing in the various locations of the s-rail is dictated by the activation energy required for recrystallization [119]. Consequently, local high strain regions, such as the inside and outside of the bend, and the section profile corners, exhibit a more pronounced softening due to annealing than do other lower strained regions. Despite

the small variations in material properties within the annealed s-rails, the residual stresses and work hardening effects are deemed to have been removed in a manner that is representative of industrial annealing practice. More importantly, the anneal does serve to reduce work hardening in the corner regions where two of the three hinges form during crash.

Chapter 3

Numerical Modelling

The ultimate objective of the numerical modelling program adopted within this research is to identify the parameters that govern s-rail crash response and understand their effect. To this end, numerical models were developed with the aim of accurately predicting the “as-formed state” and crash response of s-rails. The motivation for developing these models is to establish an analysis tool that has excellent predictive ability, that will provide additional insight to the experiments and will allow further investigation of the parameters governing the crash response of s-rails, beyond the scope of the current experiments.

3.1 Modelling Program and Implementation

3.1.1 Strategy

The identification of the main parameters governing the crash response of s-rail structures was accomplished through a parametric study that considered the initial thickness, material properties, cross-section geometry and the “as-formed” properties of the tube, as shown in Figure 3.1. The as-formed properties of the tube are a consequence of the fabrication route employed and include geometry, work hardening, thickness changes and residual stresses. A further breakdown of the parametric study is outlined in Figure 3.2 and Figure 3.3.

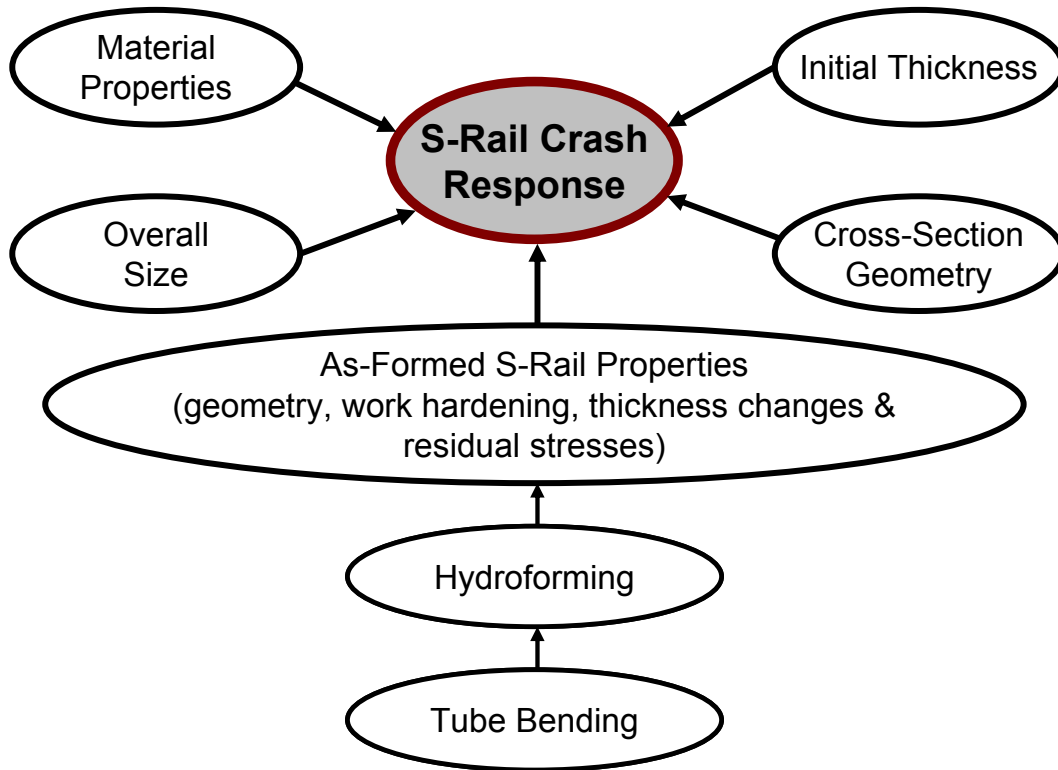


Figure 3.1: Flow chart outlining the parameters governing s-rail crash response.

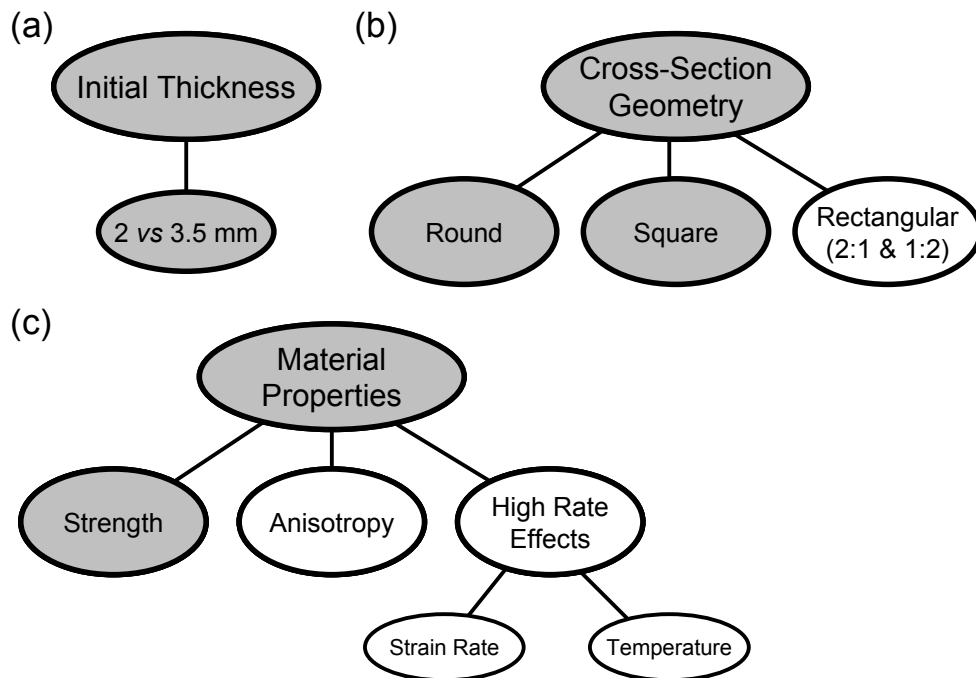


Figure 3.2: Variables governing the crash response of s-rails: (a) initial thickness; (b) cross-section geometry; and (c) material properties. Note that the variables examined in the experiments are shaded.

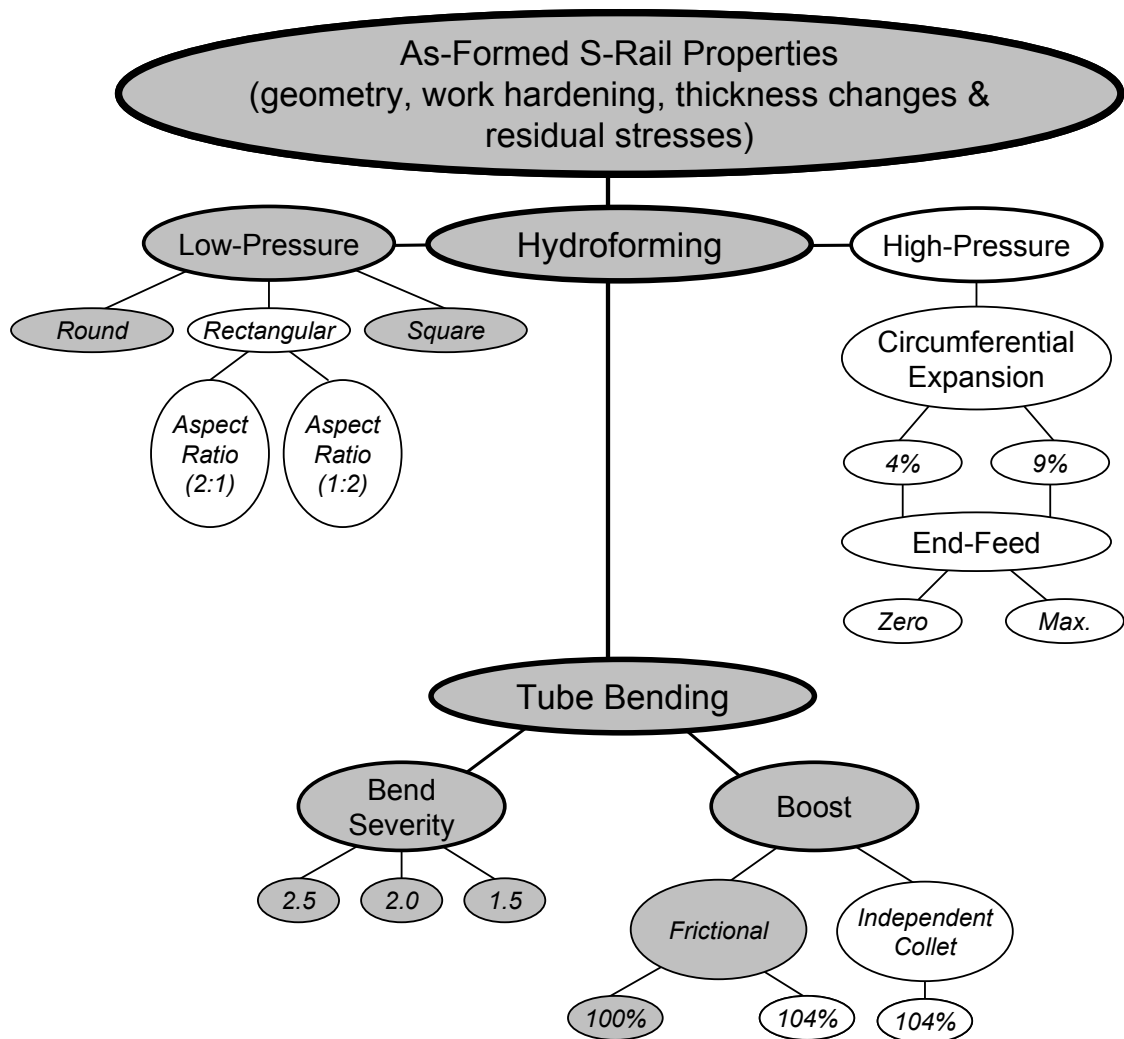


Figure 3.3: Variables that influence the as-formed properties of the s-rail. Note that the variables examined in the experiments are shaded.

There are two aspects to this study. The first assesses variations of the parameters studied in the experiments. This series of simulations also served to assess the predictive ability of the numerical modelling techniques as well as provide further insight into the parameters affecting the crash response. The second aspect of the simulations considered additional parameters not considered in the experiments. The details of the two aspects of the parametric study are presented separately in the following sections.

3.1.2 Numerical Investigations Based on Experiments

A number of parameters that affect the crash response of s-rails were investigated through simulation of the experiments. The specific parameters considered are summarized in Table 3.1.

Table 3.1: Summary of the variables governing the crash response of s-rails that are investigated through simulation of the forming and crash experiments.

Material Properties	<i>Anisotropy</i>	
	<i>Strain rate sensitivity</i>	
	<i>Thermal sensitivity</i>	
As-Formed S-Rail Properties	Tube Bending	<i>Bend severity (R/D)</i>
		<i>Degree of work hardening</i>
		<i>Thickness changes</i>
	Hydroforming (Low-Pressure)	<i>Residual stresses</i>
		<i>Degree of work hardening</i>
		<i>Thickness changes</i>
	<i>Residual stresses</i>	
Initial Thickness	<i>2 mm versus 3.5 mm</i>	
Cross-Section	<i>Round</i>	
	<i>Square</i>	

For a given strength level, the key material properties with the potential to affect crash response are the level of anisotropy, strain rate- and thermal-sensitivity. The effect of material anisotropy in the forming and crash models is examined through consideration of both an isotropic and anisotropic description of the constitutive response. The high rate material response during crash is examined in terms of the individual contributions of work-hardening, strain rate-hardening, and thermal softening on the crush force and energy absorption response of the s-rail. The three different bend severities examined in this work, as well as the subsequent hydroforming process will cause changes in the degree of work hardening, thickness change and residual stresses in the s-rail. The role that each of these forming effects plays in governing the crash response of s-rails is assessed in the numerical models of the experiments. Further investigation into the sensitivity of the crash response to tube thickness and the round versus square cross-section is also conducted.

Since numerical simulation predictions can be significantly dependent on mesh size and element formulation, the sensitivity of the models to these numerical parameters is also examined.

3.1.3 Numerical Investigations Further Examining and Isolating Physical Variables Governing the Crash Response of S-Rails

After having established the numerical modelling techniques and the predictive ability of the numerical models through comparison with experiment, additional simulations were conducted to further investigate the parameters governing the crash response of s-rails. This series of simulations considered parametric variations that were not considered in the experiments; these are summarized in Table 3.2. In particular, the models considered the effects of boost in bending (Section 1.3.7) and the adoption of the high-pressure hydroforming process (Section 1.4) rather than the low-pressure process used in the experiments. The supporting experiments for these two processes were not performed because acquisition of the tube bender tooling, hydroforming tooling, and the actual tube stock to allow hydroforming of s-rails with circumferential expansion was beyond the scope and budget of this project. Finally, the effects of more dramatic changes in the as-formed cross-section are examined by considering rectangular section s-rails.

Table 3.2: Summary of the additional variables that govern the crash response of s-rails that were not investigated through simulation of the forming and crash experiments.

As-Formed S-Rail Properties	Tube Bending	<i>Frictional Boost</i>
		<i>Independent Collet Boost</i>
	Hydroforming (High-Pressure)	<i>Circumferential expansion</i>
		<i>End-feed</i>
Cross-Section	Round	
	Square	
	Rectangular (2:1 and 1:2 aspect ratios)	
Material Properties	Strength	

The investigation into the use of boost in bending is motivated by findings that boost can reduce the level of thinning and strain in the bend region of a tube [6,11,19,20,25,27], which

in-turn should affect the overall resistance to deformation within the hinge regions of the s-rail that form during crash (Figure 1.3). Therefore, tube bending simulations with greater prescribed boost and utilizing an independent collet condition (Figure 1.6) are conducted to determine the implications on strain and thickness changes, as well as crash response.

High-pressure hydroforming processes utilize dies in which the die section perimeter exceeds the tube circumference; hence the tube must expand to fill the die. This process can result in thinning of the tube wall, and end-feed is used to counteract thinning and increase corner expansion of the material. Consequently, the high-pressure hydroforming process causes changes in thickness and strain in the hinge locations of the s-rail that are different from those in the low-pressure process. The higher level of strain in the high-pressure process also leads to greater work hardening in the as-formed condition than in low-pressure operations. Therefore, the effects of circumferential expansion and end-feed on the physical characteristics and crash response of s-rail structures is examined.

Changes in the s-rail cross-section are investigated to determine the resultant effects on crash response. Here, round, square and rectangular cross-sections are considered. The rectangular cross-sections had aspect ratios of 2:1 and 1:2. Crash simulations on uniform thickness s-rails without previous work hardening and residual stress effects for each R/D ratio were also performed to isolate the effects of bend radius on s-rail crash response. Finally, the role of material strength on the s-rail crash response is further examined through simulation by comparing AA5754 and EN-AW5018 s-rails formed from the same initial tube thickness.

3.1.4 Modelling Approach and Implementation

To conduct the parametric study outlined in Figure 3.1, Figure 3.2 and Figure 3.3, detailed finite element models of the tube bending and hydroforming processes are developed and used to simulate the fabrication of the s-rail, as well as the crash tests. Within this modelling approach, the previous deformation history of the s-rail is considered in the subsequent analysis. An important aspect of the finite element simulations is the material model used to characterize the material constitutive response and yield criterion. Both isotropic and anisotropic material models are considered in the forming and crash simulations using parameters determined from the material characterization experiments of Chapter 2. In

addition, strain-rate- and temperature-sensitive Johnson-Cook and Zerilli-Armstrong material models are employed in the simulations utilizing parameters determined based on the findings by Salisbury *et al.* [106,107].

To implement the aforementioned modelling strategy, finite element models of tube bending, hydroforming and crash were solved using LS-DYNA, version 970, an explicit dynamic finite element code [30,31]. The modelling operations are sequenced in the following manner: (i) first bend; (ii) implicit springback analysis; (iii) second bend; (iv) implicit springback analysis; (v) hydroforming; (vi) implicit springback analysis; and, (vii) impact test. Note that the fabrication of the tube from sheet was not modeled since the tubes were annealed to the O temper after tube fabrication and the as-tubed stress-strain curves were used in the simulations. After each simulation step, the nodal positions, element connectivity, thicknesses, stresses and strains are all output for use in subsequent analyses to transfer the forming history between the various forming models and eventually into the crash simulation. The same mesh is used throughout the forming and crash models to allow a direct one-to-one mapping of nodal and element data between the various simulations. To increase the computational efficiency of the numerical models, the weld seam was not modeled.

The tooling geometry for the tube bending and hydroforming models was developed using SolidWorks 2004. The Hyperworks 7.0 software suite was used as a pre-processor to generate the finite element meshes used to discretize the tooling surfaces and also for the post-processing of results.

The following sections detail the tube bending, hydroforming and crash models. Note that the material modelling aspects of the simulations are discussed in the last section of this chapter.

3.2 Tube Bending Simulation

The simulation of the s-rail pre-bend operation comprises four distinct models of the following events: (i) first bend; (ii) springback; (iii) second bend; and, (iv) springback. The bend models utilize an explicit dynamic formulation; the tube is over-bent to compensate for springback. A static implicit analysis is performed after each bend to simulate elastic

springback to reach the desired 45-degree final bend angle. Prior to the second bend model, the tube is advanced the appropriate distance depending on the R/D ratio and the tooling is rotated 180-degrees. Within LS-DYNA, the springback output option is utilized after each forming or springback stage, which generates a “dynain” file containing the nodal positions, element connectivity, thickness, stress and strain. This file is then included within the input deck for the subsequent analysis to initialize the thickness, strain and stress values to reflect the material history from the previous simulation.

The bending parameters prescribed in the models are consistent with those used in the experiments, as summarized in Table 2.5 and Table 2.6. The sequence of the prescribed displacements and loads applied to the tooling within the tube bending simulations, shown in Figure 3.4, are consistent with those prescribed in the experiments, with the exception that the time was scaled dramatically to increase computational efficiency. In order to assess the sensitivity of the model’s predictions to possible dynamic effects, caused by time-scaling, the predictions were compared to those generated from a simulation utilizing a smaller time of 0.18 ms. The predictions from both simulations, scaled differently in time, were consistent, and the dynamic effects introduced by using an 18 ms time scale were judged to not significantly influence the predictive ability of the model, which is consistent with findings by Dymant [18]. To also help reduce any dynamic effects, artificial dampers (rigid body stoppers within LS-DYNA) were prescribed on the tooling velocity to limit oscillations in force due to contact. Note that within the first two seconds of the simulation, the clamp die is closed and the pressure die load is applied. Initiation of the bend within the simulation actually begins at a time of 2 ms.

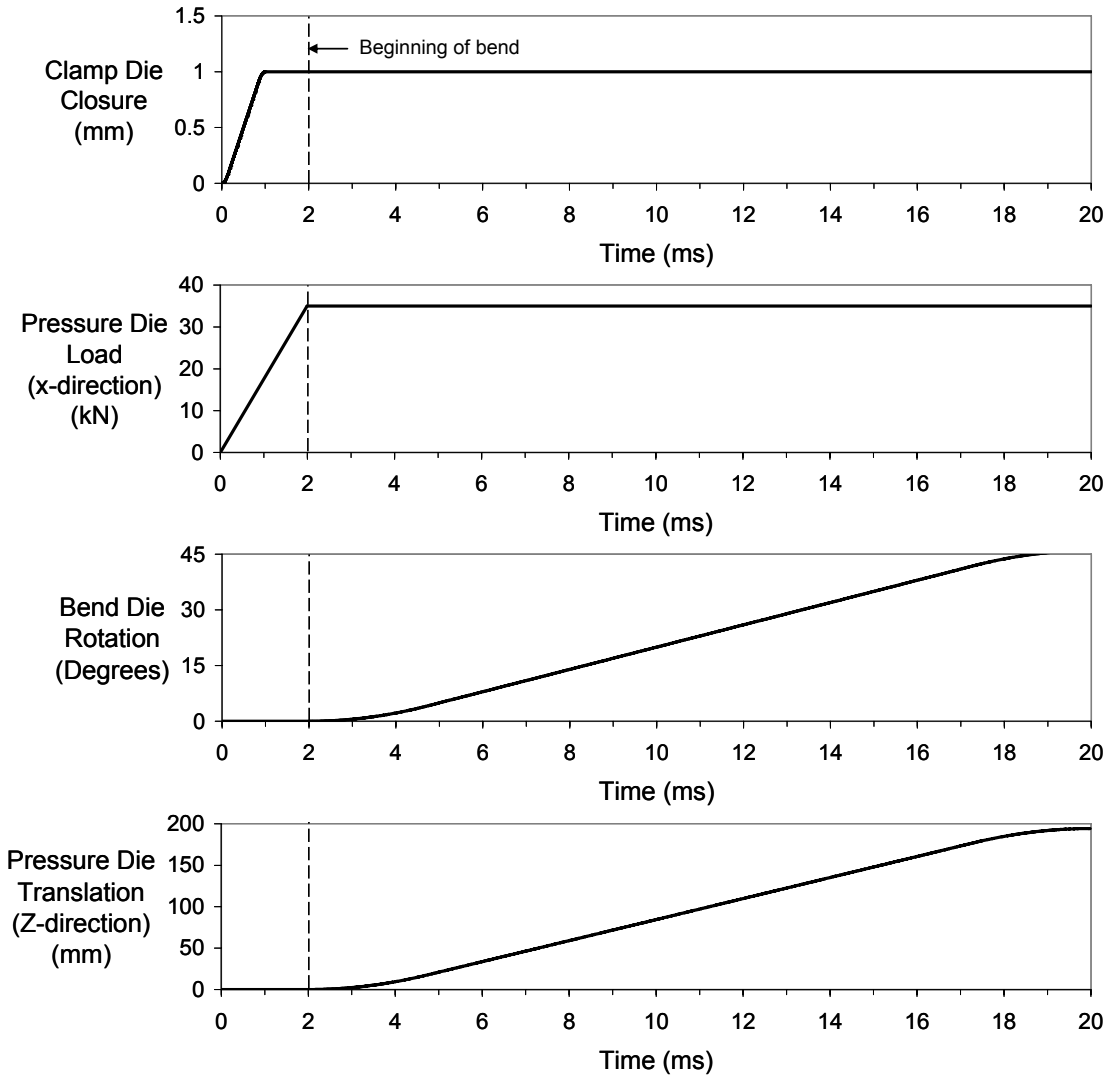


Figure 3.4: Prescribed displacement and loads of the moving tools within the tube bending simulation.

The finite element discretization used to model the tube bending operation is shown in Figure 3.5. The bend tooling surfaces were discretized using 5 mm shell elements and treated as rigid bodies. The tube bending, as well as the hydroforming models, utilized co-rotational, four-noded, fully-integrated (type 16) quadrilateral shell elements [30,31] with seven integration points through the thickness to represent the tube. Simulations considering one of three element sizes to discretize the undeformed tube, that is 2.5, 5 and 7.5 mm (Figure 3.6), allowed the mesh sensitivity of the tube bending, subsequent hydroforming and crash models to be examined. The results presented herein are primarily those using the finest mesh, with 2.5 mm elements.

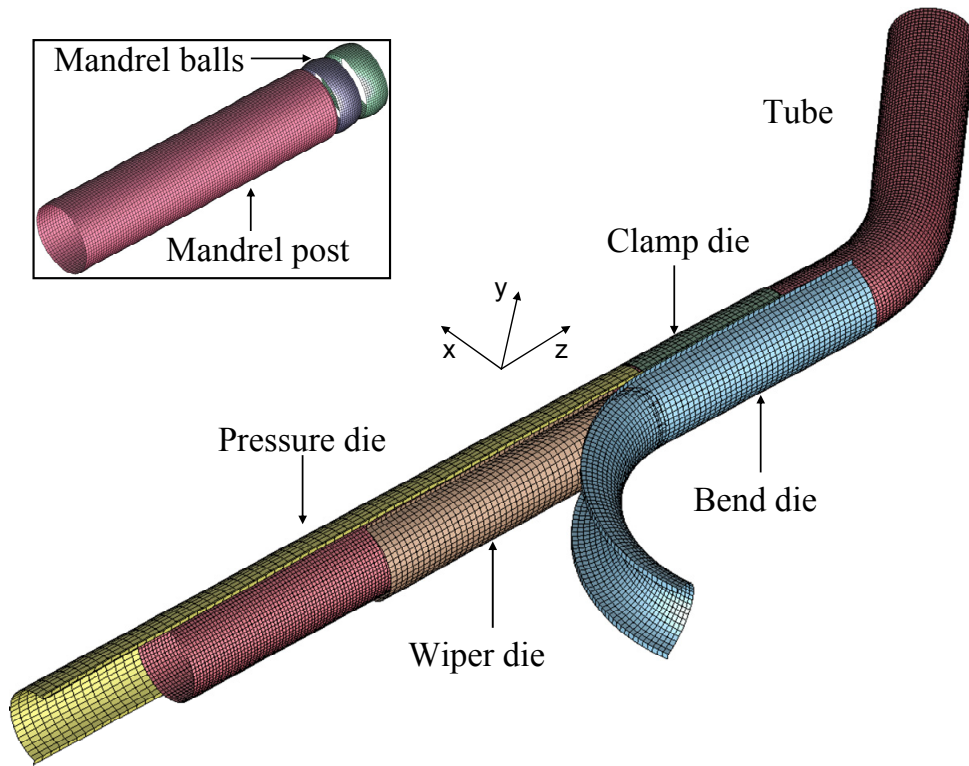


Figure 3.5: Finite element discretization used to model the tube bending operation.

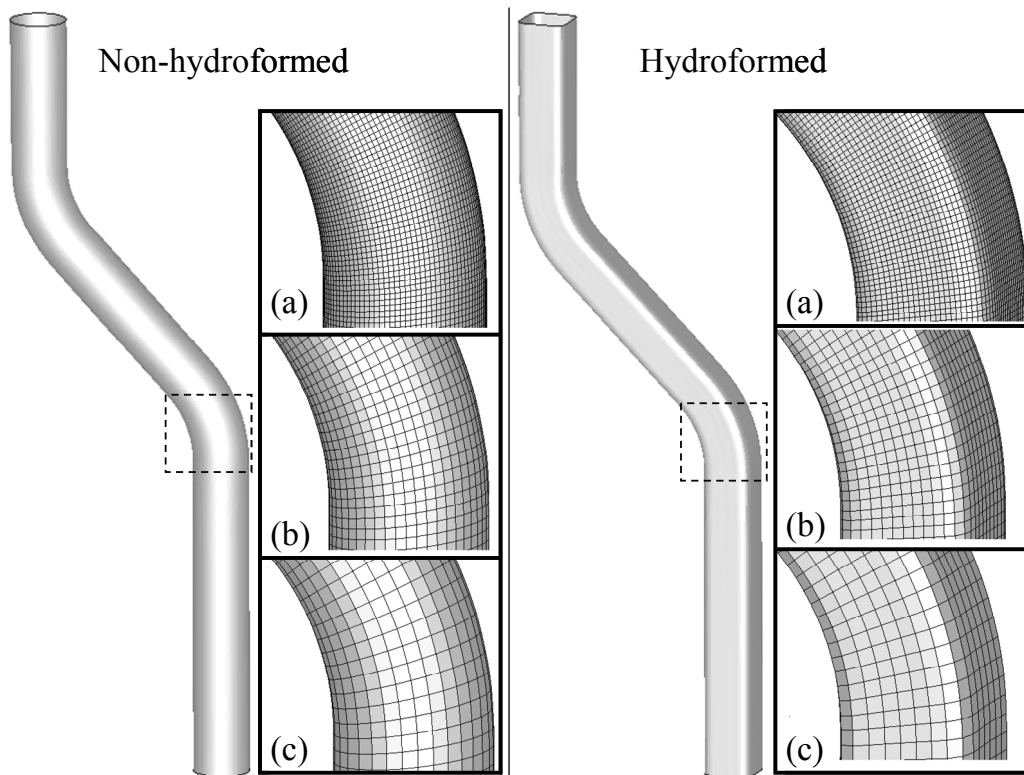


Figure 3.6: Non-hydroformed and hydroformed s-rails with element size discretizations of (a) 2.5; (b) 5; and, (c) 7.5 mm.

For the simulation of the second bend, a prescribed motion boundary condition on nodes near the clamp end of the tube was required to prevent a whipping action at the end of the tube, as shown in Figure 3.7. These nodes are prescribed the same angular displacement-time history as the bend die, allowing the bend model to be accelerated to improve computational efficiency. Without the prescribed motion boundary condition on the nodes shown in Figure 3.7a, the whipping action at the end of the tube induces localized deformation near the end of the contact region between clamp and bend dies and the tube (Figure 3.7c and Figure 3.7d). The introduction of this additional applied boundary condition did not induce additional localized deformation or stresses in the tube and was judged to provide a result that was representative of the experiment. This assessment was further verified by comparing the predicted deformation, stress and strain in the bent tube against the predictions from a model of the second bend that did not have the prescribed motion boundary condition, but was run slowly enough to avoid the whipping action of the end of the tube. The strain distributions were very close, such that the approach adopted was deemed acceptable.

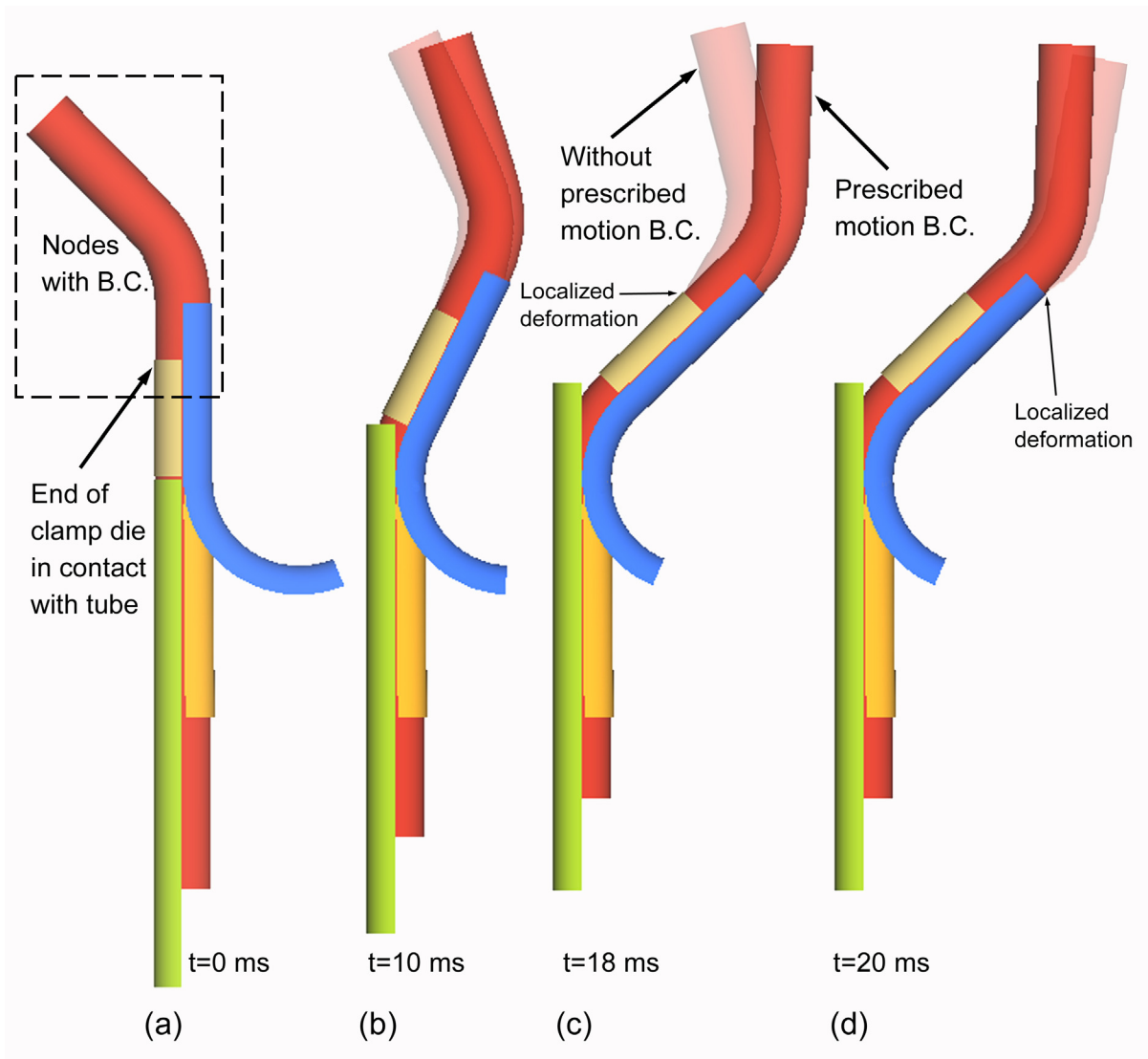


Figure 3.7: Predicted deformation of tube during second bend for models utilizing and not utilizing a prescribed motion boundary condition on nodes near the clamp die end of the tube. Predicted deformation is shown at (a) 0 ms; (b) 10 ms; (c) 18 ms; and (d) 20 ms.

A penalty function-based contact treatment [112] was prescribed between the tooling and tube. The coefficients of friction prescribed for the tooling-tube interfaces are presented in Table 3.3, and were determined from twist compression friction tests performed as part of this research (Appendix A).

Table 3.3: Coefficients of friction used in tube bending and hydroforming models.

Tooling	Coefficient of Friction	
	<i>Static</i>	<i>Dynamic</i>
Bend die	0.14	0.10
Clamp die	0.14	0.10
Pressure die	0.14	0.10
Wiper die	0.05	0.05
Mandrel	0.06	0.06
Hydroforming die	0.08	0.08

3.2.1 Bending with Additional Boost

A 100% frictional boost condition was employed in the tube bending experiments. In order to determine the degree that boost affects the crash response of s-rails, additional simulations were performed that considered the bending of a 3 mm AA5754 tube at R/D=2.0 using 104% boost under both frictional boost and independent boost conditions (Figure 1.6) (Section 1.3.7), followed by subsequent low-pressure hydroforming and crash simulations. The bending process variables for the additional boost cases are consistent with those in Table 2.5, with the exception of the pressure die clamp load, which had to be increased to 45 kN to prevent wrinkling on the inside of the bend.

To mimic the collet attached to the independent boost actuator, available in many commercial benders, that pushes on the end of the tube during bending (Figure 1.6), the nodes on the end of the tube are prescribed a boundary condition such that their axial displacement is equal to the prescribed axial displacement of the pressure die. The 104% boost case is achieved by increasing the prescribed axial displacement of the pressure die by a factor of 1.04. This condition corresponds nominally to superposition of a 4% axial compressive strain onto the imposed bending stress.

3.3 Hydroforming Models

The low- and high-pressure hydroforming models are presented separately in this section. Within the low-pressure process description, the simulations are based on the actual hydroforming experiments in which the s-rail cross-section is changed from round to square. Additional simulations are performed that examine the low-pressure hydroforming of the s-rail cross-section from round to rectangular. High-pressure hydroforming simulations are

also presented; first, the details of the process itself are given, and then a description of the numerical investigation conducted to isolate the effect of circumferential expansion and end-feed on the crash response of s-rails is provided.

The tooling surfaces for all of the hydroforming simulations were discretized using 2.5 mm sized elements. For simplicity and to reduce the computational cost of the hydroforming simulations, the floating end-seals are not modeled. Figure 3.8 shows the finite element meshes used to represent the surfaces of the low-pressure hydroforming dies. The square cross-section die used in the experiments was modeled, as well as two rectangular cross-section dies considered in the numerical parametric study.

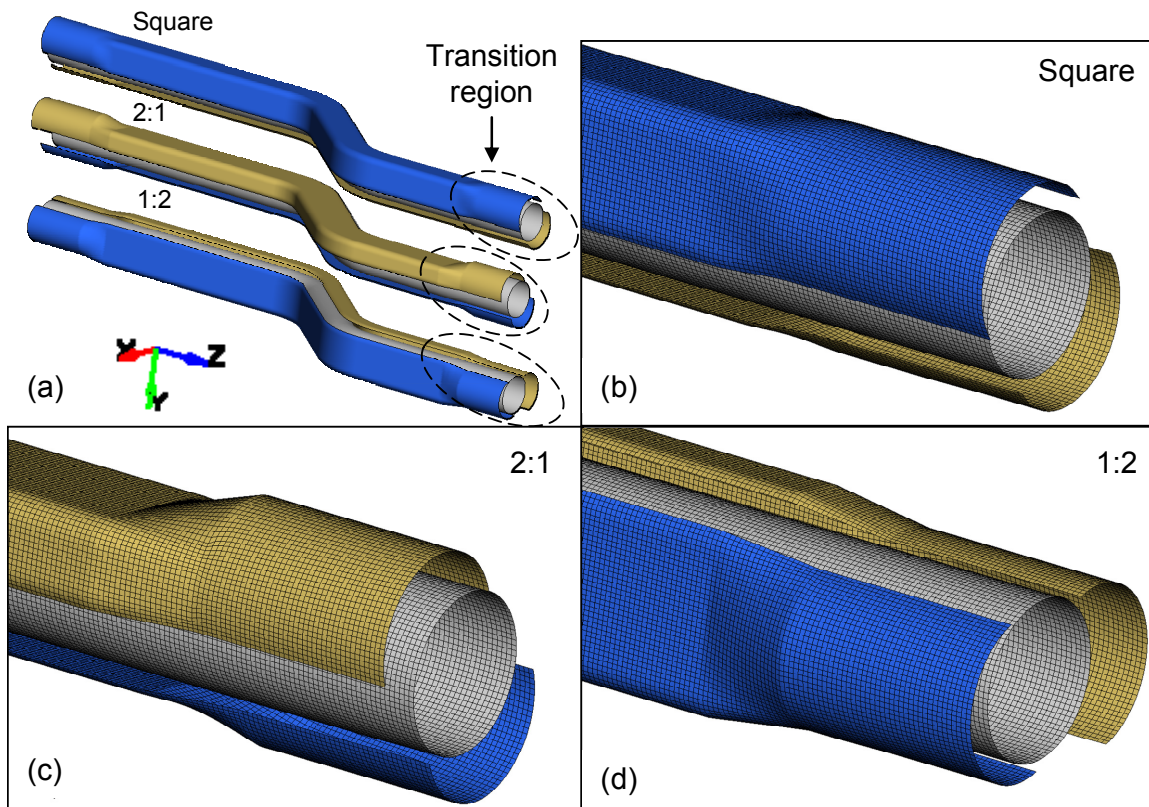


Figure 3.8: (a) Die surfaces and tube for simulating the hydroforming s-rails of square, and rectangular cross-sections with aspect ratios of 1:2 and 2:1. Close-up view of the transition region of the finite element discretization of the: (b) square; (c) rectangular with aspect ratio of 2:1; and (d) rectangular with aspect ratio 1:2 die cross-sections.

After simulation of either the low- or high-pressure hydroforming process, a static implicit analysis is performed on the tube to simulate elastic springback. After the springback analysis, the hydroformed s-rail is trimmed to eliminate the excess length at the

tube ends that is required for the transition and sealing region of the s-rail during hydroforming, as shown in Figure 2.13. As with the tube bending model, the hydroforming models also utilize co-rotational, four-noded, fully-integrated (type 16) quadrilateral shell elements [30,31] with seven integration points through the thickness to represent the tube. The coefficient of friction used in the contact algorithm is 0.08, which corresponds to the solid film lubricant in the experiments (Appendix A, Table 3.3).

3.3.1 Low-Pressure Process

The low-pressure hydroforming process simulated in this work utilizes near-zero percent expansion and zero end-feed to form the pre-bent tube. The prescribed sequence of the die closure and the internal pressurization of the tube is consistent with that prescribed in the experiments and is shown in Figure 3.9. Within the low-pressure hydroforming simulations, the die is first closed over a period of 8 ms while an internal pressure of 4.5 MPa is maintained in the tube. Upon die closure, the internal pressure is increased linearly to a maximum pressure of approximately 65 MPa in 4 ms. Dynamic effects due to the time-scaling did not influence the predictions of the model. This was verified by comparing the models predictions that considered a time-scale of 12, 0.12 and 0.012 ms.

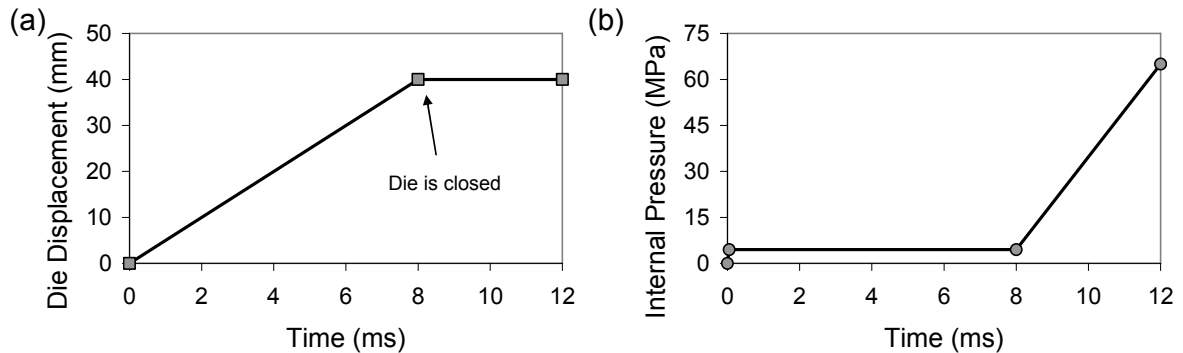


Figure 3.9: Prescribed sequence of die closure and internal pressure within the low-pressure hydroforming simulation.

A graphical comparison of all four s-rail cross-sections examined in this work is presented in Figure 3.10, and the second moment of area for each section, assuming a uniform thickness, is given in Table 3.4. The second moment of area is useful in providing an indication of the relative resistance to bending of the various cross-sections. The rectangular cross-sections have an aspect ratio of either 2:1 or 1:2 and are simulated under

the same hydroforming conditions as employed for the square cross-section s-rail. The aspect ratio is specified in terms of the section depth to width with respect to the neutral axis in bending, as also shown in Figure 3.10. Note that the four s-rail cross-sections examined in the low-pressure hydroforming simulations have the same perimeter corresponding to a near zero-percent expansion without end-feed.

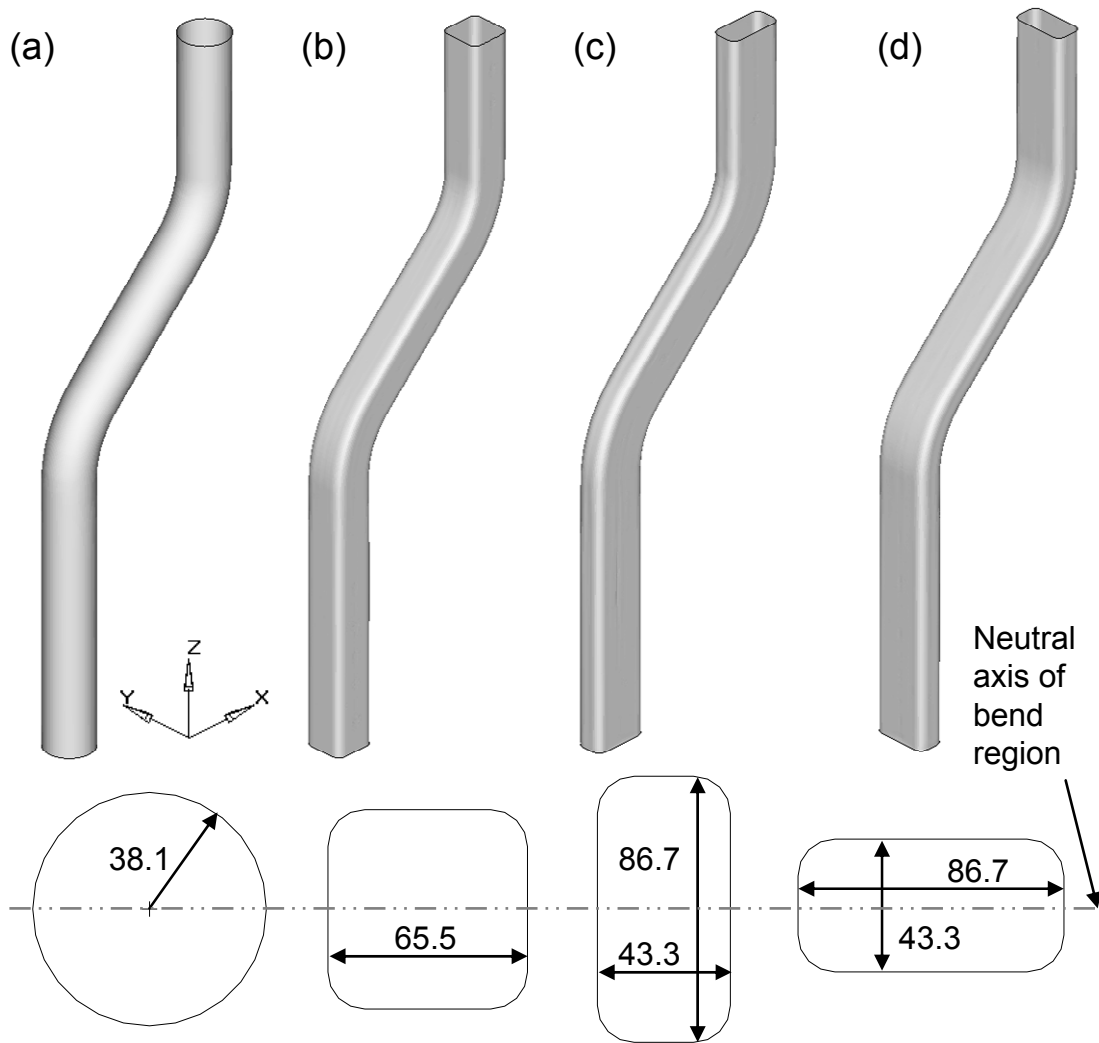


Figure 3.10: (a) Round; (b) square; (c) rectangular with an aspect ratio 2:1; and, (d) rectangular with an aspect ratio of 1:2 cross-section s-rails. Units are in millimeters.

Table 3.4: Summary of the second moment of area about the neutral axis of bending for the various cross-sections examined in the s-rail.

Cross-Section	Second Moment of Area (mm ⁴)
Round	472 x10 ³
Square	440 x10 ³
Rectangular (2:1)	628 x10 ³
Rectangular (1:2)	216 x10 ³

3.3.2 High-Pressure Process

Simulations were also undertaken that considered high-pressure hydroforming, with its associated circumferential expansion and end-feed, and the resulting effects on the thickness and strain characteristics of s-rails, and the subsequent crash response. The goal of this investigation is to model the high-pressure hydroforming of AA5754 tubes with outer diameters less than 76.2 mm within the existing square cross-section die. The tubes were sized to induce 4% and 9% circumferential expansion within the tube, while maintaining the initial tube mass constant at 2.00 kg. Maintaining the final s-rail mass approximately constant, allows better one-to-one comparisons when assessing the effect of the hydroforming process on the crash response of s-rails. The tubes are pre-bent at R/D=2.5 using the modelling techniques described in Section 3.2 and the bend parameters utilized in the experiments are adopted. The crash tests were simulated using the techniques to be described in Section 3.4, with an impact velocity of 3.35 m/s, which is also consistent with the experiments. An isotropic von Mises material model based on the 3 mm AA5754 tube was employed.

The high-pressure hydroforming process simulated in this research consists of a die closure stage, followed by a pressurization stage that utilizes end-feed. A typical internal pressure and end-feed schedule used to hydroform the various tubes is shown in Figure 3.11. During the die closure stage, the internal pressure is kept at 2.8 MPa to prevent buckling of the tube and zero end-feed is prescribed. Upon die closure, the end-feed displacement is prescribed while the internal pressure is kept low to reduce retarding frictional forces that cause lock-up of the material against the die wall. Unfortunately, the need to keep the pressure low during end-feeding also can lead to buckling near the transition region between the straight and bent sections of the s-rail, as shown in Figure 3.12, which limits the amount

of end-feed that could be achieved. To overcome buckling in this region, the internal pressure may be increased; however, this increases the frictional forces acting on the s-rail and isolates the beneficial effects of end-feed to the ends of the s-rail, which is away from the bend region.

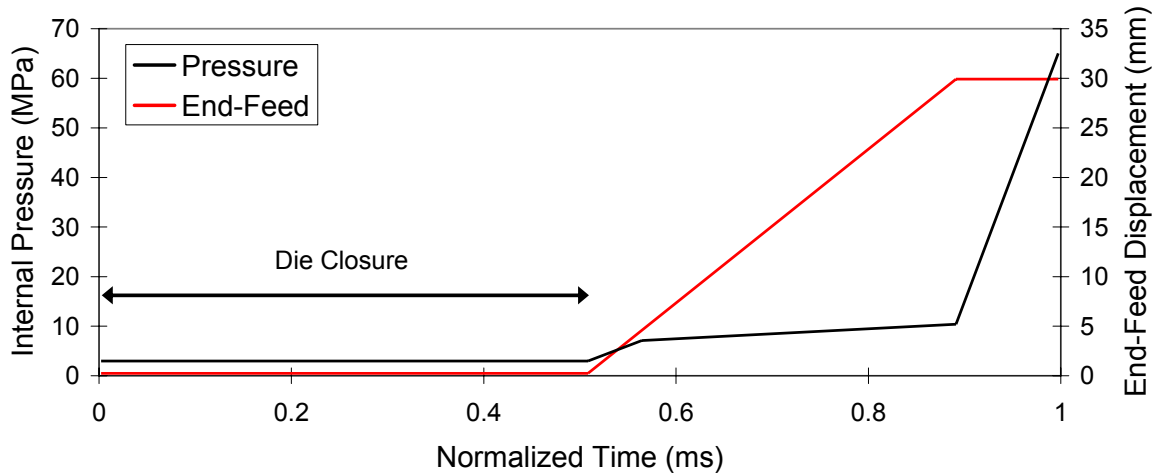


Figure 3.11: Typical internal pressure and end-feed schedule used in the high-pressure hydroforming simulations.

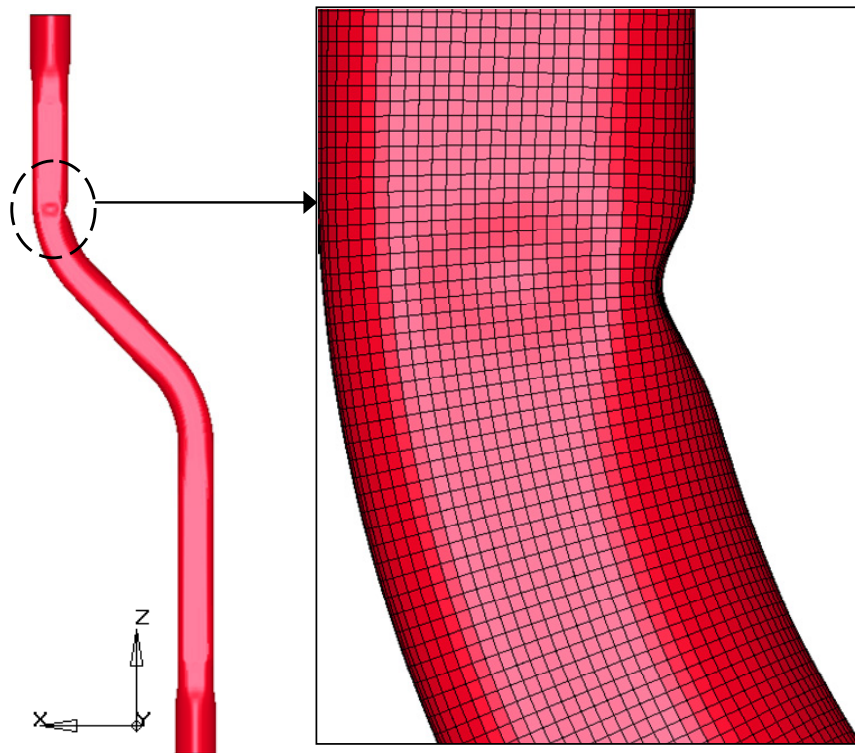


Figure 3.12: Typical buckling experienced due to excessive end-feed without sufficient internal pressure.

In order to simulate the end-feed operation during hydroforming, rigid walls are defined that push on the ends of the tube. This simplification of not modelling the end-plugs in the hydroforming operation resulted in buckling of the tube in the transition regions of the s-rail due to the lack of internal support. To avoid increasing the complexity of the models by considering the end-feed plungers, the tube was trimmed after die closure to remove the trim regions of the s-rail, shown in Figure 2.13. The end-feed boundary condition was then prescribed via rigid walls pushing directly on the ends of the square section of the s-rail, which was more resistant to buckling instability.

The test matrix for this study is presented in Table 3.5 and a schematic showing the initial outer diameter of the various tubes and final section perimeter is shown in Figure 3.13. Note that several hydroforming cases were considered that utilize a frictionless condition (Table 3.5) in order to determine the upper limit of end-feed without buckling of the s-rail. Subsequently, these hydroformed s-rails were impacted (numerically) to assess the sensitivity of the peak load and energy absorption to the hydroforming operation.

*Table 3.5: Test matrix examining the effect of the hydroforming process on the crash response of AA5754 s-rails. *Strain localization occurred; **Strain localization could not be avoided with end-feed.*

Expansion (%)	OD (mm)	Thickness (mm)	End-Feed	Static and Dynamic Coefficient of Friction
0	76.20	3.070	None	0.08
4	73.03	3.216	None	0.08
			Max (30 mm)	0.08
			Max (80 mm)	0
9	69.85	3.377	None *	0.08
			Max **	0.08
			Max (100 mm)	0

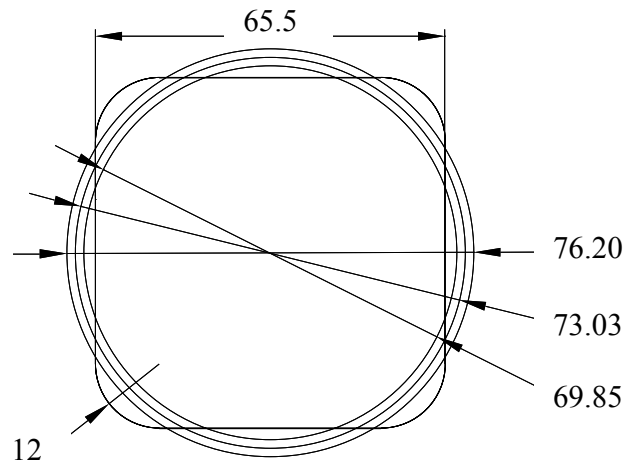


Figure 3.13: Schematic of undeformed tubes outer diameter and final hydroformed perimeter (width and corner radius). Units are in millimeters.

3.4 Crash Simulation

Simulation of the s-rail crash experiments considered a half-symmetry model of the impact structure to minimize computational cost, as shown in Figure 3.14. The nodes within 50.8 mm of the base of the structure are fixed, while the nodes within 50.8 mm of the opposite side of the s-rail near the impact plate are free to move only in the z-direction; mimicking the boundary conditions imposed by the clamps and bosses in the experiments. The impact plate, which represents both the sled and top cover plate, is assigned an inertial mass and treated as rigid. This approach allows the impact velocity (v) and the mass (m) to be prescribed directly. Note that due to symmetry, only one-half of the mass of the sled and impacted plate (567 kg, including the bosses and clamps) was assigned to the impact plate. The impact mass was modeled using shell elements and treated as rigid. A Butterworth 1 kHz filter was applied to the predicted force versus time data to be consistent with the filter on the deceleration sled [120]. Detailed examination of the effect of this filter on the measured and predicted response is presented in Section 5.3.2 and Appendix D.

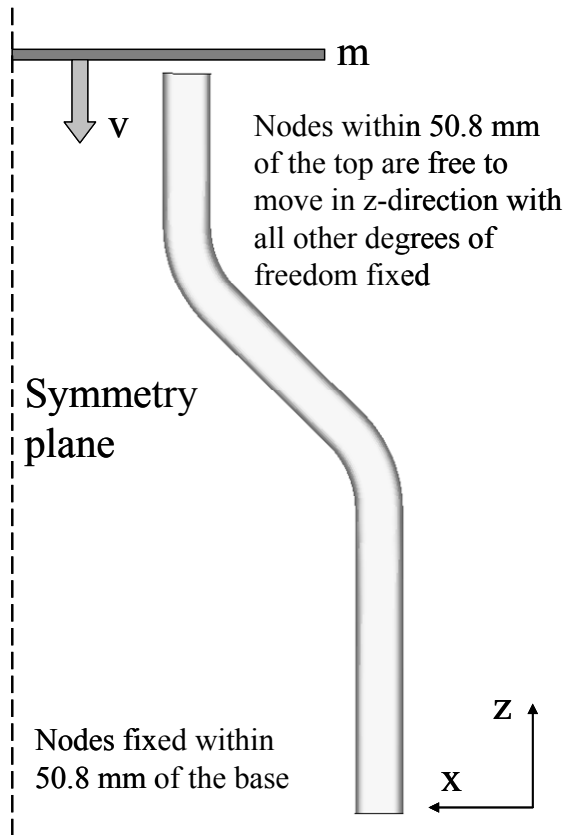


Figure 3.14: Crash model schematic and boundary conditions.

The crash simulations considered both fully integrated [30,31] and reduced integration four-noded Belytschko-Lin-Tsay [121] element formulations (element types 2 and 16, respectively, in LS-DYNA) with seven integration points through-thickness. Note that for the case of the single point quadrature Belytschko-Lin-Tsay elements, the strains and stresses output from the last springback simulation using the fully-integrated shell element were averaged prior to initializing the one-point quadrature Belytschko-Lin-Tsay elements used in the crash simulation. Use of the fully-integrated element formulation was limited to modeling the 2 and 3.5 mm EN-AW5018 non-hydroformed s-rail crash experiments since this element was found to exhibit a shear-locking phenomenon [112,122], which results in spurious losses of internal energy, as described in Chapter 5.

3.5 Material Models

Material properties corresponding to aluminium alloys AA5754 and EN-AW5018 [6] were assigned to the tube using a rate-insensitive isotropic piecewise linear hardening rule with a

von Mises yield criterion. The true stress versus true plastic strain response was curve fit using the classical Voce equation [108] to tensile data up to the point of necking and the remainder of the curve was extrapolated, as shown in Figure 2.6. Relevant elasticity constants and density typical of a 5XXX-series aluminium alloy were adopted and can be found in Table 3.6. The rate-insensitive anisotropic Barlat (1989) yield criterion [123], with a piecewise linear representation of flow stress, was also considered to assess the effect of anisotropy on thinning during forming and subsequent crash response. The anisotropic Barlat (1989) yield criterion for plane stress [30] is defined as

$$\Phi = a|K_1 + K_2|^M + a|K_1 - K_2|^M + c|2K_2|^M = 2\sigma_y^M \quad (3.1)$$

where σ_y is the yield stress, M is the yield exponent and $K_{i=1,2}$ are given by:

$$K_1 = \frac{\sigma_x + h\sigma_y}{2} \text{ and } K_2 = \sqrt{\left(\frac{\sigma_x - h\sigma_y}{2}\right)^2 + p^2\tau_{xy}^2}$$

The anisotropic material constants a , c , h and p are obtained through the Lankford parameters [30]. The associated material parameters are also shown in Table 3.6.

Table 3.6: Barlat (1989) model parameters. Lankford parameters provided by tube supplier [109].

Material	Density (kg/m ³)	Elastic modulus (GPa)	Lankford Parameters (0°, 45° and 90°)	Yield Exponent (M)
AA5754	2,700	67.9	0.64, 0.76, 0.64	8
EN-AW5018			0.75, 0.75, 0.75	

The alloys considered in this research have been shown to be relatively rate-insensitive by Smerd *et al.* [104], Salisbury *et al.* [106,107] and Worswick *et al.* [124]. Nonetheless, a series of simulations utilizing the rate-sensitive Johnson-Cook [125,126,127] and Zerilli-Armstrong [128,129,130,131] material models was performed to assess the importance of high strain rate and thermal softening effects in the AA5754 tube. Note that simulations of both forming and crash were performed using the rate-sensitive material models; the motivation for their use within the forming simulations is to determine whether a single material model can be utilized for both the forming and crash events, which simplifies the modelling process. The Johnson-Cook and Zerilli-Armstrong constitutive model parameters

were developed for the 3 mm AA5754, and 2 and 3.5 mm EN-AW5018 alloys as part of a high strain rate material characterization investigation by Salisbury *et al.* [106,107].

3.5.1 Johnson-Cook Model

The Johnson-Cook [125,126] constitutive model, as implemented in LS-DYNA, has the following form

$$\sigma = \left[A + B \varepsilon_{pl}^n \right] \left[1 + C \ln \left(\frac{\dot{\varepsilon}^*}{\dot{\varepsilon}_o} \right) \right] \left[1 - T^{*m} \right] \quad (3.2)$$

where ε_{pl} is the effective plastic strain, $\frac{\dot{\varepsilon}^*}{\dot{\varepsilon}_o}$ is the dimensionless plastic strain rate for a

reference strain rate $\dot{\varepsilon}_o$. T^* is a form of homologous temperature, given as

$$T^* = (T - T_{room}) / (T_{melt} - T_{room}) \quad (3.3)$$

The five material constants A, B, C, m and n are fit to data collected for a particular material. The first term in parentheses in Equation 3.2 represents the power-law work hardening response of the material at the reference strain rate and temperature, while the second and third terms account for the strain rate and temperature sensitivity, respectively.

A user-defined material model (UMAT) was developed by Simha [132] that uses a modified version of the Johnson-Cook model in which a Voce work hardening term replaces the power law dependence in Equation 3.2. The Voce work hardening term better captures the material stress-strain behaviour at quasi-static rates. This model was also investigated and has the following form

$$\sigma = \left[\alpha + (\beta - \alpha) (1 - \exp(-\xi \varepsilon_{pl})) \right] \left[1 + C \ln \left(\frac{\dot{\varepsilon}^*}{\dot{\varepsilon}_o} \right) \right] \left[1 - T^{*m} \right] \quad (3.4)$$

where α, β, ξ, C and m are material constants fit to data. Within the UMAT, a tolerance parameter must be prescribed for the calculation of the through thickness stress, which is normalized by current yield stress, to ensure a plane stress condition exists [132].

The values for the Johnson-Cook model parameters employed in this work are shown in Table 3.7. The simulations utilizing the “standard” Johnson-Cook model, with the power law representation of the flow stress within Equation 3.2, determined by Salisbury [106,107] experienced numerical issues that could not be resolved. Consequently, the new form of the work hardening term in Equation 3.4 was employed. The parameters for the modified Johnson-Cook model (Equation 3.4) utilizing a Voce work hardening term were determined as part of this thesis (Table 3.7), using SYSTAT [133], a statistical software package to better capture the stress-strain response of the material at high levels of strain. One of the concerns regarding the standard Johnson-Cook model is that the parameters were determined over a strain range of 0-0.15, which is a physical limitation of the apparatus. Indeed, the form of the standard Johnson-Cook model extrapolation fails to accurately capture the AA5754 material saturation stress-strain response at quasi-static rates (0.0033 s^{-1}) for strains larger than 0.3, as shown in Figure 3.15. Clearly, a larger strain range upon which to more accurately determine the parameters is needed in view of the tendency of aluminium alloys to display a saturation stress.

Table 3.7: Johnson-Cook model parameters employed based on Hopkinson bar experiments by Salisbury et al. [106,107] using a power law work hardening term, and parameters determined in this work using a Voce law work hardening term.

Parameter	Standard Johnson-Cook Using Power Law*	Parameter	Modified Johnson-Cook UMAT Using Voce Law
A	126.4	α	100
B	340.5	β	315
C	0.0102	ξ	8.5
n	0.5	C	0.001
m	2.4	m	1
		Plane stress tolerance	10^{-2}

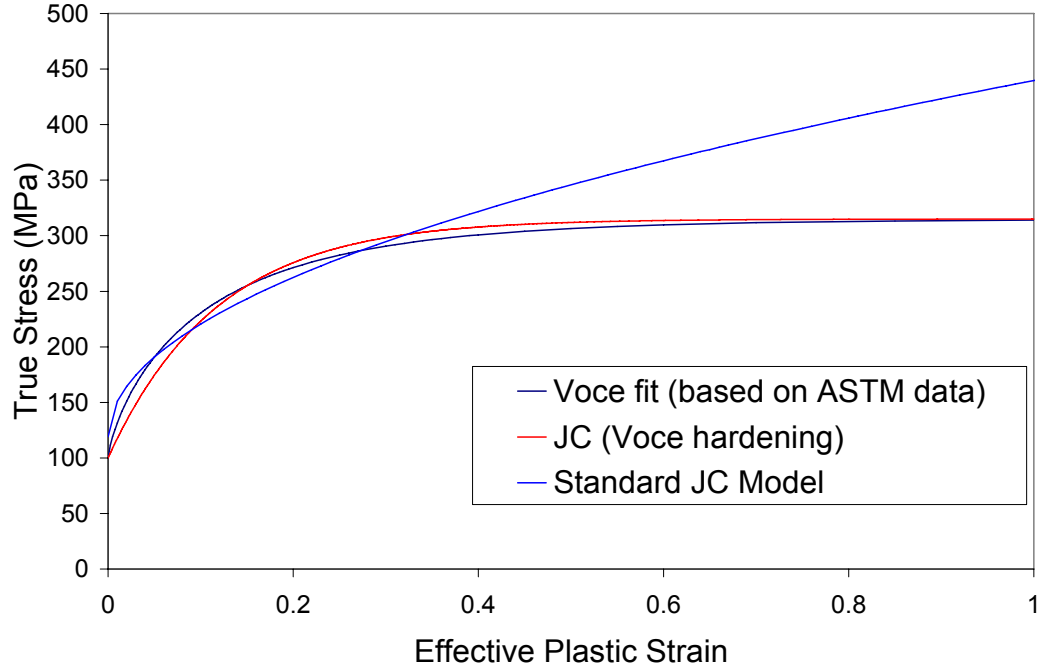


Figure 3.15: Voce curve fit based on ASTM data and predicted effective stress versus the effective plastic strain using a Johnson-Cook model with a Voce hardening term and a power-law hardening (standard) model. Stress-strain responses are at quasi-static strain rates.

3.5.2 Zerilli-Armstrong Model

The Zerilli-Armstrong [128,129,130,131] constitutive model was also considered in some of the simulations to incorporate high rate effects. This model, as implemented within LS-DYNA, has the following form

$$\sigma = C_1 + \left[C_2 \varepsilon^{1/2} e^{(-C_3 + C_4 \ln \dot{\varepsilon})^T} + C_5 \right] \left(\frac{\mu(T)}{\mu(293)} \right) \quad (3.5)$$

where

$$\left(\frac{\mu(T)}{\mu(293)} \right) = B_1 + B_2 T + B_3 T^2 \quad (3.6)$$

relates the dependence of the shear modulus on temperature. This dependence was neglected in the current work and B_1 was set to unity, and B_2 and B_3 were set equal to zero. The constant C_5 was also set to zero since the Hall-Petch relation for this material was unavailable.

The effective stress versus effective plastic strain at quasi-static rates (0.0033 s^{-1}) determined from the Voce curve fit to ASTM tensile test data (Figure 2.6) and the predicted response of the Zerilli-Armstrong model at strain rates ranging from 0.0033 s^{-1} to 500 s^{-1} are shown in Figure 3.16. The parameters employed in the Zerilli-Armstrong model, as determined by Salisbury *et al.* [106,107], are given in Table 3.8. Beyond 0.15 strain, the predicted flow stress at elevated strain rates using the Zerilli-Armstrong model is much greater than what would typically be expected for an aluminium alloy material. The effects of the Zerilli-Armstrong extrapolation of flow stress are further investigated in Chapter 5.

Table 3.8: Zerilli-Armstrong model parameters employed based on Hopkinson bar experiments by Salisbury *et al.* [106,107].

Parameter	Salisbury Parameters
C1	127 (MPa)
C2	622 (MPa)
C3	0.00201
C4	9.22E-05
C5	0
B1	1
B2	0
B3	0

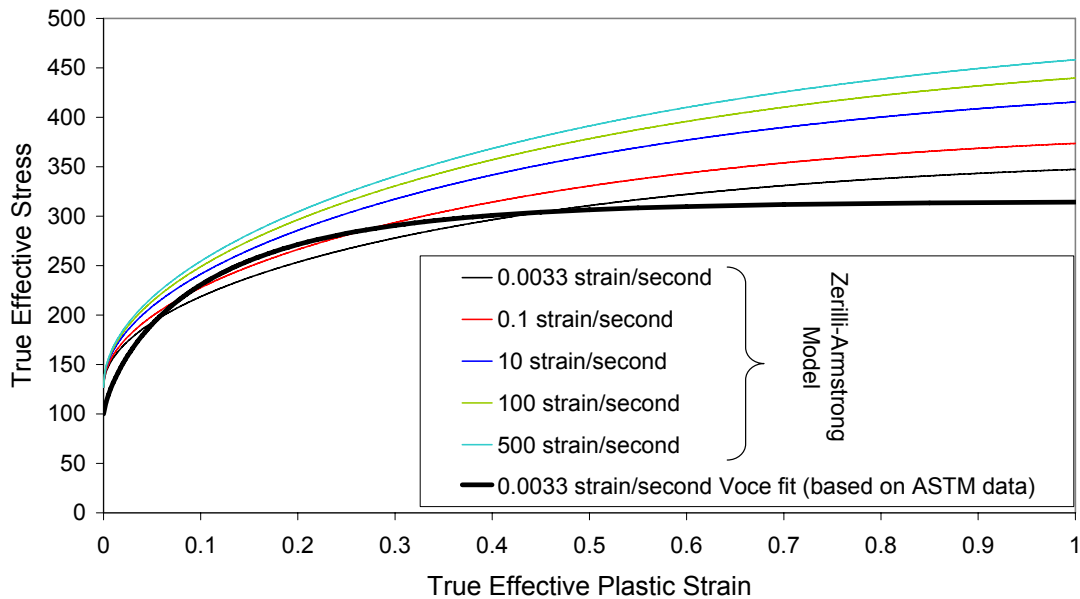


Figure 3.16: Effective stress versus effective plastic strain for a Voce fit based on ASTM data at quasi-static strain rates and predicted using the Zerilli-Armstrong model with parameters determined by Salisbury *et al.* [106,107] over a range of strain rates of $0.0033\text{-}500 \text{ s}^{-1}$.

Chapter 4

Experimental Results

The results from the tube bending, hydroforming and crash experiments are presented herein. The tube bending results are described in terms of the process variables and the as-formed tube ovality, thickness and strains. The hydroforming results are also presented in terms of the as-formed thickness and strains, followed by an examination of the interaction between the tube bending and hydroforming processes. Finally, the crash results on non-hydroformed and hydroformed s-rails are presented, with an assessment of testing repeatability and the effects of initial tube thickness, bend severity, and the low-pressure hydroforming process on the crash response of the s-rails. The effect of s-rail cross-section (round versus square) is assessed by comparing the response of hydroformed versus non-hydroformed s-rails. The results from crash experiments on annealed s-rails are also presented. These experiments are used to isolate the effects of work hardening and residual stress due to forming from thickness changes in the as-formed condition. The effect of the initial material strength (alloy) on the s-rail deformation response could not be assessed directly through the experiments since the thicknesses of the two alloys examined are different. The effect of material strength on s-rail crash response is isolated and investigated through simulation in Chapter 6.

4.1 Tube Bending Results

For brevity, the discussion of the tube bending results is limited to the 3 mm AA5754 s-rails. The general trends in terms of the relative thickness changes and strains after bending were the same for both alloys. Of course the bending loads did change with tube alloy and

thickness; however, this effect is discussed by Gholipour [137] and Oliveira *et al.* [6] and not presented here.

4.1.1 Process Variables and Ovality

The process data, comprising bend die torque, pressure die boost load and mandrel load measured during the bending of 3 mm AA5754 tubes, are plotted in Figure 4.1, Figure 4.2 and Figure 4.3, respectively. Median data with scatter bars is shown for each R/D ratio. The scatter bars provide an indication of the degree of repeatability during bending. There is little difference in bend torque for s-rails bent at the three R/D ratios, since all data fall within the experimental scatter. The respective pressure die boost loads for the s-rails bent at an R/D ratio of 2.5 and 2.0 again fall within their scatter limits and are indistinguishable; however, the s-rails bent at an R/D=1.5 require approximately 5 kN more load. This increase in pressure die boost load may be attributed to the significantly greater mandrel load resulting from the three-ball mandrel used in bending at R/D=1.5, versus the two-ball mandrel used for the R/D ratios of 2.5 and 2.0. The greater mandrel load observed in the s-rails bent at R/D=1.5 is also attributed to the tighter bend radius.

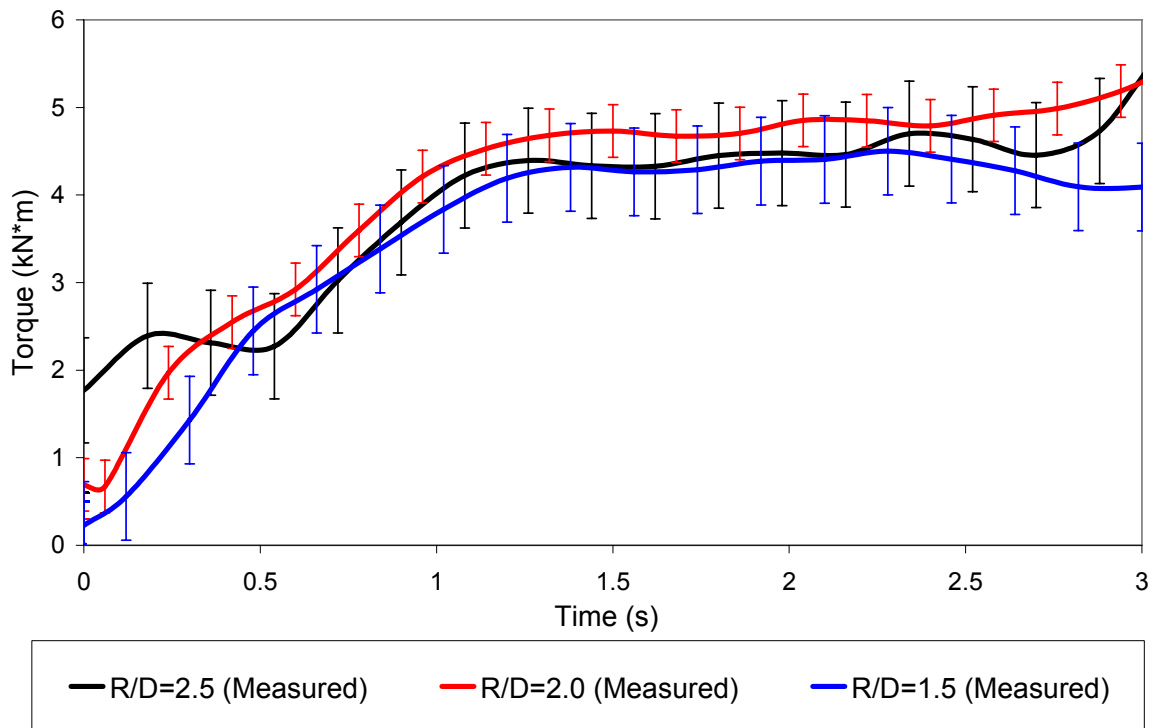


Figure 4.1: Bend die torque for 3 mm AA575 s-rails.

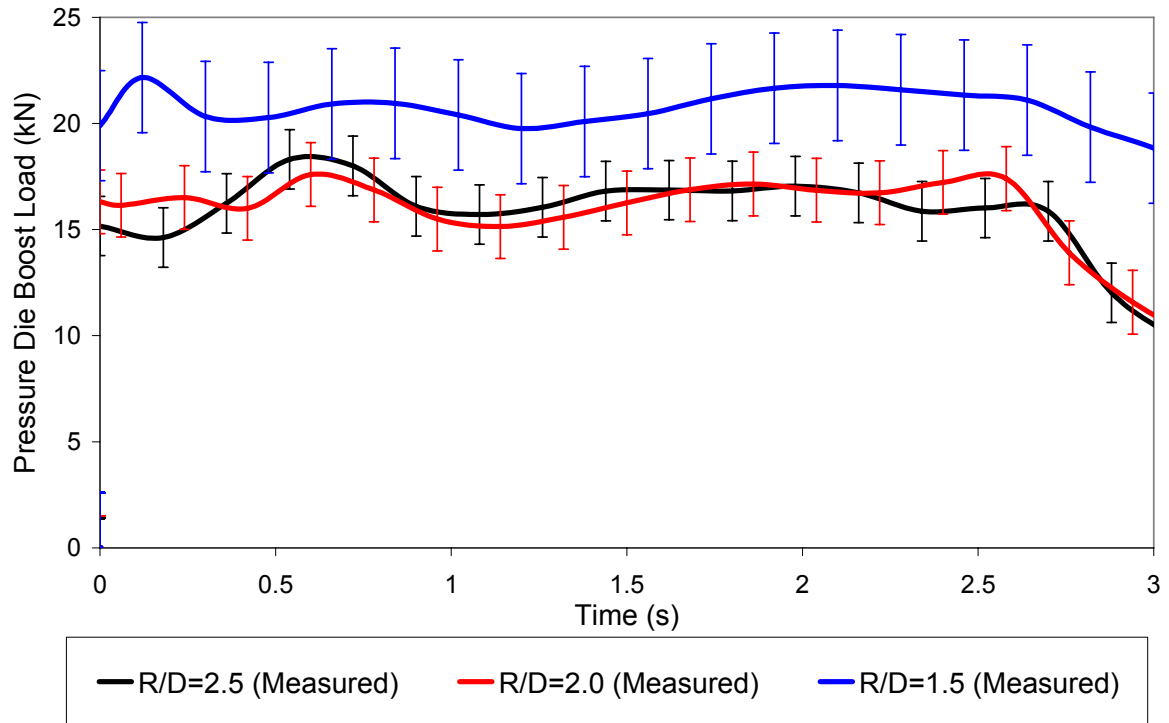


Figure 4.2: Pressure die boost load for 3 mm AA5754 s-rails.

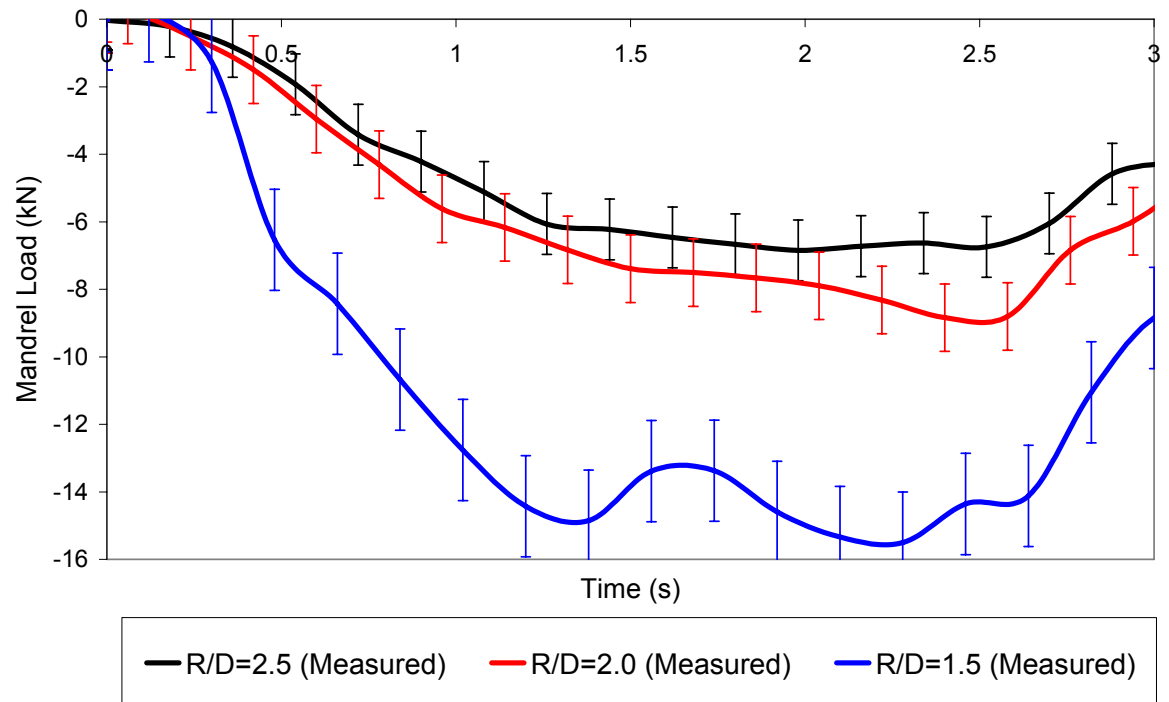


Figure 4.3: Mandrel load for 3 mm AA5754 s-rails.

The average ovality ratios, defined in Section 2.3.2, were measured in the various sections of the s-rails bent at R/D ratios of 2.5, 2.0 and 1.5 and are presented in Table 4.1. The overall degree of ovalization is very low.

Table 4.1: Ovality ratios in various sections of the 3 mm AA5754 s-rails.

Section	Ovality Ratio (%)		
	R/D=2.5	R/D=2.0	R/D=1.5
A	99.6	99.6	99.8
B	99.5	99.5	100.0
C	99.3	99.2	98.7
D	99.4	99.5	100.0
E	99.7	99.6	99.3

4.1.2 Thickness

Thickness distributions were measured on two tubes for each of the three R/D ratios and were found to lie within less than 1% of each other, indicating good repeatability; hence only results for one tube are shown for each R/D ratio in the following. The thickness distributions along the inside and outside, and around the circumference of the first bend (Figure 2.10) are shown in Figure 4.4, Figure 4.5 and Figure 4.6, respectively, for s-rails bent at each R/D ratio. The horizontal axis of Figure 4.4 and Figure 4.5 is given in terms of linear and angular measurements. The linear measurements (in centimeters) were taken just before and just after the bend in sections E and C, respectively, while the angular measurements (in degrees) were taken along the bend of the tube in section D (Figure 2.3). As the bend severity increases (smaller R/D ratio), there is an increase in the degree of thickening at the inside of the bend and thinning at the outside of the bend. Note that the thickness around the circumference, shown in Figure 4.6, does not change significantly at the neutral axis of the bend, located at approximately the 0 and 180 degree locations in Figure 4.6.

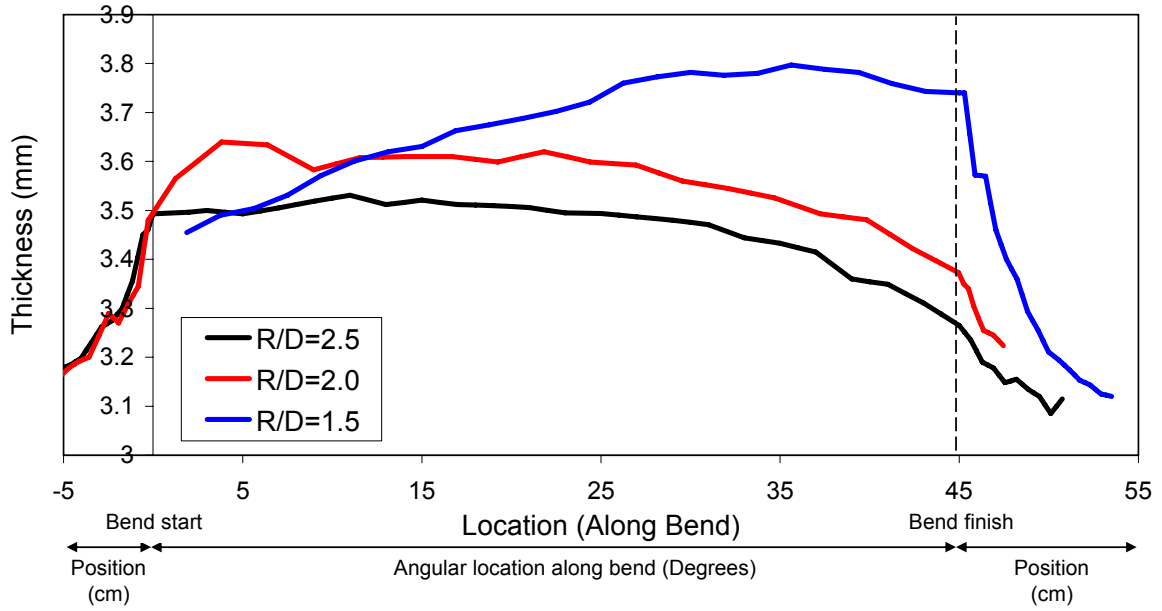


Figure 4.4: Thickness along the inside of the first bend for 3 mm AA5754 s-rails.

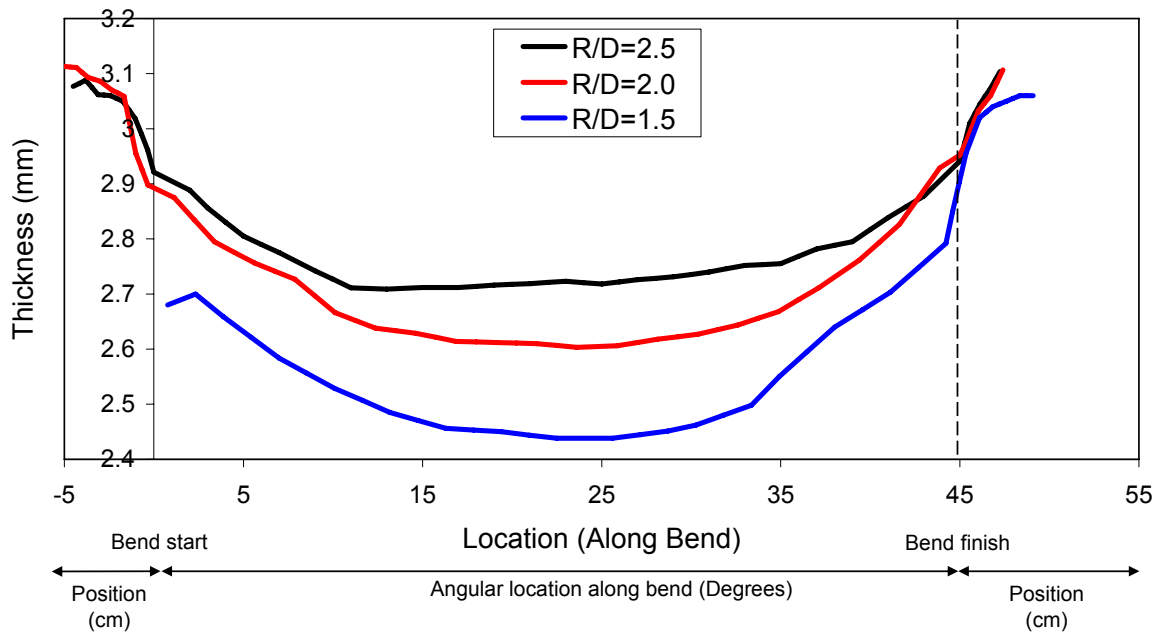


Figure 4.5: Thickness along the outside of the first bend for 3 mm AA5754 s-rails.

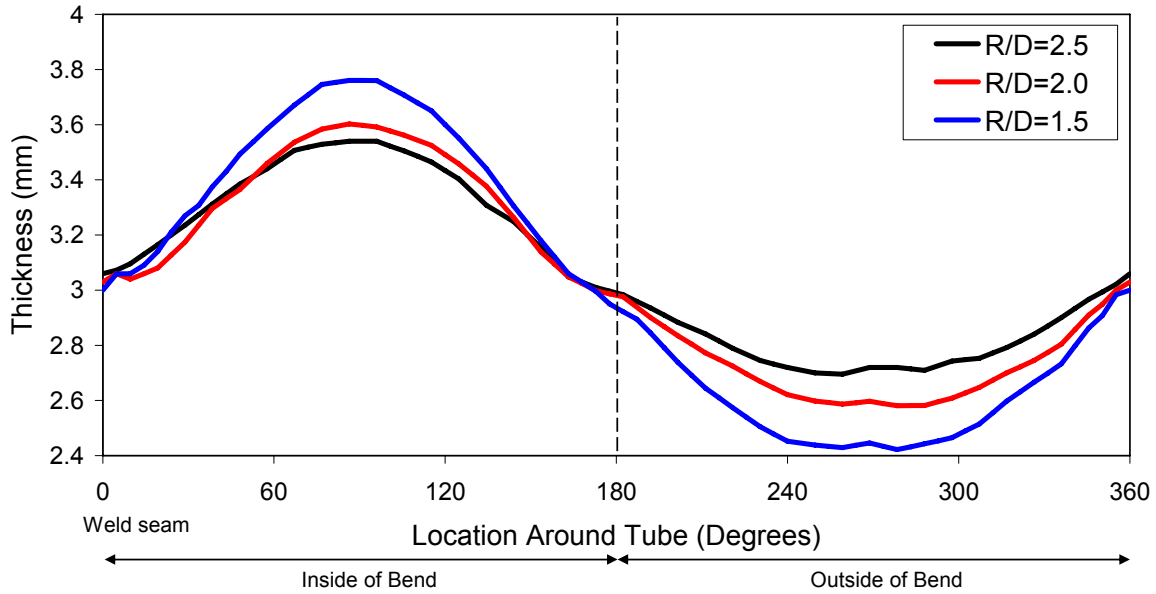


Figure 4.6: Thickness around the circumference of the first bend, at the center of the bend angle, for 3 mm AA5754 s-rails.

4.1.3 Strains

The measured strains for each R/D ratio were in very good agreement with one another and exhibited a variation of less than 3% strain, which lies within the precision of the strain measurement system employed. The major and minor engineering strains for s-rails bent at each R/D ratio, along the inside and outside, and around the circumference of the first bend are shown in Figure 4.7, Figure 4.8 and Figure 4.9, respectively. The scatter bands are not shown, but correspond to 3% strain, and results are only shown for one tube for clarity. Similar to the trends observed in the thickness measurements, as the bend severity increases (R/D ratio decreases), the magnitude of the axial strain increases. Note that the circumferential strain on the inside of the bend and the axial strain on the outside of the bend correspond to the major strain. The circumferential strains along the inside (major) and outside (minor) of the bend both have a magnitude that is less than 5% strain. Meanwhile the corresponding axial strain at the inside and outside of the bend is up to five times larger than this level. From the principle of volume constancy and, as a consequence of the near-zero (less than 5%) circumferential strains, one can infer that a near-plane strain condition exists in bending. The levels of axial strain measured at the outside of the bend at R/D ratios of 2.5, 2.0 and 1.5 are approximately 20%, 26% and 32%, respectively, which are in close accord

with those predicted through simple beam bending theory of 20%, 25% and 33%. This agreement is not surprising since the bends were performed at a boost level of 100%.

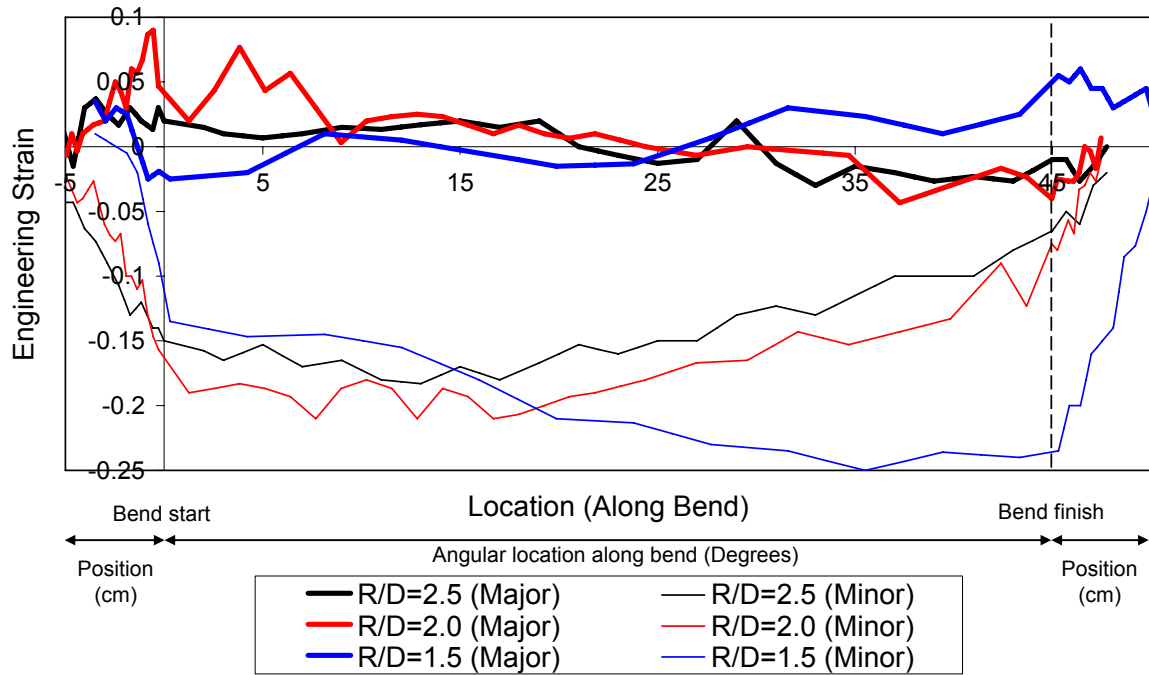


Figure 4.7: Major and minor engineering strain along the inside of the bend for 3 mm AA5754 tubes bent at R/D ratios of 2.5, 2.0 and 1.5.

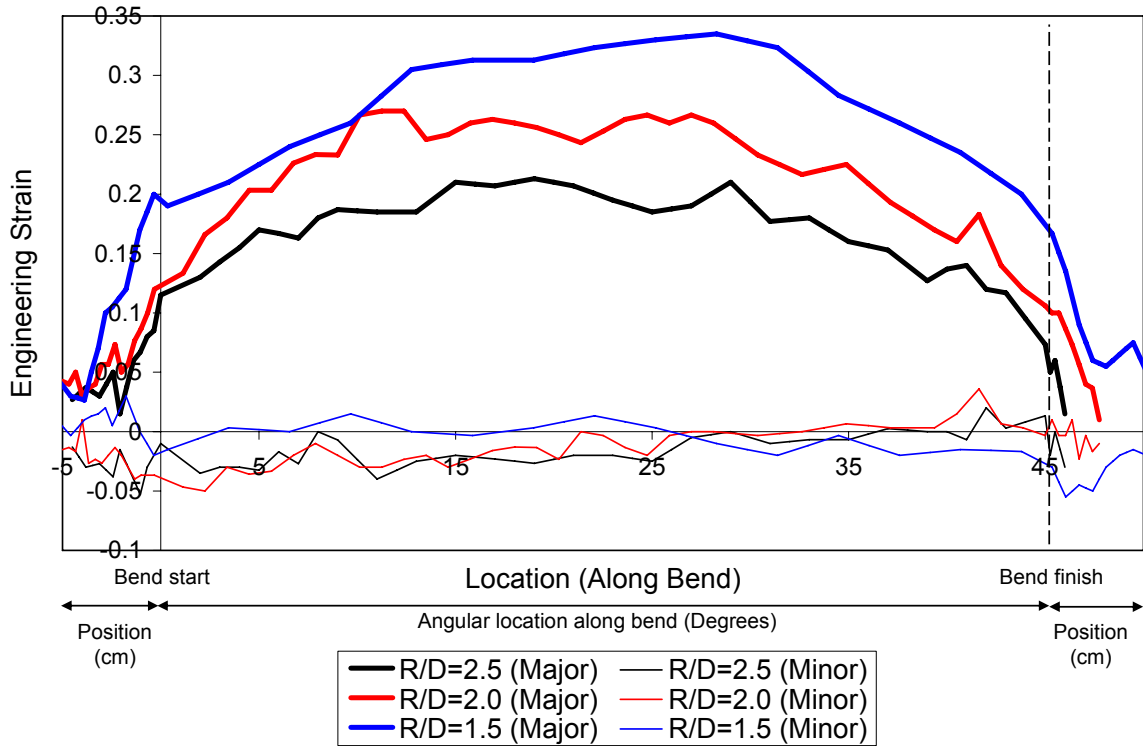


Figure 4.8: Major and minor engineering strain along the outside of the bend for 3 mm AA5754 tubes bent at R/D ratios of 2.5, 2.0 and 1.5.

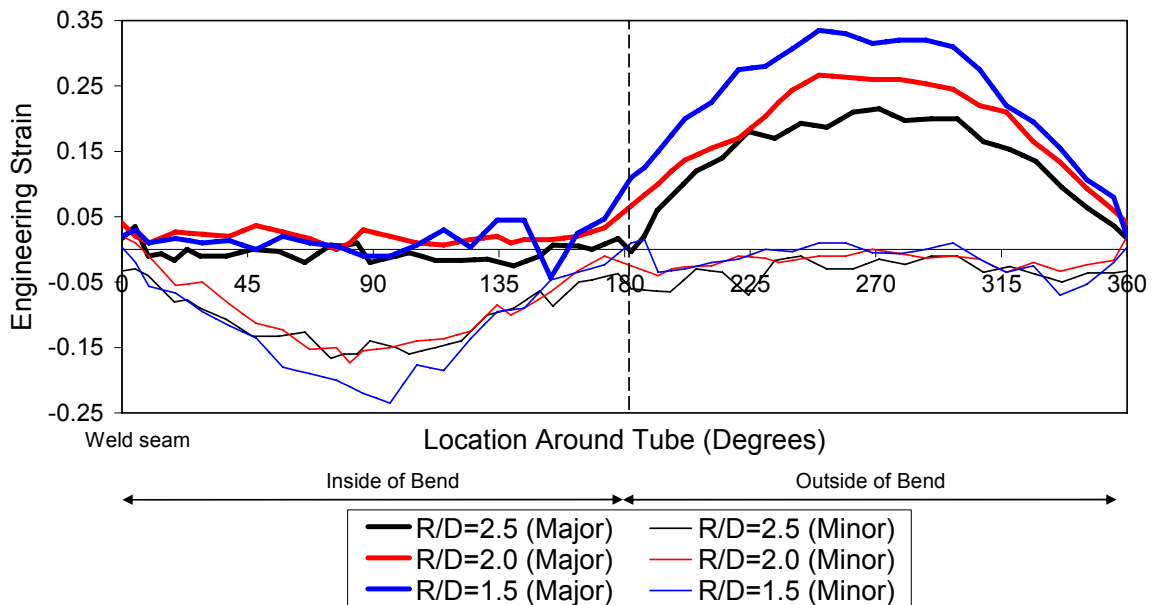


Figure 4.9: Major and minor engineering strain around the circumference of the bend for 3 mm AA5754 tubes bent at R/D ratios of 2.5, 2.0 and 1.5.

4.2 Hydroforming Results

For brevity, the hydroforming results presented are for only the 3 mm AA5754 s-rails. The hydroforming results for the EN-AW5018 tubes were consistent with those of the AA5754 s-rails.

The corner radii in the various sections of the hydroformed s-rails were found to be approximately 12.5 mm as opposed to the 12 mm radii of the die, which may be attributed to springback or possibly a need to utilize a higher hydroforming pressure.

4.2.1 Thickness

A typical measured thickness distribution around the circumference of the straight section of an as-hydroformed s-rail is shown in Figure 4.10. Note that the 30-60, 120-150, 210-240, and 300-330 degree locations around the tube correspond to the corners of the square section. The thickness varies between 3.00-3.11 mm, which lies within the initial tube thickness variation of 2.99-3.16 mm. The larger thickness measured at the 90 and 270 degree versus the 0 and 180 degree locations is consistent with the initial tube thickness variation in the 3, 6 and 9 o'clock positions (refer to Section 2.1). Note that the weld seam is located at the 0-degree location.

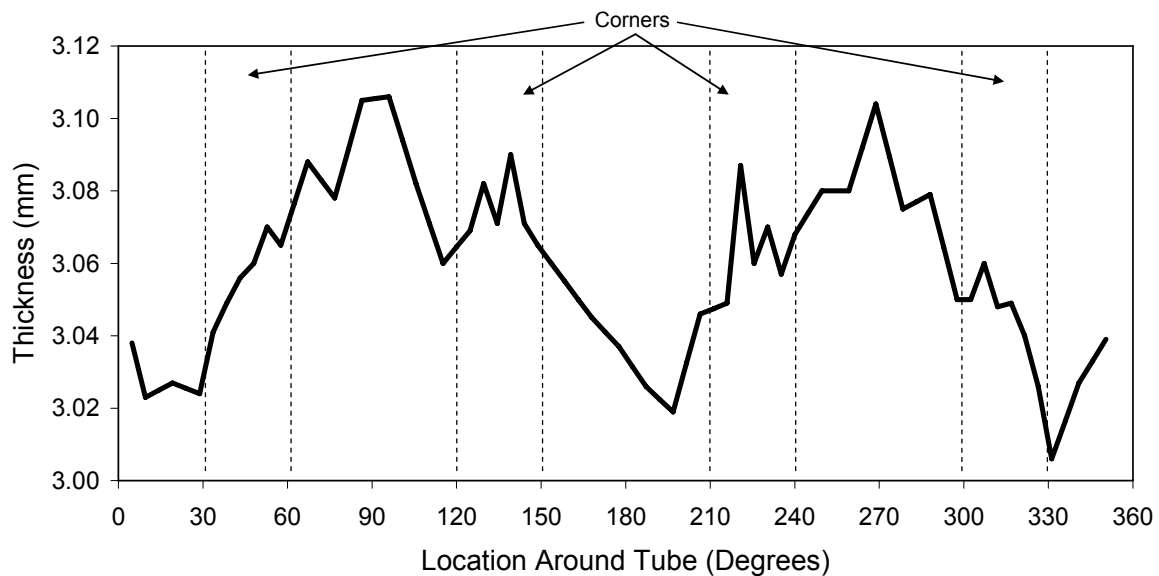


Figure 4.10: Typical thickness distribution measured around the circumference of a straight section of a 3 mm AA5754 hydroformed s-rail. Weld seam is located at the 0-degree location.

The measured thickness distributions around the circumference of the bend region for hydroformed s-rails bent at R/D ratios of 2.5, 2.0 and 1.5 are shown in Figure 4.11. The thickness increases by up to 20% at the inside of the bend and decreases by up to 19% at the outside of the bend relative to the initial tube thickness. As the severity of the bend increases, so does thickness change.

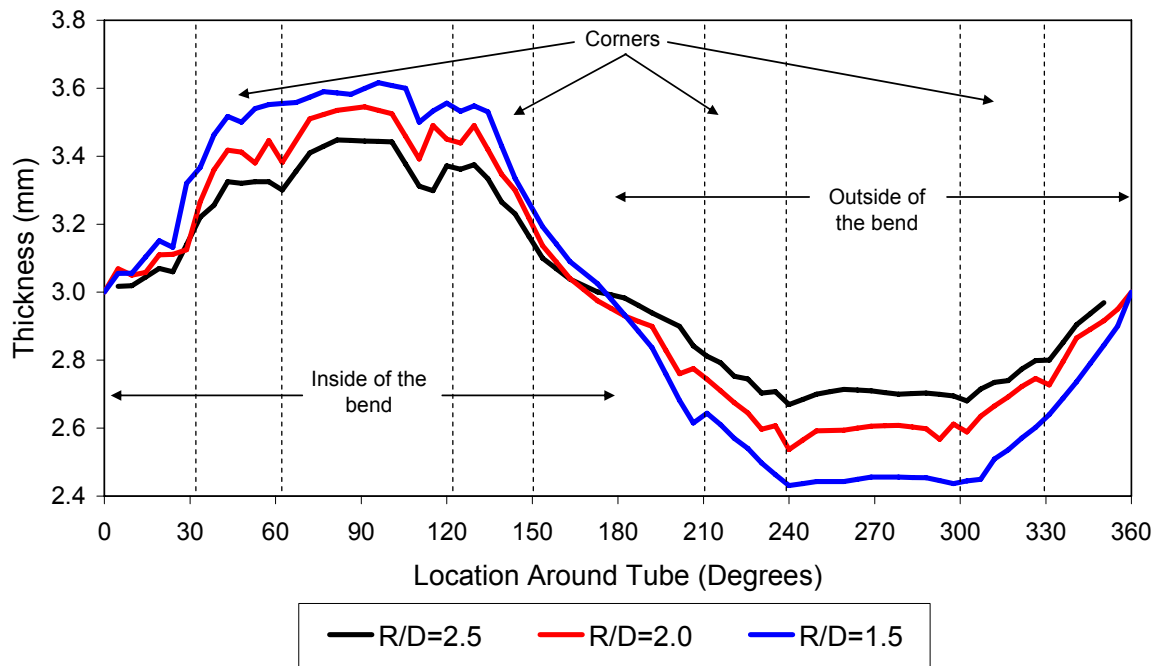


Figure 4.11: Thickness distribution around the circumference of the bend, at the center of the bend angle, for 3 mm AA5754 s-rails bent at R/D ratios of 2.5, 2.0 and 1.5.

4.2.2 Strains

The major and minor engineering strain distributions around the circumference of a straight section of an s-rail are shown in Figure 4.12. Both the major and minor strains are less than 0.04, except in the corner regions (45, 135, 225 and 315 degrees) where the major strain peaks at approximately 0.15 and the minor strain approaches zero. The measured circumferential strain at the corners of the straight section is roughly 0.15, which is greater than the value of 0.11 that can be calculated based on the r/t ratio (Equation 2.1 in Section 2.4.2).

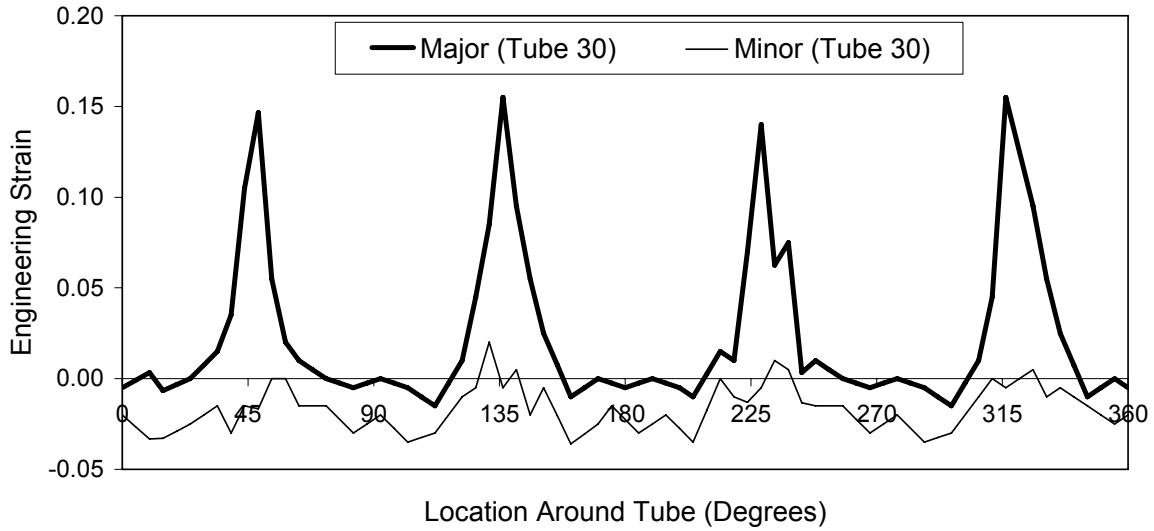


Figure 4.12: Major and minor engineering strain around the circumference of the center of a straight section in a 3 mm AA5754 hydroformed s-rail.

The major and minor engineering strains around the circumference of bend region D in hydroformed s-rails bent at the three R/D ratios are shown in Figure 4.13. Along the inside of the bend, the major strain corresponds to the circumferential strain, which peaks at approximately 0.18 in the corners (45 and 135 degree locations) of the section. Along the outside of the bend, the minor strain corresponds to the circumferential strain and peaks at approximately 0.11 in the corners of the section. As the bend severity increases, the major strain at the outside of the bend, which corresponds to the axial strain, also increases.

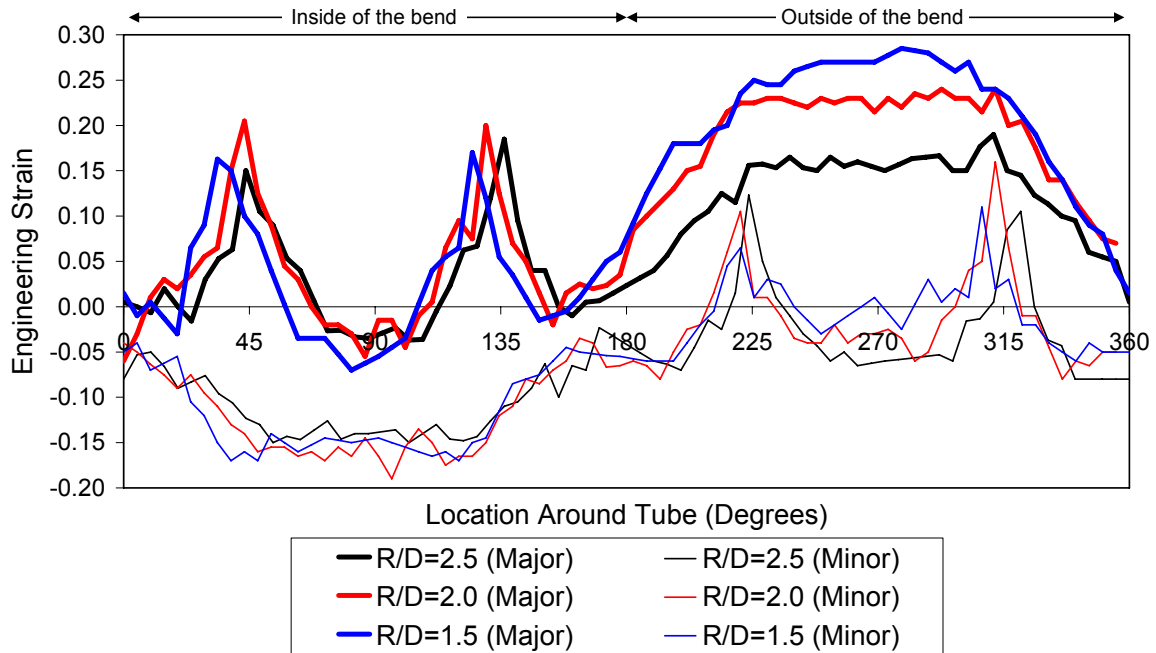


Figure 4.13: Major and minor engineering strain around the circumference of a bend region, at the center of the bend angle, in 3 mm AA5754 hydroformed s-rails bent at an R/D ratio of 2.5, 2.0 and 1.5.

4.3 Interaction of the Tube Bending and Hydroforming Processes

The measured thickness around the circumference of a bend in an s-rail bent at R/D=2.0 before and after hydroforming is shown in Figure 4.14. The tube bending operation results in thickening on the inside and thinning on the outside of the bend. The low-pressure hydroforming operation without end-feed does not cause significant expansion of the tube and consequently resulted in less than a 3% change in thickness around the circumference of the tube. These minor changes occur primarily at the inside of the bend and at the corners of the section. The lack of thickness change after hydroforming is mainly attributed to the fact that the tube perimeter is held constant (zero-percent expansion) during a low-pressure hydroforming operation.

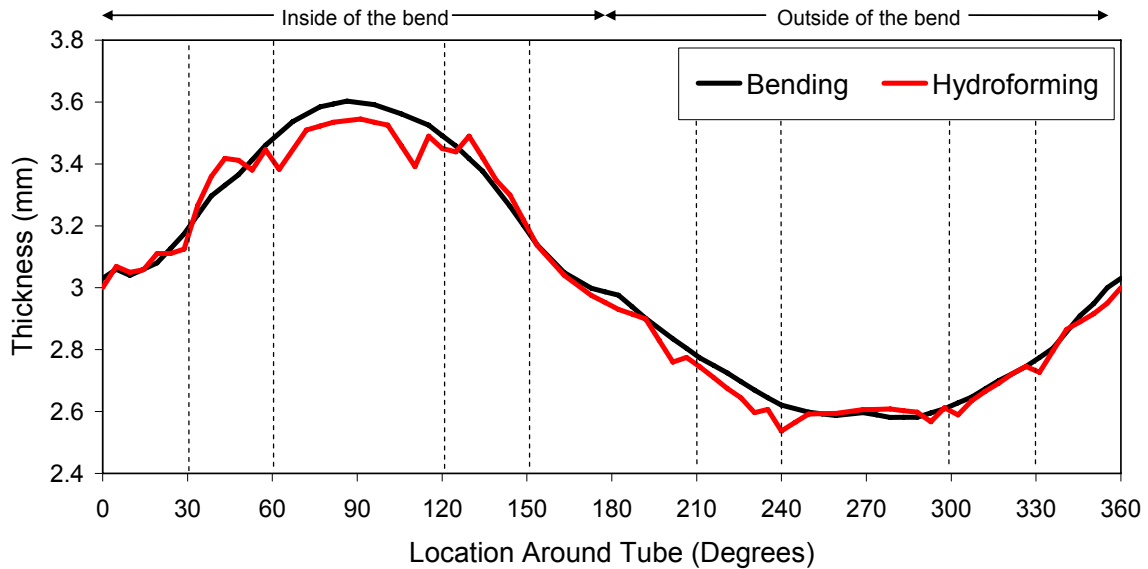


Figure 4.14: Measured thickness around the circumference of a bend, at the center of the bend angle, in a 3 mm AA5754 s-rail bent at $R/D=2.0$ before and after hydroforming.

The measured major and minor engineering strain distributions around the circumference of a bend in an s-rail bent at $R/D=2.0$ before and after hydroforming are shown in Figure 4.15. The axial strains, that is the minor and major strains at the inside and outside of the bend, respectively, correspond to the bending strains and are reduced in magnitude by less than 3% strain from the values measured prior to hydroforming. This reduction is due to flattening of the tube as it is formed from a circular to square cross-section, which reduces the depth of the bent section. However, the circumferential strains, the major and minor values at the inside and outside of the bend, respectively, change significantly. In particular, the circumferential strains change from nearly zero to up to 20% strain at the corners of the section (30-60, 120-150, 210-240 and 300-330 degrees in Figure 4.15). The increase in circumferential strain in the various sections of the s-rail is due to the circumferential bending of the tube to conform to the 12 mm corner radius of the die during hydroforming.

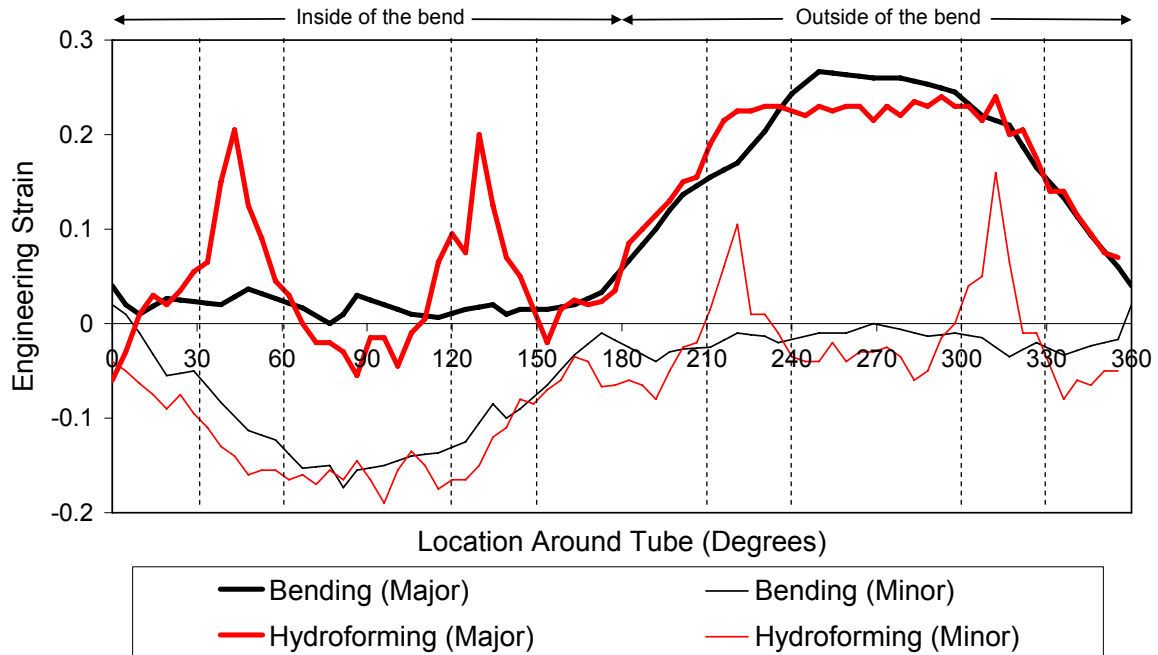


Figure 4.15: Measured major and minor engineering strain around the circumference of a bend, at the center of the bend angle, in a 3 mm AA5754 s-rail bent at $R/D=2.0$ before and after hydroforming.

4.4 Crash Results

Non-hydroformed and hydroformed 3 mm AA5754 s-rails bent at $R/D=2.5$ and impact tested using the deceleration sled are shown in Figure 4.16. Upon impact, the s-rail experiences a high initial peak load. This peak load then decays due to the formation of three local hinges, two that occur at the center of the bends and the other at the base of the longest end section, (section A in Figure 1.3). These hinges form since they are in locations that experience the largest bending moments. Progressive collapse of the hinges occurs until the s-rail has absorbed the entire kinetic energy of the impacting mass or the impact sled contacts the end-stops. The crush displacement required to deform section C of the s-rail to an orientation approximately perpendicular to the direction of impact is roughly 250 mm. Additional crush displacement beyond 250 mm is no longer representative of the deformation an s-rail would experience in a vehicle, since this would result in interactions with the engine and other structural components in an actual crash event.

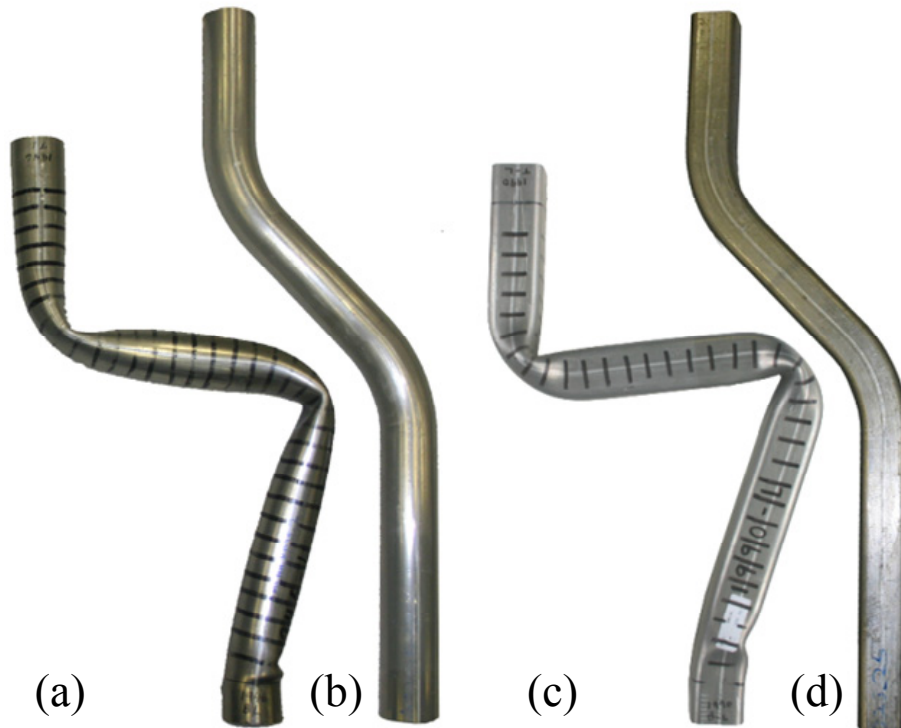


Figure 4.16: (a) Crushed; and (b) non-crushed non-hydroformed s-rails; and, (c) crushed; and (d) non-crushed hydroformed s-rails. The 3 mm AA5754 s-rails shown were bent at $R/D=2.5$.

Within the hydroformed s-rail crash experiments, both inboard and outboard buckling modes were observed at the fixed end (section A), as shown in Figure 4.17a and Figure 4.17b, respectively. The buckling mode was random and did not appear to be controlled by bend severity or whether the tube was annealed; however the buckling mode did remain consistent for each pair of s-rails comprising one impact test. There was negligible difference between the force and energy response of s-rails exhibiting inboard versus outboard buckling.

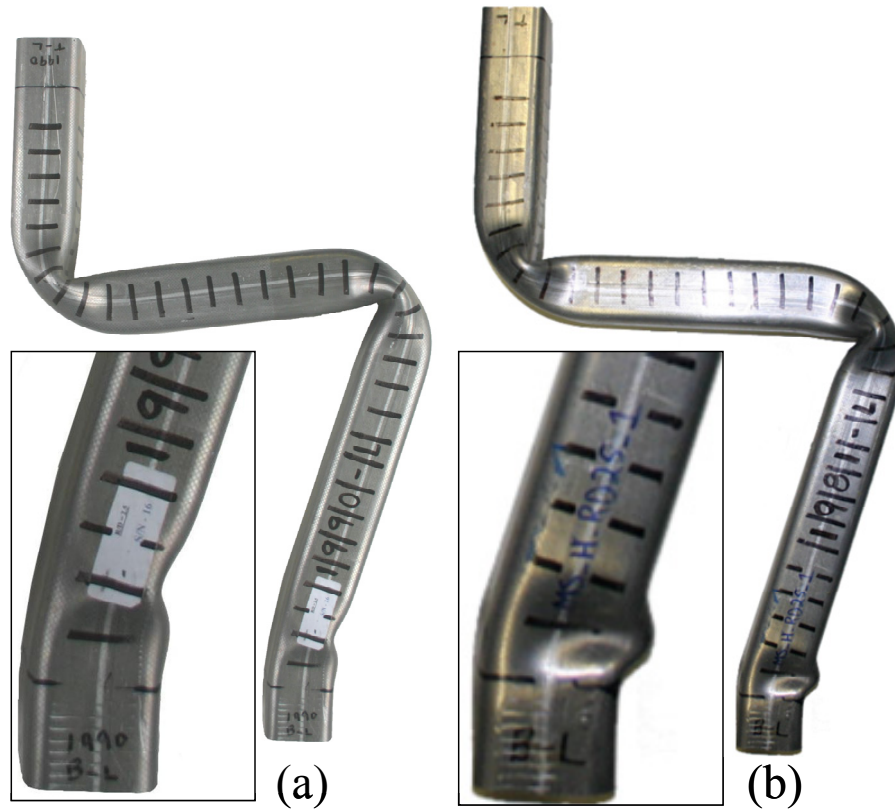


Figure 4.17: (a) Inboard; and, (b) outboard deformation modes at the fixed end of the 3 mm AA5754 s-rail.

4.4.1 Examination of Testing Repeatability

The measured force and energy versus crush displacement data from each set of three crash experiments per condition indicates an excellent degree of repeatability for both the non-hydroformed and hydroformed s-rails, as shown for example, for hydroformed AA5754 s-rails in Figure 4.18. Note that one crash test is performed on one crush structure, which is comprised of two s-rails, and the force and energy absorption results are presented for each crash structure. There were minimal differences between the three tests performed at each condition, with the exception of the final crush distance, which varied somewhat due to tearing of the s-rail near the point of contact with the clamp and boss in the EN-AW5018 s-rails and small variations in impact velocity for the AA5754 s-rails. Given the good repeatability, only one curve is presented for each test condition in the subsequent presentation of results. Note that the “median curves” of force and energy versus crush displacement response were selected for comparison purposes for the balance of this thesis.

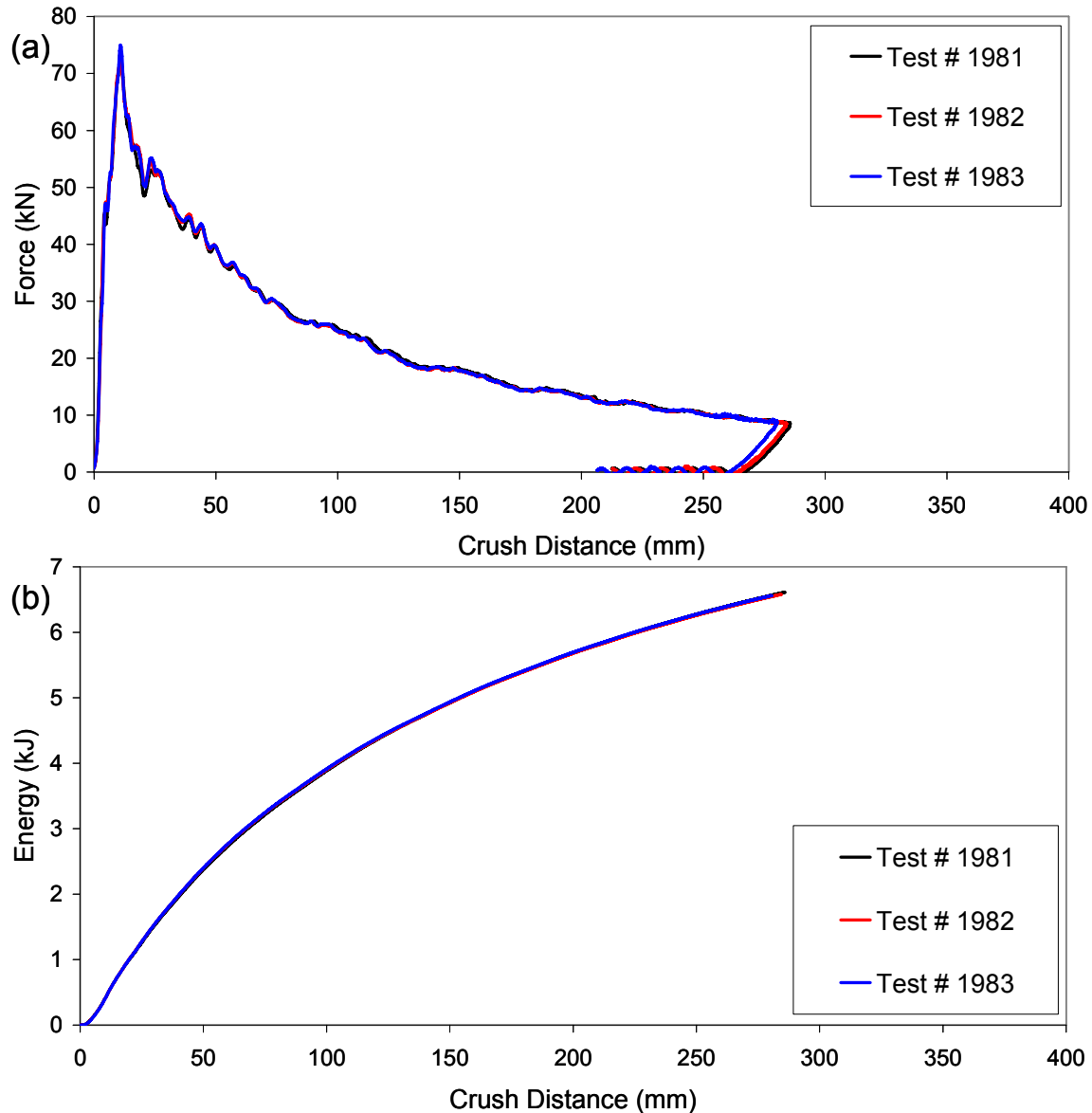


Figure 4.18: (a) Force; and (b) energy versus crush distance for three impact tests on 3 mm AA5754 hydroformed s-rails bent at $R/D=2.5$.

The force and energy absorption response of 3 mm AA5754 hydroformed s-rails bent at $R/D=2.0$ and impacted at 3.00 and 3.33 m/s are shown in Figure 4.19. The s-rails impacted at the lower velocity exhibit a force and energy versus time response that is nearly identical to that of the s-rail impacted at the greater impact velocity, except that the crush displacement of the s-rail impacted at the lower velocity deforms to a correspondingly lower crush distance. The small variations in impact velocity for each condition can be seen in Table 2.7

and had minimal effect on the force and energy response, with the exception of the final crush distance. The remaining sections of this chapter detail the effect of various tube and forming parameters on the measured crash response.

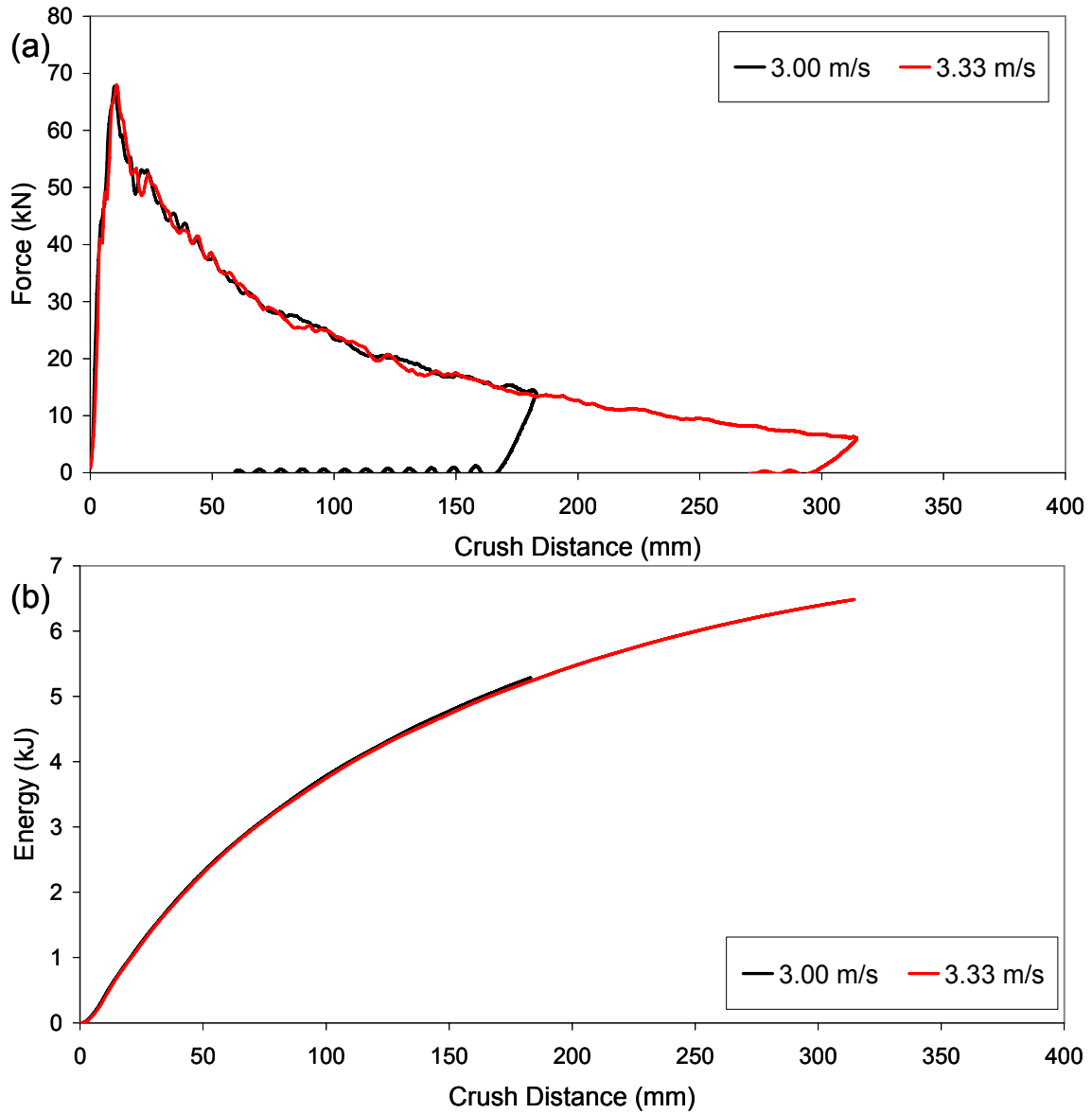


Figure 4.19: (a) Force; and (b) energy versus crush distance of 3 mm AA5754 hydroformed s-rails bent at $R/D=2.0$ and impacted at 3.00 and 3.33 m/s.

4.4.2 Effect of Initial Tube Thickness on Crash Response

The force and energy versus crush displacement for 2 and 3.5 mm EN-AW5018 non-hydroformed s-rail structures bent at $R/D=2.0$ are shown in Figure 4.20 [5]. Both the 2 and 3.5 mm s-rail structures exhibit similar trends in their crush response. The peak force, energy absorption and crush displacement measured for the 2 and 3.5 mm structures were 33.7 kN and 94.1 kN, 3.0 kJ and 9.1 kJ, and 0.29 m and 0.45 m, respectively. The thicker 3.5 mm structures exhibited approximately 2.8 times the peak crush force and experienced tearing later in the impact. In addition, the 3.5 mm tubes exhibited 3 times the energy absorption of the 2 mm structures for a given crush distance. The relative performance of the two tubes is close to the ratio of 2.54 obtained using the analytical closed-form solution of Abramowicz and Wierzbicki [134] that estimates the ratio of energy dissipation based on the ratio of thicknesses raised to the exponent $5/3$. Note that the tearing experienced by the EN-AW5018 s-rails was due to a sharp edge at the corner of the boss, which was subsequently replaced by a smooth radius for the AA5754 experiments, as discussed in Section 2.5.2.

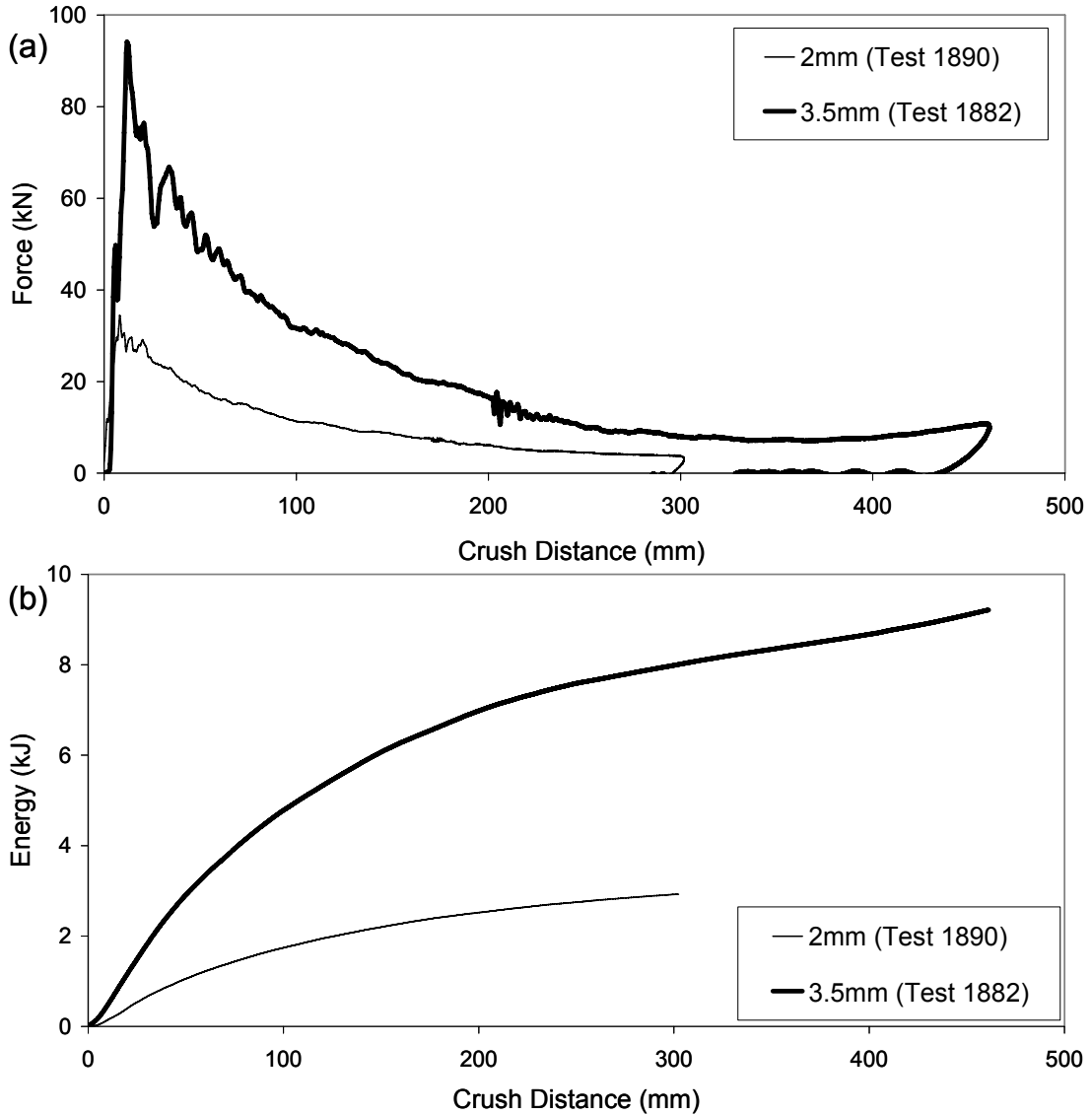


Figure 4.20: (a) Force; and (b) energy versus crush displacement response of 2 and 3.5 mm EN-AW5018 non-hydroformed s-rail structures bent at an $R/D=2.0$ [5].

4.4.3 Effect of Bend Severity on Crash Response

4.4.3.1 Non-Hydroformed S-Rails

The force and energy versus crush displacement for 3 mm AA5754 non-hydroformed s-rails bent at R/D ratios of 2.5, 2.0 and 1.5 are shown in Figure 4.21. The crush response of the 2 and 3.5 mm EN-AW5018 s-rail structures exhibited a degree of dependency on bend severity that was similar to that of the 3 mm AA5754 s-rails and is not shown for brevity. The peak load and crush displacement for s-rails bent at an R/D ratio of 2.5, 2.0 and 1.5 are 62.6, 58.1

and 52.0 kN, and 250, 310 and 414 mm, respectively. As the bend severity (R/D ratio) decreases from 1.5 to 2.0 and 1.5 to 2.5, the peak load increases by 11.7% and 20.4%, respectively, and the energy absorption at 250 mm of crush distance increases by 7.4% and 12.1%, respectively. To better understand the greater energy absorption capability of s-rails bent at larger R/D ratios, the variables affected by bend severity: (i) section length; (ii) work hardening; (iii) thickness, and (iv) residual stresses, are further isolated through numerical investigations that are presented in Chapter 6.

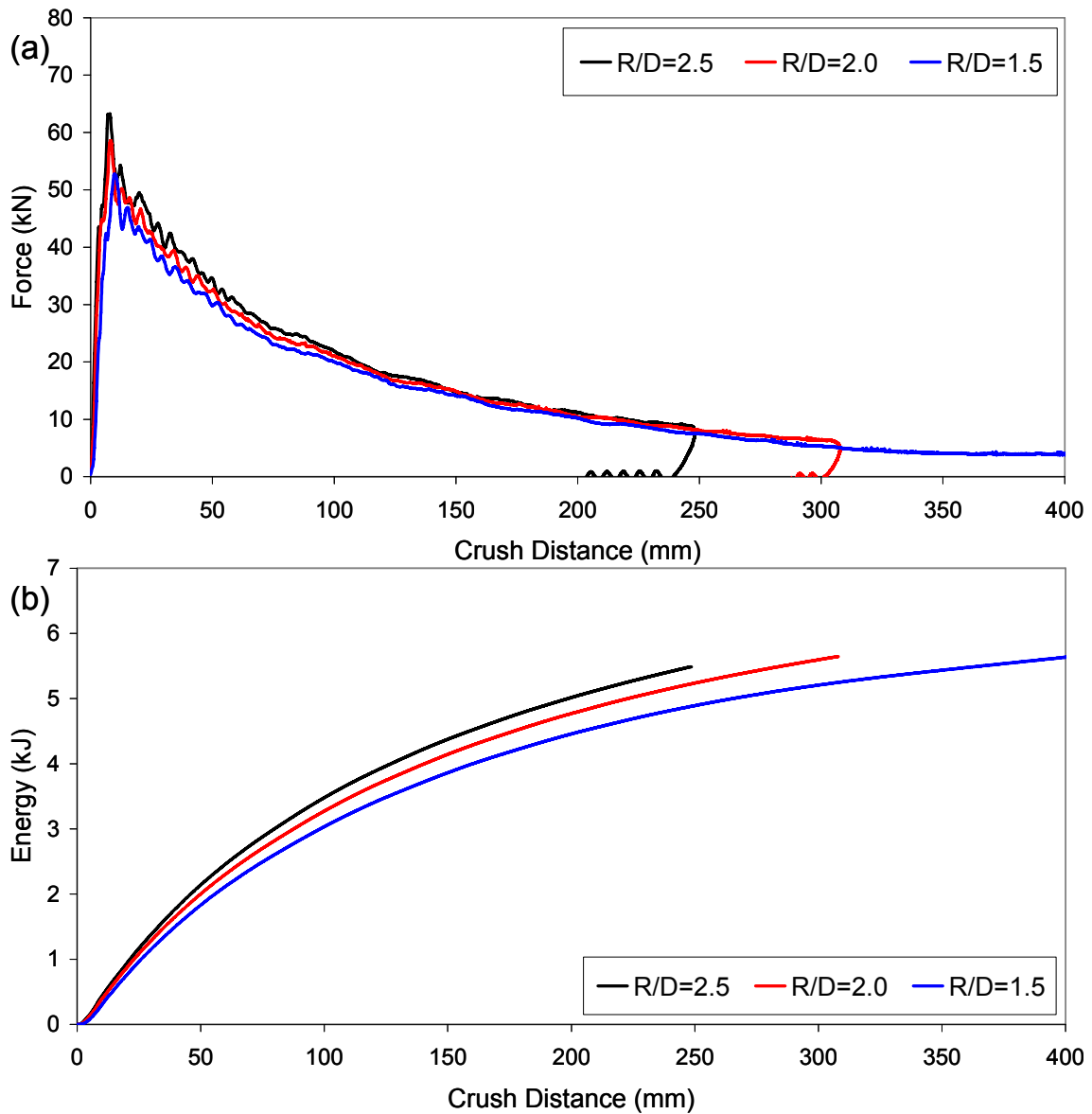


Figure 4.21: (a) Force; and (b) energy versus crush displacement of 3 mm AA5754 non-hydroformed s-rails bent at an R/D ratio of 2.5, 2.0 and 1.5.

4.4.3.2 Hydroformed S-Rails

The crush response of 3 mm AA5754 hydroformed s-rails bent at the three R/D ratios is shown in Figure 4.22. The peak load corresponding to s-rails bent at R/D ratios of 2.5, 2.0 and 1.5 are 73.1, 69.0 and 66.1 kN, respectively. As the bend severity (R/D) decreases from 1.5 to 2.0 and 1.5 to 2.5, the peak load increases by 4.4% and 10.6%, respectively. For the same change in bend severity, the energy absorption at 250 mm crush distance increases by 2.5% and 6.3%.

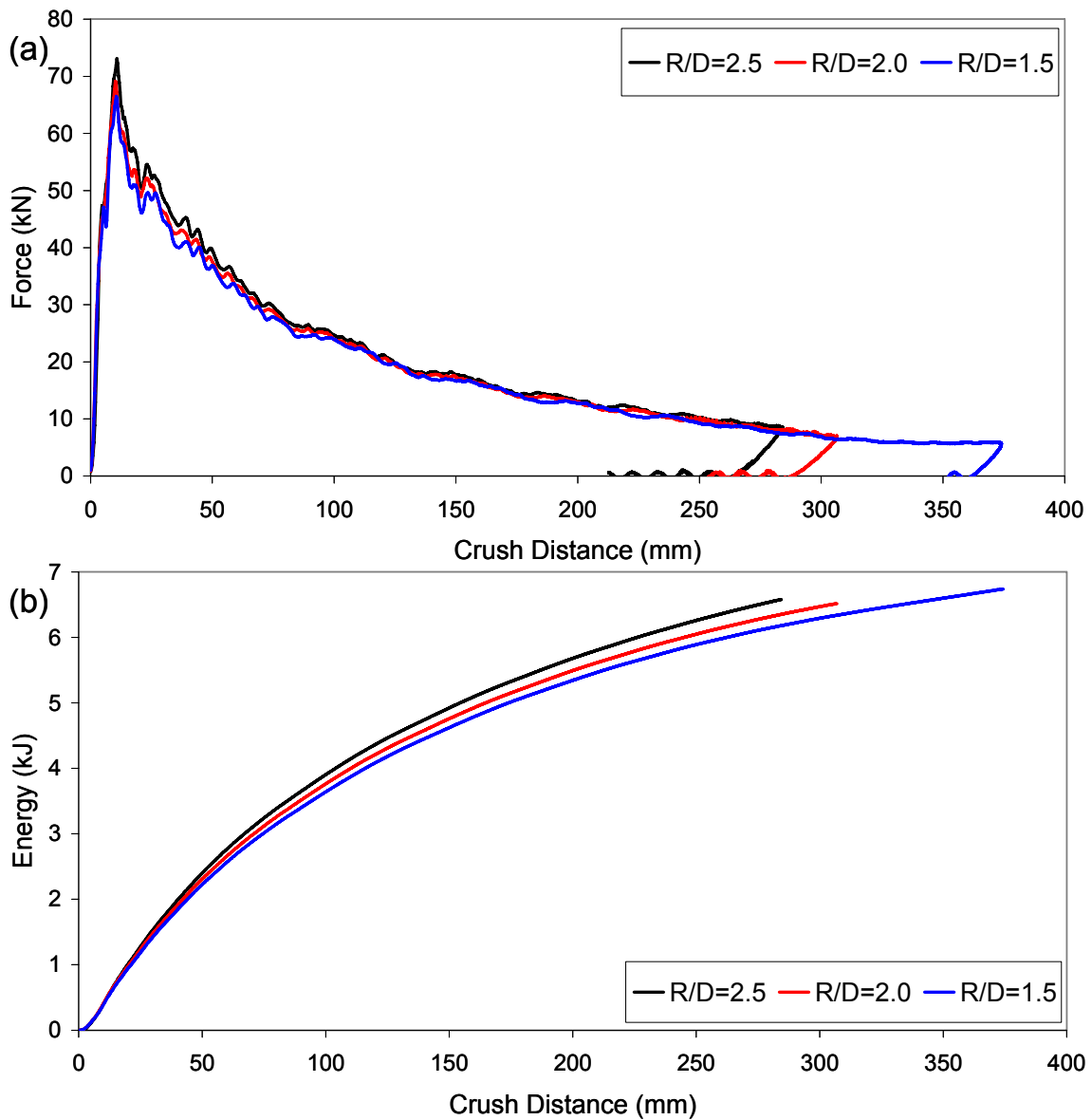


Figure 4.22: (a) Force; and (b) energy versus crush distance for 3 mm AA5754 hydroformed s-rails bent at R/D ratios of 2.5, 2.0 and 1.5.

4.4.4 Effect of Hydroforming on Crash Response

The force and energy versus crush displacement for 3 mm AA5754 non-hydroformed and hydroformed s-rails bent at $R/D=2.0$ are shown in Figure 4.23. The effect of hydroforming on the crash response of the 3 mm s-rails was an increase in peak load by 16.9% and the energy absorbed at a given crush distance by up to 15.6% relative to that measured for the non-hydroformed s-rails. This trend was consistent for the s-rails bent at the R/D ratios of 2.5 and 1.5.

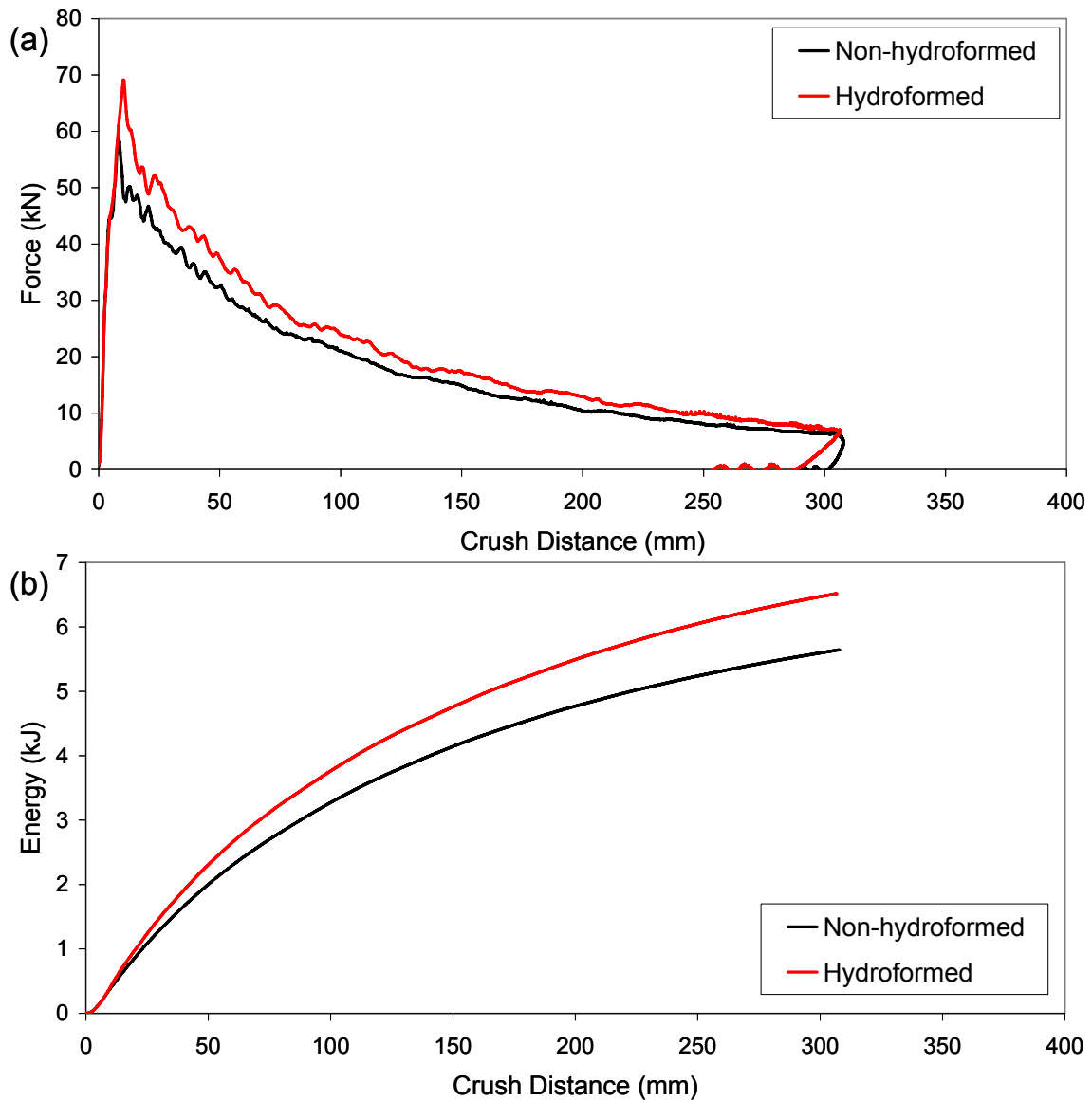


Figure 4.23: (a) Force; and (b) energy versus crush displacement for 3 mm AA5754 non-hydroformed and hydroformed s-rails bent at $R/D=2.0$.

The crash response of the 3 mm AA5754 hydroformed and non-hydroformed s-rails at each bend severity is summarized in Figure 4.24 and Table 4.2. In particular, the peak force, crush displacement, energy absorbed at 250 mm crush displacement and the percent change in these quantities with respect to the R/D=1.5 condition are listed. Hydroforming of the s-rails bent at R/D ratios of 2.5, 2.0 and 1.5 resulted in increases in peak load of 16.8%, 18.7% and 27.1%, and increases of energy absorption of 14.5%, 15.1% and 20.4%, respectively. Interestingly, the increase in peak load and energy absorption, for an s-rail bent at R/D=2.5, due to the hydroforming operation for the AA5754 and EN-AW5018 s-rails is almost identical (16.5% and 14.6% for the 2 mm EN-AW5018 s-rail versus 16.8% and 14.5% for the 3 mm AA5754 s-rails, respectively). The overall dependency of the crush response on the bend severity suggests that there is a lower resistance to crush for the s-rails bent at a lower R/D. Note that the change in crush displacement cannot be directly compared for the range of conditions due to the variation in impact velocity for each test, as given in Table 2.7.

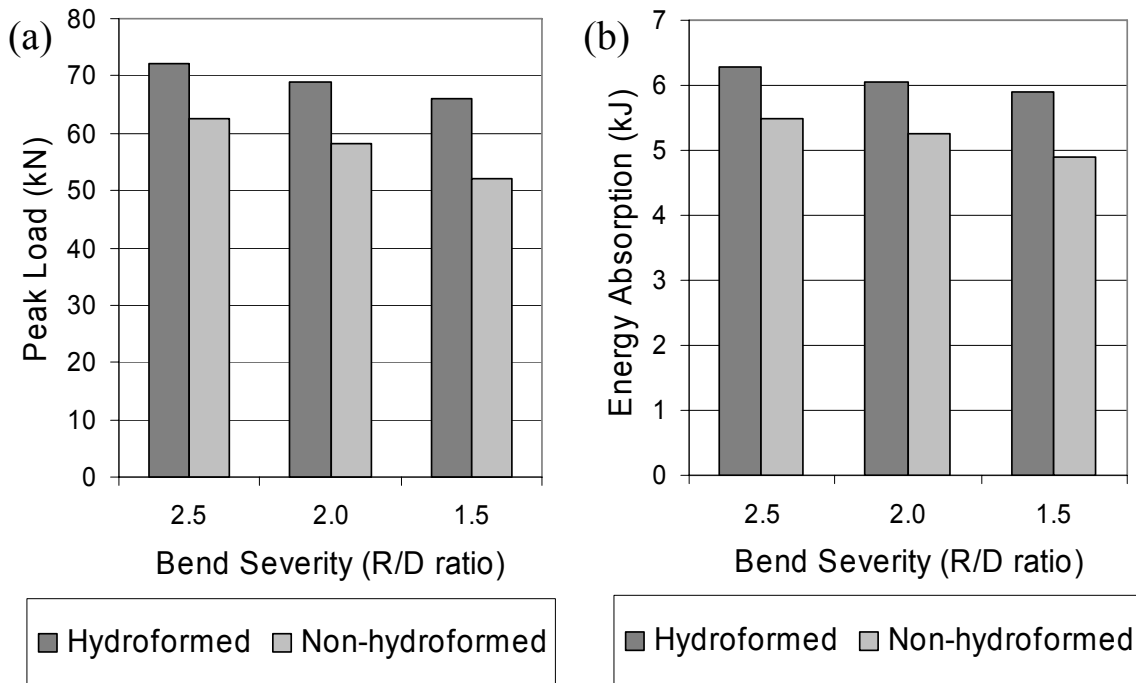


Figure 4.24: (a) Peak force; and (b) energy absorbed at 250 mm of crush distance for 3 mm AA5754 non-hydroformed and hydroformed s-rails at each bend severity.

Table 4.2: Peak force, crush displacement, energy absorbed at 250 mm crush displacement and the percent change in these quantities with respect to the R/D=1.5 condition for 3 mm AA5754 hydroformed and non-hydroformed s-rails at each bend severity.

Hydroformed (H) or Non-Hydroformed (NH)	Bend Severity (R/D)	Peak Load (kN)	Percent Increase in Peak Load	Crush Displacement (mm)	Percent Decrease in Crush Displacement	Energy Absorbed at 250 mm Crush (kJ)	Percent Increase in Energy Absorbed relative to R/D=1.5
H	2.5	73.1	10.6	282	24.0	6.3	6.3
	2.0	69.0	4.4	304	18.1	6.1	2.5
	1.5	66.1	0.0	371	0.0	5.9	0.0
NH	2.5	62.6	20.4	250	39.6	5.5	12.1
	2.0	58.1	11.7	310	25.1	5.3	7.4
	1.5	52.0	0.0	414	0.0	4.9	0.0

4.4.5 Effect of Annealing on Crash Response

The crush response of the 3 mm AA5754 hydroformed s-rails bent at the three R/D ratios and then annealed is shown in Figure 4.25. As the bend severity (R/D) decreases from 1.5 to 2.0 and from 1.5 to 2.5, the peak load increases by 3.2% and 19.8%, respectively, while the energy absorption at a given crush distance increases up to 5.6% and 11.6%, respectively. Since the effects of work hardening and residual stresses on crash response of these s-rails were largely removed in the annealing process, these changes in peak load and energy absorption are due to slight differences in the local material strength resulting from the annealing process, as well as differences in the s-rail geometry and thickness for the various bend severities. To assess the effects of annealing on the crash response, a result for a non-annealed s-rail bent at R/D=2.0 is also shown in Figure 4.25. Annealing the s-rails prior to the crash experiments reduced the peak load by 43.3% and the energy absorbed at a given crush distance (250 mm) by 23.1%.

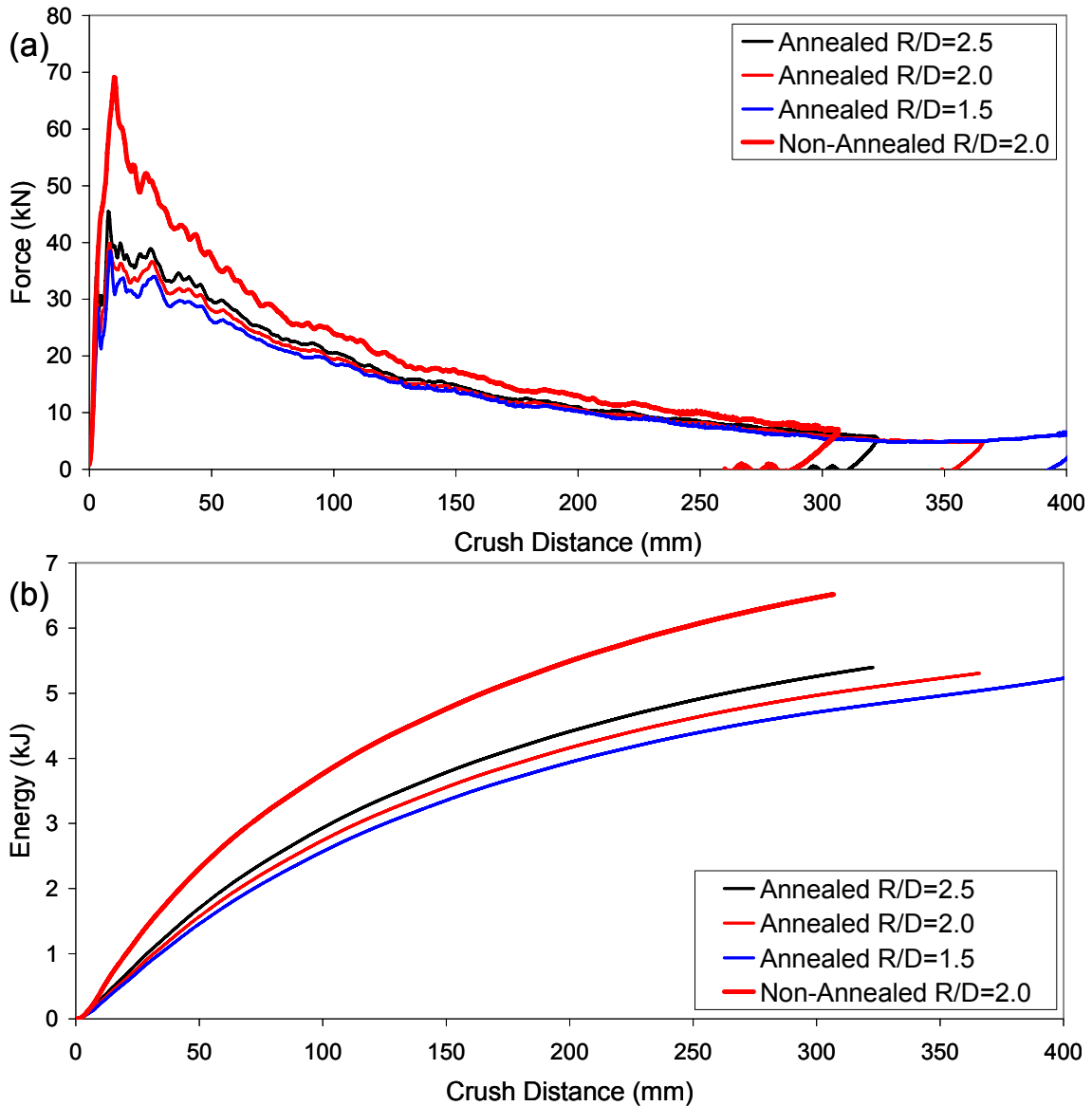


Figure 4.25: (a) Force; and (b) energy versus crush displacement for hydroformed and annealed 3 mm AA5754 s-rails bent at the three bend severities. Also shown is the force response of a non-annealed s-rail bent at $R/D=2.0$.

The peak load and energy absorption of the 3 mm AA5754 non-hydroformed and hydroformed s-rails bent at the various R/D ratios and annealed fully prior to the crash experiments are summarized in Figure 4.26 and Table 4.3. Also plotted in Figure 4.26 is the corresponding data for the non-annealed s-rails taken from Figure 4.24. There is a dramatic reduction in crush resistance due to annealing. It can also be seen that the peak load differs by less than 3% between the annealed non-hydroformed and hydroformed s-rails for each of the three bend severities examined. Similarly, the energy absorption for the annealed non-

hydroformed and hydroformed s-rails differs by 7-9% for the three bend severities examined. The larger difference between the crush resistance of the non-annealed hydroformed and non-hydroformed s-rails can be attributed to the increment in work hardening during hydroforming.

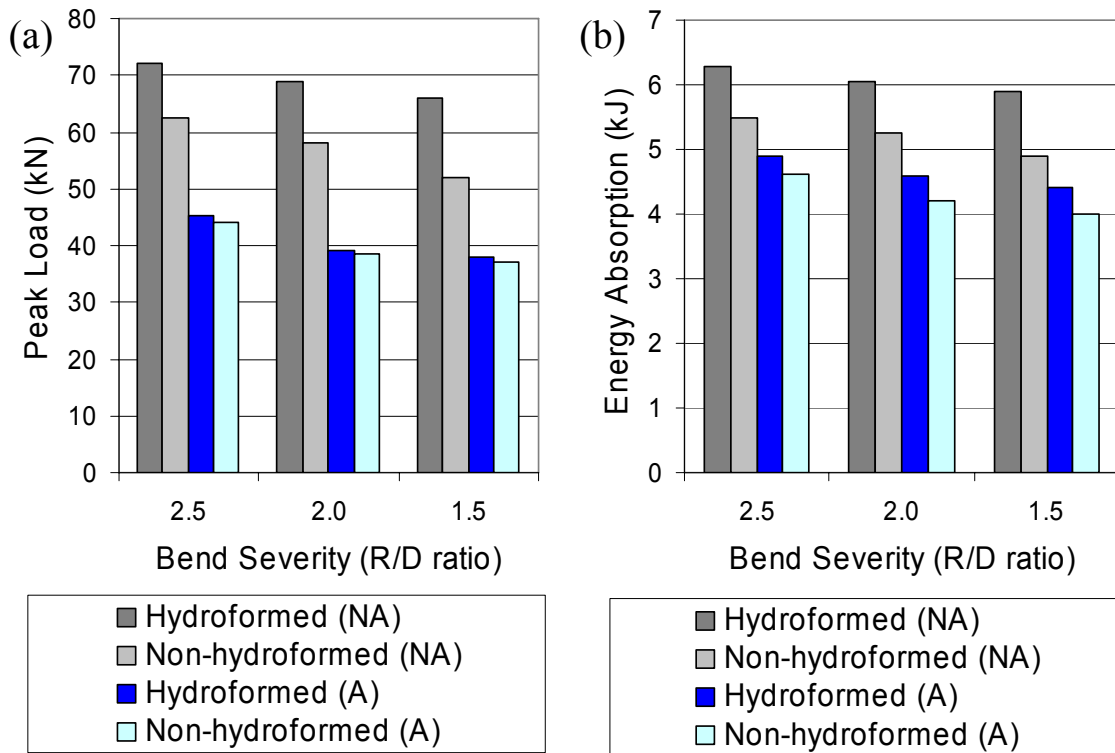


Figure 4.26: (a) Peak force; and (b) energy absorbed at 250 mm of crush distance for 3 mm AA5754 hydroformed and non-hydroformed s-rails at each bend severity that were annealed prior to the crash experiments. The corresponding data for the non-annealed s-rails from Figure 4.24 is also shown.

Table 4.3: Peak force, crush displacement, energy absorbed at 250 mm crush displacement and the percent change in these quantities with respect to the R/D=1.5 condition for 3 mm AA5754 hydroformed and non-hydroformed s-rails at each bend severity that have been fully annealed.

Hydroformed (H) or Non-Hydroformed (NH)	Bend Severity (R/D)	Peak Load (kN)	Percent Increase in Peak Load	Crush Displacement (mm)	Percent Decrease in Crush Displacement	Energy Absorbed at 250 mm Crush (kJ)	Percent Increase in Energy Absorbed relative to R/D=1.5
H	2.5	45.4	19.8	322	19.5	4.9	11.4
	2.0	39.1	3.2	365	8.8	4.6	4.5
	1.5	37.9	0.0	400	0.0	4.4	0.0
NH	2.5	44.1	19.2	240	38.0	4.6	15.3
	2.0	38.6	4.3	344	11.1	4.2	5.0
	1.5	37.0	0.0	387	0.0	4.0	0.0

From Figure 4.26, it can be seen that the crush resistance of the hydroformed s-rails was larger than that of the non-hydroformed (round) s-rails for both the annealed and non-annealed cases. This result was somewhat surprising since the initial second moment of area of the non-hydroformed s-rail cross-section is larger than that of the hydroformed s-rail cross-section, as shown in Table 3.4. This comparison suggests that the round cross-section offers less resistance to collapse of the section at the hinge locations, resulting in a lower second moment of area during crash. Thus, the higher energy absorption of the hydroformed versus non-hydroformed s-rails can be attributed to a greater resistance to bending collapse which stems from the ability of the square cross-section to better retain its shape during deformation, as will be shown in Section 5.3.1.1.

4.5 Summary

This summary section begins with the key results from the tube bending and hydroforming experiments, followed by an assessment of the variables that affect s-rail crash response.

4.5.1 Tube Bending and Hydroforming of S-Rails

A summary of the effects of tube bending and hydroforming parameters on the characteristics of the as-hydroformed s-rails is given in Table 4.4 and shown in Figure 4.27.

Table 4.4: Summary of the effect of changes in bend severity on forming process variables and strains within hydroformed s-rails.

R/D	Process Variables in Bending			Tube Ovality	Thickness Reduction at Center of Bend (%)		Work Hardening at Center of Bend						Corner Radius (Sections A-E) (mm)
							Axial Engineering Strain		Circumferential Engineering Strain		Circumferential Engineering Strain at Corners		
	Bend Torque	Boost Load	Mandrel Load		Inside of Bend	Outside of Bend	Inside of Bend	Outside of Bend	Inside of Bend	Outside of Bend	Inside of Bend	Outside of Bend	
2.5	Approx the same	Approx the same	As R/D increases the load increases	Minimal ovality	-15	10	-0.15	0.16	-0.03	-0.06	0.16	0.10	12.5
2.0					-18	13	-0.17	0.22	-0.03	-0.03	0.20	0.12	
1.5					-20	18	-0.16	0.27	-0.05	0.00	0.17	0.09	

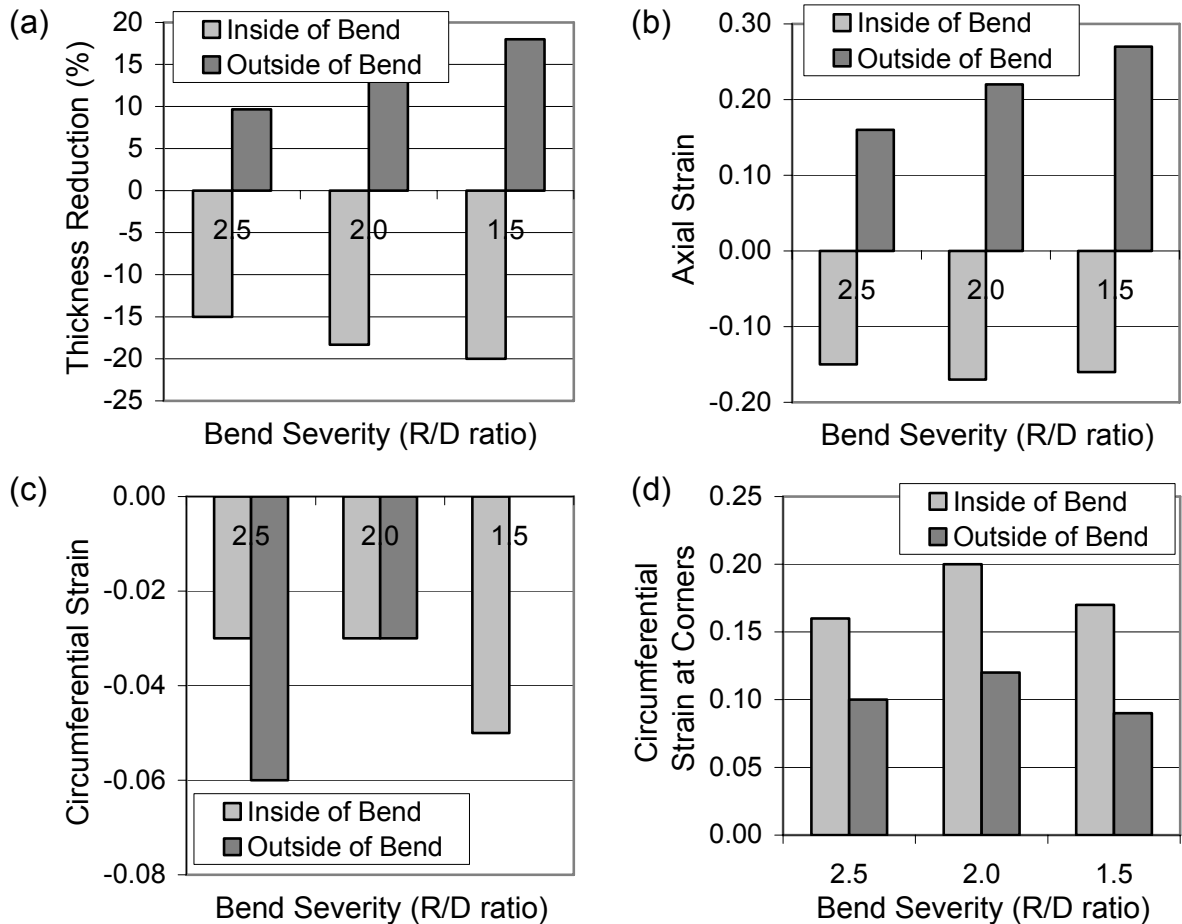


Figure 4.27: (a) Percent thickness reduction; and (b) axial; and (c) circumferential engineering strains measured at the center of the bend. (d) Circumferential engineering strain measured at corners of the bend.

The recorded tube bending process variable data provides a means upon which to assess repeatability in bending, and allows an assessment of the predictive ability of the tube bending models in Chapter 5. The tube bending process variable most significantly affected by the bend severity is the mandrel load, which influences thinning and strain in the bend. The mandrel load is greatest for tubes bent at a greater bend severity, particularly when using a set-up with additional balls attached to the post. Additional balls on the mandrel post are required for bending tubes at smaller bend radii to help prevent ovalization and wrinkling.

The most significant parameter in the tube bending operation that affects the overall level of work hardening, thickness change and residual stress in the as-formed s-rail is the bend severity. As the bend severity increases, the work hardening, thickness change and residual stresses in the bend region also increase.

The low-pressure hydroforming process used to shape the cross-section of the s-rail from round to square does not induce significant changes in the tube thickness. However, despite the constant perimeter of the section during the low-pressure hydroforming process, the changes in the thickness of the s-rail can be significant for rectangular die sections, as will be shown in Chapter 6. The level of axial strain induced in the s-rail by the low-pressure hydroforming process is minimal, while the circumferential strain can be significant, particularly in the corners of the section. The increase in circumferential strain at the corners of the sections within the s-rail is due to bending of the tube into the 12 mm corner radius of the die.

In terms of the contributions of the tube bending and hydroforming processes to the overall properties of the as-formed s-rail, the tube bending operation induces most of the thickness change and axial strain, while the low-pressure hydroforming process induces most of the circumferential strain. Overall, the level of work hardening and thickness change induced in the hydroformed (square cross-section) s-rail by the low-pressure hydroforming process is itself small. However, as will be shown in Chapter 6, the use of circumferential expansion and end-feed during a high-pressure hydroforming process can induce significant change in thickness and strains (axial and circumferential) within the s-rail that are at a level similar to those experienced due to bending.

4.5.2 Crash Response of S-Rails

For the s-rail geometry examined in the experiments, the most significant variable affecting the s-rail crash response is the tube thickness. An increase of the initial tube thickness from 2 to 3.5 mm results in an increase in peak load and energy absorption at a given crush distance by factors of 2.8 and 3, respectively.

The role of bend severity, the low-pressure hydroforming process, cross-section and the effect of annealing, prior to the crash experiments, in influencing the crash response of s-rails is summarized in Figure 4.28. An increase in the bend severity of the s-rail will increase the level of work hardening, thickness change and residual stress in the bend region, which collectively increases the crash response of the s-rails. The level of work hardening and thickness change induced in the s-rail, with a square cross-section, by the low-pressure hydroforming process is small, but significant. The increase in the peak load and energy absorption due to the hydroforming process is attributed to work hardening and due to the square versus round cross-section of the s-rail, which is better able to resist deformation of the plastic hinge during collapse, as will be shown in Chapter 5. The peak load in crushed s-rails is affected strongly by the level of previous work hardening (mainly from the bending operation), and less by the specific round or square cross-section geometries investigated experimentally. However, the effect of cross-section does become important, as seen in the rectangular sections investigated numerically in Chapter 6, which exhibited a strong dependence of force and energy absorption on cross-section.

Annealing of the s-rails bent at $R/D=2.0$ resulted in approximately 43% lower peak loads and 23% lower energy absorption, which indicates that the material strength increases due to work hardening and/or residual stresses due to the forming processes (mainly bending) play a considerable role in the crash response of s-rails. The individual effects, on the s-rail crash response, of work hardening, thickness change and residual stress changes in the bend region due to bend severity are isolated and examined through numerical simulation in Chapter 6.

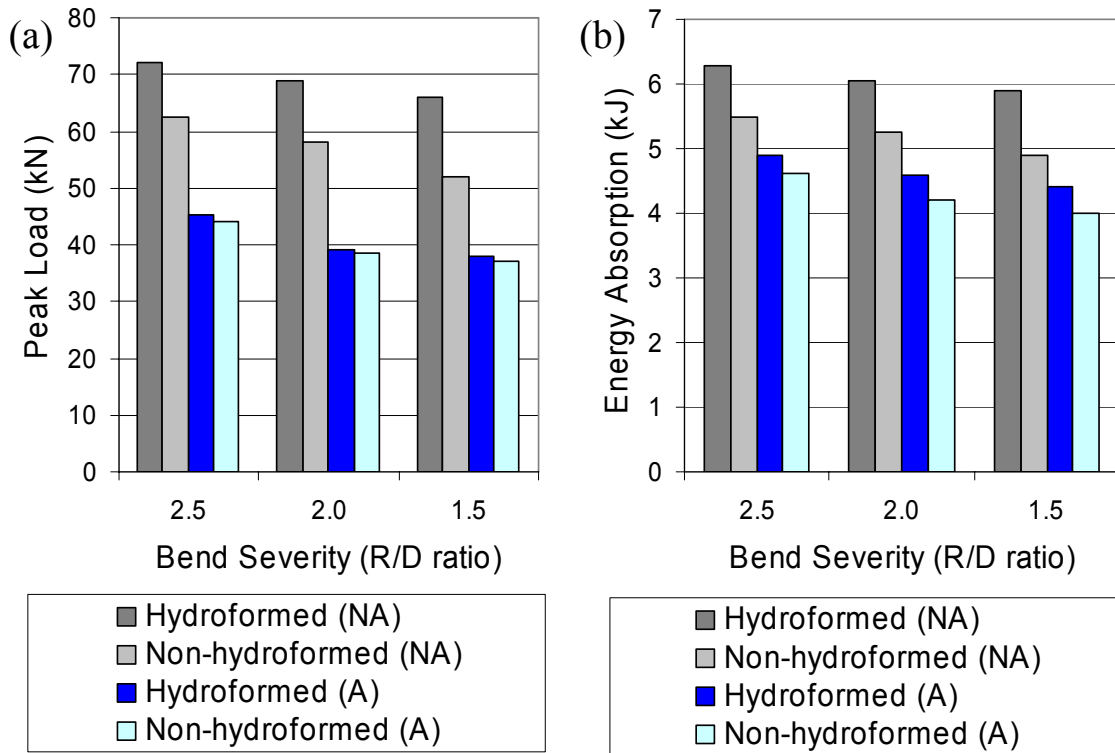


Figure 4.28: Summary of the effects of the s-rail cross-section, bend severity, low-pressure hydroforming process employed, and annealing prior to the crash experiments on the crash response of s-rails.

Although the experimental program of this research provides pertinent information on the material process and design variables that govern s-rail crash response, it is apparent that further investigation is necessary to investigate variations of the tube bending and hydroforming processes, and the effects on force and energy absorption. In addition, there is a need for further isolation and assessment of the variables that govern s-rail crash response that cannot be conducted solely through experiment. The results from the numerical models that extend the results of the experimental program are presented in Chapter 5 and Chapter 6.

Chapter 5

Numerical Results

This chapter presents results from the numerical simulation of the experiments. Here, the predictive ability of the numerical models is assessed and validation is established through comparison with measured quantities presented in Chapter 4. These include the bending process variables, the as-formed geometry, thickness and strain, as well as the degree of springback after bending. The results for the 3 mm AA5754 tubes are the main focus herein, since the predictions for the 2 and 3.5 mm EN-AW5018 tubes serve only to reinforce the trends. Note that the simulation results for the 2 and 3.5 mm EN-AW5018 material have been published by Oliveira *et al.* [5] and are included in Appendix B of this thesis. Note also that the results from additional numerical investigations that go beyond the scope of the experiments and further isolate and examine the variables governing s-rail crash response are presented in Chapter 6.

This chapter begins with the predictions for the tube bending models followed by the hydroforming models. In particular, predictions of final geometry, springback, process variables, thickness and strain changes are examined. The s-rail crash modelling results are then presented beginning with the predictions of the crushed s-rail geometry, and force and energy response. The predictions from simulations utilizing the rate-insensitive piecewise linear hardening constitutive relation with a von Mises yield criterion (loosely referred to as “isotropic von Mises” within this thesis) serve as a “baseline” for comparison with experiment and are the primary focus. Other simulations incorporating anisotropic and rate-sensitive material models are also considered. These include the anisotropic Barlat-1989 [123] and strain rate and temperature sensitive Johnson-Cook [125,126] and Zerilli-

Armstrong [128,129,130,131] material models. The majority of the results presented herein are based on a 2.5 mm element size mesh with a reduced integration four-noded Belytschko-Lin-Tsay [121] element formulation. The sensitivity of the tube bending, hydroforming and crash simulation predictions to mesh size and element formulation is also assessed, as presented in Section 5.4.

5.1 Tube Bending Predictions

Simulation of the tube bending process consists of four separate modelling stages: (i) first bend; (ii) springback; (iii) second bend; and (iv) springback. The predicted deformation in the first and second bend stages used to simulate the bending of a 3 mm AA5754 s-rail at $R/D=2.5$ are shown in Figure 5.1a and Figure 5.1c. In the first- and second-bend modelling-stages, the tube was over-bent to account for springback, hence mimicking the experiment. To obtain a 45 degree bend after the springback analysis, the prescribed bend angles in the model for simulations of the s-rails bent at R/D ratios of 2.5, 2.0 and 1.5 were 46.5, 46.0 and 45.6 degrees, respectively. These simulated values are within 1 degree of those prescribed in the experiments (Table 2.5 and Table 2.6). After the first springback analysis, the tube was reoriented in preparation for the second bend by advancing it axially by a distance corresponding to section C of the s-rail and then rotating it 180-degrees about its axis, as shown in Figure 5.1b. The second bend was then performed in a manner similar to the first bend, followed by a second implicit springback analysis.

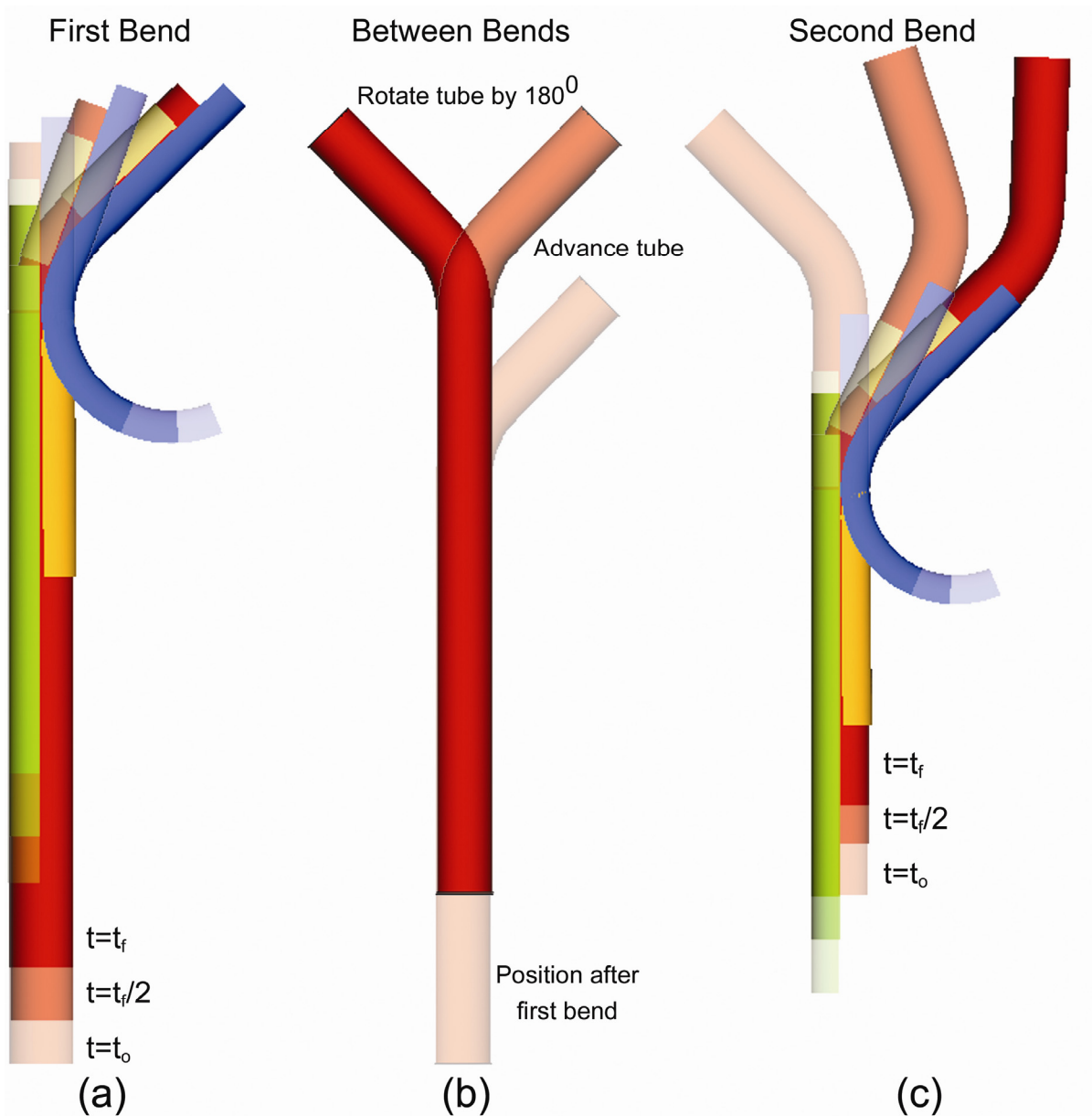


Figure 5.1: Predicted deformation at various stages of simulating the bending of a 3 mm AA5754 s-rail at $R/D=2.5$: (a) first bend; (b) tube reposition and re-orientation between bends; and (c) second bend. Note that the springback stage after each bend is not shown. The initial and final simulation times for each stage are denoted by t_o and t_f , respectively.

The actual and predicted geometry of an as-bent 3 mm AA5754 s-rail bent at $R/D=2.5$ is shown in Figure 5.2. There is very good agreement between the predicted and actual geometry of the s-rail after bending and springback. The predicted thickness in the s-rail after bending ranges from 2.71 to 3.57 mm. The maximum predicted major (axial) strain at the outside of the bend is 0.20, while the minimum predicted minor (circumferential) strain at

the inside of the bend is -0.20, which is in overall good agreement with the measured results presented in Chapter 4. The predicted thickness change and strains due to the bending operation are more closely examined and compared to the experimental results in the following sections.

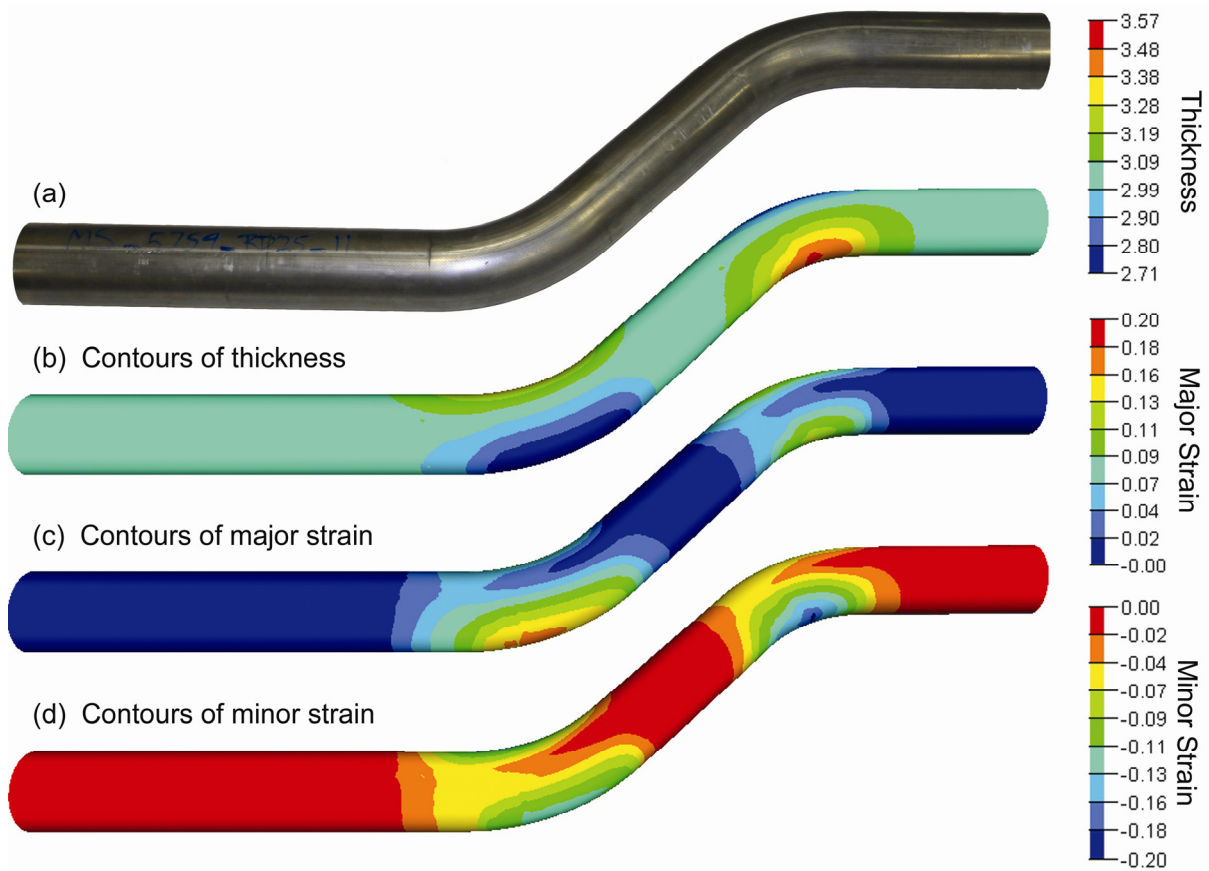


Figure 5.2: (a) Actual 3 mm AA5754 s-rail after bending at $R/D=2.5$ and trimming. Predicted s-rail geometry after bending and trimming operations with contours of (b) thickness (mm); (c) major strain; and (d) minor strain.

5.1.1 Predictions of Bending Process Variables

The measured versus predicted bend torque, pressure die boost load and mandrel load using the isotropic von Mises material model for the first bend at each R/D ratio are shown in Figure 5.3, Figure 5.4 and Figure 5.5, respectively. The predicted bend torque, pressure die boost load and mandrel load are in relatively good agreement with the experimental results. The pressure die boost load for the $R/D=1.5$ bend condition is under-predicted by approximately 5 kN, which is a discrepancy that could not be resolved.

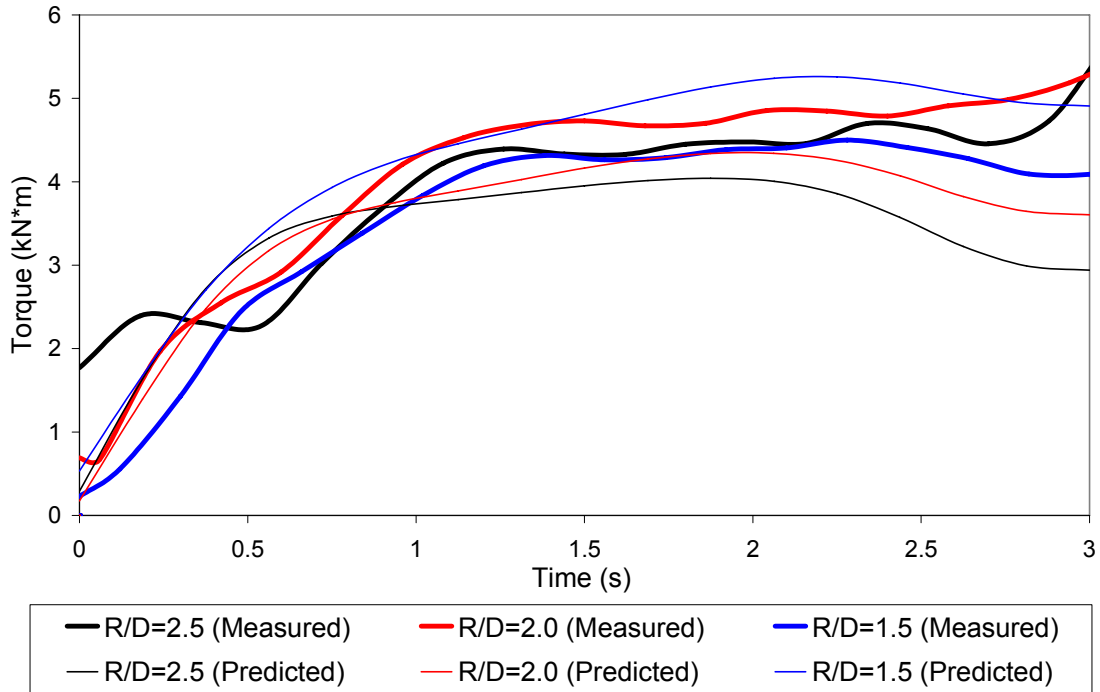


Figure 5.3: Measured bend torque for the first bend of the s-rail bent at the R/D ratios of 2.5, 2.0 and 1.5, and predictions using the piecewise linear material model with a von Mises yield criterion.

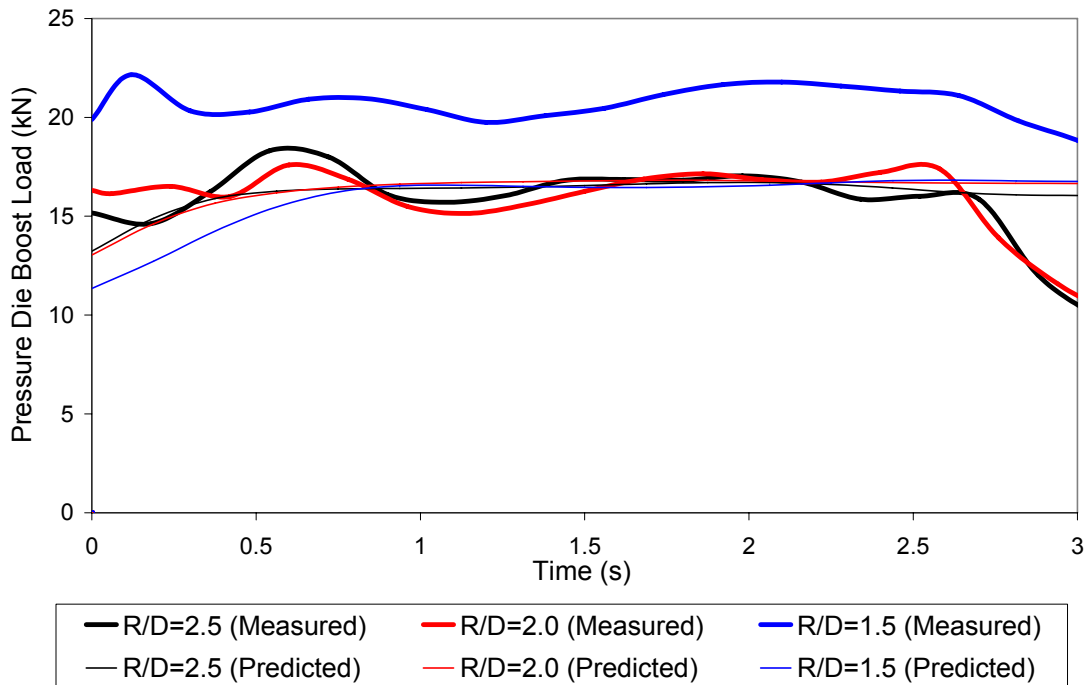


Figure 5.4: Measured pressure die boost load for the first bend of the s-rail bent at the R/D ratios of 2.5, 2.0 and 1.5, and predictions using the piecewise linear material model with a von Mises yield criterion.

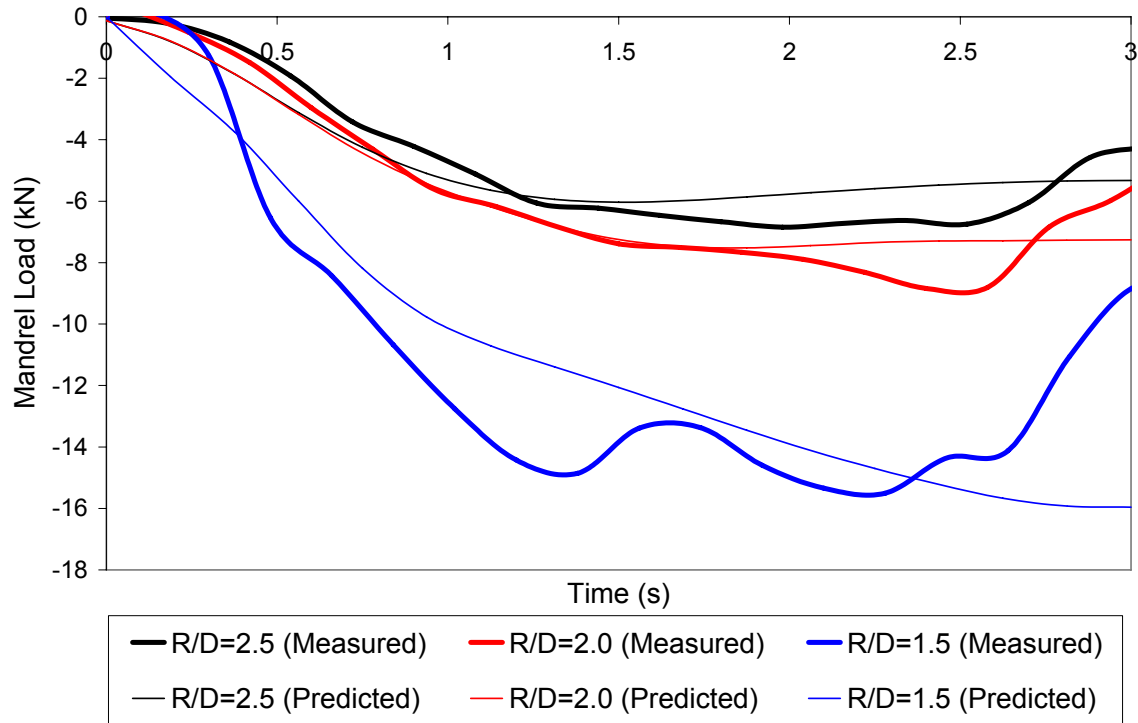


Figure 5.5: Measured mandrel load for the first bend of the s-rail bent at the R/D ratios of 2.5, 2.0 and 1.5, and predictions using the piecewise linear material model with a von Mises yield criterion.

The predicted process variables at each R/D ratio for the first and second bend comprising the s-rail are shown in Figure 5.6, Figure 5.7 and Figure 5.8. The predicted bend torque for the second bend is significantly lower than the first bend due to the prescribed motion boundary condition on nodes near the clamp end of the tube that prevent whipping of the tube, as shown in Figure 3.7. This bending condition artificially reduces the required bend die torque in the models. There is little variation in the predicted pressure die boost and mandrel loads between the two bends.

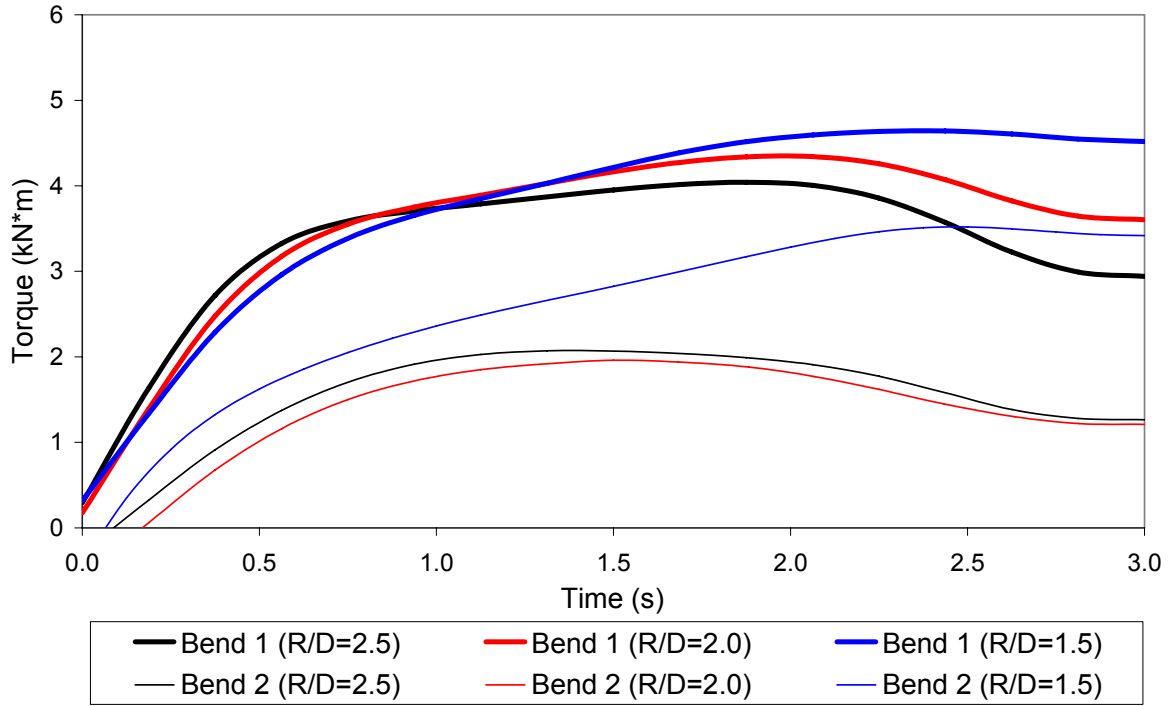


Figure 5.6: Predicted bend torque for the first and second bend of the s-rail at the R/D ratios of 2.5, 2.0 and 1.5.

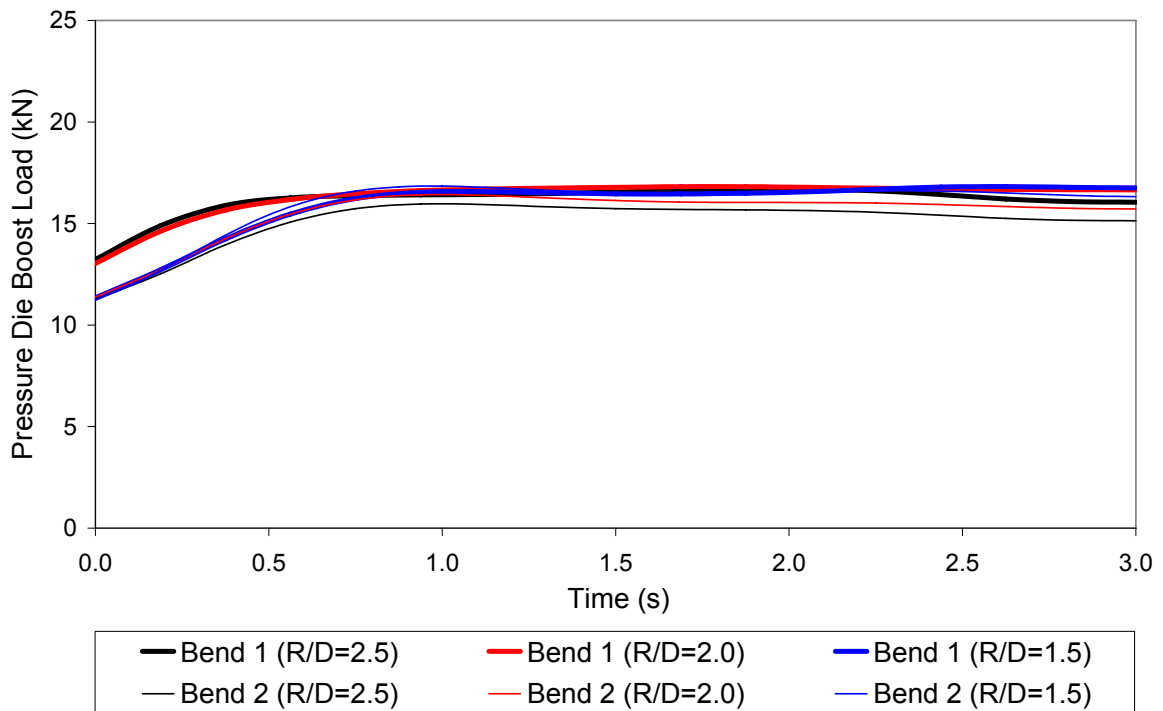


Figure 5.7: Predicted pressure die boost load for the first and second bend of the s-rail at the R/D ratios of 2.5, 2.0 and 1.5.

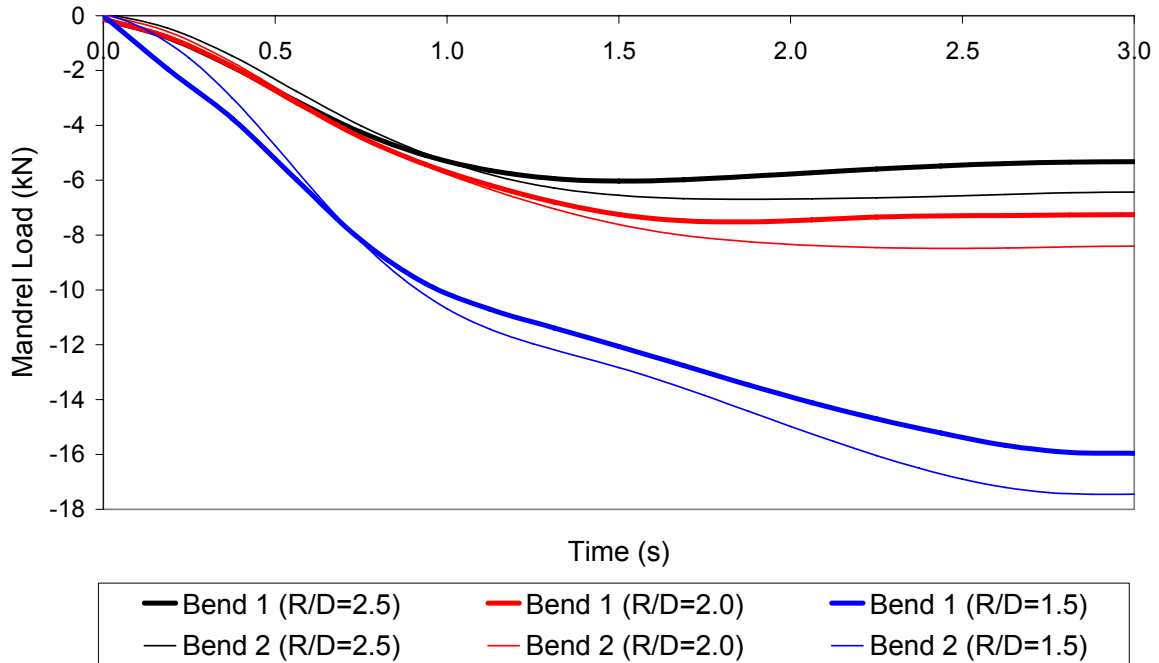


Figure 5.8: Predicted mandrel load for the first and second bend of the s-rail at the R/D ratios of 2.5, 2.0 and 1.5.

5.1.2 Predicted Thickness after Bending

The measured thickness distributions along the inside of the bend and the predictions using the isotropic von Mises (ISO) and anisotropic Barlat (1989) material models are presented in Figure 5.9, Figure 5.10 and Figure 5.11, for the three R/D ratios. The predictions utilizing the anisotropic material model are in better agreement with the measured results for all three R/D ratios, particularly for the R/D=1.5 bend condition. The discrepancy between the measured and predicted thickness, using the anisotropic model, after bending is at most 10%. The minimal sensitivity of the thickness predictions to the r-value parameters may be attributed to the near plane strain conditions experienced in bending, as shown in Section 4.1.3.

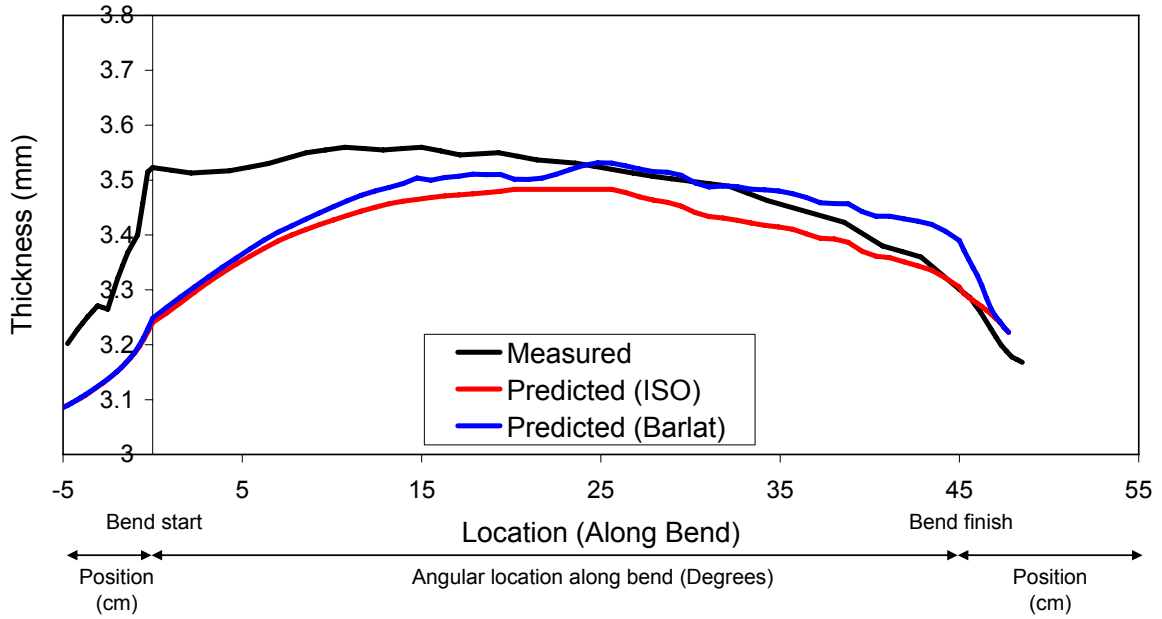


Figure 5.9: Measured thickness along the inside of the bend for $R/D=2.5$ and the predictions using the isotropic von Mises (ISO) and anisotropic Barlat (1989) material model.

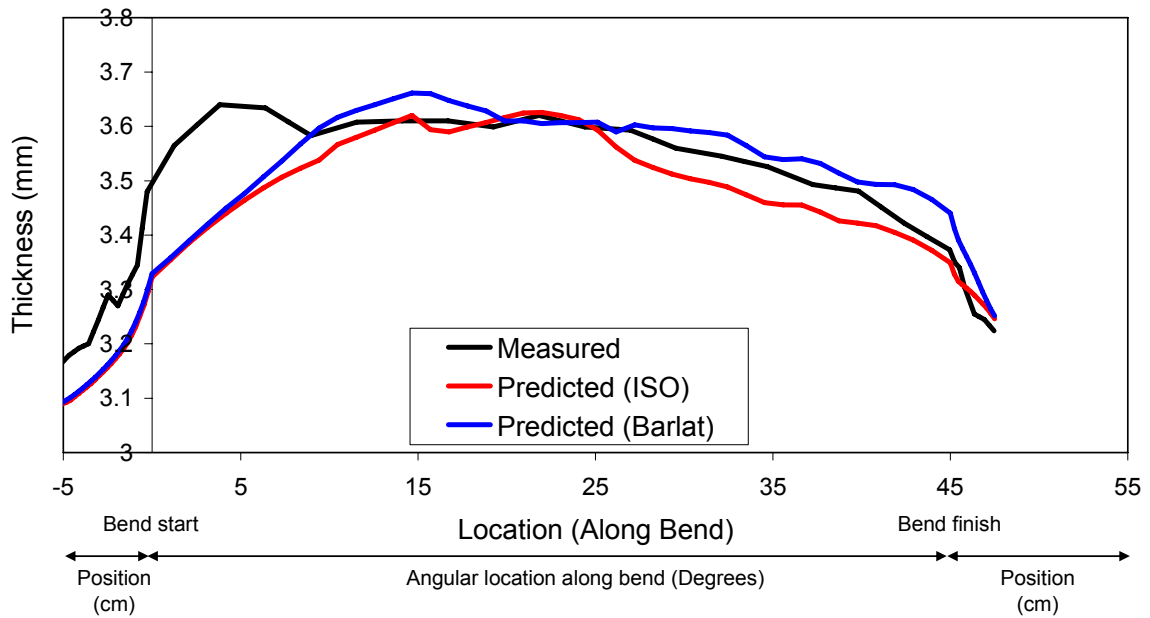


Figure 5.10: Measured thickness along the inside of the bend for $R/D=2.0$ and the predictions using the isotropic von Mises (ISO) and anisotropic Barlat (1989) material models.

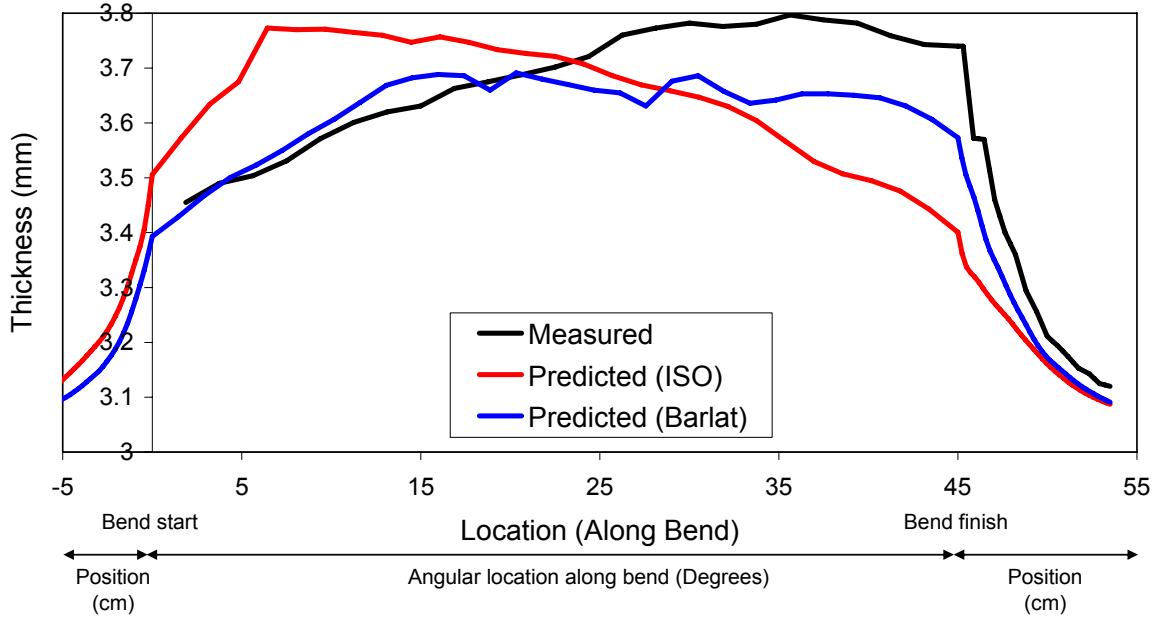


Figure 5.11: Measured thickness along the inside of the bend for $R/D=1.5$ and the predictions using the isotropic von Mises (ISO) and anisotropic Barlat (1989) material models.

The measured and predicted thickness distributions along the outside of the bend for the three R/D ratios are presented in Figure 5.12, Figure 5.13 and Figure 5.14. The predicted thickness distributions are again based on the isotropic von Mises and anisotropic Barlat (1989) material models. There is approximately 1.5% difference between the predicted thickness along the outside of the bend for the R/D ratios of 2.5 and 2.0 from the simulations utilizing the two material models. In addition, there is less than 6.3% difference in the predictions for the case of s-rails bent at $R/D=1.5$. The prediction of thickness along the outside of the bend using the anisotropic Barlat (1989) material model is in overall better agreement with the measured thickness.

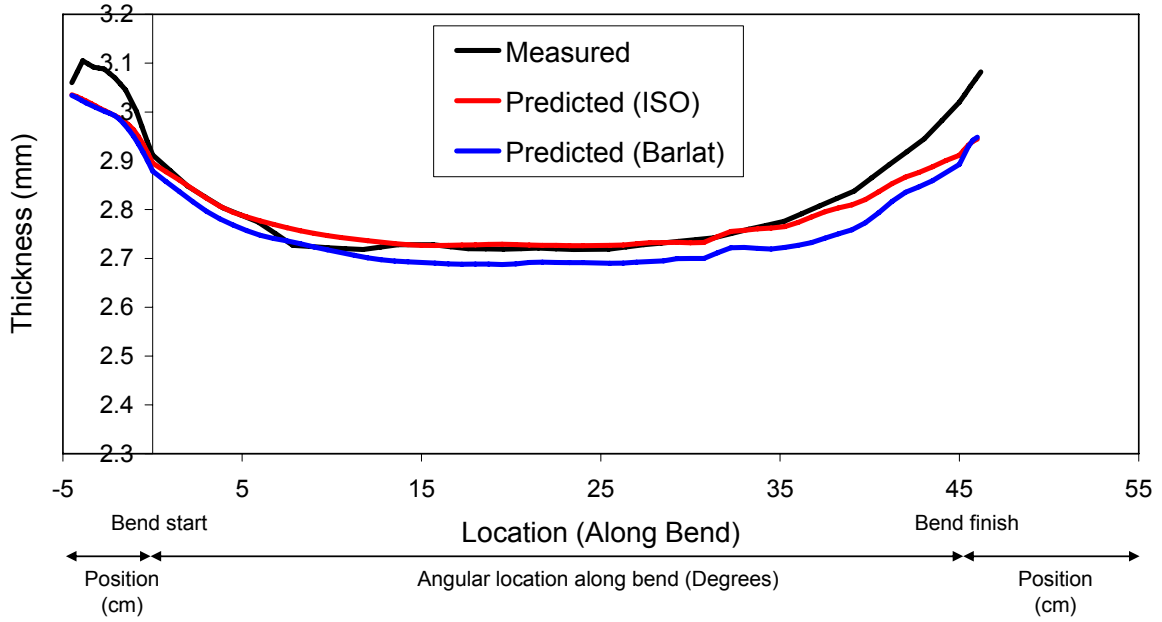


Figure 5.12: Measured thickness along the outside of the bend for $R/D=2.5$ and predictions using the isotropic von Mises (ISO) and anisotropic Barlat (1989) material models.

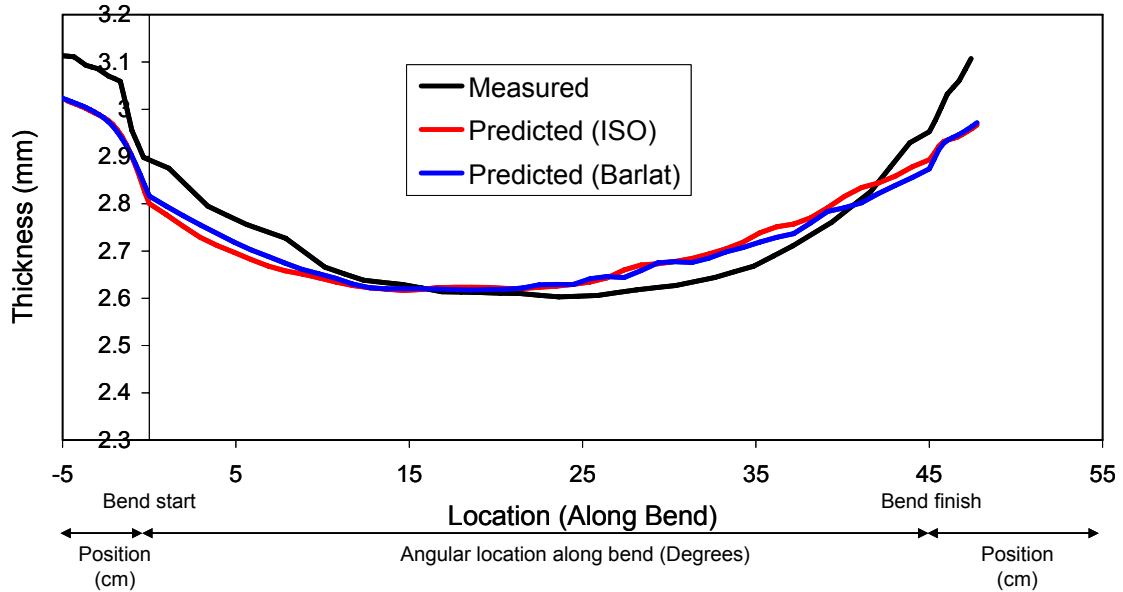


Figure 5.13: Measured thickness along the outside of the bend for $R/D=2.0$ and predictions using the isotropic von Mises (ISO) and anisotropic Barlat (1989) material models.

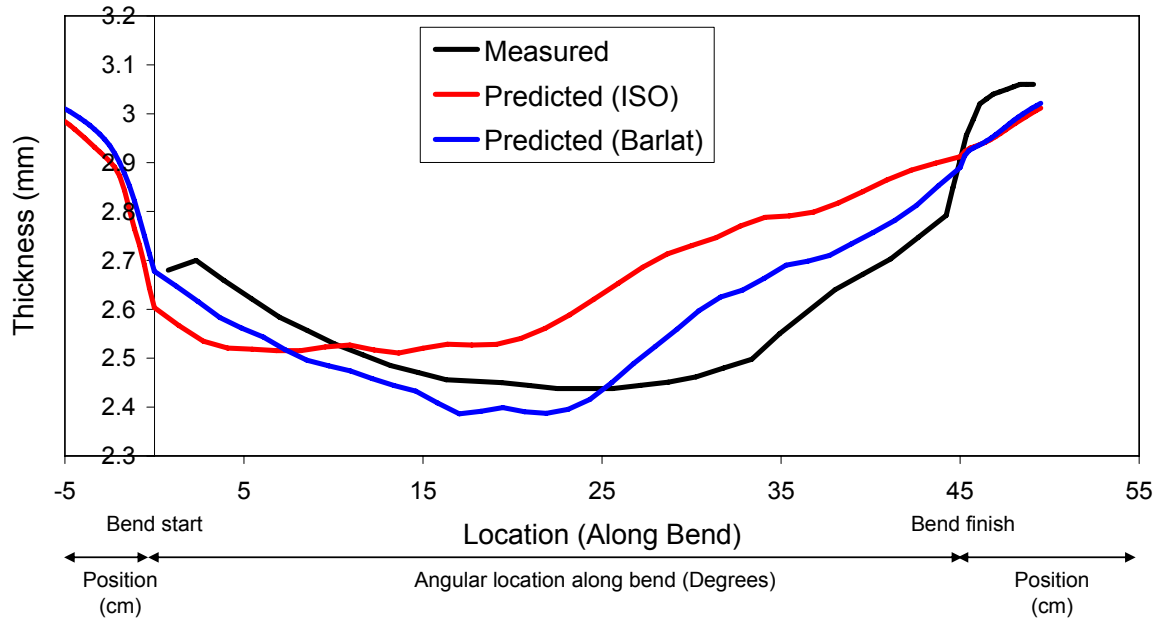


Figure 5.14: Measured thickness along the outside of the bend for $R/D=1.5$ and predictions using the isotropic von Mises (ISO) and anisotropic Barlat (1989) material models.

Figure 5.15, Figure 5.16 and Figure 5.17 show the measured thickness distribution around the circumference of the bend and the predictions using the isotropic von Mises and anisotropic Barlat (1989) models for s-rails bent at the three R/D ratios. For the case of s-rails bent at R/D ratios of 2.5 and 2.0, there is less than 3% difference in the predictions of thickness around the circumference using the two material models. Predictions utilizing the same two material models for s-rails bent at $R/D=1.5$ differ by up to 5% at the 90 and 270 degree locations corresponding to the inside and outside of the bend (Figure 5.17).

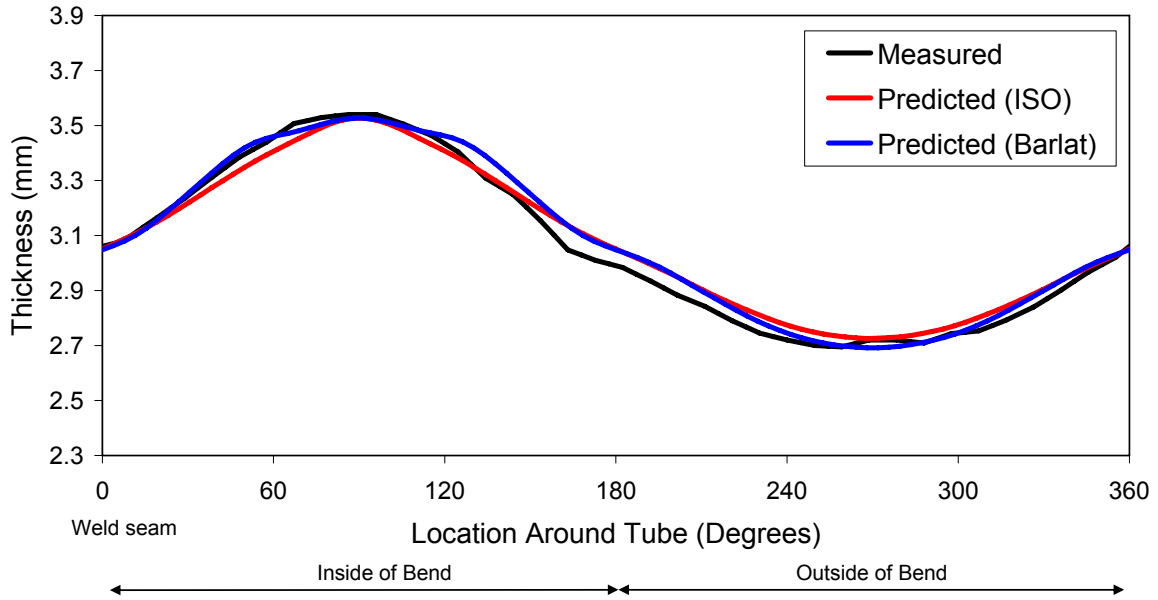


Figure 5.15: Measured thickness around the circumference of the bend for $R/D=2.5$ and predictions using the isotropic von Mises (ISO) and anisotropic Barlat (1989) material models.

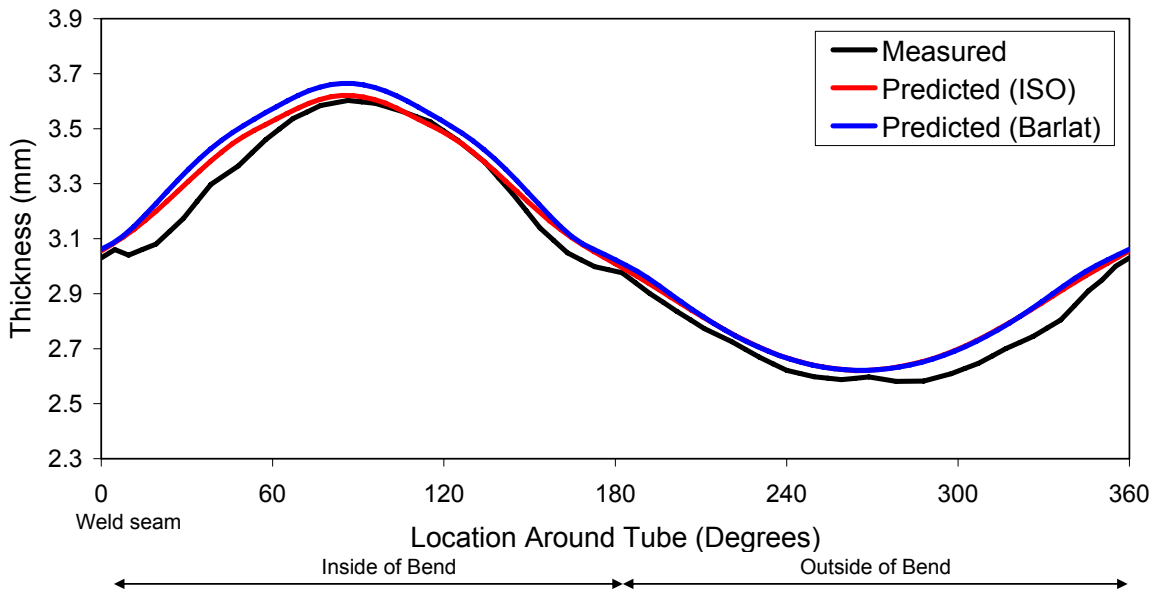


Figure 5.16: Measured thickness around the circumference of the bend for $R/D=2.0$ and predictions using the isotropic von Mises (ISO) and anisotropic Barlat (1989) material models.

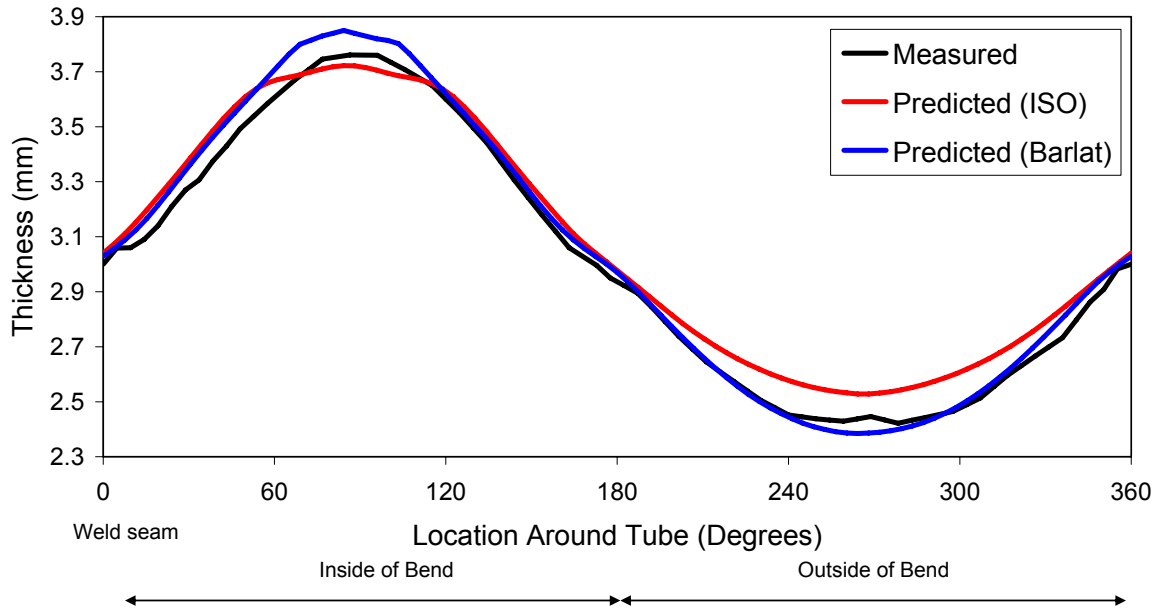


Figure 5.17: Measured thickness around the circumference of the bend for $R/D=1.5$ and predictions using the isotropic von Mises (ISO) and anisotropic Barlat (1989) material models.

A summary of the thickness predictions using the anisotropic Barlat (1989) material model along the inside, outside and around the circumference of the bend are shown in Figure 5.18, Figure 5.19 and Figure 5.20, respectively, for the various R/D ratios. As the bend severity increases from an R/D of 2.5 to 2.0, the magnitude of the predicted thickness changes at the inside and outside of the bend also increase by 4% and 3%, respectively. A further increase in bend severity, from an R/D of 2.0 to 1.5, results in a further increase in predicted thickening at the inside of the bend by 6% and thinning at the outside of the bend by 8%.

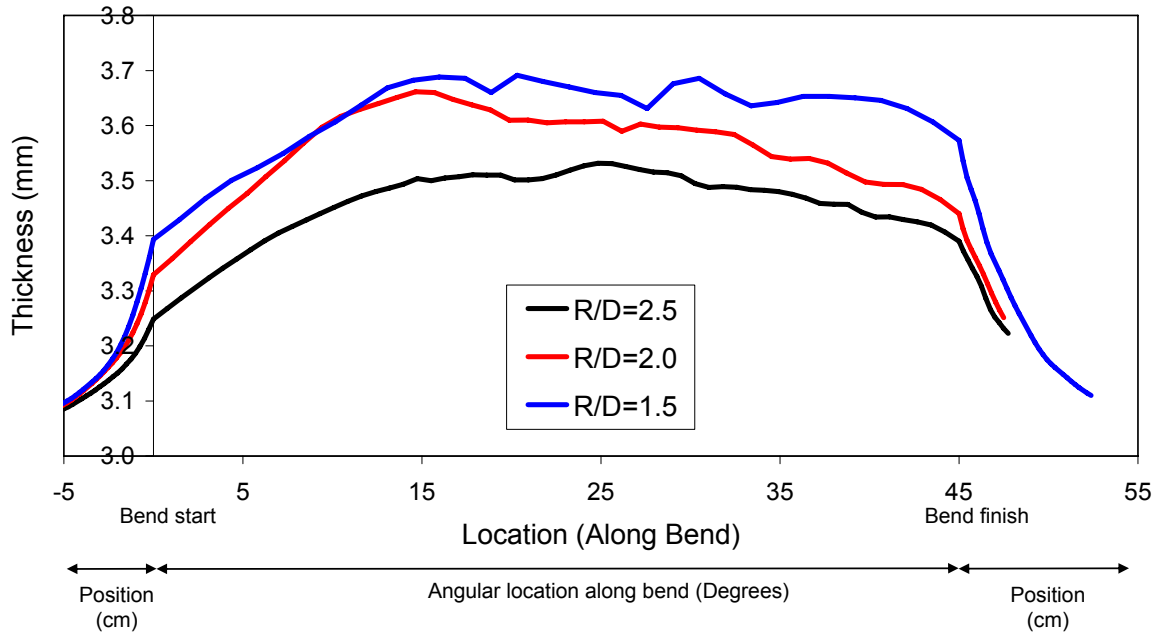


Figure 5.18: Predictions of thickness along the inside of the bend using the anisotropic Barlat (1989) material model for R/D ratios of 2.5, 2.0 and 1.5.

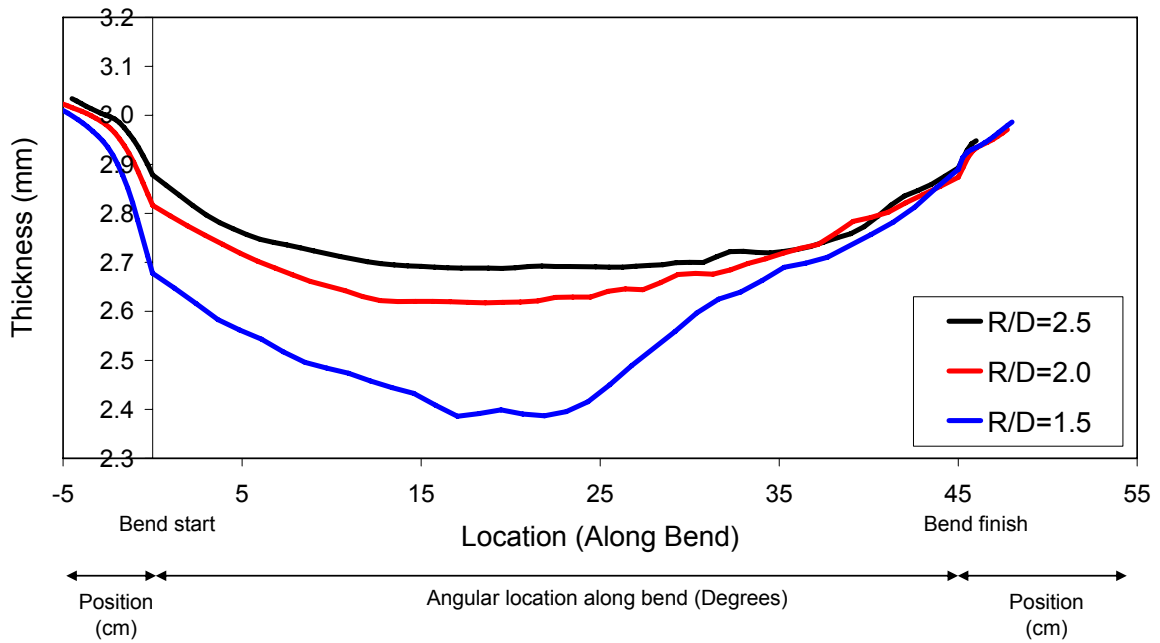


Figure 5.19: Predictions of thickness along the outside of the bend using the anisotropic Barlat (1989) material model for R/D ratios of 2.5, 2.0 and 1.5.

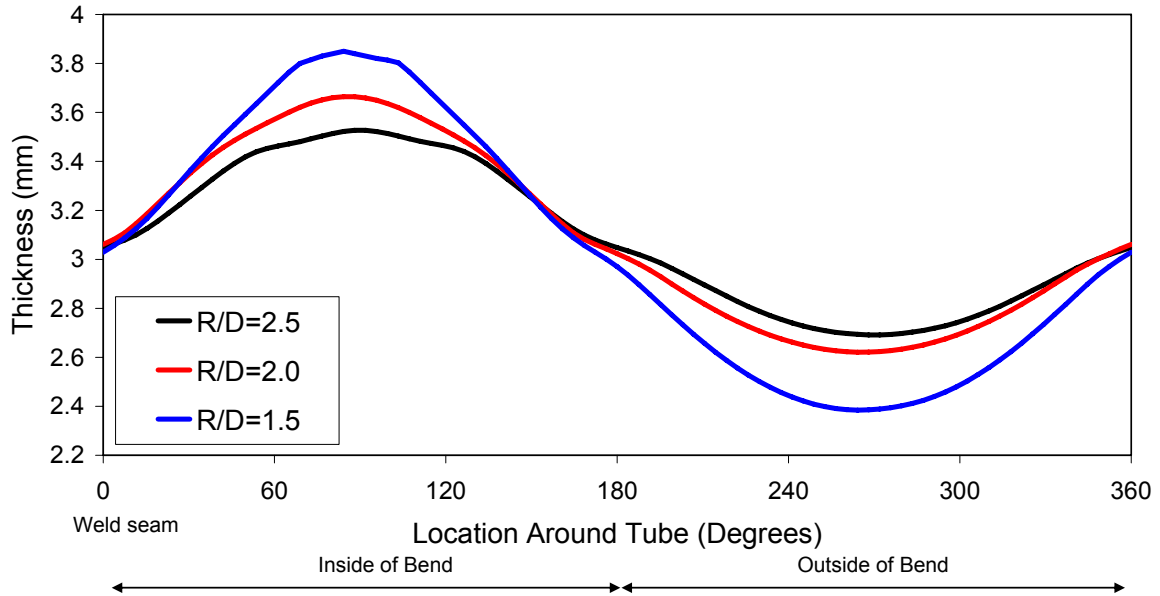


Figure 5.20: Predictions of thickness around the circumference of the bend using the anisotropic Barlat (1989) material model for R/D ratios of 2.5, 2.0 and 1.5.

5.1.3 Strains

The major and minor engineering strains from the experiments and the models using the isotropic von Mises and anisotropic Barlat (1989) material models are shown in Figure 5.21 to Figure 5.23, Figure 5.24 to Figure 5.26, and Figure 5.27 to Figure 5.29, respectively, for the three R/D ratios. There is reasonably good agreement between the predictions of major and minor strain using the two material models; however, the anisotropic model predictions of strain are in mildly better agreement with the measured results.

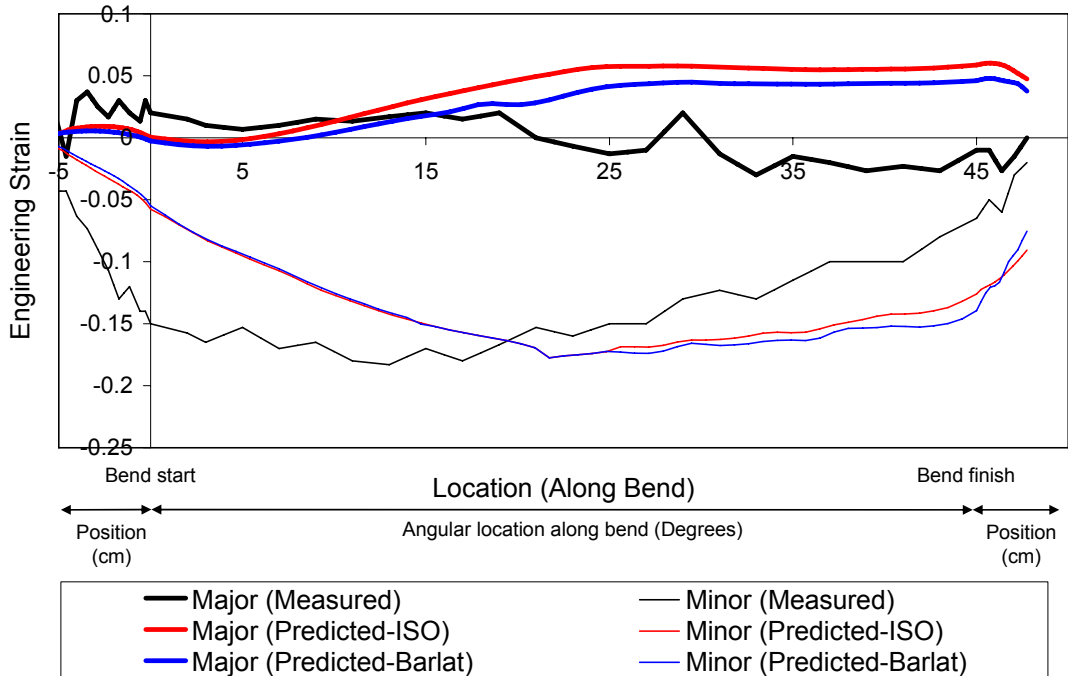


Figure 5.21: Measured major and minor engineering strains and predictions using the isotropic von Mises (ISO) and anisotropic Barlat (1989) material models along the inside of the bend for $R/D=2.5$.

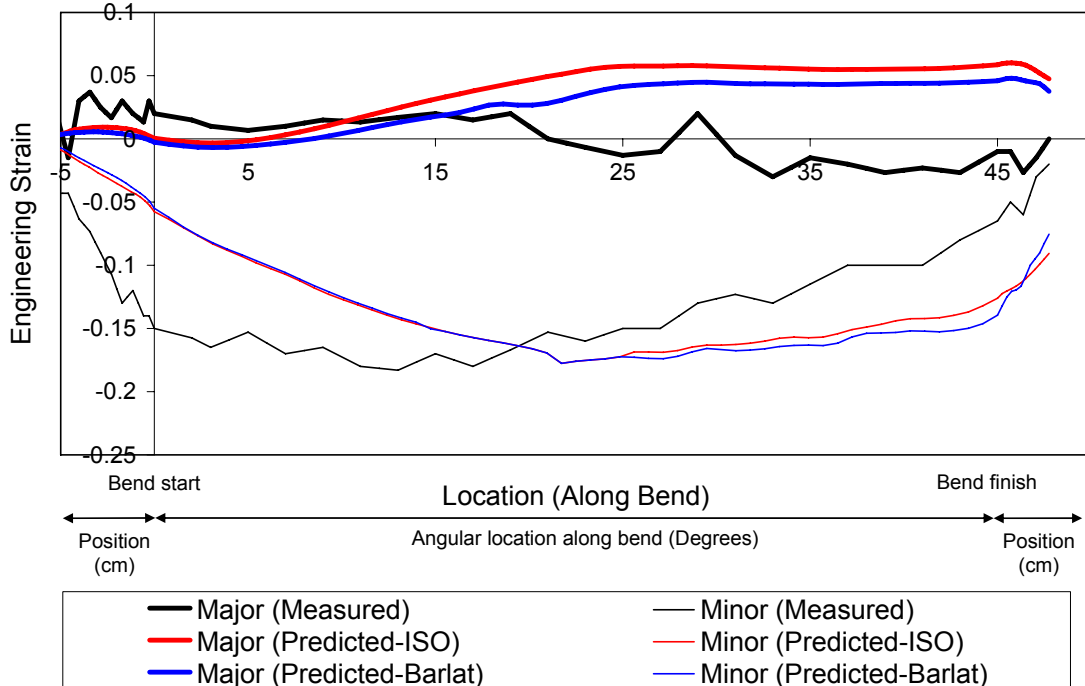


Figure 5.22: Measured major and minor engineering strains and predictions using the isotropic von Mises (ISO) and anisotropic Barlat (1989) material models along the inside of the bend for $R/D=2.0$.

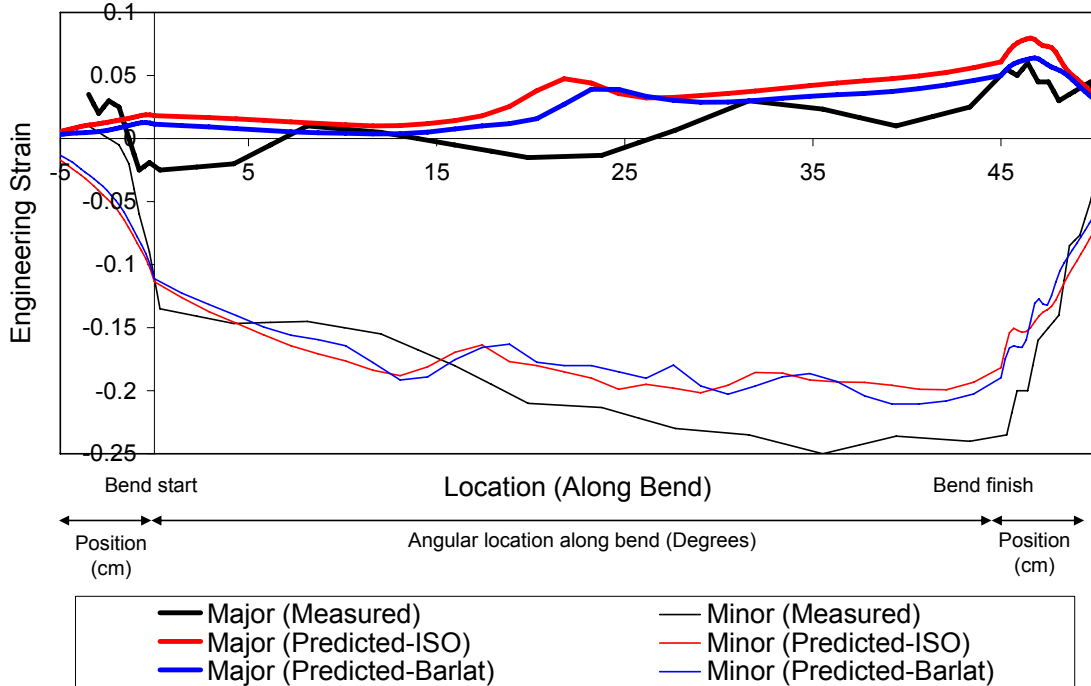


Figure 5.23: Measured major and minor engineering strains and predictions using the isotropic von Mises (ISO) and anisotropic Barlat (1989) material models along the inside of the bend for $R/D=1.5$.

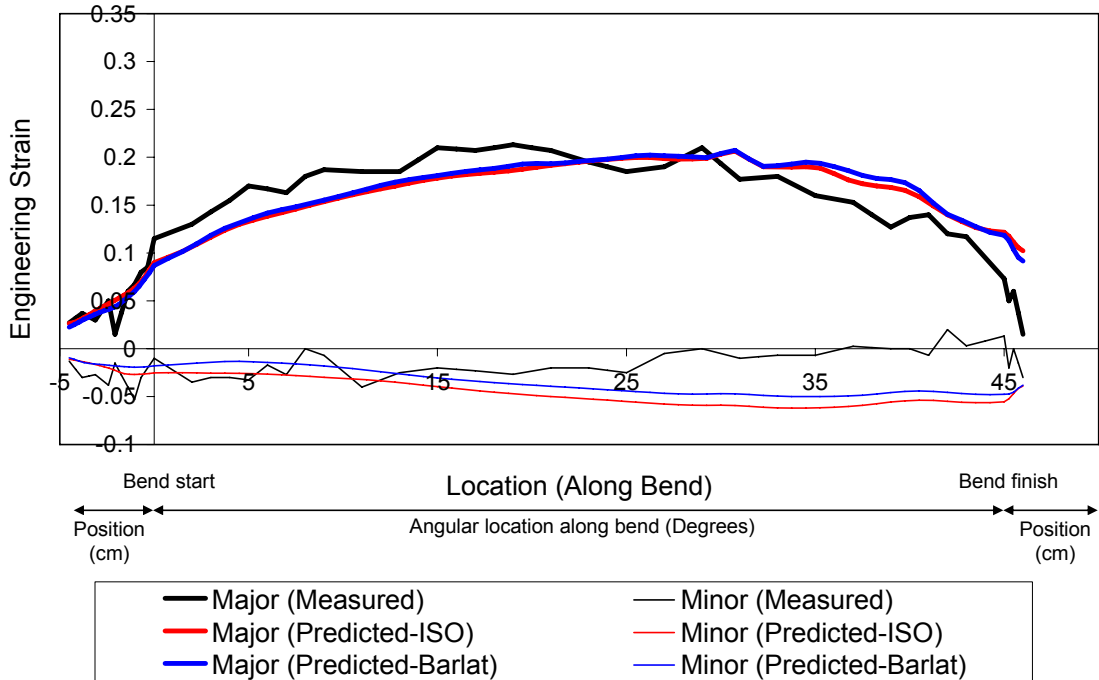


Figure 5.24: Measured major and minor engineering strains and predictions using the isotropic von Mises (ISO) and anisotropic Barlat (1989) material models along the outside of the bend for $R/D=2.5$.

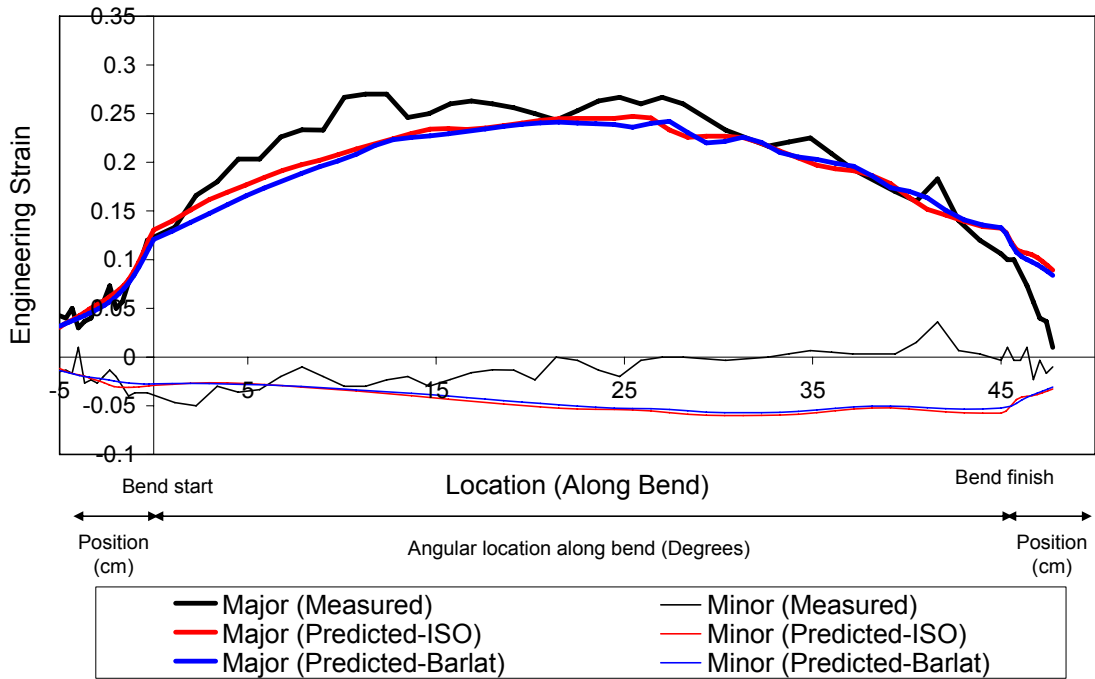


Figure 5.25: Measured major and minor engineering strains and predictions using the isotropic von Mises (ISO) and anisotropic Barlat (1989) material models along the outside of the bend for $R/D=2.0$.

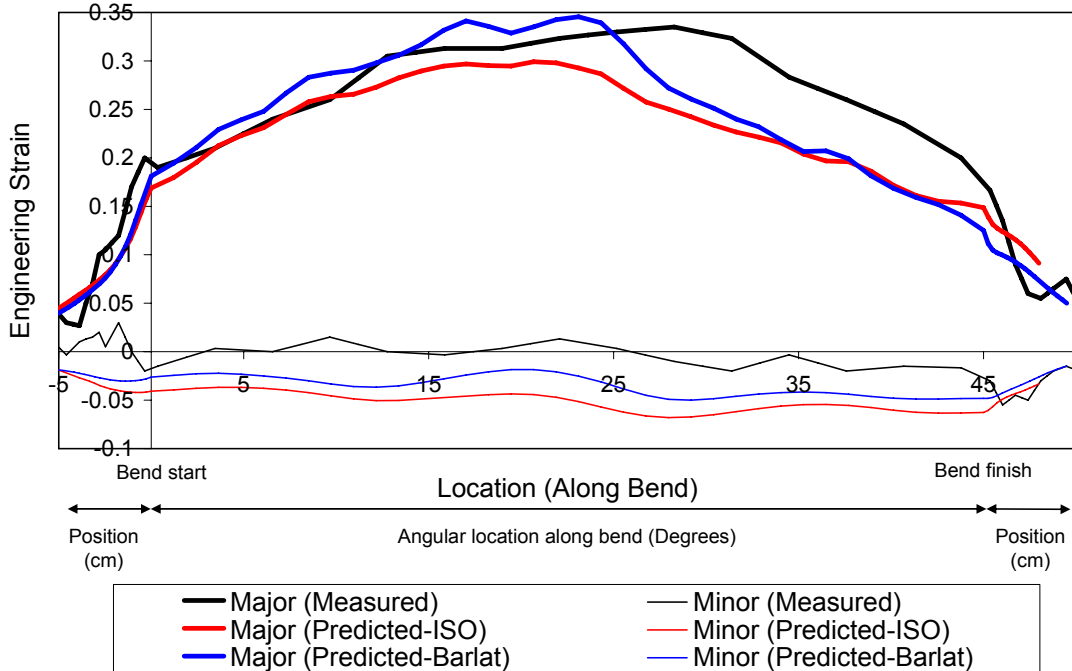


Figure 5.26: Measured major and minor engineering strains and predictions using the isotropic von Mises (ISO) and anisotropic Barlat (1989) material models along the outside of the bend for $R/D=1.5$.

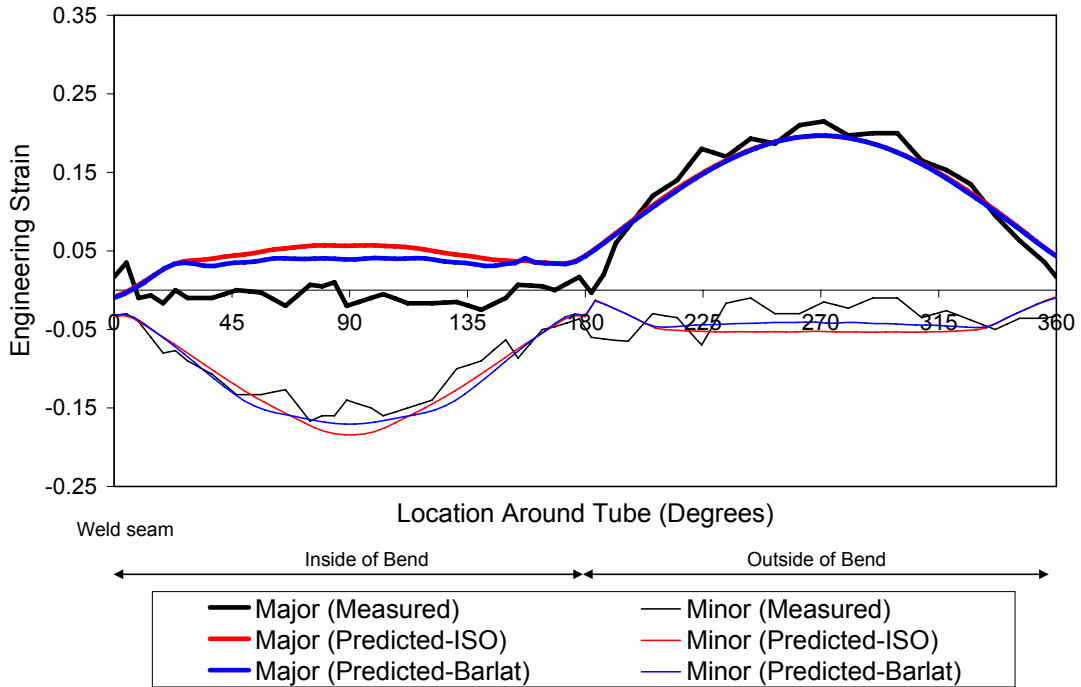


Figure 5.27: Measured major and minor engineering strains and predictions using the isotropic von Mises (ISO) and anisotropic Barlat (1989) material models around the circumference of the bend for $R/D=2.5$.

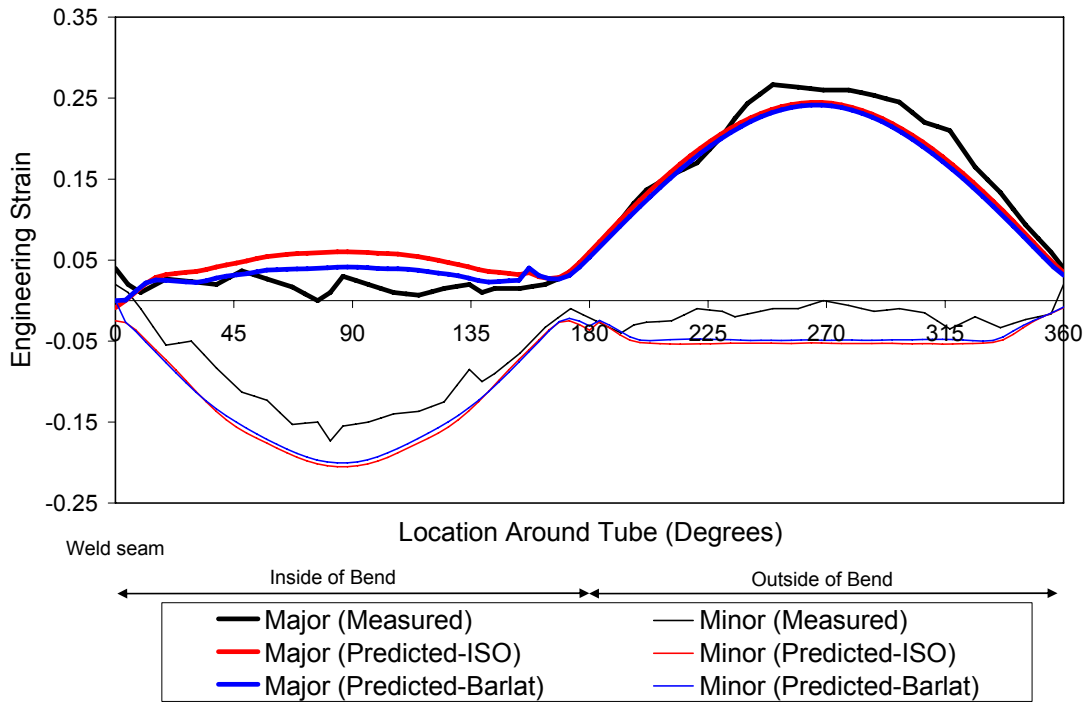


Figure 5.28: Measured major and minor engineering strains and predictions using the isotropic von Mises (ISO) and anisotropic Barlat (1989) material models around the circumference of the bend for $R/D=2.0$.

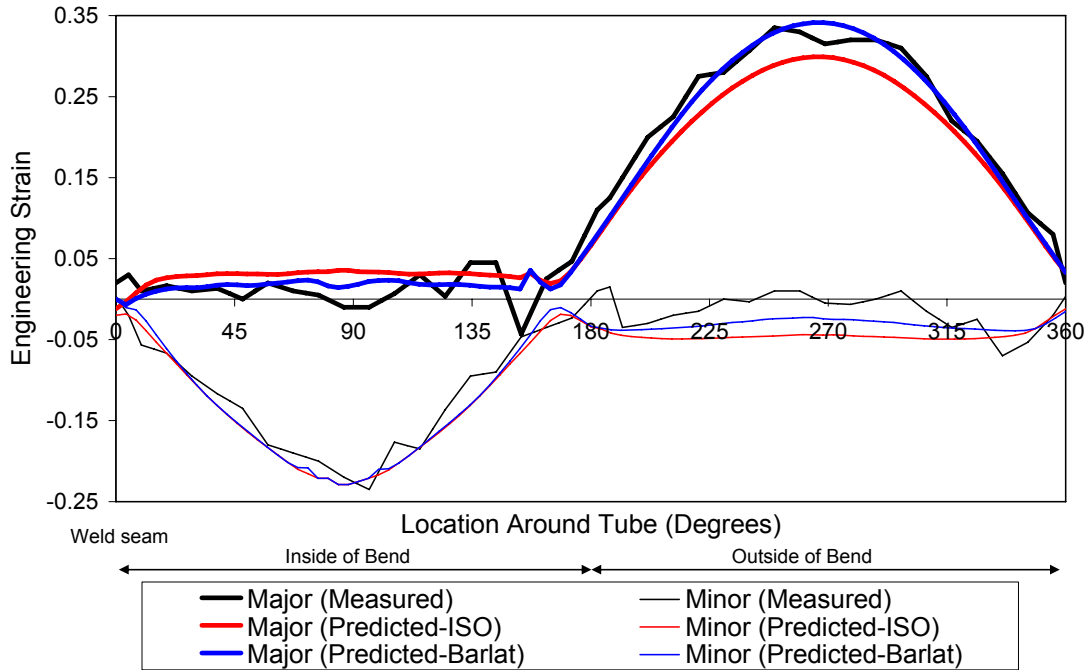


Figure 5.29: Measured major and minor engineering strains and predictions using the isotropic von Mises (ISO) and anisotropic Barlat (1989) material models around the circumference of the bend for $R/D=1.5$.

A summary of the strain predictions around the circumference of the bend at the three R/D ratios investigated using the anisotropic Barlat (1989) material model is shown in Figure 5.30. The predicted axial (minor) strains at the inside of the bend for the R/D ratios of 2.5, 2.0 and 1.5 are -17%, -20% and -23%, respectively, which is in good agreement with the values of -15%, -15% and -22% measured in the experiments. Similarly, the predicted axial (major) strains at the outside of the bend are 20%, 24% and 34%, respectively, and are also in good agreement with the values of 20%, 26% and 32% measured in the experiments.

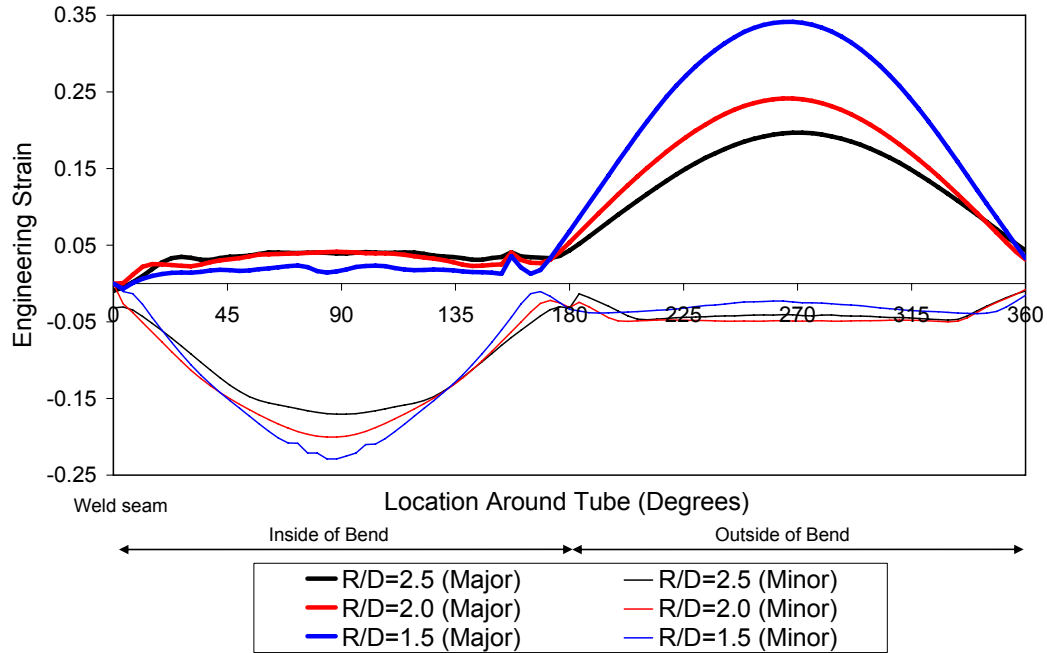


Figure 5.30: Major and minor engineering strain predictions around the circumference of the bend at R/D ratios of 2.5, 2.0 and 1.5 using the anisotropic Barlat (1989) material model.

5.2 Hydroforming Predictions

The low-pressure hydroforming simulation begins with the die closure stage that occurs within the first 8 ms of the simulation, followed by the pressurization stage over 4 ms. During the die closure stage of this process, a small internal pressure of 4.5 MPa is maintained within the tube to prevent internal collapse, after which the pressure is linearly increased to 65 MPa in the pressurization stage. The predicted deformation of a 3 mm AA5754 s-rail bent at R/D=2.5 at several instants in time during the low-pressure hydroforming process is shown in Figure 5.31. The predicted deformation of the cross-section at the center of the straight section A and bend section D (Figure 2.3) of the s-rail during this hydroforming process is also shown in Figure 5.31c and Figure 5.31d, respectively. Once the die closure portion of the low-pressure hydroforming process is completed, the straight sections of the s-rail have been mostly formed into the section of the die. After the die closure stage, the straight sections of the s-rail are not as fully formed to the profile of the die section as the bend sections (B & D), as shown in Figure 5.31d. After the pressurization stage of this low-pressure hydroforming process, the s-rail fully forms into the profile of the die.

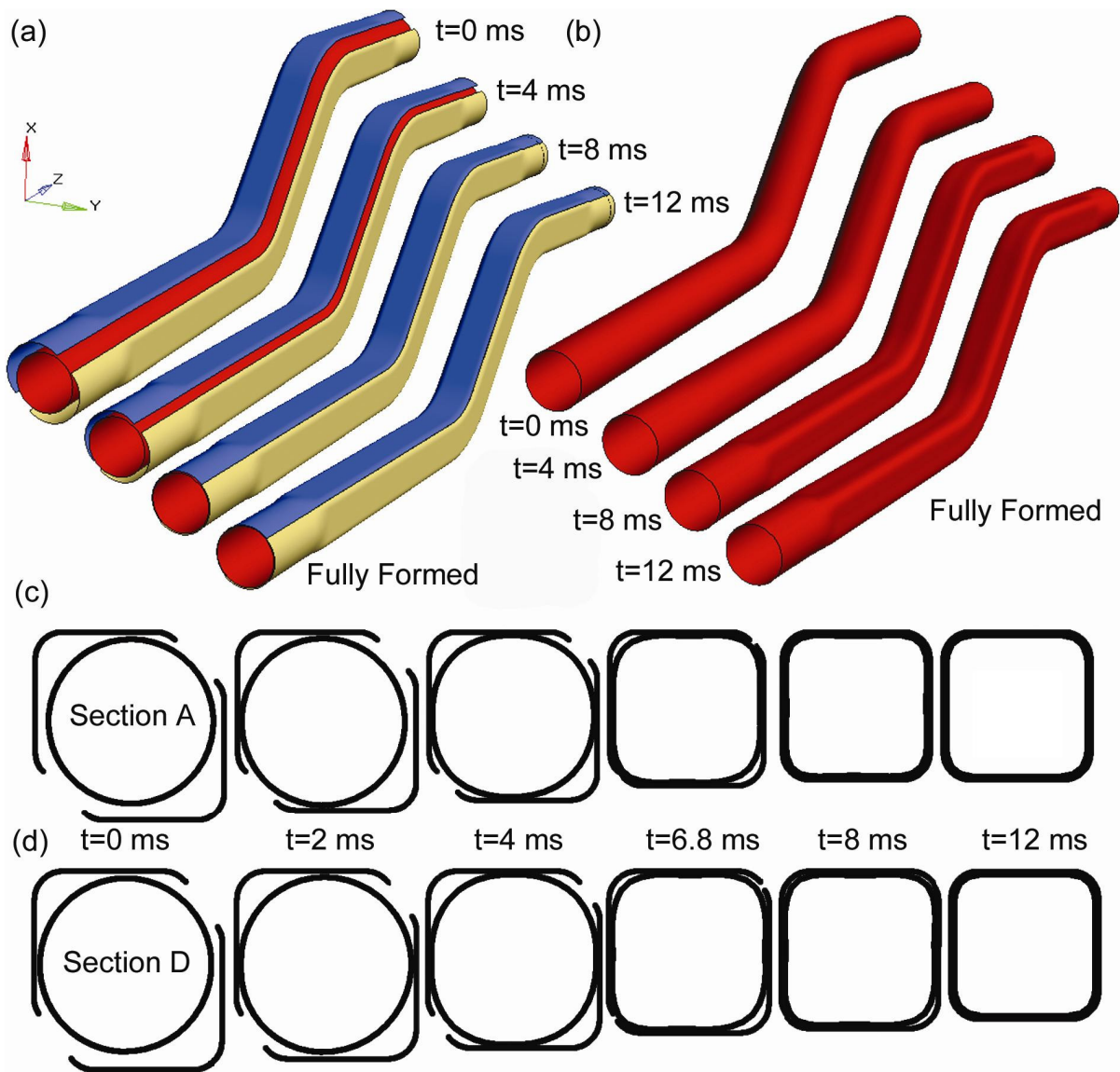


Figure 5.31: Predicted deformation of a 3 mm AA5754 s-rail bent at $R/D=2.5$ at several instants in time during the low-pressure hydroforming operation. (a) Die surfaces and s-rail; (b) s-rail; (c) cross-section view of straight section A of the s-rail; and (d) cross-section view of bent section D of s-rail.

After the low-pressure hydroforming simulation was conducted, an implicit springback analysis was performed and the s-rail was trimmed to the appropriate size, as shown in Figure 2.13. The actual and predicted final geometry of a 3 mm AA5754 s-rail bent at $R/D=2.5$ after the low-pressure hydroforming process and trimming is shown in Figure 5.32. Also shown in Figure 5.32 are the contour plots of the predicted thickness, and major and minor strain. There is excellent agreement between the actual and predicted final geometry of the s-rail after hydroforming. In addition, the predicted thickness, major and minor strains

are also in good agreement with the measured quantities presented in Section 4.2, as will be shown in detail within this section. The thickness and strain changes due to the low-pressure hydroforming operation are largely controlled by the die section geometry. Since there is almost negligible expansion of the tube in the low-pressure hydroforming process employed, the tube deforms through largely circumferential bending. Therefore changes in thickness and axial strains due to the hydroforming process are small, while circumferential strains can be large.

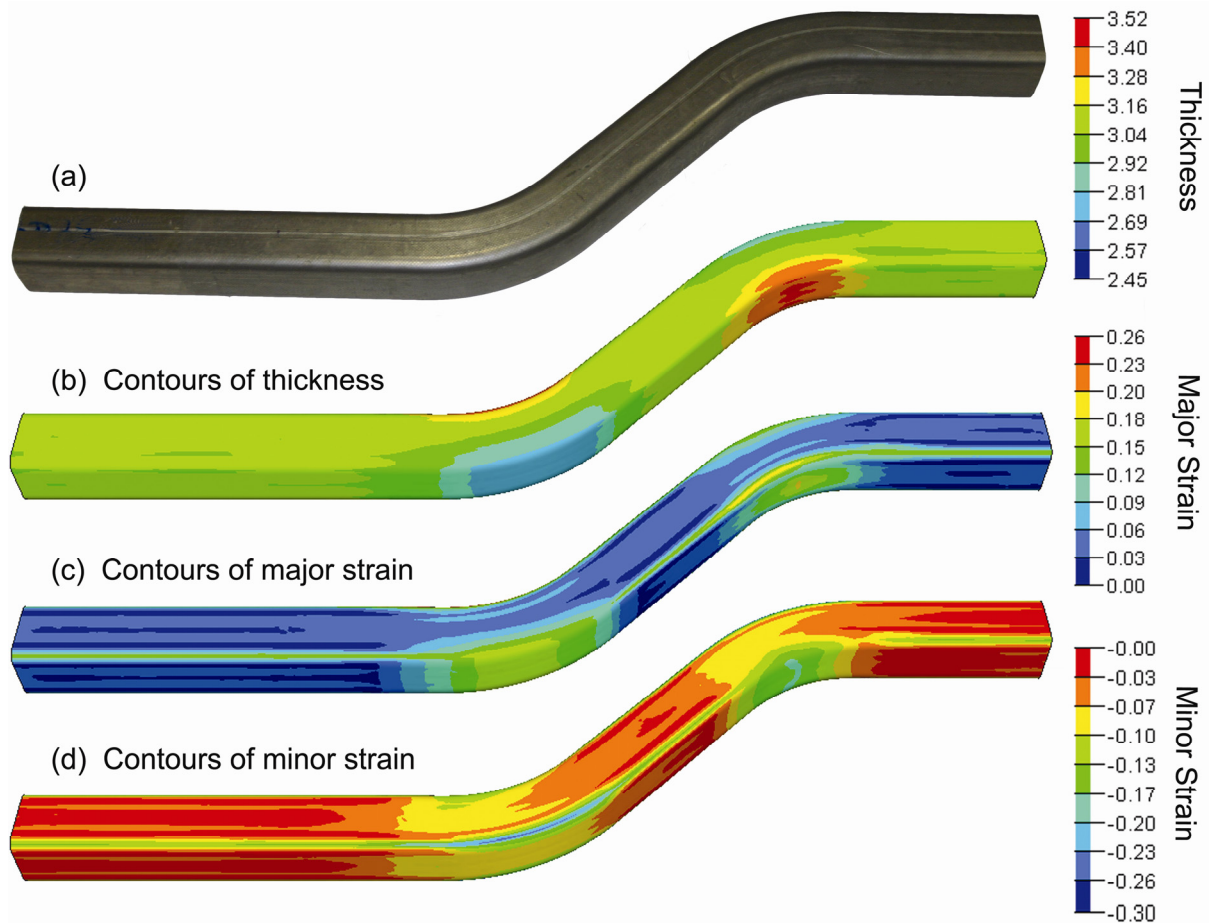


Figure 5.32: (a) Actual 3 mm AA575 s-rail bent at $R/D=2.5$ after hydroforming and trimming. Predicted s-rail geometry after low-pressure hydroforming and trimming operations and contours of (b) thickness (mm); (c) major strain; and (d) minor strain.

5.2.1 Predicted Thickness after Hydroforming

Predictions of thickness distribution around the circumference of a straight section in a hydroformed s-rail bent at R/D ratios of 2.5, 2.0 and 1.5 using the isotropic von Mises material model are shown in Figure 5.33. As expected, the predicted thickness change is low and similar within the straight sections of the s-rail.

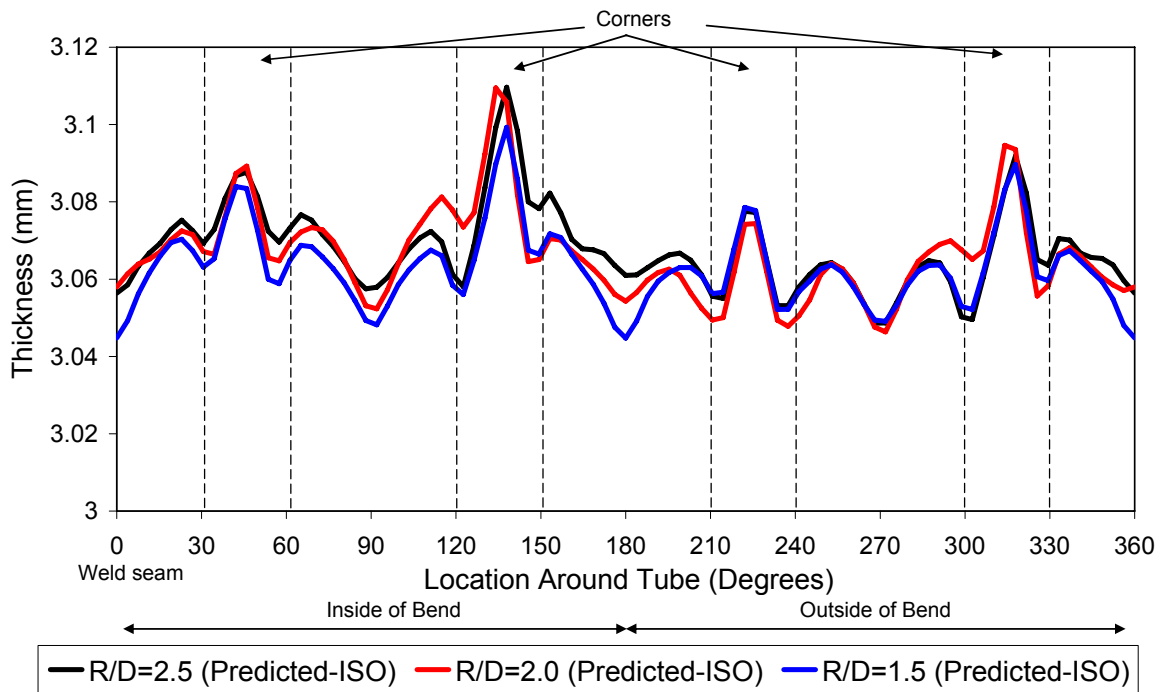


Figure 5.33: Predicted thickness distribution around the straight section C of s-rails bent and hydroformed at R/D ratios of 2.5, 2.0 and 1.5 using the isotropic material model.

The measured thickness around the circumference of the bend in the hydroformed s-rails and the predictions using the isotropic von Mises and anisotropic Barlat (1989) material models are shown in Figure 5.34, Figure 5.35 and Figure 5.36 for all three R/D ratios. Both model predictions of thickness are in very good agreement with the measured result; however, the simulation using the anisotropic model better predicts the thinning at the outside of the bend for R/D=1.5.

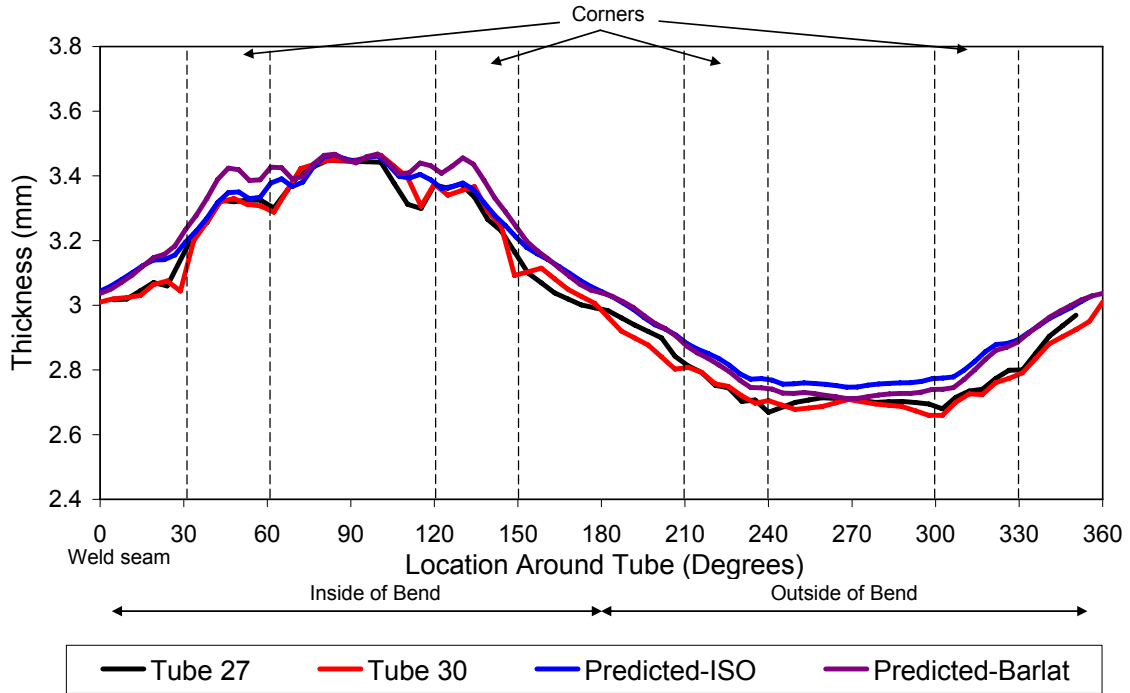


Figure 5.34: Measured thickness around the circumference of the bend and predictions using the isotropic von Mises and anisotropic Barlat (1989) material models for hydroformed s-rails bent at $R/D=2.5$.

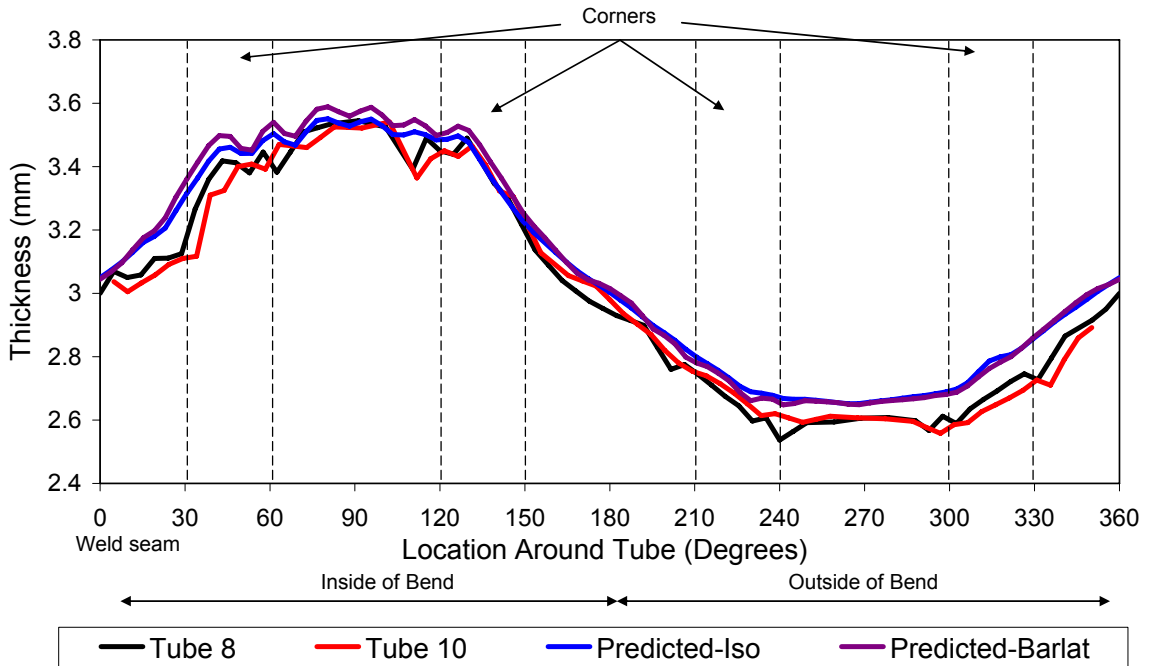


Figure 5.35: Measured thickness around the circumference of the bend and predictions using the isotropic von Mises and anisotropic Barlat (1989) material models for hydroformed s-rails bent at $R/D=2.0$.

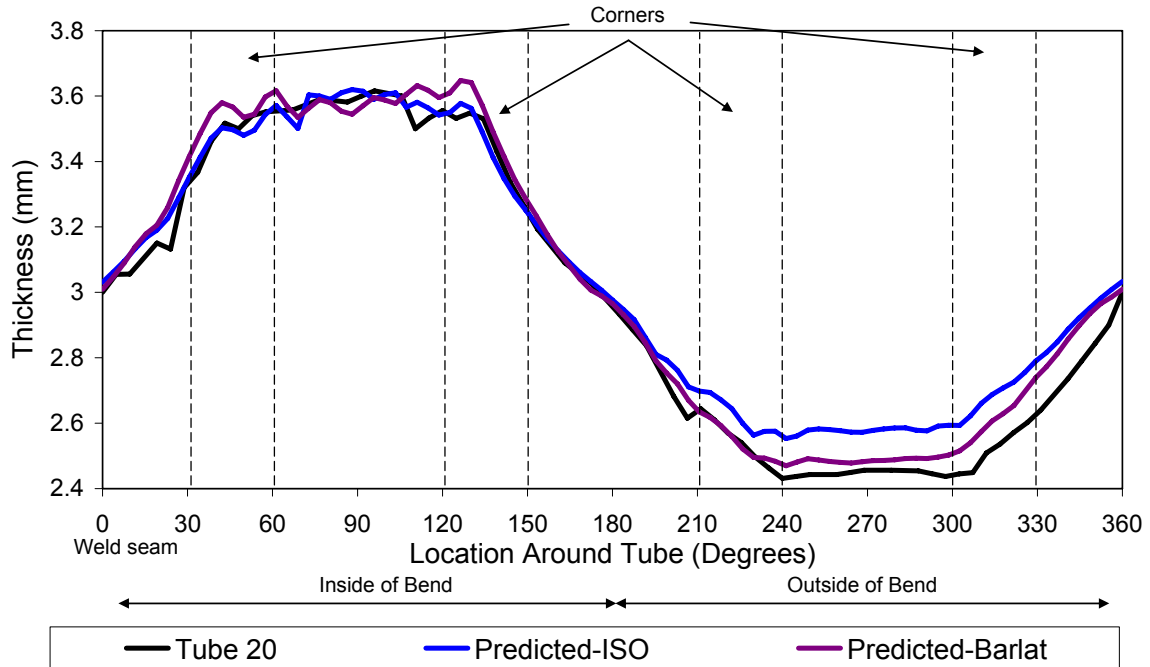


Figure 5.36: Measured thickness around the circumference of the bend and predictions using the isotropic von Mises and anisotropic Barlat (1989) material models for hydroformed s-rails bent at $R/D=1.5$.

5.2.2 Predicted Strains after Hydroforming

The measured major and minor engineering strains around the circumference of a straight section in the s-rail and predictions using the isotropic von Mises material model are shown in Figure 5.37. There is excellent agreement between the measured and predicted strains, which are characterized by a peak of approximately 15% strain in the corner regions. Note that these peak strains correspond to circumferential bending at the outside of the section profile radius. Also note that the net thickness change is nearly zero and that compressive bending strains of a similar magnitude will exist on the inside of the tubes. The analytical approach to estimating the bending strain at the corner region of the straight section of the s-rail, shown in Equation 2.1 (Section 2.4.2), under-predicts the strain by 0.04 in comparison to the measured value and numerical prediction.

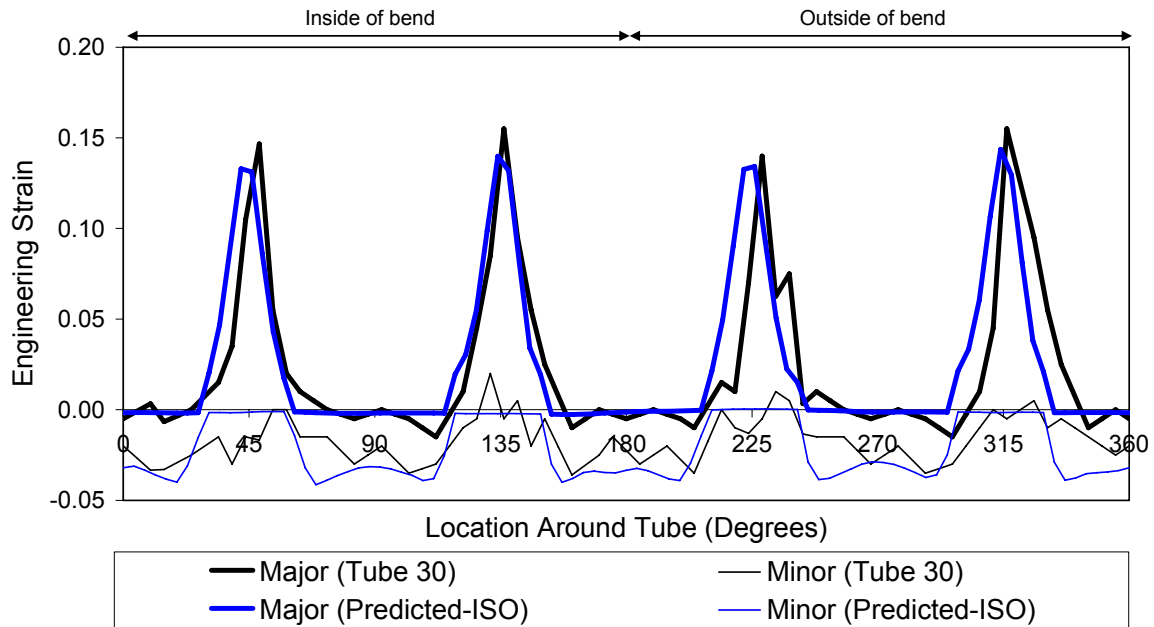


Figure 5.37: Measured versus predicted major and minor engineering strains using the isotropic von Mises material model around the circumference of straight section C of the hydroformed s-rail.

The measured major and minor engineering strains around the circumference of the bend region in s-rails bent at R/D ratios of 2.5, 2.0 and 1.5 and predictions using the isotropic von Mises and anisotropic Barlat (1989) material models are shown in Figure 5.38, Figure 5.39 and Figure 5.40. There is very good agreement between the measured and predicted results for all R/D ratios. Again, the predictions of major strain along the outside of the bend utilizing the anisotropic material model are in slightly better agreement with the measured result.

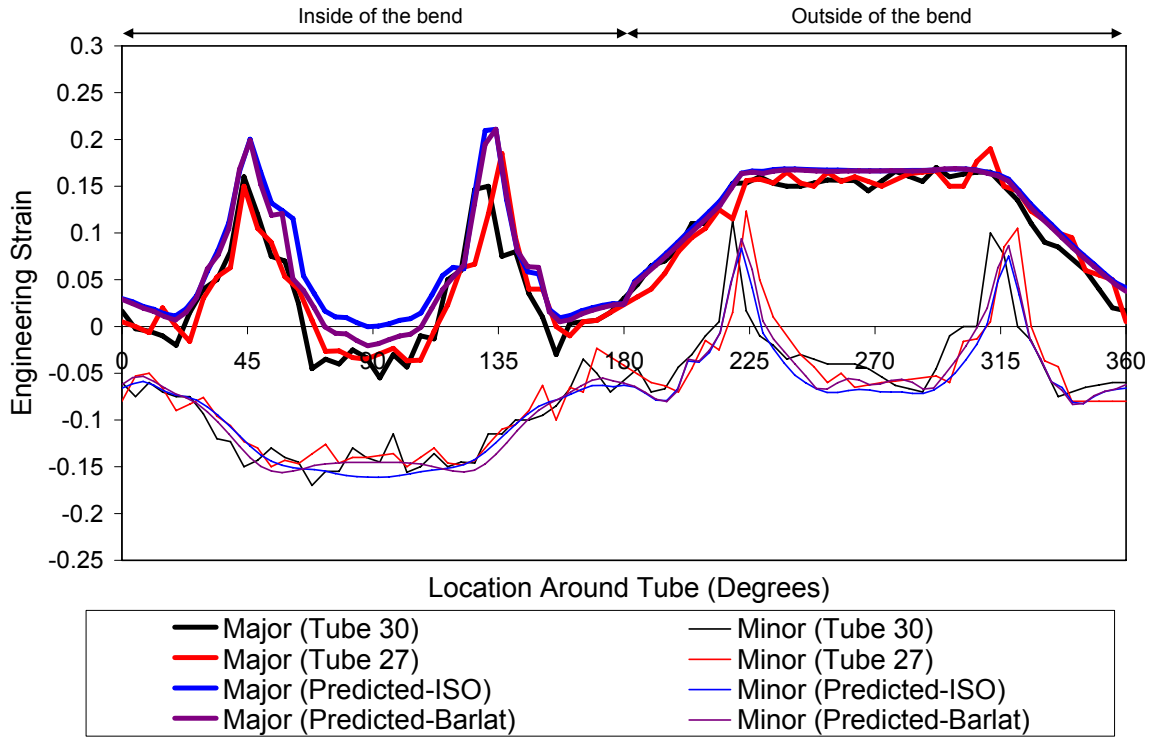


Figure 5.38: Measured major and minor engineering strains and predictions using the isotropic von Mises and anisotropic material models around the circumference of a bend in a hydroformed s-rail bent at $R/D=2.5$.

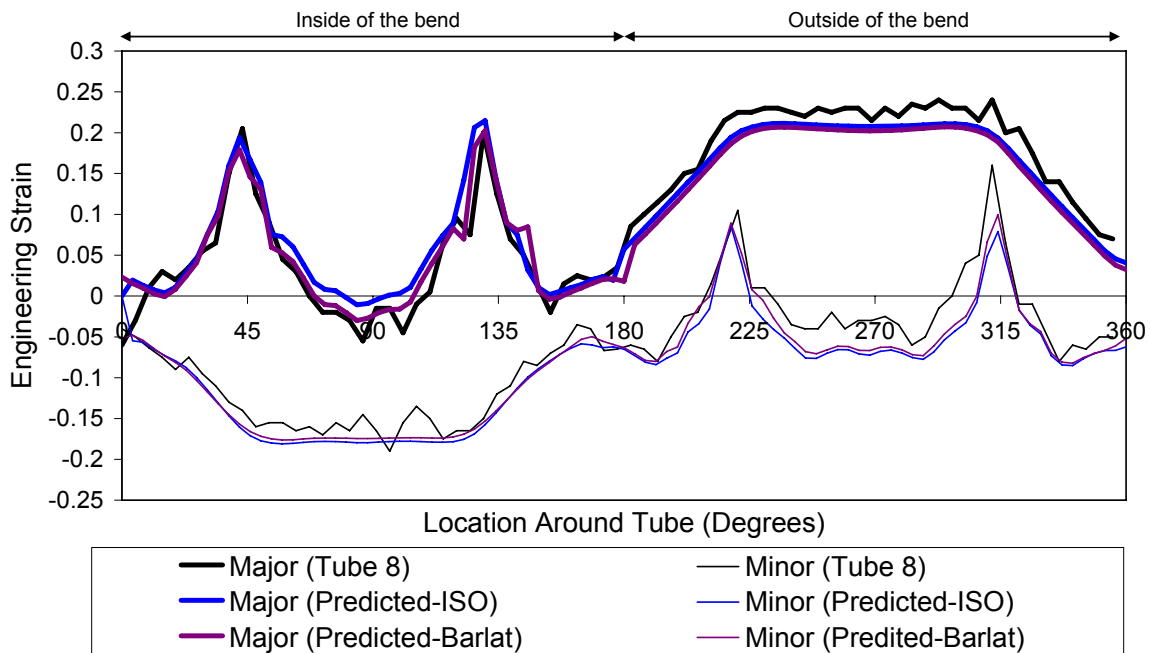


Figure 5.39: Measured major and minor engineering strains and predictions using the isotropic von Mises and anisotropic material models around the circumference of a bend in a hydroformed s-rail bent at $R/D=2.0$.

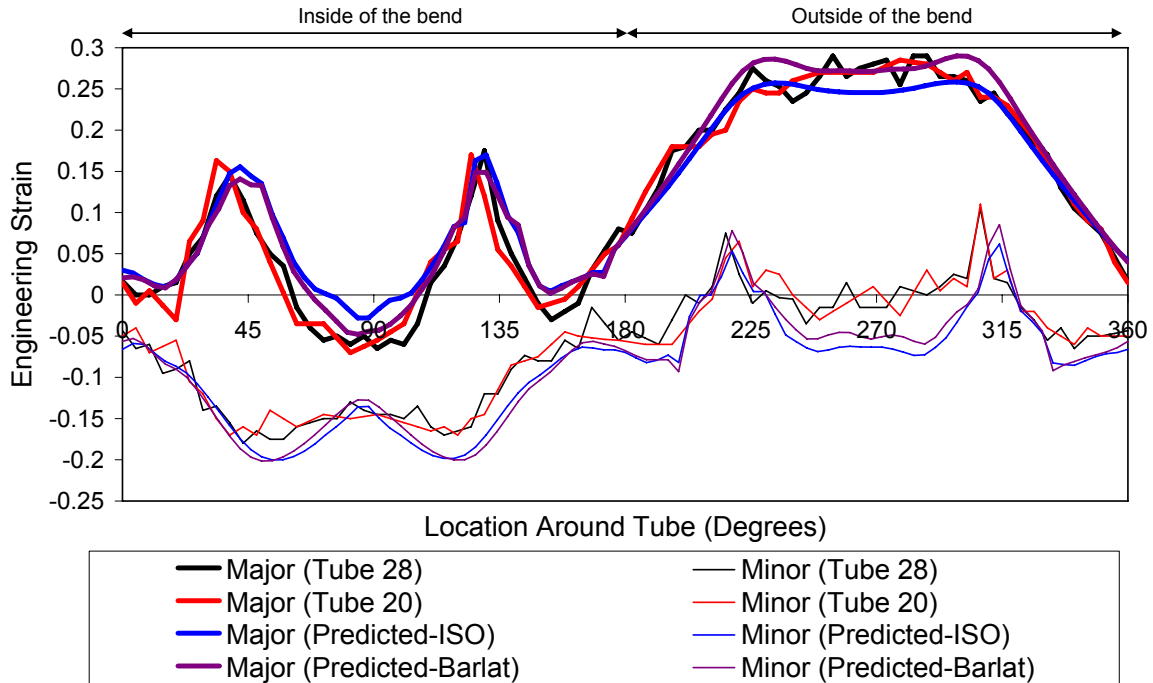


Figure 5.40: Measured major and minor engineering strains and predictions using the isotropic von Mises and anisotropic material models around the circumference of a bend in a hydroformed s-rail bent at $R/D=1.5$.

5.3 Crash Results

5.3.1 Geometry Predictions

The actual and predicted crushed s-rail geometry for a 3 mm AA5754 non-hydroformed s-rail bent at $R/D=2.5$ is shown in Figure 5.41, while the hydroformed s-rail is shown in Figure 5.42 and Figure 5.43. The predicted geometries are in very good agreement with that of the experiment, particularly when capturing details such as the buckling at the base of the s-rail. The contours of effective plastic strain indicate high local strains, up to 40% and 60% for the non-hydroformed and hydroformed s-rails, respectively, in the hinge areas of deformation; however, local strains actually reach 100%, although these are not shown explicitly in Figure 5.41, Figure 5.42 and Figure 5.43. These high strains are developed in a predominantly bending mode of deformation, and based on visual inspection of the deformed s-rails there was no evidence of material failure. The predicted deformation was also in good agreement with the actual crushed geometry for the other bend severities, which are not shown here for brevity.

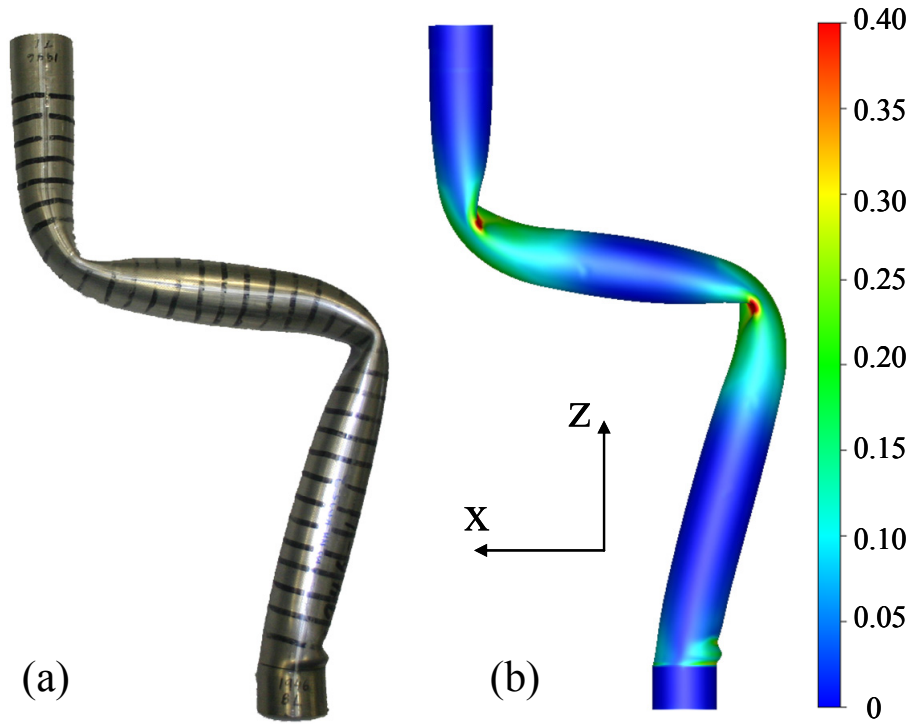


Figure 5.41: (a) Actual and (b) predicted 3 mm AA5754 crushed non-hydroformed s-rail geometry with contours of effective plastic strain. S-rail was bent at $R/D=2.5$.

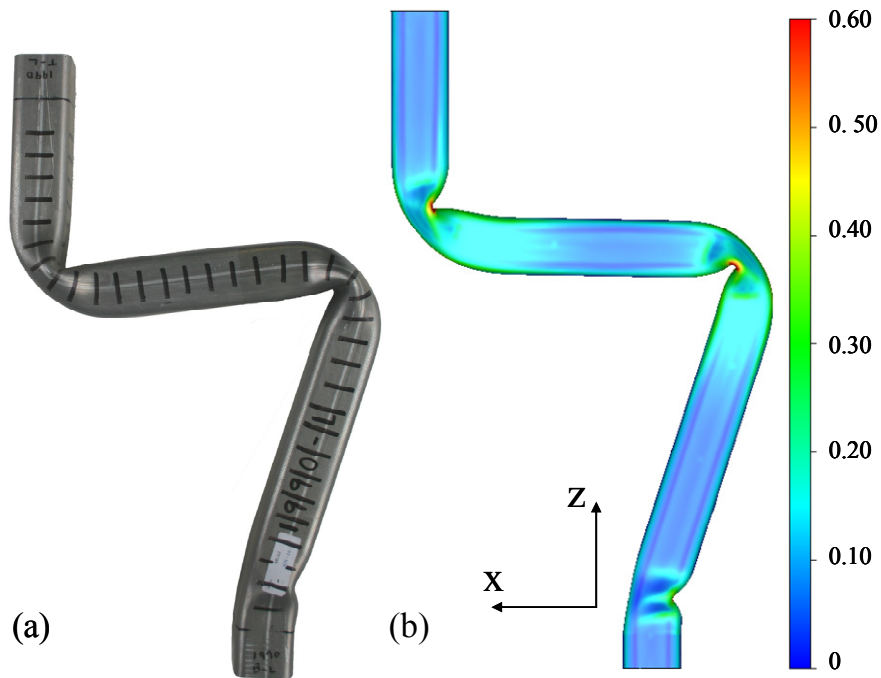


Figure 5.42: Top view of (a) actual and (b) predicted 3 mm AA5754 crushed hydroformed s-rail geometry with contours of effective plastic strain. S-rail was bent at $R/D=2.5$.

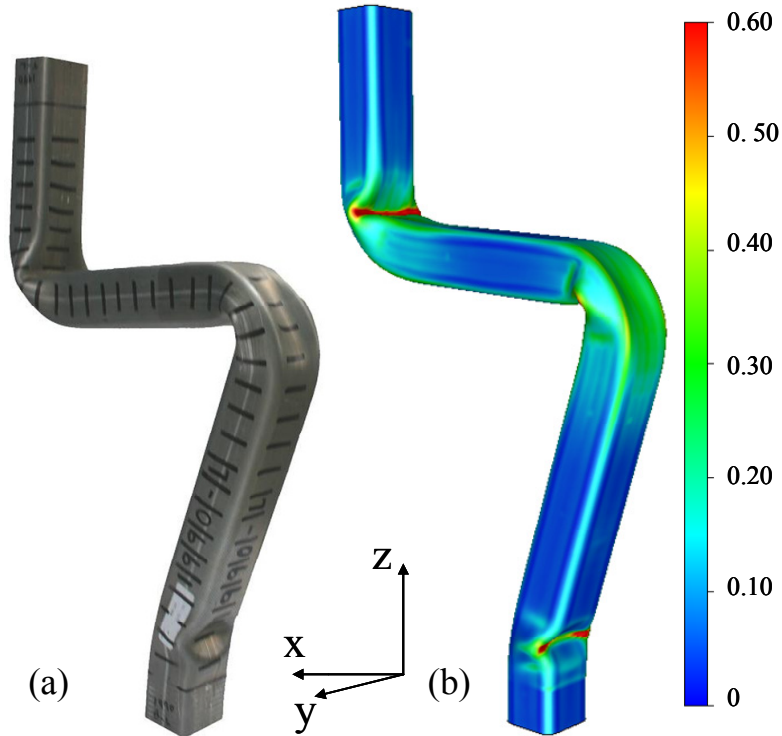


Figure 5.43: Isometric view of (a) actual and (b) predicted 3 mm AA5754 crushed hydroformed s-rail geometry with contours of effective plastic strain. S-rail was bent at $R/D=2.5$.

5.3.1.1 Development of Plastic Hinges during Deformation of the S-Rails

The mode of deformation of the s-rails due to impact is characterized by the formation of three plastic hinges at the center of the two bend regions and at the base of the longer section of the s-rail, as shown earlier in Figure 1.3. The locations of the hinges correspond to the location of largest bending moment, as will be shown in Section 6.1.1. The development of these plastic hinges within the non-hydroformed and hydroformed s-rail are shown in Figure 5.44 and Figure 5.45, respectively.

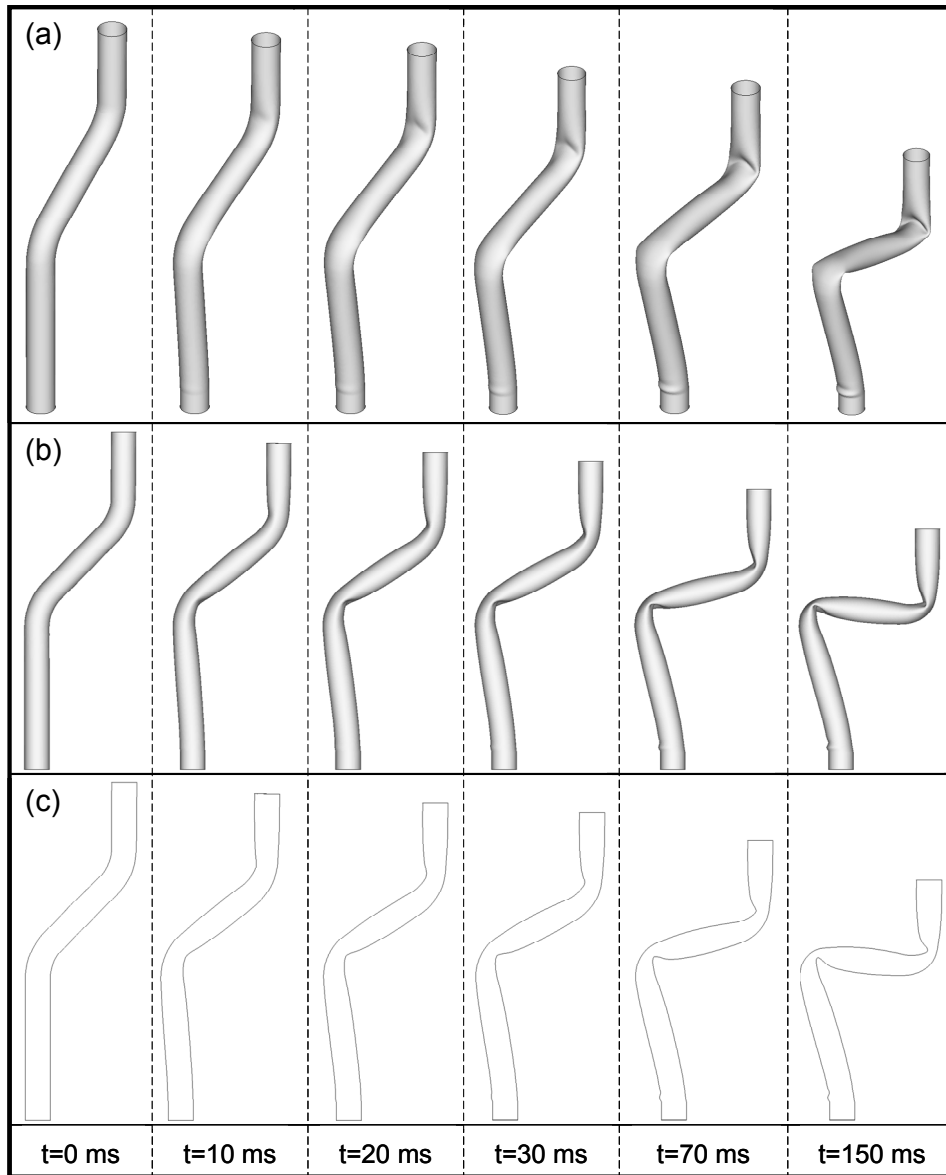


Figure 5.44: (a) Isometric; (b) front; and (c) front sectioned views of deformation in the 3 mm AA5754(bent at $R/D=2.5$) non-hydroformed s-rail at various increments in time.

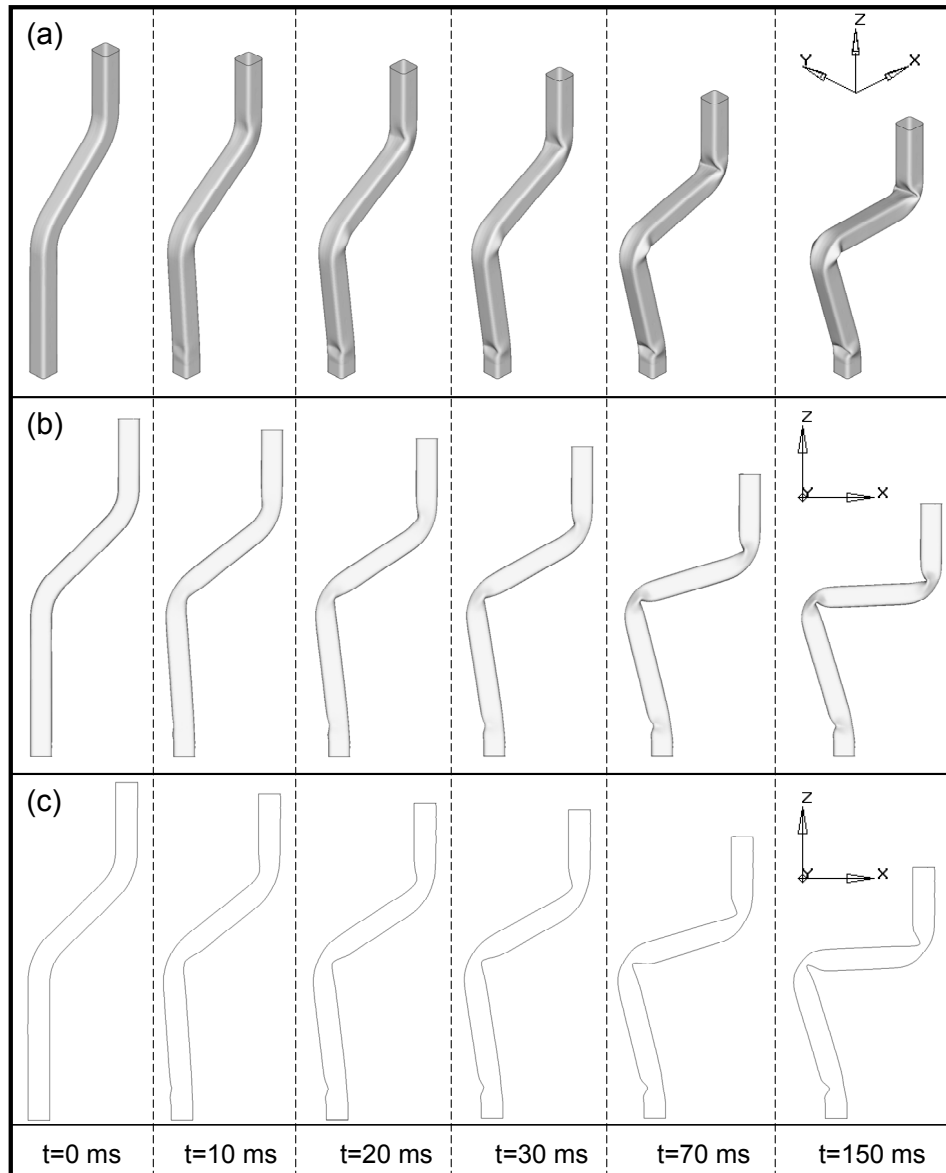


Figure 5.45: (a) Isometric; (b) front; and (c) front sectioned views of deformation in the 3 mm AA5754(bent at $R/D=2.5$) hydroformed s-rail at various increments in time.

The predicted deformation of a cross-section of the hinge that forms in section D (Figure 2.3) for both the non-hydroformed and hydroformed 3 mm AA5754 s-rails bent at $R/D=2.5$ at several instants in time is shown in Figure 5.46. Note that the cross-section examined is located at the center of the bend region within Section D of the s-rail, as shown in Figure 2.10. To better understand the resistance to deformation of the hinges within the non-hydroformed (round cross-section) and hydroformed (square cross-section) s-rails, the second moment of area at several instants in time during collapse is given in Table 5.1 and plotted versus time in Figure 5.47. Note that the second moment of area is an indicator of the

geometric resistance of the section to bending. It can be seen that the cross-section of the non-hydroformed (round cross-section) s-rail initially has a slightly larger second moment of area; however, the round section collapses more quickly and the second moment area of the hinge within the hydroformed s-rail is greater from a time of 20 ms onwards. Therefore, the hinges of the hydroformed (square cross-section) s-rail provide greater overall resistance to deformation throughout the collapse, and consequently, greater energy absorption, as was shown in Chapter 4.

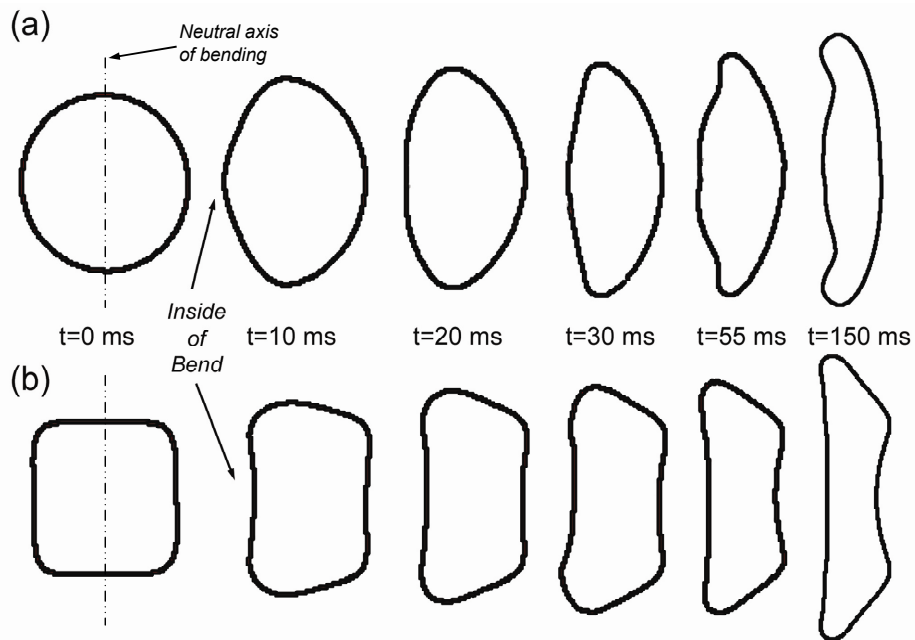


Figure 5.46: Predicted deformation of a cross-section of the hinge in section D of 3 mm AA5754 non-hydroformed and hydroformed s-rails bent at $R/D=2.5$.

Table 5.1: Predicted second moment of area for the round (non-hydroformed) and square (hydroformed) cross-section of the hinge location corresponding to section D of the 3 mm AA5754 s-rails bent at R/D=2.5.

S-Rail Cross-Section	Time (ms)	Second Moment of Area (mm^4)
Round (Non-hydroformed)	0	472×10^3
	10	294×10^3
	20	179×10^3
	30	84×10^3
	55	63×10^3
	150	26×10^3
Square (Hydroformed)	0	440×10^3
	10	278×10^3
	20	192×10^3
	30	155×10^3
	55	83×10^3
	150	51×10^3

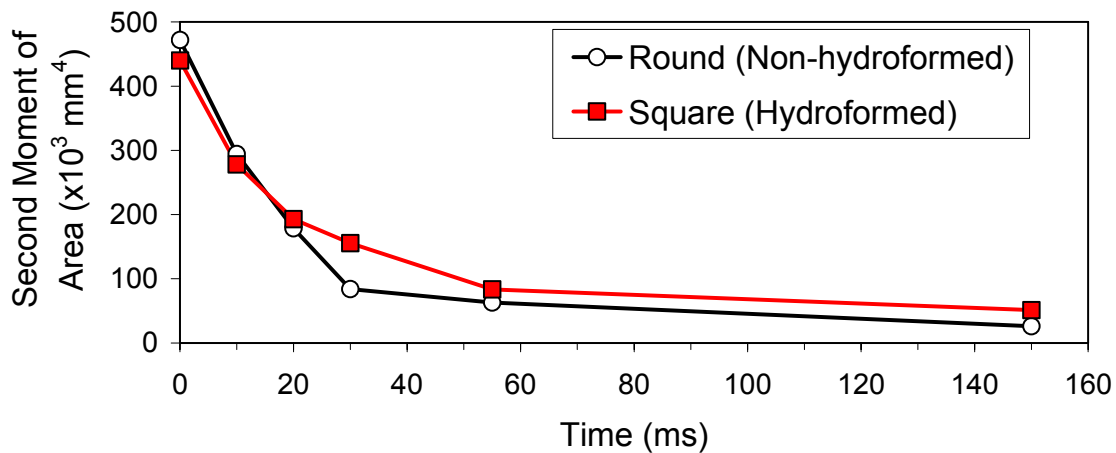


Figure 5.47: Predicted second moment of area for the round (non-hydroformed) and square (hydroformed) cross-section of the hinge location corresponding to section D of the 3 mm AA5754 s-rails bent at R/D=2.5.

5.3.2 Understanding the Force-Time Response in S-Rail Crash

In the s-rail crash experiments, the force response was captured in a filtered form using a low-pass 1 kHz Butterworth filter within the data acquisition system, as described in Section 2.5.1. To allow consistent comparisons between the model predictions and the experimental data, this filter was also applied to the predicted force-time response. In this section, some

insight into the oscillatory nature of the early predicted force-time response and the effect of the 1 kHz Butterworth filter is presented. In addition, the initial period of the force-time response and how it is governed by stress wave propagation is also examined. To better understand the non-filtered force-time response of s-rails in the actual crash experiments, the sensitivity of the model prediction to a damping element, which mimics the rubber pad and plywood on the top cover plate in the crash test set-up (Figure 2.15), and consideration of forming history are examined and shown in Appendix D.

5.3.2.1 Oscillatory Nature of Early Force-Time Response

The predicted filtered and non-filtered force versus time response of a 3 mm AA5754 hydroformed s-rail bent at $R/D=2.0$ using the modeling techniques described in Chapter 3 is shown in Figure 5.48. Also shown in Figure 5.48 is the level of s-rail deformation corresponding to 0, 10, 70 and 150 ms, and the approximate time duration that stress wave propagation significantly influences the force-time response. Within roughly the first 5 ms of impact, large fluctuations in the force-time response are observed, after which the oscillations dampen and decay in a smooth manner. The 1 kHz Butterworth filter employed significantly reduces the amplitude and the number of oscillations in the predicted force-time response. Interestingly, this reduction in the amplitude and number of oscillations in the predicted force-time response that is filtered is consistent with the effect of considering the damping element (rubber pad and plywood in the crash test set-up) in the model's predictions, which is shown in Appendix D for brevity.

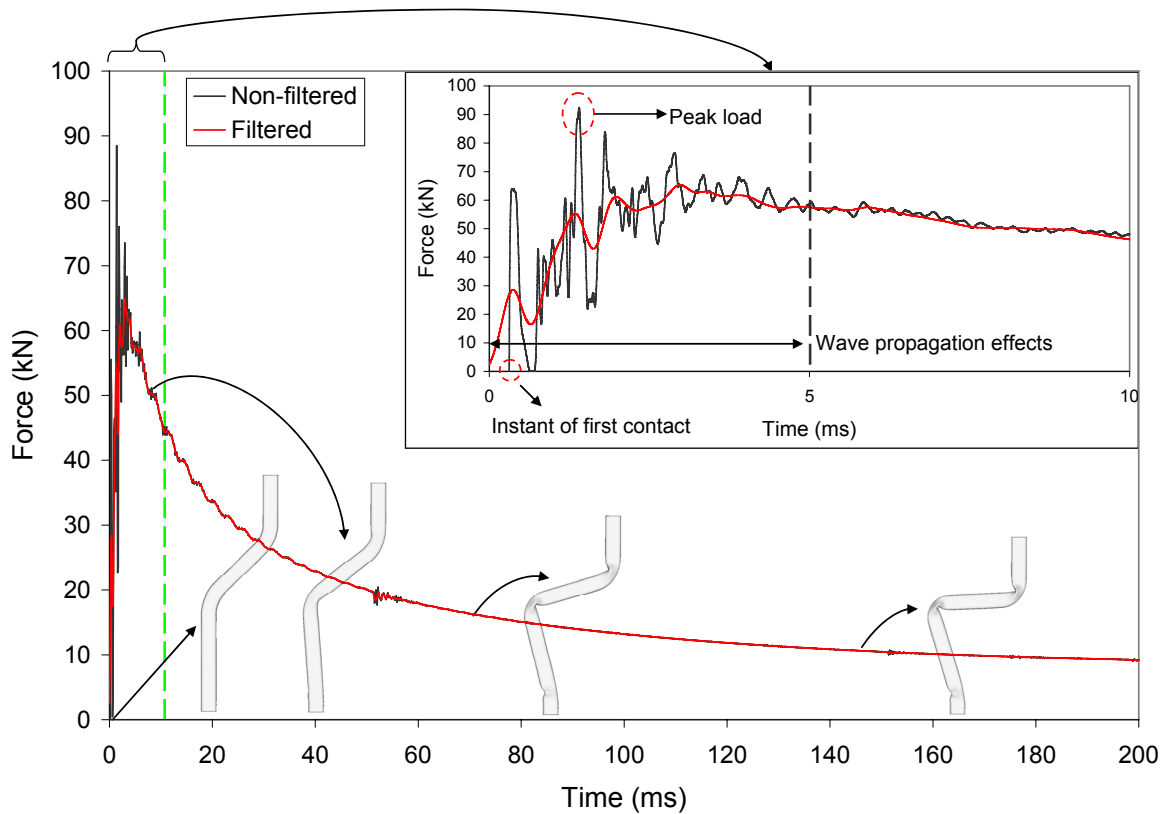


Figure 5.48: Predicted, filtered and non-filtered crush force versus time for a 3 mm AA5754 hydroformed s-rail bent at an $R/D=2.0$. Level of deformation, instant of first contact, peak load and time duration that wave propagation effects are significant are shown.

5.3.2.2 Wave Propagation in S-Rail Crash

The impact of the sled on the s-rail generates a compressive stress wave that propagates from the impact location to the fixed end while experiencing multiple interactions with geometric and rigid boundaries (Figure 5.49), as well as reflected waves (Figure 5.50). The geometric boundaries are located at the bend regions of the s-rail and are due to its' curvature which changes the direction of the local particle velocity, resulting in a complex transmission and reflection of the waves. The travel distance and the time interval for a longitudinal stress wave to traverse the regions between boundaries of the s-rail are shown in Figure 5.49, while Figure 5.50 shows contours of axial or z-stress at various instants in time up to the start of the second peak of force.

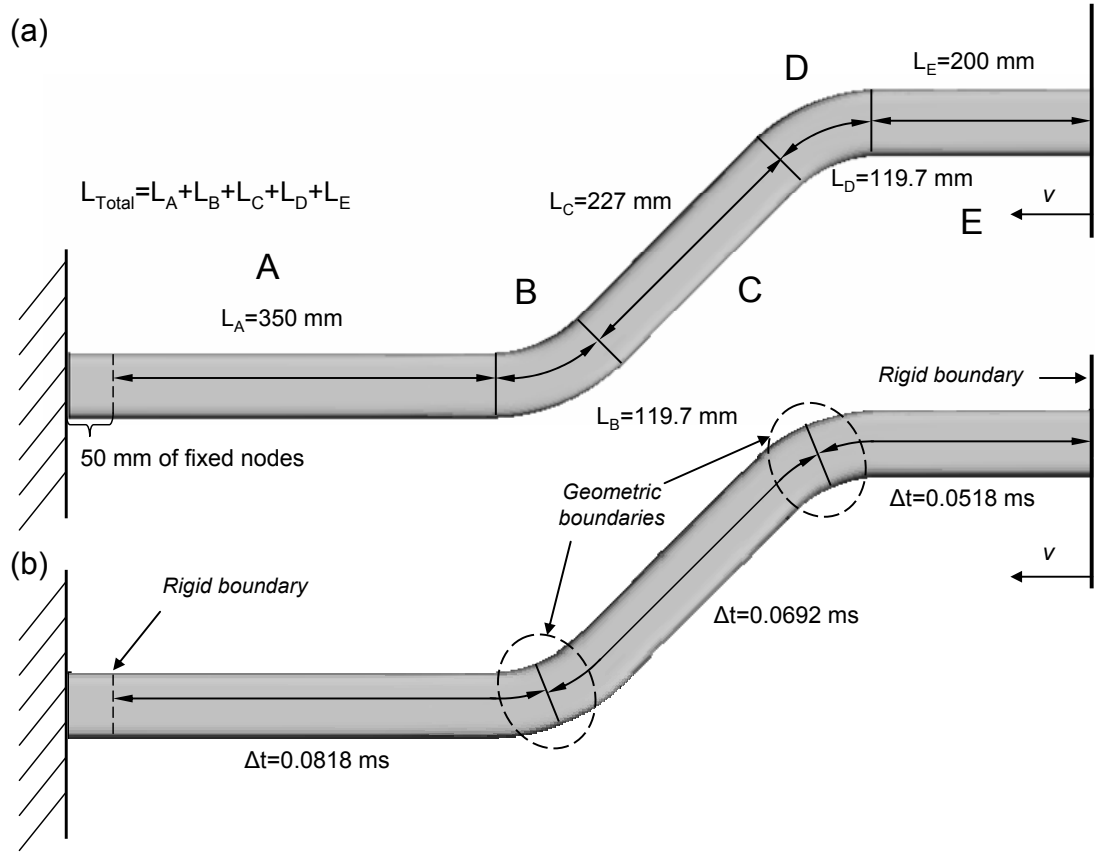


Figure 5.49: (a) Traverse distances; and (b) time intervals for a stress wave to propagate between the geometric and rigid boundaries of the s-rail.

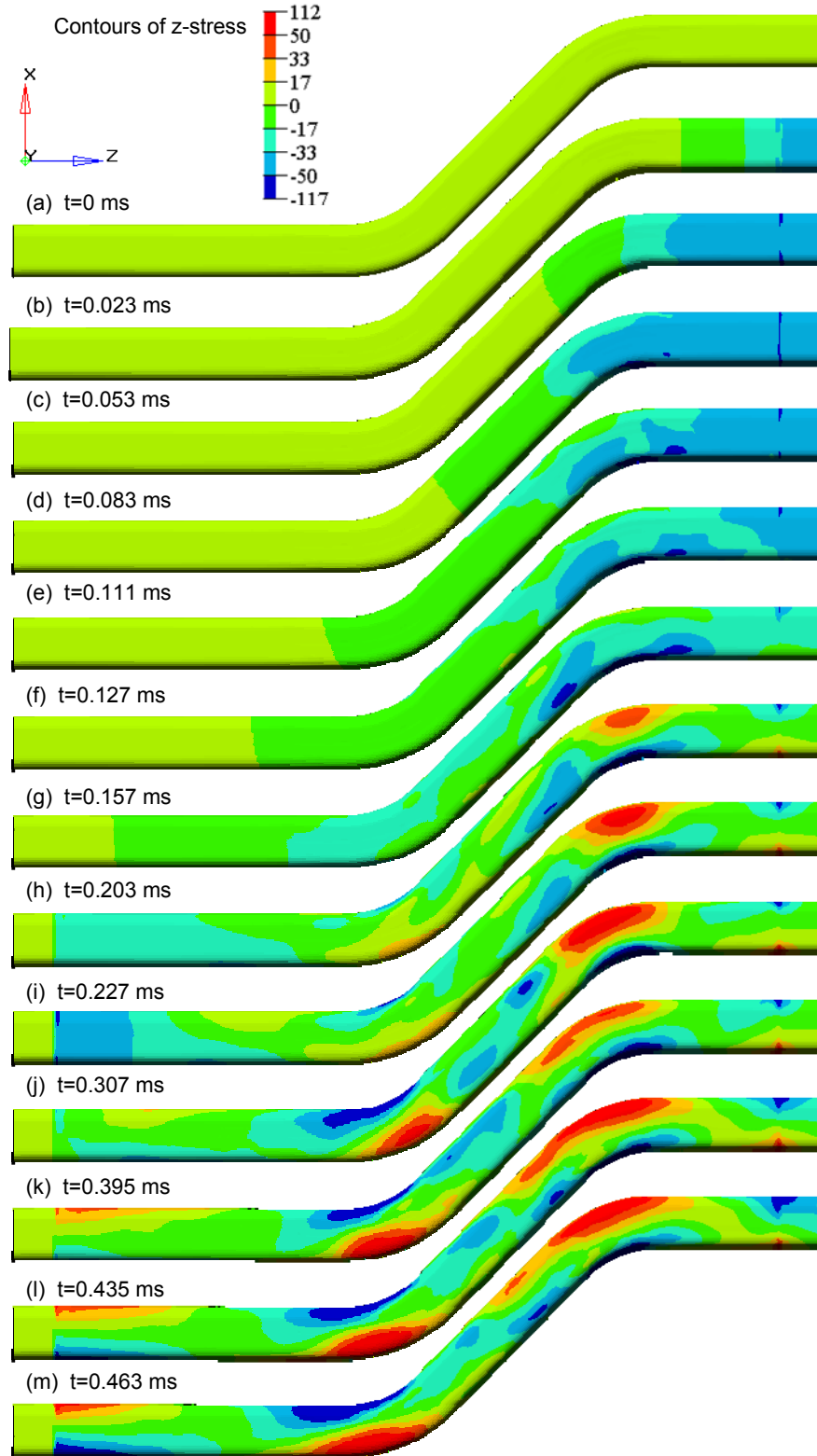


Figure 5.50: Contours of stress in the z-direction at various instants in time due to impact showing the progression of first loading wave. The units of stress are MPa.

The predicted force versus time signature for an s-rail impact event up to the second peak of force is shown in Figure 5.51. To better understand the influence of the wave interactions on the predicted force acting on the impact plate, the points in time that the reflected stress waves from the first and second bends, and fixed end of the s-rail reach the impact plate were calculated based on the longitudinal wave speed ($C = \sqrt{E/\rho}$; E =modulus of elasticity and ρ =density) and are also shown in Figure 5.51. Note that for simplicity, additional wave reflections due to waves interacting with one another are not considered. After impact ($t=0$ ms), a compressive stress pulse is generated and travels along the s-rail at the speed of sound in the material, which is 5,015 m/s. After reaching the first bend region (Section D), the wave encounters a geometric boundary (first bend) and therefore part of the wave is transmitted and part reflected. The reflected wave from the first bend is tensile and propagates towards the impact plate, while the transmitted wave remains compressive. There will also be a large bending wave initiated at this geometric discontinuity. The bending wave speed generated under such an impact scenario is much lower than the longitudinal component, and for this reason, this discussion is centered on the longitudinal waves. Arrival of the reflected tensile wave from the first bend at the impact plate occurs at 0.104 ms and causes the stress/force at the boundary to begin to decrease as can be seen in Figure 5.51. The force on the impact plate continues to decrease rather abruptly until the second reflection of stress from the first bend arrives back at the impact plate, which causes a change in the rate of its' deceleration. Shortly thereafter, tensile stress waves from the first reflection at the second bend and the third reflection at the first bend arrive at the impact plate causing the net force to become zero due to the superposition of stresses that occur in that local region. The net force on the impact plate remains zero until the first reflected compressive stress waves from the fixed end of the s-rail (arrive at 0.406 ms) and the fourth reflection from the first bend (at 0.414 ms) arrive back at the impact plate. Beyond this point in time, the level of complexity of the stress wave interactions increases significantly (Figure 5.50) such that they cannot be tracked using simple wave velocity calculations.

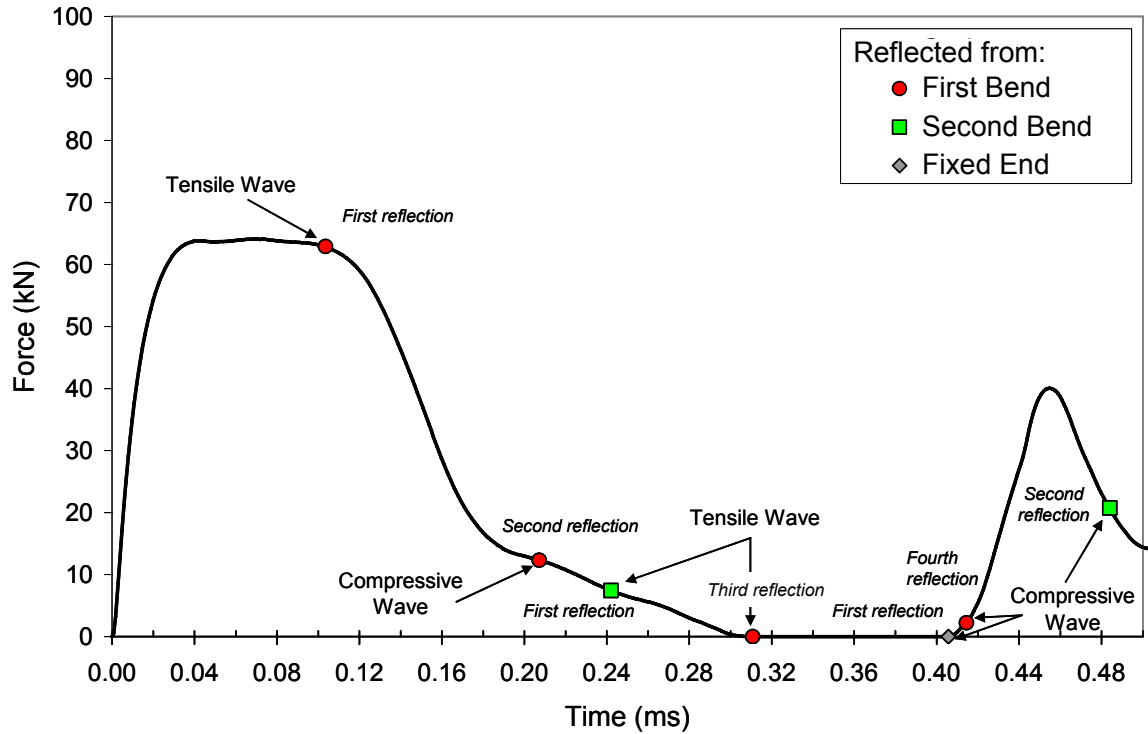


Figure 5.51: Predicted force versus time signature of s-rail. Points in time that the stress waves reflected from the first and second bends, and the fixed end of the s-rail reach the impact plate.

5.3.3 Predicted Force and Energy Response

5.3.3.1 Non-Hydroformed S-Rails

The measured force and energy versus crush displacement for a 3 mm AA5754 non-hydroformed s-rail bent at $R/D=2.0$ and predictions using the isotropic von Mises and anisotropic Barlat (1989) material models are shown in Figure 5.52. The force and energy response of the 3 mm non-hydroformed s-rails bent at R/D ratios of 2.5 and 1.5 are shown in Appendix C. Both predictions utilizing the two material models were in good agreement with the experiment. For the three bend severities examined, the predictions using the isotropic von Mises material model better captures the peak load and energy response, while the anisotropic Barlat (1989) model predicts lower peak load and total energy.

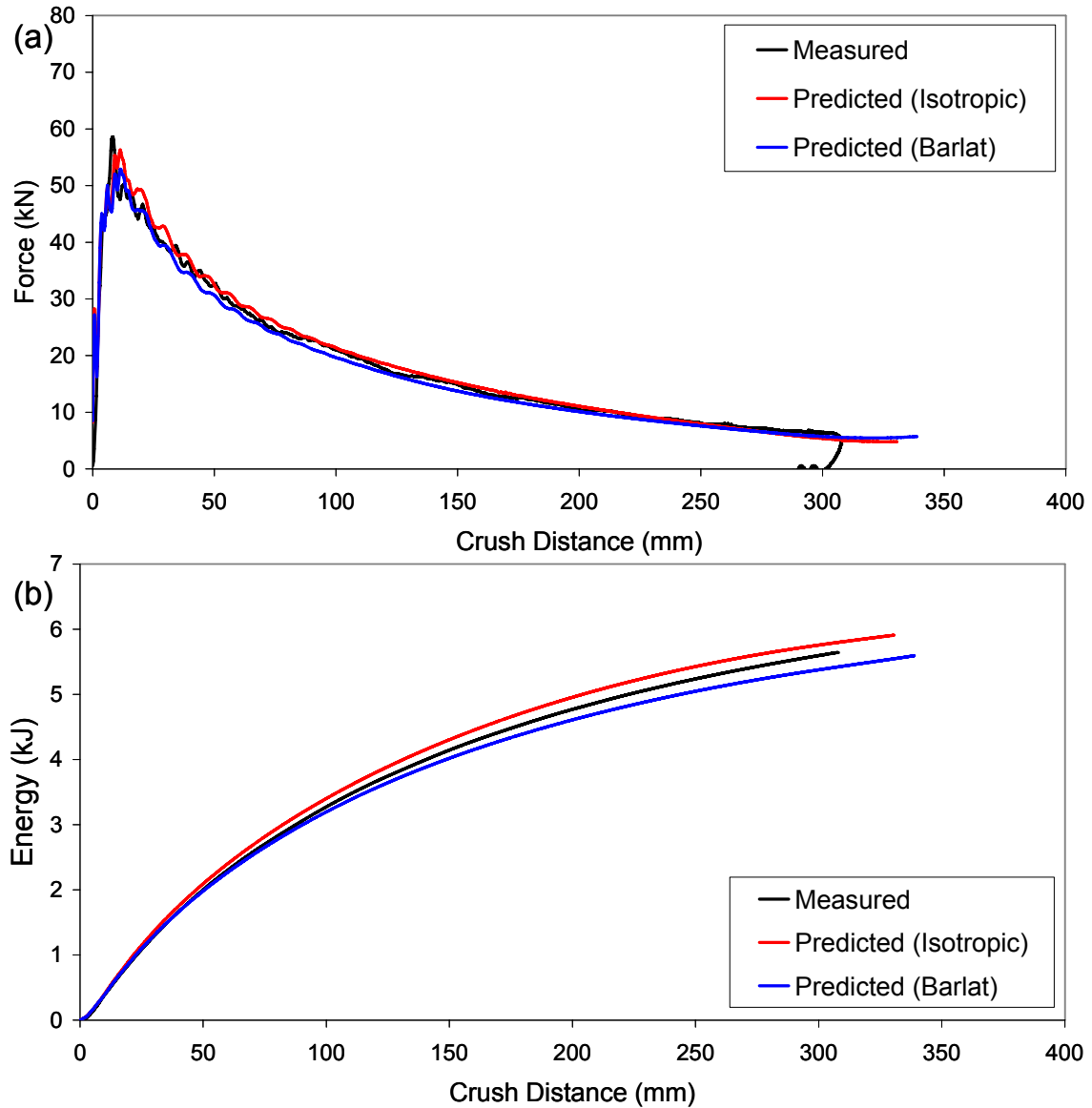


Figure 5.52: Measured and predicted (a) force; and (b) energy versus crush distance for a 3 mm AA5754 non-hydroformed s-rail bent at $R/D=2.0$ using the isotropic von Mises and anisotropic Barlat (1989) material models.

5.3.3.2 Hydroformed S-Rails

The measured force and energy versus crush distance and predictions using the isotropic von Mises and anisotropic Barlat (1989) material models for a hydroformed 3 mm AA5754 s-rail bent at $R/D=2.0$ are shown in Figure 5.53. Consistent with the predictions of crash response for the non-hydroformed s-rails, the predictions of crash response for the hydroformed s-rail utilizing the isotropic von Mises material model are in excellent agreement with the

measured response. Note that the simulation utilizing the anisotropic Barlat (1989) material model under-predicts both the force and energy; in fact, the under-prediction is greater than in the case for the non-hydroformed s-rails. Similar agreement between the measured and predicted force and energy response was observed for s-rails bent at the R/D ratios of 2.5 and 1.5, as shown in Appendix C.

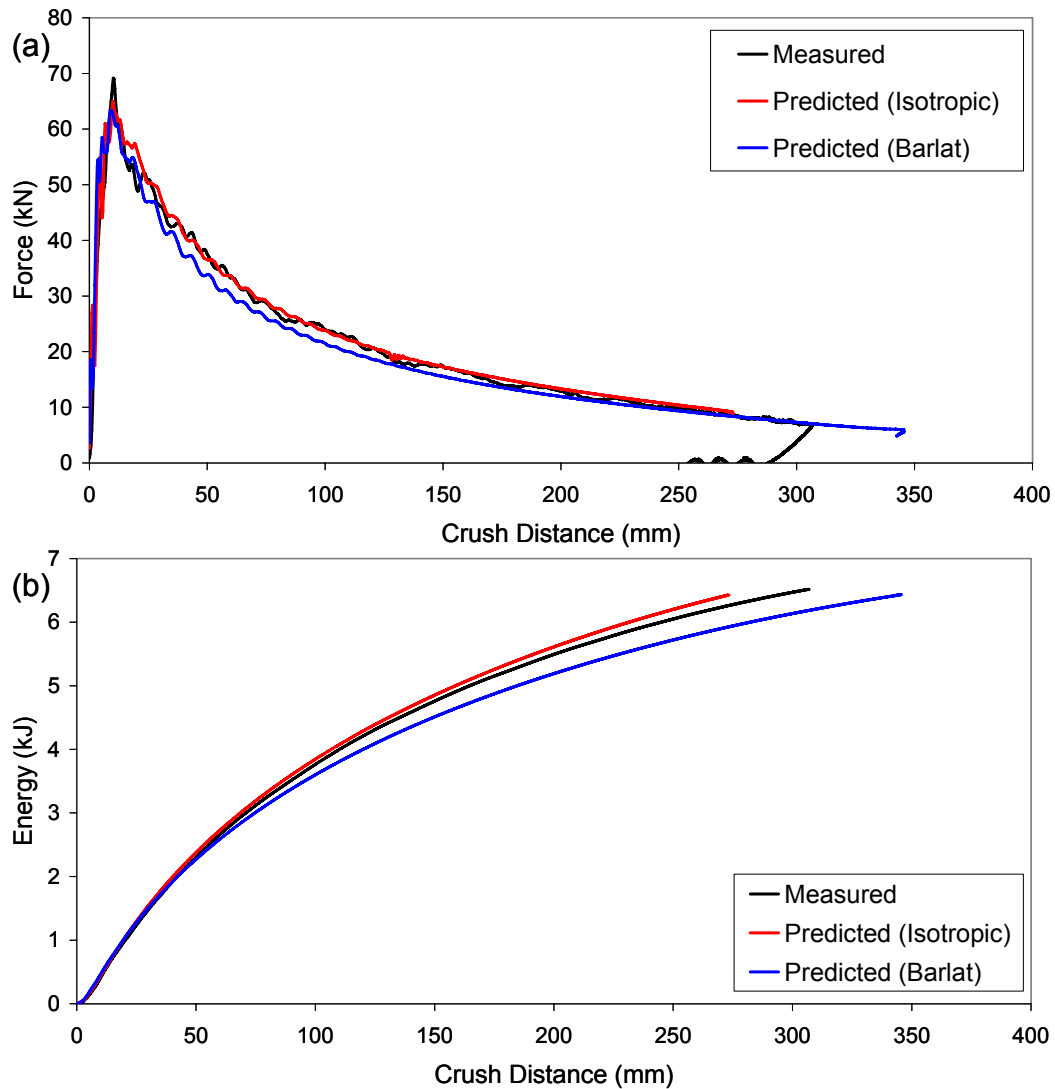


Figure 5.53: Measured and predicted (a) force; and (b) energy versus crush distance for a 3 mm AA5754 hydroformed s-rail bent at R/D=2.0 using the isotropic von Mises and anisotropic Barlat (1989) models.

5.3.4 Predicted Force and Energy Response of Annealed S-Rails

The effects of an intermediate anneal between the forming operations and the crash test was examined experimentally, as presented in Section 4.4.5. Here, the ability of the models to

capture the effect of this annealing stage is examined. The measured force and energy response of 3 mm AA5754 annealed non-hydroformed s-rails bent at $R/D=2.0$ and predictions using the isotropic von Mises material model are shown in Figure 5.54, while the corresponding hydroformed s-rail results are shown in Figure 5.55. The model slightly over-predicts the force and energy response of the annealed s-rails. Similar agreement was observed for the R/D ratios of 2.5 and 1.5 (not shown for brevity).

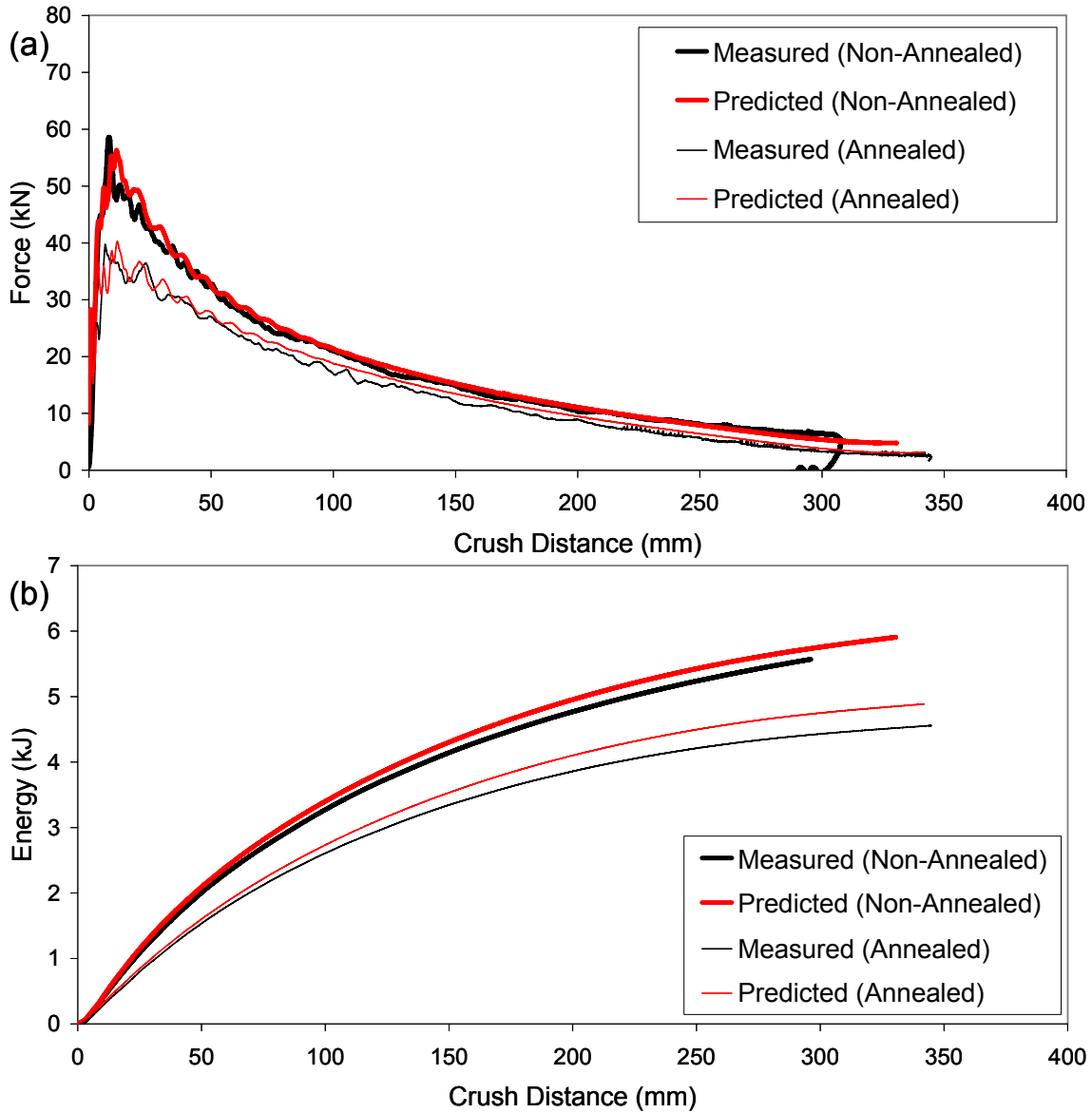


Figure 5.54: Measured and predicted (a) force; and (b) energy versus crush distance for 3 mm AA5754 annealed and non-annealed non-hydroformed s-rails bent at an R/D ratio of 2.0 using the isotropic von Mises material model.

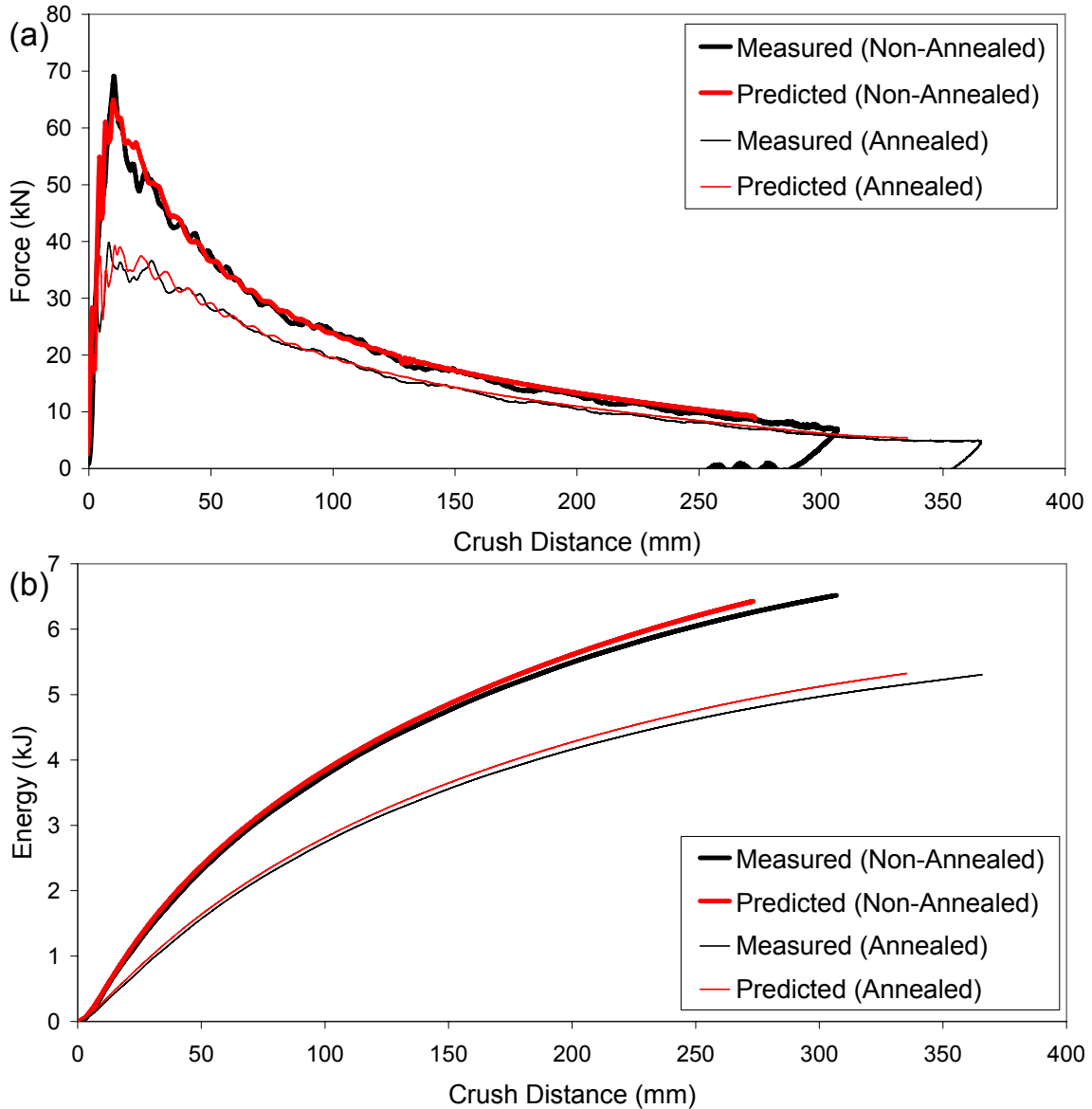


Figure 5.55: Measured and predicted (a) force; and (b) energy versus crush distance for 3 mm AA5754 annealed and non-annealed hydroformed s-rails bent at an R/D ratio of 2.0 using the isotropic von Mises material model.

5.3.5 Effect of Strain Rate Sensitivity and Thermal Softening on Crash Response

The predicted crash response of hydroformed s-rails considering strain rate effects and thermal softening due to the adiabatic temperature rise during deformation was assessed using the Johnson-Cook and Zerilli-Armstrong constitutive models. In particular 3 mm, AA5754 hydroformed s-rails bent at R/D=2.0 were modeled using the material parameters presented in Sections 3.5.1 and 3.5.2.

To understand the strain rate regime within which the s-rails deform, the strain rate was calculated in elements throughout the s-rail by numerically differentiating the effective plastic strain with respect to time. The maximum strain rate and temperature increase are predicted to occur in section B of the s-rail (Figure 2.3), in an element at the corner of the inside of the bend corresponding to the location of the plastic hinge, as shown in Figure 5.56. The effective plastic strain rate versus time in this element is shown in Figure 5.57a. The predicted maximum strain rate in the hinge region of deformation is approximately 150 s^{-1} , which occurs over a 1.5 ms period. The average strain rate over the period of active plastic deformation, which is roughly 55 ms, is 27 s^{-1} , as indicated in Figure 5.57a, which is relatively low. The majority of the plastic strain occurs in the first 55 ms of deformation, as shown in Figure 5.57c.

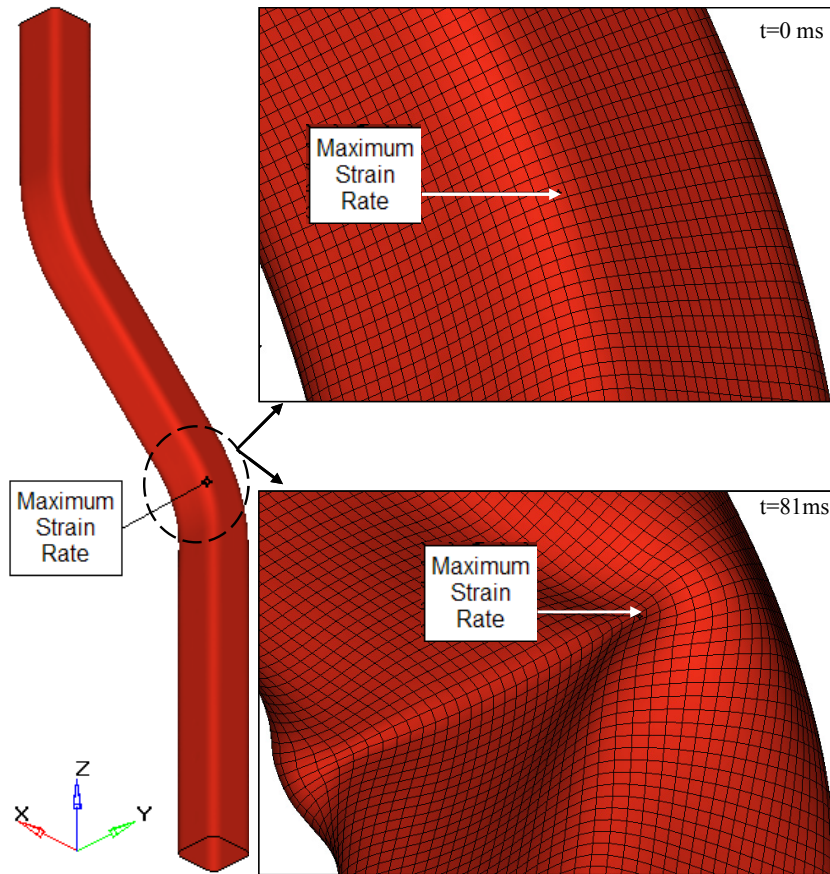


Figure 5.56: Location of maximum strain rate.

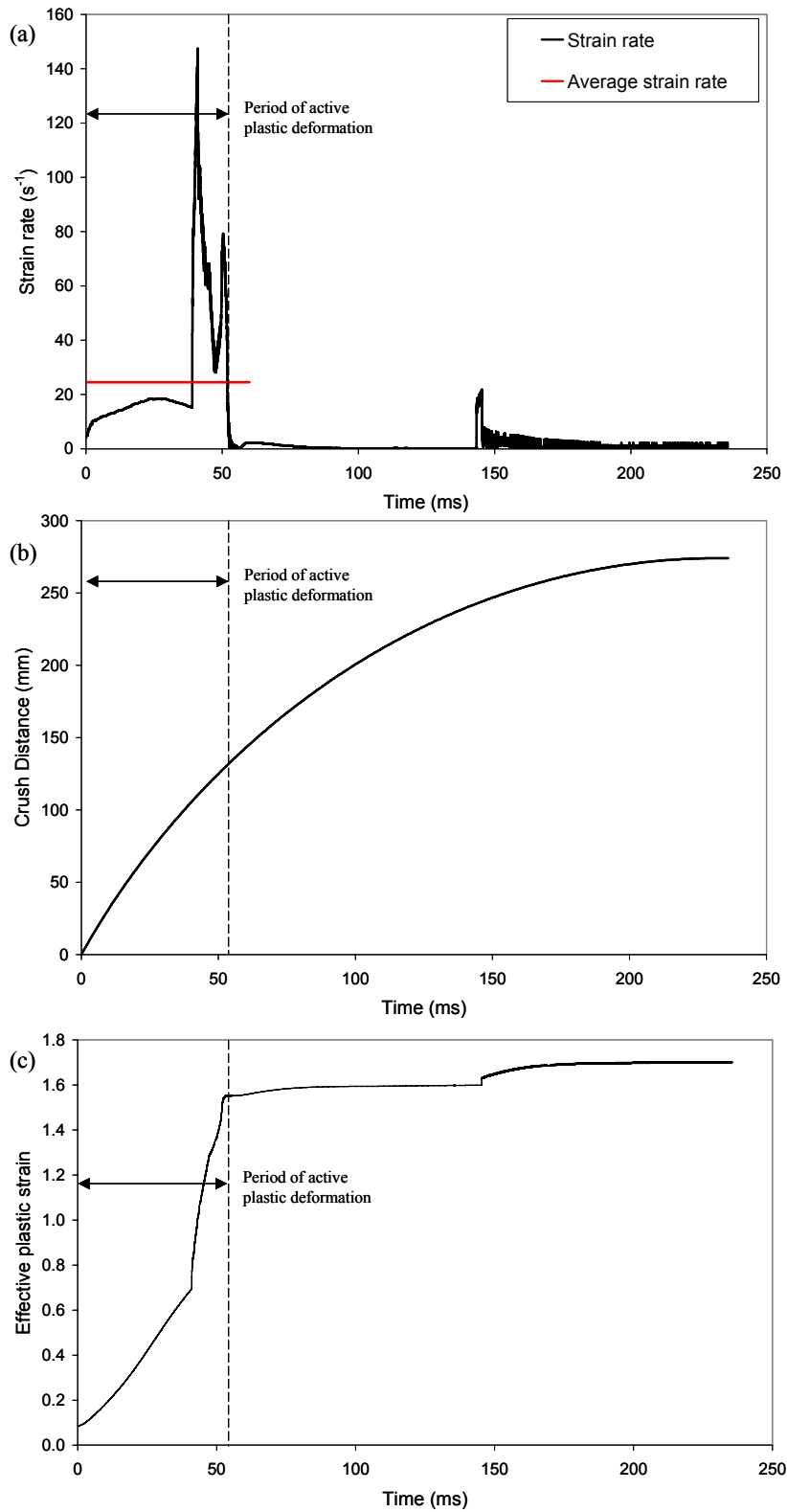


Figure 5.57: Predicted (a) maximum strain rate; (b) crush distance; and, (c) effective plastic strain versus time experienced in an element at the hinge location of the s-rail.

The maximum adiabatic temperature rise is also predicted to occur locally in the hinge region of deformation, as shown in Figure 5.58. The adiabatic temperature increase versus crush distance and time for the element that experiences the largest increase in temperature is shown in Figure 5.59. The maximum predicted temperature experienced by the material is 376 degrees Celsius; however, this temperature increase is very localized, as can be seen from Figure 5.58.

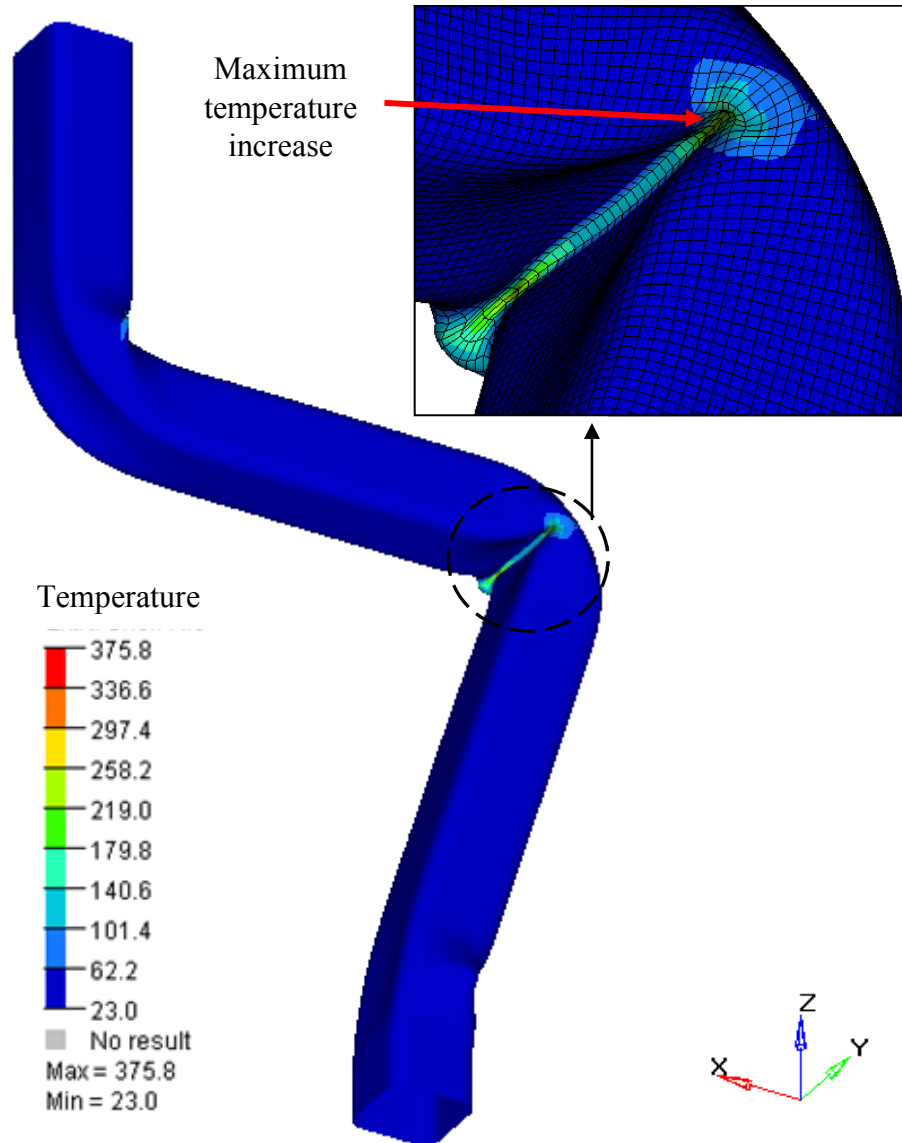


Figure 5.58: Contour plot of temperature in the s-rail. Units are in degrees Celsius.

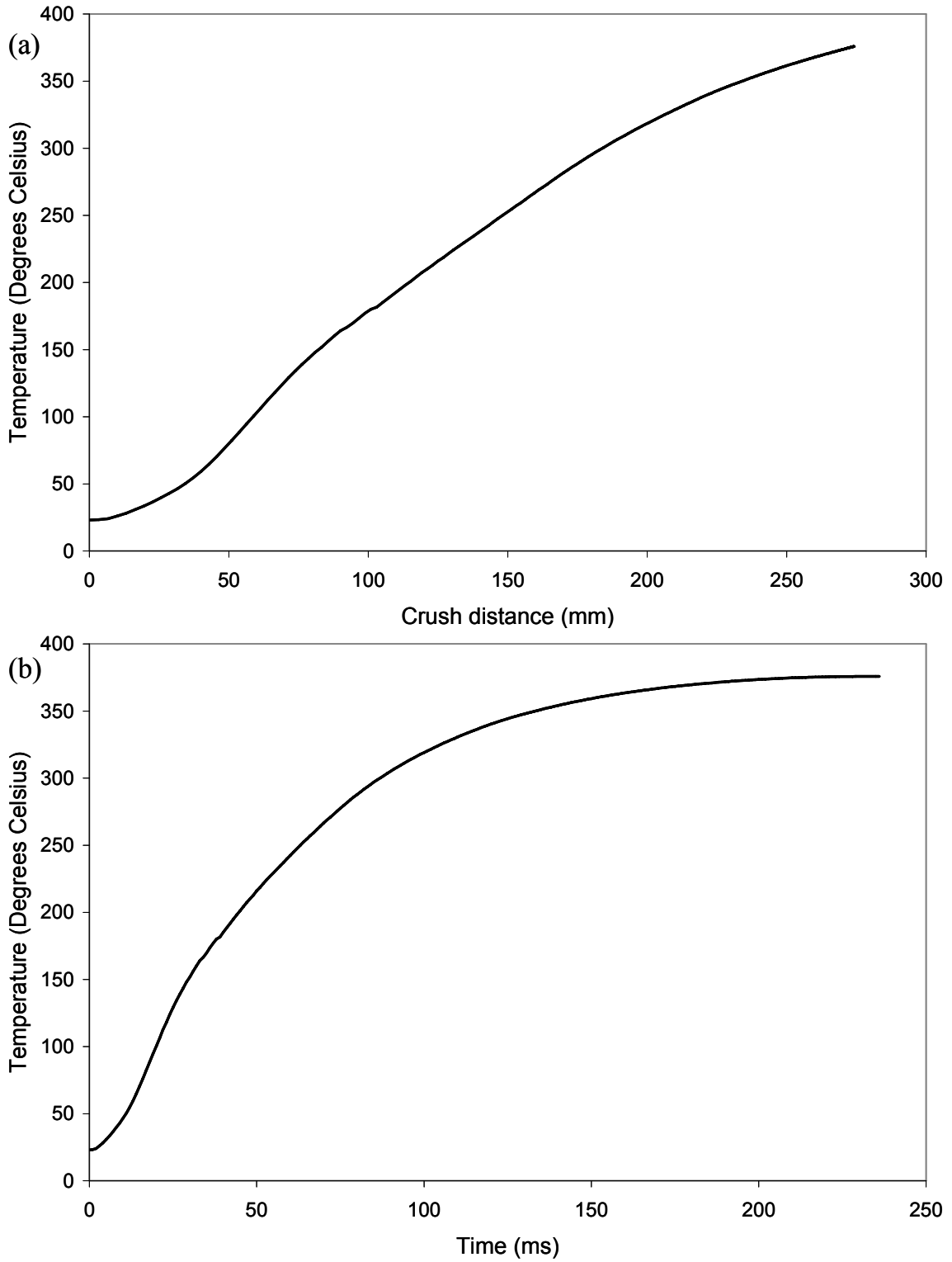


Figure 5.59: Predicted temperature versus (a) crush distance, and (b) time in the element experiencing the largest adiabatic temperature rise and strain rate.

To assess and quantify the effects of strain rate and thermal softening on the s-rail crash response, two rate-sensitive material models were employed: (i) Johnson-Cook [125,126] and (ii) Zerilli-Armstrong [128,129,130,131]. Employing the Johnson-Cook material model within the crash simulations allows the effects of strain rate and thermal softening to be decoupled with the aim of understanding their relative contributions to the overall s-rail crash response.

5.3.5.1 Johnson-Cook Predictions

The measured force and energy versus crush displacement for a 3 mm AA5754 hydroformed s-rail bent at R/D=2.0 and the predictions using the Johnson-Cook material model with a Voce hardening law (Equation 3.4), are shown in Figure 5.60. The predicted crash response of the model utilizing the Johnson-Cook UMAT (JC-Voce) is in excellent agreement with the experimental result. Interestingly, these predictions, which consider material rate-sensitivity and thermal softening, lie within 1% of predictions using a standard rate-insensitive von Mises formulation (presented earlier). This comparison suggests that the rate sensitivity of these alloys is not very strong. To further examine the importance of material rate-sensitivity, strain rate effects were artificially removed from the Johnson-Cook UMAT by setting the parameter $C=0$ (JC-Voce ($C=0, m=1$)), which resulted in less than a 0.5% reduction in the predicted energy absorption. This small effect of strain rate hardening of the aluminium alloy on the crash response of the s-rail is consistent with the findings of Salisbury *et al.* [106,107] that this aluminium alloy is relatively rate-insensitive. The effect on crash response of thermal softening due to the adiabatic temperature rise within the material was isolated by artificially suppressing the thermal softening parameter in the Johnson-Cook material model. This was done by setting the thermal softening exponent m in Equation 3.4 to a very large value (10^{+20}). Using $m=10^{+20}$ in this manner to suppress thermal softening results in a 2.5% increase in predicted softening as can be seen in Figure 5.60.

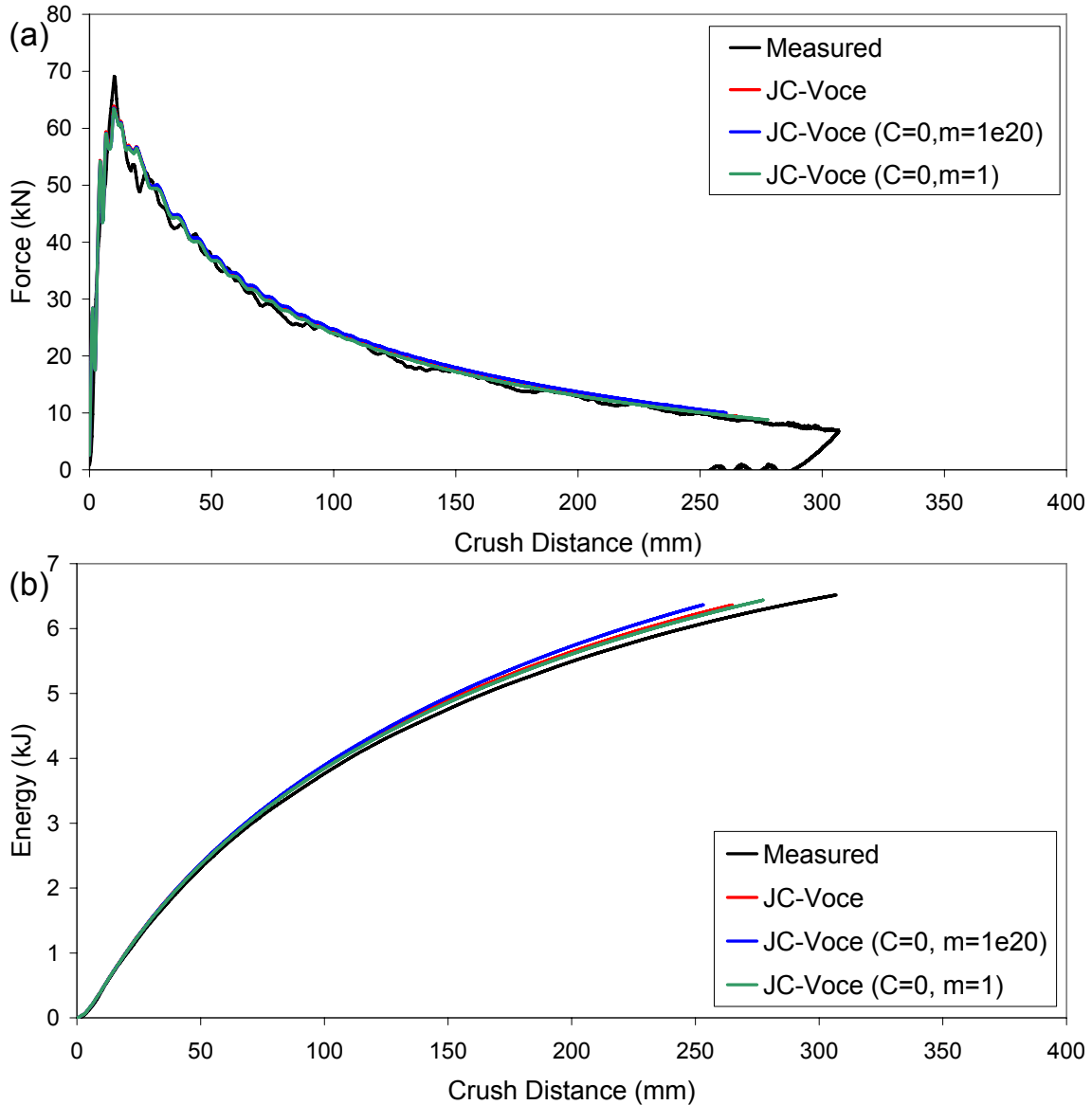


Figure 5.60: Predictions of (a) force; and (b) energy versus crush distance using the Johnson-Cook UMAT with a Voce hardening law for 3 mm AA5754 hydroformed s-rails bent at $R/D=2.0$.

5.3.5.2 Zerilli-Armstrong Predictions

Simulations were performed to assess the accuracy of predictions utilizing the Zerilli-Armstrong constitutive model to account for material rate-sensitivity. Two scenarios were modelled; in the first, the Zerilli-Armstrong model was used to simulate both the forming and crash events. The second scenario utilized the Zerilli-Armstrong model to simulate the crash event, but adopted a rate-insensitive formulation for the forming operations. Note that the

forming predictions utilizing the rate-insensitive and rate-sensitive material models were in reasonably good agreement, as shown in Appendix C.

First of all, it was found that the two scenarios resulted in energy absorption predictions that differed by only 0.5%. This result is beneficial since it demonstrates that a less-expensive rate-insensitive model can be used for the forming models.

The accuracy of the crash predictions using the Zerilli-Armstrong model are shown in Figure 5.61, which shows the measured and predicted force and energy response for 3 mm AA5754 s-rails bent at $R/D=2.0$. The peak load using the Zerilli-Armstrong material model lies consistently above the measured data, and the energy absorption is over-predicted by 9.4%. Due to the coupled nature of the strain rate and temperature contributions to the flow stress in the Zerilli-Armstrong model, isolation of strain rate and thermal softening effects is challenging. However, it is thought that the over-prediction of absorbed energy is due more to the extrapolation of the Zerilli-Armstrong constitutive model beyond the 0.15 failure strain upon which the parameters were determined. This extrapolation results in over-predictions of flow stress, as shown previously in Figure 3.16.

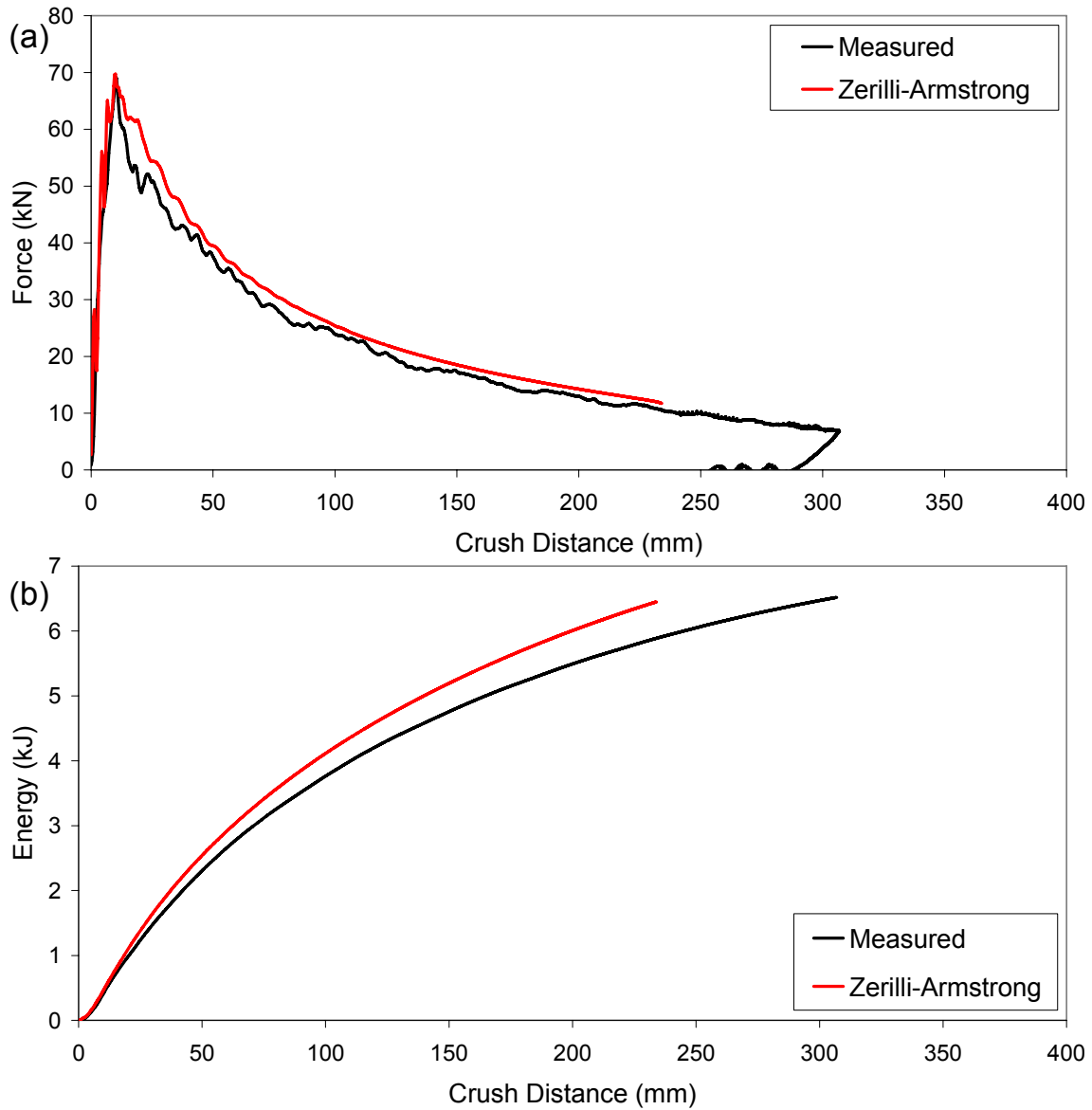


Figure 5.61: Measured (a) force; and (b) energy response and predictions using the Zerilli-Armstrong material model for 3 mm AA5754 hydroformed s-rails bent at R/D=2.0.

5.4 Sensitivity of Models to Element Formulation and Size

To assess the dependency of the predictions on the element formulation and size, simulations were performed using two element types and three levels of mesh refinement. Both the fully-integrated [30,31] (type 16 in LS-DYNA) and reduced-integration Belytschko-Lin-Tsay [121] (type 2 in LS-DYNA) formulations were considered and elements of sizes of 2.5, 5 and 7.5 mm.

The results of the element type and mesh size sensitivity study are given in Appendix C. In general, it was found that the forming models predictions were quite insensitive to the selection of fully versus reduced integration element type. It was also found that the predictions of process variables (forming loads) were only mildly sensitive to element size. The use of the finest mesh resulted in a slightly more accurate prediction of strain, but at a much greater computational cost (Section 5.4.1).

In order to examine the sensitivity of the crash response, predictions of force and energy response using the isotropic von Mises material model for the 3.5 mm EN-AW5018 non-hydroformed s-rail bent at $R/D=2.0$ are shown in Figure 5.62. The peak load is significantly under-predicted using the fully integrated element formulation, whereas predictions utilizing the Belytschko-Lin-Tsay element are in much better agreement with the measured result. The predictions of energy absorption using both element types are similar when utilizing 5 and 7.5 mm element size discretizations. Both element types exhibit mesh sensitivity, but this was most pronounced for the fully integrated element that significantly under-predicts the impact response with a finer mesh size and does not exhibit mesh convergence. The lack of mesh convergence utilizing the fully-integrated element formulation is due to unaccounted internal energy losses, which results in failure to conserve total energy. This behaviour was particularly true for finer mesh sizes, which may explain the strong mesh sensitivity of the model using the fully-integrated element type. In general, the predictions utilizing the reduced integration Belytschko-Lin-Tsay elements were in good agreement with the experiment.

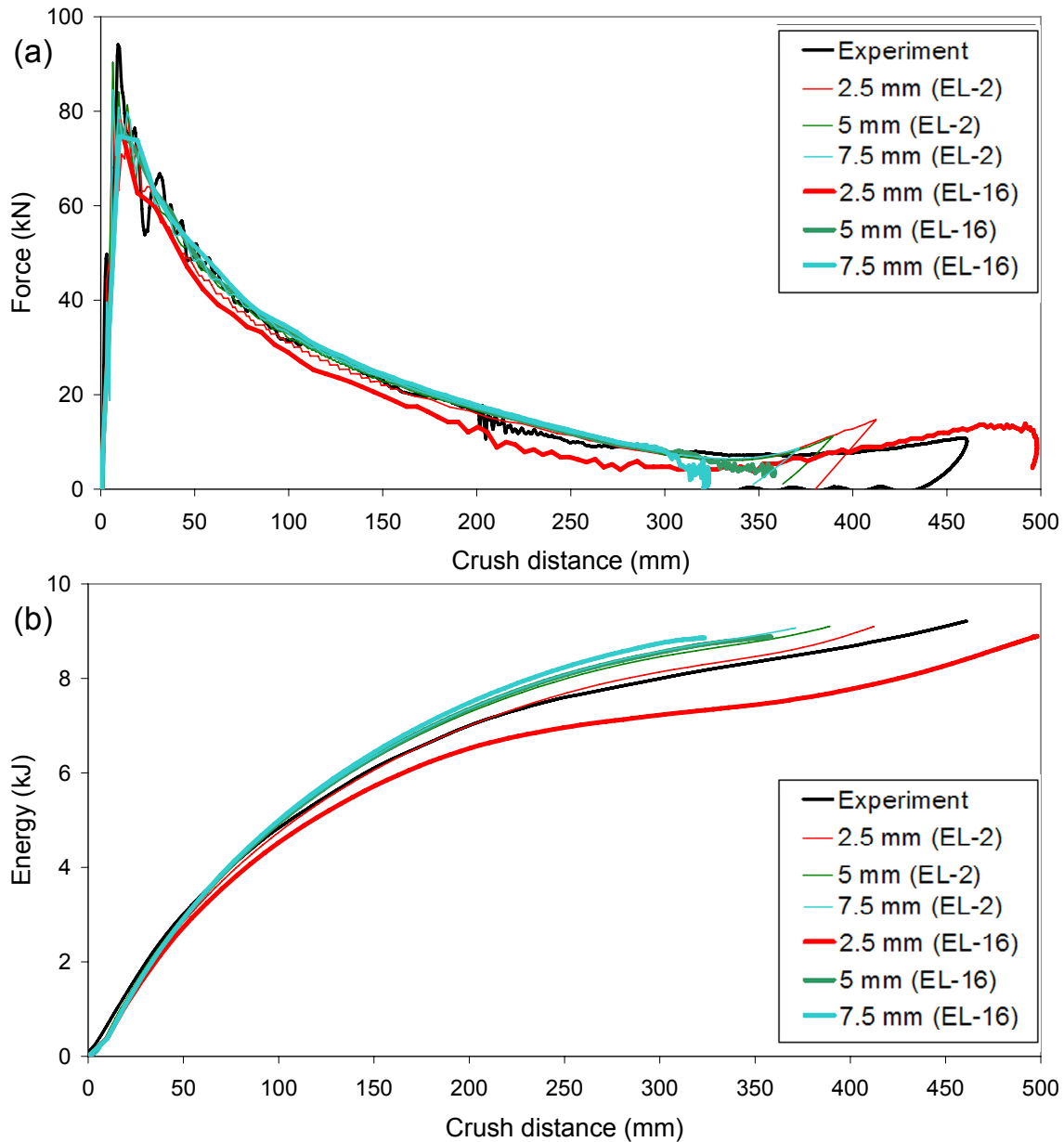


Figure 5.62: Predicted: (a) force; and, (b) energy response of 3.5 mm EN-AW5018 s-rails bent at an $R/D=2.0$, simulated using fully-integrated (FI) and Belytschko-Lin-Tsay (BT) elements and 2.5, 5 and 7.5 mm element sizes.

In view of the strong mesh sensitivity and energy loss using the fully integrated elements, the predicted force and energy response presented for the balance of this thesis are from simulations utilizing the Belytschko-Lin-Tsay element formulation. Stronger mesh sensitivity also occurred in the thinner 2 mm versus the 3.5 mm EN-AW5018 s-rails using the fully-integrated element, which is not shown for brevity. It is speculated here that the stronger mesh sensitivity of the fully integrated elements is a consequence of shear-locking

phenomena associated with continuum-based shell elements under buckling and pinching, as described by Hughes and Hinton [122], and Belytschko *et al.* [112].

The mesh sensitivity of the predicted crash response using the isotropic von Mises material model for the 3 mm AA5754 hydroformed s-rails was also investigated using the Belytschko-Lin-Tsay (type 2) element formulation. Note that the forming models retained the fully-integrated (type 16) element formulation mainly for its better accuracy in the prediction of springback [135]. The predicted force and energy versus crush distance using 2.5, 5 and 7.5 mm elements is shown in Figure 5.63. The energy absorption is over-predicted by up to 4.5% using the coarse 7.5 mm element size mesh compared to the 2.5 mm element size mesh. The model utilizing this finer mesh of 2.5 mm provides predictions in excellent agreement with the measured results, as shown in Section 5.3.3. Further refinement of the mesh could lead to less mesh discretization error; however, the meshes are certainly already finer than those utilized in industrial simulation of vehicle crash events and were judged to be adequate for the current research.

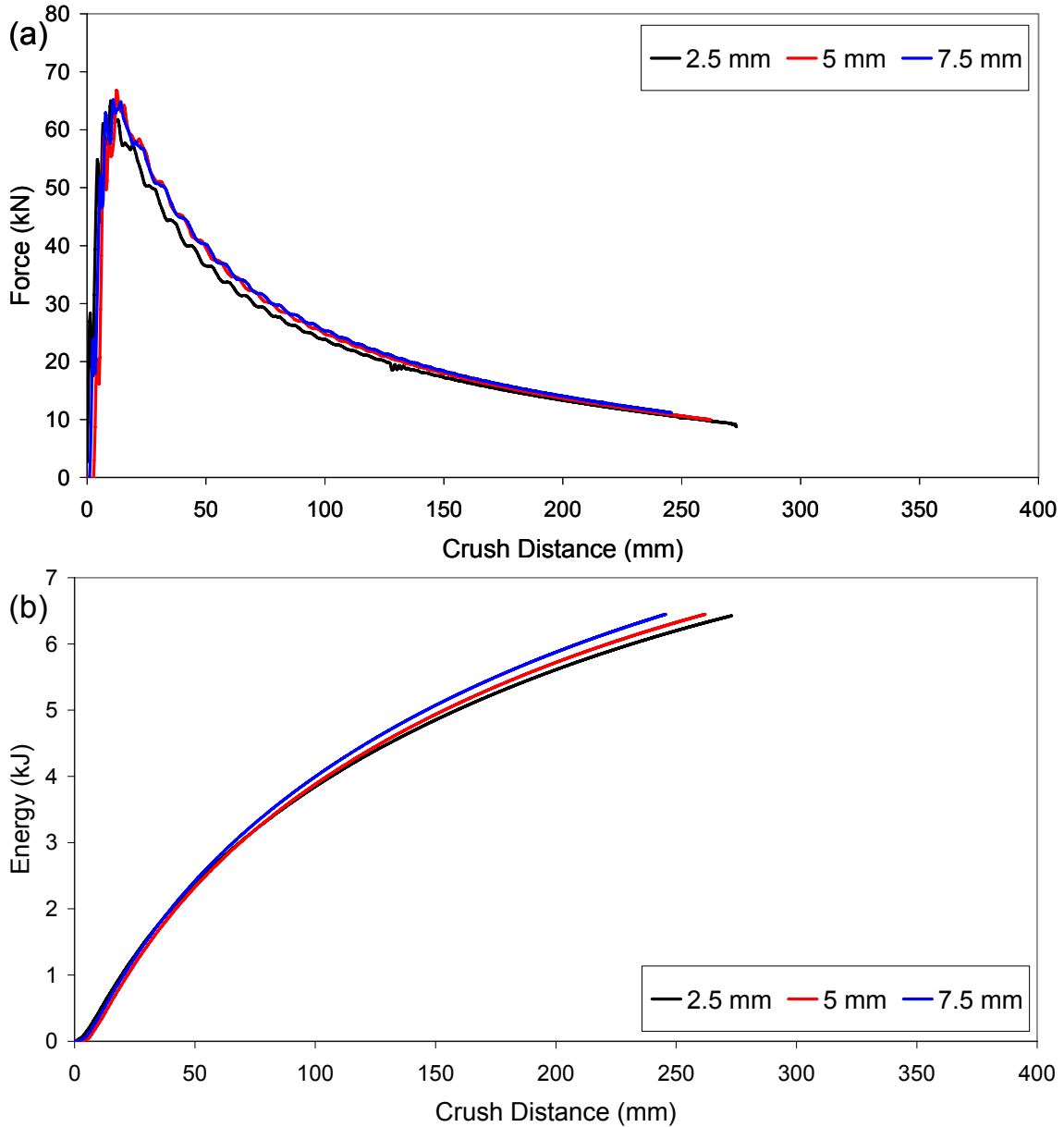


Figure 5.63: Predicted (a) force; and (b) energy versus crush distance using 2.5, 5 and 7.5 mm element size discretizations for 3 mm AA5754 hydroformed s-rails bent at an $R/D=2.0$ and the isotropic von Mises material model.

5.4.1 Computational Cost of Mesh Size

The finite element simulations utilized a 24 processor Linux cluster with 3.06 GHz Pentium-4 processors. The duration of the computations for the various simulations used to fabricate and crash the s-rail are shown in Table 5.2. Note that the comparison is made based on a single processor utilizing the reduced integration Belytschko-Lin-Tsay [121] element

formulation. Also shown is a breakdown of the computational time for each simulation using 2.5, 5 and 7.5 mm element size discretizations. There are significant computational cost savings by utilizing a large element size discretization; however, the resulting degradation in the accuracy of the predictions can be quite large. The crash model requires roughly 10 times the computation time required for the bend and hydroforming models, while the springback analyses are relatively very inexpensive.

Table 5.2: Duration of the various models computation used to simulate the forming and crash response of a 3 mm AA5754s-rail bent at R/D=2.0. The durations of the models computation are for 2.5, 5 and 7.5 mm element size discretizations. A single Pentium-4 3.06 GHz processor was used for each simulation.

SIMULATION	Simulation Duration (hours)		
	Element Size (mm)		
	2.5	5	7.5
First bend	8.3	1.1	0.4
First springback	0.120	0.020	0.006
Second bend	10.9	1.4	0.5
Second springback	0.180	0.020	0.006
Low-pressure hydroforming	10.2	1.0	0.4
Post-hydroforming springback	0.160	0.020	0.006
Crash	100.0	11.0	3.2

5.5 Summary

This summary of the numerical models is presented in two parts. The first part focuses on the predictions of the tube bending and hydroforming models, while the second part focuses on the predictions of the crash simulation. The overall predictive ability of the tube bending, hydroforming and crash models has been established within this chapter through validation with the experiments of Chapter 4. These models can now be confidently applied to provide additional insight into variations in the forming processes and the effect on the subsequent crash response, as will be presented in Chapter 6.

5.5.1 Tube Bending and Hydroforming Models

A summary of the measured process variables, thickness and strain due to bending and hydroforming of a 3 mm hydroformed s-rail along with the predictions using the isotropic von Mises, anisotropic Barlat and Zerilli-Armstrong material models is given in Table 5.3.

The corresponding thickness changes and strain in the as-formed s-rail are shown graphically in Figure 5.64. The tube bending and hydroforming model predictions of geometry, bending process variables, springback, thickness and strain were in good agreement with the measured results of Chapter 4. The predictions using the rate-insensitive material models are in better agreement with the measured result than the rate-sensitive Zerilli-Armstrong model. In particular, the model utilizing the anisotropic Barlat (1989) material model together with the fully-integrated element formulation provided predictions in slightly better agreement with the experiments.

Table 5.3: Summary of the measured process variables, thickness and strain in a 3 mm hydroformed s-rail versus the predictions using the isotropic von Mises, anisotropic Barlat and Zerilli-Armstrong material models.

	R/D	Process Variables in Bending			Thickness Reduction at Center of Bend (%)		Work Hardening at Center of Bend						Corner Radius (Sections A-E) (mm)
							Axial Engineering Strain		Circumferential Engineering Strain		Circumferential Engineering Strain at Corners		
		Bend Torque	Boost Load	Mandrel Load	Inside of Bend	Outside of Bend	Inside of Bend	Outside of Bend	Inside of Bend	Outside of Bend	Inside of Bend	Outside of Bend	
Measured	2.5	<i>Predicted bend torque is consistent with measured result</i>	<i>Predicted boost load is consistent with measured result</i>	<i>Predicted mandrel load is consistent with measured result</i>	-15	10	-0.15	0.16	-0.03	-0.06	0.16	0.10	12.5
	2.0				-18	13	-0.17	0.22	-0.03	-0.03	0.20	0.12	
	1.5				-20	18	-0.16	0.27	-0.05	0.00	0.17	0.09	
Isotropic von Mises	2.5				-15	8	-0.16	0.17	0	-0.07	0.2	0.08	
	2.0				-18	12	-0.17	0.21	0	-0.06	0.2	0.09	
	1.5				-21	14	-0.16	0.25	-0.02	-0.06	0.16	0.06	
Anisotropic Barlat	2.5				-15	10	-0.15	0.17	-0.02	-0.06	0.2	0.09	
	2.0				-19	12	-0.17	0.2	-0.01	-0.06	0.2	0.09	
	1.5				-19	17	-0.15	0.27	-0.04	-0.05	0.16	0.08	
Zerilli-Armstrong	2.5	NA	NA	NA	NA	NA	NA	NA	NA				
	2.0	-19	11	-0.18	0.21	-0.03	-0.07	0.17	0.08				
	1.5	NA	NA	NA	NA	NA	NA	NA	NA				

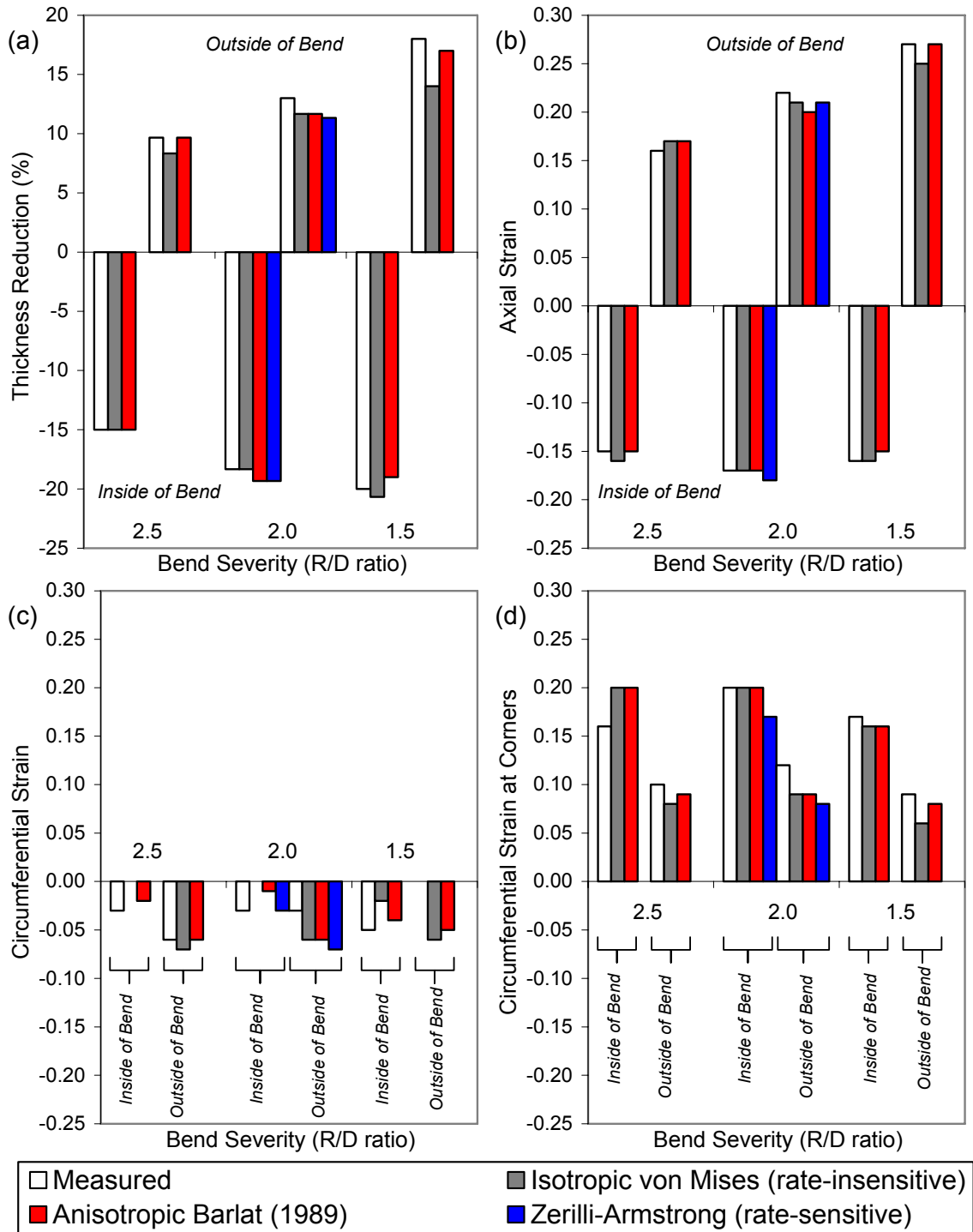


Figure 5.64: Summary of measured and predicted (a) thickness reduction; (b) axial strain; (c) circumferential strain; and (d) circumferential strain at the corners in a 3 mm hydroformed s-rail bent at various bend severities.

5.5.2 Crash Models

A summary of the measured peak load and energy absorption for 3 mm AA5754 hydroformed s-rails that have been annealed and not-annealed prior to the crash experiments versus the predictions utilizing the various material models is given in Table 5.4 and shown graphically in Figure 5.65.

Table 5.4: Summary of the measured peak load and energy absorption for 3 mm AA5754 hydroformed s-rails that have been annealed and not-annealed prior to the crash experiments versus the predictions utilizing the various material models.

			Measured			Predicted using isotropic von Mises material model (rate-insensitive)			Predicted using anisotropic Barlat (1989) material model (rate-insensitive)			Predicted using Johnson-Cook material model (rate-sensitive)			Predicted using Zerilli-Armstrong material model (rate-sensitive)		
			2.5	2.0	1.5	2.5	2.0	1.5	2.5	2.0	1.5	2.5	2.0	1.5	2.5	2.0	1.5
Non-Annealed	Non-Hydroformed	Peak Load (kN)	62.6	58.1	52.0	59.2	56.3	51.4	56.8	52.9	48.8	NA	NA	NA	NA	NA	NA
		Energy Absorption (kJ)	5.5	5.3	4.9	5.6	5.4	5.1	5.3	5.0	4.7	NA	NA	NA	NA	NA	NA
	Hydroformed	Peak Load (kN)	73.1	69.0	66.1	69.2	65.0	59.9	65.9	63.4	57.1	NA	63.9	NA	NA	69.7	NA
		Energy Absorption (kJ)	6.3	6.1	5.9	6.4	6.2	5.9	5.9	5.7	5.3	NA	6.2	NA	NA	6.7	NA
Annealed	Non-Hydroformed	Peak Load (kN)	44.1	38.6	37.0	NA	40.2	NA	NA	NA	NA	NA	NA	NA	NA	NA	NA
		Energy Absorption (kJ)	4.6	4.2	4.0	NA	4.5	NA	NA	NA	NA	NA	NA	NA	NA	NA	NA
	Hydroformed	Peak Load (kN)	45.4	39.1	37.9	NA	39.3	NA	NA	NA	NA	NA	NA	NA	NA	NA	NA
		Energy Absorption (kJ)	4.9	4.6	4.4	NA	4.8	NA	NA	NA	NA	NA	NA	NA	NA	NA	NA

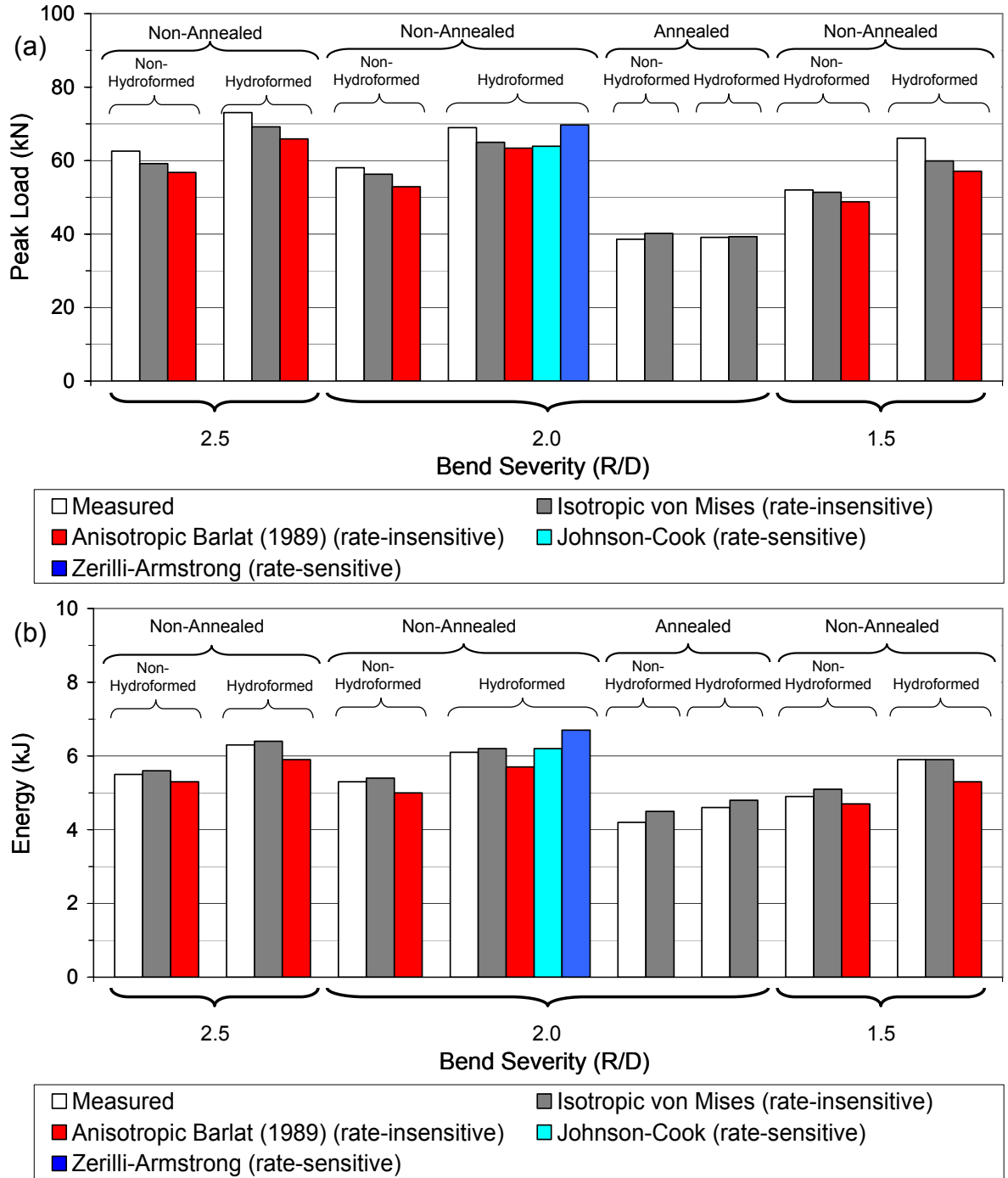


Figure 5.65: Summary of the measured peak load and energy absorption for 3 mm AA5754 hydroformed s-rails that have been annealed and not-annealed prior to the crash experiments versus the predictions utilizing the various material models.

The crash models utilizing the reduced integration Belytschko-Lin-Tsay element formulation and the piecewise linear isotropic representation with the von Mises yield criterion provided predictions of geometry and crash response in best agreement with the

measured result. The fully integrated element formulation, which served the forming models well, performed poorly in the crash models and exhibited poor mesh convergence. This poor performance is attributed to the shear locking phenomena associated with shell elements under buckling type loads as discussed in Section 5.3.5. Implementation of the Belytschko-Lin-Tsay element formulation within the crash models provided crash results in better agreement with the experiment. Much less mesh sensitivity was observed for this element type versus the fully-integrated element. The finer 2.5 mm mesh implemented in the models was found to provide predictions in better agreement with the measured values than the coarser 5 and 7.5 mm meshes.

The crash simulation utilizing the Zerilli-Armstrong material model significantly over-predicted the force and energy absorption, while use of the Johnson-Cook material model provided crash response predictions in excellent agreement with the measured result. The Johnson-Cook and Zerilli-Armstrong material models are not required for modeling the crash response of these alloys because: (i) these aluminium alloys were found to be strain rate insensitive [106,107]; and, (ii) the average strain rate over the period of active plastic deformation is roughly 27 s^{-1} , which is relatively low.

The early force-time response is governed by stress wave propagation effects only up to roughly 5 ms in time since the stress wave oscillations dissipate rapidly due to the large number of reflections from the various boundaries. After this initial period, the s-rail can be described as being in a state of dynamic equilibrium.

The greater energy absorption of the hydroformed versus non-hydroformed s-rail is attributed to the overall greater resistance to deformation throughout collapse provided by the square versus round cross-section of the s-rail. The performance of rectangular cross-sections in the crash response of s-rails is assessed in Chapter 6.

Chapter 6

Numerical Investigations into the Variables Governing the Physical Characteristics and Crash Response of S-Rails

In the previous chapter, the numerical models of tube bending, hydroforming and crash response were validated using the experimental data from Chapter 4. Here, the validated numerical models are used to provide further insight by examining additional variables affecting the characteristics of s-rails and their subsequent crash response. These numerical investigations isolate the influence of tube geometry, forming variables and the nature of the adopted hydroforming process (low-pressure versus high-pressure) on s-rail crash response.

The balance of this chapter begins with a presentation of the results from investigations examining the effects of s-rail geometry on crash response. Within this section, the s-rail R/D ratio (section lengths) and cross-section are examined. The results from the investigations examining the influence of forming process parameters on s-rail crash response are then presented, and include: (i) material strength effects; (ii) boost in bending; and (iii) forming history effects. The investigation into the role of the high-pressure hydroforming process, although a forming variable, on s-rail crash response is presented separately thereafter.

6.1 Effect of S-Rail Geometry on Crash Response

6.1.1 R/D Ratio and Section Lengths

For the s-rail examined in this work, the total length, width and bend angle of the s-rails (Figure 2.3) were constrained. Thus, a consequence of a change in the bend severity or R/D ratio would be a change in the section lengths between the bend regions (Table 2.1). Here, the geometric effect of bend severity on the crash response of s-rails is isolated, and then the degree to which the section length is affected by bend severity and the influence of section length on the crash response are examined.

The effect of geometrical differences in the 3 mm AA5754 hydroformed s-rails due to the three bend severities was examined numerically by simulating the crash experiments on uniform thickness s-rails for which residual stresses and work hardening effects were removed. Essentially, simulations of impact tests on uniform thickness hydroformed s-rails with virgin material properties are considered for each corresponding bend severity. Thus, thinning and work hardening due to forming are eliminated such that geometric effects can be isolated. The force and energy response of these s-rails were predicted using the rate-insensitive isotropic von Mises material model and are shown in Figure 6.1. As the bend severity decreased from an R/D ratio of 1.5 to 2.5, the peak force and energy absorption increased by 10.6% and 6.3%, respectively, which is a significant change. Thus the geometric effect of decreasing bend severity is to actually increase crush resistance in the absence of work hardening and thickness changes.

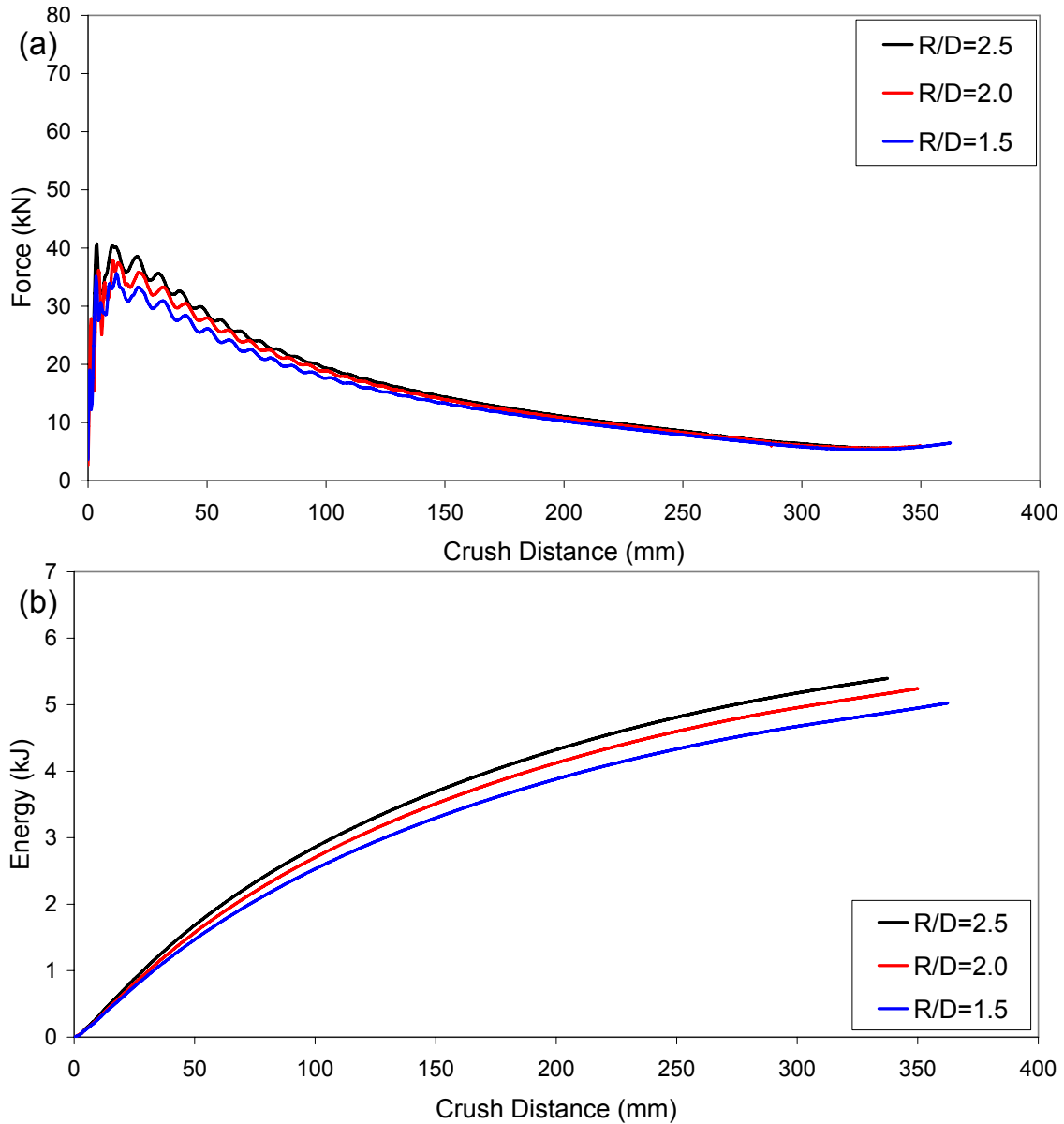


Figure 6.1: Predicted (a) force; and (b) energy versus crush distance for 3 mm AA5754 hydroformed s-rails with uniform thickness and virgin material properties bent at R/D ratios of 2.5, 2.0 and 1.5.

To better understand the effect of section length differences of the s-rails bent at the various bend severities on the crash response, the collapsing s-rail can be considered to act as a three-bar linkage with the formation of three plastic hinges, two at the bends and one near the base of section A (Figure 2.3). To illustrate the geometric differences (Table 2.1) between s-rails bent at the three R/D ratios, a schematic of the centre line geometry is shown in Figure 6.2. Note that the centre line geometry corresponding to R/D ratios of 2.5, 2.0 and

1.5 are denoted by green, blue and red lines, respectively. In simulations of the crash event, the formation of the hinge, regardless of the bend severity, was observed to occur at the centre of the bends and just above the longer fixed section A of the s-rail as shown in Figure 6.3. The geometry of the higher severity bend ($R/D=1.5$) results in a shift of the hinge by 6.28 mm along the line perpendicular to the tangent of the bend when compared to an $R/D=2.5$ bend, as shown in Figure 6.2b and Figure 6.3c. Consequently, for higher bend severities, the lengths of the “links” that form between the two corner hinges (Figure 6.2) also increases, which decreases the ability of the hinge to resist deformation during crash. Consequently, s-rails bent with greater bend severity experience a decrease in their energy absorption capability (Figure 6.1), that can be directly attributed to geometry effects.

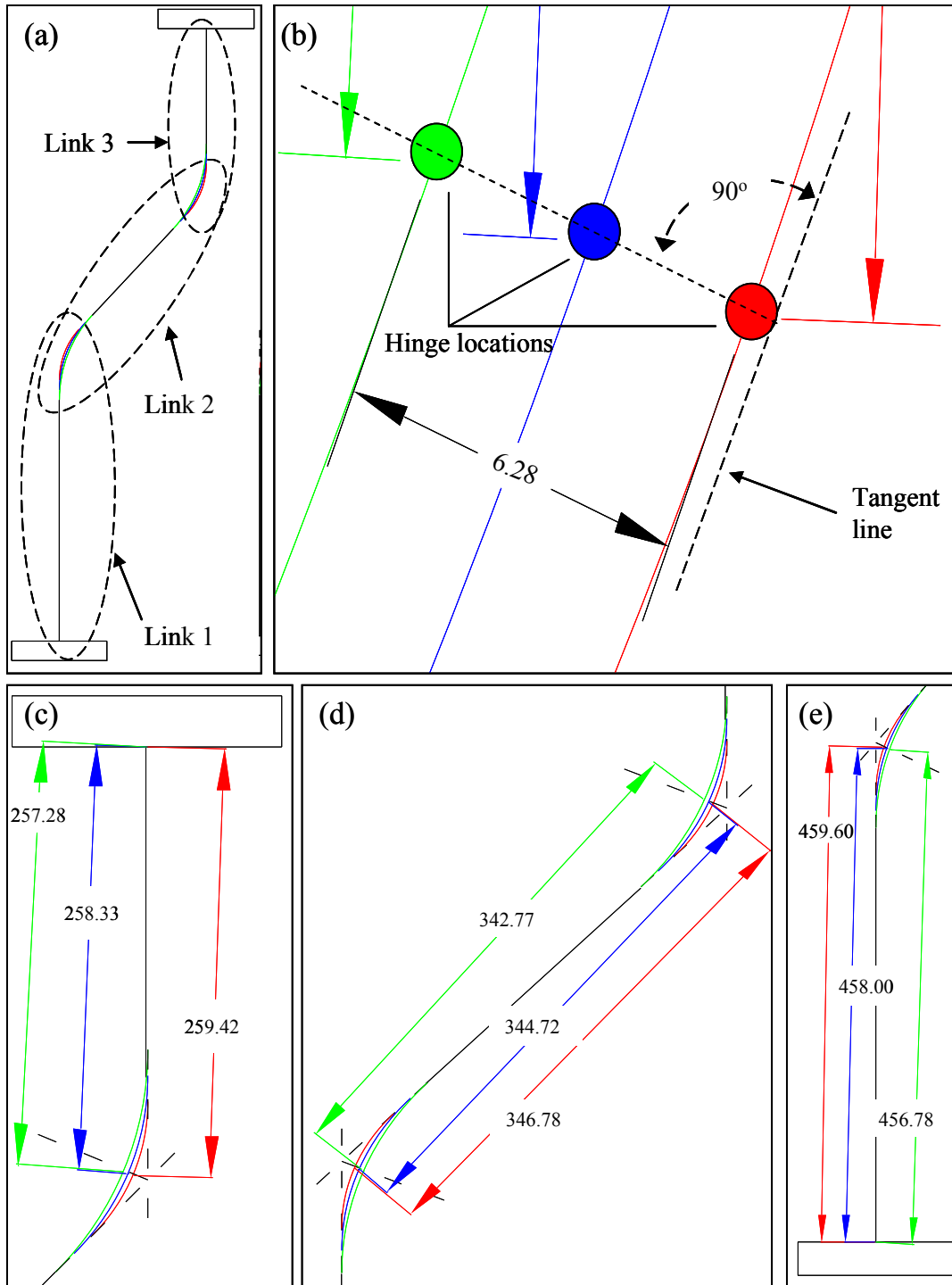


Figure 6.2: Schematic of centre line geometry of s-rails bent at R/D ratios of 2.5 (green), 2.0 (blue), and 1.5 (red): (a) links 1, 2 and 3; (b) close-up of the distance between the fixed end of the s-rail and the location of hinge in the linkage corresponding to section E; (c) length of the bar linkage (section C) between hinges in bend regions; (d) distance between the fixed end of the s-rail and the location of hinge in linkage corresponding to section A; and (e) close-up view of the hinge location occurring at the bends of the s-rail. Units are in millimeters.

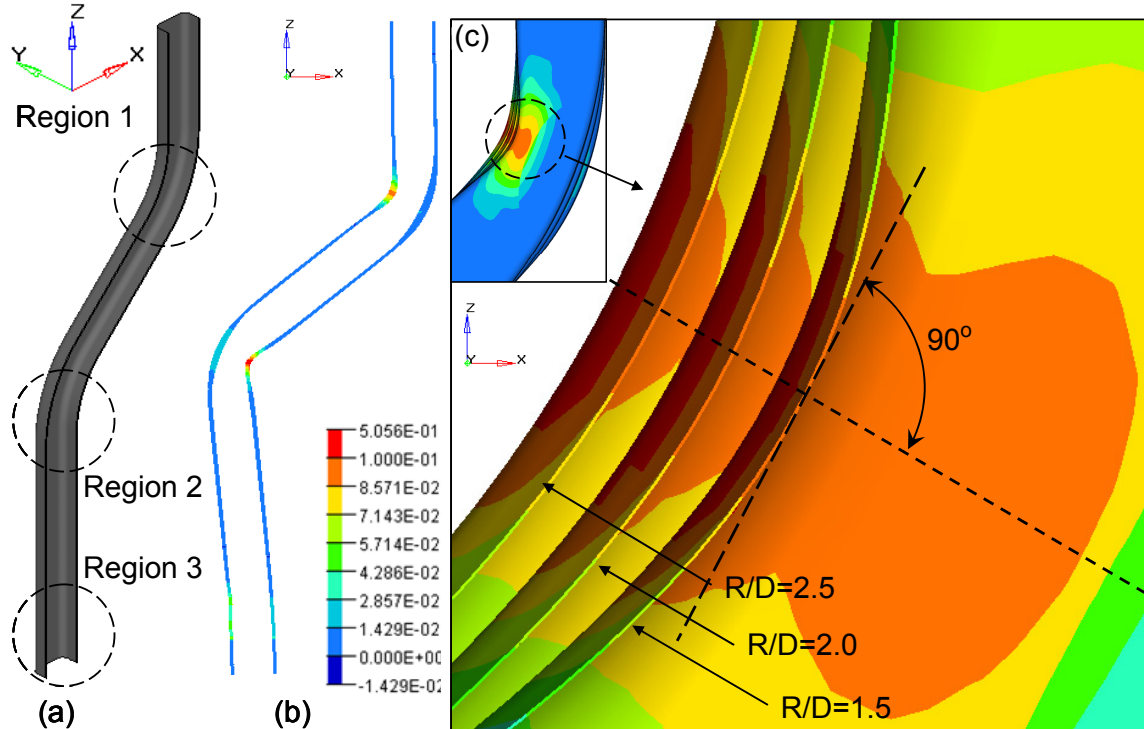


Figure 6.3: (a) Section view of hydroformed s-rail (time=0 ms); (b) contours of effective plastic strain in the corresponding cross-section (time=12 ms); and, (c) contours of effective plastic strain in of the hinge in region 1 of three s-rails with different bend severities superimposed on one another (time=12 ms).

6.1.2 S-Rail Cross-Section

Thus far, the forming and crash results for only two s-rail cross-section geometries (round and square) have been presented. Here, predictions of forming and s-rail crash response for two additional s-rail cross-sections, rectangular with aspect ratios of 2:1 and 1:2 (Figure 3.10), are presented. These rectangular cross-section s-rails were pre-bent from 3 mm AA5754 tube at $R/D=2.0$ and hydroformed using the simulation techniques described in Chapter 3. The forming and crash results for the two rectangular cross-section s-rails are compared to the corresponding round and square cross-sections s-rails presented in Chapter 5. Note that all four cross-section s-rails have identical mass and the impact tests were modelled under the same conditions described in Chapter 3. To further isolate the effect of cross-section on the s-rail crash response, the impacts on the four s-rails were also simulated without considering previous forming history effects (i.e. thickness changes, work hardening and residual stresses). The rate-insensitive isotropic von Mises material model was utilized within both the forming and crash simulations.

The change in cross-section due to the hydroforming process induced significantly different levels of thickness change and work hardening in the s-rails, the latter of which has already been shown to significantly affect the subsequent crash response. The predicted thickness, and major and minor engineering strains were extracted around the circumference of the bend section (Figure 2.10) for the four s-rails and are shown in Figure 6.4. As the depth of the section increases (2:1 versus 1:1 and 1:2 aspect ratio), the degree of thickening on the inside of the bend and thinning on the outside of the bend increases. Similarly, as the depth of the section increases, the magnitude of the major (axial) strain along the outside of the bend and the minor (axial) strain along the inside of the bend increase. Hydroforming of the rectangular cross-section s-rail with an aspect ratio of 2:1 induces the greatest amount of work hardening in the s-rail. Note that forming of the square cross-section of the s-rail using the low-pressure hydroforming operation induced significantly less change in thickness than was predicted for the rectangular sections. This observation indicates that changes in thickness due to the low-pressure hydroforming process are dependant on the geometry of the die section.

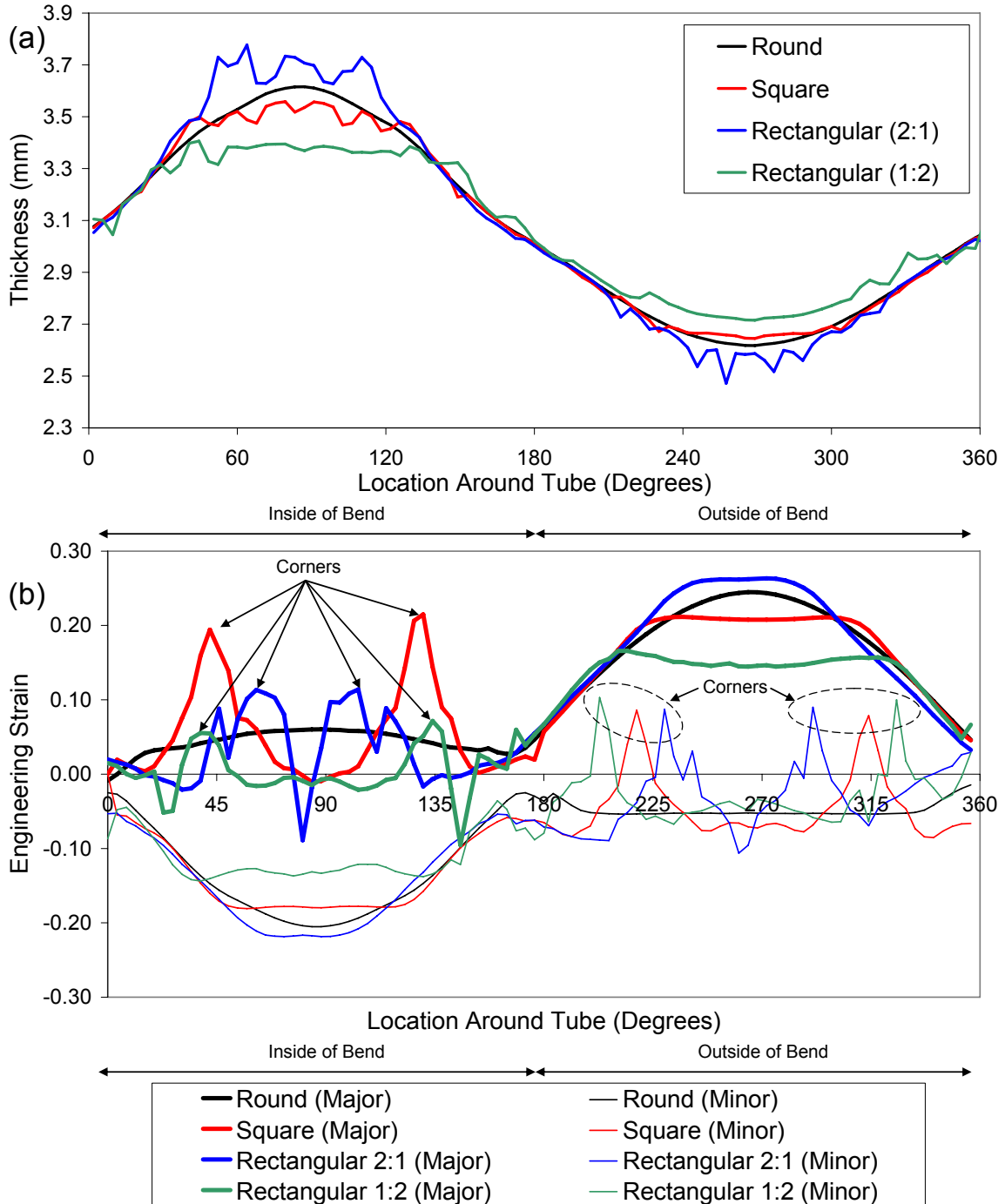


Figure 6.4: Predicted (a) thickness; and (b) major and minor strain around the circumference of the center section of the bend for the various s-rail cross-section geometries.

The predicted contours of effective plastic strain in the rectangular cross-section s-rails with aspect ratios of 2:1 and 1:2 at a time of 0 and 35 ms after impact are shown in Figure 6.5. The three plastic hinges in the rectangular cross-section s-rails develop in a similar

manner as the round and square sections shown earlier. The predicted strains in the hinge regions of the rectangular s-rails are greater than 100%, which is consistent with the strains in the round and square cross-section s-rails, although the extent of deformation is more severe in the deeper cross-section.

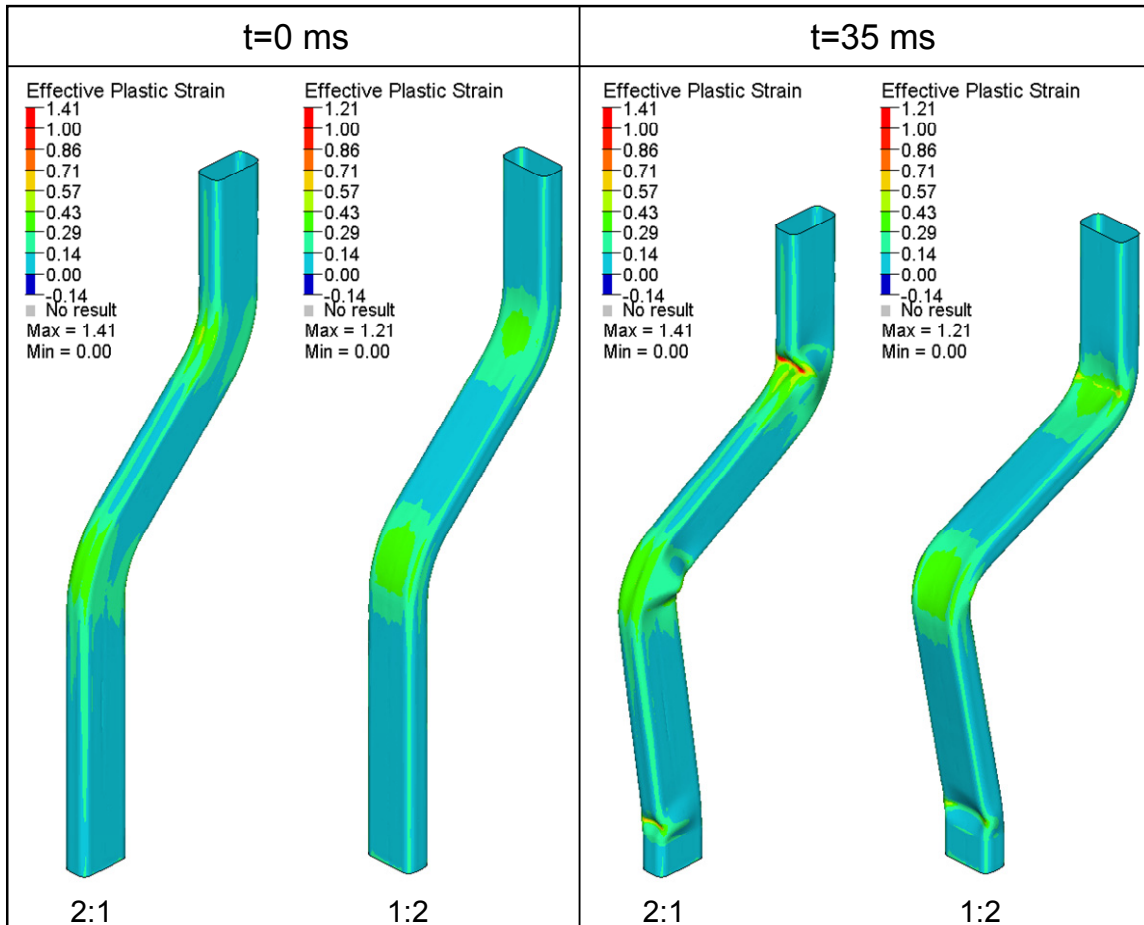


Figure 6.5: Predicted contours of effective plastic strain in the rectangular cross-section s-rails with aspect ratios of 2:1 and 1:2 at a time of 0 ms and 35 ms.

The predicted peak load and energy absorption for the four s-rail cross-sections (Figure 3.10) both with and without consideration of previous forming history effects, are summarized in Table 6.1 and Figure 6.6. For brevity, the predicted force and energy absorption as a function of crush distance are given in Appendix E. Assessing the predictions of peak load and energy absorption from the model that does not consider previous forming history effects allows the effects of cross-section geometry on crash response to be isolated. The rectangular cross-section s-rail with an aspect ratio of 2:1

demonstrated the greatest peak load and energy absorption; whereas the predicted peak load and energy absorption for the rectangular cross-section s-rail with an aspect ratio of 1:2 is approximately one-half of that predicted for the s-rail with an aspect ratio of 2:1. Comparing the predicted crash response of the square and rectangular (aspect ratio 2:1) cross-section s-rails reveals a 42% increase in peak load when previous forming history effects are considered and a 38% increase when previous forming history effects are not considered. Interestingly, the predicted energy absorption for the rectangular (2:1 aspect ratio) cross-section is 30% greater than that of the square cross-section for both cases either with or without consideration of previous forming history effects. Meanwhile, the increase in predicted peak load and energy absorption due to consideration of previous forming history effects for the square and both rectangular cross-sections (2:1 and 1:2) is 69-78% and 36%, respectively. Based on these findings, the predicted crash response of an s-rail is strongly dependant on the effects of cross-section geometry, but to a slightly greater extent on the effects of previous forming history. As will be shown in Section 6.2.3, the work hardening associated with the forming history is the predominant parameter affecting s-rail crash response.

Table 6.1: Peak load and energy absorbed for the s-rails with varying cross-sections examined considering and not considering forming history.

Forming History Condition	Cross Section Geometry	Peak Load (kN)	Energy Absorbed at 150 mm of Crush Distance (kJ)
Forming History Considered	Round	56.6	4.3
	Square	65.0	4.9
	Rectangular (2:1)	92.6	6.4
	Rectangular (1:2)	39.1	3.1
Forming History Not Considered	Round	38.2	3.5
	Square	37.7	3.6
	Rectangular (2:1)	52.0	4.7
	Rectangular (1:2)	23.2	2.3

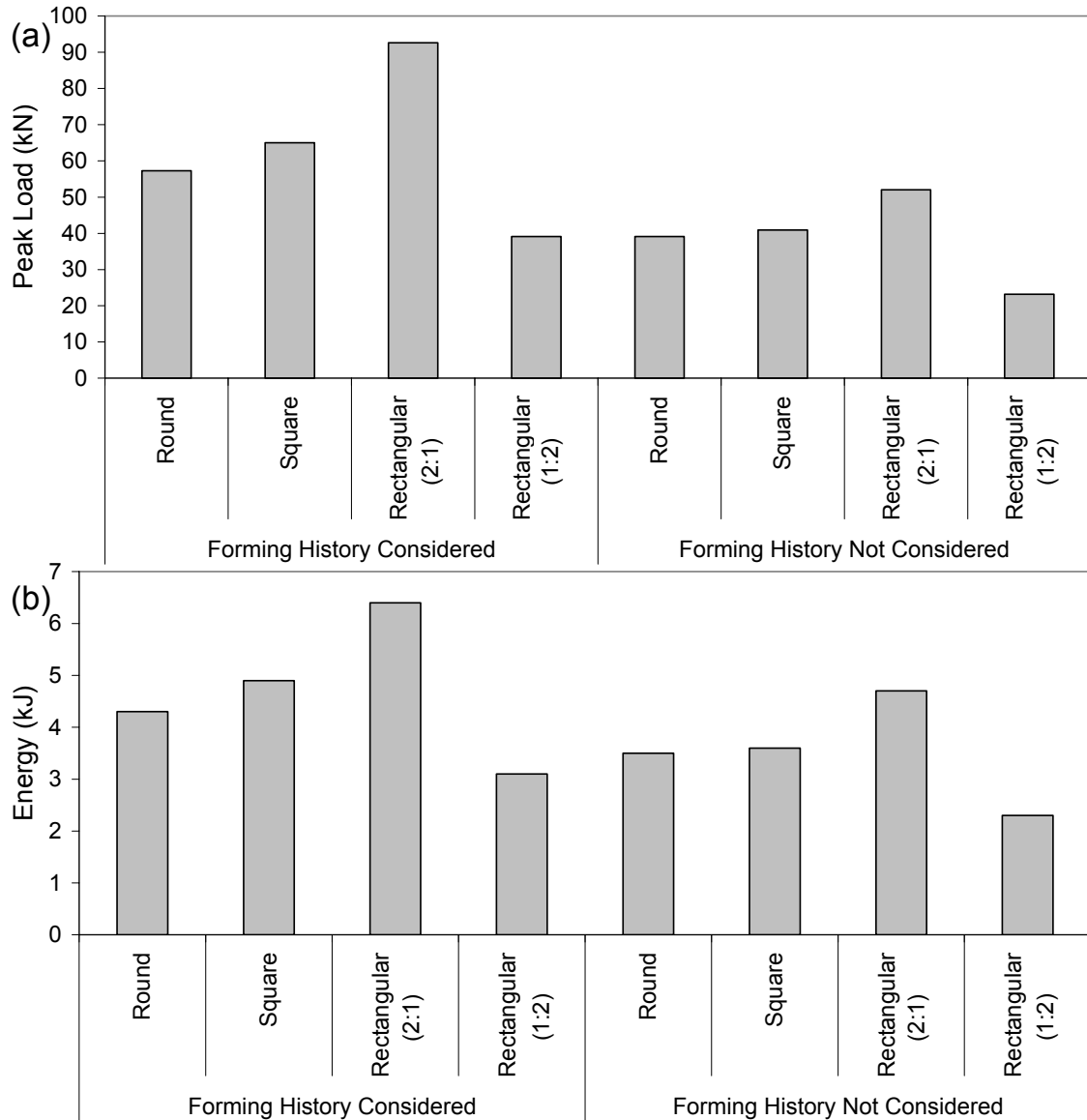


Figure 6.6: Predicted (a) peak load; and (b) energy absorbed for the s-rails with varying cross-sections examined considering and not considering forming history.

6.2 Effect of Forming Parameters on Crash Response

6.2.1 Material Strength

Direct assessment of the effect of strength for the two alloys considered in this research was confounded by the different tube thicknesses available. Thus numerical simulations were performed to facilitate this comparison.

To isolate the effect of the material strength, the effective stress versus effective plastic strain curve of the higher strength EN-AW5018 material was assigned to a numerical model of a 3 mm thick tube with a 76.2 mm outer diameter. As shown earlier in Figure 2.6, the strength of the EN-AW5018 alloy is roughly 20% higher than the strength of AA5754. Simulations were then performed considering the “3 mm EN-AW5018 tubes” that underwent bending and hydroforming under the same prescribed conditions as the 3 mm AA5754 hydroformed s-rail, which allowed a one-to-one comparison of their subsequent crash response. The crash response of two s-rails bent at $R/D=2.0$ was predicted using the rate-insensitive isotropic von Mises material model and is shown in Figure 6.7. The EN-AW5018 hydroformed s-rail experienced higher crush forces and up to 16.4% greater energy absorption than the AA5754 material. This increase in energy absorption is less than the theoretical prediction of 20%, which is based on analytical techniques that suggest the crush load is directly proportional to the material strength [136]. However, the increase in predicted energy absorption by 16.4% due to a 20% increase in material strength is consistent with findings by Reid [85] that suggest a 20% increase in material strength will result in a 14.6% increase in energy absorption.

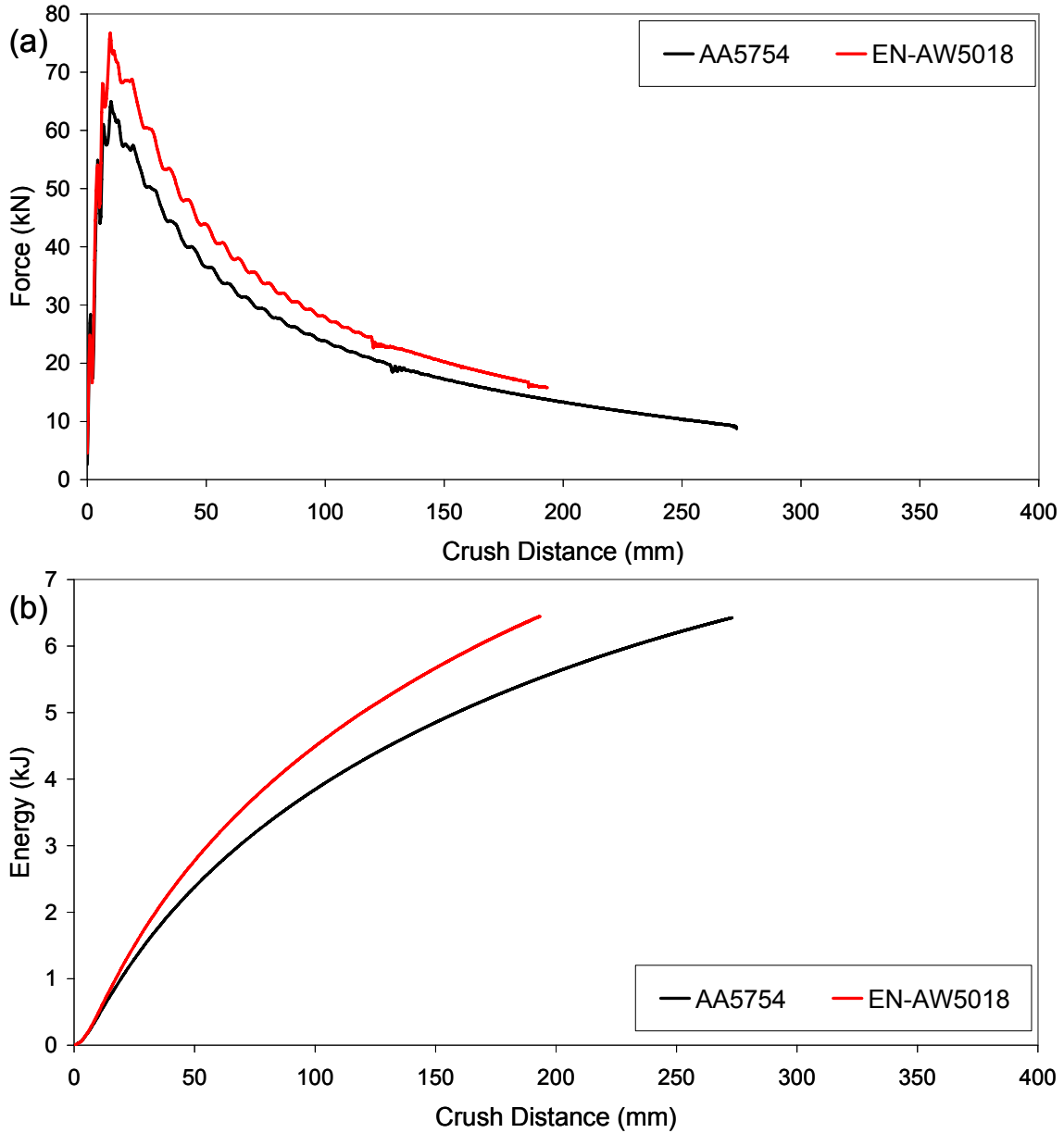


Figure 6.7: Predicted (a) force; and (b) energy versus crush distance for 3 mm AA5754 and 3 mm EN-AW5018 hydroformed s-rails bent at R/D=2.0, and fabricated under the same prescribed conditions.

6.2.2 Bending Boost

To determine the degree that bending boost affects the crash response of s-rails, the bending of a 3 mm AA5754 tube at R/D=2.0 is simulated using a 104% boost level under both frictional boost and independent collet boost conditions (Figure 1.6) (Section 1.3.7), followed by subsequent hydroforming and crash simulations. The predicted bending process variables

for the two additional boost cases are consistent with those in Table 2.5, with the exception of the pressure die clamp load, which had to be increased to 45 kN to prevent wrinkling on the inside of the bend. The results from the simulations considering these two additional boost cases are compared to predicted results for the 100% frictional boost condition employed in the experiments, with the exception that the pressure die clamp load is increased to 45 kN. This approach allowed a direct one-to-one comparison of the predicted results considering the three boost conditions.

6.2.2.1 Effect of Boost on Thickness and Strain

The predicted thickness after bending along the inside and outside of the bend (Figure 2.10) for the three boost conditions is shown in Figure 6.8 and Figure 6.9, respectively. Bending with a 104% frictional boost condition has a minimal effect on the degree of thickness changes both on the inside and outside of the bend, which is attributed to slip of the tube from the pressure die during the bend. However, bending under a 104% independent collet boost condition results in up to a 6% increase in thickness along the inside and outside of the bend over the 100% frictional boost condition.

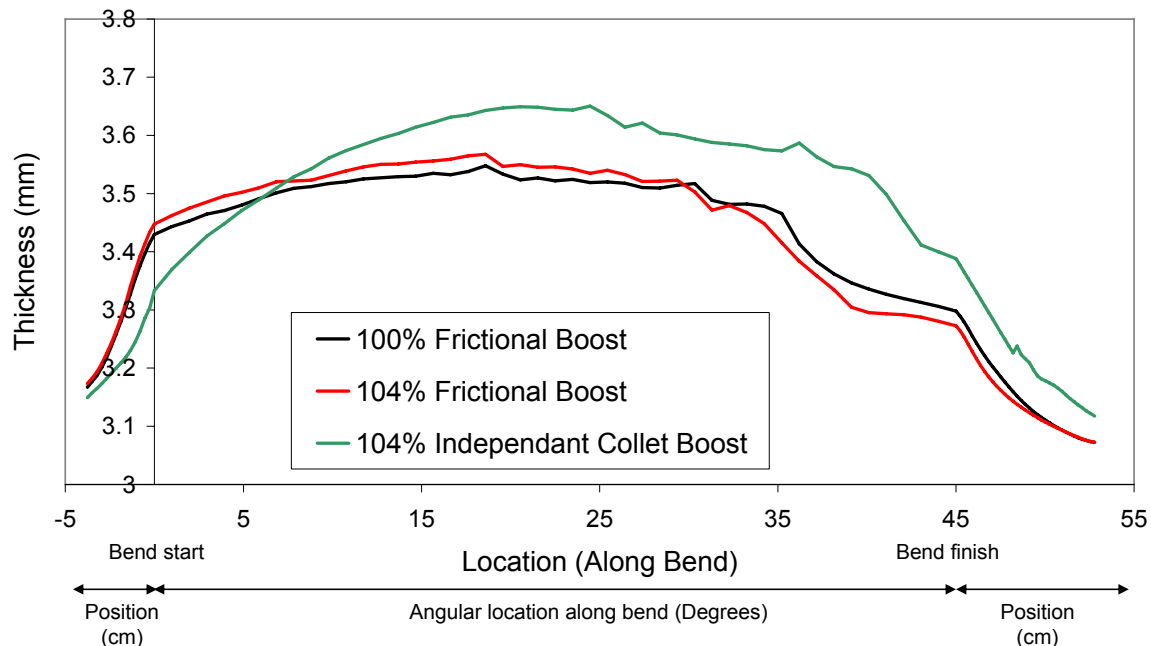


Figure 6.8: Predicted thickness along the inside of the bend for (i) 100% frictional boost; (ii) 104% frictional boost; and (iii) 104% independent collet boost bending conditions.

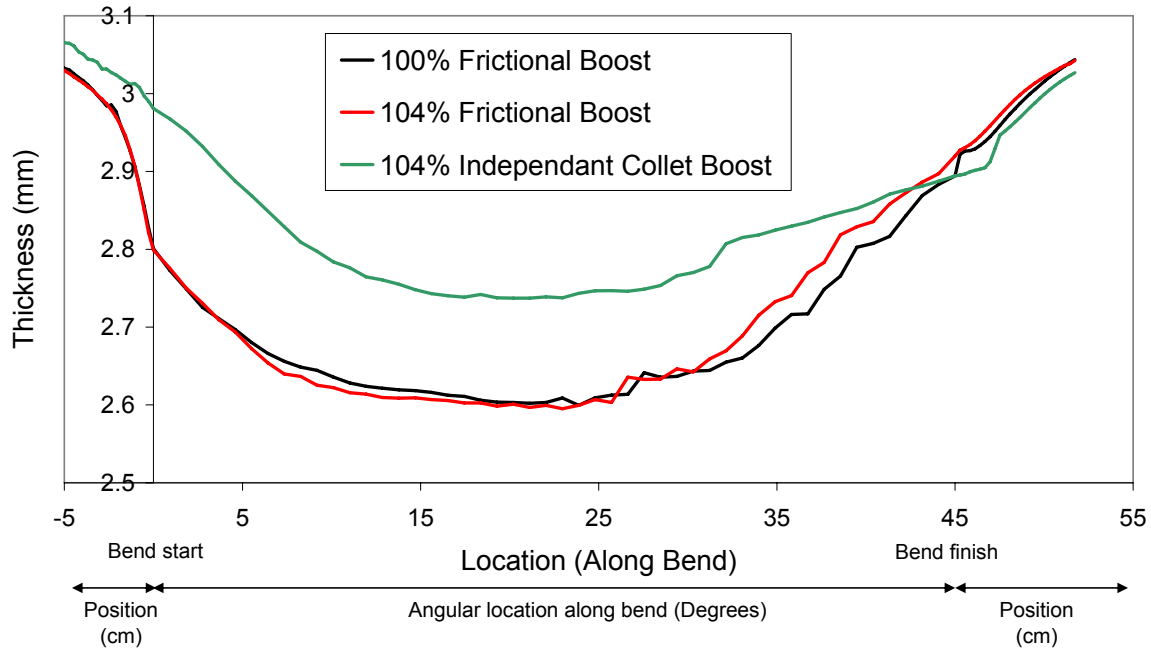


Figure 6.9: Predicted thickness along the outside of the bend for (i) 100% frictional boost; (ii) 104% frictional boost; and (iii) 104% independent collet boost bending conditions.

The predicted effective plastic strain along both the inside and outside of the bend for the three conditions of boost is shown in Figure 6.10 and Figure 6.11, respectively. As observed in the thickness measurements, bending with 104% frictional boost has little effect on the level of plastic strain, again likely due to slip of the tube on the pressure die during bending. However, bending with an independent collet boost condition results in a 12% increase in the predicted effective plastic strain at the inside center of the bend (22.5 degrees) over the frictional boost case. Use of an independent collet boost condition during bending also resulted in a 25% decrease in effective plastic strain at the outside center of the bend over the frictional boost case. This decrease in the predicted effective plastic strain is due to less stretching of the material as a result of greater material being fed into the bend region.

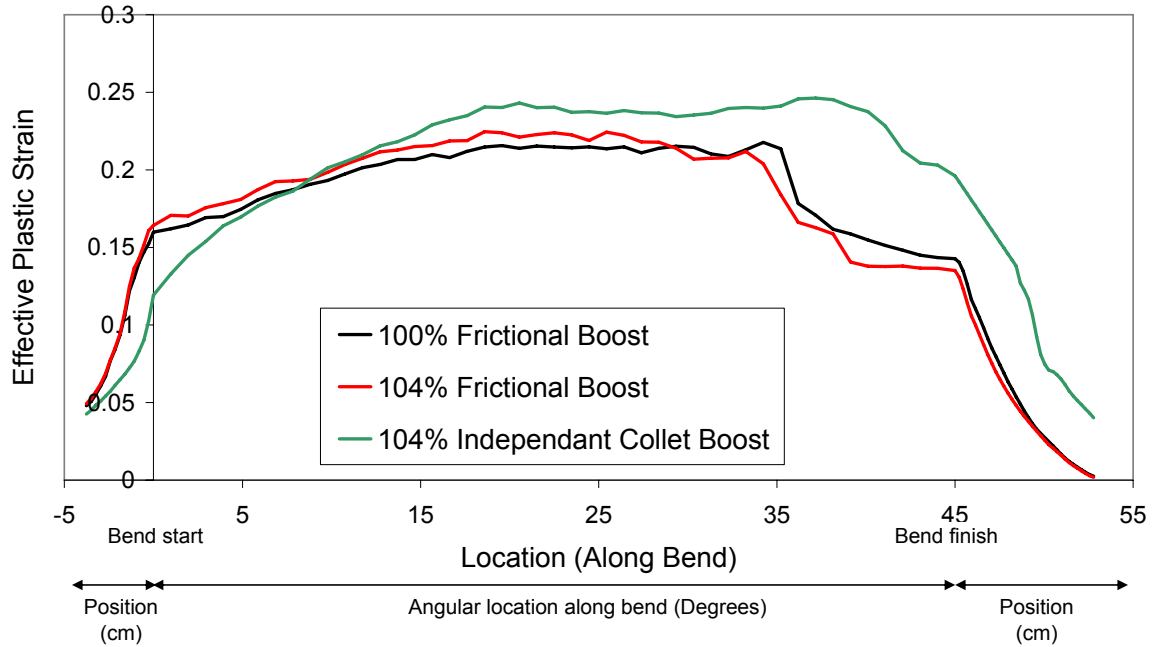


Figure 6.10: Predicted effective plastic strain along the inside of the bend for (i) 100% frictional boost; (ii) 104% frictional boost; and (iii) 104% independent collet boost bending conditions.

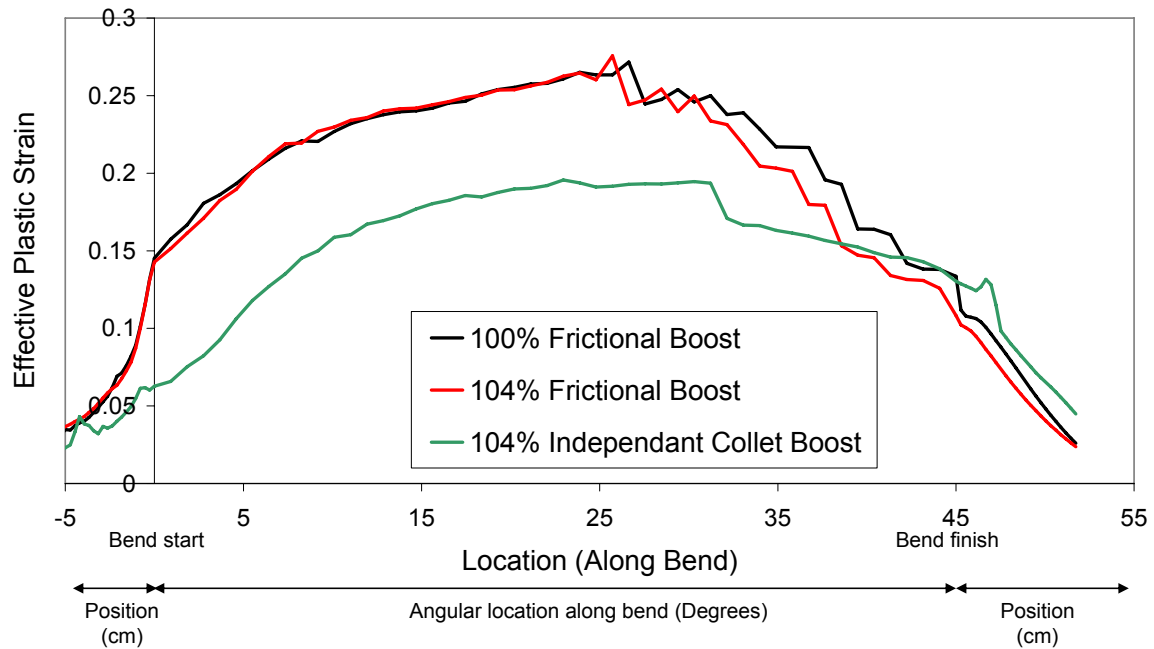


Figure 6.11: Predicted effective plastic strain along the outside of the bend for (i) 100% frictional boost; (ii) 104% frictional boost; and (iii) 104% independent collet boost bending conditions.

6.2.2.2 Effect of Boost on Crash Response

The predicted force and energy absorption for the s-rails bent under the three boost conditions is shown in Figure 6.12. There is a negligible difference in crash response for the s-rails bent at 100% and 104% frictional boost conditions; however, the energy absorption at 250 mm of crush distance for the s-rail bent under the 104% independent collet boost condition increases by 4.3%.

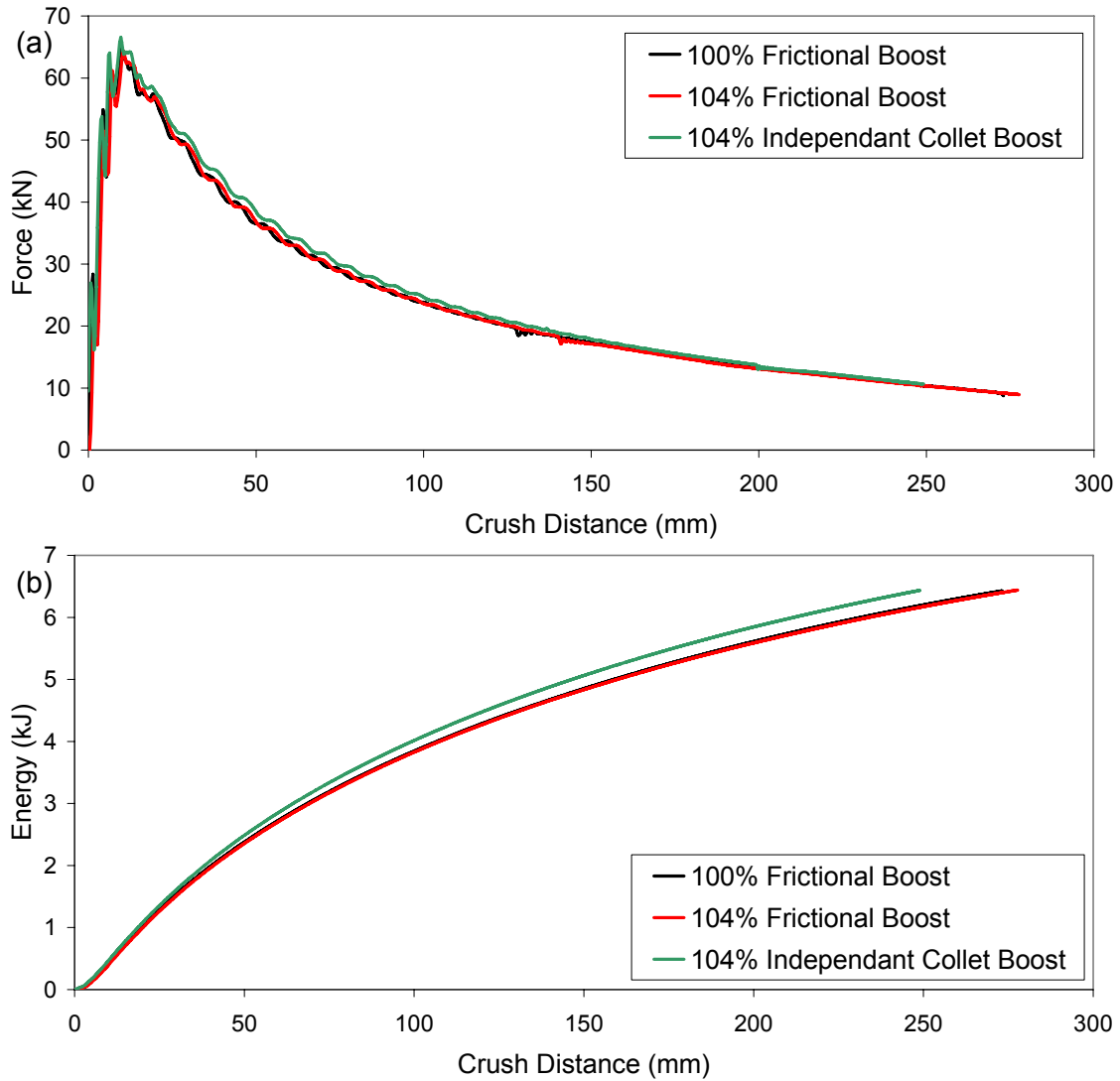


Figure 6.12: Predicted (a) force; and (b) energy absorption for hydroformed s-rail bent under the three boost conditions.

6.2.3 Forming History

To isolate the effects of residual stresses, thickness changes and work hardening on the crash response of both non-hydroformed and hydroformed s-rails, the following crash simulations were performed using the rate-insensitive isotropic von Mises material model:

- i) entire forming history considered;
- ii) entire forming history minus the residual stresses;
- iii) entire forming history minus the residual stresses and work hardening; and,
- iv) entire forming history minus the residual stresses, work hardening and thickness changes (i.e. no forming effects at all).

The predicted force and energy response of non-hydroformed and hydroformed 3 mm AA5754 s-rails bent at $R/D=2.0$ is summarized in Table 6.2 and Figure 6.13, while the predicted force and energy absorption versus crush distance is shown in Appendix E. The residual stresses due to the forming operations had a negligible effect on the crash response. The effect of work hardening was very significant; not considering the work hardening due to tube bending and hydroforming results in an under-prediction of peak force by 33% and 41%, in the non-hydroformed and hydroformed s-rails, respectively. Furthermore, the energy absorption is under-predicted by up to 19% and 23% in the non-hydroformed and hydroformed s-rails, respectively, when work hardening effects are neglected. The predicted crash response of both types of s-rails appears to be relatively unaffected by consideration of the thickness changes in the bend regions. This result is somewhat unexpected; however, the increase in thickness at the inside of the bend, which stiffens the s-rail, is offset by the reduced thickness on the outside of the bend. This result challenges the “conventional wisdom” arising from similar studies of stamped structures that thickness change is offset by work hardening when predicting the crash response of structural components.

Table 6.2: Summary of peak load and energy absorption at 250 mm of crush distance for the various forming history conditions considered in the s-rail crash simulation.

S-Rail Type	Forming History	Peak Load (kN)	Energy Absorbed at 250 mm crush (kJ)
Non-hydroformed	Entire forming history considered	56.6	5.4
	Residual stresses removed	56.6	5.4
	Residual stresses and work hardening removed	39.7	4.5
	Residual stresses, work hardening and thickness changes removed	38.2	4.4
Hydroformed	Entire forming history considered	65.0	6.2
	Residual stresses removed	65.0	6.2
	Residual stresses and work hardening removed	39.3	4.8
	Residual stresses, work hardening and thickness changes removed	37.7	4.6

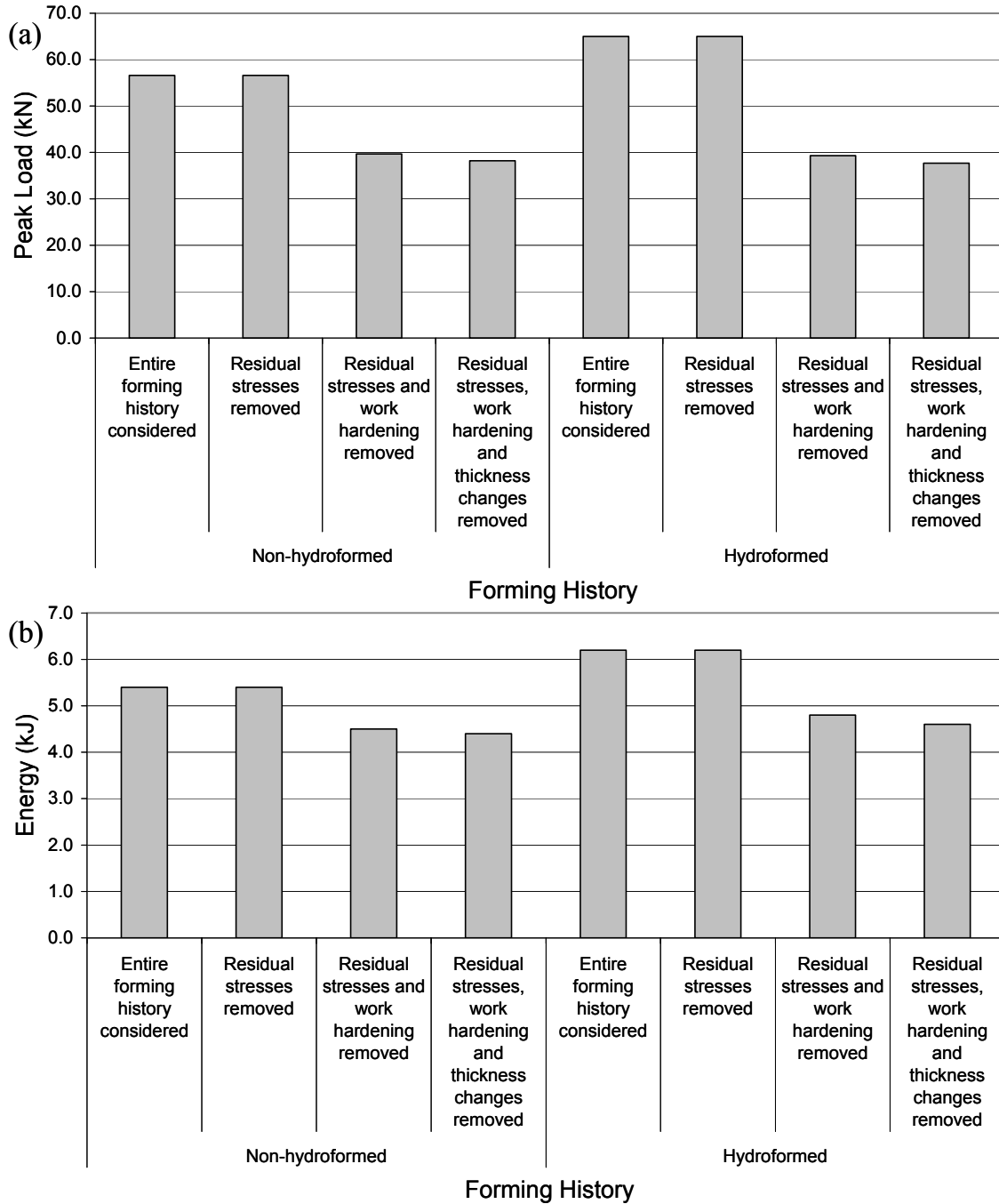


Figure 6.13: Summary of predicted (a) peak load and (b) energy absorption of non-hydroformed and hydroformed s-rails bent at $R/D=2.0$ for the various forming history considerations.

6.3 Effect of Hydroforming Process Type

6.3.1 Overview

Up until now, all of the hydroformed s-rails presented in this thesis have considered a so-called low-pressure hydroforming process with essentially zero circumferential expansion and end-feed. In this section, the effect of the adoption of a high-pressure hydroforming process with circumferential expansion and end-feed is considered. The thickness and strain distribution and subsequent crash response of the high-pressure hydroformed s-rails is compared directly to the previous low-pressure results.

6.3.2 Results

6.3.2.1 High-Pressure Hydroforming Predictions

Simulations of high-pressure hydroforming of the s-rails were performed for the range of cases outlined in Section 3.3.2. Figure 6.14 shows contours of thickness and effective plastic strain for each condition, summarized as:

- (i) zero-percent circumferential expansion and zero end-feed (this corresponds to the low-pressure hydroforming process);
- (ii) four-percent circumferential expansion and zero end-feed;
- (iii) four-percent circumferential expansion with 30 mm of end-feed;
- (iv) four-percent circumferential expansion with a frictionless condition and 80 mm of end-feed;
- (v) nine-percent circumferential expansion and zero end-feed; and,
- (vi) nine-percent circumferential expansion with a frictionless condition and 100 mm of end-feed.

As the level of circumferential expansion increases, the overall effective plastic strain and degree of local thinning increase, particularly in the section corners. In the four- and nine-percent expansion cases, the following observations were made:

- As the level of end-feed increases, the degree of plastic strain increases, particularly in the two straight sections, A and E, and near their transition regions within the bends. Section C does not experience significant change in the level of strain.
- End-feed can reduce the overall thinning in the straight sections, A and E, of the s-rail, but not significantly in the bend regions or in section C.
- Strain localization was observed in both the 4% and 9% expansion cases with zero end-feed near the outside corner of the bends, which may indicate possible material failure. End-feed eliminated this instability.

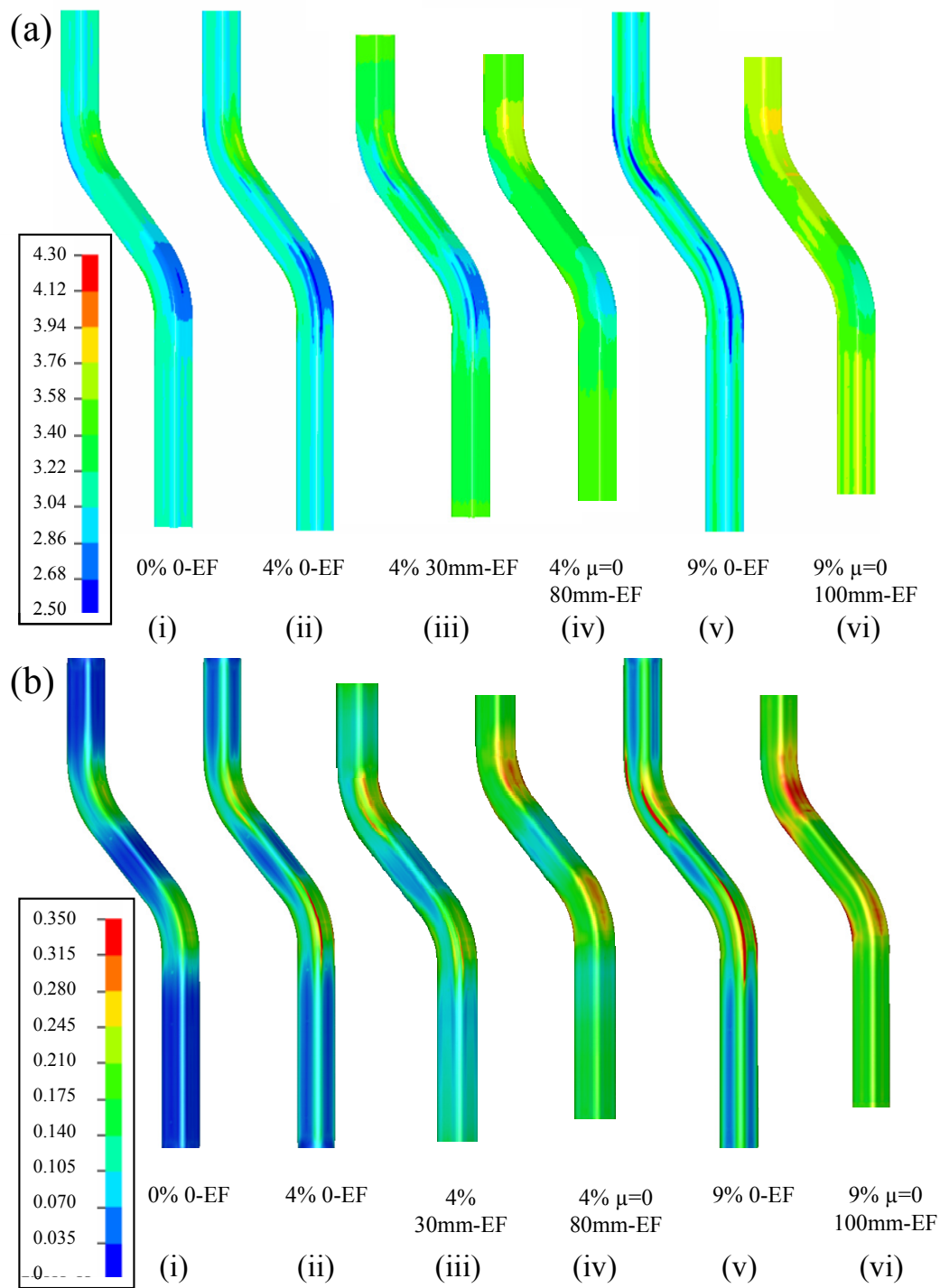


Figure 6.14: Contours of (a) thickness; and (b) effective plastic strain: (i) zero-percent expansion and zero end-feed; (ii) four-percent expansion and zero end-feed; (iii) four-percent expansion with a frictionless condition and 80 mm of end-feed; (iv) four-percent expansion with 30 mm of end-feed; (v) nine-percent expansion with zero end-feed; and (vi) nine-percent expansion with a frictionless condition and 100 mm of end-feed.

In both the four- and nine-percent expansion cases with zero end-feed, strain localization was observed along the outside of section D and near the neutral axis of section B of the s-rail, as shown in Figure 6.15. Similar strain localization has been observed by Dymnt [18] in the hydroforming of pre-bent steel tubes with circumferential expansion, and initiation of this instability corresponded well with the failure of the part during his validation experiments. As the level of circumferential expansion increases, the degree of strain localization also becomes more pronounced. Through the use of end-feed, strain localization was suppressed for the four- and nine-percent expansion conditions. However, strain localization could only be prevented under frictionless conditions in the nine-percent expansion case; hence this represents a limiting case that likely could not be achieved experimentally.

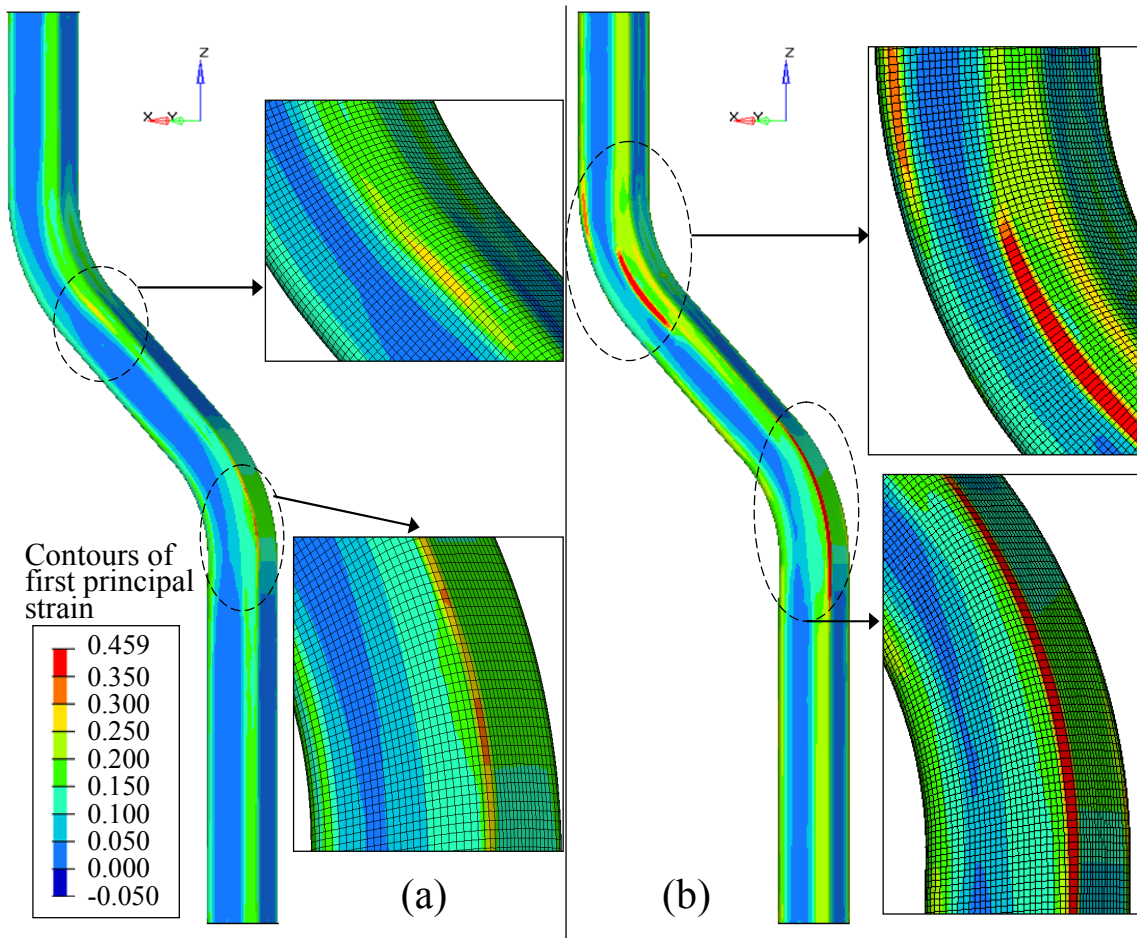


Figure 6.15: Strain localization observed in high-pressure hydroforming simulations using: (a) four-percent expansion with zero end-feed; and, (b) nine-percent expansion with zero end-feed.

6.3.2.2 Crash Response of High-Pressure Hydroformed S-Rails

The predicted peak load and energy absorption per unit mass versus the crush distance are presented in Table 6.3 and Figure 6.16 for the tubes modelled in the high-pressure hydroforming simulation, while the force and energy versus crush displacement curves are shown in Appendix E, for brevity. Due to variations in the final masses of the s-rails resulting from end-feed during the hydroforming operation, the specific force and energy response are presented, which allows a more direct comparison.

The increase in circumferential expansion from 0% to 4% without end-feed results in a 5.9% increase in energy absorption per unit mass at the 120 mm crush distance; however, a further increase in circumferential expansion to 9% results in a reduction of energy absorption by 0.9%. Here, the energy absorption at 120 mm of crush distance is reported since it is the highest crush distance reached by all of the s-rails modelled. The crush distances, which can be seen in Appendix E, is a consequence of the s-rail impact mass and velocity being held constant for the various simulation conditions. The s-rail hydroformed with 9% expansion and zero end-feed had elements that experienced strain localization during the hydroforming simulation, which resulted in significant regions of exaggerated thinning and straining. Consequently, the predicted crash results for the s-rail hydroformed with 9% expansion and zero end-feed should not be considered, since the material would likely fail during hydroforming. The use of end-feed in hydroforming of s-rails that underwent 4% expansion resulted in a 7.7% increase in energy absorption per unit mass relative to the 0% expansion condition, which is only slightly higher than the case without end-feed; however, when formed under frictionless conditions, the energy absorption increased by 20.4%, which is a limiting case. Interestingly, the predicted energy absorption increased by 23.1% relative to the 0% expansion condition for the s-rail hydroformed under frictionless conditions with 9% circumferential expansion and maximum end-feed. The increases in peak load and energy absorption in the s-rails hydroformed with circumferential expansion are due to increased thickness in the bend section and work hardening of the material during hydroforming. Increased levels of end-feed reduced the degree of thinning and increased the work hardening in the straight sections of the s-rail, A and E, which results in higher peak loads and energy absorption during crash.

Table 6.3: Summary of s-rail crash results for each hydroforming process.

Expansion (%)	End-Feed	Mass (kg)	Coefficient of Friction	Peak Load Per Unit Mass (kN/kg)	Percent Increase in Peak Load Per Unit Mass w.r.t. Zero Expansion Case	Energy Per Unit Mass at 120 mm of Crush Displacement (kJ/kg)	Percent Increase in Energy Per Unit Mass w.r.t. Zero Expansion Case
0	None	2.00	0.08	34.0	0.0	2.21	0
4	None	2.00	0.08	38.4	12.9	2.34	5.9
	Max (30mm)	2.13	0.08	39.1	15.0	2.38	7.7
	Max (80mm)	2.26	0	42.5	25.0	2.66	20.4
9	None	2.00	0.08	38.4	12.9	2.32	5.0
	Max(100mm)	2.35	0	41.9	23.2	2.72	23.1

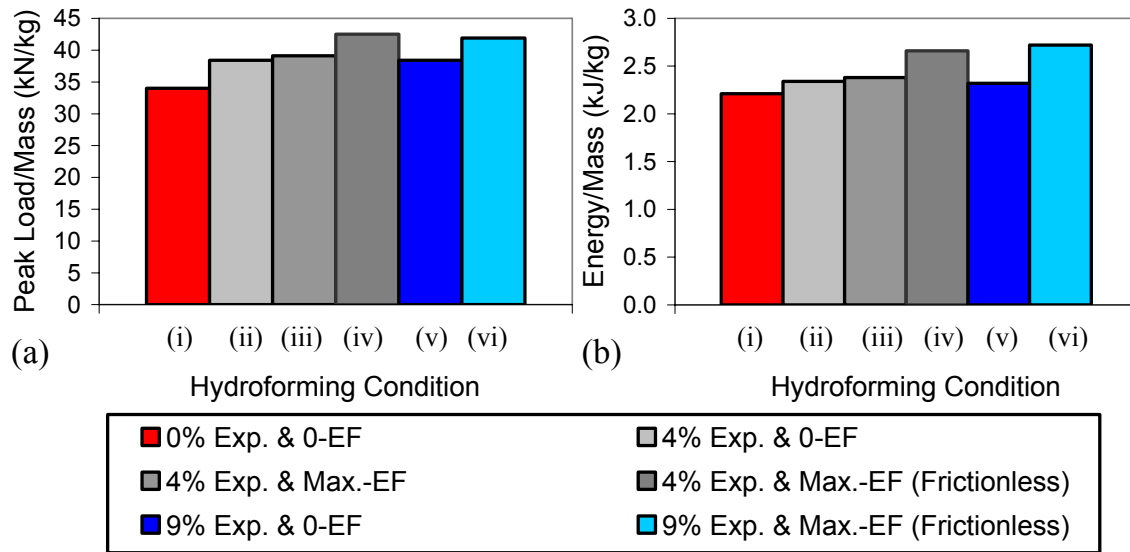


Figure 6.16: Predicted (a) force; and (b) energy per unit mass versus crush distance for hydroformed s-rails: (i) zero-percent expansion and zero end-feed; (ii) four-percent expansion and zero end-feed; (iii) four-percent expansion with 30 mm of end-feed; (iv) four-percent expansion with a frictionless condition and 80 mm of end-feed; (v) nine-percent expansion with zero end-feed; and (vi) nine-percent expansion with a frictionless condition and 100 mm of end-feed.

6.3.3 Summary

The pressure versus end-feed schedule used in this study has not been optimized since such an effect was considered beyond the scope of this work; however, general trends in the effect of hydroforming with circumferential expansion and end-feed on crush response were determined. High frictional forces caused lock-up of the material against the die, which does

not allow significant thickening in the bend regions of the s-rail. To reduce these high frictional forces, the internal pressure during end-feed was reduced, which allowed material to move more freely. However due to a lack of internal support, buckling occurred at the inside of the bends at the transition with the straight end sections, A and E, as shown in Figure 3.12. The buckling limit could have been avoided by reducing the amount of end-feed stroke but at least an 80 mm end-feed stroke is required for the effects of end-feed to be experienced within the bend region, as shown in the frictionless cases. There appears to be a narrow forming window within which the aluminium alloy s-rails can be expanded circumferentially using hydroforming with end-feed.

A summary of the predicted peak load and energy per unit mass at 120 mm of crush distance for the various s-rail hydroforming conditions was shown in Figure 6.16. Circumferential expansion of the s-rail during hydroforming will increase the overall effective plastic strain and work hardening, which has been shown to play a major role in the crash response of the s-rail. The degree of thinning, particularly in the corners, due to the high-pressure hydroforming process was also shown to increase, while the low-pressure process had little effect on thickness distribution for the square cross-section examined. Although the large differences in thickness between the inside and outside of the bend were shown to cancel each other in terms of the crash response of the low-pressure hydroformed s-rail, an overall lower thickness in the hinge regions of the s-rail will reduce the energy absorption capability.

The use of end-feed in hydroforming can suppress material failure and has the potential to significantly increase the energy absorption within the s-rail under optimized pressure-end-feed schedules. The main challenge in end-feeding the s-rail is to overcome frictional lock-up or wrinkling of the material and yet maintain enough internal pressure within the tube to prevent collapse, which can only be done by minimizing the coefficient of friction. For the current process, end-feed during hydroforming did increase the level of plastic strain and thickness within the straight sections of the s-rail, but not in the bend regions, where two of the three hinges occur during crash. Under frictionless conditions, increased levels of work hardening and thickness increases can be achieved, particularly in the hinge regions of the s-rail, which results in significant increases in the crash response.

Chapter 7

Discussion

The crash performance of an s-rail is governed by the geometric features of its design, the inherent material properties of the as-received material, and changes in those properties due to the fabrication techniques employed. Of the various methods in which s-rails may be fabricated, the tube bending followed by hydroforming route is commonly used due to the structural performance and economic advantages discussed in Chapter 1. In this chapter, the variables influencing this fabrication route and the implications on crash response are isolated and discussed. The discussion is divided into three sections: the first addresses the tube bending and hydroforming aspects of s-rail fabrication, and the effects of the forming variables on its' characteristics; the second section elaborates on the crash response of s-rails and the geometric design, material properties and forming variables that govern its performance. Finally, the third section outlines the significance of these findings to improving the design of s-rails for increased energy absorption by redesigning the s-rail examined in this thesis for a crash event.

7.1 Influence of Tube Bending and Hydroforming on the Characteristics of S-Rails

The tube bending operation used to fabricate an s-rail results in thinning on the outside and thickening on the inside of the bends, which are locations at which two of the three hinges form during collapse (Figure 1.3). Also, axial strain, tensile and compressive, occurs on the outside and inside of the bend, respectively. The major variable affecting the degree of thickness and strain changes is the bend severity. To this effect, bend severity increases

cause the level of thickness change and strain in the bend region to intensify. To determine the effect of initial tube thickness and material properties on the strains in the bend region, strain measurement data (Figure 2.10) from several researchers [6,18,137,138,139,140] on aluminium and steel tubes bent at 100% boost was examined and compared to that of this thesis. After careful comparison of the strains, which are given in Table 7.1 and shown graphically in Figure 7.1, an interesting observation can be made. The level of strain at the outside and inside of a bend of given R/D ratio for all of the steel and aluminium alloy materials and gauges is very similar. In fact, the scatter in the axial and hoop strain measurements at the inside and outside of the bend falls within the $\pm 3\%$ strain error associated with the circle grid measurement technique employed. Also note that these tubes were all bent under different tooling set-ups, and that for the same boost and R/D ratio all of the strains are close to the analytical prediction. Based on these findings, it is apparent that the level of strain resulting from mandrel-rotary draw bending of tubes is mainly dictated by the final bend geometry (R/D ratio) and is nearly independent of the tube thickness and strength.

Table 7.1: Axial and circumferential strain measured at the center of the inside and outside of the bend for various tubes bent under a 100% boost condition. Theoretical estimate of axial strain at outside of bend is based on beam bending theory [112]. The strain data sources for the various materials are: (i) Δ - Oliveira et al. [6] and Gholipour et al. [137]; (ii) φ - Grantab [138]; (iii) ξ - Dyment [18]; (iv) β - Bardelcik [139]; and (v) α - Sorine [140].

Source	Material	R/D Ratio											
		2.5				2.0				1.5			
		Bend Location				Bend Location				Bend Location			
		Outside		Inside		Outside		Inside		Outside		Inside	
		Axial	Circ.	Axial	Circ.	Axial	Circ.	Axial	Circ.	Axial	Circ.	Axial	Circ.
Theory	Any	0.2	-	-	-	0.25	-	-	-	0.33	-	-	-
Current thesis	3 mm AA5754	0.20	-0.02	-0.15	0.02	0.26	-0.02	-0.15	0.02	0.32	-0.02	-0.18	0.02
Δ -Oliveira et al. & Gholipour et al.	3.5 mm EN-AW5018	0.21	0.01	-0.16	0.01	0.26	-0.03	-0.23	0.06	-	-	-	-
	2.0 mm EN-AW5018	0.20	0.01	-0.15	0.01	0.24	-0.05	-0.23	0.03	-	-	-	-
φ -Grantab	1.5 mm HSLA350	-	-	-	-	0.25	-0.04	-0.18	0.04	-	-	-	-
	1.8 mm HSLA350	-	-	-	-	0.26	-0.03	-0.20	0.04	-	-	-	-
	1.8 mm DP600	0.19	-0.03	-0.18	0.03	0.25	-0.03	-0.20	0.03	0.32	-0.03	-0.26	0.03
	1.8 mm DDQ	-	-	-	-	0.26	-0.03	-0.21	0.04	-	-	-	-
ξ -Dyment	1.5 mm AKDQ	0.20	-0.05	-0.17	0.03	0.26	-0.06	-0.23	0.06	-	-	-	-
β -Bardelcik	1.8 mm IF	-	-	-	-	0.26	-0.08	-0.21	0.06	-	-	-	-
α -Sorine	1.8 mm DDQ	-	-	-	-	0.25	-0.06	-0.21	0.02	-	-	-	-
	1.8 mm HSLA350	-	-	-	-	0.25	-0.06	-0.21	0.02	-	-	-	-
	1.8 mm DP600	-	-	-	-	0.28	-0.05	-0.21	0.02	-	-	-	-

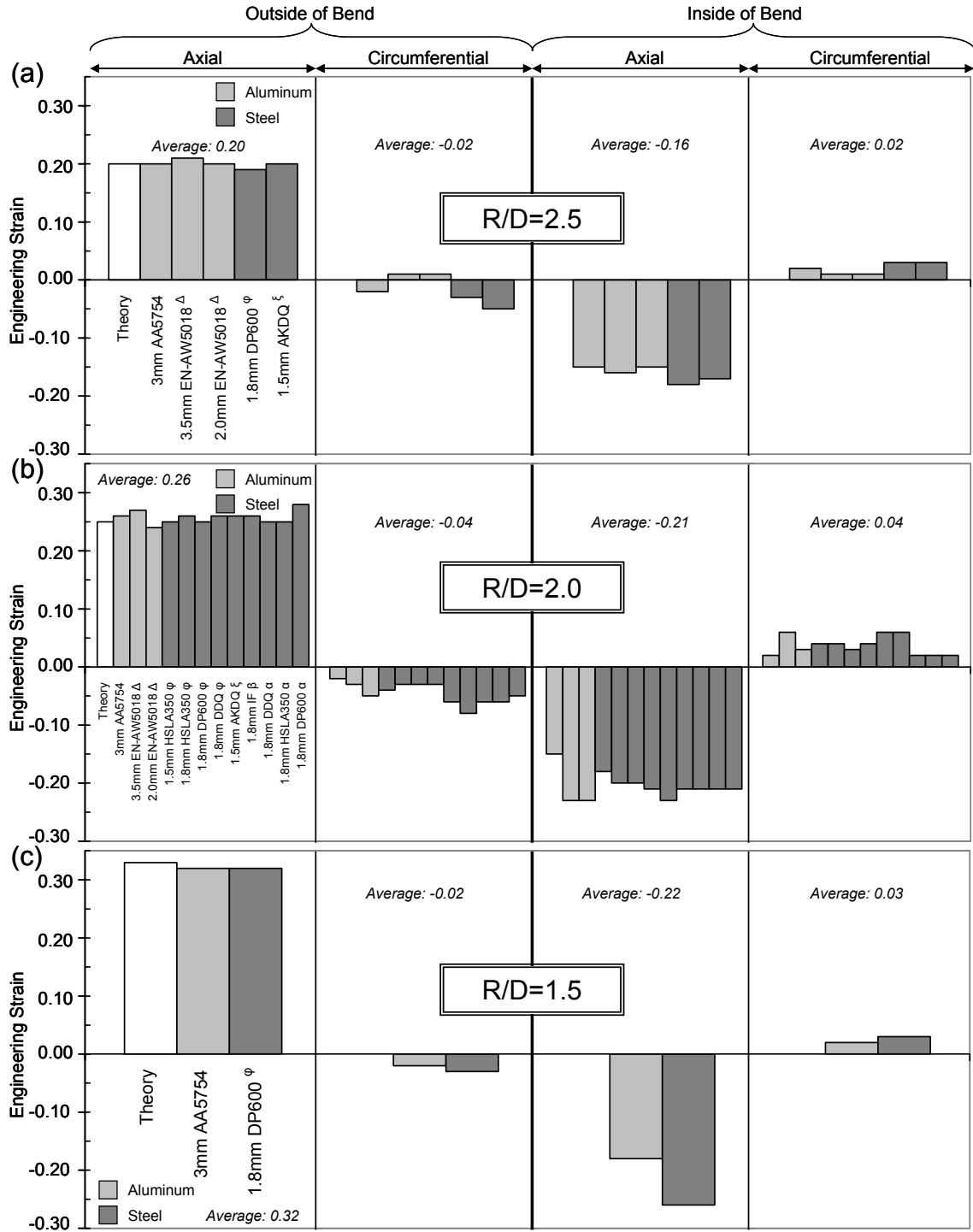


Figure 7.1: Axial and circumferential strain measured at the center of the inside and outside of the bend for various tubes bent under a 100% boost condition at: (a) $R/D=2.5$; (b) $R/D=2.0$; and (c) $R/D=1.5$. Theoretical estimate of axial strain at outside of bend is based on beam bending theory [112]. The strain data sources for the various materials are: (i) Δ -Oliveira et al. [6] and Gholipour et al. [137]; (ii) ϕ - Grantab [138]; (iii) ξ - Dyment [18]; (iv) β - Bardelcik [139]; and (v) α - Sorine [140].

Boost in bending is an approach that can be used to further increase the overall thickness in the bend region of the tube by axially feeding material into the deformation zone during bending. Boost in bending will also increase the degree of effective plastic strain on the inside of the bend while reducing the effective plastic strain on the outside of the bend. On average, the effective plastic strain over the entire section increases due to boost in bending. Bending with boost has been shown to consume less material ductility during bending, which allows a higher subsequent formability of the tube in hydroforming [137,139,140], which is attractive when considering lower formability materials such as advanced high strength steels. In this work, bending with greater than 100% independent collet boost has been shown to strengthen the s-rail by increasing the overall thickness and work hardening.

For a given material, the recorded process variables during bending, such as bend torque, pressure die feed load and mandrel load are sensitive to the mandrel clearance, wiper die rake angle, lubricant and clamping loads. To obtain the best quality bends, careful lubricant selection is required to eliminate scoring and pick-up in aluminium alloys, and minimize mandrel drag and overall load requirements of the bender. Usage of a mandrel with a larger clearance has the benefit of reducing the frictional loads on the tube, while also allowing greater tube ovalization. When bending tube that will undergo subsequent hydroforming, tube ovalization is not necessarily a disadvantage as it can assist in allowing a better (easier) fit of the part within the tight tolerances of a hydroforming die. Generally speaking, the mandrel clearance needs to be smaller when bending higher strength and thinner walled tube, which is more prone to wrinkling.

The zero-percent expansion hydroforming operation without end-feed results in a very small change in the thickness and axial strain within the square cross-section s-rail. However, when this low-pressure process is used to form s-rails with a rectangular cross-section, significant changes in thickness and strains do occur. In particular, s-rails hydroformed with greater section depth (2:1 vs. 1:1 or 1:2 aspect ratios) experience increased work hardening, and greater thickening on the inside and thinning on the outside of the bends. The circumferential strains in both the straight and bend sections of the s-rail due to the low-pressure hydroforming process change significantly, particularly in the corners of the section, and do not exhibit a clear dependence on section depth. The resulting thickness and axial strain distributions in the hydroformed s-rail are mostly influenced by the bending

operation, whereas the circumferential strain that is nearly zero after bending is mostly influenced by the hydroforming operation. To further extend the consideration of manufacturing processes on crash performance, numerical models were developed of the so-called high-pressure process. This process introduces circumferential expansion which tends to decrease thickness in the corners of the section and can also utilize end-feeding to increase the overall thickness in the s-rail. Note that the additional strain associated with both circumferential expansion and end-feed will result in further work hardening. The high-pressure process results in increased thickness and axial compressive strains at the ends of the straight sections, A and E of the s-rail, but not in the bend regions due to friction. The thicker section A increases the resistance to deformation of the third hinge that forms at the base of the s-rail during crash. The lack of end-feed into the bend region is mainly attributed to the difficulty in overcoming frictional forces that lock-up the material against the die wall. One disadvantage of the hydroforming process with circumferential expansion is that it further consumes material ductility, particularly in the bend regions, which may lead to material failure.

The finite element models of tube bending and hydroforming developed in this work provide an accurate means by which to predict the final geometry, strains, thickness changes and springback. A number of material representations were employed in the forming simulations, with the anisotropic Barlat (1989) material model providing a slightly better representation of the actual deformation. Overall, the forming simulations utilizing the isotropic von Mises and Zerilli-Armstrong material representations provided predictions of final geometry, thickness and strain that were in very good agreement with the experimental results. Of particular importance in accurately simulating the forming experiments is the coefficient of friction prescribed for the contact treatment between the various interacting tools with the workpiece. The twist compression tests employed to determine the coefficient of friction between the various tool-lubricant-workpiece interactions provided excellent data to better capture the frictional forces acting on the workpiece. The robustness of the modeling techniques developed here have been further tested, since they have since been successfully utilized by Grantab *et al.* [84,138] to simulate the forming of various steel s-rails. These numerical models are an invaluable design tool that can be used to provide additional insight into the tube bending and hydroforming operations that is not available in

the experiments. A limitation to the current simulation technique is the lack of a material model that can predict material failure, such as the damage-based constitutive model implemented by Gholipour [137].

7.2 Variables Governing the Crash Response of S-Rails

Finite element models of the s-rail crash event that consider the entire fabrication history have been developed and shown to accurately predict the crush response in terms of geometry, force and energy absorption. The simulation tools developed in this thesis have allowed the variables influencing the crush response to be isolated and assessed, which cannot be done through experiment alone. A ranking indicating the significant variables and the degree to which they influence the crash response of aluminium hydroformed s-rails is shown in Figure 7.2. To facilitate this discussion, a summary of the sensitivity of the force and energy response to each of these variables is shown in Figure 7.3, and structured such that the variables are focused upon in order of greatest influence on s-rail crash response.

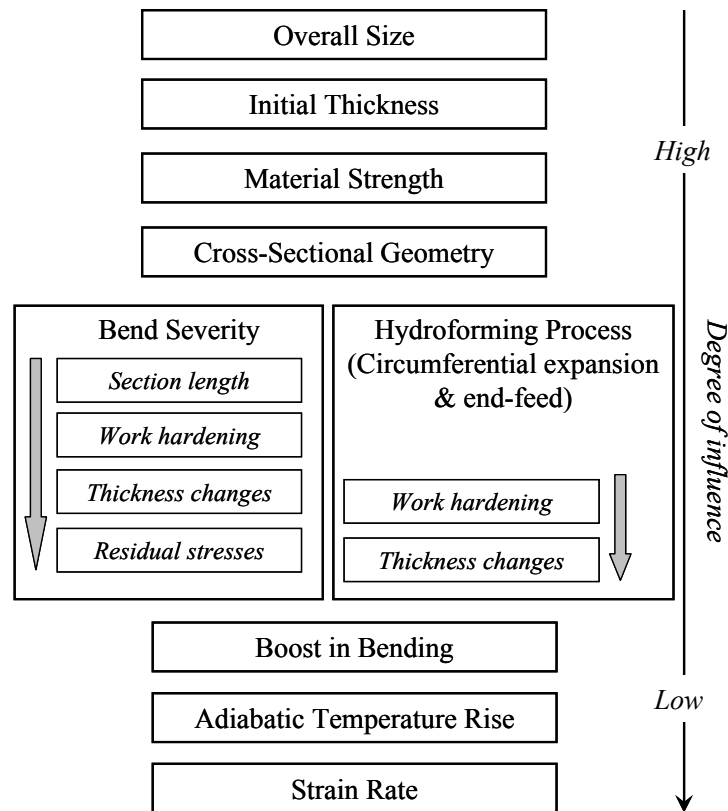


Figure 7.2: Ranking chart indicating variables and the degree to which they affect the crash response of aluminium alloy hydroformed s-rails.

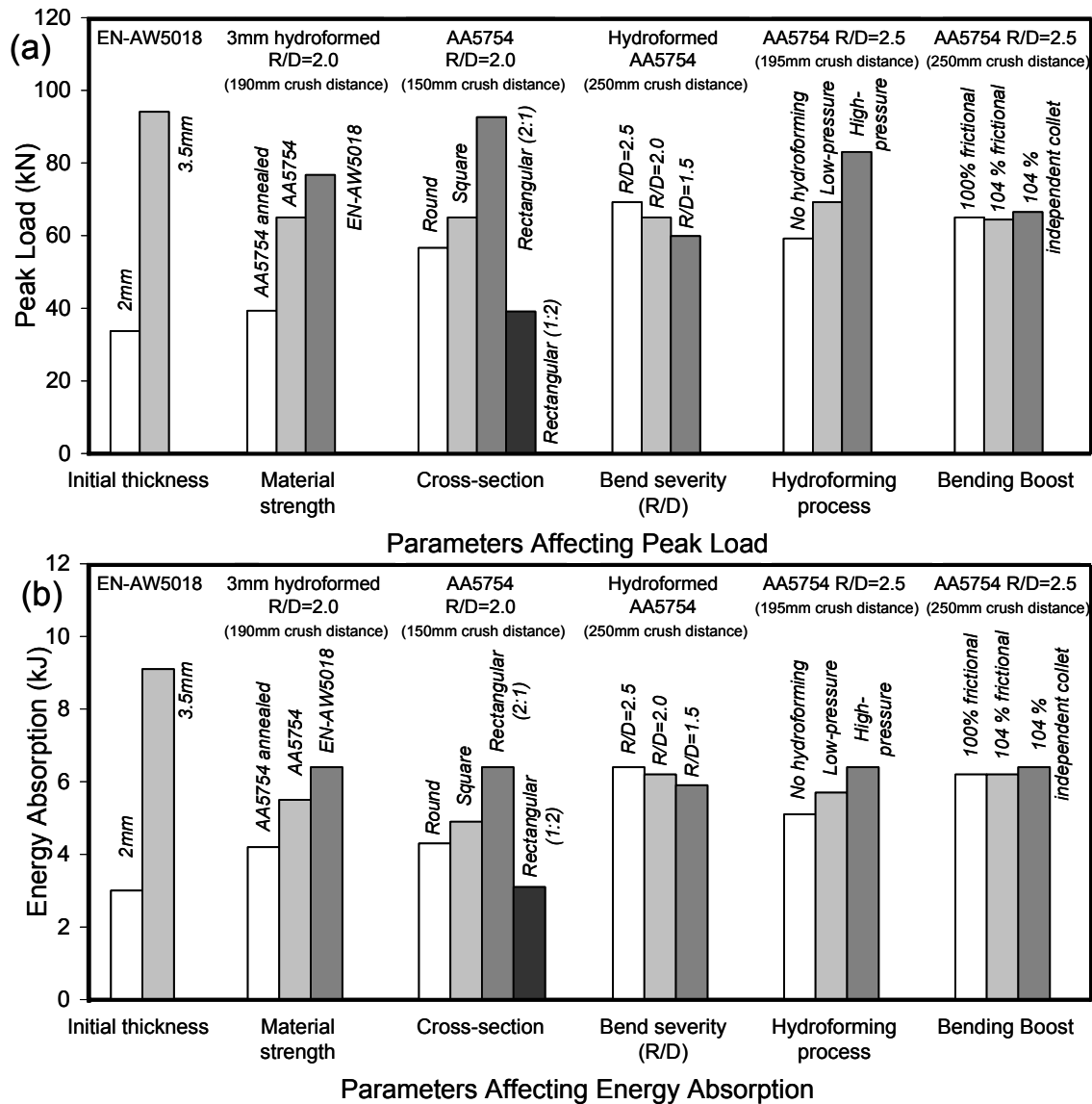


Figure 7.3: Predicted (a) force and (b) energy absorption of the various parameters affecting s-rail crash response.

For a given material strength, the overall size of an s-rail in terms of length, width, section dimensions and thickness plays the largest role in determining the crash response. To this end, an overall “larger” sized s-rail will absorb greater energy during a crash event. The energy absorption capability of an s-rail is ultimately determined by the ability of the three hinges to resist the bending moments generated by impact. Therefore, a reduction in the length of the moment arm acting at the location where the hinges form, by manipulating the lengths of sections A, C and E, will increase the energy absorbing capability of the s-rail. In particular, the length of section C within the s-rail is the most influential parameter in

determining the overall stiffness and resistance to deformation, since it interacts directly with two of the three hinges, which are located at the bends. In the limiting case where the length of section C approaches zero and the s-rail becomes an axial crush member, the crash response in terms of geometric optimization is maximized.

For a given size, cross-section and material strength, the most dominant variable controlling the crash response of an s-rail is the initial tube thickness, as shown in Figure 7.3. A 75% increase in material thickness from 2 to 3.5 mm increased the peak load and energy absorption by up to 2.8 and 3 times, respectively, which is consistent with findings by Abramowicz and Wierzbicki [134] using analytical techniques. The larger thickness in the locations of the s-rail where hinges form results in a greater stiffness and resistance to bending and collapse of the cross-section. In turn, this increases the energy absorption capability of the s-rail. By interpolating these results, one can estimate that a 20% increase in a tube that is 3 mm thick results in roughly a 33% increase in peak load and energy absorption. In comparison, a 20% increase in material strength for an s-rail formed from a 3 mm thick tube was shown to increase the energy absorption by only 16% (Figure 7.3). Therefore the influence of thickness on the crash response of s-rails is significantly greater than the effect of material strength, which is the next most significant variable to thickness and the overall size.

The effect of material strength on the crash response of hydroformed s-rails was also investigated by Grantab [138] by performing a material substitution exercise in which HSLA350 and DP600 steel alloys were used to replace DDQ in 1.8 mm wall thickness s-rails of the same geometry as those investigated in this thesis. The dependency of energy absorption on the material strength for the aluminium alloys examined in this thesis and the steel materials examined by Grantab [138] are shown in Figure 7.4. Note that the thickness of the substituting HSLA350 and DP600 steel alloys were also 1.8 mm. Performing a simple linear regression on the data revealed an interesting trend that allows the following guideline, which is useful for the design engineer, to be made: the increase in energy absorption is roughly 86% of the increase in material strength. This guideline, based on the laboratory-scale s-rail examined in this thesis, is consistent with the findings of a numerical investigation examining a commercial s-rail by Reid [85], which suggests that the increase in energy absorption is 73% of the increase in material strength.

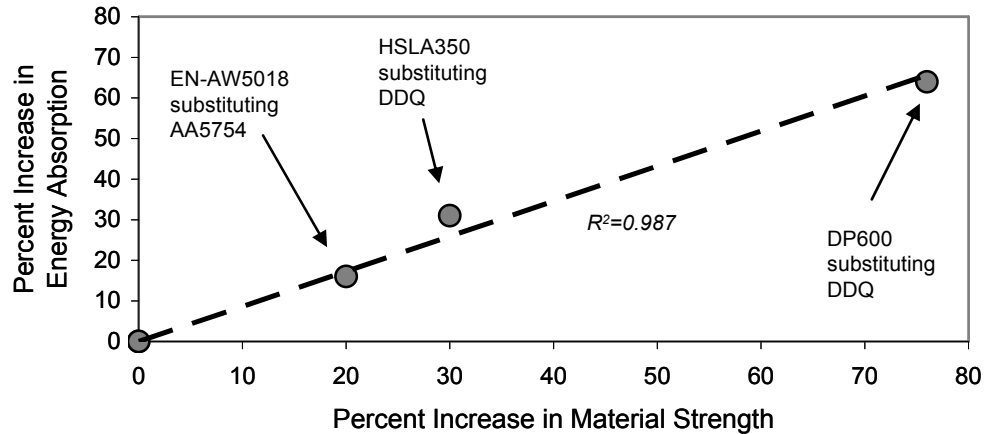


Figure 7.4: Increase in energy absorption versus increase in material strength data for various material substitutions. The data for the HSLA350 and DP600 substitutions for DDQ steel are taken from Grantab [138].

The geometry of the cross-section significantly contributes to the energy absorbing capability of the s-rail by affecting the hinge moment of rotation [74,75,76,77,78,79,80]. A change in s-rail cross section that increases the second moment of area will increase the resistance to bending of the hinges. In addition, an s-rail with a cross-section that better maintains its shape, and therefore its second polar moment of area, during collapse will ultimately absorb greater energy. To this effect, foam filled tubes have been shown to provide substantial gains in energy absorption by better supporting the sectional collapse of the hinges within the s-rail during crash [141]. The hydroformed s-rail with a rectangular cross-section aspect ratio of 2:1 (Figure 3.10) had the largest second polar moment of area (Table 3.4) and exhibited the largest energy absorbing capability for the various sections examined, as shown in Figure 7.3. The findings that the cross-section of the s-rail plays a significant role in s-rail crash response supports the conclusions of other researchers [73,74].

Increasing the bend severity used in fabrication of the hydroformed s-rails results in increased work hardening, thickness changes and residual stresses in the hinge regions of collapse. These changes to the properties of the hinge regions within the s-rail increase the resistance to deformation during impact resulting in higher peak loads and energy absorption. However, these gains in peak load and energy absorption due to an increased bend severity are partially offset by the longer moment arms acting at the three hinges of the s-rail, which decrease its overall resistance to deformation. Specifically, the overall effect of decreasing the bend severity from an R/D ratio of 1.5 to 2.5, was to increase the peak load and energy

absorption by 10.6% and 6.3%, respectively, which is a relatively small change in comparison to the effects of initial thickness, strength and cross-section (Figure 7.3). The additional benefit of utilizing less severe bends within the s-rail is that less of the material's ductility is consumed during bending. From a material formability standpoint, the reduced consumption of ductility in the bending operation opens the door to utilizing higher strength (less formable) materials with more complex sections for the s-rails. An additional method in which to increase the overall energy absorption capability of the s-rail is to bend with a greater than 100% independent collet boost condition. The tubes bent with a 104% independent collet boost condition experienced an increase in energy absorption by 4.3%. Bending under such a boost condition increases the overall thickness in the bend region, and work hardening at the inside of the bend, which strengthens the s-rail. Boost in bending is the directly controllable design parameter that least influences s-rail crash response, as shown in Figure 7.3.

The crash response of an s-rail is dependant on the type of hydroforming process used to form its cross-section, as shown in Figure 7.3. The predicted peak load and energy absorption of a square cross-section s-rail hydroformed using the high-pressure process are greater by 20% and 12%, respectively, than for the s-rail formed using the low-pressure process. The effects of the type of hydroforming process employed contribute as much (if not more) to the crash response of s-rails as the effects of the bending process, as shown in Figure 7.3. Direct comparison of the predicted crash response between the s-rails formed using the low- and high-pressure hydroforming processes is possible since the hydroforming of the pre-bent tubes was simulated using the same representation of the die geometry, and with tubes of identical mass. As a consequence of the tubes having identical mass prior to forming, the tube's outer diameter was prescribed to be smaller and the thickness larger (Table 3.5). The increased peak load and energy absorption of the s-rail hydroformed using the high- versus low-pressure process is attributed to:

- (i) end-feed, which further increases the thickness and work hardening in the straight sections, particularly at the hinge near the base of the s-rail; and,
- (ii) circumferential expansion, which causes a higher degree of work hardening throughout the s-rail.

A consequence of the increased thickness in the straight sections of the s-rail due to end-feed in the hydroforming process is that the overall mass of the s-rail is increased (7% for the 4% circumferential expansion and 30 mm end-feed case shown in Figure 7.3). Both the increased thickness and strength at the hinge location near the base of the s-rail and the increased strength at the hinges located at the two bends of the s-rail due to the high-pressure hydroforming process increase the overall resistance to deformation. Although the high-pressure hydroforming process is attractive from the point of view of improving the crash response of an s-rail, there are some concerns that can impede its use. The first concern is that the monetary cost of implementing the high- versus low-pressure hydroforming process is greater due to increased requirements on the clamping capacity of the press and the capacity of the end-feed actuators [7]. The second concern is that materials with a lower formability such as 6XXX-series aluminium alloy or dual phase steels may experience failure due to expansion during the high-pressure hydroforming process. The advantage of using the low-pressure hydroforming process is that such a higher strength and lower formability material can be formed to more complex shapes than the high-pressure process.

The strain rate sensitivity for the aluminium alloys investigated in this thesis is very minor [106,107], and its influence on the crash response of s-rails is negligible within the range of strain rates typical of an automotive crash event. For the s-rail examined in this thesis, the average strain rate predicted in the hinge region of deformation during crash is approximately 27 s^{-1} , while the peak predicted strain rate is 140 s^{-1} , which occurs over a small 1.5 ms interval. Therefore, based on these results, there is little need for a constitutive model that considers high strain rate effects for modelling the crash response of aluminium alloy s-rails, as considered in this work. However, it was shown by Grantab [138] that the rate sensitivity of steel alloys, which are generally strain rate sensitive [142], must be considered when simulating the impact of steel s-rails. Failure to consider high strain rate effects when predicting the crash response of steel structures will result in significant under-predictions. For the AA5754 aluminium alloy examined in this thesis, the adiabatic temperature rise considered in the Johnson-Cook material model influences the predicted crash response of the s-rail significantly more than the strain rate sensitivity. Consideration of the adiabatic temperature rise within the Johnson-Cook model utilized in the simulations

results in a lower prediction of energy absorption by up to 2.5%, whereas strain rate effects are increase the prediction of energy absorption by less than 0.5%.

Prediction of the energy absorption of an s-rail utilizing the rate-insensitive: (i) isotropic piecewise linear von Mises; and (ii) anisotropic Barlat (1989); and, rate-sensitive isotropic (iii) Johnson-Cook; and (iv) Zerilli-Armstrong material models are shown in Figure 7.5. The overall crash response of the AA5754 aluminium alloy s-rail is most accurately predicted using the isotropic von Mises material model, followed by the Johnson-Cook material model that utilizes a Voce representation of the hardening response. The disadvantage of utilizing the Johnson-Cook material model when simulating the forming operations in an s-rail is the significant computational cost, which makes it impractical to use with a fine mesh, particularly for simulations of full vehicle crash events.

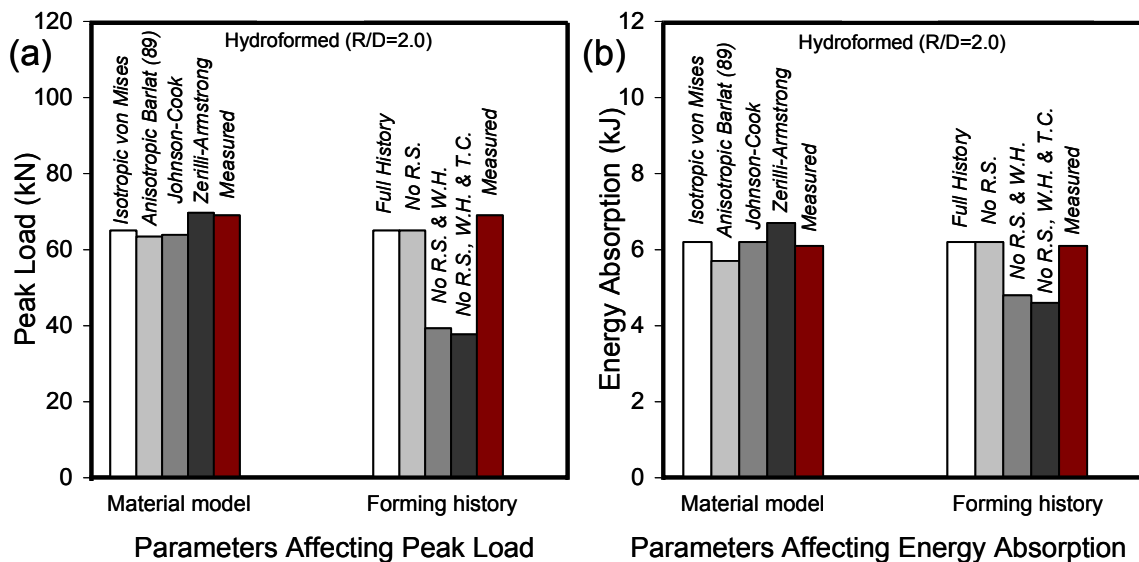


Figure 7.5: Predicted (a) peak load and (b) energy absorption for hydroformed AA5754 s-rails that were bent at $R/D=2.0$: (i) utilizing the various material models examined, and (ii) with various forming history effects isolated.

Accurate predictions of the crash response of s-rails must consider previous material forming history effects such as work hardening, thickness changes and residual stresses, as shown in Figure 7.5. Not accounting for previous material forming history effects due to tube bending and hydroforming operations results in an under-prediction of the force and energy response by up to 42% and 26%, respectively. Neglecting the effects of work hardening during forming comprises roughly 24.7% of the 26% under-prediction of energy

absorption of the s-rail, whereas the effects of thickness change in the bend regions comprise the other 1.3%. The effect of residual stresses due to forming has a negligible effect on the crash response of s-rails, which is consistent with findings by other researchers that have examined stamped parts [99,100,101]. Thickness changes in the s-rails due to tube bending and hydroforming using the low-pressure process do not play a significant role in the crash response, which is contrary to findings by other authors [85] based on sheet metal stamped components. This discrepancy is a consequence of the increases in stiffness and resistance to deformation on the inside of the bend (due to thickening of the tube) cancelling the decreases in stiffness and resistance to deformation on the outside of the tube (due to thinning).

Particular care should be given to selecting the element formulation to represent the s-rail during crash within a finite element model. The fully integrated element formulation, which served the forming models so well, performed very poorly in the crash models, and exhibits very strong mesh sensitivity, as shown in Figure 7.6. These numerical issues are likely attributed to the shear locking phenomena associated with shell elements under buckling type loads. Implementation of the Belytschko-Lin-Tsay element formulation within the crash models provided predictions of crash response in better agreement with the experiment. Much less mesh sensitivity was observed for this element type versus the fully-integrated element. The finer 2.5 mm element size mesh discretization implemented in the models was found to be in better agreement with the experimentally measured values than the coarser 5 and 7.5 mm element sized meshes.

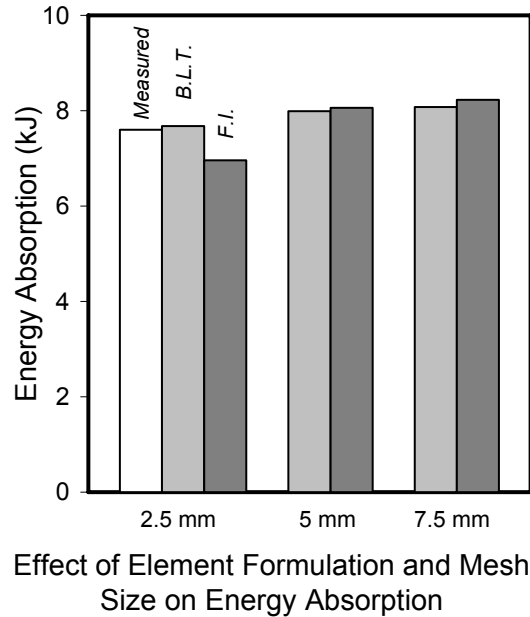


Figure 7.6: Influence of element formulation and mesh size on the predicted energy absorption of hydroformed s-rails. B.L.T.- Belytschko-Lin-Tsay [121]; F.I.-fully integrated [31].

7.3 Demonstration of S-Rail Crash Response Improvement through Better Design and Forming Techniques

In the discussion up to this point, initial tube thickness, material strength, cross-section geometry, bend severity, hydroforming process and boost in bending have been shown to significantly affect the crash response of s-rails. In the design of an s-rail for improved crashworthiness, these parameters and the nature of the hydroforming process are specified by the designer under some constraints, i.e. mass, size, formability, cost, etc. The aim of the work presented in this section is to demonstrate the manner in which the crash resistance of the 3 mm AA5754 hydroformed s-rail bent at R/D=2.0 can be improved (increased) through the knowledge developed in this thesis.

The constraints of this problem are such that the initial mass of the aluminium alloy s-rail, and the overall width and length, are the same as the baseline design (Figure 2.3). The validated modeling techniques for bending, hydroforming and crash employed throughout this work are used here with an isotropic piecewise linear representation of the hardening response with a von Mises yield rule. The following design and process variables were focused upon to improve the energy absorption of the s-rail:

- material strength: fabricate s-rail using higher strength EN-AW5018 aluminium alloy,
- cross-section: utilize a rectangular shaped die with an aspect ratio of 2:1 as shown in Figure 3.10,
- bend severity: bend at an R/D ratio of 2.5, which was shown to provide greater energy absorption,
- hydroforming process: use a process with 4% circumferential expansion and 30 mm end-feed, and
- boost in bending: bend using a 104% independent collet boost condition.

As a consequence of using the hydroforming process with 4% circumferential expansion and end-feed, a 73.03 mm outer diameter tube of 3.22 mm thickness (Table 3.5) was used to fabricate the s-rail and ensure equal mass with the baseline.

7.3.1 Crash Results and Summary

The undeformed geometry of the baseline and so-called “improved” s-rail and deformed geometry after impact of a 1,134 kg mass (Section 2.5.2) at 3.33 m/s (Table 2.7) are shown in Figure 7.7. The overall crush distance of the improved s-rail is much less than that of the baseline. The force and energy response comparison between the baseline and improved s-rail is shown in Figure 7.8, upon which the overall energy absorption of the improved s-rail is 6.32 kJ at 90 mm of crush distance versus 3.61 kJ for the baseline. The improved s-rail experienced an increase in energy absorption over the baseline by a factor of 1.75. Further increases in energy absorption can be accomplished by changing the overall size (width and length) of the s-rail and utilizing a thicker tube, as discussed previously.

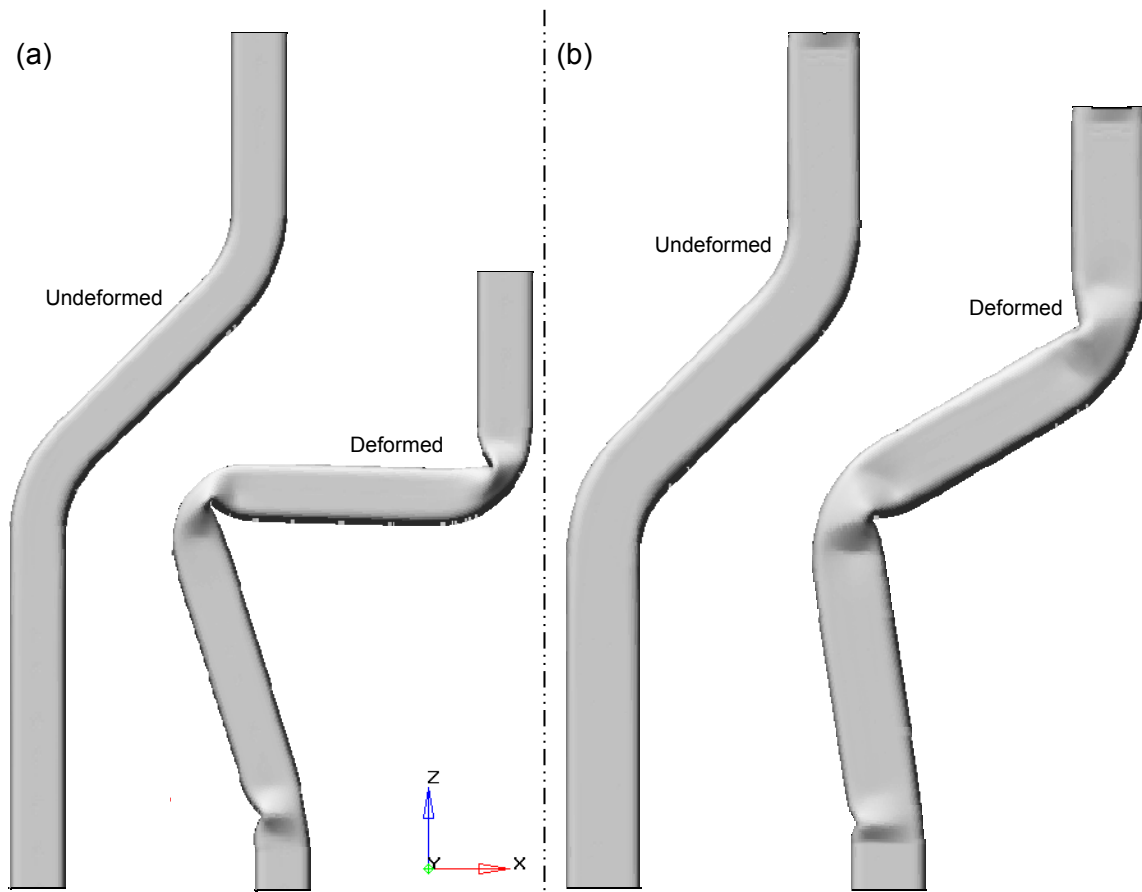


Figure 7.7: (a) Baseline s-rail; and, (b) improved s-rail before and after impact.

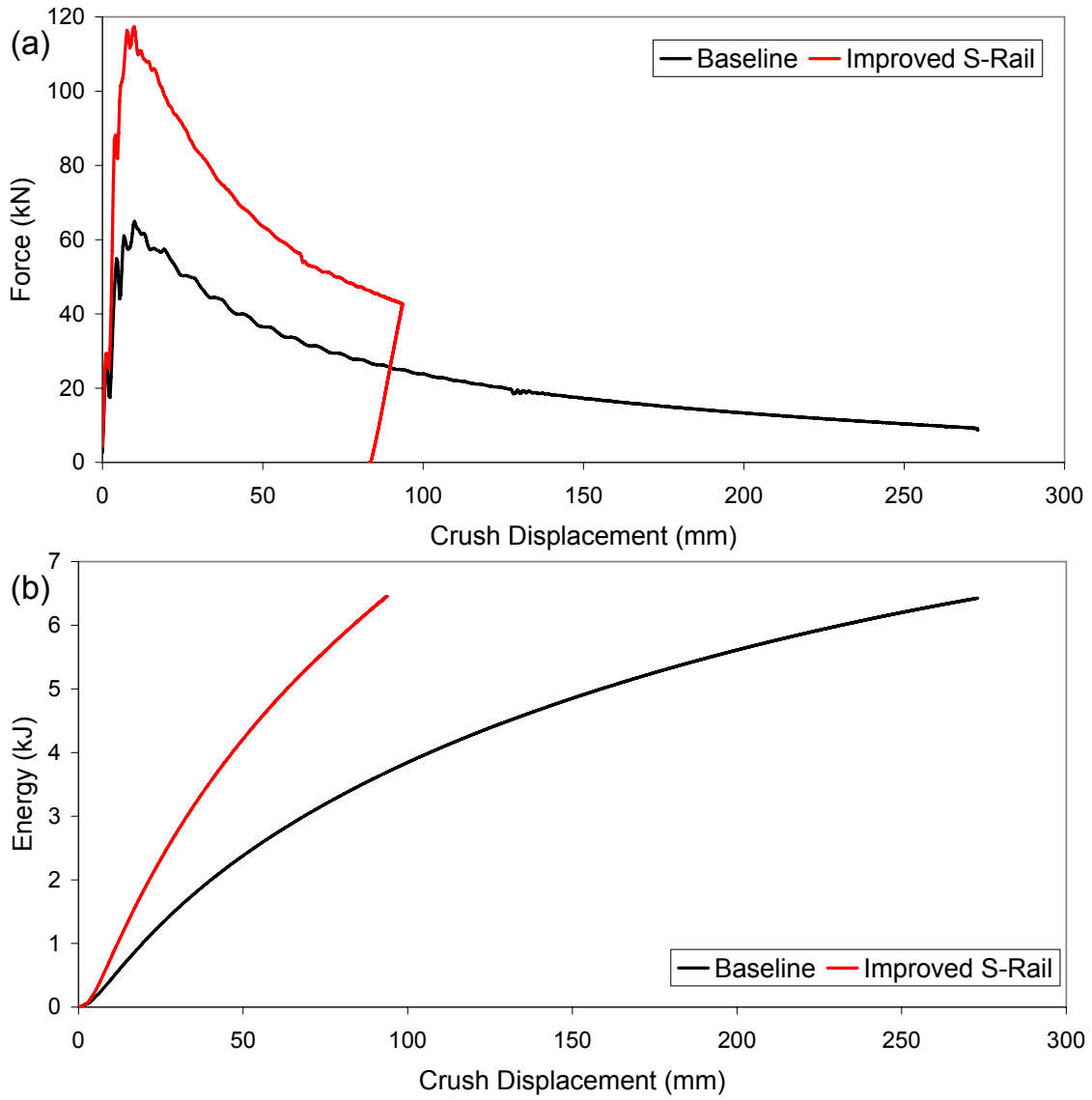


Figure 7.8: (a) Force; and, (b) energy absorption comparison between the baseline and improved s-rails.

Chapter 8

Conclusions and Recommendations

8.1 Conclusions

The following conclusions, which are grouped in terms of crash response, tube bending, hydroforming and numerical modelling, can be made from this work:

8.1.1 S-Rail Crash Response

1. Through the knowledge developed in this work, there now exists data and simulation techniques which form the basis upon which a set of design guidelines can be developed to optimize the energy absorption capability of an s-rail or minimize the thickness/mass of an s-rail to meet a given energy absorption requirement.
2. Careful manipulation of the following variables will increase the crash energy absorption capability of the s-rail:
 - decreasing the moment arm at the hinges by reducing the offset distance of the two bends,
 - increasing the initial wall thickness of the s-rail,
 - optimizing the forming process to increase the thickness and work hardening of the material at the local hinge locations,
 - increasing the material strength of the tube used to fabricate the s-rail,
 - increase the second moment of area of the cross-section,

- decreasing the bend severity, and
 - increase boost in bending.
3. The early force-time response in s-rail crash is governed by stress wave propagation effects only up to roughly 5 ms in time, after which dynamic equilibrium is established and discrete wave propagation effects are obscured and diminish.

8.1.2 Tube Bending

1. The process variables during bending are sensitive to the mandrel clearance, wiper die rake angle, lubricant and clamping loads. To obtain the best quality bends, careful lubricant selection is required to eliminate scoring and pick-up, and minimize the overall load requirements of the bender.
2. Bending of a tube results in thinning on the outside and thickening on the inside of the bend, due to the axial strains in those regions. The major variable affecting the degree of thickness change and strain in the bend is the bend severity. As the bend severity increases, the level of thickness and strain changes intensify, as does the degree of work hardening.
3. The level of strain in the bend region of an aluminium or steel pre-bent tube is mainly dictated by the final bend geometry and is nearly independent of the tube thickness and strength.
4. Boost in bending can increase the overall thickness in the bend region and the degree of work hardening at the inside of the bend, which reinforces the s-rail during crash by increasing the overall resistance to deformation of the hinge.

8.1.3 Hydroforming

1. For the square cross-section s-rail, the low-pressure hydroforming operation without end-feed results in no expansion of the tube circumference with only a very small change in the thickness and axial strain. However, the simulations of the rectangular s-rails, hydroformed using the low-pressure process, predicted greater thickness change at the inside and outside of the bend. The

circumferential strains around the s-rail in both the straight and bend sections change significantly from the as-bent condition, particularly in the corners of the section. The resulting thickness and axial strain distributions in the hydroformed s-rail are mostly influenced by the bending operation, whereas the circumferential strain is mostly influenced by the hydroforming operation.

2. The so-called high-pressure hydroforming process with end-feed results in an increase in thickness and axial compressive strains at the ends of the straight sections, A and E, of the s-rail. In addition, greater work hardening is experienced throughout the s-rail since it undergoes circumferential expansion. The increase in thickness and work hardening at the base of the s-rail, and the increased work hardening in the bend regions serve to increase the energy absorption capability of the s-rail. This beneficial effect is limited, however, by friction which prevents a larger level of end-feeding within the bend region.

8.1.4 Numerical Modelling

1. The finite element models of tube bending, hydroforming and crash developed in this work provide an accurate means by which to predict the final geometry, strains, thickness changes, springback and crash response of s-rails.
2. Consideration of material anisotropy in the constitutive representation of the aluminium alloys provides slightly more accurate forming predictions, while the isotropic von Mises material representation performs better for predicting crash response. The simulations utilizing the isotropic von Mises material model are computationally more efficient.
3. By neglecting work hardening effects due to the tube bending and hydroforming operations, an under-prediction of the force and energy response results by up to 41% and 23%, respectively. The residual stresses due to the forming operations had a negligible effect on the crash response. The crash response of bent and hydroformed s-rails are relatively unaffected by the thickness changes at the bend regions. Essentially, the increase in stiffness and resistance to deformation due to

thickening at the inside of the bend is cancelled by the effect of the decrease in thickness at the outside of the tube.

4. The fully integrated element (type 16 in LS-DYNA) performed very well in representing the s-rail in the forming simulations, but very poorly in the crash simulations. The reduced integration Belytschko-Lin-Tsay element formulation provided good results for the forming models and excellent results in the crash model. Both element types exhibit mesh sensitivity, but this effect was stronger for the fully-integrated element.
5. There is little need for a constitutive model that considers high strain rate effects for modelling the crash response of aluminium alloy s-rails due to the inherent rate-insensitive nature of this material.
6. The Voce hardening law provides a better representation of the constitutive response of the aluminium alloy tubes at quasi-static rates when compared to the power law hardening representation.

8.2 Recommendations

The following recommendations are suggested for further research and development.

1. The development of a robust constitutive model that can be used to predict material damage and failure during forming. Such a model would allow the high-pressure hydroforming of a structural member to be better optimized for good crash response within the formability limit of the material.
2. The interaction of the s-rail with the many subcomponents and attachments within a vehicle should be investigated. This would provide a better understanding of the global response of the s-rail in full-vehicle crash.
3. Methods by which s-rails can be further reduced in weight while maintaining their energy absorption capability should be investigated. Such methods would include filling the tube with a crushable foam, adoption of tailor welded tubes, integral stiffeners and the use of variable wall thickness tubes.

References

- [1] <http://corvette-info.tripod.com/id61.html>
- [2] B. Williams. The study of the axial crush response of hydroformed aluminium alloy tubes. Doctoral Thesis, Department of Mechanical Engineering, University of Waterloo, To be completed in 2007.
- [3] F. Vollertsen, A. Sprenger, J. Kraus, H. Arnet. Extrusion, channel, and profile bending: a review. *Journal of Materials Processing Technology* 87 (1999) 1-27.
- [4] J. Yang, B. Jeon, S. Oh. The tube bending technology of a hydroforming process for an automotive part. *Journal of Materials Processing Technology* 111 (2001) 175-181.
- [5] D.A. Oliveira, M.J. Worswick, R. Grantab, B. Williams, R. Mayer. Effect of forming process variables on the crashworthiness of aluminium alloy tubes. *International Journal of Impact Engineering*, Volume 32, Issue 5, May 2006, pages 826-846.
- [6] D.A. Oliveira, M.J. Worswick, G. Khodayari, J. Gholipour. Effect of bending variables on the characteristics of EN-AW5018 tubes for subsequent hydroforming. *Canadian Metallurgical Quarterly*, Vol 46, No2 pp 145-154, 2007.
- [7] T. Altan, G. Ngaile. Tube and sheet hydroforming fundamentals and applications. Recent Development on Tube and Sheet Hydroforming, A Short Course and International Conference, Columbus, Ohio, June 2003.
- [8] R.R. Strange, Tube and Pipe Bending –Principals, methods, tooling, techniques and developments. Tools For Bending Inc., 194 West Dakota Avenue, Denver CO 80223-2195 USA. www.toolsforbending.com
- [9] J. Gillanders. Pipe and tube bending manual. Fabricators & Manufacturers Association, International Rockford, Illinois.
- [10] G. McDaniel. Bending tube with short tangents: meeting the challenge when there is no alternative. *Tube and Pipe Journal*, p.22-23.
- [11] K. Inoue, P.B. Mellor, Radial-draw bending of stainless steel tubes, *Journal of Mechanical Working Technology*, vol.3, pp. 151-166, 1979.
- [12] F. Paulsen, T. Welo. Application of numerical simulation in the bending of aluminium-alloy profiles. *Journal of Materials Processing Technology* 58 (1996) 274-285.

- [13] K. Trana. Finite element simulation of the tube hydroforming process –bending, preforming and hydroforming. *Journal of Materials Processing Technology* 127 (2002) 401-408.
- [14] V.P. Luk'yanov and A.I. Zubkov. Investigation of tube bending on a tube bending machine with mandrel. *Khimicheskoe I Neftyanoe Mashinostroenie*, no. 11, pp.22-23.
- [15] K.P. Staudhammer, L.E. Murr. The effect of prior deformation on the residual microstructure of explosively deformed stainless-steels. *Materials Science and Engineering* 44 (1): 97-113, 1980.
- [16] M. Gold, W.E. Leyda, R.H. Zeisloft. Effect of varying degrees of cold work on stress-rupture properties of type 304 stainless-steel. *Journal of Engineering Materials and Technology-Transactions of the ASME* 97 (4): 305-312, 1975.
- [17] N. Dwyer, M. Worswick, J. Gholipour, C. Xia, G. Khodayari. Pre-bending and subsequent hydroforming of tube: simulation and experiment, *Proceedings of Numisheet 2002*, pp. 447-452, 2002.
- [18] J. Dymant. Effect of the bending process on hydroformability of steel tubes, Masters Thesis, Department of Mechanical Engineering, University of Waterloo, 2004.
- [19] A. Bardelcik, M.J. Worswick. Numerical investigation into the effects of bending boost and hydroforming end-feed on the hydroformability of DP600 tube. *SAE Congress Proceedings 2005*, paper 2005-01-0094.
- [20] A. Bardelcik, M.J. Worswick. The effect of element formulation on the prediction of boost effects in numerical tube bending. *Numisheet Proceedings 2005*.
- [21] J. Gholipour, M.J. Worswick, D. Oliveira. Application of damage models in bending and hydroforming of aluminium alloy tube. *SAE congress proceedings*, 2004.
- [22] J. Gholipour, M.J. Worswick and D.A. Oliveira. Severity of the bend and its effect on the subsequent hydroforming process for aluminium alloy tube. *Proceedings of the 8th international conference on Numerical Methods in Industrial Forming Processes, NUMIFORM 2004*, Columbus, Ohio, 13-17 June 2004, pp. 1089-1094.
- [23] W.C. Wang, K.A. Stelson. Computer aided manufacturing for three-dimensional tube bending with on-line springback compensation. *North American Manufacturing Research Conference 19th 1991*, Rolla, Missouri, pp.70-76.
- [24] D.A. Oliveira, M.J. Worswick, R. Grantab. Effect of lubricant in mandrel-rotary draw tube bending of steel and aluminium. *Canadian Metallurgical Quarterly*, Vol 44, No 1, 2005.
- [25] J.N. Dymant, M.J. Worswick, F. Normani, D.A. Oliveira, G. Khodayari. Effect of endfeed on the strains and thickness during bending and on the subsequent hydroformability of steel tubes. *IBEC 2003 Conference Proceedings*, pp. 717-722, 2003.
- [26] F. Normani. Analytical modelling of tube bending and hydroforming. Masters Thesis, Department of Mechanical Engineering, University of Waterloo, 2004.

- [27] F. Stachowicz. Bending with upsetting of copper tube elbows. *Journal of Materials Processing Technology* 100 (2000) 236-240.
- [28] T. Welo, F. Paulsen, L.J. Solheim. On the use of 3D finite element simulation in design of industrial bending processes for aluminium alloy profiles. *Proceedings of the 4th International MARC Users Conference, Tokyo, Japan, 29 August, 1994.*
- [29] T. Welo, F. Paulsen, K.F. Moen. On the use of numerical simulation for predicting bendability and geometric tolerances of AA7xxx extrusions formed in stretch bending. *Proc. Formability' 94, Ostrava, Czech Republic, 24-27 October. 1994.*
- [30] J.O., Hallquist LS-DYNA – Keyword User's Manual, Version 970. Livermore Software Technology Corporation 2003.
- [31] J.O. Hallquist. LS-DYNA – Theory Manual. Livermore Software Technology Corporation March 2006.
- [32] P. Gantner, H. Bauer, D.K. Harrison, A.K.M. De Silva. FEA – Simulation of bending processes with LS-DYNA. *8th International LS-DYNA Users Conference, Section 2, pp. 33-40, 2004.*
- [33] N. Utsumi, S. Sakaki. Countermeasures against undesirable phenomena in the draw-bending process for extruded square tubes. *Journal of Materials Processing Technology* 123 (2002) 264-269.
- [34] M. Zhan, H. Yang, Z.Q. Jiang, Z.S. Zhao, Y. Lin. A study on a 3D FE simulation method of the NC bending process of thin-walled tube. *Journal of Materials Processing Technology, vol. 129, pp. 273-276, 2002.*
- [35] M. Geiger, P. Hein. New ideas in internal high pressure forming. *Blech Rohr Profile* 2 (1) (1996).
- [36] M. Ahmegotlu, T. Altan. Tube hydroforming – state of the art and future trends. *Proceedings of International Conference on Tube Welding for Hydroforming Applications, Columbus Ohio, September, 1999.*
- [37] N. Asnafi, T. Nilsson, G. Lassl. Tubular hydroforming of automotive side members with extruded aluminium profiles. *Journal of Materials Processing Technology* 142 (2003) 93-101.
- [38] M. Koc, T. Altan. An overall review of the tube hydroforming (THF) technology. *Journal of Materials Processing Technology, vol. 108, pp. 384-393, 2001.*
- [39] F. Dohmann, C. Hartl. Tube hydroforming – research and practical application. *Journal of Materials Processing Technology, vol. 71, pp. 174-186, 1997.*
- [40] F.U. Leitloff, D. Pohler. Tolerances in hydroforming –process layout and tool design. *Hydroforming of Tubes and Extrusions, Volume 1, 1999.*
- [41] A. Birkert, J. Neubert. Tool and part design for tube hydroforming. *Hydroforming of Tubes and Extrusions, Volume I, 1999.*
- [42] H.J. Kim, B.H. Jeon, H.Y. Kim, J.J. Kim. Finite element analysis of the liquid bulge forming processes. *Proceedings of the Fourth International Conference on Technology of Plasticity.*

- [43] P. Ray, B.J. MacDonald. Intelligent control of tube hydroforming processes using finite element analysis. Numiform 2004 Proceedings, pp.1071-1076.
- [44] M. Ahmed, M.S.J. Hashmi. Three-dimensional finite-element simulation of bulge forming. *Journal of Materials Processing Technology* 119 (2001) 387-392.
- [45] W.H. Sillekens, R.J. Werkhoven, B.R. Depoers. Optimisation of hydroforming processes for tubular parts by means of adaptive and iterative FEM simulation. *Proceedings of the Fourth International ESAFORM Conference on Material Forming, Liege, 2001*, pp. 357-360.
- [46] B.J. MacDonald, M.S.J. Hashmi. Finite element simulation of bulge forming of a cross-joint from a tubular blank. *Journal of Materials Processing Technology*, 103 (2000) 333-342.
- [47] B.J. MacDonald, M.S.J. Hashmi. Three-dimensional finite element simulation of bulge forming using a solid bulging medium. *Finite Elements in Analysis and Design* 37 (2001) 107-116.
- [48] M. Krei. State of the art sealing techniques for hydroforming tools. *Hydroforming of Tubes and Extrusions, Volume I, 1999*.
- [49] G.T. Kridli, L. Bao, P.K. Mallick, Y. Tian. Investigation of thickness variation and corner filling in tube hydroforming, *Journal of Materials Processing Technology*, vol. 133, pp. 287-296, 2003.
- [50] C.L. Chow, X. J. Yang. Bursting for fixed tubular and restrained hydroforming, *Journal of Materials Processing Technology*, vol. 130-131, pp. 107-114, 2002.
- [51] Z.C. Xia. Failure analysis of tubular hydroforming. *Journal of Engineering Materials and Technology*, vol. 123, pp. 423-429, 2001.
- [52] P.B. Mellor. Tensile instability in thin-walled tubes. *Journal of Mechanical Engineering Science, Volume 4, No. 3, 1962*.
- [53] J. Tirosh, A. Neuberger, A. Shirizly. On tube expansion by internal fluid pressure with additional compressive stress. *International Journal of Mechanical Sciences*, No. 8-9, pp. 839-851, 1996.
- [54] F. Dohmann, C. Hartl. Hydroforming – A method to manufacture light-weight parts. *Journal of Materials Processing Technology. Vol. 60*, pp.669-676.
- [55] K. Roll. Finite element simulation of internal and external high pressure forming. *Proceedings of the Sheet Forming Technology Conference, Technical University of Stuttgart, June 1995*.
- [56] N. Asnafi. Analytical modelling of tube hydroforming. *Thin-Walled Structures* 34 (1999) 295-330.
- [57] N. Asnafi, A. Skigsgardh. Theoretical and experimental analysis of stroke-controlled tube hydroforming. *Materials Science and Engineering A279* (2000) 95-110.
- [58] N. Abedrabbo, N. Zafar, R. Averill, F. Pourboghraat, R. Sidhu. Optimization of a tube hydroforming process. *NUMIFORM 2004*, pp. 1172-1177.

- [59] L. Lei, J. Kim, B. Kang. Bursting failure prediction in the tube hydroforming processes by using rigid-plastic FEM combined with ductile fracture criterion. *International Journal of Mechanical Sciences*, vol. 44, pp. 1411-1428, 2002.
- [60] J. Kim, L. Lei, S. Hwang, S. Kang, B. Kang. Manufacture of an automobile lower arm by hydroforming. *International Journal of Machine Tools & Manufacture*, vol. 42, pp. 69-78, 2002.
- [61] G. Khodayari, H. Reid, J.V. Reid. Report- The influence of the lubricant during tube hydroforming. Industrial Research and Development Institute, Midland, Ontario, Canada, 2003.
- [62] J.A. Schey and P.C. Nautiyal. Effects of surface roughness on friction and metal transfer in lubricated sliding of aluminium alloys against steel surfaces. *Wear*, v146, n 1, May 30, 1991, p. 37-51.
- [63] F. Vollertsen, M. Plancak. On possibilities for the determination of the coefficient of friction in hydroforming of tubes. *Journal of Materials Processing Technology*, vol. 125-126, pp. 412-420, 2002.
- [64] H. Singh. Fundamentals of hydroforming. Society of Manufacturing Engineers.
- [65] B.F. Kuvin. Pressure sequencing expands the use of hydroforming. *Metal Forming Magazine*, June 2000, pp.30-35.
- [66] G. Morphy. Pressure-sequence and high-pressure hydroforming: knowing the processes can mean boosting profits. *The Tube & Pipe Journal*, February 19, 2001.
- [67] Y.M. Hwang, T. Altan. Finite element analysis of tube hydroforming processes in a rectangular die. *Finite Elements in Analysis and Design*, vol. 39, pp. 1071-1082, 2002.
- [68] L. Wu, Y. Yu. Computer simulations of forming automotive structural parts by hydroforming process. *Numisheet Proceedings 1996*, pp. 324-329.
- [69] T. Stoughton. A general forming limit criterion for sheet metal forming. *International Journal of Mechanical Science* 42 (2000) 1-27.
- [70] C.H.M. Simha, J. Gholipour, A. Bardelcik, M.J. Worswick. Prediction of necking in tubular hydroforming using an extended stress-based forming limit curve. *Journal of Engineering Materials and Technology*, Transactions of the ASME Paper no. MATS-05-1169.
- [71] C.H.M. Simha, R. Grantab, M.J. Worswick. Application of an extended stress-based forming limit curve to predict necking in stretch flange forming. Submitted to *Transactions of the ASME Journal of Manufacturing Science and Engineering*, November 2006.
- [72] A. Reyes, M. Langseth, O.S. Hopperstad. Crashworthiness of aluminium extrusions subjected to oblique loading: experiments and numerical analyses. *International Journal of Mechanical Sciences*, 44 (2002) 1965-1984.
- [73] H.S. Kim, T. Wierzbicki. Effect of the cross-sectional shape of hat-type cross-sections on crash resistance of an s-frame. *Thin-Walled Structures* 39 (2001) 535-554.

- [74] D. Kecman. Bending collapse of rectangular and square cross-section tubes. *International Journal of Mechanical Science*, Vol. 25, No. 9-10, pp.623-636, 1983.
- [75] W. Abramowicz. Simplified crushing analysis of thin-walled columns and beams. *Engineering Transactions*, 29, 3-27 (1983).
- [76] G.H. Tidbury, D. Kecman. Investigation into the behaviour of hinges produced by bending collapse of vehicle structural components. XVII FISITA Congress, Budapest, Vol. 2, pp.849-864 (1978).
- [77] J.C. Brown, G.H. Tidbury. An investigation of the collapse of thin-walled rectangular beams in biaxial bending. *International Journal of Mechanical Science* Vol. 25, No.9-10, pp.733-746, 1983.
- [78] W. Chen, T. Wierzbicki. Torsional collapse of thin walled prismatic columns. *Thin-walled Structures* 36 (2000) 181-196.
- [79] W. Abramowicz, N. Jones. Transition from initial global bending to progressive buckling of tubes loaded statically and dynamically. *International Journal of Impact Engineering*, Vol. 19, Nos 5-6, pp.415-437, 1997.
- [80] N. Jones. Several phenomena in structural impact and structural crashworthiness. *European Journal of Mechanics and Solids*, 22 (2003) 693-707.
- [81] T-E Chung, Y-R Lee, C-S Kim, H-S Kirr. Design of aluminium space frame for crashworthiness improvement. SAE paper no. 960167, 1996.
- [82] C.M. Ni. Impact response of curved box beam-columns with large global and local deformations. Proceedings of the 14th Structures, Structural Dynamics, and Materials Conference, King of Prussia, PA, USA. AIAA Paper No. 73-401, 1976.
- [83] H.S. Kim, T. Wierzbicki. Closed-form solution for crushing response of three-dimensional thin-walled s frames with rectangular cross-sections. *International Journal of Impact Engineering* 30 (2004) 87-112.
- [84] R. Grantab, D.A. Oliveira, B.W. Williams, M.J. Worswick, R. Mayer. Numerical modelling of a dual crush mode welded aluminium crash structure. *International Journal of Crashworthiness*, Volume 11 No. 2, pp.165-175, 2006.
- [85] J.D. Reid. Crashworthiness of automotive steel midrails: thickness and material sensitivity. *Thin-Walled Structures*, Vol. 26, No. 2, pp.83-103, 1996.
- [86] I. Nishimura, T. Sakurai. Prediction of the crashworthiness of vehicle body aided computer. 6th International Pacific Conference on Automotive Engineering, Seoul, Korea, Oct. 28-Nov. 1, 1991, SAE Report No. 900461.
- [87] T-E Chung, R-R Lee, C-S Kim, H-S Kim. Design of aluminium space frame for crashworthiness improvement. SAE Paper No. 960167, 1996.
- [88] D.J. Meadows, A.D. Seeds, I.J. McGregor, M. Kenyon. Aluminium crash member in axial and bending collapse. SAE Paper No. 922113, 1992.
- [89] A. Yoshitake, K. Sato, T. Okita. Impact absorbed energy of hat square column in high strength steels. SAE Paper No. 960020, 1996.

- [90] M. Seitzberger, S. Willminger. Versagensmechanismen zur kollapsanalyse axial gedruckter aluminiumschaum-gefüllter profile. *Mat.-wiss. U. Werkstofftech* 31, 459-461 (2000).
- [91] M. Seitzberger, S. Willminger. Application of plastic collapse mechanisms for the axial crushing analysis of tubular steel structures filled with aluminium foam. In: *Proc. Icrash 2000, RAS* (Chirwa, E.C., Otte, D., eds.) Service Point (UK) Lmt. 2000.
- [92] M. Seitzberger, F.G. Rammerstorfer, R. Gardinger, H.P. Degisher, M. Blaimschein, C. Walch. Experimental studies on the quasi-static axial crushing of steel columns filled with aluminium foam. *International Journal of Solid Structures*, 37, 4125-4147 (2000).
- [93] R. Gardinger, M. Seitzberger, F.G. Rammerstorfer, H.P. Degisher, M. Blaimschein, C. Walch. Aluminium foam filled steel tubes as composite shock absorbers. In: *Metal foams and porous metal structures* (Banhart, J., Fleck, N.A., eds) MIT Press 1999.
- [94] R. Gardinger, F.G. Rammerstorfer. On the influence of mesoinhomogeneities on the crush worthiness of metal foams. *Acta Mater.* 47, 143-148, (1999).
- [95] M. Seitzberger, F.G. Rammerstorfer, R. Gardinger, H.P. Degisher. Crushing of axially compressed steel tubes filled with aluminium foam. *Acta Mech.* 125, 93-105 (1997).
- [96] W. Chen, D. Nardini. Experimental study of crush behaviour of sheet aluminium foam-filled sections. *International Journal of Crashworthiness* 5, 447-468 (2000).
- [97] W. Chen, T. Wierzbicki and S. Santosa. Bending collapse of thin-walled beams with ultralight filler: numerical simulation and weight optimization. *Acta Mechanica* 153, 183-206 (2002).
- [98] S. Santosa, J. Banhart, T. Wierzbicki. Experimental and numerical analysis of bending of foam-filled sections. *Acta Mech.* 48, 199-213 (2001).
- [99] T. Dutton, A. Kellicut, B. Cowell, K. Kavikondala, S. Iregbu, R. Sturt. Application of the results of forming simulation in Crash Models. *Numisheet'99 Conference Proceedings*, pp. 509-514, Besancon, France.
- [100] T. Dutton, S. Iregbu, R. Sturt, A. Kellicut, B. Cowell, K. Kavikondala. The effect of forming on the crashworthiness of vehicles with hydroformed frame side rails. *SAE Proceedings*, paper no. 1999-01-3208, 1999.
- [101] H. Ryou, K. Chung, J. Yoon, F. Pourboghrat. Crash simulations considering sheet forming effects based on ideal forming theory and hybrid membrane/shell method. *Proceedings of the Eighth International Conference on Numerical Methods in Industrial Forming Processes*, Ohio (Columbus, USA): 2004. p. 1034-1039.
- [102] M. Kaufman, D. Gaines, K. Kundrick, S.D. Liu. Integration of chassis frame forming analysis into performance models to more accurately evaluate crashworthiness. *SAE Proceedings*, paper no. 980551, 1998.
- [103] M. Langseth, O.G. Lademo. Tensile and torsion testing of AA6060-T4 and T6 aluminium alloys at various strain rates. *Technical Report*, Department of Structural Engineering, Norwegian University of Science and Technology, 1994.

- [104] R. Smerd, S. Winkler, C. Salisbury, M. Worswick, D. Lloyd, M. Finn. High strain rate testing of automotive aluminium alloy sheet. *International Journal of Impact Engineering*. Volume: 32, Issue: 1-4, December, 2005, pp. 541-560.
- [105] A. Rahem, G. D'Amours, H.R. Shakeri. Interaction Between Forming and Crashworthiness of Aluminium Alloy Tubes. Summary report for General Motors of Canada and University of Waterloo. Aluminium Technology Center. February 2005.
- [106] C. Salisbury, and M.J. Worswick. Interaction between forming and crashworthiness of aluminium alloy tubes. Task 1 Report for General Motors of Canada and the Aluminium Technology Centre. December 22, 2004.
- [107] C. Salisbury, D. Wowk, M.J. Worswick, K. Pilkey. Interaction Between Forming and Crashworthiness of Aluminium Alloy Tubes, Task 1 Report for General Motors of Canada and the Aluminium Technology Centre, High Rate Characterization of Aluminium Alloy Tubes. November 30, 2005.
- [108] E. Voce. The relationship between stress and strain for homogeneous deformation, *Journal of the Institute for Metals* 74 (11): 537-562, 1948.
- [109] Jana Heuer and Michael Opitz. Hydro Aluminium. Personal Communication. 2005
- [110] D.A. Stuart Data Sheet, Drawsol Al 20, www.dastuart.com
- [111] T. Altan, G. Ngaile. Tube and sheet hydroforming fundamentals and applications. Recent Development on Tube and Sheet Hydroforming, A Short Course and International Conference, Columbus, Ohio, June 2003.
- [112] T. Belytschko, W.K. Liu, B. Moran. Nonlinear finite elements for continua and structures. John Wiley and Sons, 2001.
- [113] D.A. Oliveira. Electromagnetic Forming of Aluminium Alloy Sheet: Experiment and Model. Masters Thesis, Department of Mechanical Engineering, University of Waterloo, Waterloo, Ontario, Canada, 2002.
- [114] D.A. Stuart Data Sheet, Hydrodraw 625, www.dastuart.com
- [115] J.A. Schey. Introduction to Manufacturing Processes, Second Edition. McGraw-Hill Company, 1987, pp. 298.
- [116] R.R. Mayer, S. Webb, J. McCleary, R. Gusko, D.A. Oliveira, M.J. Worswick. S-rail sled testing with deceleration sled. Proceedings of the 2005 International Mechanical Engineering Congress and Exposition, Nov. 5-11, 2005, Orlando, Florida.
- [117] R.D. Strum, D.E. Kirk. First Principles of Discrete Systems and Digital Signal Processing. Addison-Wesley Publishing Company, 1988, pp. 623-630, 690-693.
- [118] Jana Leschke, Personal communication. Hydro Aluminium Alutubes GmbH
- [119] Donald R. Askeland. The science and engineering of materials, Third S.I. Edition, Chapman and Hall, pp.202-207, 1996.
- [120] R. Mayer. Personal Communication, General Motors, Warren, Michigan, 2006.

- [121] T. Belytschko, J.I. Lin, C. Tsay. Explicit algorithms for the nonlinear dynamics of shells. *Computer Methods in Applied Mechanics and Engineering*, Vol. 42, 1984, pp. 225-251.
- [122] T.J.R. Hughes and E. Hinton. *Finite element methods for plate and shell structures. Vol. 2: Formulations and Algorithms.*
- [123] F. Barlat, J.I. Lian. Plastic Behavior and Stretchability of Sheet Metals Part I: A Yield Function for Orthotropic Sheets Under Plane Stress Conditions, *International Journal of Plasticity*, Vol. 5, pp. 51-56, 1989.
- [124] M.J. Worswick, R. Smerd, C. Salisbury, S. Winkler, D.J. Lloyd. High strain rate behaviour of aluminium alloy sheet. *International Conference on Aluminium Alloys*, July 9-13, 2006, Vancouver, Canada.
- [125] G.R. Johnson, W.H.A. Cook. Constitutive model and data for metals subjected to large strains, high strain rates, and high temperatures. *Proceedings of the Seventh International Symposium on Ballistics*, The Hague (Netherlands): 1983. p. 541-547.
- [126] G.R. Johnson, W.H. Cook. Fracture characteristics of three metals subjected to various strains, strain Rates, temperatures and pressures. *Engineering Fracture Mechanics* 1985; 21(1): 31-48.
- [127] M.A. Meyers. *Dynamic behavior of materials*. New York: John Wiley & Sons, Inc., 1994.
- [128] F.J. Zerilli, and R.W. Armstrong. The effect of dislocation drag on the stress-strain behavior of F.C.C. metals. *Acta Metallurgica et Materialia*, vol. 40, no. 8, 1992, pp. 1803-1808.
- [129] F.J. Zerilli, and R.W. Armstrong. Dislocation-mechanics-based constitutive relations for material dynamics calculations. *Journal of Applied Physics*, Vol.61, no. 5, 1987, pp. 1816-1825.
- [130] F.J. Zerilli, and R.W. Armstrong. Dislocation mechanics based constitutive relations for dynamic straining to tensile instability. *Shock Compression of Condensed Matter*, 1989, pp. 357-360.
- [131] F.J. Zerilli, and R.W. Armstrong. Dislocation mechanics based analysis of material dynamics behavior: enhanced ductility, deformation twinning, shock deformation, shear instability, dynamic recovery. *Journal de Physique IV*, 1997, pp. C3-637-C3-642.
- [132] C.H.M. Simha. Personal Communication, Department of Mechanical Engineering, University of Waterloo, Waterloo, Canada, 2006.
- [133] L. Wilkinson. *SYSTAT: The System for Statistics*. Evanston, IL: SYSTAT Inc., 1990.
- [134] W. Abramowicz, T. Wierzbicki. Axial crushing of multicorner sheet metal columns. *Journal of Applied Mechanics* 1989;56:113-20.
- [135] B.N. Maker. *Implicit Analysis with LS-DYNA version 960 and 970*. Livermore Software Technology Corporation, June 2002.

- [136] T. Wierzbicki, W. Abramowicz. On the crushing mechanics of thin-walled structures. *Journal of Applied Mechanics*, 50 (1983), pp. 727-734.
- [137] J.G. Gholipour. Damage in hydroforming of pre-bent aluminium alloy tubes. Doctoral Thesis, Department of Mechanical Engineering, University of Waterloo, Waterloo, Ontario, Canada, 2004.
- [138] R. Grantab. Interaction between forming and crashworthiness of advanced high strength steel s-rails. Masters Thesis, Department of Mechanical Engineering, University of Waterloo, Waterloo, Ontario, Canada, 2006.
- [139] A. Bardelcik. Effect of pre-bending and hydroforming parameters on the formability of advanced high strength steel tube. Masters Thesis, Department of Mechanical Engineering, University of Waterloo, Waterloo, Ontario, Canada, 2006.
- [140] M. Sorine. Personal communication. Department of Mechanical Engineering, University of Waterloo Waterloo, Ontario, Canada, 2006.
- [141] S.P. Santosa, T. Wierzbicki, A.G. Hanssen, M. Langseth. Experimental and numerical studies of foam-filled sections. *International Journal of Impact Engineering* 24 (2000) 509-534.
- [142] A. Thompson. High strain rate characterization of advanced high strength steel s-rails. Masters Thesis, Department of Mechanical Engineering, University of Waterloo, Waterloo, Ontario, Canada, 2006.
- [143] J.A. Schey and P.C. Nautiyal. Effects of surface roughness on friction and metal transfer in lubricated sliding of aluminium alloys against steel surfaces. *Wear*, v146, n 1, May 30, 1991, p. 37-51.
- [144] J.A. Schey, Personal Communication.
- [145] D. Cronin. Personal communication, Department of Mechanical Engineering, University of Waterloo, Waterloo, Canada, 2006.
- [146] R.C. Hibbeler. *Mechanics of Materials*, Third Edition. Prentice Hall In, Upper Saddle River, New Jersey 07458, 1997.

Appendix A: Twist Compression Tests for Tube Bending and Hydroforming of AA5754 Tube

A.1 Introduction

This Appendix documents research into estimating the coefficient of friction for various tool/lubricant/workpiece interactions in rotary draw tube bending and hydroforming of AA5754 aluminium alloy tube. The so-called twist compression test (TCT), originally developed by Schey [143], is shown in Figure A.1 and Figure A.2. This test considers large interface pressures and sliding distances, which are experienced in rotary draw tube bending and hydroforming operations and was therefore used to estimate the friction coefficient. In the TCT, an anvil (Figure A.1c) of a known radius (r) and contact area (A) is prescribed an angular velocity and is then brought into contact with a stationary workpiece using a normal pressure (P). The applied pressure and velocity should mimic the tool/workpiece contact pressures and relative velocity experienced during the forming operation. Under the applied pressure (P), the anvil rotates on the workpiece, which transmits a torque. The coefficient of friction is given by

$$\mu = \frac{T}{rPA} \quad (\text{A.1})$$

The anvil should be of the same material and be representative of the surface roughness and hardness of the actual tool under investigation. Similarly, the workpiece should be representative of the part in terms of material, surface roughness, hardness and lubrication.

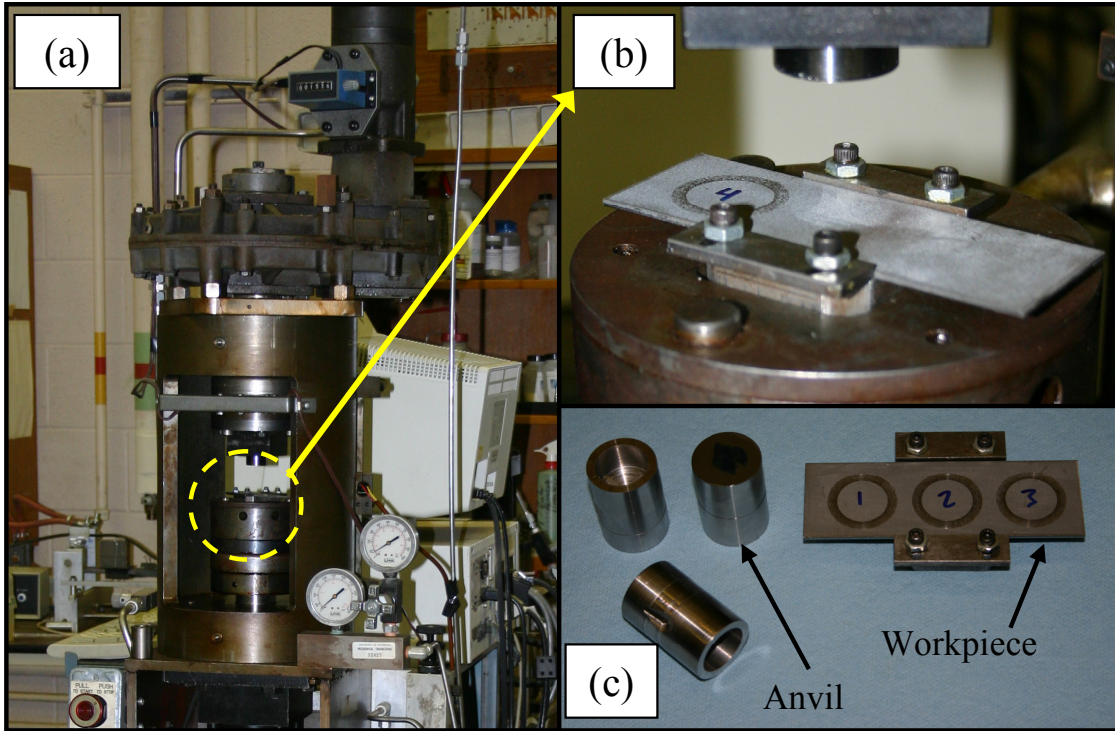


Figure A.1: (a) Twist compression test rig; (b) close-up of test rig; and, (c) anvil and workpiece.

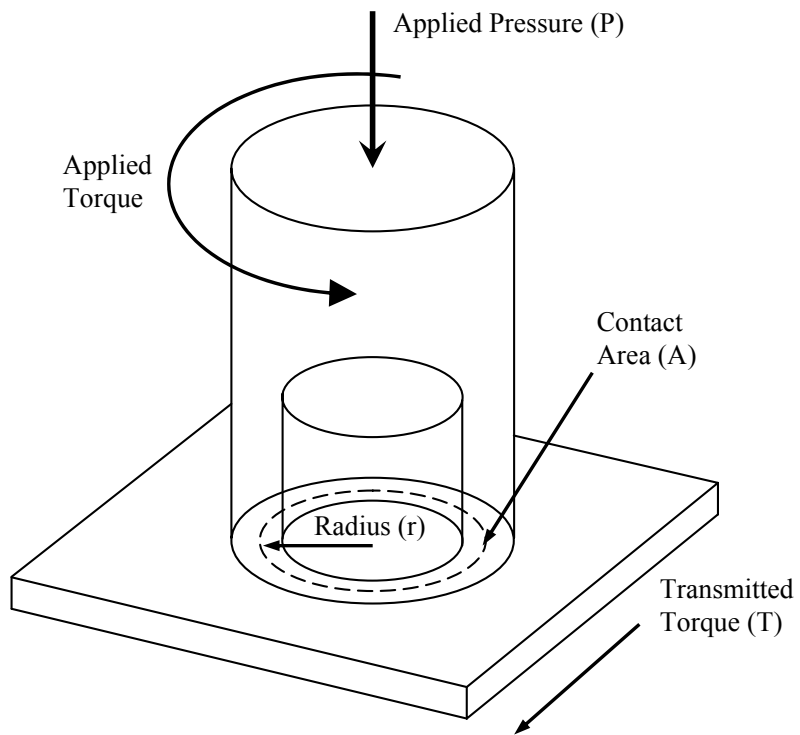


Figure A.2: Schematic of the tool/workpiece interaction.

A.2 Twist Compression Tests

A.2.1 Testing Conditions

The frictional conditions in mandrel rotary draw tube bending and hydroforming experiments presented in this thesis are mimicked in these twist compression tests. The tool/workpiece interactions in tube bending and hydroforming experiments are summarized in Table A.1. The bend, clamp and pressure dies were all made from 4130 steel and nitrided to a hardness of 60-62 Rc (Rockwell C scale). The wiper die was also made from 4130 steel; however it was not hardened, while the mandrel used in bending is made from 8620 steel and has an industrial chrome finish. The hydroforming die is made from 4140 steel and was not hardened, although the die inserts were hardened to 60-62 Rc.

Table A.1: Tube bending and hydroforming tooling specification.

Tooling	Material	Treatment	Hardness (Rc)
Bend die	4130 steel	Nitrided	60-62
Clamp die	4130 steel	Nitrided	60-62
Pressure die	4130 steel	Nitrided	60-62
Wiper die	4130 steel	None	???
Mandrel	8620 steel	Chrome finish	58-62
Hydroforming die	4140 steel	None	???

The interface pressures between the various tools and the workpiece are summarized in Table A.2. The normal force and contact areas on the bend, clamp and wiper dies were estimated based on the numerical models of these experiments described in Chapter 3. The normal force on the pressure die was prescribed to be 35 kN and the mandrel transmits this force via the tube to the bend and wiper dies. The interface pressure between the tube and hydroforming die ranged from 3.45-65.5 MPa in s-rail hydroforming experiments and up to 200 MPa in straight tube axial crush experiments by Williams *et al.* [2].

Table A.2: Estimates of interface pressures.

Interaction with tube	Normal Force (kN)	Pressure Range (MPa)	Pressure Range (psi)
Bend die	5-15	1.64-8.2	238-1200
Clamp die	5-30	0.27-1.64	39-238
Pressure die	35	0.44-0.54	64-78
Wiper die	10-35	1.97-6.89	286-1000
Mandrel	35	0.44-0.54	64-78
Hydroforming die		3.45-207	500-30,000

The lubricants used in tube bending and hydroforming experiments were both D.A. Stuart lubes, Drawsol AL20 and Hydrodraw 625, respectively [110,114]. The Drawsol AL20 is a lubricant developed for aluminium wire drawing and has been shown to be an excellent lubricant for tube bending of 5000-series aluminium alloys [24], while the Hydrodraw 625 is a solid film lubricant.

Due to significant variation in the surface roughness of the tooling, the anvil specimens were lapped to a 0.2 μm RMS roughness scale, as suggested by Schey [144].

A.2.2 Test Plan

The test plan for the twist compression tests is presented in Table A.3. Due to limitations in the TCT rig at the University of Waterloo, the minimum applicable pressure that could be applied on the workpiece was 6.9 MPa. Three film thicknesses of solid film lubricant (Hydrodraw 625) were investigated in order to account for film thickness variation on parts due to the manual spraying application in the hydroforming experiments as discussed in Chapter 2. The dry condition mimics the clamp, pressure and bend die interactions with the tube and also serves as a reference point for evaluating the bending lubricant. Two relative speeds between the anvil and workpiece were chosen, 2 and 19 rpm (2 and 22 mm/s), which represent the lower and upper bounds of tool/workpiece relative velocity estimated from the tube bending finite element models. Similarly, the relative velocity of the anvil/workpiece that mimics the low- and high-pressure hydroforming operations is 0.4 and 0.8 rpm (0.46 and 0.93 mm/s), and up to 4 rpm (4.6 mm/s), respectively. The workpiece is AA5754 aluminium alloy sheet stock from which the tube used in bending and hydroforming experiments was fabricated.

Table A.3: Test plan for twist compression tests.

	Material interacting with workpiece	Lubricant	Film Thickness	Pressure (MPa)	Number of Repeats	Speed (rpm)
Bending	4130 steel (Hardened)	DRY	medium	6.9	3	2
		DRY	medium	6.9	3	19
		Drawsol AL20	medium	6.9	3	19
	4130 steel (Non-Hardened)	Drawsol AL20	medium	6.9	2	2
		Drawsol AL20	medium	6.9	3	19
		Drawsol AL20	medium	13.8	2	19
	Chromed 8620	Drawsol AL20	medium	6.9	2	19
		DRY	medium	6.9	3	19
Hydroforming	4140 steel	Hydrodraw 625	medium	6.9	2	0.8
		Hydrodraw 625	medium	13.8	2	0.8
		Hydrodraw 625	medium	62.0	2	0.4
		Hydrodraw 625	medium	124	2	0.4
		Hydrodraw 625	medium	193	2	0.4
		Hydrodraw 625	medium	193	1	4
	4140 steel	Hydrodraw 625	thin	13.8	2	0.8
		Hydrodraw 625	thick	13.8	1	0.8

A.3 Friction Coefficients for Tube Bending

A.3.1 Bend, Clamp and Pressure Dies

The median coefficient of friction as a function of the number of revolutions for hardened 4130 steel that compares the lubricated versus dry workpiece is shown in Figure A.3. Note that the maximum sliding distance on the bend, clamp and pressure dies during the tube bending experiments was measured to be 13 mm, which corresponds to one-quarter revolution in the TCT. The addition of lubricant lowers the coefficient of friction up to roughly 40% within a one-quarter of a revolution.

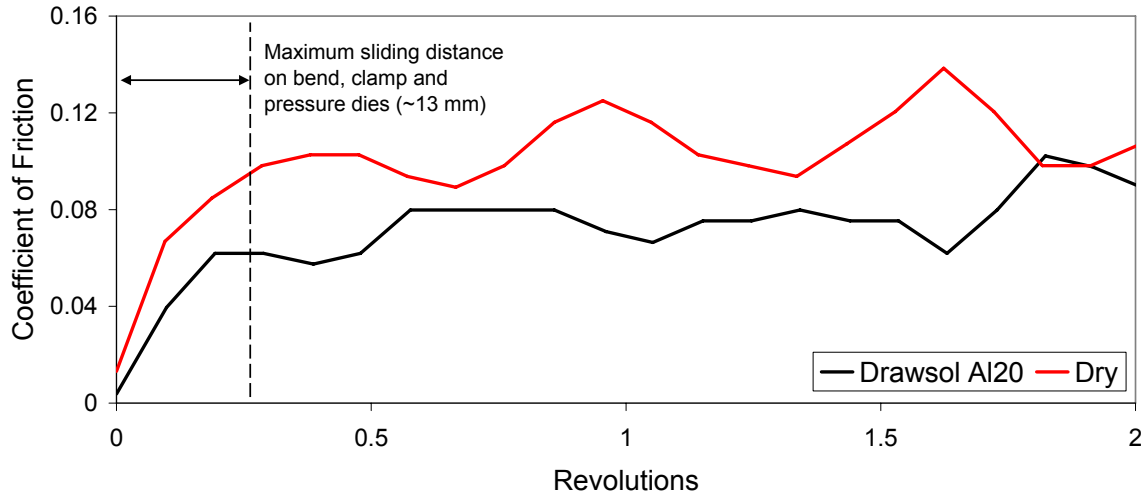


Figure A.3: Coefficient of friction for hardened 4130 steel interacting with a lubricated and dry workpiece.

The coefficient of friction using 4130 hardened steel anvils in a dry condition at 2 and 19 rpm is shown in Figure A.4. Within the first one-quarter revolution, the tests with the higher rotational speed demonstrated a lower coefficient of friction. At the 19 rpm speed there is quite a significant variation in the tests after the first quarter revolution, mainly due to “pick-up” of the aluminium on the anvil, which resulted in severe scratching of the workpiece surface.

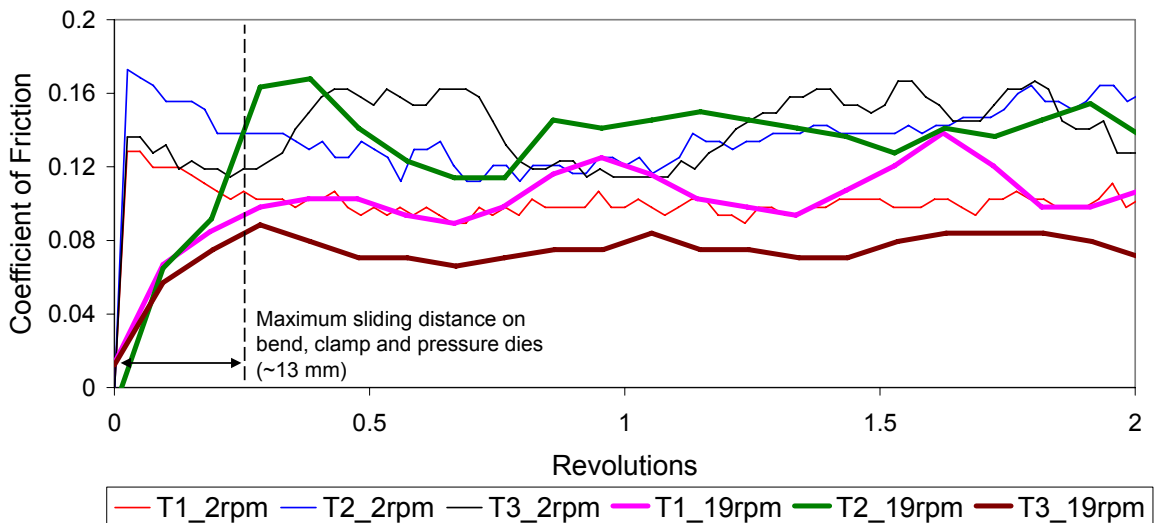


Figure A.4: Coefficient of friction for hardened 4130 steel interacting with a dry workpiece at 2 and 19 rpm.

A.3.2 Wiper Die

The coefficient of friction for non-hardened 4130 steel at interface pressures of 6.9 and 13.8 MPa is shown in Figure A.5. At the higher interface pressure, the Drawsol AL20 lubricant broke down quickly, which resulted in severe scratching of the samples. Despite the lubricant breakdown, the coefficient of friction was approximately 50% lower at the lower interface pressure.

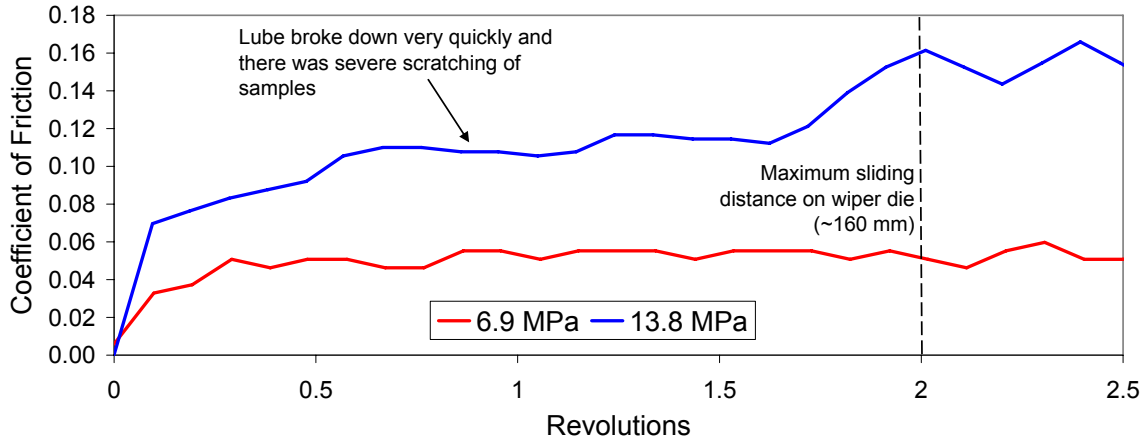


Figure A.5: Coefficient of friction for non-hardened 4130 steel and the Drawsol AL20 lubricant at 6.9 and 13.8 MPa.

The effect of rotational speed on the coefficient of friction for non-hardened 4130 steel is shown in Figure A.6. The coefficient of friction is reduced by up to 50% at the 19 rpm higher speed.

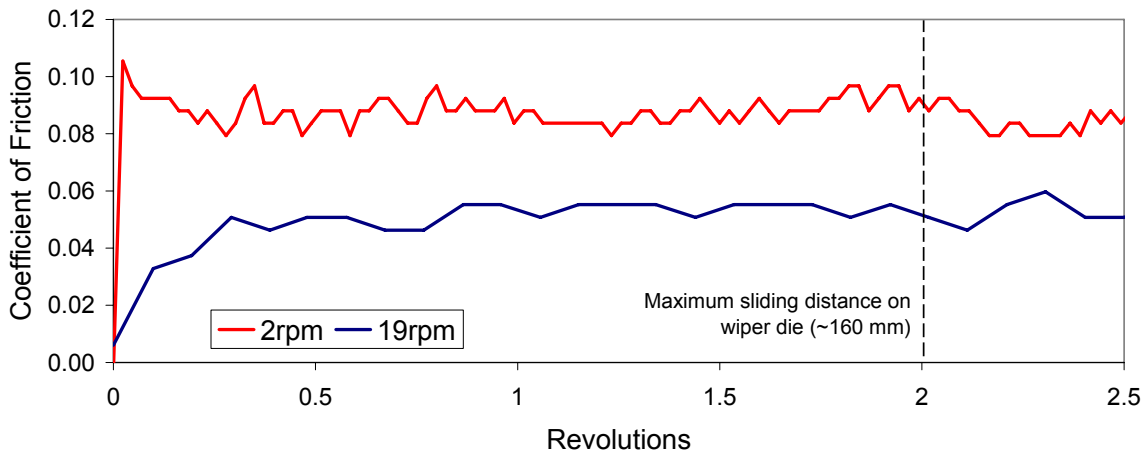


Figure A.6: Coefficient of friction for non-hardened 4130 steel at 2 and 19 rpm.

A.3.3 Mandrel

The coefficient of friction for 8620 chromed steel under lubricated and dry workpiece conditions is shown in Figure A.7. The effect of lubricant results in more than a 50% reduction in the coefficient of friction.

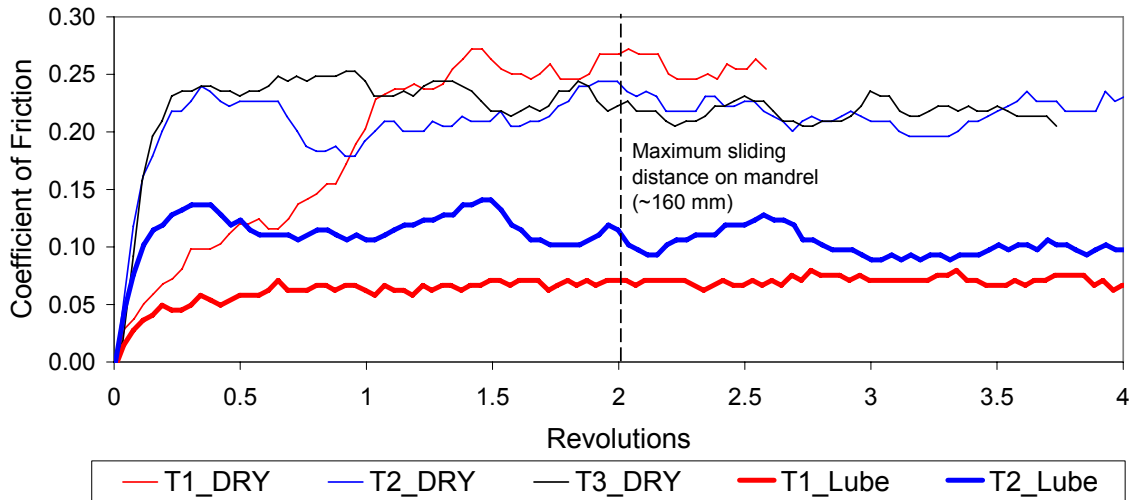


Figure A.7: Coefficient of friction for 8620 chromed steel interacting with lubricated and dry workpiece.

The effect of interface contact pressure on the coefficient of friction for 8620 chromed steel is shown in Figure A.8. At the higher interface pressure, the coefficient of friction increases by a factor of 2.5-5.

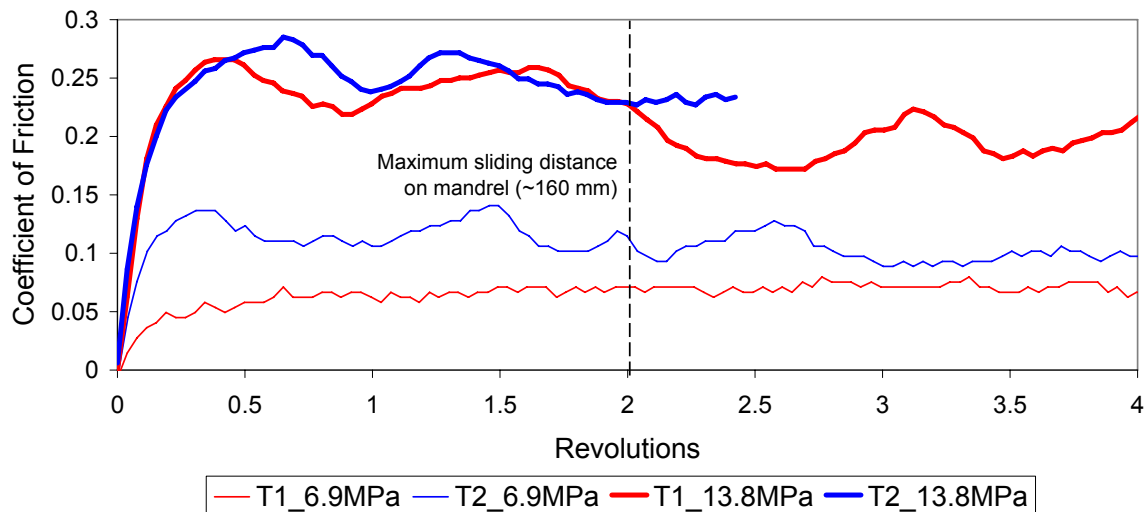


Figure A.8: Coefficient of friction for 8620 chromed steel at 6.9 and 13.8 MPa.

A.4 Friction Coefficients for Hydroforming

The effect of interface pressure on the coefficient of friction for 4140 steel and the Hydrodraw625 lubricant is shown in Figure A.9. As the interface pressure increases, the coefficient of friction decreases considerably.

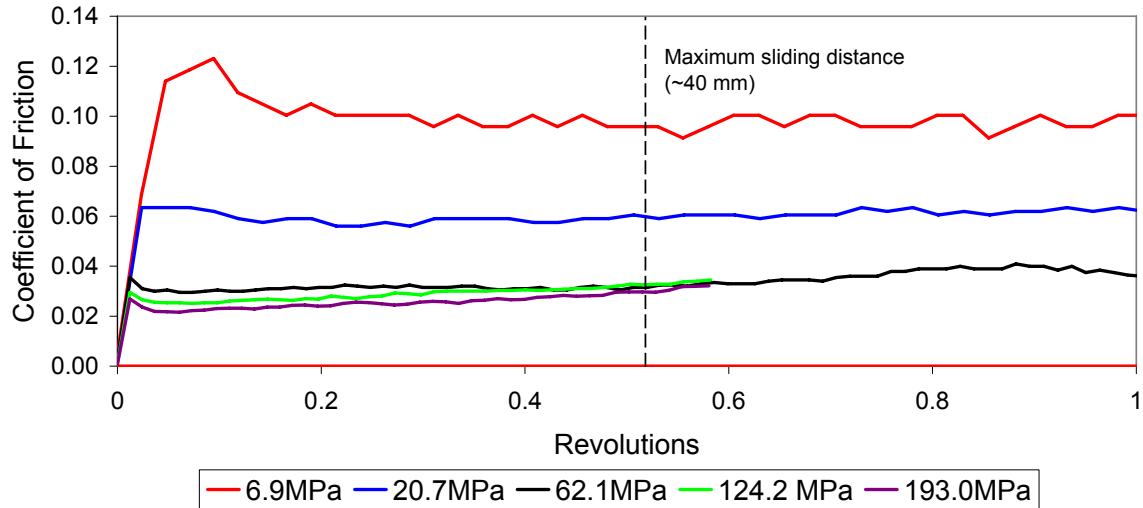


Figure A.9: Coefficient of friction for 4140 steel and Hydrodraw625 lubricant at various levels of interface pressure.

The effect of sliding velocity on the coefficient of friction for 4140 steel is shown in Figure A.10. The larger sliding velocity results in a reduction in the coefficient of friction of less than 0.01.

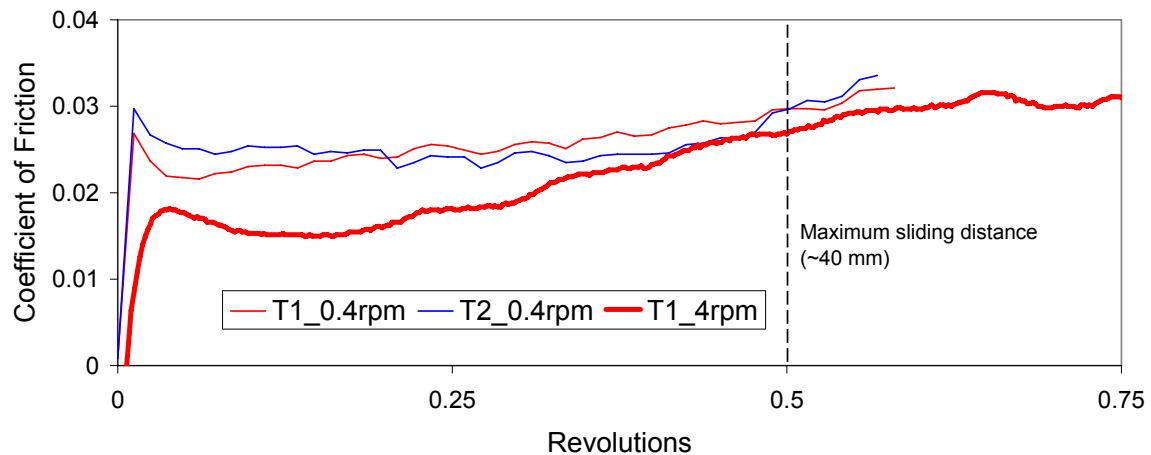


Figure A.10: Coefficient of friction for 4140 steel at 0.4 and 4 rpm.

The effect of lubricant film thickness on the coefficient of friction for 4140 steel is shown in Figure A.11. The variation in lubricant film thickness did not significantly affect the coefficient of friction.

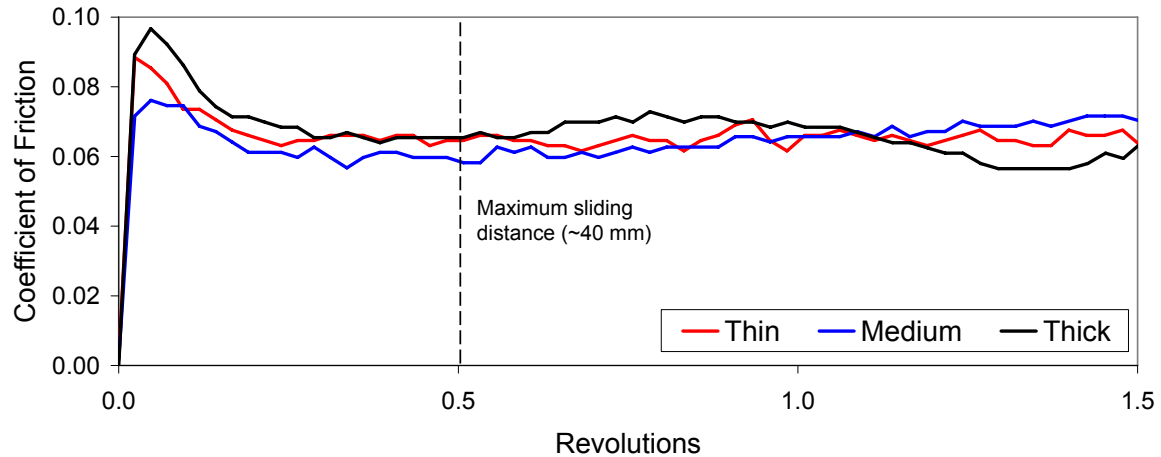


Figure A.11: Coefficient of friction for 4140 steel with various lubricant film thicknesses using a rotational speed of 0.8 rpm.

A.5 Summary

An estimate of the static and dynamic coefficients of friction for tube bending and hydroforming of AA5754 aluminium alloy tubes is given in Table A.4 and Table A.5, respectively. The static coefficient of friction was estimated based on the first peak in the coefficient of friction versus revolution plots, while estimates for the dynamic coefficient of friction considered values after this peak and up to the maximum sliding distance. The coefficients of friction determined herein provide data that may be used within finite element models of tube bending and hydroforming of AA5754 aluminium alloy tube.

Table A.4: Summary of the friction coefficients for bending of AA5754 tube.

				Velocity				Coefficient of Friction	
Tooling	Material	Treatment	Interface Pressure (MPa)	rpm	mm/s	Max Sliding Distance (mm)	Lubricant	Static	Dynamic
Bend, clamp and pressure dies	4130 steel	Nitrided	6.9	2	2	13	DRY	0.14	0.12
			6.9	19	22	13	DRY	0.10	0.10
			6.9	19	22	13	Drawsol AL20	0.05	0.05
Wiper die	4130 steel	None	6.9	2	2	160	Drawsol AL20	0.10	0.09
			6.9	19	22	160	Drawsol AL20	0.05	0.05
			13.8	19	22	160	Drawsol AL20	0.07	?
Mandrel	8620 steel	Chrome finish	6.9	19	22	160	Drawsol AL20	0.06-0.12	
			6.9	19	22	160	DRY	0.23	0.23
			13.8	19	22	160	Drawsol AL20	0.25	0.25

Table A.5: Summary of the friction coefficients for hydroforming of AA5754 tube.

				Velocity				Coefficient of Friction	
Tooling	Material	Treatment	Interface Pressure (MPa)	rpm	mm/s	Max Sliding Distance (mm)	Hydrodraw 625 Lube Thickness	Static	Dynamic
Hydroforming die	4140 steel	Nitrided	6.9	0.8	0.93	40	Med	0.11	0.09
			20.7	0.8	0.93	40	Med	0.07	0.06
			62.0	0.4	0.46	40	Med	0.03	0.03
			124	0.4	0.46	40	Med	0.03	0.03
			193	0.4	0.46	40	Med	0.03	0.03
			193	4	4.6	40	Med	0.02	0.02
			20.7	0.8	0.93	40	thin	0.08	0.06
			20.7	0.8	0.93	40	thick	0.10	0.07

Appendix B: Results for the 2 and 3.5 mm EN-AW5018 S-Rails

The results for the 2 and 3.5 mm EN-AW5018 s-rails shown here are taken from the publication by Oliveira *et al.* [5], which is based on this work.

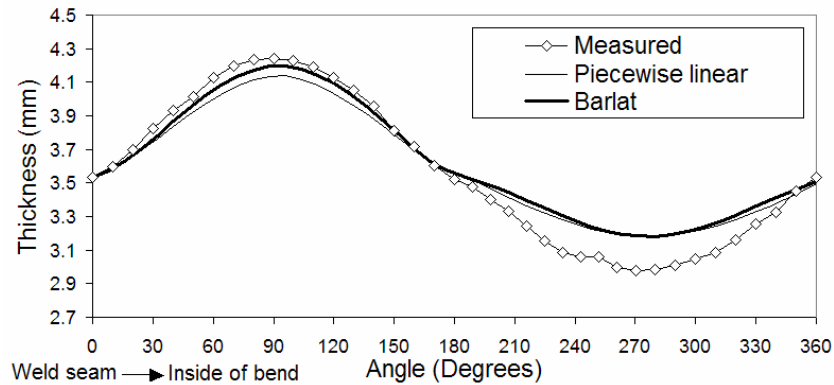


Figure B.1: Measured and predicted thickness results along the circumference of the 3.5 mm s-rail bent at an $R/D=2.0$.

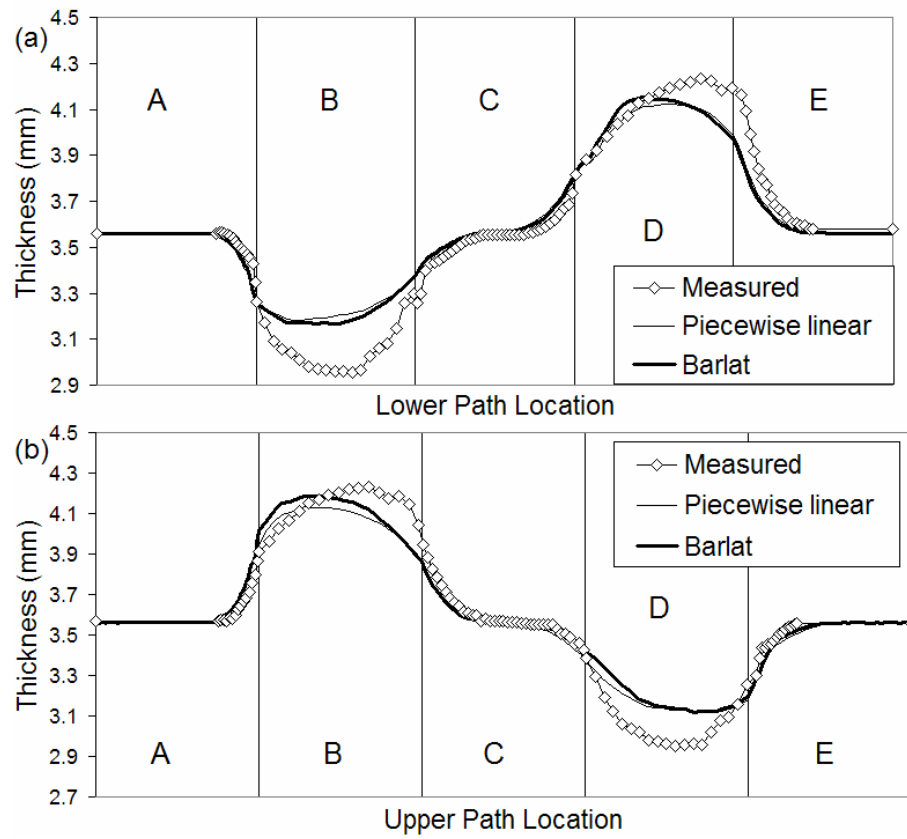


Figure B.2: Measured and predicted thickness results along the: (a) lower path; and, (b) upper path of the 3.5 mm s-rail bent at an $R/D=2.0$.

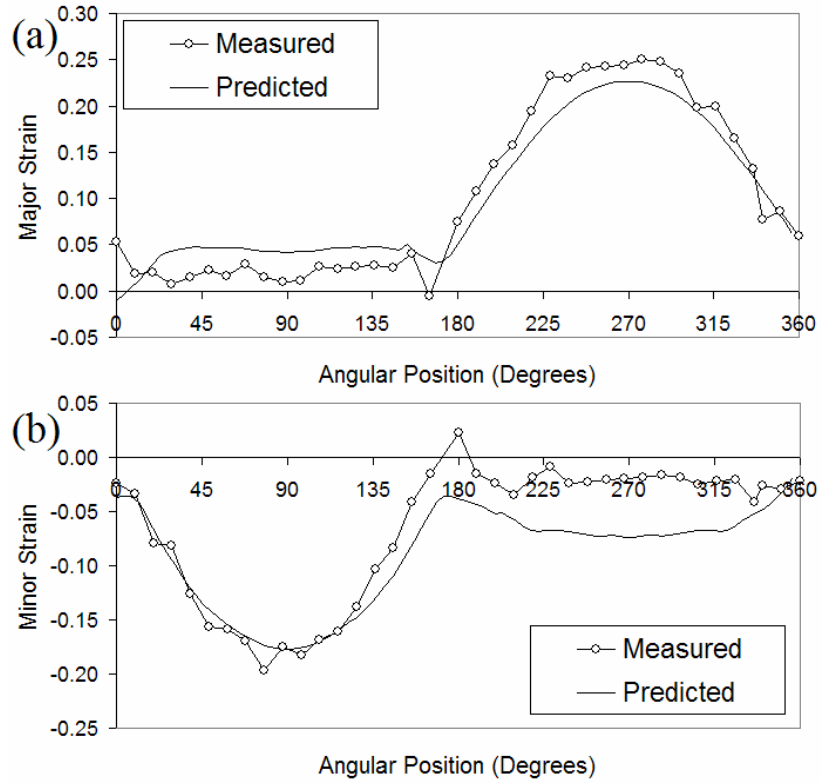


Figure B.3: Measured and predicted: (a) major; and, (b) minor strain along the circumference of the first bend of a 3.5 mm s-rail bent at an $R/D=2.0$.

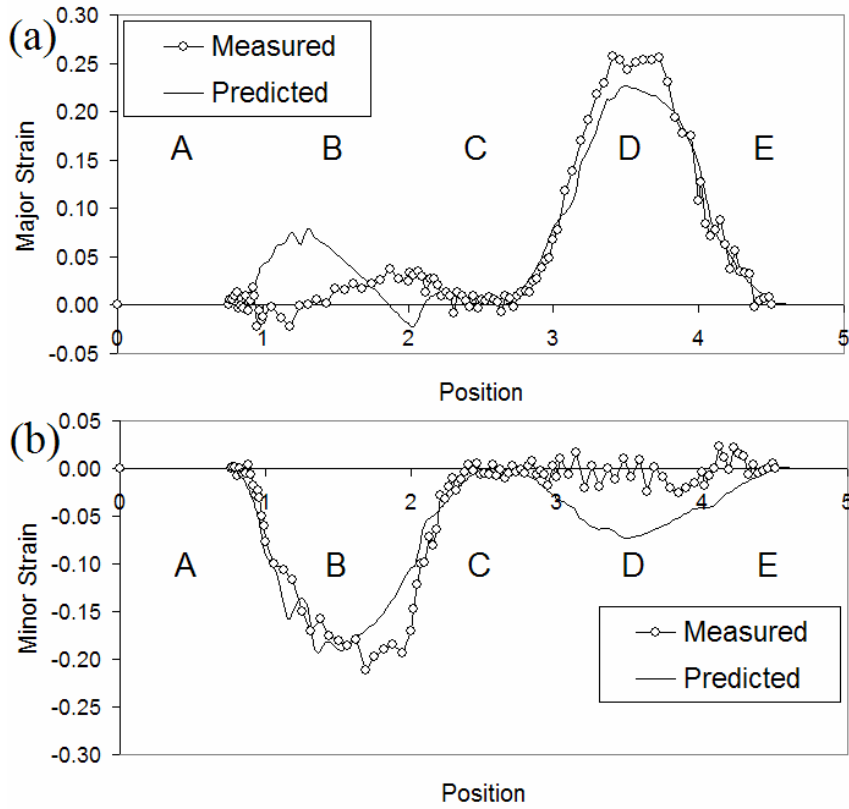


Figure B.4: Measured and predicted strains for a 3.5 mm s-rail, bent at an $R/D=2.0$, along the lower path: (a) major strains; and, (b) minor strains.

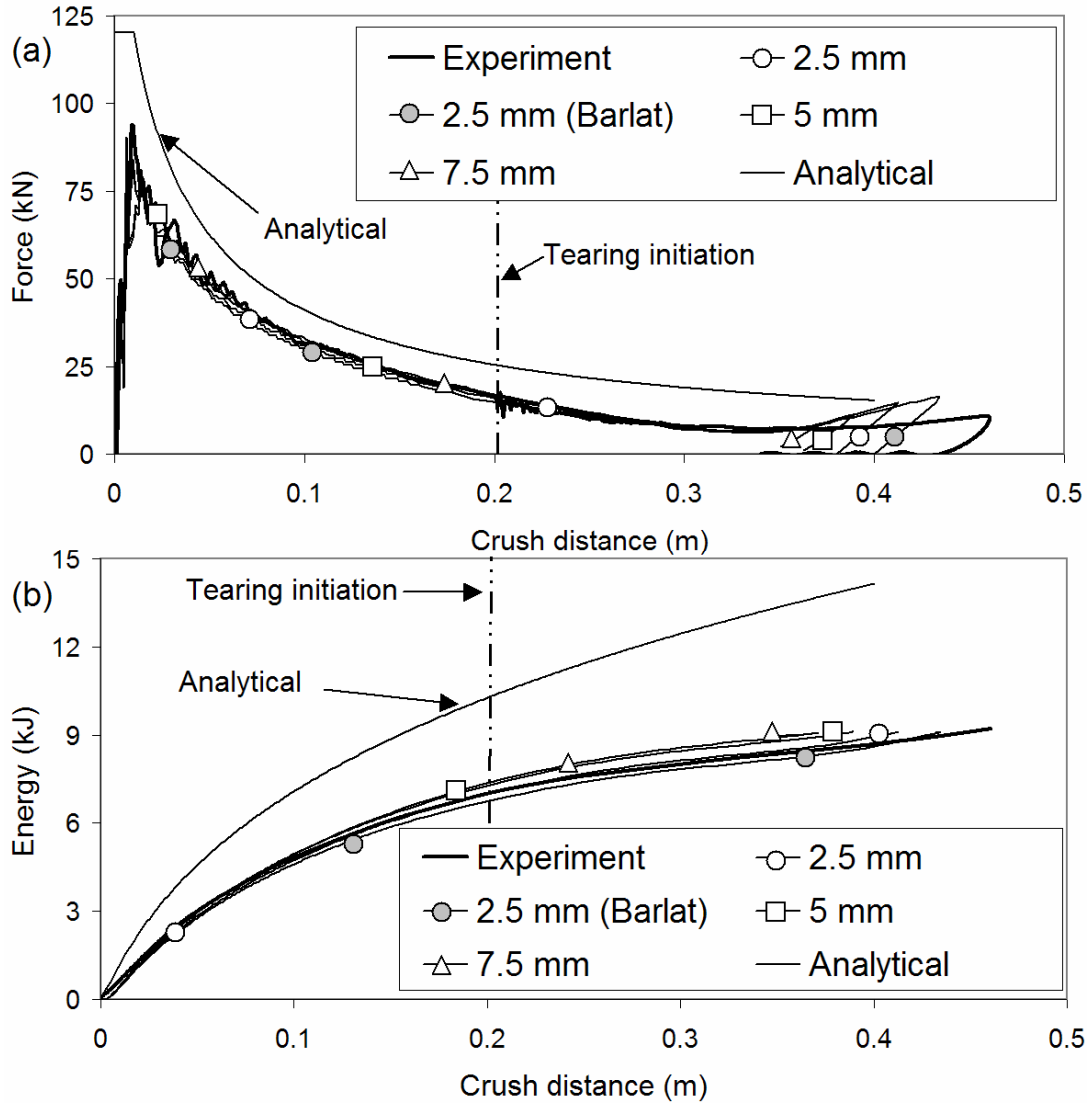


Figure B.5: Measured and numerically predicted: (a) force; and, (b) energy versus displacement response of 3.5 mm s-rail structures bent at an $R/D=2.0$ for various mesh sizes. Analytical prediction is included for comparison purposes.

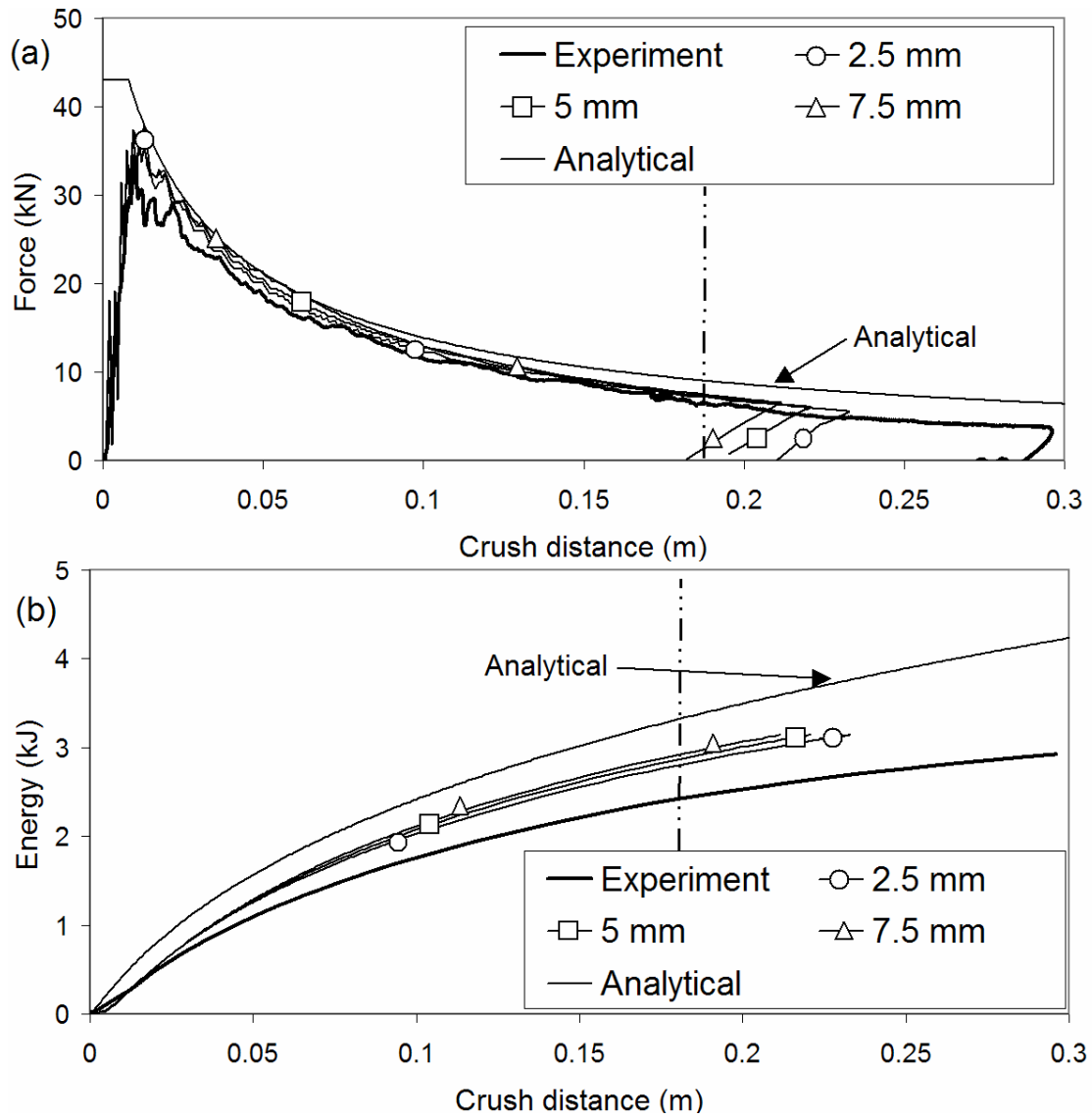


Figure B.6: Measured and predicted: (a) force; and, (b) energy versus displacement response of 2 mm s-rail structures bent at an $R/D=2.0$ for various mesh sizes. Analytical prediction is included for comparison purposes.

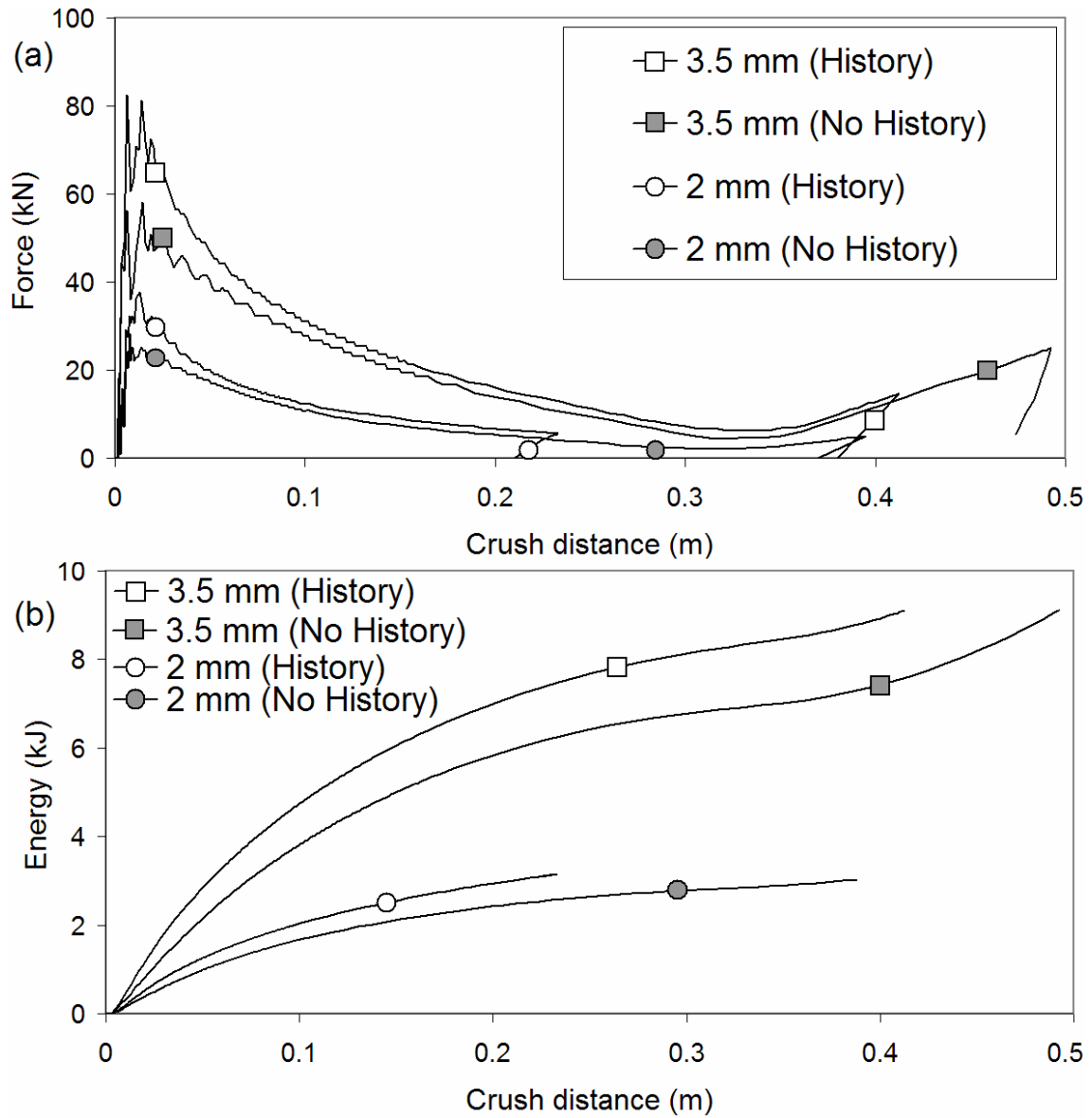


Figure B.7: The effect of considering forming history on the: (a) force; and, (b) energy versus displacement response of a 2 and 3.5 mm s-rail crash structure bent at an R/D of 2.0. Crush response was calculated using the 2.5 mm sized elements.

Appendix C: Predicted Tube Bending, Hydroforming and Crash Results

C.1 Tube Bending Predictions

C.1.1 Process Variables

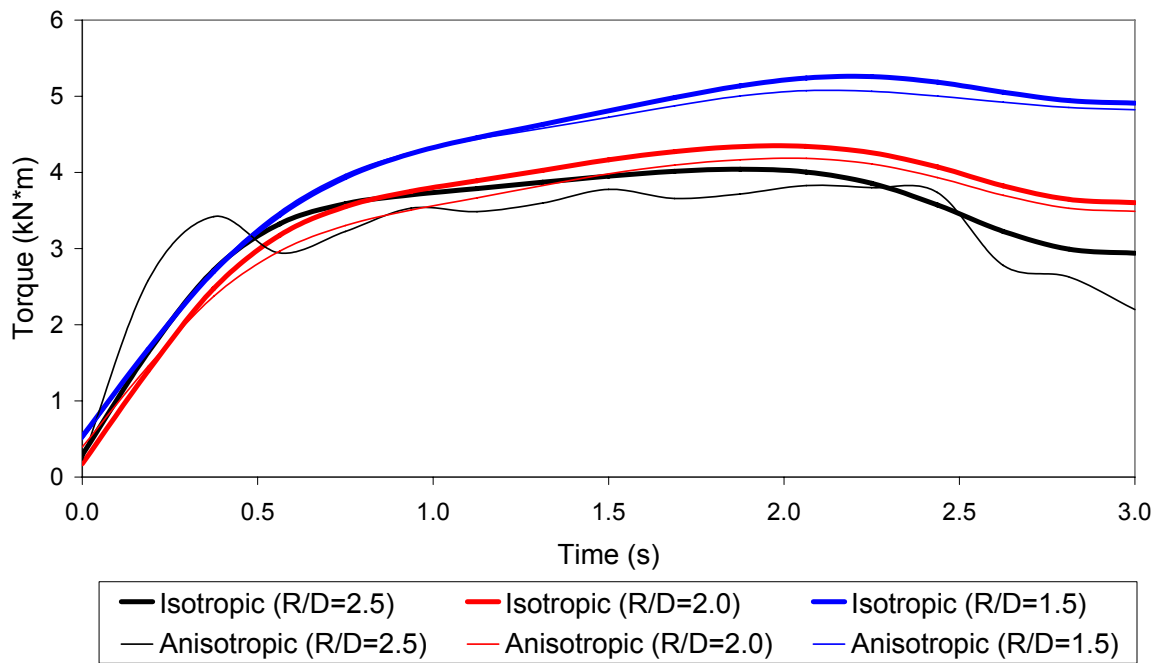


Figure C.1: Predicted bend torque using the isotropic von Mises versus anisotropic Barlat (1989) material models.

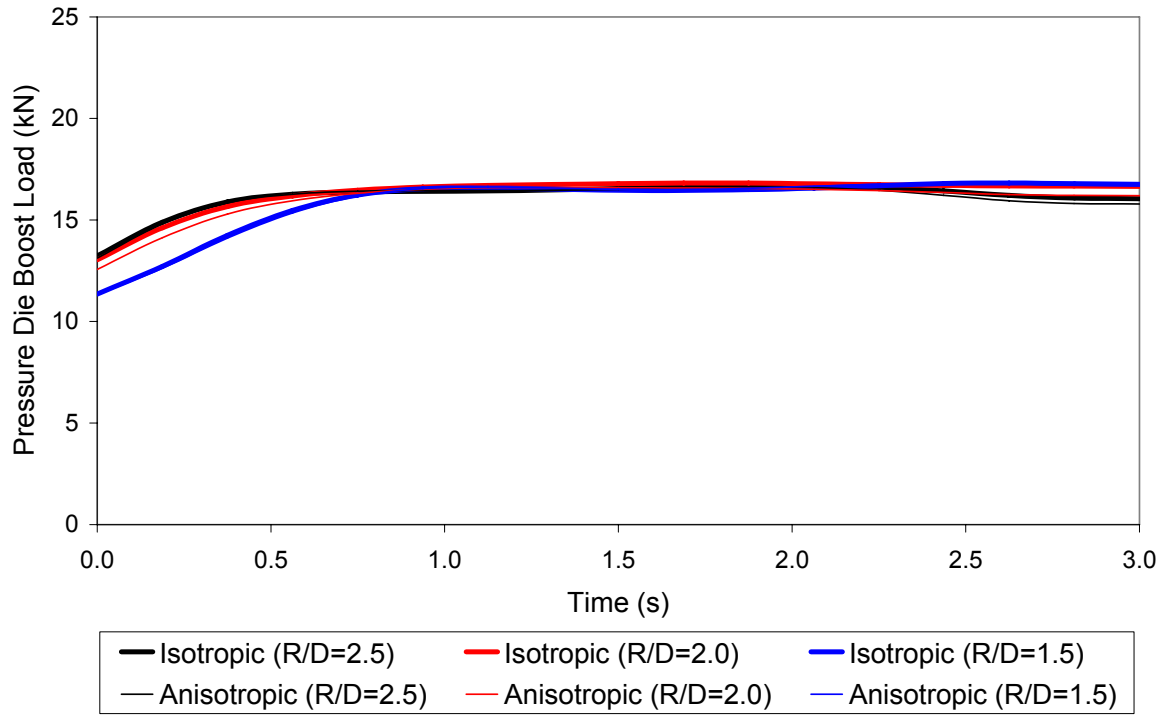


Figure C.2: Predicted pressure die boost load using the isotropic von Mises versus anisotropic Barlat (1989) material models.

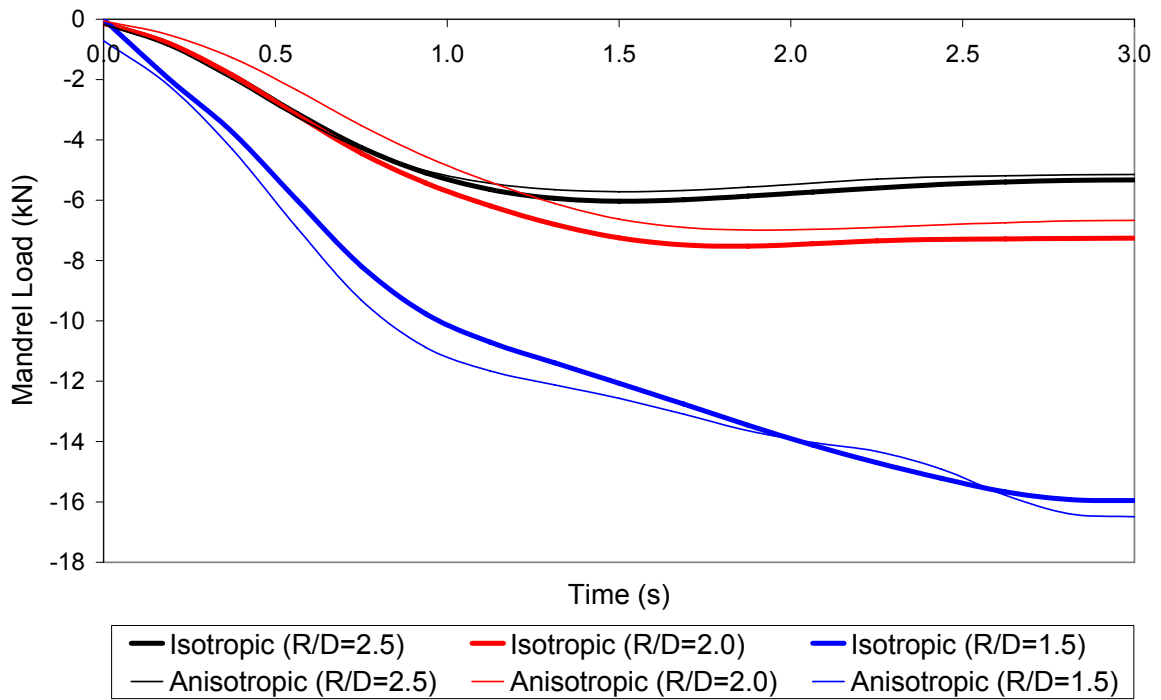


Figure C.3: Predicted mandrel load using the isotropic von Mises versus anisotropic Barlat (1989) material models.

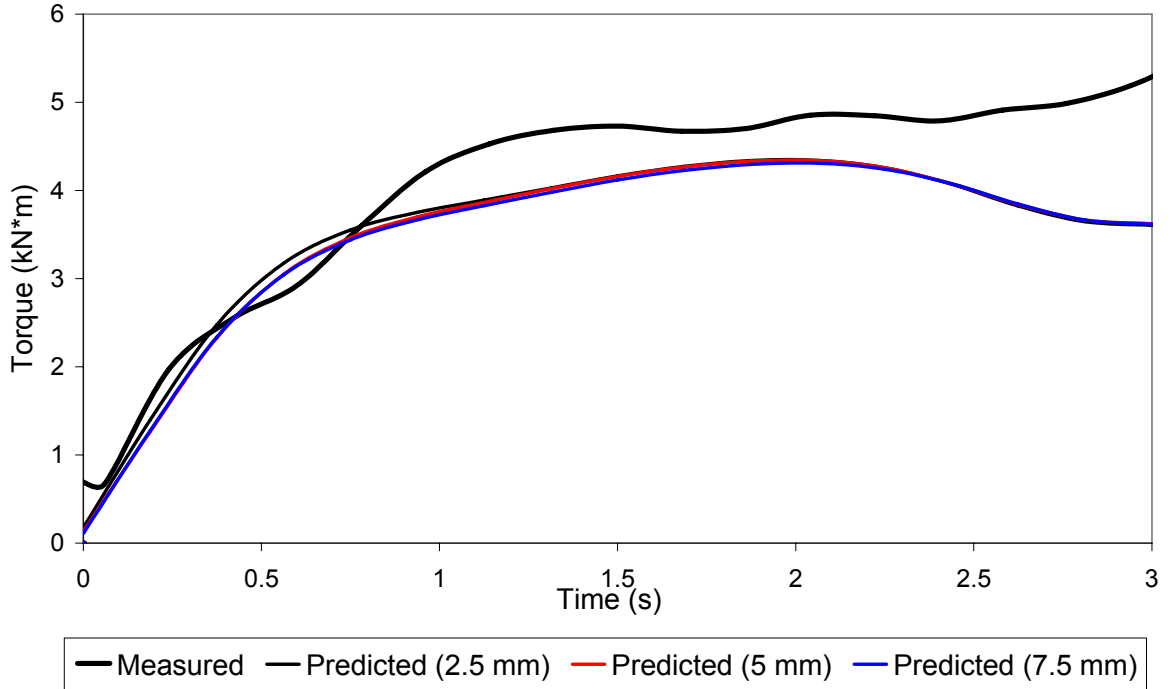


Figure C.4: Measured and predicted bend torque using 2.5, 5 and 7.5 mm element sized mesh discretizations for s-rails bent at $R/D=2.0$ using the anisotropic Barlat (1989) material model.

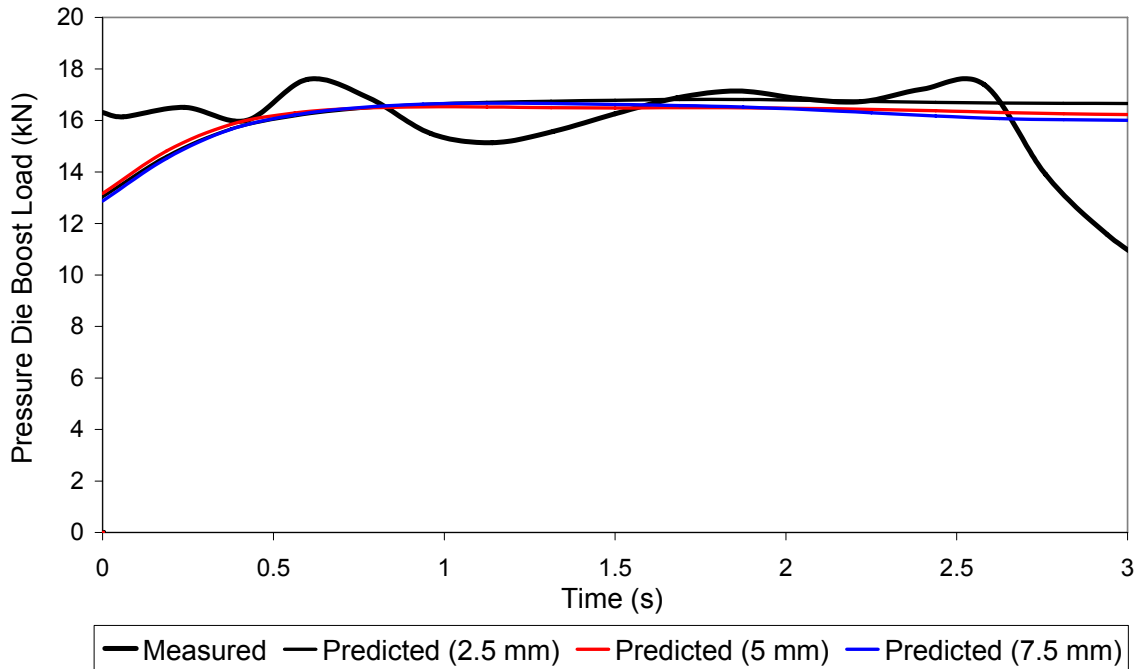


Figure C.5: Measured and predicted pressure die boost load using 2.5, 5 and 7.5 mm element sized mesh discretizations for s-rails bent at $R/D=2.0$ using the anisotropic Barlat (1989) material model.

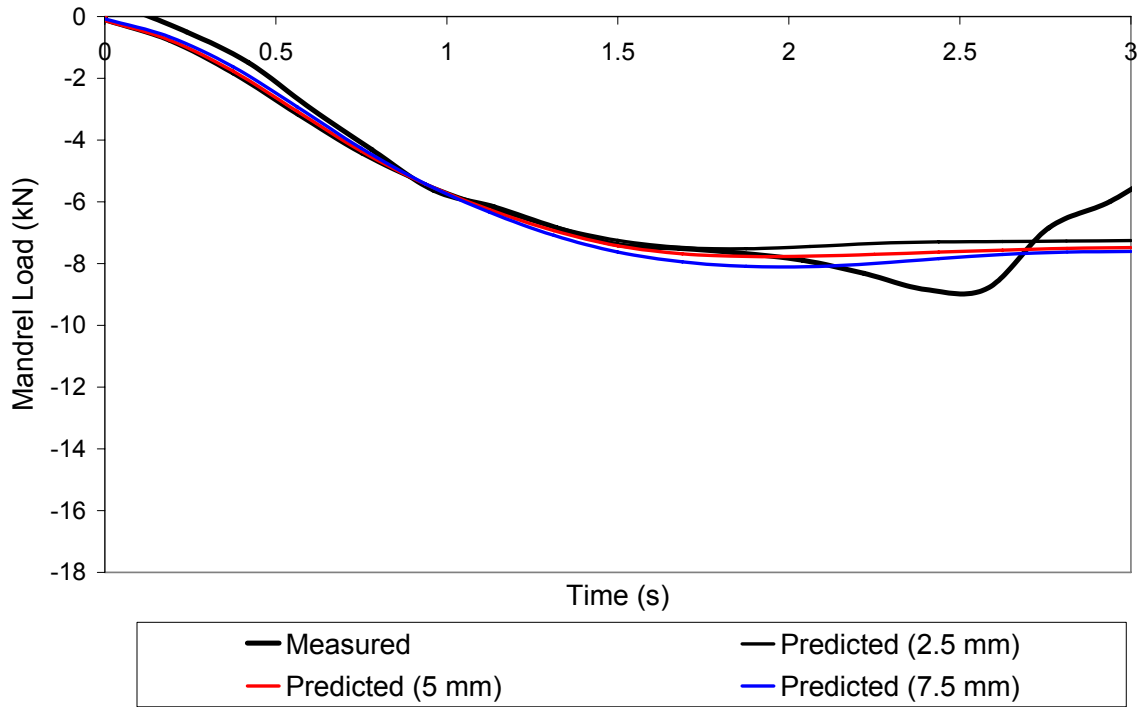


Figure C.6: Measured and predicted mandrel load using 2.5, 5 and 7.5 mm element sized mesh discretizations for s-rails bent at $R/D=2.0$ using the anisotropic Barlat (1989) material model.

C.1.2 Thickness

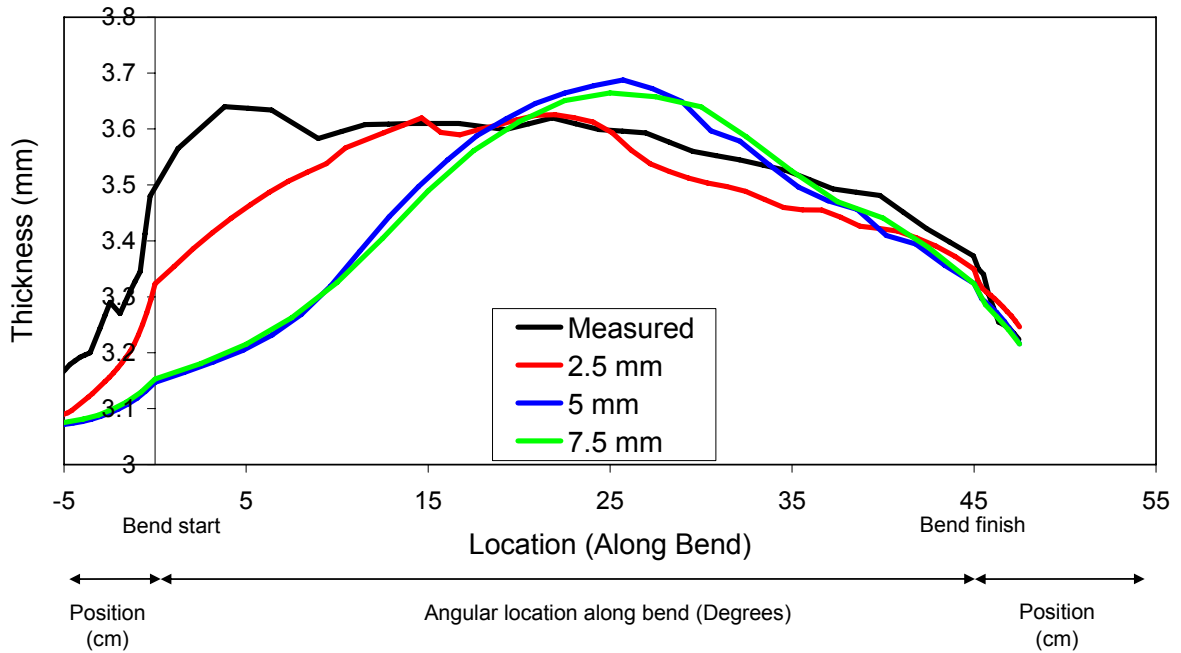


Figure C.7: Predictions of thickness along the inside of an $R/D=2.0$ bend using 2.5, 5 and 7.5 mm element size discretizations and an isotropic von Mises material model.

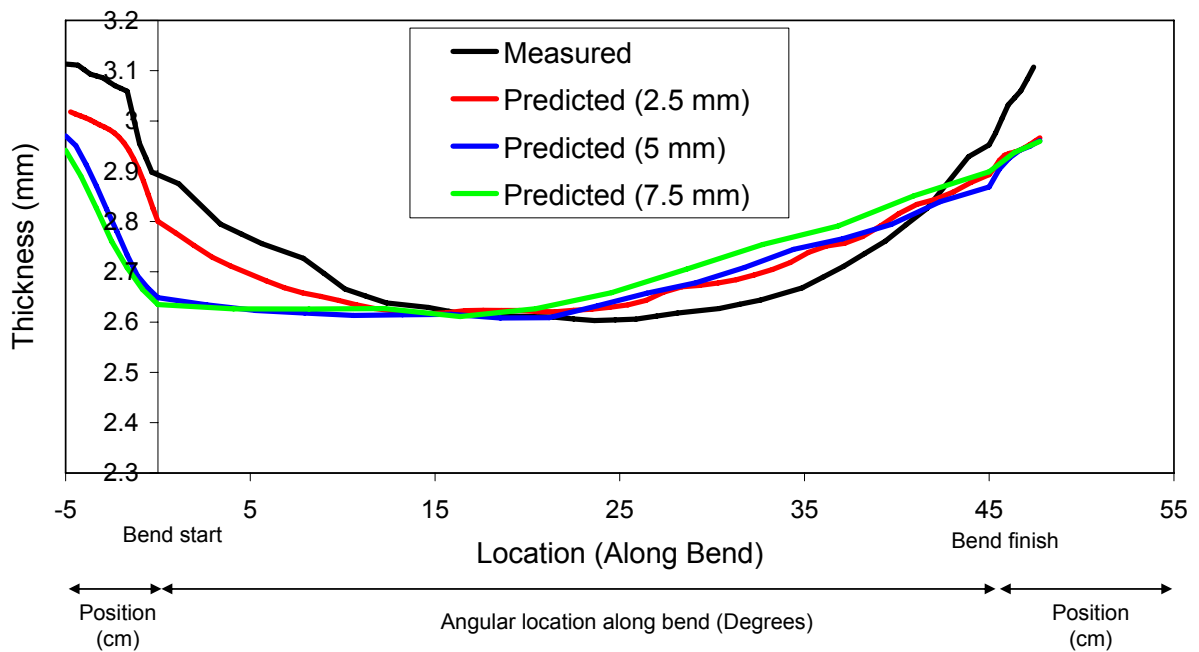


Figure C.8: Predictions of thickness along the outside of an $R/D=2.0$ bend using 2.5, 5 and 7.5 mm element size discretizations and an isotropic von Mises material model.

C.1.3 Strains

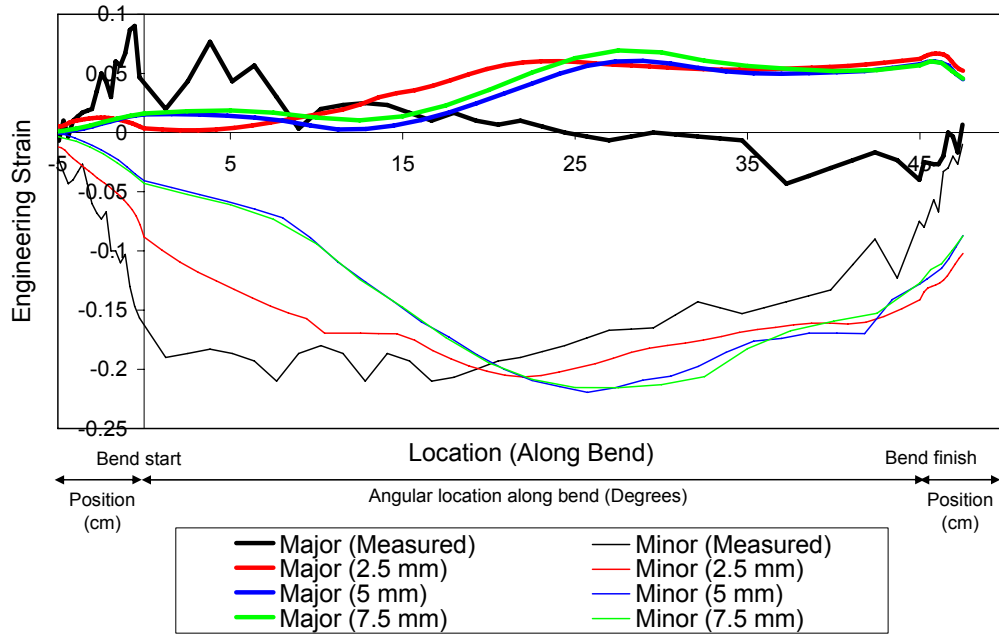


Figure C.9: Predictions of major and minor engineering strains along the inside of an $R/D=2.0$ bend using 2.5, 5 and 7.5 mm element size discretizations and an isotropic von Mises material model.

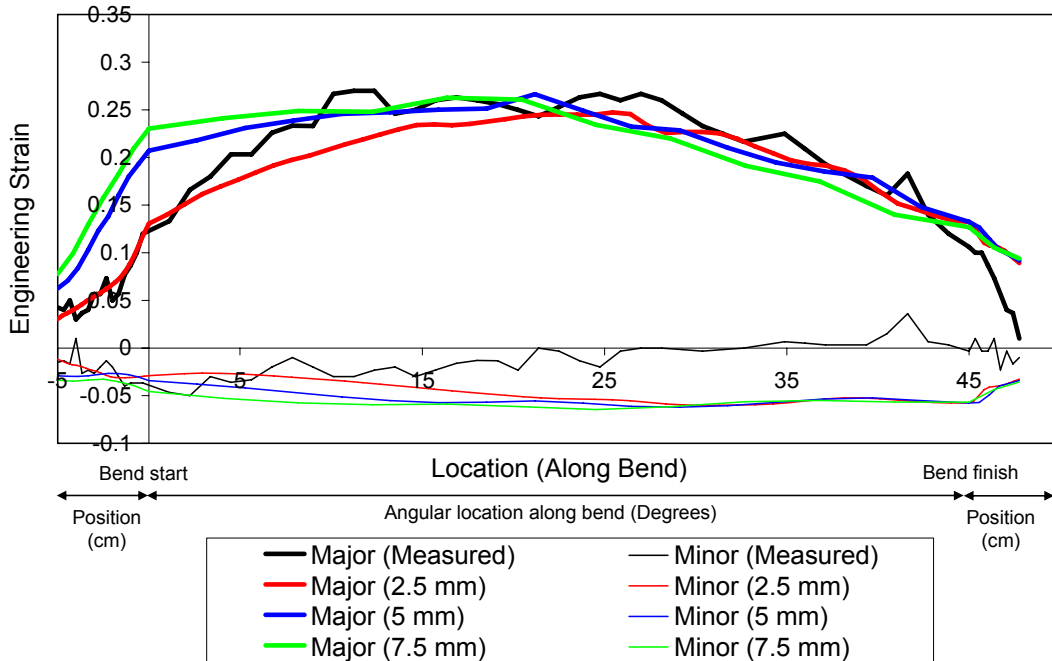


Figure C.10: Predictions of major and minor engineering strains along the outside of an $R/D=2.0$ bend using 2.5, 5 and 7.5 mm element size discretizations and an isotropic von Mises material model.

C.1.4 Predictions of Process Variables, Thickness and Strain utilizing the Zerilli-Armstrong Material Model

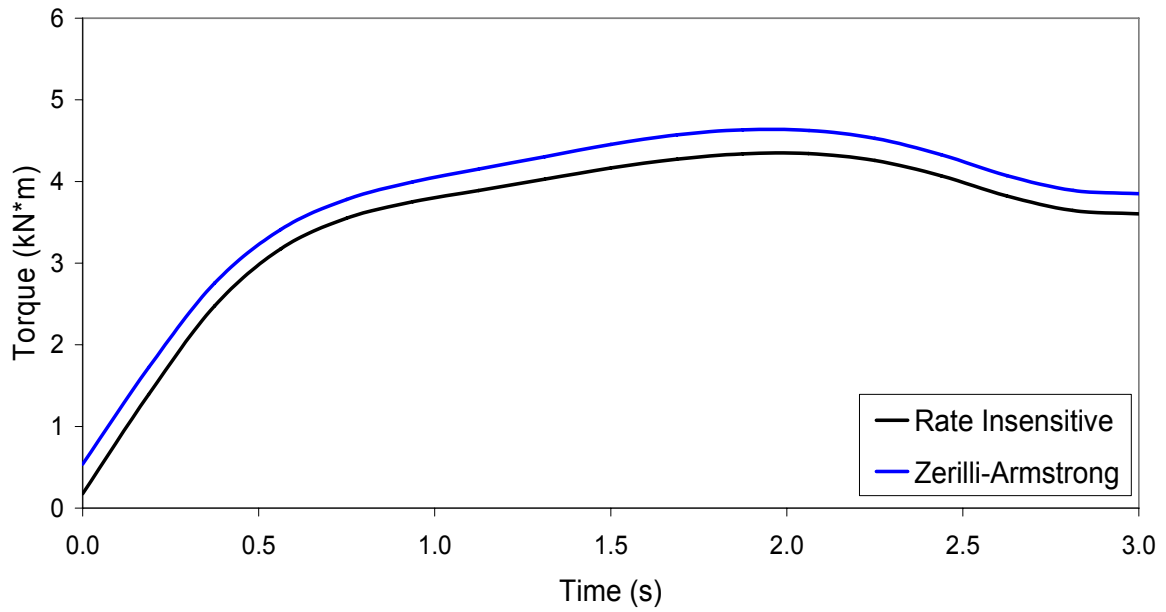


Figure C.11: Predicted bend torque using the rate-insensitive material model and rate-sensitive Zerilli-Armstrong material model.

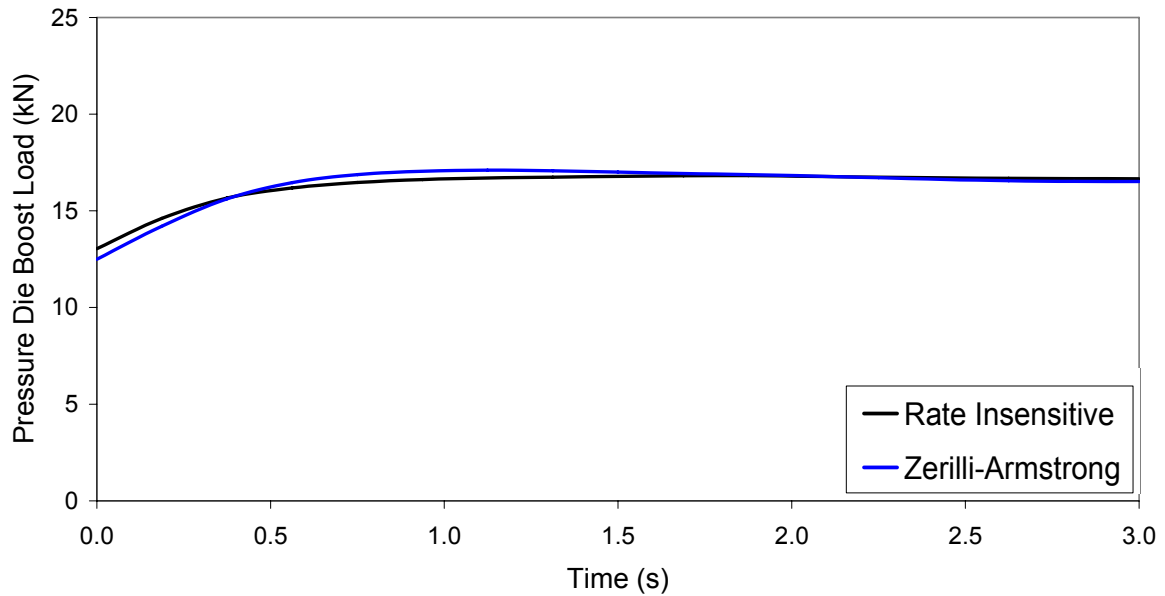


Figure C.12: Predicted boost load using the rate-insensitive material model and rate-sensitive Zerilli-Armstrong material model.

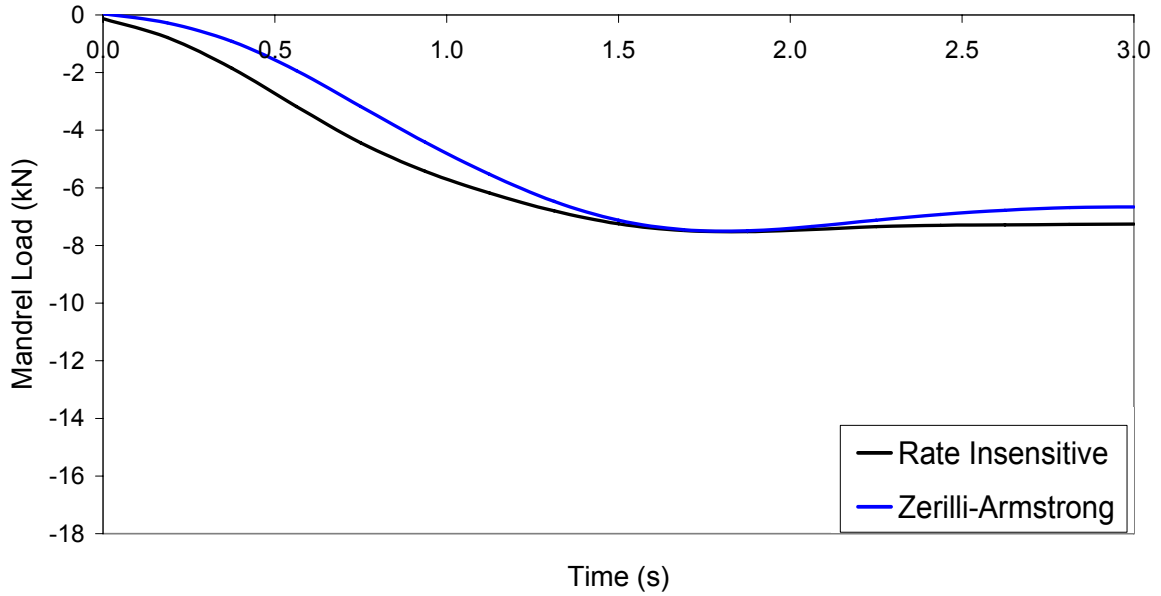


Figure C.13: Predicted mandrel load using the rate-insensitive material model and rate-sensitive Zerilli-Armstrong material model.

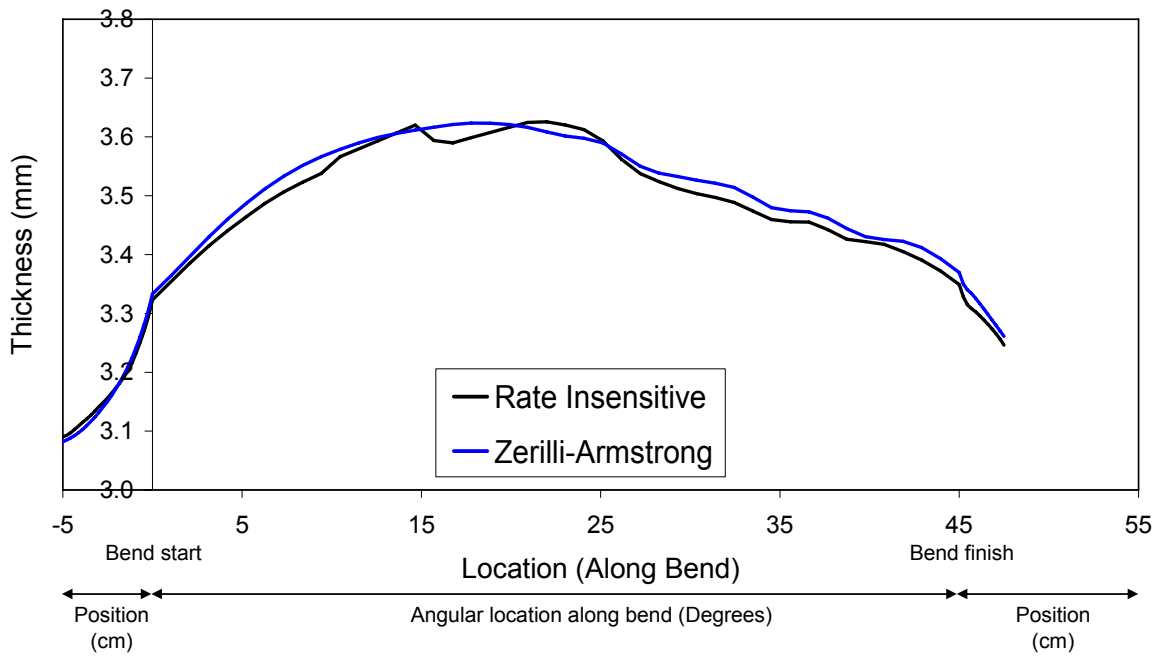


Figure C.14: Predicted thickness along the inside of the bend using the rate-insensitive material model and rate-sensitive Zerilli-Armstrong material model.

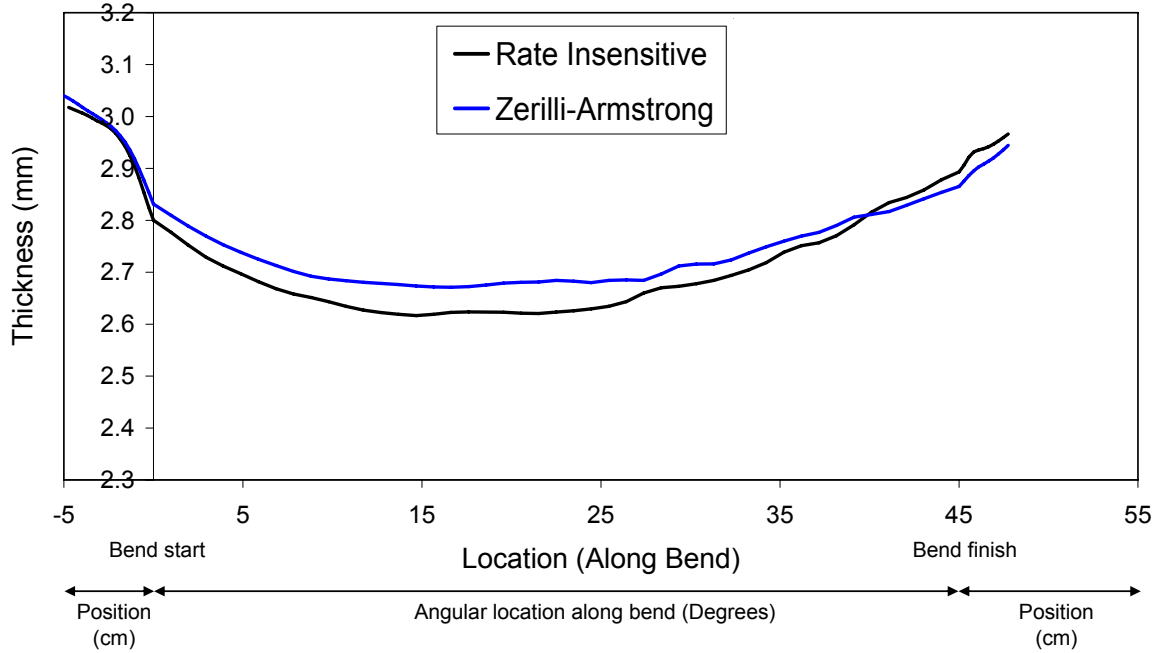


Figure C.15: Predicted thickness along the outside of the bend using the rate-insensitive material model and rate-sensitive Zerilli-Armstrong material model.

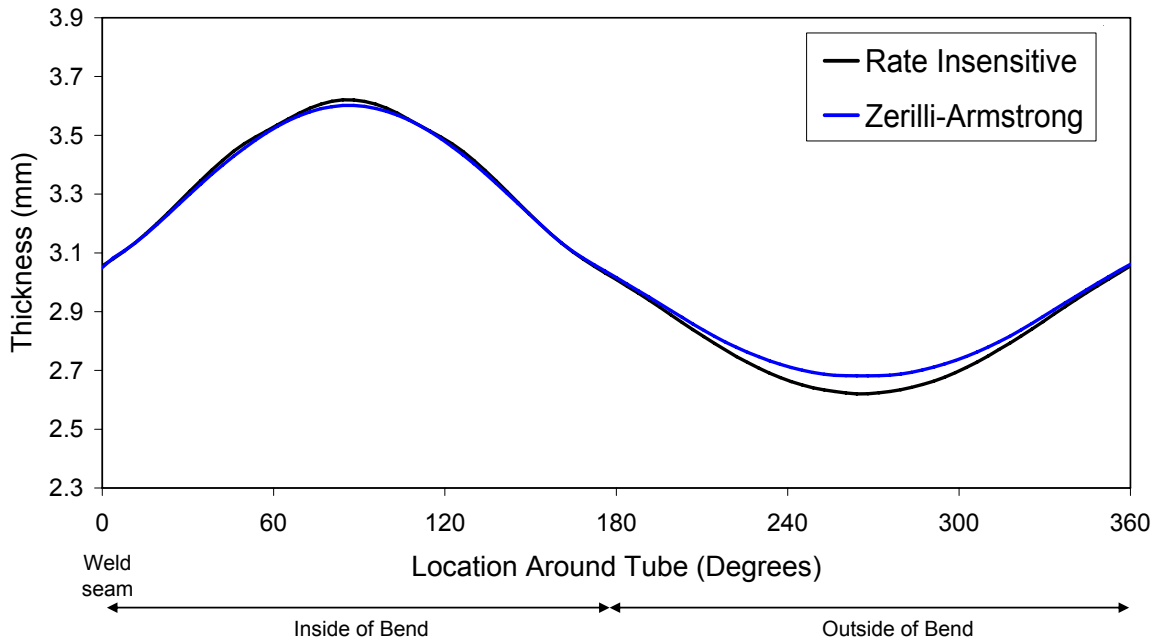


Figure C.16: Predicted thickness around the circumference of the bend using the rate-insensitive and rate-sensitive Zerilli-Armstrong material models.

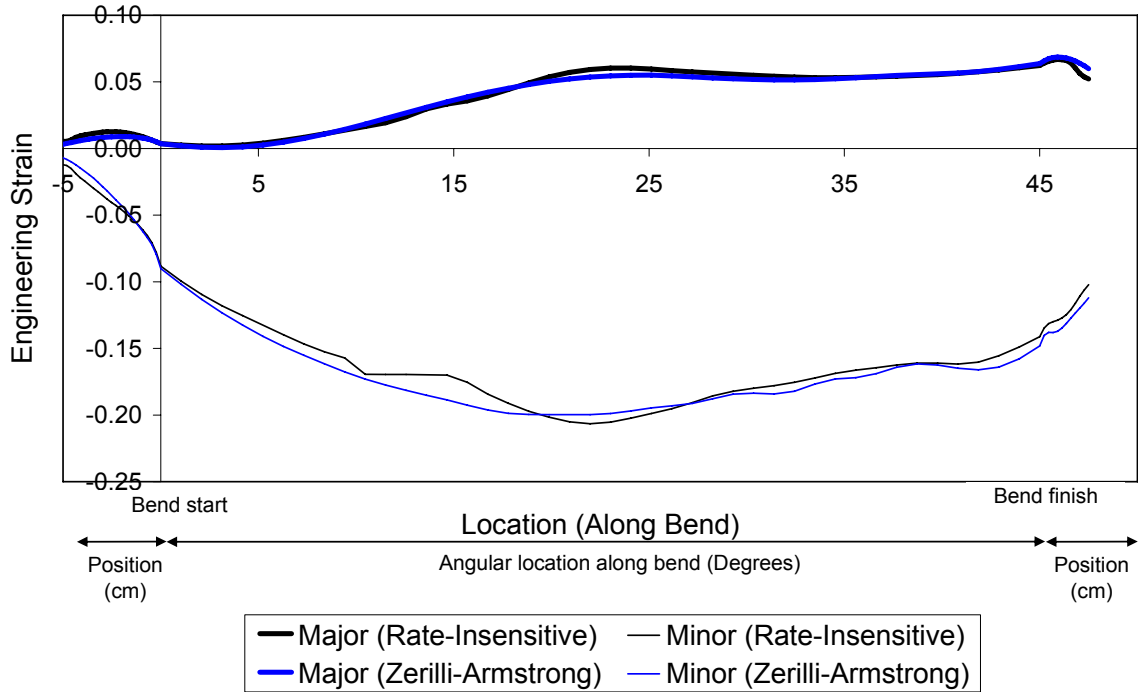


Figure C.17: Predicted major and minor engineering strains along the inside of the bend using the rate-insensitive material model and rate-sensitive Zerilli-Armstrong material model.

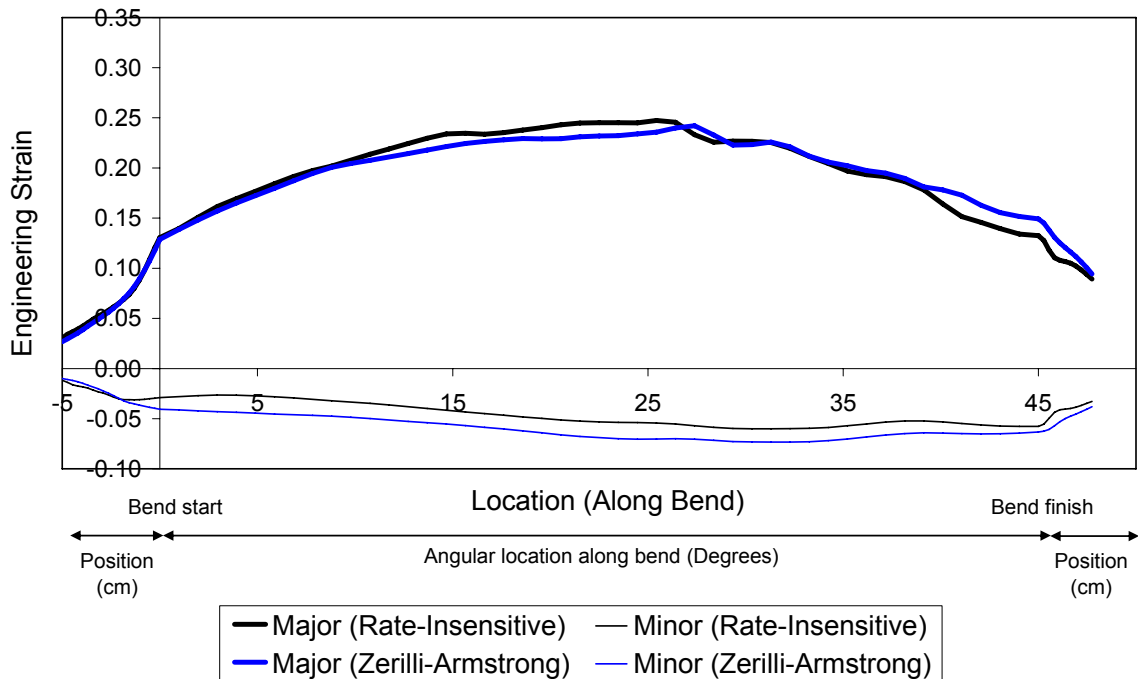


Figure C.18: Predicted major and minor engineering strains along the outside of the bend using the rate-insensitive material model and rate-sensitive Zerilli-Armstrong material model.

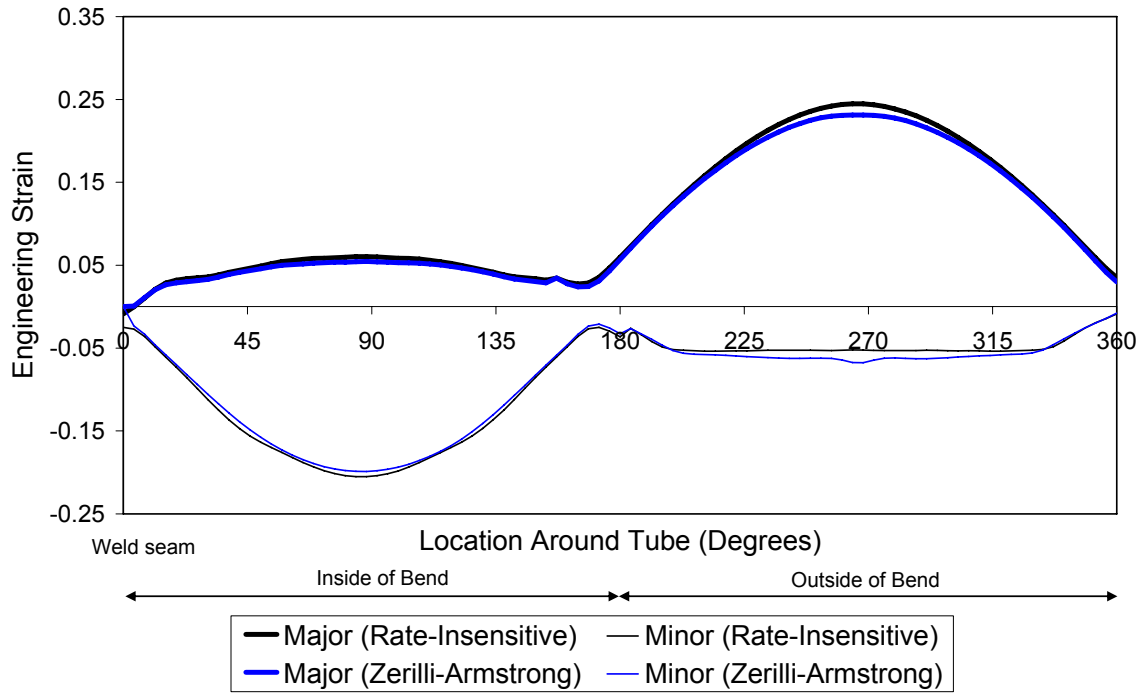


Figure C.19: Predicted major and minor engineering strains around the circumference of the bend using the rate-insensitive and rate-sensitive Zerilli-Armstrong material models.

C.2 Hydroforming

C.2.1 Thickness

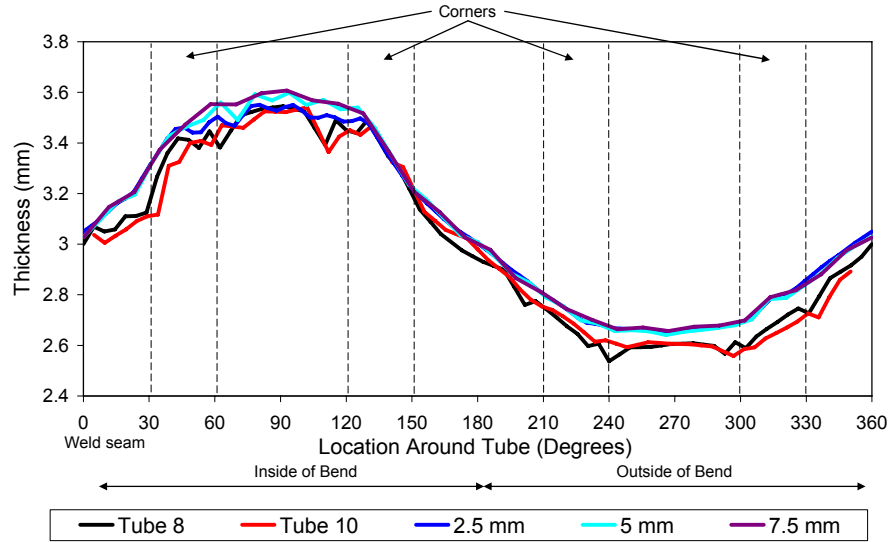


Figure C.20: Measured thickness and predictions using 2.5, 5 and 7.5 mm element size discretizations and the rate-insensitive isotropic von Mises material model around the circumference of the hydroformed bend section $R/D=2.0$.

C.2.2 Strains

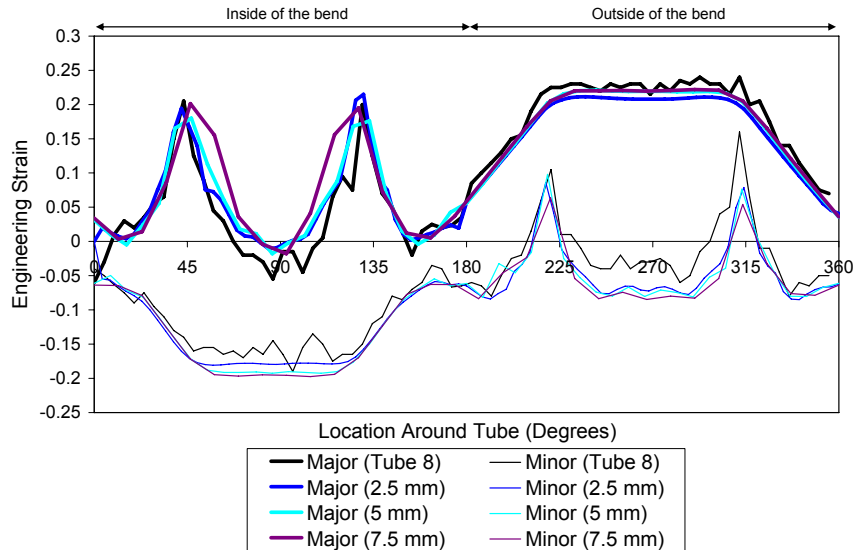


Figure C.21: Measured major and minor engineering strains and predictions using the rate-insensitive isotropic von Mises material model with element size discretizations of 2.5, 5 and 7.5 mm around the circumference of the hydroformed bend section $R/D=2.0$.

C.2.3 Predictions of Thickness and Strain utilizing the Zerilli-Armstrong Material Model

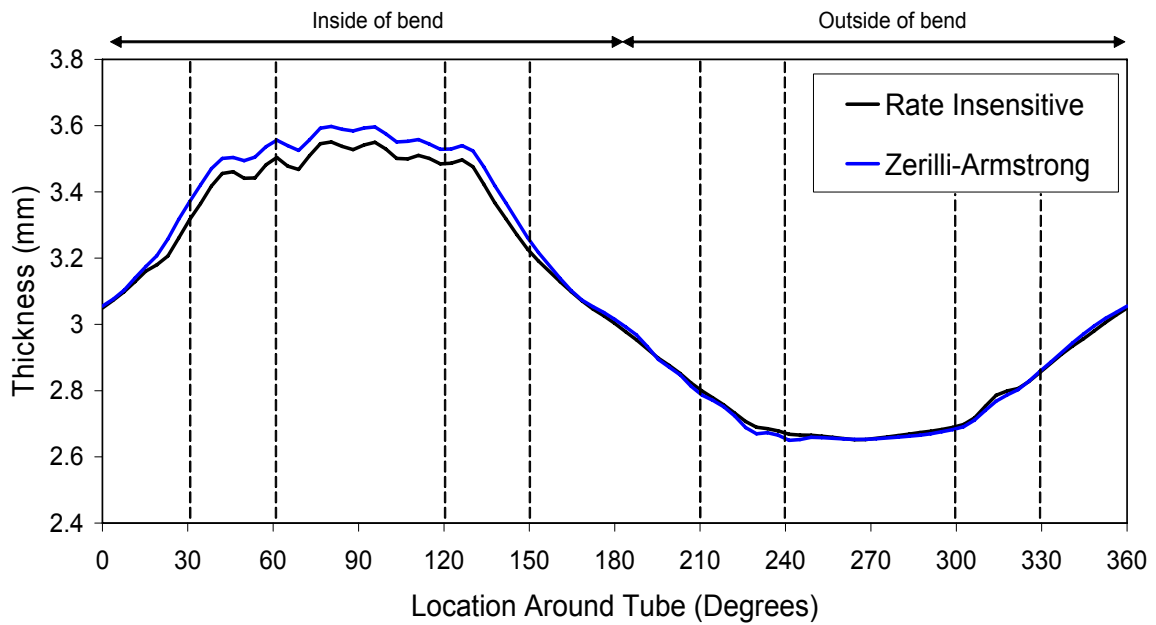


Figure C.22: Predicted thickness around the circumference of the bend region after hydroforming using the rate-insensitive and rate-sensitive Zerilli-Armstrong material models.

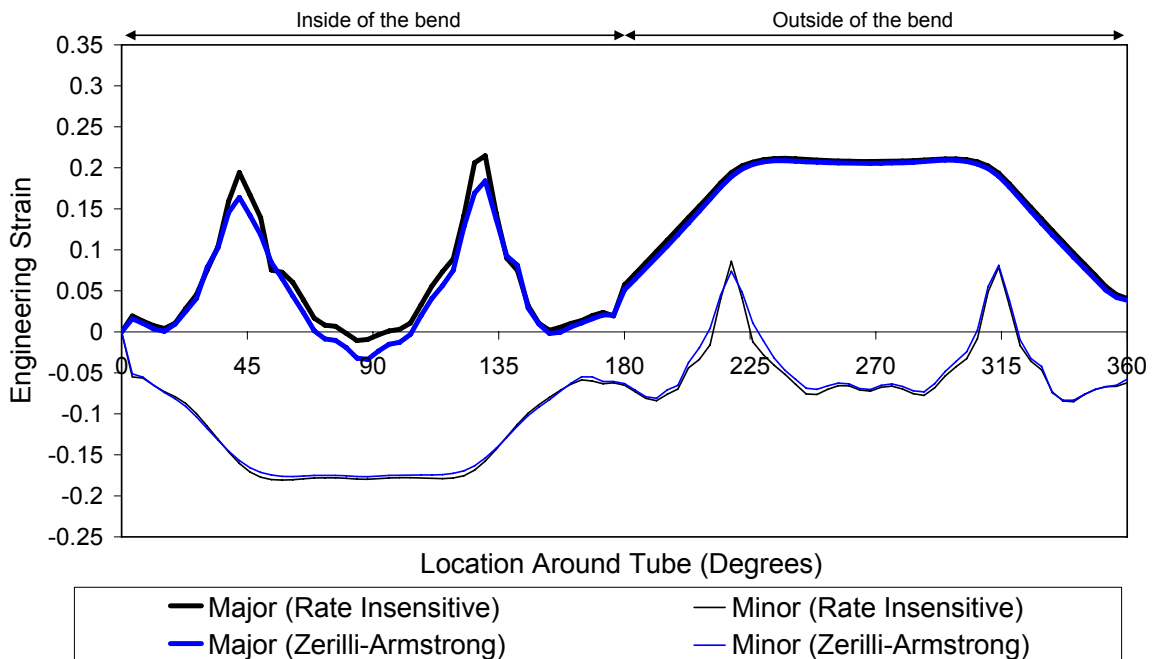


Figure C.23: Predicted major and minor engineering strains around the circumference of the bend region after hydroforming using the rate-insensitive and rate-sensitive Zerilli-Armstrong material models.

C.3 Crash Predictions

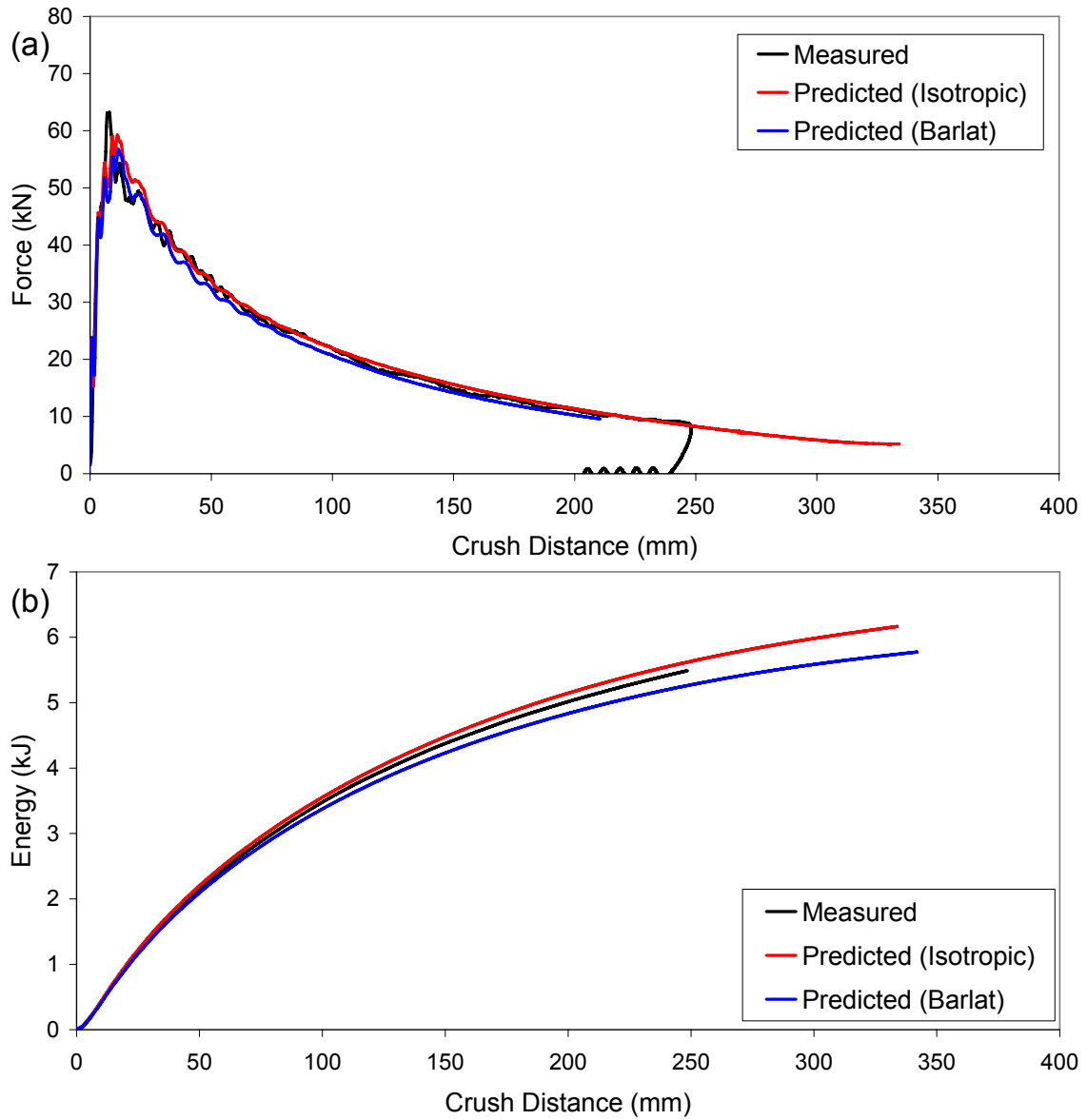


Figure C.24: Measured and predicted (a) force; and (b) energy versus crush distance for a 3 mm AA5754 non-hydroformed s-rail bent at $R/D=2.5$ using the isotropic and anisotropic models.

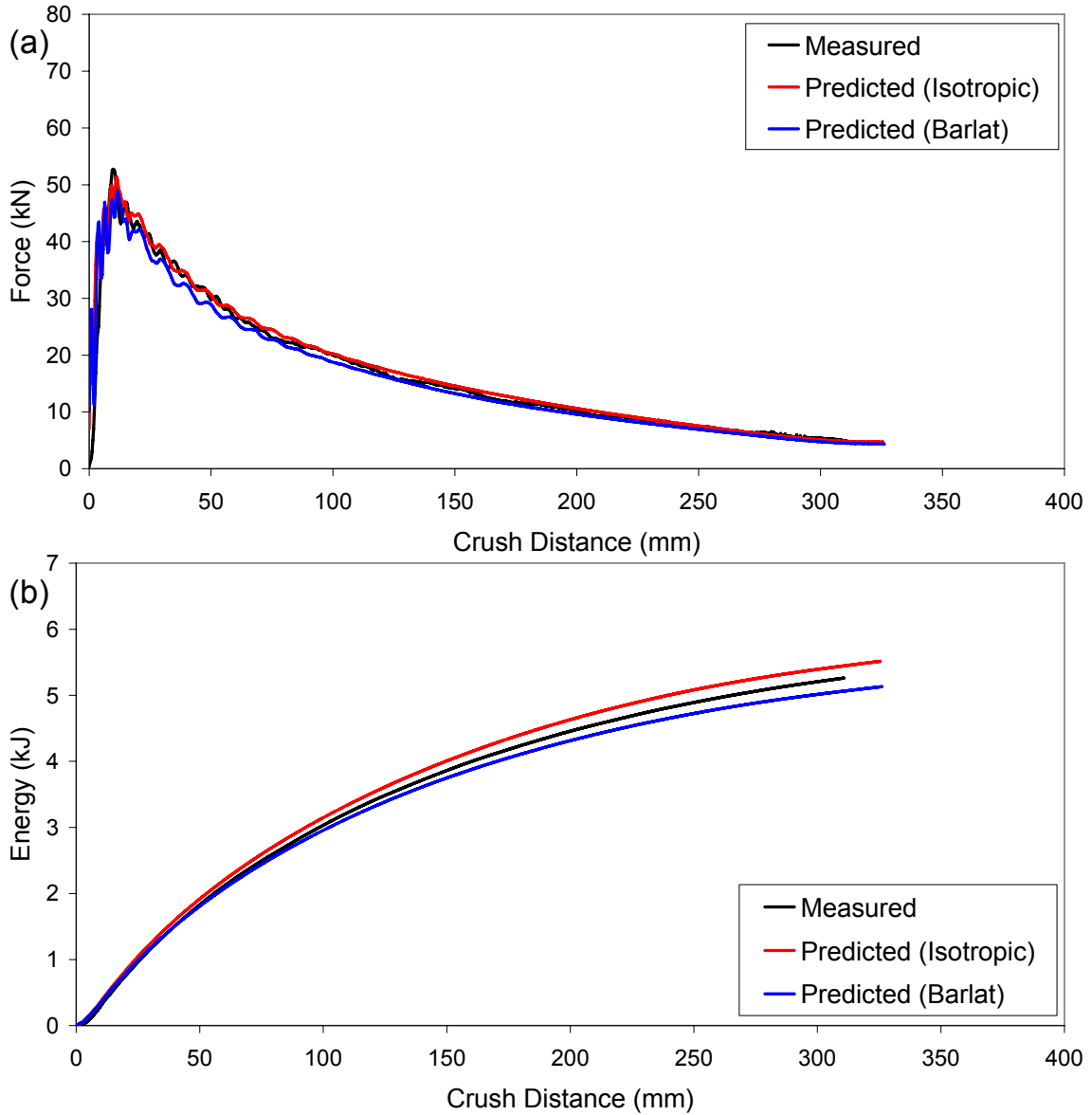


Figure C.25: Measured and predicted (a) force; and (b) energy versus crush distance for a 3 mm AA5754 non-hydroformed s-rail bent at $R/D=1.5$ using the isotropic and anisotropic models.

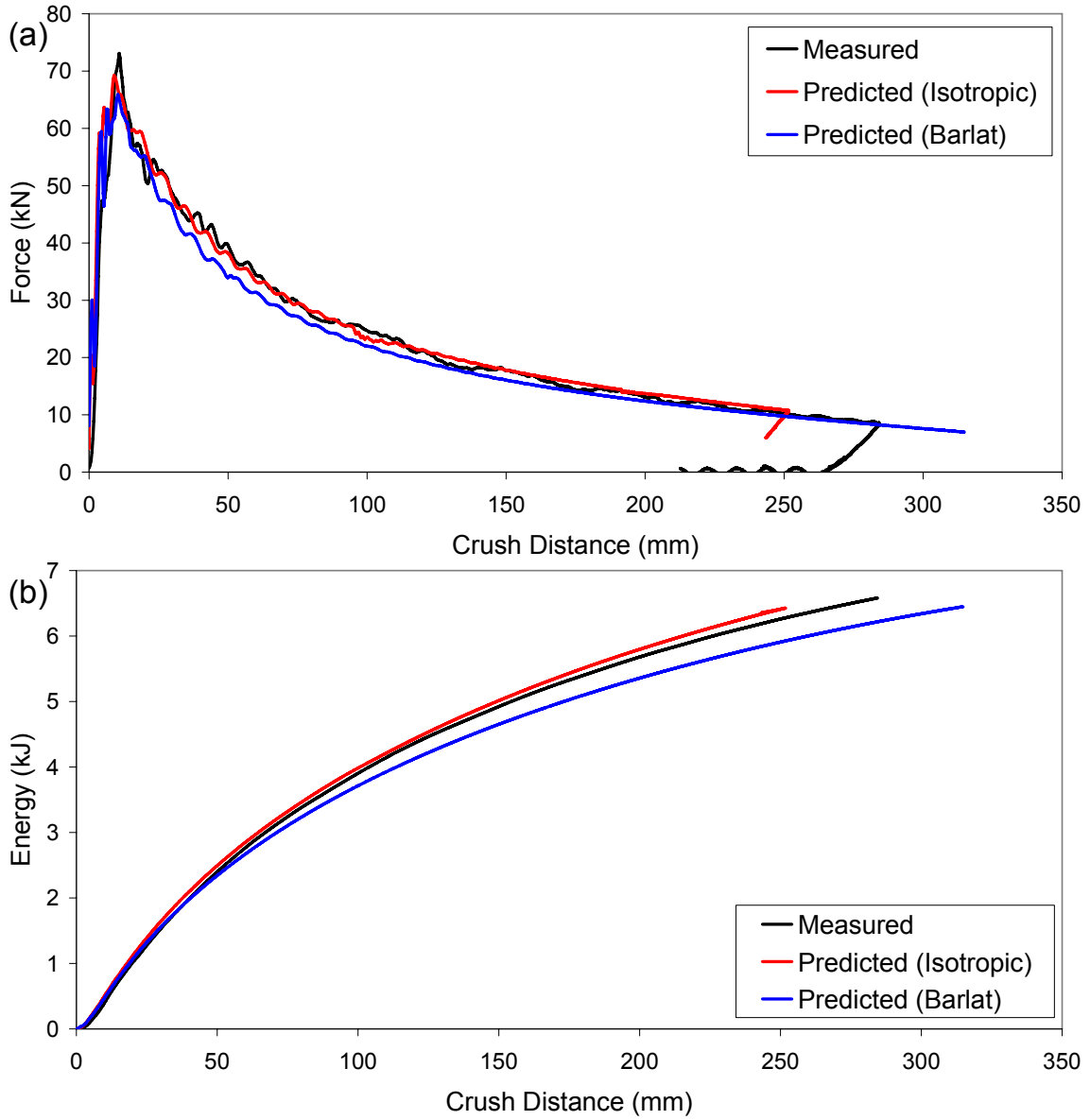


Figure C.26: Measured and predicted (a) force; and (b) energy versus crush distance for a 3 mm AA5754 hydroformed s-rail bent at $R/D=2.5$ using the isotropic and anisotropic models.

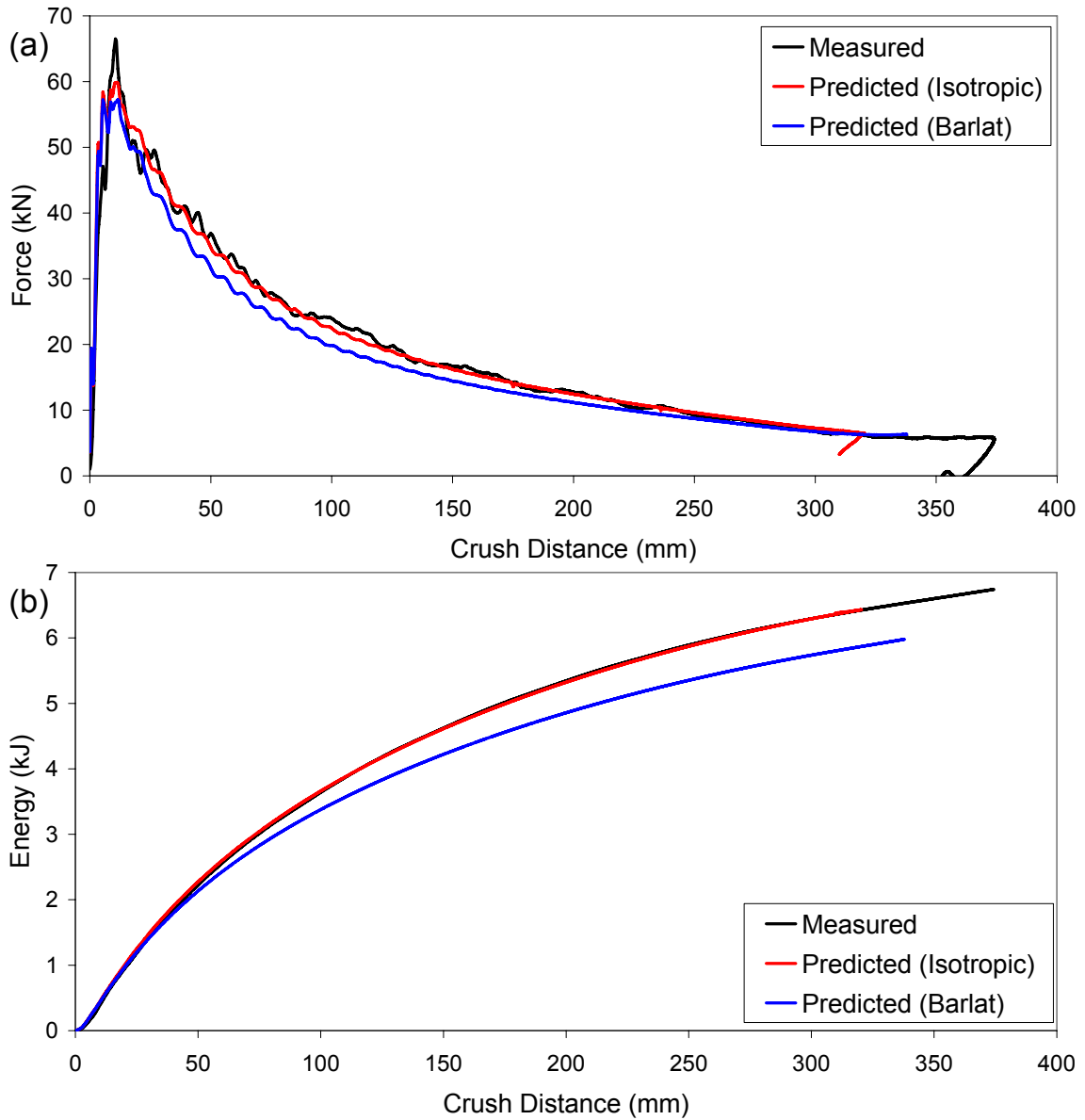


Figure C.27: Measured and predicted (a) force; and (b) energy versus crush distance for a 3 mm AA5754 hydroformed s-rail bent at $R/D=1.5$ using the isotropic and anisotropic models.

Appendix D: Understanding the Force Response in S-Rail Crash

D.1 Overview

In the s-rail crash experiments, the force response was captured in a filtered form using a low-pass 1 kHz Butterworth filter within the data acquisition system, as described in Section 2.5.1. To allow consistent comparisons between the model predictions and the experimental data, this 1 kHz Butterworth filter was also applied to the predicted force-time response. In this section, some insight into the oscillatory nature of the early predicted force-time response, and the initial period of the force-time response and how it is governed by stress wave propagation is given. To better understand the non-filtered force-time response of s-rails in the actual crash experiments, the sensitivity of the model prediction to a damping element, which mimics the rubber pad and plywood on the top cover plate in the crash test set-up (Figure 2.15), and consideration of forming history are examined.

D.1.1 Oscillatory Nature of Early Force-Time Response

The predicted filtered and non-filtered force versus time response of a 3 mm AA5754 hydroformed s-rail bent at $R/D=2.0$ using the modeling techniques described in Chapter 3 is shown in Figure D.1. Also shown in Figure D.1 is the level of s-rail deformation corresponding to 0, 10, 70 and 150 ms, and the approximate time duration that stress wave propagation significantly influences the force-time response. Within roughly the first 5 ms of impact, large fluctuations in the force-time response are observed, after which the oscillations dampen and decay in a smooth manner. The 1 kHz Butterworth employed significantly reduces the amplitude and the number of oscillations in the predicted force-time response.

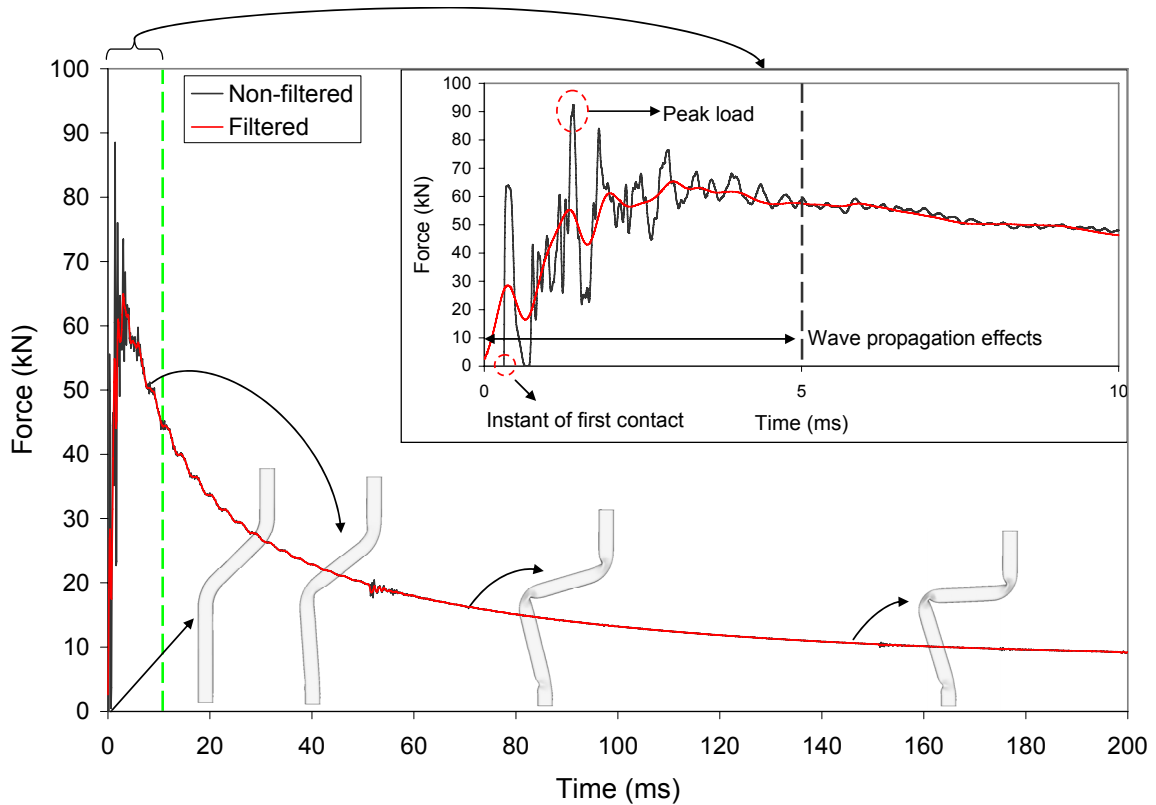


Figure D.1: Predicted, filtered and non-filtered crush force versus time for a 3 mm AA5754 hydroformed s-rail bent at an $R/D=2.0$. Level of deformation, instant of first contact, peak load and time duration that wave propagation effects are significant are shown.

D.2 Wave Propagation Theory

A comprehensive presentation of wave propagation theory is given in the book by Meyers [127]. Here, only the relevant equations required to describe the one-dimensional elastic stress wave propagation due to impact in a simple cylindrical bar are presented, which will be sufficient to understand the s-rail wave propagation analysis of the next section.

Consider the impact of two elastic cylindrical bars for which the bar diameter is much smaller than the bar length and the length of incident bar is much greater than the striker. The striker bar (A) traveling at velocity v impacts the stationary incident bar (B), as shown in Figure D.2. Just after the moment of impact two compressive stress waves traveling at speed

$$C = \sqrt{\frac{E}{\rho}}, \quad (D.1)$$

are generated in the bars,

where E = the modulus of elasticity of the bars and

ρ = the density of the bars.

The magnitude of the stress pulse in the bars is given by

$$\sigma = \frac{1}{2} \rho C v \quad (D.2)$$

The stress wave in the striker bar propagates and reflects from the free surface and is transferred into the incident bar. The duration of the pulse in the incident bar after contact with the striker bar is twice the length of the striker bar ($2L_A$).

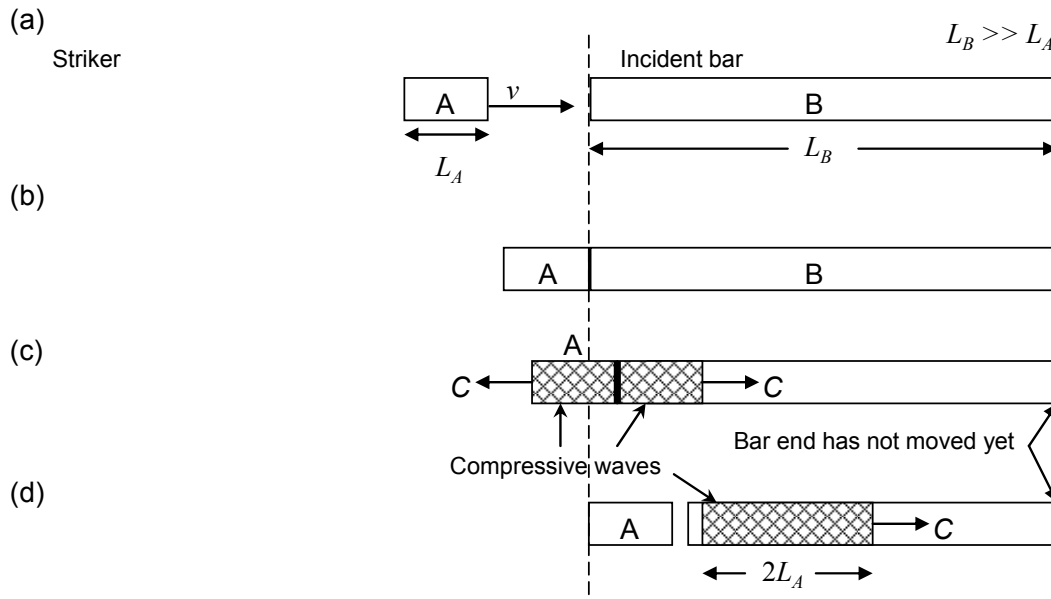


Figure D.2: Impact of two cylindrical bars: (a) before impact; (b) at the moment of impact; (c) shortly after impact; and, (d) after the stress wave from the striker bar has been transferred to the incident bar.

D.2.1 Wave Reflection and Transmission

If a stress wave encounters a boundary or adjacent material of different impedance, part of the wave will be transmitted and part will be reflected. Impedance changes can be due to variations in geometry or material properties, for example. A geometric impedance change is experienced when a wave propagates across a boundary of different cross-sectional areas, while material impedance changes are due to differences in the material density, as shown in Figure D.3. For equilibrium to exist when a stress wave encounters a boundary of constant

cross-section, the sum of the incident and reflected forces must equal the transmitted force. For continuity to exist at the interface (no gaps or overlap of the materials), the sum of the velocities of the incident and reflected waves must equal that transmitted wave velocity. The reflected stress and particle velocity (U_p) of a wave encountering a free surface or a rigid boundary are summarized in Table D.1 [127]. In terms of our simplified example presented earlier, a rigid object impacting a rod results in a stress pulse that is twice in magnitude than that given by Equation D.2.

$$\sigma = \rho C v \tag{D.3}$$

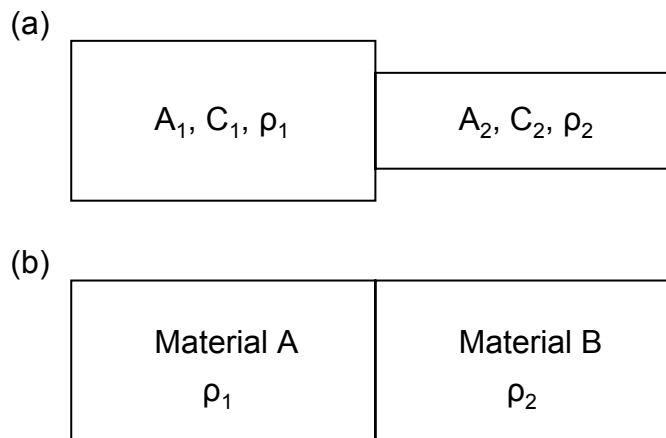


Figure D.3: (a) Geometric; and, (b) material impedance changes.

Table D.1: Wave property relations at free and rigid boundaries. Note that the incident, reflected and transmitted wave properties are denoted by sub- and super-script symbols I , R and T , respectively [127]. U_p refers to the particle velocity.

Boundary	Wave Property Relations
Free surface	$\sigma_T=0$; $\sigma_R=(-\sigma_I)$ & $U_p^T=2U_p^I$; $U_p^R=U_p^I$
Rigid boundary	$\sigma_T=2\sigma_I$; $\sigma_R=\sigma_I$ & $U_p^T=0$; $U_p^R=(-U_p^I)$

D.3 Wave Propagation in S-Rail Crash

The impact of the sled on the s-rail generates a compressive stress wave that propagates from the impact location to the fixed end while experiencing multiple interactions with geometric and rigid boundaries (Figure D.4), as well as reflected waves (Figure D.5). The geometric boundaries are located at the bend regions of the s-rail and are due to its' curvature which changes the direction of the local particle velocity, resulting in a complex transmission and reflection of the waves. The travel distance and the time interval for a longitudinal stress

wave to traverse the regions between boundaries of the s-rail are shown in Figure D.4, while Figure D.5 shows contours of axial or z-stress at various instants in time up to the start of the second peak of force.

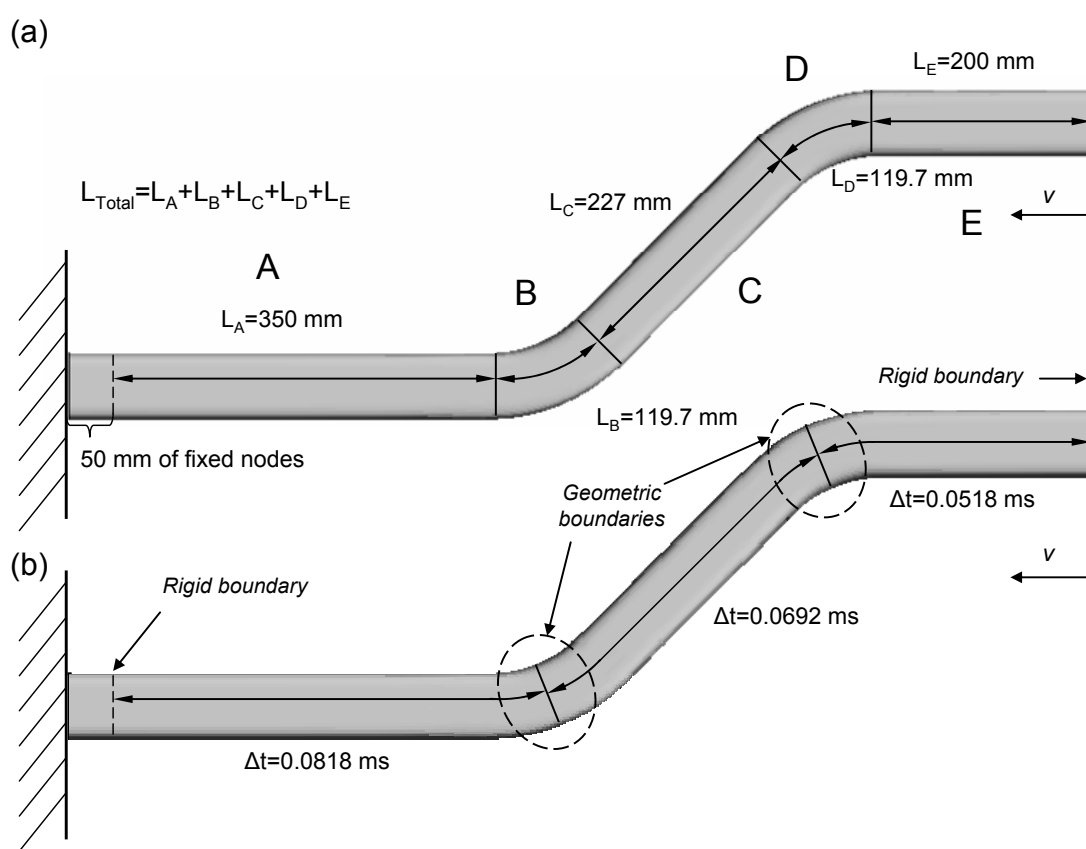


Figure D.4: (a) Traverse distances; and (b) time intervals for a stress wave to propagate between the geometric and rigid boundaries of the s-rail.

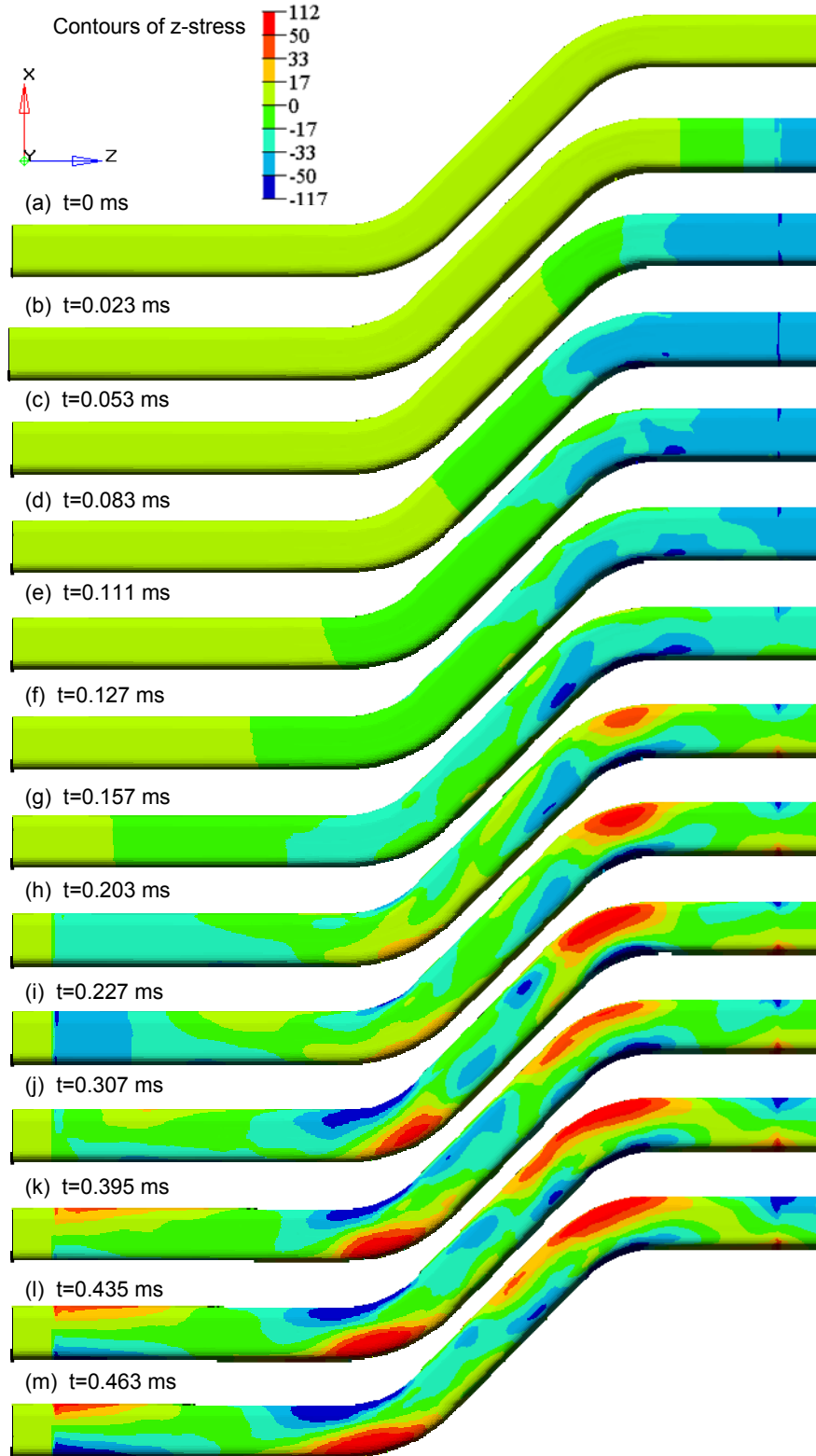


Figure D.5: Contours of stress in the z-direction at various instants in time due to impact showing the progression of first loading wave.

The predicted force versus time signature for an s-rail impact event up to the second peak of force is shown in Figure D.6. To better understand the influence of the wave interactions on the predicted force acting on the impact plate, the points in time that the reflected stress waves from the first and second bends, and fixed end of the s-rail reach the impact plate were calculated based on the longitudinal wave speed (Equation D.1) and are also shown in Figure D.6. Note that for simplicity, additional wave reflections due to waves interacting with one another are not considered. After impact ($t=0$ ms), a compressive stress pulse is generated and travels along the s-rail at the speed of sound in the material, which is 5,015 m/s. After reaching the first bend region (Section D), the wave encounters a geometric boundary (first bend) and therefore part of the wave is transmitted and part reflected. The reflected wave from the first bend is tensile and propagates towards the impact plate, while the transmitted wave remains compressive. There will also be a large bending wave initiated at this geometric discontinuity. The bending waves generated under such an impact scenario are much lower than the longitudinal component, and for this reason, this discussion is centered on the longitudinal waves. Arrival of the reflected tensile wave from the first bend at the impact plate occurs at 0.104 ms and causes the stress/force at the boundary to begin to decrease as can be seen in Figure D.6. The force on the impact plate continues to decrease rather abruptly until the second reflection of stress from the first bend arrives back at the impact plate, which causes a change in the rate of its' deceleration. Shortly thereafter, tensile stress waves from the first reflection at the second bend and the third reflection at the first bend arrive at the impact plate causing the net force to become zero due to the superposition of stresses that occur in that local region. The net force on the impact plate remains zero until the first reflected compressive stress waves from the fixed end of the s-rail (arrive at 0.406 ms) and the fourth reflection from the first bend (at 0.414 ms) arrive back at the impact plate. Beyond this point in time, the level of complexity of the stress wave interactions increase significantly (Figure D.5) such that they cannot be tracked using simple wave velocity calculations.

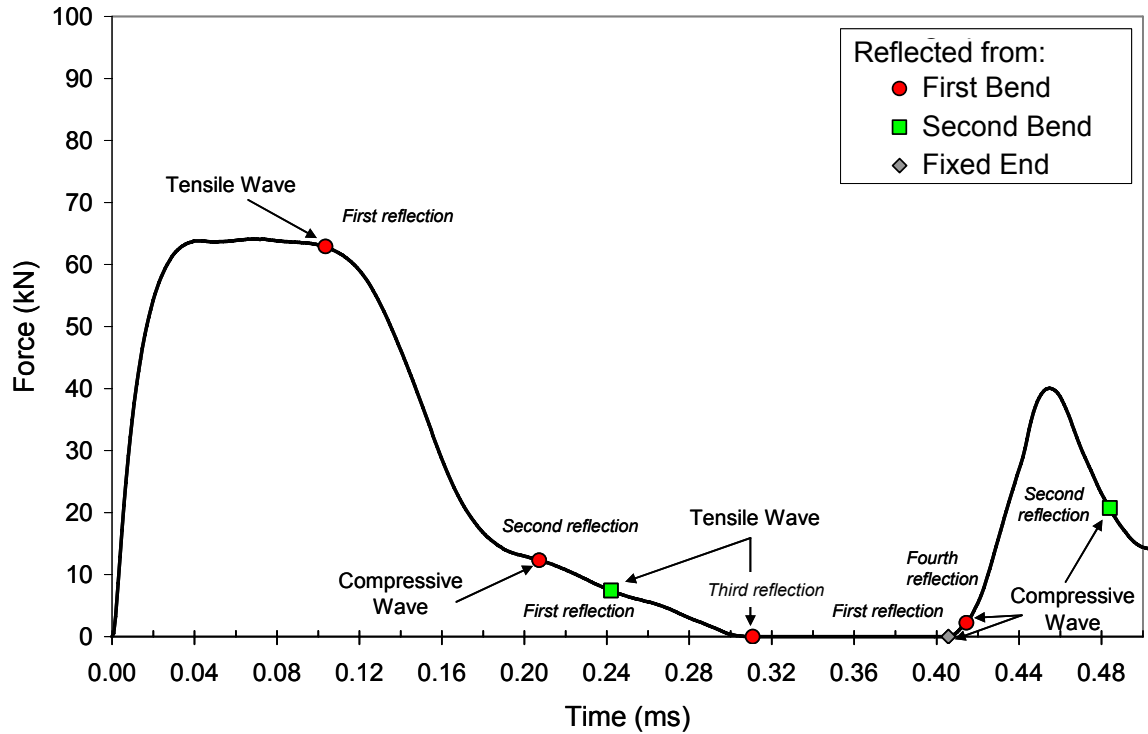


Figure D.6: Predicted force versus time signature of s-rail. Points in time that the stress waves reflected from the first and second bends, and the fixed end of the s-rail reach the impact plate.

D.3.1 Data Filtering

Depending on the manner in which the force-time data is processed, different representations can be obtained. The effect of applying the 1 kHz Butterworth filter to the predicted force versus time response of an as-formed s-rail can be seen in Figure D.7. The filter effectively reduces the amplitude of the force oscillations and is more consistent with the experimental result (Figure D.7), which was also filtered as described in Section 2.5.1.

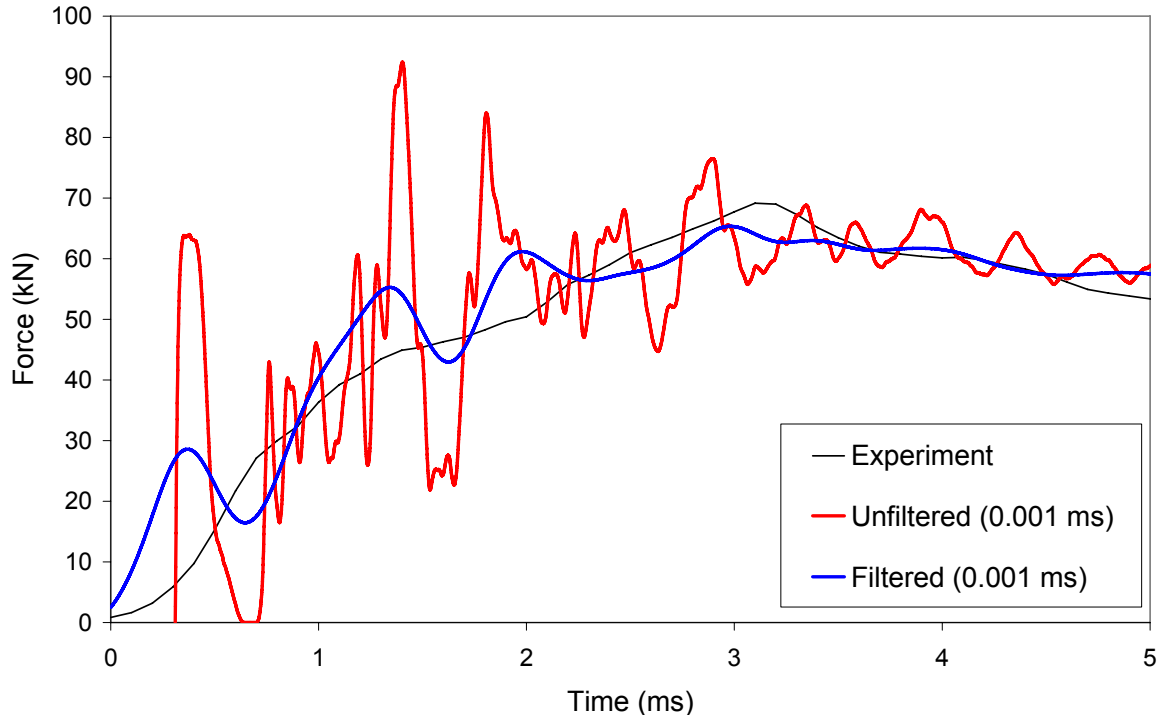


Figure D.7: Experimental and predicted (filtered and non-filtered) force versus time data.

D.3.2 Effect of a Damper at the Impact Interface

As shown in Figure 2.15, the experimental set-up incorporated a rubber pad and sheet of plywood placed on the top impact plate to prevent ringing in the system that could damage the load cells. For simplicity, the rubber pad and plywood were not considered in the crash model, and despite this simplification the model was shown to provide excellent predictions of force and energy absorption as shown in Chapter 5. It is evident, however, in the comparison of measured and predicted force-time histories in Figure D.7, that the rise time of the predictions is much shorter than seen in the experiments. This comparison suggests that damping effects in the experiments could be important, particularly during the early stages of impact. To provide insight into the effect of damping at the contact interface on the force versus time response, a model was developed that considers the rubber pad and top cover plate at the impact interface. To simplify the model, the plywood, which is extremely challenging to accurately represent numerically, is neglected. A schematic of the impact scenario is shown in Figure D.8. The rubber pad was modeled using an Ogden linear viscoelastic formulation within LS-DYNA [30,31], and the material parameters were provided by Cronin [145], and are shown in Table D.2. Eight-node hexahedron constant

stress solid elements were used to represent the rubber pad and top cover plate within the simulation. The top cover plate was treated as elastic and assigned elastic properties corresponding to steel [146], and the impact plate was treated as a rigid body, as described in Chapter 3.

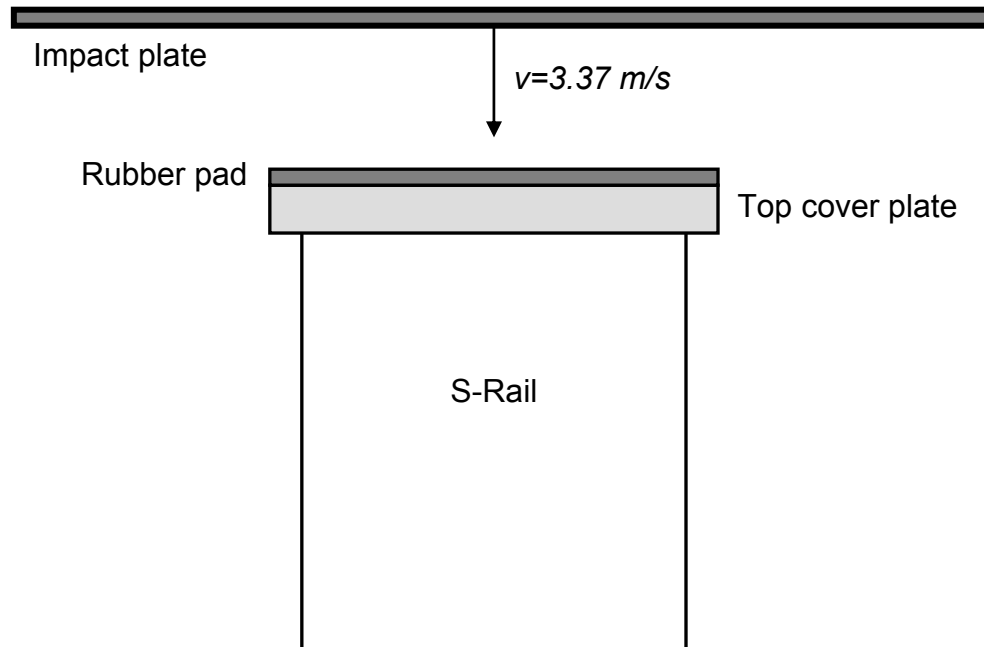


Figure D.8: Schematic of s-rail impact interface for the model considering a rubber damper.

Table D.2: Material properties and parameters utilized within the Ogden linear viscoelastic formulation within LS-DYNA [30,31] that was used to represent the rubber pad within the simulation prediction. Parameters provided by Cronin [145].

Density	1500 x10-6 (g/mm ³)
Poisson's ratio	0.497
Order of fit	0
Number of terms in fit	1
μ_1	1.72
α	6.73

The predicted force-time response of the model that considers a rubber pad at the interface is given in Figure D.9. Consideration of the rubber pad results in a predicted force-time response that is significantly different in terms of amplitude and frequency to the model that does not consider a damper or top cover plate. Note that the high frequency oscillations in the predicted force response that considers the rubber pad is a consequence of the contact algorithm and stiffness between the two materials. Consideration of the rubber pad in the

model reduced the peak load from 91 kN to 67 kN, which is close to the 65 kN found in the filtered force-time response from Section 6.2.2. Also note that the predicted peak load occurs later in time for the model considering the rubber pad. Consideration of the rubber pad is important for any study aimed at accurately predicting the peak load in s-rail crash.

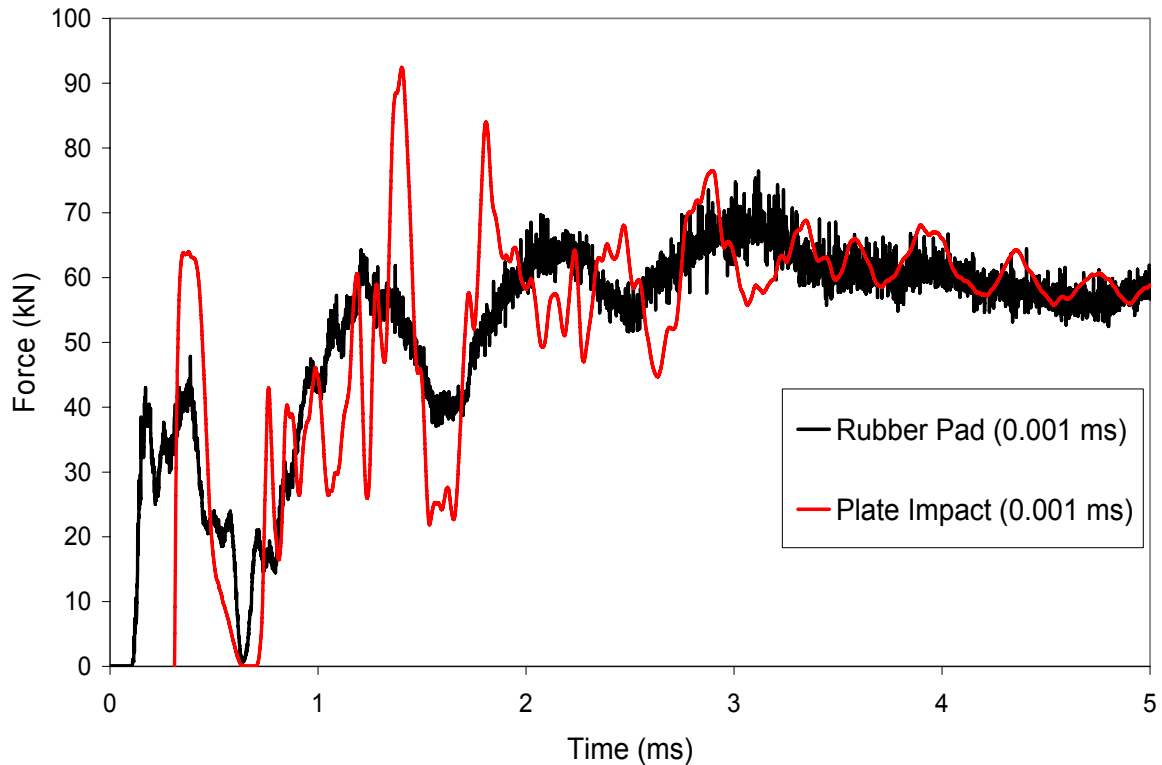


Figure D.9: Predicted force versus time response with and without a rubber pad at impact interface. The output interval of the data is shown within brackets within the legend.

D.3.3 Forming History Effects

As shown in Section 6.2.2, consideration of forming history effects is important to better predict s-rail force response due to crash. The effect of considering residual stress, work hardening and thickness changes on the predicted force-time response in the time that stress wave propagation effects are significant is shown in Figure D.10. Within the first peak of force, the predicted force response is independent of the previous forming history effects, which is expected since the initial stress wave propagates elastically within the s-rail. Consideration of thickness changes and residual stresses did not significantly change the predicted force response of the s-rail, however, work hardening effects resulted in a considerable increase in the predicted force levels. The increased force response prediction,

when considering work hardening effects, is due to the higher material strength due to forming, which stiffens the s-rail.

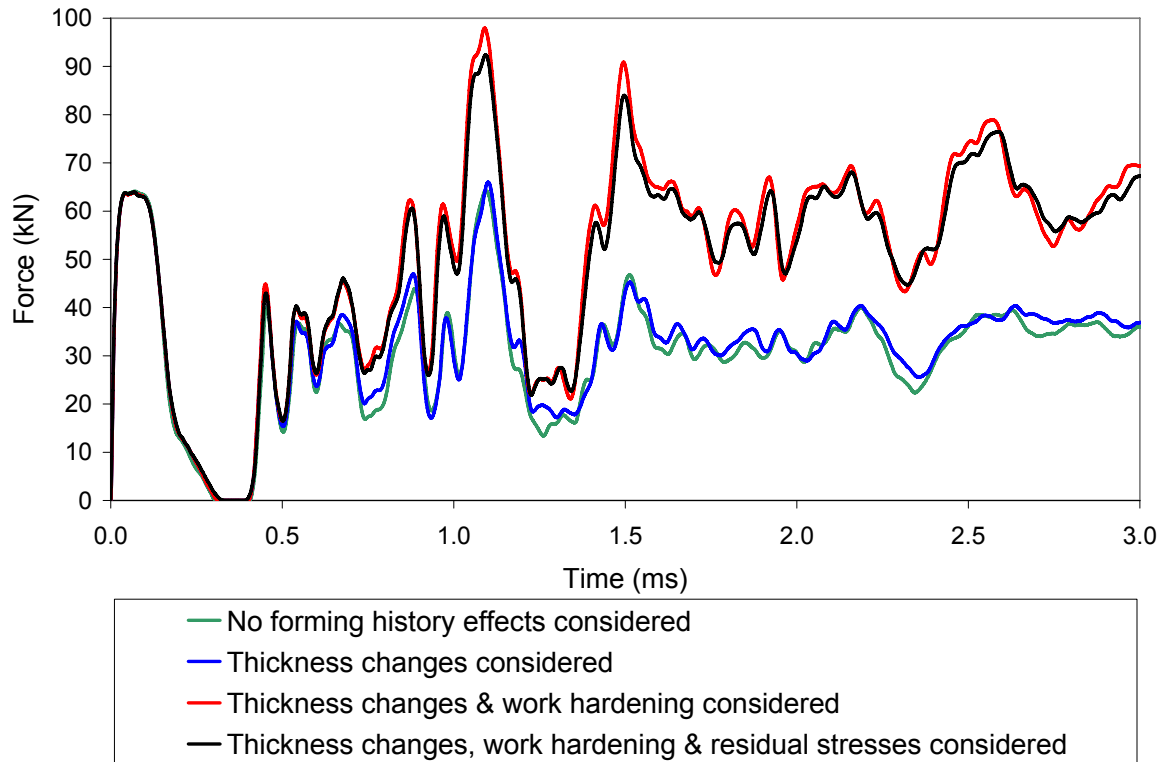


Figure D.10: Predicted force-time response of s-rail considering various forming history effects.

D.4 Summary and Discussion

Stress wave propagation effects influence the force-time response of the s-rail only within the first 5 ms in time since the stress waves dissipate rapidly due to the large number of reflections from the various boundaries. After this initial period, the s-rail can be described as being in a state of dynamic equilibrium.

The force-time response over the first two oscillations is governed by the geometry of the s-rail and very little by forming history effects. Beyond this point, the forming history effects, particularly work hardening, play a significant role in the prediction of force-time response. Accurately tracking the stress wave propagation throughout the s-rail beyond the first two oscillations is very challenging. The complexity arises due to the varying geometric and material impedances resulting from the changes in curvature and thickness at the bends of the s-rail during collapse, as well as the different levels of work hardening. With such a

high number of boundaries for reflecting and transmitting stress waves in the s-rail, it becomes quite difficult to post-process the magnitude and direction of the stress waves predicted by the finite element model developed in this work.

Any model that attempts to accurately predict the oscillatory force-time response in order to capture the measured peak load must consider previous forming history effects and the damping components used to reduce ringing in the system. It is recommended here that to better capture the stress wave propagation effects that occur in the experiment and influence the peak load, the entire test should set-up be carefully modeled. For instance, the assumption of a fixed base is not representative of the experiment since some wave transmission will occur through the top and bottom load cell plates (Figure 2.15) via the load cells. Although most of the waves would be reflected due to the large impedance of the steel plates, there is some elasticity to the entire s-rail fixture due to the mating tolerances of the many interacting components. Accurately representing this complex interaction of components within a finite element model remains a serious challenge.

The largest predicted force experienced by the impact plate occurs at the third peak in the force-time response of the s-rail and is much greater than the measured value from the experiments. Without unfiltered data from the experiment it is not possible to validate the prediction of peak load in the model that considers the rubber pad. The higher predicted peak load in the crash model that does not consider the damper is a consequence of not accounting for the rubber pad which dampens the oscillations in force. The effect of the not considering the damping element in the models prediction of force-time response is compensated by the 1 kHz Butterworth filter.

Appendix E: Numerical Investigations into the Variables Governing the Characteristics and Crash Response of S-Rails

E.1 Effect of S-Rail Cross-Section

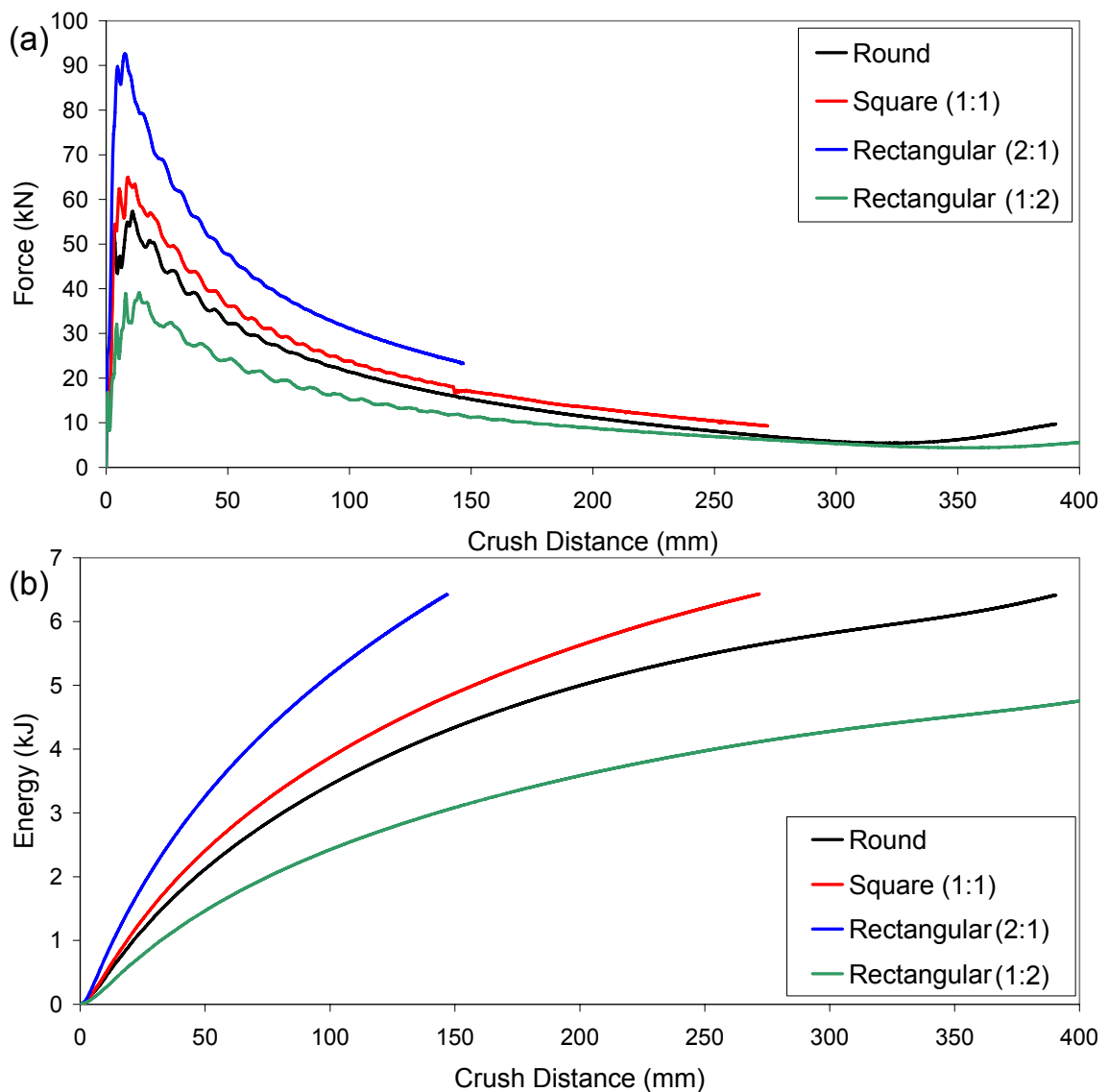


Figure E.1: (a) Peak load; and (b) energy absorbed for the s-rails with varying cross-sections examined considering forming history.

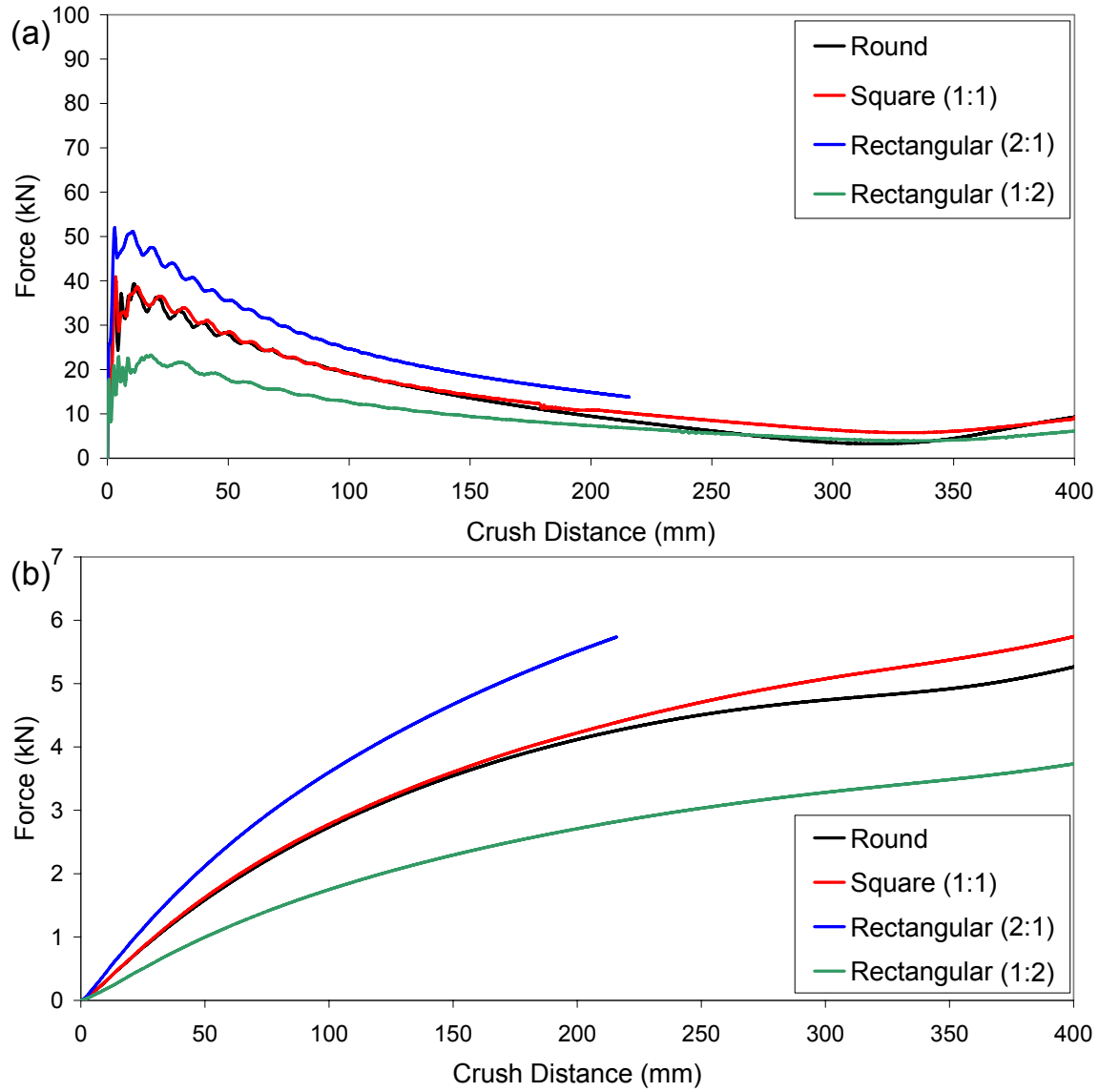


Figure E.2: (a) Peak load; and (b) energy absorbed for the s-rails with varying cross-sections examined not considering forming history.

E.2 Forming History

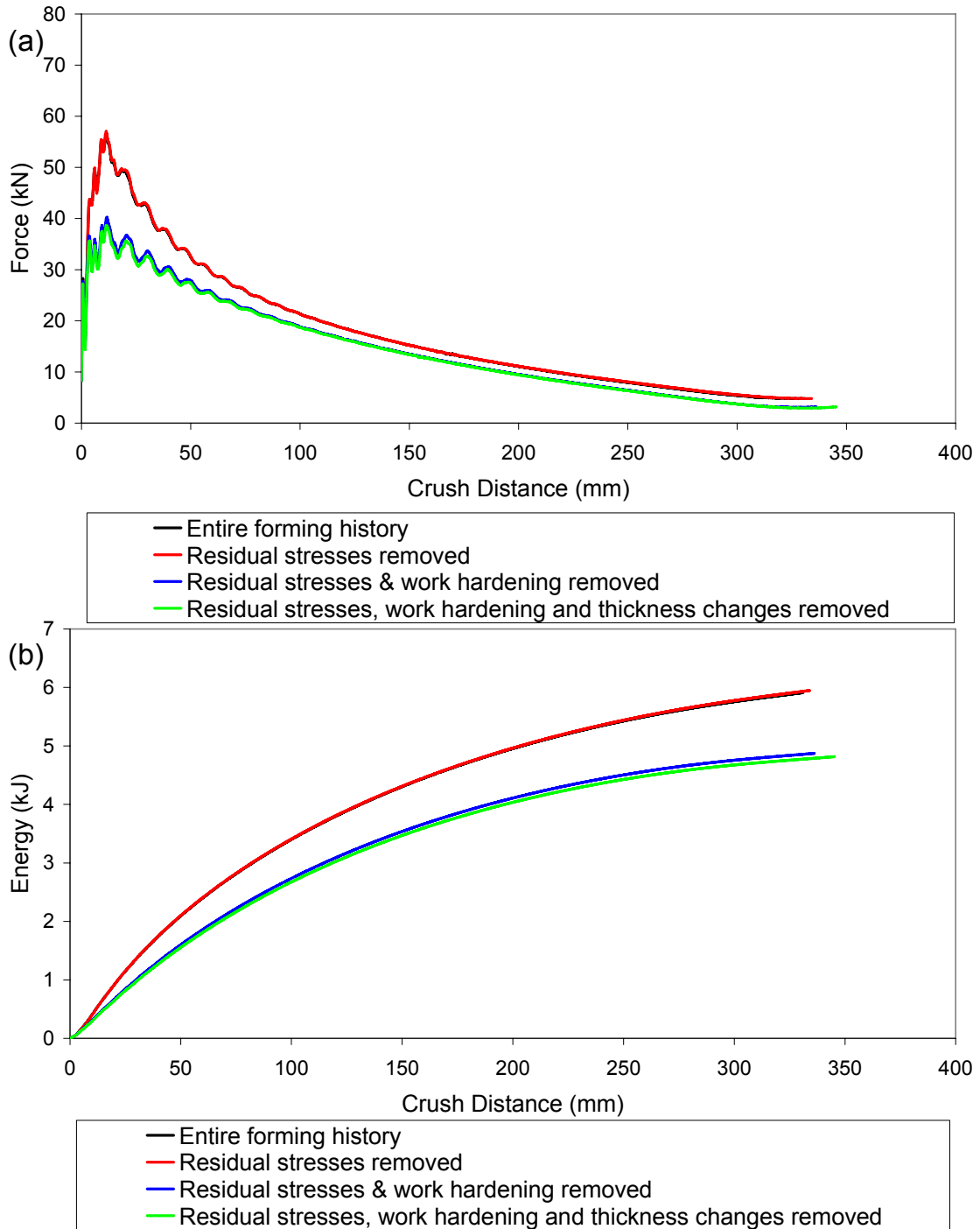


Figure E.3: Predicted (a) force; and (b) energy versus crush distance for non-hydroformed s-rails with (i) entire forming history considered; (ii) residual stresses removed; (iii) residual stresses and work hardening removed; and, (iv) residual stresses, work hardening and thickness changes removed.

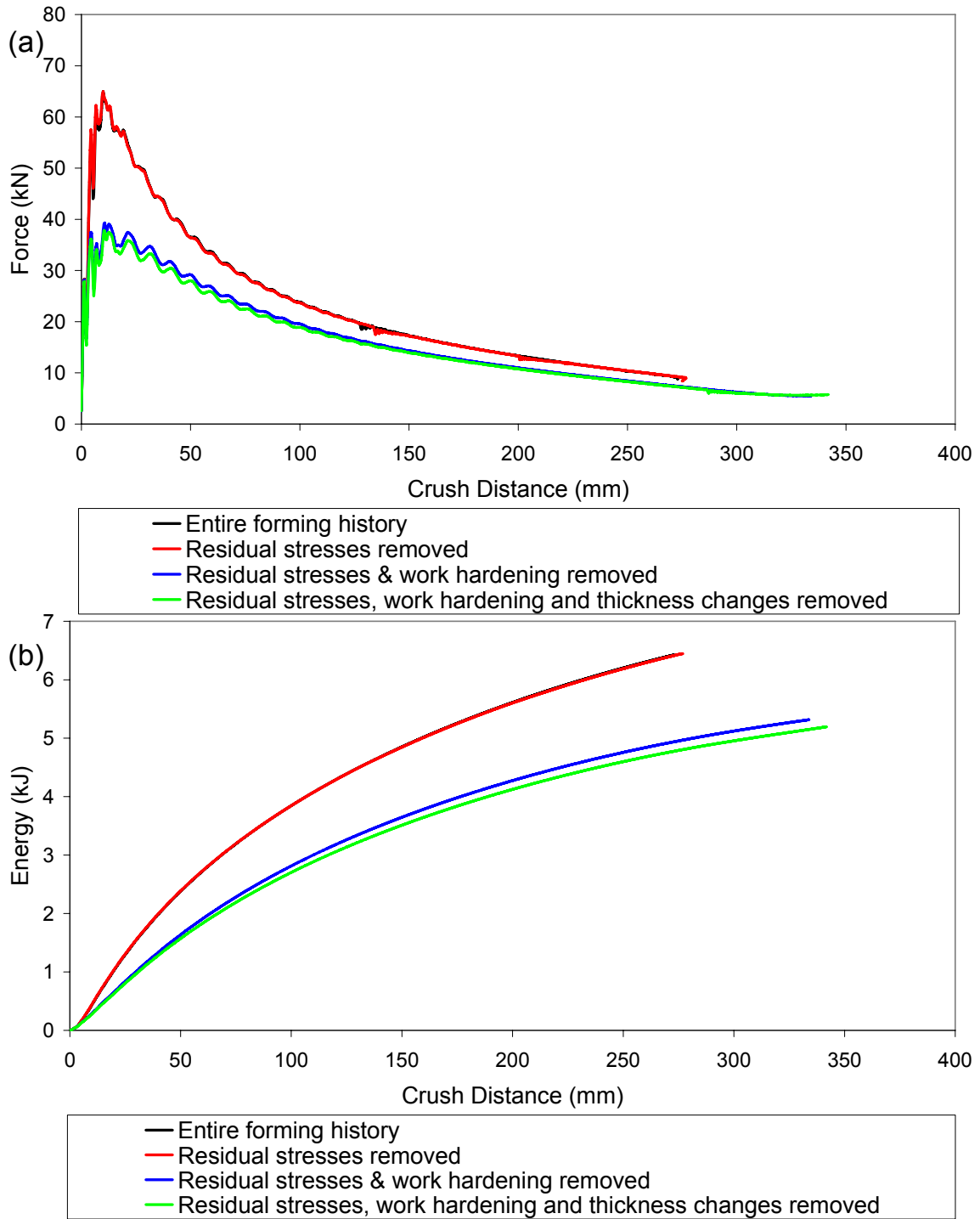


Figure E.4: Predicted (a) force; and (b) energy versus crush distance for hydroformed s-rails with (i) entire forming history considered; (ii) residual stresses removed; (iii) residual stresses and work hardening removed; and, (iv) residual stresses, work hardening and thickness changes removed.

E.3 Effect of the Hydroforming Process on the Characteristics and Crash Response of Hydroformed S-Rails

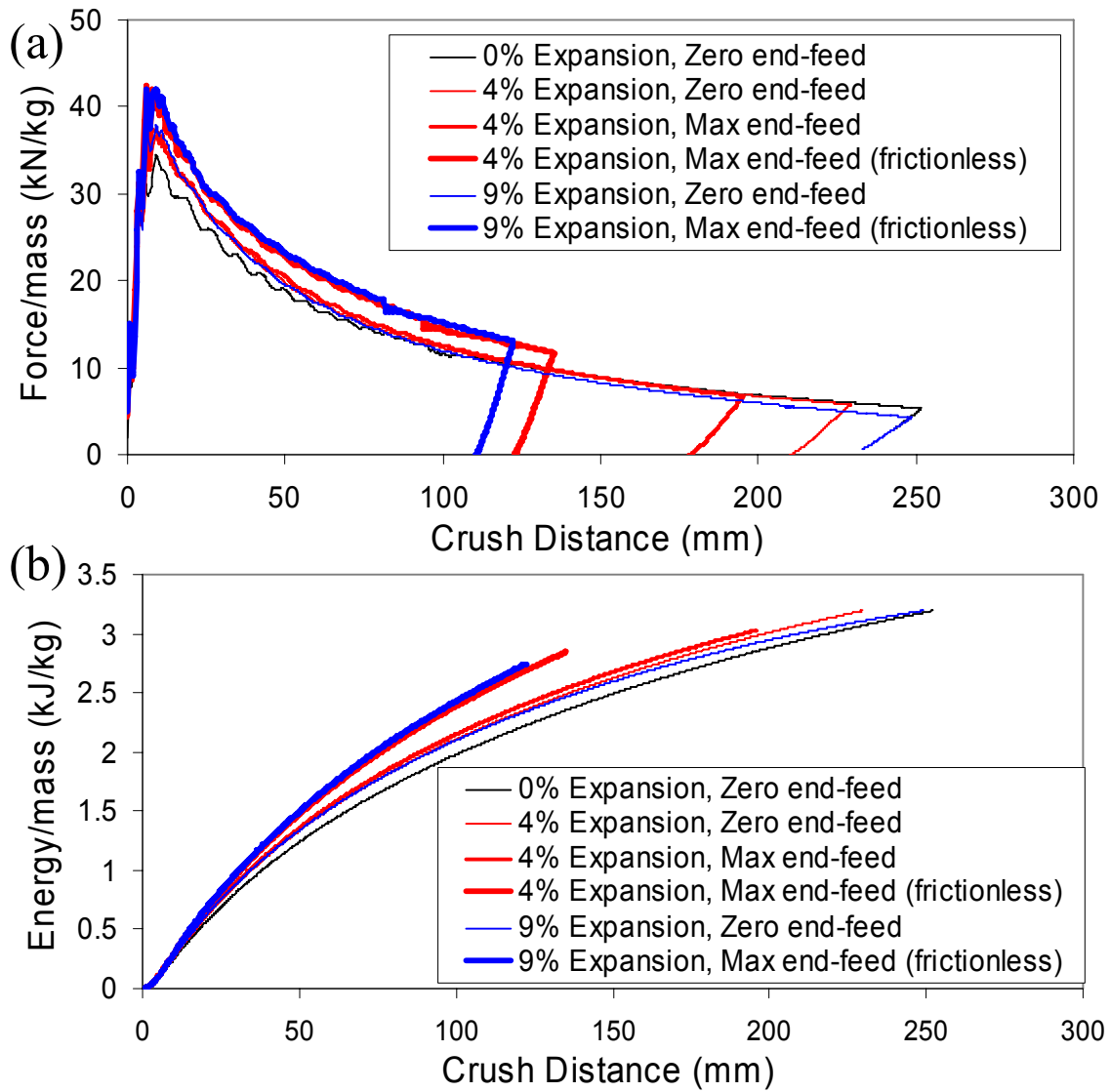


Figure E.5: Predicted (a) force; and (b) energy per unit mass versus crush distance for hydroformed s-rails: (i) zero-percent expansion and zero end-feed; (ii) four-percent expansion and zero end-feed; (iii) four-percent expansion with 30 mm of end-feed; (iv) four-percent expansion with a frictionless condition and 80 mm of end-feed; (v) nine-percent expansion with zero end-feed; and (vi) nine-percent expansion with a frictionless condition and 100 mm of end-feed.